

Characterization of Minerals, Metals, and Materials 2022

EDITED BY

Mingming Zhang

Jian Li

Bowen Li

Sergio Neves Monteiro

Shadia Ikhmayies

Yunus Eren Kalay

Jiann-Yang Hwang

Juan P. Escobedo-Diaz

John S. Carpenter

Andrew D. Brown

Rajiv Soman

Zhiwei Peng

TMS



Springer

The Minerals, Metals & Materials Series

Mingming Zhang · Jian Li · Bowen Li ·
Sergio Neves Monteiro · Shadia Ikhmayies ·
Yunus Eren Kalay · Jiann-Yang Hwang ·
Juan P. Escobedo-Diaz · John S. Carpenter ·
Andrew D. Brown · Rajiv Soman · Zhiwei Peng
Editors

Characterization of Minerals, Metals, and Materials 2022

TMS

 Springer

Editors

Mingming Zhang
Wood Mackenzie
Chicago, IL, USA

Jian Li
CanmetMATERIALS
Hamilton, ON, Canada

Bowen Li
Michigan Technological University
Houghton, MI, USA

Sergio Neves Monteiro
Military Institute of Engineering
Rio De Janeiro, Brazil

Shadia Ikhmayies
Amman, Jordan

Yunus Eren Kalay
Middle East Technical University
Ankara, Turkey

Jiann-Yang Hwang
Michigan Technological University
Houghton, MI, USA

Juan P. Escobedo-Diaz
University of New South Wales
Canberra, ACT, Australia

John S. Carpenter
Los Alamos National Laboratory
Los Alamos, NM, USA

Andrew D. Brown
United States Army Research Laboratory
Abingdon, MD, USA

Rajiv Soman
Eurofins EAG, Materials Science, LLC
Liverpool, NY, USA

Zhiwei Peng
Central South University
Changsha, China

ISSN 2367-1181

ISSN 2367-1696 (electronic)

The Minerals, Metals & Materials Series

ISBN 978-3-030-92372-3

ISBN 978-3-030-92373-0 (eBook)

<https://doi.org/10.1007/978-3-030-92373-0>

© The Minerals, Metals & Materials Society 2022

This work is subject to copyright. All rights are solely and exclusively licensed by the Publisher, whether the whole or part of the material is concerned, specifically the rights of translation, reprinting, reuse of illustrations, recitation, broadcasting, reproduction on microfilms or in any other physical way, and transmission or information storage and retrieval, electronic adaptation, computer software, or by similar or dissimilar methodology now known or hereafter developed.

The use of general descriptive names, registered names, trademarks, service marks, etc. in this publication does not imply, even in the absence of a specific statement, that such names are exempt from the relevant protective laws and regulations and therefore free for general use.

The publisher, the authors and the editors are safe to assume that the advice and information in this book are believed to be true and accurate at the date of publication. Neither the publisher nor the authors or the editors give a warranty, expressed or implied, with respect to the material contained herein or for any errors or omissions that may have been made. The publisher remains neutral with regard to jurisdictional claims in published maps and institutional affiliations.

Cover illustration: From Chapter “Surface Modification of Jamesonite During Flotation; Effect of the Presence of Ferric Ion”, M. R. Pérez et al., Figure 3: SEM, EDS, and elemental mapping image of jamesonite ore. https://doi.org/10.1007/978-3-030-92373-0_42.

This Springer imprint is published by the registered company Springer Nature Switzerland AG
The registered company address is: Gewerbestrasse 11, 6330 Cham, Switzerland

Preface

Materials characterization is a vital part in all science and engineering practice, as it is a fundamental process to achieve a good understanding of the processing-microstructure-property relationship. Various advances in characterization techniques and instruments in recent years have contributed, in a significant way, to an in-depth understanding of materials properties and structure on different scales. This enhanced understanding has also made profound impacts on process efficiency of existing industrial processes, and the ways of minerals, metals, and materials application in many fields.

This year, the Characterization of Minerals, Metals, and Materials symposium received 126 abstract submissions, of which 46 papers were accepted in 8 technical sessions. This symposium is among one of the largest in the TMS Annual Meeting & Exhibition. The proceedings volume includes state-of-art techniques used in modern minerals, metals, and materials characterization, and the latest research in the field of materials engineering and technologies. This proceedings publication is a valuable reference for academia scholars and industry professionals who are interested in advanced characterization methods and instrumentations that cover a wide range of research subjects. Readers will enjoy the diversity of topics in this book with innovative approaches to process and characterize materials at various scales and levels.

The Characterization of Minerals, Metals, and Materials 2022 symposium is sponsored by the Materials Characterization Committee under the Extraction & Processing Division (EPD) of TMS. The main focuses of this symposium include, but are not limited to, advanced characterization of extraction and processing of minerals, process-microstructure-property relation of metal alloys, ceramics, polymers, and composites. New characterization methods, techniques, and instrumentations are also emphasized.

As a lead organizer of this symposium, I would like to take this opportunity to express my sincere gratitude to all authors for their contribution and generosity to share their research work. On behalf of the organizing committee, I would like to thank TMS for providing us the valuable opportunity to publish this stand-alone

proceedings volume. Much appreciation is also extended to the EPD for sponsoring this symposium.

Most importantly, the success of this proceedings publication would not be possible without the fabulous contribution and support from all members of the Materials Characterization Committee. I also would like to thank our publisher, Springer, for their timely and quality publication of this book.

Mingming Zhang
Lead Organizer

Contents

Part I Advanced Microstructural Characterization Methods

Challenges Concerning the Characterization of Cementite in Low Carbon Steel Using Electron Backscatter Diffraction	3
M. K. O'Brien, S. K. Lawrence, and K. O. Findley	

Part II Characterization of Mechanical Properties

Strength and Failure Characterization of the Gibeon (IVA) Iron Meteorite	17
M. Fazle Rabbi, Khaled H. Khafagy, Laurence A. J. Garvie, Erik Asphaug, Desireé Cotto-Figueroa, and Aditi Chattopadhyay	
Effect of Equal-Channel Angular Pressing and Targeted Heat Treatment on Aluminum AA7075 Sheet Metal	25
Maximilian Gruber, Thomas Spoerer, Christian Illgen, Philipp Frint, Martin F.-X. Wagner, Philipp Lechner, and Wolfram Volk	

Part III Characterization of Polymers, Composites, Coatings and Ceramics

Application of Flue Gas Desulfurization Waste for the Production of Geopolymer Tiles	39
M. T. Marvila, A. R. G. Azevedo, F. D. Gama, E. B. Zanelato, S. N. Monteiro, and C. M. F. Vieira	
Lowering the Presence of Heavy Metals in Textured Coat Using Recycled Post Consumer Glass	47
A. O. Adejo, A. D. Garkida, C. M. Gonah, and E. V. Opoku	

Microstructural Characterisation of AA5083 in AA5083/SiC Co-Continuous Ceramic Composites (C4) Fabricated by Gravity and Gas Pressure Infiltration	57
Georgia Warren, Jianshen Wang, Krishna Shankar, V. Krishnaraj, A. S. Prasanth, R. Ramesh, and Juan Pablo Escobedo-Diaz	
Part IV Metallurgical Processing Analysis and Characterization	
Study on the Degradation Behavior of Organic Humic Acid from the Wastewater by Refractory High-Titanium Slag After Metallurgical Transformation	71
Yubi Wang, Shengpeng Su, Bingbing Liu, Guihong Han, and Yanfang Huang	
Adsorption of Iron, Copper, Lead, Chromium, and Cadmium in Cobalt Sulfate Solution by Goethite	81
Sujun Lu, Jiang Cao, Yuanyuan Li, Guoju Chen, Jesika, and Guanwen Luo	
Study on Efficient Burdening for Preparation of Fused Calcium Magnesium Phosphate Fertilizer from Low-Grade Phosphate Ores	91
Tingting Wang, Luyi Li, Cuihong Hou, Haobin Wang, Shouyu Gu, and Jie Wang	
Characterization of Nano-crystalline Metallurgical-Grade Silicon Prepared from Rice Husk Ash	101
B. O. Ayomanor, C. Iyen, I. S. Iyen, V. Mbah, D. I. Anyaogu, D. N. Dawuk, S. D. Ndiriza, S. O. Aniko, and M. Omonokhua	
Separation of Nickel and Cobalt from Nickel and Cobalt Solution by Cyanex272	113
Ganggang Yan, Zibiao Wang, Dinghao Le, Xijun Zhang, Xintao Sun, and Dalin Chen	
Low-Temperature Preparation and Mechanism Study of Vanadium Nitride	123
Yongjie Liu, Qingqing Hu, Donglai Ma, Yue Wang, and Zhixiong You	
Part V Mineralogical Analysis and Process Improvement	
Leaching Cobalt from a Nickel-Containing Copper-Cobalt Zebesha Ore	135
Foibe D. L. Uahengo, Yotamu R. S. Hara, Rainford Hara, Nachikonde Fumpa, Alexander Old, and Golden Kaluba	
Interaction Between Iron Ore and Magnesium Additives During Pellet Roasting Process	143
Lian-Da Zhao, Hong-Su, Qing-Guo Xue, and Jing-Song Wang	

Chemical Analysis of Mineral Surfaces Using Digital Image Processing	155
Juan C. González-Islas, Abdon R. Aparicio-Durán, Gildardo Godfnez-Garrido, Karime A. González-García, and Mizraim U. Flores-Guerrero	
Degradation of Structure and Properties of Coke in Blast Furnace: Effect of High-Temperature Heat Treatment	163
Jingbo Chen, Wei Ren, Yan Guo, and Shengfu Zhang	
Coking Coal Macromolecular Structural Characteristic and Its Correlations with the Compressive Strength of CaO-Containing Carbon Pellets	177
Xiaomin You, Xuefeng She, Jingsong Wang, and Qingguo Xue	
Part VI Poster Session	
An Investigation of the Relationship Between Raw Coal Caking Characteristics and Its Petrographic Properties	195
Yucen Kuang, Wei Ren, Lechi Zhang, and Shengfu Zhang	
Application of Grinding, Pyrometallurgical Pretreatment, and Silver Leaching of Mineral Tailings from the State of Morelos, Mexico	207
Jesús Iván Martínez Soto, Aislinn M. Teja-Ruiz, Martin Reyes-Perez, Miguel Pérez-Labra, Víctor Esteban Reyes-Cruz, José A. Cobos-Murcía, Gustavo Urbano-Reyes, and Julio Cesar Juárez-Tapia	
Application of Subnanosecond-Pulsed Dielectric Barrier Discharge in Air to Structural and Technological Properties Modification of Natural Minerals	219
Igor Zh. Bunin, Natalia E. Anashkina, Irina A. Khabarova, and Maria V. Ryazantseva	
Characterization and Stain Analysis in Natural and Artificial Rocks ...	229
M. G. S. Freitas, E. D. F. Castilho, A. R. G. Azevedo, J. A. T. Linhares júnior, M. T. Marvila, and S. N. Monteiro	
Characterization of Blast Furnace Slag for Preparing Activated Alkali Cements	239
M. T. Marvila, A. R. G. Azevedo, E. B. Zanelato, S. N. Monteiro, and C. M. F. Vieira	
Characterization of Mortar in Fresh State with the Addition of Açai Fiber	247
A. R. G. Azevedo, D. L. Rocha, T. E. S. Lima, M. T. Marvila, E. B. Zanelato, J. Alexandre, S. N. Monteiro, and H. Colorado	

Characterization of Slag and Growth of Ferronickel Grains During Smelting of Nickel Laterite Ore	257
Donglai Ma, Jianbo Zhao, Hanghang Zhou, and Zhixiong You	
Characterization of Soil from Areas Degraded by Mining Activity in Campos Dos Goytacazes-RJ, Brazil	267
A. R. G. Azevedo, J. G. F. Brainer, M. T. Marvila, G. C. Xavier, and S. N. Monteiro	
Comparative Study of Staining Resistance for Polished and Resined Silicatic Ornamental Rocks	277
S. Rocha, E. D. F. Castilho, A. R. G. Azevedo, L. R. Cruz, M. T. Marvila, and S. N. Monteiro	
Comparative Study of the Flexural Strength of Rock Materials for Applications in Civil Construction	287
L. M. Campos, E. D. F. Castilho, A. R. G. Azevedo, T. R. Silva, M. T. Marvila, E. B. Zanelato, and S. N. Monteiro	
Comparison of Ceramic Blocks Incorporated with Ornamental Rock Waste in Hoffman and Caieira Furnace	295
E. B. Zanelato, A. R. G. Azevedo, M. T. Marvila, J. Alexandre, and S. N. Monteiro	
Cooling Rate and Roughness Dependence of the Undercooling for One Single Sn Droplet with Si Thin Film Substrate by Nanocalorimetry	305
Shun Li, Li Zhang, Bingge Zhao, Kai Ding, and Yulai Gao	
Determination of Strength to the Hard Body Impact of Raw, Resinate, and Screened Ornamental Rocks	315
A. C. Hilário, E. D. F. Castilho, A. R. G. Azevedo, T. E. S. Lima, M. T. Marvila, and S. N. Monteiro	
Development of Metakaolin-Based Geopolymer Mortar and the Flue Gas Desulfurization (FGD) Waste	323
L. B. Oliveira, A. R. G. Azevedo, M. T. Marvila, C. M. Vieira, N. A. Cerqueira, and S. N. Monteiro	
Effects of Natural Aging on Figue Fabric-Reinforced Epoxy Composites: An Analysis by Charpy Impact Energy	333
Michelle Souza Oliveira, Fernanda Santos da Luz, Artur Campos Pereira, Fabio da Costa Garcia Filho, Noan Tonini Simonassi, Lucio Fabio Cassiano Nascimento, and Sergio Neves Monteiro	
Evaluation of Recyclable Thermoplastics for the Manufacturing of Wind Turbines Blades H-Darrieus	341
Andres F. Olivera, Edwin Chica, and Henry A. Colorado	

Evaluation of the Rheology of Mortars with Incorporation of Ornamental Stone Waste	349
E. B. Zanelato, A. R. G. Azevedo, M. T. Marvila, J. Alexandre, and S. N. Monteiro	
Fundamental Study on Wettability of Pure Metal Using a Low Melting Temperature Alloy: A Theoretical Approach	359
Jun-ichi Saito, Yohei Kobayashi, and Hideo Shibutani	
Influence of pH Regulating Additives on the Performance of Granite Waste-Based Paints	369
Márcia Maria Salgado Lopes, Leonardo Gonçalves Pedroti, Hellen Regina de Carvalho Veloso Moura, José Maria Franco de Carvalho, José Carlos Lopes Ribeiro, and Gustavo Henrique Nalon	
Influence of the Sand Content on the Physical and Mechanical Properties of Metakaolin-Based Geopolymer Mortars	381
Igor Klaus R. Andrade, Beatryz C. Mendes, Leonardo G. Pedroti, Carlos M. F. Vieira, and J. M. Franco de Carvalho	
Mechanical and Microstructural Evaluation of Eco-Friendly Geopolymer Produced from Chamotte and Waste Glass	391
Beatryz Mendes, Leonardo Pedroti, José Maria Carvalho, Carlos Maurício Vieira, Igor Klaus Andrade, and Pedro Henrique Drumond	
Recycling Glass Packaging into Ceramic Bricks	403
G. C. G. Delaqua and C. M. F. Vieira	
Study of the Collectorless Flotation Behavior of Galena in the Presence of Ferric Ion	411
Martín Reyes Pérez, Jimena Detzamin Trejo Martínez, Elia Palacios Beas, Iván A. Reyes Domínguez, Mizraim U. Flores Guerrero, Aislinn Michelle Teja Ruiz, Miguel Pérez Labra, Julio Cesar Juárez Tapia, and Francisco Raúl Barrientos Hernández	
Study of the Determination of Hardbody Impact Resistance of Screened and Non-screened Ornamental Rocks of Different Thicknesses	421
M. F. Braga, E. D. F. Castilho, A. R. G. Azevedo, A. S. A. Cruz, M. T. Marvila, and S. N. Monteiro	

Surface Modification of Jamesonite During Flotation; Effect of the Presence of Ferric Ion	431
Martín Reyes Pérez, Jazmin Terrazas Medina, Elia Palacios Beas, Iván. A. Reyes Domínguez, Mizraim U. Flores Guerrero, Aislinn Michelle Teja Ruiz, Miguel Pérez Labra, Julio Cesar Juárez Tapia, and Francisco Raúl Barrientos Hernández	
Synthesis and Electrical and Magnetic Characterization of Electroceramics Type $Ba_{1-x}Eu_xTi_{1-x/4}O_3$ ($x = 0.001$ and $x = 0.005\%$ by Weight Eu^{3+})	443
J. P. Hernández-Lara, M. Pérez-Labra, A. Hernández-Ramírez, J. A. Romero-Serrano, F. R. Barrientos-Hernández, J. C. Juárez-Tapia, M. Reyes-Pérez, and V. E. Reyes-Cruz	
The Collectorless Flotation of Pyrrargyrite, Surface Analysis via FTIR	453
Martín Reyes Pérez, Zaida Peralta García, Elia Palacios Beas, Iván. A. Reyes Domínguez, Mizraim U. Flores Guerrero, Aislinn Michelle Teja Ruiz, Miguel Pérez Labra, Julio Cesar Juárez Tapia, and Francisco Raúl Barrientos Hernández	
The Elastic Constants Measurement in a Medical Ti-6Al-4V ELI Alloy by Using Ultrasonic Means	463
Hector Carreon and Maria Carreon-Garcidueñas	
Use of Glass Waste as a Geopolymerization Reaction Activator for Ceramic Materials	473
A. R. G. Azevedo, M. T. Marvila, L. B. Oliveira, D. Cecchin, P. R. Matos, G. C. Xavier, C. M. Vieira, and S. N. Monteiro	
Author Index	481
Subject Index	485

About the Editors



Mingming Zhang is currently a principal consultant at Wood Mackenzie. He has more than 15 years of experience in the field of mining, mineral processing, smelting and refining, and materials engineering. Before joining Wood Mackenzie, Dr. Zhang held lead engineer position at ArcelorMittal Global R&D in East Chicago, Indiana. He obtained his Ph.D. in Metallurgical Engineering from The University of Alabama and his master's degree in Mineral Processing from the General Research Institute for Non-ferrous Metals in China. Prior to joining ArcelorMittal, he worked with Nucor Steel in Tuscaloosa, Alabama where he was a metallurgical engineer leading the development of models for simulating slab solidification and secondary cooling process. Dr. Zhang has conducted a number of research projects involving mineral beneficiation, thermodynamics and kinetics of metallurgical reactions, electrochemical processing of light metals, metal recycling, and energy-efficient and environmentally cleaner technologies. He has published more than 50 peer-reviewed research papers and he is the recipient of several U.S. patents. Dr. Zhang also serves as editor and reviewer for a number of prestigious journals including *Metallurgical and Materials Transactions A and B*, *JOM*, *Journal of Phase Equilibria and Diffusion*, and *Mineral Processing and Extractive Metallurgy Review*. Dr. Zhang has made more than 30 research presentations at national and international conferences including more than 10 keynote presentations. He was the recipient of the 2015 TMS Young Leaders Professional Development Award. He has served as conference/symposium

organizer and technical committee chair in several international professional organizations including The Minerals, Metals & Materials Society (TMS), the Association for Iron & Steel Technology (AIST), and the Society for Mining Metallurgy & Exploration (SME).



Jian Li is a senior research scientist and program manager at CanmetMATERIALS in Natural Resources Canada. He obtained his B.Sc. in Mechanical Engineering from Beijing Polytechnique University, M.Sc. in Metallurgical Engineering from the Technical University of Nova Scotia, and Ph.D. in Materials and Metallurgical Engineering from Queen's University, Kingston, Ontario, Canada. He has broad experience in materials processing and characterization including alloys deformation, recrystallization, and micro-texture development. Dr. Li has extensive experience in Focused Ion Beam (FIB) microscope techniques. He is also an expert in various aspects of SEM-EDS and EPMA techniques. Dr. Li has authored three book chapters and published more than 160 papers in scientific journal and conference proceedings.



Bowen Li is a research professor in the Department of Materials Science and Engineering and Institute of Materials Processing at Michigan Technological University. His research interests include materials characterization and analysis, metals extraction, ceramic process, antimicrobial additives and surface treatment, porous materials, applied mineralogy, and solid waste reuse. He has published more than 140 technical papers in peer-reviewed journals and conference proceedings, authored/co-authored 3 books, and edited/co-edited 12 books. He also holds 16 patents and has delivered more than 30 invited technical talks.

Dr. Li received a Ph.D. degree in Mineralogy and Petrology from China University of Geosciences Beijing in 1998 and a Ph.D. degree in Materials Science and Engineering from Michigan Technological University in 2008. He has been an active member in The Minerals, Metals & Materials Society (TMS), Society for Mining, Metallurgy & Exploration (SME), and China Ceramic Society. At TMS, he has served as the chair of the Materials Characterization Committee and as a member

of the Powder Materials Committee and the Biomaterials Committee. He has also served as an EPD Award committee member, a *JOM* subject advisor, and a key reader for *Metallurgical and Materials Transactions A*. He has been organizer/co-organizer of a number of international symposia and sessions. He also served as an editorial board member of the *Journal of Minerals and Materials Characterization and Engineering*, *Reviews on Advanced Materials Science*, and *FUTO Journal Series*.



Sergio Neves Monteiro graduated as a metallurgical engineer (1966) at the Federal University of Rio de Janeiro (UFRJ). He received his M.Sc. (1967) and Ph.D. (1972) from the University of Florida, followed by a 1975 course in energy at the Brazilian War College, and a postdoctorate (1976) at the University of Stuttgart. In 1968, he joined the Metallurgy Department of UFRJ as full professor of the postgraduation program in engineering (COPPE). He was elected as head of department (1978), coordinator of COPPE (1982), Under-Rector for Research (1983), and was invited as Under-Secretary of Science for the State of Rio de Janeiro (1985) and Under-Secretary of the College Education for the Federal Government (1989). He retired in 1993 from the UFRJ and joined the State University of North Rio de Janeiro (UENF), where he retired in 2012. He is now a professor at the Military Institute of Engineering (IME), Rio de Janeiro. Dr. Monteiro has published more than 1,900 articles in journals and conference proceedings and has been honored with several awards including the ASM Fellowship and several TMS awards. He is the top researcher (1A) of the Brazilian Council for Scientific and Technological Development (CNPq) and Emeritus Scientist of State of Rio de Janeiro (FAPERJ). He was president of the Superior Council of the State of Rio de Janeiro Research Foundation, FAPERJ (2012), and currently is coordinator of the Engineering Area of this foundation. He has also served as president of the Brazilian Association for Metallurgy, Materials and Mining (ABM, 2017–2019), as a consultant for the main Brazilian R&D agencies, and as a member of the editorial board of five international journals as well as associate editor-in-chief of the *Journal of Materials Research and Technology*. He is the author of 130

patents and a top world researcher in “Natural Fiber Composites” and “Ballistic Armor”, Scopus 2020.



Shadia Ikhmayies received a B.Sc. and M.Sc. from the physics department at the University of Jordan in 1983 and 1987, respectively, and a Ph.D. in producing CdS/CdTe thin film solar cells from the same university in 2002. Her research is focused on producing and characterizing semiconductor thin films and thin film CdS/CdTe solar cells. She also works in characterizing quartz in Jordan for the extraction of silicon for solar cells and characterizing different materials by computation. She has published 59 research papers in international scientific journals, 85 research papers in conference proceedings, and 3 chapters in books. She is the founder and editor of the eBook series *Advances in Material Research and Technology* published by Springer, and the editor-in-chief/editor of several books.

Dr. Ikhmayies is a member of The Minerals, Metals & Materials Society (TMS) where she was the chair of the TMS Materials Characterization Committee (2016–2017), and the leading organizer of three symposiums; Solar Cell Silicon 2017–2020, Mechanical Characteristics and Application Properties of Metals and Non-metals for Technology: An EPD Symposium in Honor of Donato Firrao, and Green Materials Engineering: An EPD Symposium in Honor of Sergio Monteiro. Dr. Ikhmayies is also a member of the World Renewable Energy Network/Congress (WREN/WREC) 2010–present. She is a member of the international organizing committee and the international scientific committee in the European Conference on Renewable Energy Systems (ECRES2015–ECRES2022). She is a guest editor and a member of the editorial board of several journals including *JOM* and the *Journal of Electronic Materials*. Dr. Ikhmayies is a reviewer of 24 international journals and several international conference proceedings. She has received several international awards including the TMS Frank Crossley Diversity Award 2018 and World Renewable Energy Congress 2018 Pioneering Award.



Yunus Eren Kalay is an associate professor in the Metallurgical and Materials Engineering Department and assistant to the president at Middle East Technical University (METU), Ankara, Turkey. Dr. Kalay received his Ph.D. degree with Research Excellence award from Iowa State University in 2009. His Ph.D. topic was related to the metallic glass formation in Al-based metallic alloy systems. Following his Ph.D., he pursued postdoctoral research at Ames National Laboratory. In 2011, Dr. Kalay joined the Department of Metallurgical and Materials Engineering (METE) of METU as an assistant professor and in 2014 he was promoted to associate professor. His research interests span microstructural evolution in metallic alloys, rapid solidification of metallic alloys, nanostructured and amorphous alloys, high-entropy alloys, electronic packaging, and advanced characterization techniques such as scanning and transmission electron microscopy, electron and X-ray spectroscopy, atom probe tomography, and synchrotron X-ray scattering. Dr. Kalay was awarded the METU Prof. Dr. Mustafa Parlar Foundation Research Incentive Award, which is a very prestigious award that recognizes young scientists in Turkey with exceptional achievements and research productivity. He is also an active member of the TMS Materials Characterization Committee and served on organizing committees of three international and one national congress including IMMC, MS&T, and TMS. Dr. Kalay has also been involved in many synergistic activities such as being founding editor of Turkey's first undergraduate research journal, *MATTER*, and organizing the Materials Science Camps for K-12 students.



Jiann-Yang Hwang is a professor in the Department of Materials Science and Engineering at Michigan Technological University. He is also the Chief Energy and Environment Advisor at the Wuhan Iron and Steel Group Company, a Fortune Global 500 company. He has been the editor-in-chief of the *Journal of Minerals and Materials Characterization and Engineering* since 2002. He has founded several enterprises in areas including water desalination and treatment equipment, microwave steel production, chemicals, fly ash processing, antimicrobial materials, and plating wastes treatment. Several universities have honored him as a guest professor, including

the Central South University, University of Science and Technology Beijing, Chongqing University, Kunming University of Science and Technology, and Hebei United University. Dr. Hwang received his B.S. from National Cheng Kung University in 1974, M.S. in 1980 and Ph.D. in 1982, both from Purdue University. He joined Michigan Technological University in 1984 and served as its Director of the Institute of Materials Processing from 1992 to 2011 and the Chair of Mining Engineering Department in 1995. He has been a TMS member since 1985. His research interests include the characterization and processing of materials and their applications. He has been actively involved in the areas of separation technologies, pyrometallurgy, microwaves, hydrogen storage, ceramics, recycling, water treatment, environmental protection, biomaterials, and energy and fuels. He has more than 28 patents and has published more than 200 papers. He has chaired the Materials Characterization Committee and the Pyrometallurgy Committee in TMS and has organized several symposia. He is the recipient of the TMS Technology Award and of Michigan Tech's Bhakta Rath Research Award.



Juan P. Escobedo-Diaz is a senior lecturer in the School of Engineering and Information Technology (SEIT) at UNSW Canberra. He obtained his doctoral degree in Mechanical Engineering at Washington State University. Prior to taking up this academic appointment, he held research positions at the Institute for Shock Physics at Los Alamos National Laboratory. His main research interests center on the dynamic behavior of materials under extreme conditions, in particular high pressure and high strain rate. His focus has been on investigating the effects of microstructural features on the dynamic fracture behavior of metals and metallic alloys. He has published primarily in the fields of shock physics and materials science. He has been a member of The Minerals, Metals & Materials Society (TMS) since 2011. During this time, he has co-organized more than five symposia at the Annual Meetings including the symposium on Characterization of Minerals, Metals, and Materials since 2014. He was awarded a 2014 SMD Young Leaders Professional Development Award.



John S. Carpenter is a scientist within the manufacturing and metallurgy division at Los Alamos National Laboratory. Dr. Carpenter received his Ph.D. in Materials Science and Engineering from The Ohio State University in 2010 after performing his undergraduate studies at Virginia Tech.

Dr. Carpenter's research focus is on enabling advanced manufacturing concepts through experiments employing novel processing techniques, advanced characterization, and small-scale mechanical testing. Currently, he is working on projects related to the qualification of additively manufactured components, development of new materials for high field magnets using severe plastic deformation, and using high energy X-rays to study phase transformations during solidification in MIG cladding. Throughout his career he has utilized many characterization techniques including neutron scattering, X-ray synchrotron, XCT, PED, TEM, EBSD, and SEM.

He has more than 60 journal publications, one book chapter, and 45 invited technical talks to his credit.

With regard to TMS service, Dr. Carpenter is a past chair for both the Materials Characterization and Advanced Characterization, Testing & Simulation Committees. He is current chair for the Joint Commission for *Metallurgical and Materials Transactions A* and the SMD representative on the Content Development and Dissemination Committee. He is also the Program Committee Representative for the MS&T Conference. He recently received the McKay-Helm Award from the American Welding Society and is the 2018 recipient of the Distinguished Mentor Award at Los Alamos National Laboratory.



Andrew D. Brown is a mechanical engineer at the U.S. Army Combat Capabilities Development Command (CCDC) Army Research Laboratory (ARL), Aberdeen Proving Grounds, Maryland, USA. He obtained his B.S. in Mechanical Engineering at North Carolina State University (2009) and his doctoral degree in Mechanical Engineering at Arizona State University (2015). He spent three years (2015–2018) at UNSW Canberra as a postdoctoral researcher where he oversaw the daily operations of the Impact Dynamics Laboratory, mentored undergraduate and graduate student research projects, and performed teaching duties. His research expertise is understanding microstructural effects on the mechanical performance and damage processes of materials subjected to high dynamic pressures (shock) and high strain rates. Since joining ARL in 2018 he has shifted focus to high-rate injury biomechanics research to improve injury outcome prediction and protect the U.S. Warfighter. He has been an active member of TMS since 2011; was a co-organizer for the symposium on Characterization of Minerals, Metals, and Materials in 2018; and has been the symposium's EPD Award Representative from 2017–present. Dr. Brown has published 41 peer-reviewed articles in the fields of mechanical engineering, materials science, and biomechanics.



Rajiv Soman is currently with Purity Survey Analysis, Materials Sciences Division at Eurofins EAG Laboratories, USA, where he is responsible for developing new strategic partnerships and R&D initiatives. Prior to his current responsibilities, he served as Director, Purity Survey, Eurofins EAG Laboratories. He has over 32 years of professional experience in analytical chemistry and materials sciences. He earned a doctorate in Analytical Chemistry from Northeastern University, Boston. He received his B.Sc. (Chemistry—*Principal*; Physics—*Subsidiary*) with Honors, from Bombay University, India, and M.Sc. in Applied Chemistry from the Faculty of Technology & Engineering, Maharaja Sayajirao University of Baroda, India. He commenced his professional career as an Advanced Analytical Chemist in the Engineering Materials Technology Laboratories of General Electric Aircraft Engines. Prior to joining EAG Laboratories, Dr. Soman served as Professor (Full) of Chemical Engineering, Chemistry,

and Chemical Technology, and served as a faculty member for 21 years. He also served as Department Head and Associate Dean. He has received numerous awards for excellence in teaching and twice has been listed in *Who's Who Among America's Teachers*.

Dr. Soman's research interests are in the areas of atomic and mass spectrometry, with an emphasis on trace element determination and chemical speciation in a wide range of complex sample matrices. He was an invited guest scientist at the prestigious research institute, Forschungszentrum Jülich, Germany, where he conducted research in elemental mass spectrometry. He has co-authored several peer reviewed publications in international journals and has made numerous presentations at national and international conferences. He holds two U.S. patents.

Dr. Soman has been a member of the Society for Applied Spectroscopy (SAS) and the American Chemical Society (ACS) since 1986 and has served in numerous leadership positions in the societies. He was an invited panel member for the American Chemical Society's National Initiative on *Preparing for the Workforce 2015*. He is also a member of ASM International, and TMS, where he serves as a member of the Materials Characterization Committee and as Chair of the Poster Awards Committee.



Zhiwei Peng is a professor in the School of Minerals Processing and Bioengineering at Central South University, China. He received his B.E. and M.S. degrees from Central South University in 2005 and 2008, respectively, and his Ph.D. degree in Materials Science and Engineering from Michigan Technological University, USA, in 2012. His research interests include dielectric characterization, ferrous metallurgy, microwave processing, comprehensive utilization of resources, waste valorization, powder agglomeration, low-carbon technology, process simulation, electromagnetic shielding, and synthesis of functional materials.

Dr. Peng has published over 170 papers, including more than 120 peer-reviewed articles in journals such as *International Materials Reviews*; *Journal of Hazardous Materials*; *ACS Sustainable Chemistry & Engineering*; *Resources, Conservation & Recycling*; *Journal of Cleaner Production*; *Waste Management*; *Metallurgical and Materials Transactions A*; *Metallurgical and Materials Transactions B*; *JOM*; *Journal of*

Power Sources; Fuel Processing Technology; Energy & Fuels; IEEE Transactions on Magnetics; IEEE Transactions on Instrumentation and Measurement; Ceramics International; Powder Technology; and Separation and Purification Technology. He holds 56 Chinese patents and has served as an associate editor for *Mining, Metallurgy & Exploration*, as a guest editor for *JOM and Metals*, and as an editor for *PLOS ONE* and *Cogent Chemistry*. He has also been a member of editorial boards of *Scientific Reports*, *Journal of Central South University*, and *Journal of Iron and Steel Research International*, and has served as a reviewer for more than 70 journals.

Dr. Peng is an active member of The Minerals, Metals & Materials Society (TMS). He has co-organized 10 TMS symposia and co-chaired 24 symposia sessions since 2012. He is a member of the Pyrometallurgy Committee and the vice chair of the Materials Characterization Committee. He was a winner of the TMS EPD Young Leaders Professional Development Award in 2014 and the TMS EPD Materials Characterization Award Best Paper—1st Place in 2020.

Part I
Advanced Microstructural
Characterization Methods

Challenges Concerning the Characterization of Cementite in Low Carbon Steel Using Electron Backscatter Diffraction



M. K. O'Brien, S. K. Lawrence, and K. O. Findley

Abstract Understanding the location and morphology of cementite precipitation in steel has long been addressed almost exclusively with transmission electron microscopy, particularly in low carbon steels. However, scanning electron beam techniques such as electron backscatter diffraction (EBSD) could leverage automated diffraction pattern analysis and high scan rates to improve statistics in cementite analysis. This paper discusses challenges specific to EBSD through the lens of a case study concerning low carbon microalloyed pipeline steel. Correlations between secondary electron (SE) and EBSD micrographs of a low carbon, microalloyed steel etched with 2 pct nital could not effectively verify the presence of cementite identified using EBSD. Pixels identified as cementite by the EBSD software often held a $43.6^\circ \parallel \langle 100 \rangle$ axis/angle relationship reflected in grain boundary texture misorientation distributions. Further investigations of the ferrite/cementite interfaces displaying this $43.6^\circ \parallel \langle 100 \rangle$ relationship were undertaken by utilizing pole figures of three well-known orientation relationships (OR) between ferrite and cementite, which resulted in the best match with the Bagaryatskii OR. Some questions concerning interaction volumes and indexing/phase identification algorithms are presented with respect to cementite characterization, as well as a proposal for future work to consider possible pseudosymmetric phenomena in specific ferrite orientations.

Keywords EBSD · Cementite · Phase identification

Introduction

Low carbon, microalloyed steels are often used in applications where weldability is a concern. Strength is achieved using complex thermo-mechanical processing

M. K. O'Brien (✉) · S. K. Lawrence
Los Alamos National Laboratory, P.O. Box 1663, Los Alamos, NM 87545, USA
e-mail: mkobrien@lanl.gov

K. O. Findley
Colorado School of Mines, Golden, CO 80401, USA

© The Minerals, Metals & Materials Society 2022
M. Zhang et al. (eds.), *Characterization of Minerals, Metals, and Materials 2022*,
The Minerals, Metals & Materials Series,
https://doi.org/10.1007/978-3-030-92373-0_1

schemes. Microalloying elements such as niobium and vanadium are added with the intention of high temperature precipitation in austenite during rolling such that subsequent rolling at temperatures below the temperature for recrystallization results in grain refinement as the precipitates pin grain boundaries. Further strengthening can also be achieved by accelerated cooling upon completion of finish rolling, which can result in non-equiaxed ferrite with M/A constituents, also known as granular bainite.

There are several techniques that have traditionally been used to characterize the size and spatial distribution of cementite in low carbon steels. The predominant technique is transmission electron microscopy (TEM), utilizing diffraction, bright field, and dark field modalities. If the cementite precipitates in known orientation relationships with ferrite, a combination of diffraction and dark field techniques can be used to unequivocally identify cementite. However, due to the small sample size inherent in TEM samples, it is time consuming and difficult to obtain a statistically significant number of precipitates. Capitalizing on nital etchant response and secondary electron micrographs to provide larger sampling regions and thus a higher number of precipitates is another common technique of cementite characterization, but this technique suffers from both resolution limits and ambiguity regarding the interpretation of cementite as opposed to retained austenite, or other precipitates. Lastly, the use of TEM carbon extraction replicas offers some reduction in ambiguity relative to SEM etching techniques, and an increase in the number of precipitates analyzed relative to thin foils, but removes the ability to relate the location and size of cementite precipitates to any characteristics of the original matrix. Improvement of scanning electron beam diffraction techniques of bulk samples could overcome the small statistical sampling size inherent in TEM-based techniques, while providing options for confirming cementite identification by means of dynamical diffraction techniques such as EBSD.

Orientation Relationships Between Cementite and Ferrite

Cementite precipitation can occur by several different mechanisms tied to different orientation relationships between the parent ferrite and daughter cementite. Determining the orientation relationships could assist in identifying when the cementite precipitated during thermo-mechanical processing, in addition to being a verification tool for understanding the veracity of cementite phase identification using EBSD. Cementite is orthorhombic with lattice parameters $a = 0.452$ nm, $b = 0.674$ nm, and $c = 0.509$ nm [1, 2]. The cementite unit cell has 12 iron atoms and 4 carbon atoms, as shown schematically in Fig. 1. Three orientation relationships, the Bagaryatskii, Isaichev, and Pitsch-Petch relationships, are shown in Table 1. In pearlitic steels, the cementite and ferrite lamellae nucleate and grow simultaneously according to a Pitsch-Petch relationship [3–5]. The Pitsch-Petch relationship is also observed when cementite forms at the austenite/ferrite interphase boundary in upper bainite [6]. When cementite precipitation occurs in supersaturated ferrite or martensite during

-P 2ac 2n [P n m a] #62
 a=5.069Å
 b=6.736Å
 c=4.518Å
 $\alpha=90.000^\circ$
 $\beta=90.000^\circ$
 $\gamma=90.000^\circ$

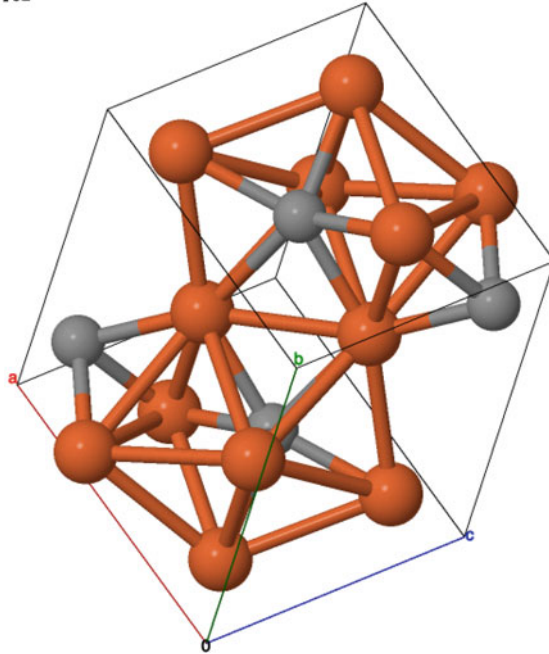


Fig. 1 Three-dimensional representation of the cementite unit cell where the orange atoms represent iron and the grey atoms represent carbon [2] (Color figure online)

Table 1 Three orientation relationships between ferrite and cementite

Bagaryatskii	Isaichev	Pitsch-Petch
$[100]c \parallel [110]f$	$[100]c \parallel [111]f$	$[100]c$ 2.6° from $[311]f$
$[010]c \parallel [111]f$	$(031)c \approx \parallel (101)f$	$[010]c$ 2.6° from $[131]f$
$(001)c \parallel (112)f$		$(001)c \parallel (215)f$

tempering, the Bagaryatskii and Isaichev ORs are often observed [5, 6]. The Bagaryatskii and Isaichev ORs are closely related; the Isaichev OR deviates from the Bagaryatskii OR by a rotation of 3.8° about the a -axis of the cementite lattice [3, 7–12].

Experimental

The chemical compositions of the X70 steel used in this investigation are shown in Table 2. The thermo-mechanical processing path for the X70 steel is not known, although steels of this grade are usually assumed to be accelerated cooled upon finish rolling. The samples were mounted in Bakelite®, ground and polished to 1 μm

Table 2 Chemical composition of X70 plate steel [13, 14]

wt pct	C	Mn	Si	Ni	Cr	Ti	Mo	Nb
X70	0.050	1.59	0.3	0.01	0.26	0.013	0.09	0.066
wt pct	V	Al	N	S	P	Cu	Ca	
X70	0.005	0.026	0.0081	0.003	0.010	0.01	–	

grit using standard metallographic procedures, and vibro-polished using 0.02 μm colloidal silica suspension for several hours. Electron backscatter diffraction patterns were obtained using a JEOL[®]-7000 field emission scanning electron microscope (FE-SEM). All EBSD scans were obtained using an accelerating voltage of 20 kV. Step sizes were varied depending on the size of the scan. All data analysis was performed using OIM Data Analysis and no clean-up procedures were applied to the data sets.

Results and Discussion

Questions about the efficacy of using EBSD to reliably characterize cementite distribution in low carbon steels arose from work in which the effect of microstructure on hydrogen induced cracking in pipeline steels was assessed [13]. In particular, the work focused on characterizing intergranular cracks by comparing misorientation distributions of the uncracked microstructure to misorientations across cracks [13]. Using a misorientation distribution function (MDF) in Rodriguez-Frank (RF) space allowed for the identification of grain boundaries that occur with a higher frequency than others, as shown in Fig. 2. The MDF of the uncracked microstructure is represented by a color gradient map where red represents boundaries that occur at ~ 24 multiples of a random distribution (MRD) and blue represents boundaries present in amounts equivalent to a random distribution. Individual cracked grain boundaries measured by manually assessing misorientations across the crack are overlaid and represented by black dots. The boundary that appears with the highest MRD in the uncracked microstructure is the $43.6^\circ \parallel \langle 100 \rangle$ axis/angle pair. This axis/angle pair is of particular interest due to the lack of cracked boundaries (black dots in Fig. 2) measured upon hydrogen introduction, which could indicate that there are particular boundaries that are less susceptible to cracking than others in the low carbon steel of interest.

However, when attempting to characterize the spatial distribution of these $43.6^\circ \parallel \langle 100 \rangle$ boundaries, it was discovered that these boundaries appeared as clusters within particular ferrite grains, indicating that they are not grain boundaries. Figure 3a is an image quality (IQ) map from a scan obtained using a 50 nm step size in the ND-TD plane, with a region rich in $43.6^\circ \parallel \langle 100 \rangle$ boundaries outlined in white. Figure 3b includes a PRIAS[™] top micrograph with cementite and austenite phases with >0.2 confidence index (CI) overlaid in green and red, respectively. PRIAS[™] is an imaging modality available in EDAX[®] EBSD systems that uses the variation

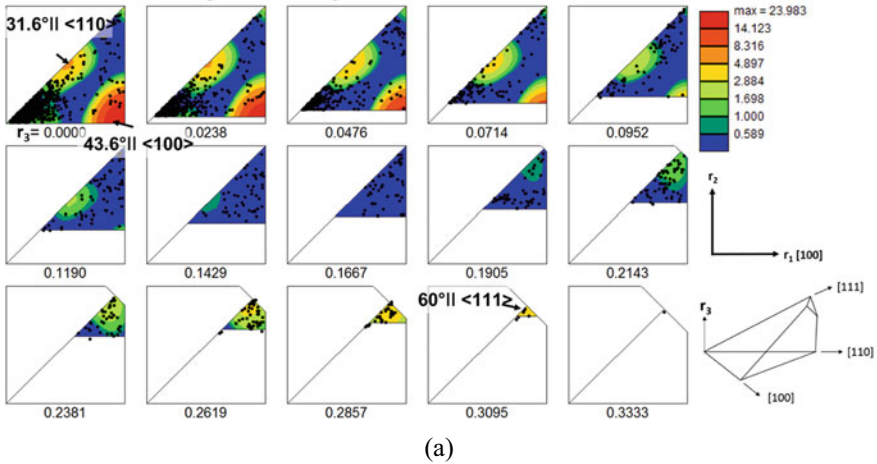


Fig. 2 MDF in RF space for the steel with discrete misorientation angle/axis pairs from cracked boundaries overlaid as black dots. Locations of three special boundaries with relatively high multiples of a random distribution are also overlaid for reference [13]

in the intensity of the diffracting electrons on the phosphor screen to create micrographs with varying diffraction contrast modes [15]. When comparing the EBSD micrographs in Fig. 3a and b, it is clear that the same regions that are rich in $43.6^\circ \parallel \langle 100 \rangle$ boundaries are also rich in regions classified as cementite by the EBSD phase identification. It is also interesting to note that the regions rich in $43.6^\circ \parallel \langle 100 \rangle$ boundaries in Fig. 3a are directly adjacent to grains that do not have any $43.6^\circ \parallel \langle 100 \rangle$ boundaries present, indicating that the pixels identified as cementite are likely not universal errors in phase identification, but rather either correct indexing of cementite that precipitated in specific grains or a pseudosymmetry related error. The term pseudosymmetry is often used when discussing multiple orientation solutions possible for a given experimental Kikuchi pattern, which in practice often results in “speckling”, or systematic color variation within a single grain.

In order to attempt to verify the accuracy of the EBSD software phase identification, fiducial marks were created near the region of interest using a focused ion beam, and the samples were etched with 2 pct nital. A secondary electron (SE) micrograph was then obtained, which is the bottom micrograph in Fig. 3b. Several raised and light-colored constituents are apparent on the surface due to the nital etchant. It is assumed that nital preferentially attacks the ferrite grains and leaves carbon-rich constituents like austenite and cementite in relief. Several observations come about as a result of comparing the light-colored constituents in the SE micrograph to the phase map produced by EBSD. Constituents identified as austenite in the EBSD phase map correlate well with constituents visible in SE upon nital etching and are identified by black arrows. In contrast, isolated pixels identified as cementite occur along boundaries and sporadically within the ferrite grains and do not correlate well to individual light-colored constituents in the SE micrograph. Several constituents

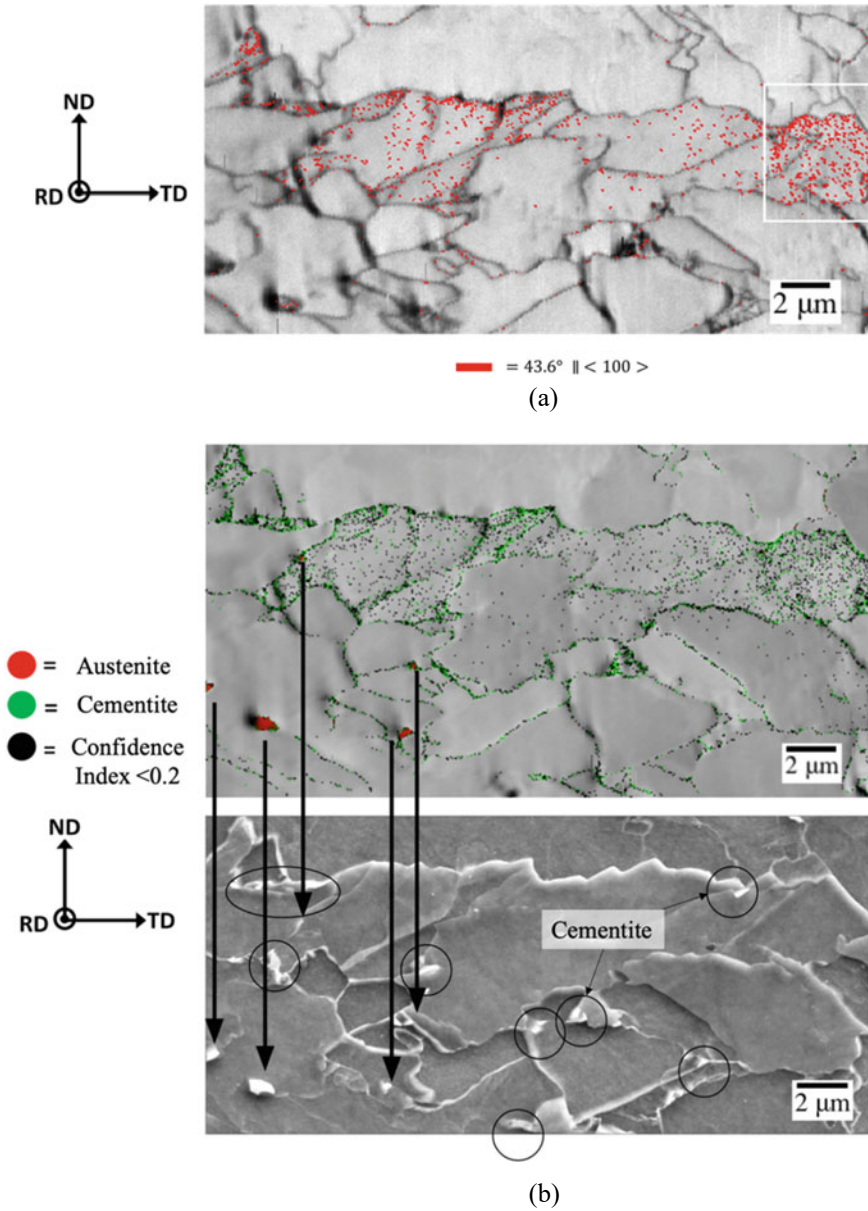


Fig. 3 **a** EBSD image quality map with red regions representing $43.6^\circ \parallel \langle 100 \rangle$ boundaries and subsequent region of interest outlined in white and **b** EBSD PRIAS™ top micrograph (top) with austenite and cementite phases indicated by red and green, respectively, and (bottom) secondary electron micrograph of 2 pct nital etched steel, with arrows pointing to austenite regions and circles indicating possible cementite precipitates (Color figure online)

that might be classified as cementite using SE micrographs of the nital etched steel are indicated by black circles in Fig. 3b, but cannot be as convincingly tied to regions identified as cementite in the EBSD maps. Therefore, a separate, diffraction-based verification modality was undertaken.

Figure 4a is an inverse pole figure (IPF) map of the white outlined region in Fig. 3a with boundaries within 5° of a $43.6^\circ \parallel \langle 100 \rangle$ boundary indicated in black. Figure 4b is a PRIAS™ top micrograph of the same region in Fig. 4a with pixels indexed as cementite shown in green and $43.6^\circ \parallel \langle 100 \rangle$ boundaries shown in red. Data points indexed as cementite appear largely as isolated individual pixels in Fig. 4b and often have red boundaries indicating a $43.6^\circ \parallel \langle 100 \rangle$ boundary surrounding the pixel. The three different colors (e.g. orientations) of cementite are shown below the IPF micrograph in Fig. 4a. The fact that cementite surrounded by the special boundaries only has 3 different colors in the IPF map may be indicative of 3 separate variants. This observation might then in turn indicate that the cementite data points have an orientation relationship with the ferrite, which is described by the $43.6^\circ \parallel \langle 100 \rangle$ axis/angle pair. To investigate if the axis/angle pair correlates to one of the three most common ferrite/cementite orientation relationships discussed in the background section, pole figures were created from several adjacent data points with a common $43.6^\circ \parallel \langle 100 \rangle$ boundary.

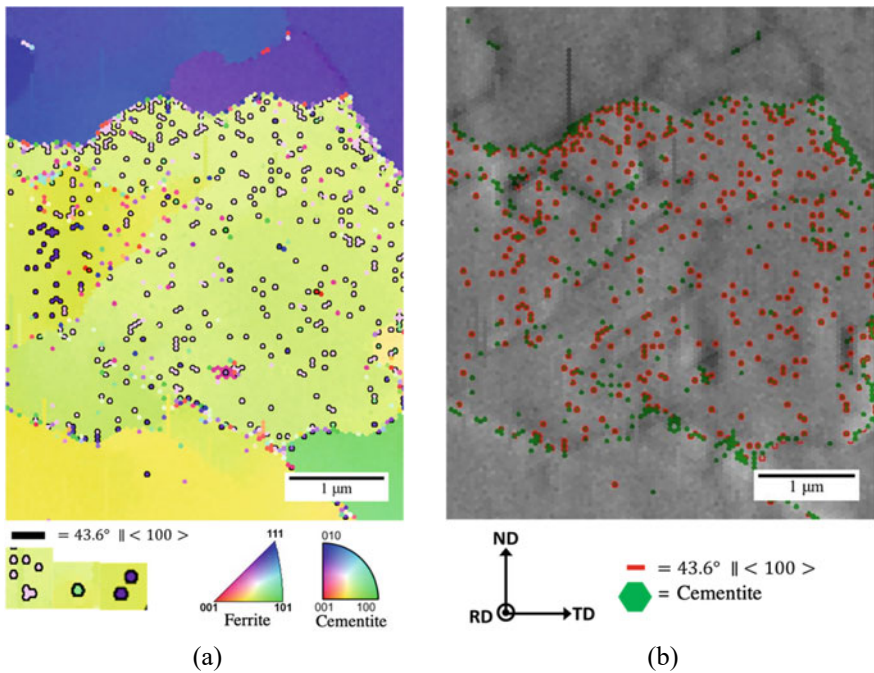


Fig. 4 EBSD maps from a region selected from Fig. 3a where **a** is an IPF map with $43.6^\circ \parallel \langle 100 \rangle$ boundaries indicated as black outlines and **b** is a PRIAS top micrograph with data points indexed as cementite in green and $43.6^\circ \parallel \langle 100 \rangle$ boundaries indicated in red. Each pixel represents data indexed by the EBSD software (Color figure online)

Figure 5 is a series of pole figures from adjacent ferrite and cementite data points with $43.6^\circ \parallel \langle 100 \rangle$ boundary relationships reflecting the most common cementite/ferrite ORs as presented in Table 1. The black circles (open and closed) in the pole figures in Fig. 5 correspond to the ferrite poles, while the red and pink correspond to the cementite poles. The closed black circles correspond to ferrite poles in the positive hemisphere, while the open black circles correspond to ferrite poles in the

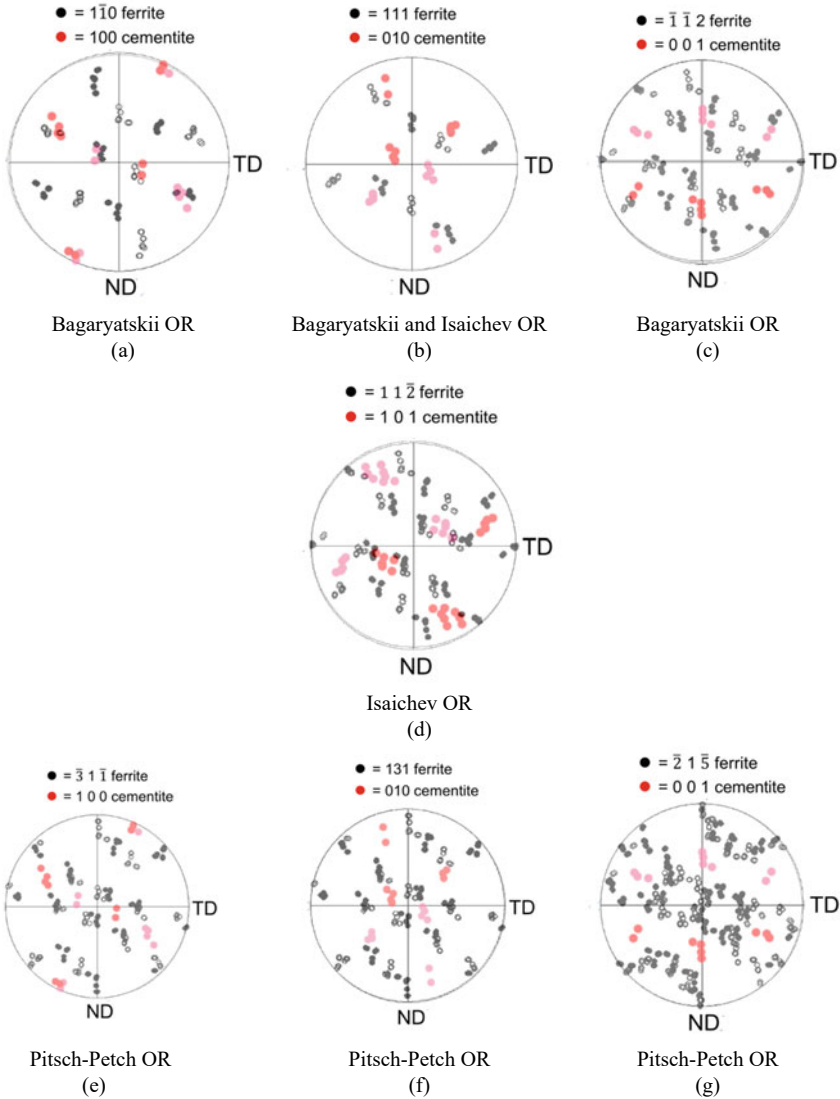


Fig. 5 Pole figures obtained from adjacent cementite/ferrite data points representing the most common cementite/ferrite orientation relationships

negative hemisphere. Similarly, the darker red circles correspond to cementite poles in the positive hemisphere, while the pink circles correspond to cementite poles in the negative hemisphere. The pole figures with specific cementite poles that coincide with a given ferrite pole indicate that those planes are parallel. Two or more of the pole figures for a given OR that have coinciding ferrite and cementite poles could indicate cementite precipitation according to the specified OR. The ferrite/cementite relationships shown in Fig. 5a, where (100)_c cementite planes are parallel to (110)_f ferrite planes, have the most coinciding ferrite/cementite data points indicating (100)_c and (110)_f planes could be parallel. Data points in Fig. 5b, c, corresponding to the (010)_c|| (111)_f and (001)_c|| (112)_f planes, respectively, are close to matching.

The first set of parallel planes necessary to fulfill the Isaichev OR coincides with the second set of parallel planes for the Bagaryatskii OR and is shown in Fig. 5b, with some poles being close to matching. The second set of parallel planes necessary to fulfill the Isaichev OR is shown in Fig. 5d. Figure 5d does not have ferrite and cementite poles that match as well as Fig. 5a, but instead has cementite poles that are close to more than one cluster of ferrite poles. In contrast, the cementite poles in Fig. 5e–g do not appear to be close to any ferrite planes, indicating that the Pitsch-Petch OR likely does not hold. The absence of ferrite and cementite poles consistent with the Pitsch-Petch OR would be consistent with the lack of pearlite observed in this steel. The proximity of the ferrite and cementite poles for the Bagaryatskii OR could indicate that the cementite precipitated from supersaturated ferrite, as the Bagaryatskii OR is often observed in the tempering of martensite. Autotempering could have occurred during the air-cooling step that occurs after accelerated cooling [4].

In order to assess the veracity of cementite phase identification by EBSD, the definition and calculation procedures for boundary analysis in the OIM software are presented. EBSD data is gathered by rastering the electron beam and pausing at a given step size to collect a Kikuchi pattern. Figure 6 is a schematic demonstrating the process of rastering the electron beam, collecting and indexing Kikuchi patterns, and creating a phase map from the indexed points in OIM Analysis. Phase indexing in multiphase materials occurs by comparing measured and calculated interplanar angles and choosing the best fit between the user-input-based options for possible phases [16]. The software does a similar calculation and fitting/voting scheme to index orientations. During the indexing process, several possible orientations may come close to satisfying the experimentally derived Kikuchi pattern. The software ranks those solutions based on a voting scheme, and the confidence index value is a ratio of the difference between the highest two ranked solutions divided by the total number of votes [16]. It is unclear in what order this process occurs, i.e. if the phase identification occurs in parallel or in series with the orientation indexing. This ambiguity has important ramifications for user interpretation of data, particularly in regards to the interpretation of confidence index values associated with data points. It may be tempting for a user to interpret the “confidence index” assigned to a data point to also have some meaning regarding how confident the software is in phase identification, which may not be the case. As a specific example, ambiguity arises upon

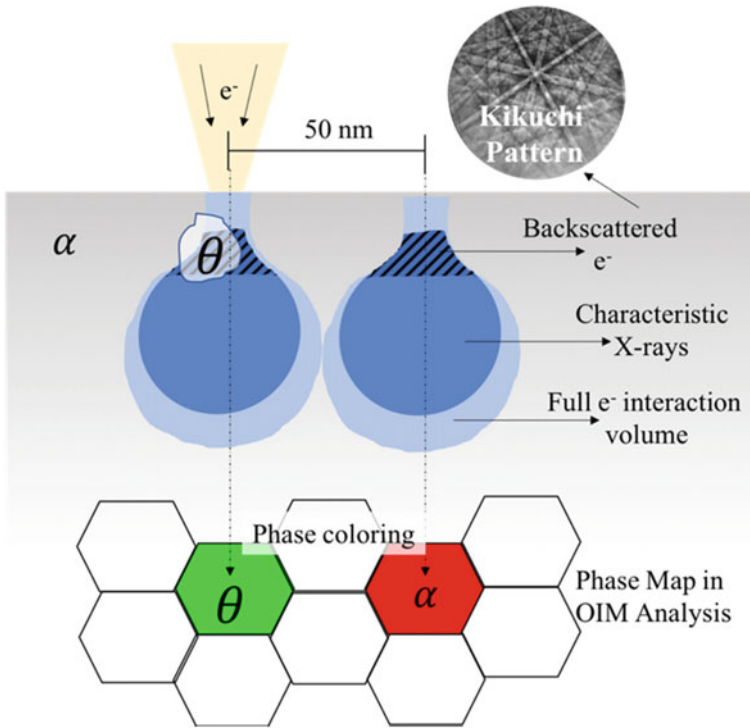


Fig. 6 Schematic of an electron beam interacting with a ferrite sample with a cementite precipitate in part of the electron beam interaction volume. The schematic gives a 50 nm step size as an example of the distance between where the electron beam rasters and a schematic output of a phase map from OIM analysis. This schematic demonstrates the possibility of backscatter electrons coming from two phases simultaneously

orientation indexing and phase identification of grain boundary regions. Two overlapping Kikuchi patterns could cause smaller interplanar angle measurements, even between two cubic grains. The smaller interplanar angles would be more indicative of a lower symmetry phase than the cubic one, resulting in the software identifying the pixel as cementite.

Individual pixels identified as cementite within a ferrite crystal, unlike grain boundary cementite, are more difficult to verify without either believing that the software has successfully identified a nano-scale cementite particle below the surface (i.e. not visible in SE upon etching), or that there is a pseudosymmetry effect in certain ferrite grain orientations. The backscatter electrons that create Kikuchi patterns for indexing only come from a small portion of the total electron beam interaction volume. As an illustration, Fig. 6 shows a small cementite (θ) precipitate within the backscatter electron interaction volume. The backscatter interaction volume is partially filled with the cementite particle, but the remaining volume is filled by the ferrite matrix. Here it is assumed that the cementite particle is much smaller than

the 50 nm step size such that the backscatter volume is only partially filled with the cementite precipitate. The resulting Kikuchi pattern has overlapping bands associated with both orthorhombic and cubic symmetries resulting from the two phases. The overlapping patterns are more difficult for the software to index, and low confidence index values often result. Understanding the algorithm used for phase ID of EBSD data could either be adjusted to ensure more accurate phase ID or could help users make informed assessments of EBSD data. In interpreting the veracity of the phase identification of cementite in these steels with nano-scale cementite precipitation, it would be important to know the algorithm by which the software is assigning both phase IDs and orientations. It is also worth further investigations into possible pseudosymmetric phenomena in certain ferrite orientations that could be resulting in the measurement of the special $43.6^\circ \parallel \langle 100 \rangle$ boundary.

Conclusions

This work was initiated to understand if hydrogen induced cracking in pipeline steels favored some grain boundary orientations over others. From comparisons of misorientation distribution functions of the uncracked steels to misorientations measured across cracks, it appeared that a boundary of abundance in the microstructure ($43.6^\circ \parallel \langle 100 \rangle$) might be less susceptible to cracking. However, upon characterization of the spatial distribution and locations of these special boundaries, it was noted that the special $43.6^\circ \parallel \langle 100 \rangle$ boundaries were not grain boundaries, but rather interphase boundaries between pixels identified as cementite and the matrix ferrite. Because correlations between SE micrographs of the steel etched with 2 pct nital could not effectively verify the presence of cementite, pole figures were created to understand if the special $43.6^\circ \parallel \langle 100 \rangle$ boundaries were actually reflective of an orientation relationship between the cementite and ferrite. The resulting pole figures seem to support the phase identification by the EBSD software, as the cementite and ferrite correlated better with the Bagaryatskii OR. It is apparent from the EBSD maps that the $43.6^\circ \parallel \langle 100 \rangle$ boundaries identified using the MDF were not grain boundaries but rather interphase cementite/ferrite boundaries. The inclusion of interphase boundaries in MDFs is important for users of OIM Data Analysis to note while interpreting MDFs in multiphase materials, as these maps were produced by using the “grain boundary texture” feature in the software. Further, if the EBSD software is correctly indexing cementite precipitates on the scale of tens of nanometers, then even nano-scale precipitates could need to be taken into account as secondary phases for misorientation distributions to be interpreted correctly. However, in order to understand if the EBSD software is correctly identifying nano-scale precipitation, all possible pseudosymmetry effects must be categorically ruled out. Investigating possible pseudosymmetry effects on cementite phase identification and misorientation boundary calculation is proposed as a future direction of this work, in addition to attempting cementite phase ID in systems with much larger and more easily identifiable cementite constituents such as pearlitic steels.

References

1. Krauss G (2005) Steels-processing, structure, and performance. ASM International (2005)
2. Cementite (Fe₃C) Crystal Structure. https://materials.springer.com/isp/crystallographic/docs/sd_1623041
3. Zhou DS, Shiflet GJ (1992) Ferrite: cementite crystallography in pearlite. *Metall Trans A* 23(4):1259–1269
4. Shackleton DN, Kelly PM (1967) The crystallography of cementite precipitation in the Bainite transformation. *Acta Metall* 15(6):979–992
5. Andrews KW (1963) The structure of cementite. *Acta Metall* 11:939–946
6. Ohtani, Okaguchi S, Fujishiro Y, Ohmori Y (1990) Morphology and properties of low-carbon Bainite. *Metall Trans A* 21(3):877–888 (1990)
7. Bhadeshia HKDH (2018) Solution to the Bagaryatskii and Isaichev Ferrite–cementite orientation relationship problem. *Mater Sci Technol (United Kingdom)* 34(14):1–3
8. Wei FG, Tsuzaki K (2005) Crystallography of [0 1 1]/54.7° Lath boundary and cementite in tempered 0.2C steel. *Acta Mater* 53(8):2419–2429
9. Bagaryatskii YA (1950) Possible mechanism of martensite decomposition. *Dokl Akad Nauk SSSR* 73:1161–1164
10. Isaichev IV (1947) Orientatsiya tsementita v otpushchennoi uglerodistoi stali [Orientation of cementite in tempered carbon steel]. *Zhurnal Tekhnicheskoi Fiziki* 17:835–838
11. Pitsch W (1962) Der orientierungszusammenhang zwischen zementit und ferrit im perlit. *Acta Metall* 10:79–80
12. Petch NJ (1953) The orientation relationships between cementite and α -iron. *Acta Crystallogr A* 6:96
13. O'Brien M (2018) Effect of microstructure on hydrogen induced cracking in pipeline steels. MS thesis, Colorado School of Mines, Golden, CO
14. Angus G (2014) Hydrogen induced damage in pipeline steels. MS thesis, Colorado School of Mines, Golden, CO
15. Wright SI, Nowell MM, De Kloe R, Camus P, Rampton T (2015) Electron imaging with an EBSD detector. *Ultramicroscopy* 148:132–145
16. OIM Analysis Version: 7.2 (2013) User Manual: TexSEM Laboratories Inc., Draper

Part II
Characterization of Mechanical Properties

Strength and Failure Characterization of the Gibeon (IVA) Iron Meteorite



M. Fazle Rabbi, Khaled H. Khafagy, Laurence A. J. Garvie, Erik Asphaug, Desirée Cotto-Figueroa, and Aditi Chattopadhyay

Abstract Most iron meteorites are thought to be remnants of the cores of differentiated planetesimals, exposed to interplanetary space by collisional events. Many display a Widmanstätten pattern, an intergrowth of kamacite (bcc α -iron) and a high Ni-iron material called taenite. This coarse structure, which is formed by slow cooling over millions of years in space, may influence the material properties and failure mechanisms. In this study, eight samples are used to characterize the strength and failure mechanism of the Gibeon (IV) iron meteorite under quasi-static compressive and tensile loading. Here is shown the full-field strain and displacement contours using an in-situ three-dimensional digital image correlation (DIC) technique that provides insights into the initiation and propagation of damage. Further microstructural characterization of the post-fracture surfaces is conducted and correlated to the DIC effective strain contours to better investigate the influence of the different phases on the failure mechanisms.

Keywords Iron meteorite · Gibeon · Digital image correlation · Failure mechanism

M. F. Rabbi (✉) · K. H. Khafagy · A. Chattopadhyay
School for Engineering of Matter Transport and Energy, Arizona State University, Tempe, AZ, USA
e-mail: mrabbi1@asu.com

L. A. J. Garvie
Center for Meteorite Studies, Arizona State University, Tempe, AZ, USA

E. Asphaug
Lunar & Planetary Laboratory, University of Arizona, Tucson, AZ, USA

D. Cotto-Figueroa
Department of Physics and Electronics, University of Puerto Rico at Humacao, Humacao, PR, USA

Introduction

Iron meteorites provide insight into the formation of early planetary bodies [1]. Many are thought to be from the cores of differentiated planetesimals that have lost the outer rocky layer by numerous collisions: pieces deorbit and fall onto the Earth as iron meteorites [2–4]. Iron meteorites can display a unique Widmanstätten pattern microstructure, with its formation controlled by the composition and cooling rate of the parent body [5]. The primary metal phases include the body-centered cubic (BCC) α -iron phase, alloyed with $\sim 7\%$ Ni named kamacite, and the face-centered cubic (FCC) iron phase that contains ~ 30 – 40% Ni known as taenite [6]. Nucleation and growth of kamacite from the taenite phase occur during very slow cooling of approximately 1 K temperature over a few hundreds of thousands of years that form the Widmanstätten pattern [1, 7].

Due to the unique microstructure of iron meteorites, many studies were conducted to understand their origin, structure, and compositional variation of Fe–Ni contents within the Widmanstätten pattern [1, 5, 8]. The mechanical properties of these material systems were also studied at different temperatures and strain rates to understand their failure mechanisms and the effect of ductile to brittle transition temperature on the breakage of the parent body [6, 9–11]. The characterization of mechanical properties such as hardness [12], strength [13], and elastic modulus [14] for the metallic microconstituents was reported using microhardness, micro-tension, and nanoindentation tests. However, very few studies were performed to characterize the failure using in-situ digital image correlation (DIC), which can provide in-and out-of-plane full-field displacement and strain contours to analyze the mechanical response and failure mechanisms of iron meteorites under quasi-static compression and tension load conditions. The DIC technique is an optical method that correlates a reference image with a series of images from the deformed sample taken during mechanical tests. This correlation provides information on the material behaviors by measuring the strain at any points of the area of interest at different loads [15–17]. It has been proved as an effective and efficient strain measurement technique and used in many laboratory tests [18–21].

In this paper, the strength and failure mechanisms of the Gibeon (IVA) iron meteorite is characterized using quasi-static compression and tension tests with in-situ digital image correlation. Full-field strains, calculated using the DIC system, are utilized to investigate the damaged surface that aid the understanding of failure initiation and propagation in the tested specimens. Optical and scanning electron micrographs of the post-failure surface with the DIC strain fields are utilized to correlate the influence of different phases of Gibeon to the failure mechanisms.

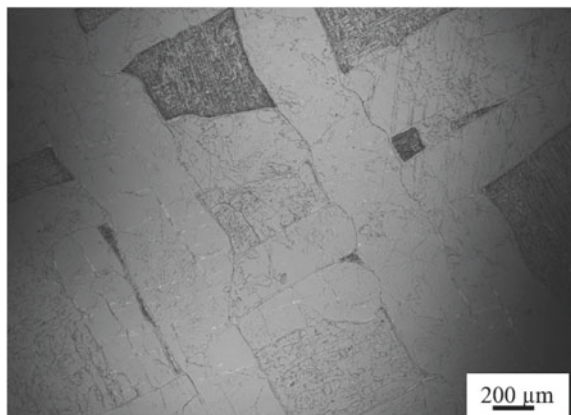
Material and Methods

Test specimens, received from the Center for Meteorite Studies at Arizona State University, were prepared from a bar of the Gibeon meteorite. Four cubic specimens of 10 mm and four sub-sized tensile specimens of gauge length 32 mm, width 6 mm, and thickness 2 mm were used for the uniaxial compression and tension experiments according to ASTM E8-21/E9. Tests were conducted at a displacement rate of 0.25 mm/min at ambient temperature using a universal testing machine Instron 5985 frame with a load cell of the capacity of 250 kN. In-situ DIC was utilized for all tests using the ARAMIS 5M DIC system to record the deformations and compute the strain evolution. The DIC system was calibrated to compensate for lens distortion and to maintain dimensional consistency of the measuring system using a calibration cube provided by ARAMIS. It computes the displacement and strain fields both in the longitudinal and transverse direction from the stochastic speckle pattern of deformed images and provides local and global strain fields, useful for identifying crack initiation and propagation. Additionally, post-failure surfaces of the tested specimens were analyzed using the JEOL JXA-8530F at an accelerating voltage of 20 kV with a beam current of ~80 nA to further investigate the failure mechanisms. Samples for optical and SEM imaging were prepared from the original Gibeon and pieces after the compression and tension tests. Pieces were embedded in epoxy, ground flat, polished, and etched with nital.

Results and Discussion

The optical imaging of the Gibeon meteorite displays the typical Widmanstätten pattern dominated by the oriented kamacite lamellae separated by the thin taenite boundaries (Fig. 1). The average size of the kamacite bands was measured at $220.8 \pm 77.2 \mu\text{m}$ and they are several millimeters long with an intersecting pattern.

Fig. 1 Optical micrograph of the original Gibeon meteorite specimen showing the Widmanstätten pattern. Visible are the elongated kamacite laths (light-colored regions) and dark-etched plessite. Plessite is a fine-scale intergrowth of kamacite and taenite. The sample is etched with nital



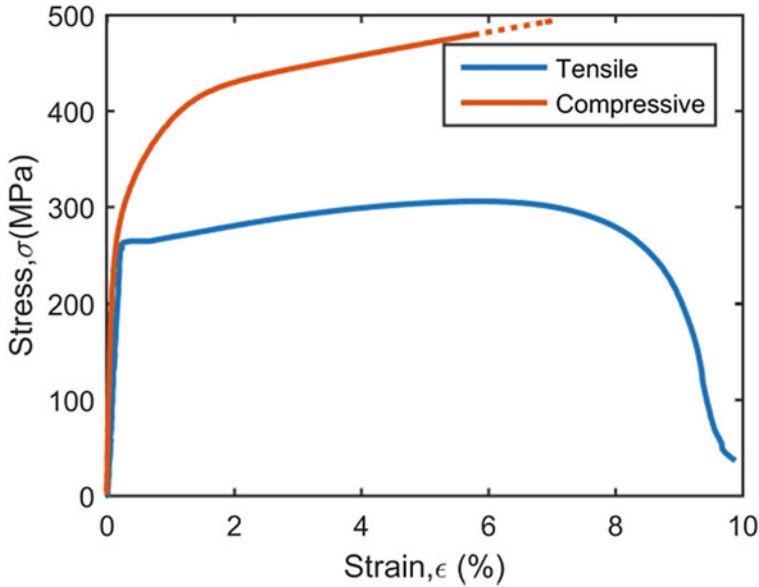


Fig. 2 A typical quasi-static response of the Gibeon meteorite at ambient temperature

Under both tensile and compressive loads, the specimens exhibit a linear increase of strain to yield point, then strain hardening and large nonlinear plastic deformations followed by ductile failure (Fig. 2). Failure of the tensile specimens occurred at an average strength of 305.7 ± 4.6 MPa at a failure strain of $6.3 \pm 0.95\%$. The quasi-static compression tests were interrupted at a strain of $\sim 50\%$. In compression, specimens were permanently deformed without fracture, showing an average yield strength of 308 ± 64.9 MPa at 0.2% strain that conforms with the previous studies [6, 22].

The taenite exhibits higher strength, by up to three orders of magnitude, compared to the kamacite [13]: this difference in mechanical properties is confirmed by the in-situ DIC displacement and strain contour results. A localized strain around the kamacite is shown in axial and von Mises strain contours (Fig. 3). Strain measurements show uniform distribution during the elastic region where more variation was observed in strain values during the plastic region of the mechanical tests. The evolution of the axial strains was studied using multiple virtual extensometers in order to calculate the local strains and identify the region of failure initiation. Failure patterns were observed in the von Mises strain contours during the plastic deformation and shear bands were possibly induced by the piled-up dislocations [23]. Strain concentration in the gauge region, for compression and tension, resulted in the initiation of new fracture surfaces (Fig. 3). The tensile specimens showed necking before fracture, a common failure mechanism of ductile materials. From a micro-mechanical perspective, tensile failure can be explained such as when the shear component of an

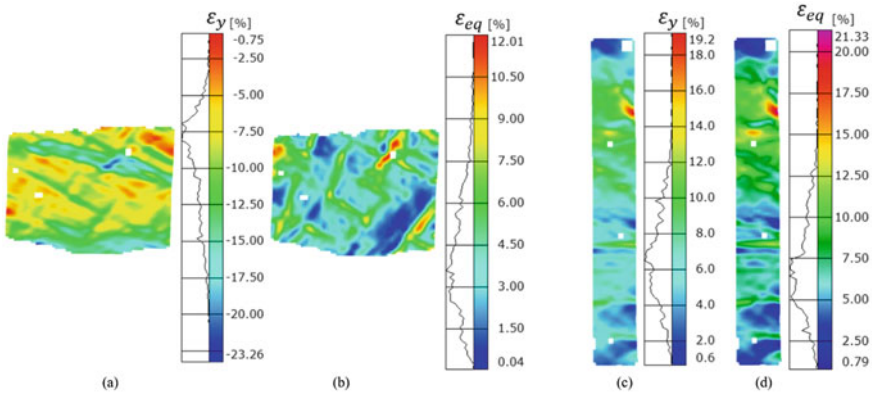


Fig. 3 Contours of axial and von Mises strain for compression (a–b) and tension (c–d) experiments showing the location of high strains and region of failure initiation

applied stress is resolved along a slip plane, slip system activates, and failure occurs due to the shear acting on the slip planes [13].

Both the kamacite and taenite of Gibeon deform plastically, although in areas a serrated boundary was observed between the kamacite and taenite (Fig. 4a). Micrographs of a compressed specimen show that Widmanstätten patterns stretched along the transverse direction of load. The applied load was primarily supported by kamacite phases with relatively low strength and hardness compared to the taenite, followed by taenite since it also exhibits significant ductility [6, 13] (Fig. 4a). Furthermore, fractography of the tensile specimen reveals that the specimens were slipping along the plane of shear and a smooth ductile ridge appears on the fracture surface (Fig. 4b). Observations from optical and scanning electron micrographs correlate

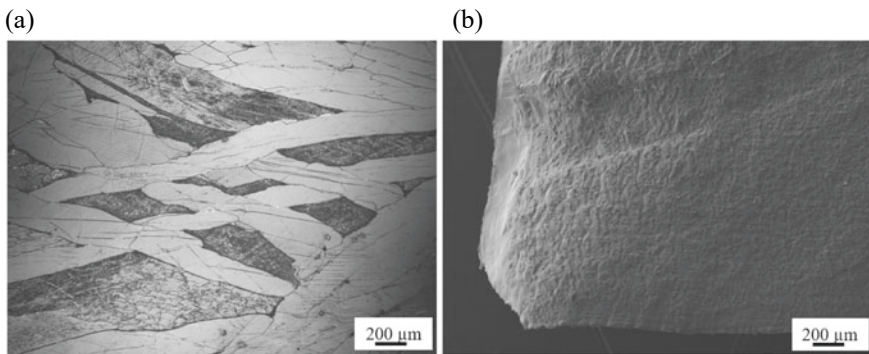


Fig. 4 **a** Optical photograph of a nital-etched surface through a compressed cube showing the deformed Widmanstätten pattern along the transverse direction of the load after the compression test. **b** Failure surface of the tensile specimen showing shear band

well with the DIC strain contours. Further investigation on the fracture surface along the boundary of kamacite and taenite and their influence on failure under different load conditions will be reported in future work.

Conclusion

Mechanical behaviors of the Gibeon meteorite were characterized at ambient temperature by combining quasi-static mechanical tests under compression and tension conditions with in-situ full-field DIC analyses. Specimens, under both loading conditions, showed significant deformation in their Widmantätten pattern. The deformations that proceed to fracture in the specimens are also identified from the DIC strain contours revealing the location of failure initiation and propagation. Post-failure surfaces were analyzed under optical and scanning electron microscopes showing the deformation marks on the kamacite phases and the shear band on the fracture planes, which are in good agreement with the strain localization shown in the DIC strain contours. Since the formation, collisions, and disintegration of the planetary bodies largely depend on their physical and mechanical properties, this work on strength and failure characterization of the Gibeon meteorite demonstrates the effectiveness of failure analysis of iron meteorites using the DIC technique and improves understanding of the asteroidal breakup of iron-rich bodies.

Acknowledgements The authors are grateful to the Center for Meteorite Studies at Arizona State University for supplying the Gibeon meteorite for the experiments. This work is supported by the National Aeronautics and Space Administration under Grant/Contract/Agreement No. 80NSSC18K1444 issued through the SSO Near-Earth Object Observations Program.

Conflict of Interest The authors declare no conflict of interest.

References

1. Goldstein JI, Scott ERD, Chabot NL (2009) Iron meteorites: crystallization, thermal history, parent bodies, and origin. *Geochemistry* 69:293–325. <https://doi.org/10.1016/j.chemer.2009.01.002>
2. Katsura T, Nakamura AM, Takabe A et al (2014) Laboratory experiments on the impact disruption of iron meteorites at temperature of near-earth space. *Icarus* 241:1–12. <https://doi.org/10.1016/j.icarus.2014.06.007>
3. Yang J, Goldstein JI, Scott ERD (2007) Iron meteorite evidence for early formation and catastrophic disruption of protoplanets. *Nature* 446:888–891. <https://doi.org/10.1038/nature05735>
4. Slyuta EN (2013) Physicomechanical properties and gravitational deformation of metallic asteroids. *Sol Syst Res* 47:109–126. <https://doi.org/10.1134/S0038094613010085>
5. Yang J, Goldstein JI, Scott ERD (2010) Main-group pallasites: thermal history, relationship to IIIAB irons, and origin. *Geochim Cosmochim Acta* 74:4471–4492. <https://doi.org/10.1016/j.gca.2010.04.016>

6. Knox R (1970) The yield strength of meteoritic iron. *Meteoritics* 5:63–74. <https://doi.org/10.1111/j.1945-5100.1970.tb00391.x>
7. Short JM, Andersen CA (1965) Electron microprobe analyses of the Widmanstätten structure of nine iron meteorites. *J Geophys Res* 1896–1977(70):3745–3759. <https://doi.org/10.1029/JZ070i015p03745>
8. Bunge HJ, Weiss W, Klein H et al (2003) Orientation relationship of Widmannstätten plates in an iron meteorite measured with high-energy synchrotron radiation. *J Appl Crystallogr* 36:137–140. <https://doi.org/10.1107/S0021889802021386>
9. Auten TA (1973) On the brittleness of gibeon meteoritic iron. *Meteoritics* 8:189–196. <https://doi.org/10.1111/j.1945-5100.1973.tb01247.x>
10. Gordon RB (1970) Mechanical properties of iron meteorites and the structure of their parent planets. *J Geophys Res* 75:439–447. <https://doi.org/10.1029/JB075i002p00439>
11. Petrovic JJ (2001) Review mechanical properties of meteorites and their constituents. *J Mater Sci* 36:1579–1583
12. Jain AV, Gordon RB, Lipschutz ME (1972) Hardness of kamacite and shock histories of 119 meteorites. *J Geophys Res* 77:6940–6954. <https://doi.org/10.1029/JB077i035p06940>
13. Ueki S, Mine Y, Takashima K (2021) Excellent mechanical properties of taenite in meteoric iron. *Sci Rep* 11:4750. <https://doi.org/10.1038/s41598-021-83792-y>
14. Wheeler JM (2021) Mechanical phase mapping of the Taza meteorite using correlated high-speed nanoindentation and EDX. *J Mater Res* 36:94–104. <https://doi.org/10.1557/s43578-020-00056-7>
15. Ackermann F (2006) Digital image correlation: performance and potential application in photogrammetry. *Photogramm Rec* 11:429–439. <https://doi.org/10.1111/j.1477-9730.1984.tb00505.x>
16. Pan B, Qian K, Xie H, Asundi A (2009) Two-dimensional digital image correlation for in-plane displacement and strain measurement: a review. *Meas Sci Technol* 20:062001. <https://doi.org/10.1088/0957-0233/20/6/062001>
17. Wu H, Zhao G, Liang W (2019) Mechanical response and fracture behavior of brittle rocks containing two inverted U-shaped holes under uniaxial loading. *Appl Sci* 9:5327. <https://doi.org/10.3390/app9245327>
18. Rege A, Schwan M, Chernova L et al (2020) Microstructural and mechanical characterization of carbon aerogels: an in-situ and digital image correlation-based study. *J Non-Cryst Solids* 529:119568. <https://doi.org/10.1016/j.jnoncrysol.2019.119568>
19. Miao S, Pan P-Z, Yu P et al (2020) Fracture analysis of Beishan granite after high-temperature treatment using digital image correlation. *Eng Fract Mech* 225:106847. <https://doi.org/10.1016/j.engfracmech.2019.106847>
20. Gehri N, Mata-Falcón J, Kaufmann W (2020) Automated crack detection and measurement based on digital image correlation. *Constr Build Mater* 256:119383. <https://doi.org/10.1016/j.conbuildmat.2020.119383>
21. Farahani BV, Amaral R, Tavares PJ et al (2020) Material characterization and damage assessment of an AA5352 aluminium alloy using digital image correlation. *J Strain Anal Eng Des* 55:3–19. <https://doi.org/10.1177/0309324719892727>
22. Ostrowski D, Bryson K (2019) The physical properties of meteorites. *Planet Space Sci* 165:148–178. <https://doi.org/10.1016/j.pss.2018.11.003>
23. Parz P, Leitner M, Sprengel W et al (2013) Defect investigations of an iron-nickel meteorite. *J Phys Conf Ser* 443:012032. <https://doi.org/10.1088/1742-6596/443/1/012032>

Effect of Equal-Channel Angular Pressing and Targeted Heat Treatment on Aluminum AA7075 Sheet Metal



Maximilian Gruber, Thomas Spoerer, Christian Illgen, Philipp Frint, Martin F.-X. Wagner, Philipp Lechner, and Wolfram Volk

Abstract In this study, equal-channel angular pressing (ECAP) was used to improve the mechanical properties of Aluminum AA7075 sheet metal. Various approaches were tested for ECAP route C, involving either channel geometry, forming temperature, or post-treatment time. The specimens were evaluated by tensile testing and compared with reference specimens in artificially aged T6 conditions. The goal was to optimize the time- and energy-consuming artificial aging procedure. The results show that a 75% reduction in artificial aging time still leads to an increase in yield strength due to ECAP. In addition, the elongation at fracture is strongly influenced by ECAP. Furthermore, tensile tests were performed on a resistance-heated test bench to determine its potential for hot forming processes. These results show that the use of ECAP with sheet metal enables efficient production of high-strength aluminum and thus contributes to a more sustainable production.

Keywords Equal-channel angular pressing (ECAP) · Aluminum AA7075 · Resistance heating · Hot tensile test

Introduction

Not just in aerospace but also in the automotive sector, lightweight components have been used in large quantities for decades. Interest is growing due to the increasingly stringent environmental regulations governing the levels of harmful emissions [1]. Aspects such as passenger safety, weight reduction, and product costs, which can of course be reduced by minimizing the use of materials, also play an important role. In addition to developing innovative manufacturing processes, materials

M. Gruber (✉) · T. Spoerer · P. Lechner · W. Volk
Chair of Metal Forming and Casting, Technical University of Munich, Walther-Meissner-Str. 4,
85748 Garching, Germany
e-mail: Maximilian.gruber@utg.de

C. Illgen · P. Frint · M. F.-X. Wagner
Institute of Materials Science and Engineering, Chemnitz University of Technology,
Erfenschlager Str. 73, 09125 Chemnitz, Germany

© The Minerals, Metals & Materials Society 2022
M. Zhang et al. (eds.), *Characterization of Minerals, Metals, and Materials 2022*,
The Minerals, Metals & Materials Series,
https://doi.org/10.1007/978-3-030-92373-0_3

research is concerned with lightweight construction, in particular with regard to high-strength steels and, above all, high-strength aluminum alloys [2]. The 6000 and 7000 series aluminum alloys are precipitation-hardenable and exhibit high strength at low density, excellent corrosion resistance, good fatigue properties, and ductility. Since the mechanical properties of these series can be modified by applying heat treatments or thermomechanical processing, the alloys can be used in a wide range of engineering applications [3]. The increased ductility resulting from hot forming allows more complex geometries with less material springback [4]. However, since both heat treatment and hot forming are very energy-intensive, several studies are now addressing how to reduce the temperatures and time intervals of these processes [5, 6].

In this context, equal-channel angular pressing (ECAP) has attracted increasing scientific and technological interest in recent years. ECAP denotes the process of pressing material through an angled channel, which introduces a severe plastic, predominantly shear deformation that creates a fine-grained microstructure [7, 8]. In conventional ECAP, a bar stock with a square or round cross-section is pressed through the channel. The geometry of the semi-finished product is preserved to enable the material to be passed through the ECAP tool several times, and it can also go through different processing routes [9]. While many important and scientifically interesting studies have been conducted on conventional ECAP processing, one important and still unsolved problem is the suitability of ECAP for use in an industrial environment. The processing of sheet metals and, in particular, high-strength aluminum alloys, is of great interest, especially in automotive applications. The tool considered in this study is used for ECAP processing of sheet materials with a thickness of 1.8 mm [10]. Previous studies have demonstrated the possibility of using this tool to process 5000 series aluminum at room temperature [11]. In addition, various process routes could already be carried out and numerical studies were performed to improve the process [12, 13]. This study is based on AA7075 under elevated ECAP temperatures and channel geometries. In addition, the influence of post-treatment is investigated and compared with that of conventional heat treatments. By investigating the fundamentals of ECAP with sheet materials, a contribution is made to the subsequent industrialization and application of the process.

Experimental Investigations

This section describes the experiments performed in the ECAP tests and the determination of the mechanical properties. The present work involved processing rolled AA7075 sheets with a thickness of 1.8 mm (Si 0.064%, Fe 0.139%, Cu 1.519%, Mn 0.045%, Mg 2.419%, Cr 0.183%, Zn 6.310%, and Ti 0.0252%). To create a homogeneous microstructure, the sheets were solution-annealed at 475 °C for one hour and then quenched in a water bath. A T6 heat treatment was subsequently performed on some of the samples, which served as a reference. For this purpose, the samples were heat-aged after quenching, first for 18 h at 125 °C and then again for 4 h at

175 °C (referred to as the 22 h treatment). Solution-annealed samples were used for the ECAP tests. In the initial position of the ECAP tool (see Fig. 1a), a sheet with the dimensions $200 \times 100 \times 1.8 \text{ mm}^3$ was inserted into the ECAP channel. The long edge corresponded both to the rolling direction and the ECA-pressing direction. The sheet was pressed through the channel at a constant stamp speed of 5 mm/s, using two different configurations with channel angles of $\Phi = 110^\circ$ or 120° , respectively. The 110° channel had an inner radius r of 2 mm and an outer radius R of 4 mm. A width w of 2 mm and a height h of 1.9 mm were used for this angle. The 120° ECAP channel had an inner radius r of 0.5 mm and an outer radius R of 0.5 mm, and a width w of 2.1 mm and height h of 2 mm were used for this ECAP die. The experiments were performed at different temperatures. For this purpose, holes were made in the channel parts, to enable heating cartridges to be inserted. The temperature was precisely controlled by Type K thermocouples in the respective channel part, using a temperature control unit (hotcontrol cDT+, Hotset GmbH, Germany). The testing temperatures were room temperature (RT), 150, 180, and 210 °C. The specimens were held inside the ECAP tool for 30 s prior to pressing. Previous studies showed that route C in particular displayed good potential for employing ECAP with sheet materials. After the first pass, the ECAP sheets were therefore rotated by 180° around the ECAP axis and again subjected to pressing. To reduce friction during the tests, Bechem Beruforge 150D lubricant was used [14]. Following the ECAP process, the samples were subjected to heat treatment for 4 h at 125 °C plus a further 2 h at 175 °C (referred to as the 6 h treatment). This corresponds to a 75% shorter heat treatment time than the conventional heat treatment used to obtain the T6 specimens.

To determine the mechanical properties of the material at room temperature, tensile specimens (DIN 50125, shape H, width 12.5 mm, and parallel length 75 mm) were machined from both the unprocessed and the ECAP material [15]. The loading direction corresponds to the rolling or ECAP direction, respectively. The specimens were tested in a Zwick ZT150 Allround Line universal testing machine according

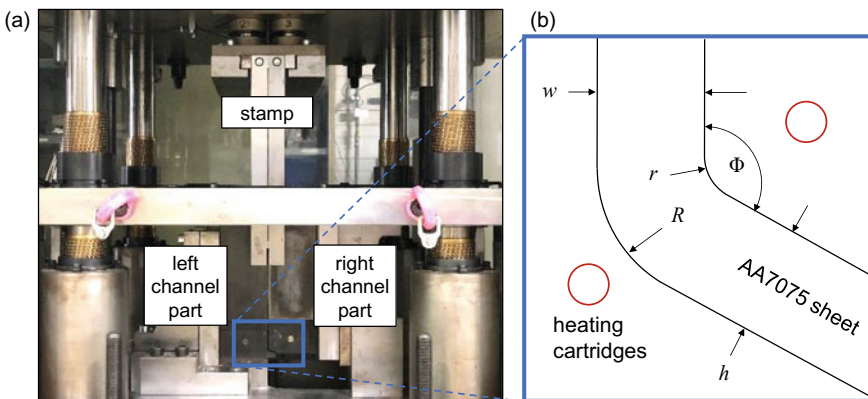


Fig. 1 **a** ECAP tool for sheet metal with a thickness of 1.8 mm; **b** Schematic sketch of the channel geometry and the heating cartridges for the ECAP process under elevated temperatures

to [16]. A test speed of 2.25 mm/min was selected with displacement control. The strain was measured using Digital Image Correlation (DIC) with a GOM Aramis SRX system. Three tests were performed with each setup.

The highly plastic material deformation resulting from ECAP is generally accompanied by an increased driving force for recovery and recrystallization of the microstructures. This circumstance must be taken into account when characterizing the behavior of the ECAP sheets in hot tensile tests [17]. As the low heating rates and long heating cycles of conventionally used chamber furnaces appear unsuitable for the mechanical characterization of thermally unstable microstructures, a resistance-heated test bench was developed, see Fig. 2. The application of an electric current enabled a very high heating rate and significantly reduced or even suppressed the recrystallization and structural transformation effects that would otherwise result from slow heating. The test bench was mounted in a Zwick ZT150 Allround Line universal testing machine. Power was supplied by a pe3000-6-D (Plating electronic GmbH, Germany) DC power station. The current was introduced into the tensile specimen using copper cables and conductors. The conductors were mounted in vertical guides to ensure that the specimen was not affected by transverse forces. Insulation in the clamping jaws enabled a closed circuit and prevented any major heat losses during the test. The current supply was controlled by the specimen temperature. A pyrometer (CT-SF22-C3, Micro-Epsilon Messtechnik GmbH & Co. KG, Germany) was placed at a measuring distance of 200 mm to optically record the actual temperature at the center of the sample. A PID controller was used to process the measured signal in the LabVIEW software and to regulate the current to the nominal temperature specified for the tensile specimen. Errors due to heat transfer and damage to

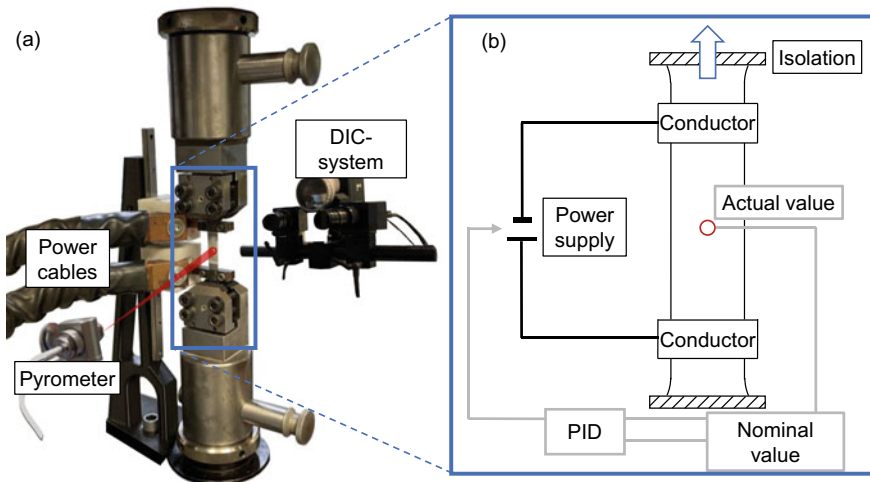


Fig. 2 a Tensile test bench with resistance heating implemented by a DC power supply; b Schematic sketch of the process control; the temperature is measured with a pyrometer and controlled by the electrical current

the specimen were avoided by using non-contact measurement. Since reflections on the aluminum surface can lead to errors in determining the optical temperature, the samples were first coated in a temperature-resistant varnish. The emission coefficient was calibrated iteratively by comparison with welded-on thermocouples, resulting in a value of $\epsilon = 0.96$ (the spectral range of the pyrometer was 8–14 μm) [18]. Since the crosshead of the testing machine moved upwards and the lower specimen clamp remained stationary, the pyrometer also had to be moved upwards to ensure that measurements were always taken at the center of the specimen. This was done using a pulley block to make the pyrometer move at half the test speed. During the test, the strain was measured inline by the GOM Aramis DIC-system. This is important in conductive testing because it means that strain can always be evaluated at the point measured by the pyrometer, which is necessary because the temperatures are at their maximum level in the center of the tensile specimen and decrease slightly toward the outside. The evaluation of the plastic strains is based on the findings of Mueller, who in his studies on resistance heating determined the initial gauge length for the strain calculation as a function of the test temperature [19]. An initial gauge length of 10 mm was used for the temperatures of 180 and 250 $^{\circ}\text{C}$. A temperature-resistant paint was also used to provide a speckle pattern for DIC measurements.

Results and Discussion

Figure 3 shows different ECAP samples after one pass using a channel angle of 110° at different temperatures. In each case, the ECAP direction (ED) for the specimens was from left to right. It was not possible to process the sheet at room temperature because the material’s elongation at fracture was exceeded, and the ECAP test had to be aborted. Other studies have shown that cracking already occurs at a plastic strain of 0.37 for the AA7075 alloy [20]. Iwahashi’s formula is used to calculate the plastic strain φ for ECAP:

$$\varphi = \frac{2 \cot\left(\frac{\phi'}{2} + \frac{\psi}{2}\right) + \psi \operatorname{cosec}\left(\frac{\phi'}{2} + \frac{\psi}{2}\right)}{\sqrt{3}} \tag{1}$$



Fig. 3 ECAP specimens after one pass at different processing temperatures with a channel angle of 110°

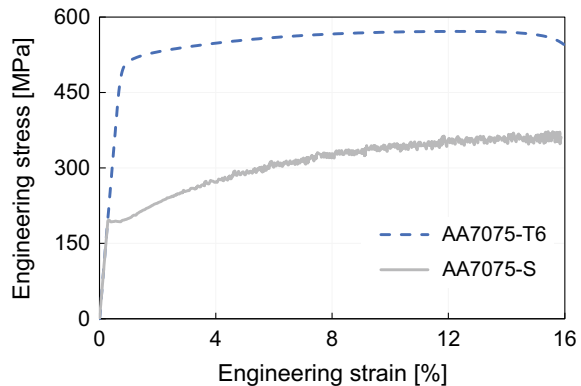
The angle Φ' describes the specimen's deformation at the inner channel radius, while ψ describes the angle at the channel's outer radius [21]. With the given configurations, one ECAP pass for the channel with the 110° die results in a plastic strain of approx. 0.6 ($\Phi' = 110^\circ$, $\psi \approx 61^\circ$). Due to the smaller radii, this value was even higher for the 120° die. The values consequently exceed the reference value of 0.37, which clearly indicates that heating is needed to perform ECAP on the material.

Processing of the sheets was possible at an ECAP temperature of 150°C . However, due to the strong deformation, which was higher at the inner radius than at the outer radius, the sheet was bent. In addition, slight areas of damage can be seen on the surface of the inner channel radius. At an ECAP temperature of 180°C , the sheet was more uniformly deformed, resulting in only a slight curvature of the sheet, such that further processing was unproblematic. The results at an ECAP temperature of 210°C are similar to those obtained at 180°C , and similar behavior is observed with the 120° ECAP die.

Tensile specimens were taken from the sheets in ED and tested. To enable comparison of the ECAP specimens with reference treatments, artificially aged (T6) and solution-annealed (S) specimens were also tested. The results are shown in Fig. 4. A representative sample for each case is presented in the results. In the text, the standard deviation is given. It can be seen that with the T6 treatment, the yield strength (YS) increases by 140%. Also, the ultimate tensile strength (UTS) increases from 358 ± 4.7 MPa to 572 ± 0.5 MPa (+60%), while the elongation at fracture (EF) decreases slightly from $17.4 \pm 1.5\%$ to $16.3 \pm 0.5\%$. It is also noticeable that the solution-annealed specimens exhibit a pronounced yield drop and PLC effect. This is different in the T6 specimens, due to the thermal stabilization of the material [22].

Figure 5a represents the mechanical behavior (in terms of engineering stress–strain curves) of the sheets processed with the ECAP angle 110° . A second ECAP pass could not be performed for a process temperature of 150°C without damaging the sheet, so specimens were only processed at 180°C and 210°C . For an ECAP temperature of 210°C with a post-heat treatment of 6 h (A110 210 6 h), this results in a UTS of 503 ± 5.3 MPa with an EF of $9.4 \pm 1.1\%$. The specimens formed at an

Fig. 4 Engineering stress–strain curves of Aluminum AA7075, artificially aged (T6) and solution-annealed (S)



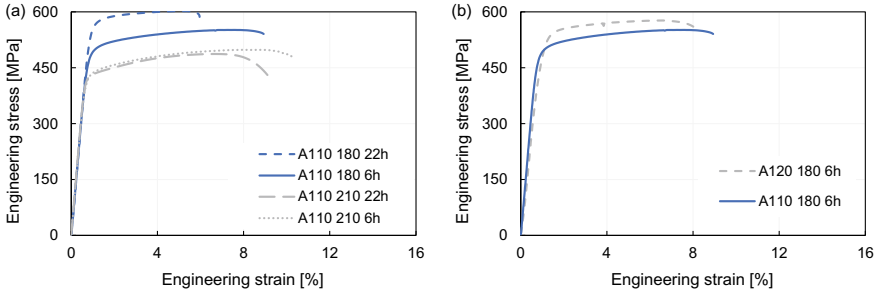


Fig. 5 **a** Engineering stress–strain curves of different parameter setups (ECAP temperature and age treatment) with the ECAP die of 110°; **b** Engineering stress–strain curves with the ECAP die of 110° compared to the 120° die

ECAP temperature of 180 °C and after heat treatment for 6 h exhibit a UTS of 525 ± 35.3 MPa at an EF of $8.9 \pm 1.3\%$ (A110 180 6 h). There is no PLC effect at either forming temperature, which in principle indicates thermal stability of both specimens. For the specimen formed at 180 °C, there is a higher strength with slightly lower EF. Both effects are due to a higher defect density (dislocation density and formation of substructures) as a result of the greater strain hardening at the lower temperature. A time reduction of 75% can thus be achieved compared with T6 heat treatment, and similar strengths can be obtained by the ECAP process at an ECAP temperature of 180 °C. The considerable reduction of the ECAP specimen in EF compared to the T6 condition is due to defects in the microstructure introduced during the deformation of the material. Due to the low thickness of the sheet materials, these defects have an even greater effect on the elongation at fracture than is the case with bulk material in conventional ECAP. For conventional ECAP of AA7075, Shaeri et al. concluded that ECAP performed at lower temperatures is more effective for grain refinement than pressing at high temperatures [23]. The increase in grain size as the ECAP temperature increases can be attributed to dynamic recovery processes and grain growth [24].

Moreover, for both ECAP temperatures, specimens were also tested at the same temperature and duration as for the T6 treatment (22 h treatment). For an ECAP temperature of 210 °C, a slight reduction in the mechanical properties can be observed (A110 210 22 h). For an ECAP temperature of 180 °C, the longer treatment leads to a further increase in strength with further reduced EF (A110 180 22 h). The reason for the negligible effect of the aging treatment on the mechanical properties of the specimen at higher ECAP temperature (210 °C) can be based on dynamic strain aging during the ECAP process at elevated temperatures [25]. Shaeri et al. found this effect already occurred at an ECAP temperature of 120 °C. This may be due to the increased deformation and finer grains resulting from the use of back pressure in the ECAP process in their study.

Figure 5b shows the mechanical properties with the 120° ECAP tool compared to the 110° tool. The specimens formed with an ECAP temperature of 180 °C and

the 120° channel angle exhibit a UTS of 585 ± 10 MPa and an EF of $8 \pm 0.2\%$. The increase in strength and lower EF again suggest an increased density of defects in the microstructure. This is consistent with the results of the calculation using Iwahashi's formula.

The results show that the mechanical properties at room temperature can be adjusted within certain limits by performing ECAP on aluminum sheets with subsequent heat treatment. The process times can be shortened using the described procedure, but only limited improvements in properties can be achieved. These findings can also be found in a similar form for bulk material [20]. However, the ratio of sheet thickness to width for sheet materials with ECAP means that damage in the material has a greater influence than is the case for bulk material with conventional ECAP. This means that the elongation at fracture is lower than with conventional ECAP. For example, in order to test more ECAP runs and lower process temperatures without failure of the material, Shaeri et al. use a back pressure of 180 MPa [25]. This approach could also be used for ECAP of sheet materials to obtain further improvements in terms of material properties and will be investigated in future studies of sheet materials.

To demonstrate the potential with regard to hot forming processes, additional tests were carried out at elevated temperatures. First, the suitability of the resistance heating used is demonstrated. Figure 6 shows the temperature and current curve of a tensile test on an aluminum AA7075-T6 at 180 °C. The temperature at the beginning of the test exceeds that at the end of the test. It can be seen that the temperature drops slightly for the first 20 s at the beginning of the test. This range coincides with the elastic range of the tested specimen and can be attributed to the Joule-Thompson effect. Vitzthum et al. previously demonstrated this effect for sheet materials [26]. Subsequently, there are only small changes in the temperature. The measured unsmoothed temperature signal lies in a range of maximum 178.5 and 182.5 °C. According to the DIN EN ISO 6892-2 standard, for temperatures below

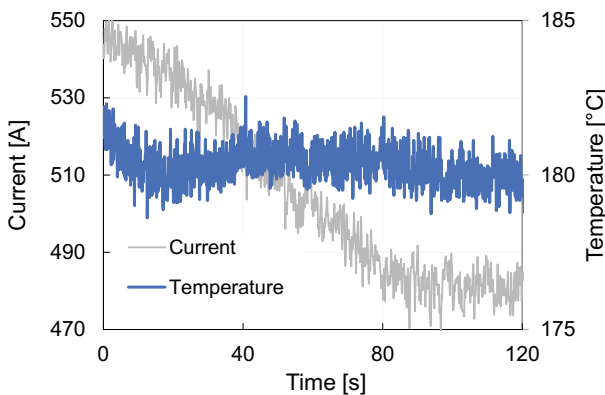


Fig. 6 Temperature and current measurement of a heated tensile test of the material AA7075-T6 at 180 °C

600 °C, a temperature variation of the test of ± 3 °C must be observed [27]. This dimension can be maintained for each of the tests carried out. The current intensity is reduced over the duration of the experiment as the cables and conductors heat up and the electrical resistance decreases. Thus, a lower amperage is required to heat both the system and the specimen.

Due to the complex ECAP process and the complexity of the heated tensile tests, three valid tests could not always be performed. This is indicated in the text. Figure 7 shows the engineering stress–strain curves for the reference material AA7075-T6 at 180 and 250 °C. At 180 °C, UTS is 334 ± 8.6 MPa and EF is $32.7 \pm 0.6\%$. For 250 °C, the values are 177.4 ± 7.7 MPa and $29 \pm 2.3\%$. This is in line with the observations of Shojaei et al., who argued that the strength decreases for the increased temperature because higher deformation temperatures increase the dislocation motion, thus favoring dynamic softening mechanisms [28].

Figure 8a shows the engineering stress–strain curves for the reference material AA7075-T6 under 180 °C and an ECAP specimen formed with the 110° tool at 180 °C. The ECAP specimen shows a slightly increased UTS of 360 ± 1.4 MPa and an EF of $31.8 \pm 0.5\%$ (two tested specimens). The peculiarity of the curve is that the specimen reaches its maximum very quickly after the yield point and then drops. This behavior was observed by Sajadifar et al. for thermo-mechanically processed specimens at a tensile test temperature of 250 °C [3]. That this behavior occurs already at a temperature of 180 °C in the materials studied here suggests a more strongly deformed microstructure prior to the heated tensile test.

Finally, the mechanical properties were tested at 250 °C, see Fig. 8b. Here, a further increase in elongation to $43.4 \pm 0.4\%$ is shown for the specimens processed with the 110° ECAP die at an ECAP temperature of 180 °C (two tested specimens). For this temperature, three samples of the 120° die were also tested, showing that a further increase in elongation to a value of $53.1 \pm 1.6\%$ is possible. While the heat-treated reference material already failed at strains of about 30% at both forming temperatures, the ECAP specimens for higher forming temperatures achieved progressively higher

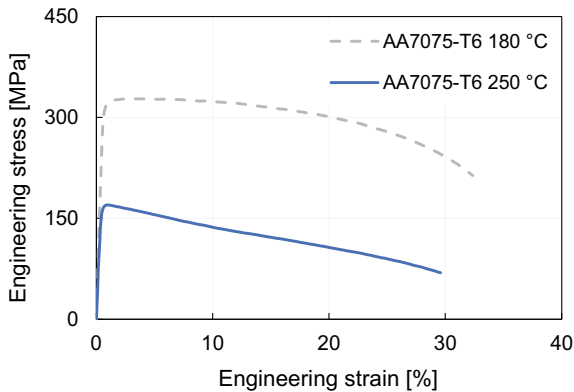


Fig. 7 Engineering stress–strain curves for AA7075-T6 at 180 and 250 °C

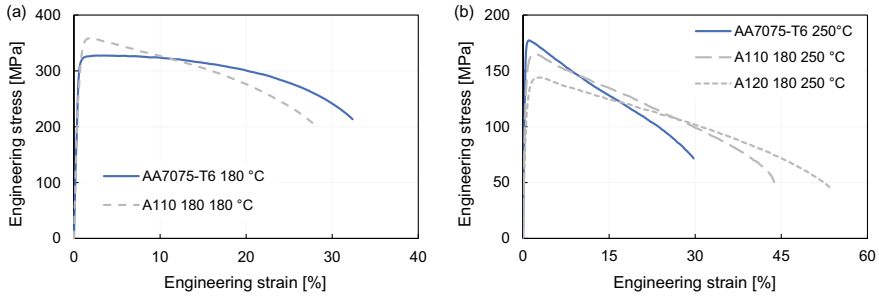


Fig. 8 **a** Engineering stress–strain curves at 180 °C for AA7075-T6 and ECAP processed specimens with the 110° channel die at 180 °C ECAP temperature; **b** Engineering stress–strain curves for AA7075-T6 and ECAP processed specimen with the 110° and 120° channel die at 250 °C

strains as a function of temperature. According to Zhou et al. this effect can be attributed to a finer microstructure. The activation of grain boundaries at elevated temperatures also results in improved dislocation slip with multiple slip systems for the fine-grained microstructures [28, 29]. Grain boundary sliding (GBS) is regarded as the main mechanism in superplastic forming and can be observed at temperatures high enough for grain boundary diffusion mechanisms to be effective [30, 31]. Future work may consider this potential in the industrialization and economic utilization of the ECAP process.

Conclusion and Outlook

In the present study, ECAP tests were performed on high-strength AA7075 sheets. It was shown that the mechanical properties at room temperature can be adjusted by control of both the geometry of the ECAP channel and the ECAP temperature. The process time can be reduced by 75% compared with that for T6 heat treatment. The literature research showed that back pressure in the ECAP process can potentially be used to improve the mechanical properties even further. In addition, a conductive heated tensile test bench was developed to demonstrate the potential for hot forming processes. Due to the deformed microstructure, strains can be increased by up to 80% in the ECAP sheets at a temperature of 250 °C. Further in-depth microstructural investigations need to be carried out to provide experimental proof of the mechanisms and relationships suggested in this work. Such an analysis will be the subject of follow-up studies.

Acknowledgements The authors gratefully acknowledge the funding by the German Research Foundation (Deutsche Forschungsgemeinschaft, DFG) in supporting this work within the framework of the collaborative research projects VO 1487/32-2 and WA 2602/13-2. A big thank you also goes to Philipp Leitner and Gylxhane Maqedonci, who contributed to the control of the heated tensile test in their student research projects.

References

1. Jaeger H, Gude M (2019) Lightweight materials in tomorrow's automotive industry. *Lightweight Des Worldwide* 12:20–23. <https://doi.org/10.1007/s41777-019-0065-9>
2. Tisza M, Czinege I (2018) Comparative study of the application of steels and aluminium in lightweight production of automotive parts. *Int J Lightweight Mater Manuf* 1(4):229–238. <https://doi.org/10.1016/j.ijlmm.2018.09.001>
3. Sajadifar SV, Scharifi E, Weidig U, Steinhoff K, Niendorf T (2020) Performance of thermo-mechanically processed AA7075 alloy at elevated temperatures—from microstructure to mechanical properties. *Metals* 10(7):884. <https://doi.org/10.3390/met10070884>
4. Noder J, George R, Butcher C, Worswick MJ (2021) Friction characterization and application to warm forming of a high strength 7000-series aluminum sheet. *J Mater Process Technol* 293(38):e117066. <https://doi.org/10.1016/j.jmatprotec.2021.117066>
5. Kilic S, Kacar I, Sahin M, Ozturk F, Erdem O (2019) Effects of aging temperature, time, and pre-strain on mechanical properties of AA7075. *Mat Res* 22(5):4273. <https://doi.org/10.1590/1980-5373-mr-2019-0006>
6. Omer K et al (2018) Process parameters for hot stamping of AA7075 and D-7xxx to achieve high performance aged products. *J Mater Process Technol* 257:170–179. <https://doi.org/10.1016/j.jmatprotec.2018.02.039>
7. Bruder E (2019) Formability of ultrafine grained metals produced by severe plastic deformation—an overview. *Adv Eng Mater* 21(1):1–18. <https://doi.org/10.1002/adem.201800316>
8. Wagner MF-X, Nostitz N, Frint S, Frint P, Ihlemann J (2020) Plastic flow during equal-channel angular pressing with arbitrary tool angles. *Int J Plast* 134. <https://doi.org/10.1016/j.ijplas.2020.102755>
9. Iwahashi Y, Furukawa M, Horita Z, Nemoto M, Langdon TG (1998) Microstructural characteristics of ultrafine-grained aluminum produced using equal-channel angular pressing. *Metall Mater Trans A* 29A:2245–2252
10. Suh J et al (2014) Improvement of ductility at room temperature of Mg-3Al-1Zn alloy sheets processed by equal channel angular pressing. *Proc Eng* 81(2):1517–1522. <https://doi.org/10.1016/j.proeng.2014.10.183>
11. Gruber M, Illgen C, Frint P, Wagner MF-X, Volk W (2019) Numerical and experimental study on ECAP-processing parameters for efficient grain refinement of AA5083 sheet metal. *KEM* 794:315–323. <https://doi.org/10.4028/www.scientific.net/KEM.794.315>
12. Illgen C, Frint P, Gruber M, Volk W, Wagner MF-X (2020) Evolution of grain refinement in AA5083 sheet metal processed by ECAP. In: *Light metals. The minerals, metals and materials series*. Springer International Publishing, Cham, pp 362–369
13. Gruber M, Yang Y, Illgen C, Frint P, Wagner MF-X, Volk W (2021) Thermomechanical analysis and experimental validation of ECAP for aluminum sheet metal. In: *Forming the future. The minerals, metals and materials series*. Springer International Publishing, Cham, pp 1775–1790
14. Frint P, Wagner MF-X, Weber S, Seipp S, Frint S, Lampke T (2017) An experimental study on optimum lubrication for large-scale severe plastic deformation of aluminum-based alloys. *J Mater Process Technol* 239:222–229. <https://doi.org/10.1016/j.jmatprotec.2016.08.032>
15. DIN 50125 (2004) Prüfung metallischer Werkstoffe – Zugproben
16. DIN EN ISO 6892-1 (2014) Metallische Werkstoffe – Zugversuch – Teil 1: Prüfverfahren bei Raumtemperatur
17. Zhao YH, Liao XZ, Jin Z, Valiev RZ, Zhu YT (2004) Microstructures and mechanical properties of ultrafine grained 7075 Al alloy processed by ECAP and their evolutions during annealing. *Acta Mater* 52(15):4589–4599. <https://doi.org/10.1016/j.actamat.2004.06.017>
18. Gerhardt KW (2015) Untersuchungen zur konduktiven Erwärmung für Warmzugversuche an Blechen. Dissertation, Shaker Verlag GmbH
19. Müller K (1999) Werkstoffkundliche Qualifizierung des Randschichthärtens mit Laserstrahlung. Dissertation, Fakultät für Angewandte Naturwissenschaften, Universität Bayreuth

20. Fritsch S, Hockauf M, Schönherr R, Hunger S, Meyer LW, Wagner MF-X (2010) Untersuchungen zum Einfluss von ECAP und Tieftemperaturwalzen auf die mechanischen Eigenschaften der Aluminiumlegierung 7075. *Mat Werkstofftech* 41(9):697–703. <https://doi.org/10.1002/mawe.201000655>
21. Iwahashi Y, Wang J, Horita Z, Nemoto M, Langdon TG (1996) Principle of equal-channel angular pressing for the processing of ultra-fine grained materials. *Scripta Mater* 35(2):143–146
22. Thevenet D, Mliha-Touati M, Zegloul A (1999) The effect of precipitation on the Portevin-Le Chatelier effect in an Al–Zn–Mg–Cu alloy. *Mater Sci Eng A* 266:175–182
23. Shaeri MH, Salehi MT, Seyyedein SH, Abutalebi MR, Park JK (2014) Microstructure and mechanical properties of Al-7075 alloy processed by equal channel angular pressing combined with aging treatment. *Mater Des* 57(4):250–257. <https://doi.org/10.1016/j.matdes.2014.01.008>
24. Cardoso KR, Travessa DN, Botta WJ, Jorge AM (2011) High strength AA7050 Al alloy processed by ECAP: microstructure and mechanical properties. *Mater Sci Eng A* 528(18):5804–5811. <https://doi.org/10.1016/j.msea.2011.04.007>
25. Shaeri MH, Shaeri M, Salehi MT, Seyyedein SH, Abutalebi MR (2015) Effect of equal channel angular pressing on aging treatment of Al-7075 alloy. *Progress Natl Sci Mater Int* 25(2):159–168. <https://doi.org/10.1016/j.pnsc.2015.03.005>
26. Vitzthum S, Hartmann C, Eder M, Volk W (2019) Temperature-based determination of the onset of yielding using a new clip-on device for tensile tests. *Proc Manuf* 29(1):490–497. <https://doi.org/10.1016/j.promfg.2019.02.166>
27. DIN EN ISO 6892-2 (2011) Metallische Werkstoffe - Zugversuch - Teil 2: Prüfverfahren bei erhöhter Temperatur
28. Shojaei K, Sajadifar SV, Yapici GG (2016) On the mechanical behavior of cold deformed aluminum 7075 alloy at elevated temperatures. *Mater Sci Eng A* 670:81–89. <https://doi.org/10.1016/j.msea.2016.05.113>
29. Zhou M, Lin YC, Deng J, Jiang Y-Q (2014) Hot tensile deformation behaviors and constitutive model of an Al–Zn–Mg–Cu alloy. *Mater Des* 59:141–150. <https://doi.org/10.1016/j.matdes.2014.02.052>
30. Langdon TG (1982) The mechanical properties of superplastic materials. *Metall Trans A* 13A:689–701
31. Illgen C, Bohne B, Wagner MF-X, Gruber M, Volk W, Frint P (2021) Facing the issues of sheet metal equal-channel angular pressing: a modified approach using stacks to produce ultrafine-grained high ductility AA5083 sheets. *Adv Eng Mater* 1:2100244. <https://doi.org/10.1002/adem.202100244>

Part III
**Characterization of Polymers, Composites,
Coatings and Ceramics**

Application of Flue Gas Desulfurization Waste for the Production of Geopolymer Tiles



M. T. Marvila, A. R. G. Azevedo, F. D. Gama, E. B. Zanelato, S. N. Monteiro, and C. M. F. Vieira

Abstract Geopolymers are eco-friendly materials that efficiently replace cementitious and ceramic materials. In this context, the objective of this work was to carry out the production of geopolymer tiles using commercial metakaolin (MK) and flue gas desulfurization waste (FGD). The tiles were produced in the molar ratio $\text{SiO}_2/\text{Al}_2\text{O}_3 = 3.00$, using a composition with 0, 10, and 20% substitution of metakaolin by FGD. Prismatic specimens were produced, with tests of tensile strength, mass density, water absorption, and linear shrinkage being carried out. Curing was carried out at 25 and 65 °C for a period of 7 days. The results obtained demonstrate that the use of FGD improved the mechanical behavior of the tiles, due to the formation of phases different from geopolymerization of metakaolin alone. It is concluded that the application of geopolymer tiles with FGD is viable, as the values obtained are compatible with the proposed application.

Keywords Ceramics · Mechanical properties · Geopolymers

M. T. Marvila (✉) · F. D. Gama · C. M. F. Vieira
LAMAV – Advanced Materials Laboratory, UENF – State University of the Northern Rio de Janeiro, Av. Alberto Lamego, 2000, Campos dos Goytacazes, Rio De Janeiro 28013-602, Brazil

F. D. Gama
e-mail: 00118110311@pq.uenf.br

C. M. F. Vieira
e-mail: vieira@uenf.br

A. R. G. Azevedo · E. B. Zanelato
LECIV – Civil Engineering Laboratory, UENF – State University of the Northern Rio de Janeiro, Av. Alberto Lamego, 2000, Campos dos Goytacazes, Rio De Janeiro 28013-602, Brazil

S. N. Monteiro
Department of Materials Science, IME – Military Institute of Engineering, Square General Tibúrcio, 80, Rio de Janeiro 22290-270, Brazil

Introduction

Geopolymers are materials that are gaining more prominence in the development of new building components, due to the properties obtained by these materials [1, 2]. In general, they can be applied replacing Portland cement, being applied in the production of mortars and concrete, or even in replacement of ceramic materials, obtained by calcining clays [3, 4].

The advantages obtained by using these materials are related to high mechanical strength, at short ages, low porosity, and low water absorption, consequently increasing the durability of the material [5]. They also have the advantages of high performance in situations of saturation and high temperatures [6] and the possibility of immobilizing hazardous waste [7].

The geopolymerization process is complex, but it can be simplified as a reaction that takes place between two essential components: a precursor rich in aluminosilicates, and an alkaline liquid solution called an activator [8]. During the step of mixing the two components, the alkaline solution dissolves the phases present in the precursor, originating species of the aluminate and silicate type. These species condense and enter into chemical equilibrium, forming elongated chains called gels. These materials are sequentially reorganized, crystallized, and hardened, forming long chains of inorganic polymers, of high strength and brittleness [2].

Depending on the chemical composition of the precursor, the molarity of the alkaline solution, and the conditions of temperature and pressure, geopolymers can originate different hardened products, known as zeolites [9]. This process can be used in the production of geopolymer tiles, which substitute ceramic tiles, with the advantage of high mechanical properties and durability.

Some relevant works have already proven the possibility of using geopolymers in roof tiles, as mentioned below: Marvila et al. [6] evaluated the performance of geopolymer tiles produced with metakaolin and sodium hydroxide and silicate solution in durability situations and varying the $\text{SiO}_2/\text{Al}_2\text{O}_3$ molar ratio. Azevedo et al. [10] and Azevedo et al. [11] evaluated the possibility of using glass waste as a complementary precursor to metakaolin in geopolymer tiles, obtaining satisfactory results in mechanical strength and durability. Thus, the feasibility of applying geopolymeric materials used as roof tiles is proven.

The aim of this article is to evaluate the effect of the incorporation of flue gas desulfurization waste (FGD) on the properties of geopolymer tiles produced with commercial metakaolin (MK). FGD is a material rich in calcium, different from MK, presenting a type of reaction that complements this commercial precursor. Therefore, the use of FGD together with MK presents a great potential for application in the development of geopolymer tiles, as investigated in this work.

Table 1 Chemical composition of precursors

Precursor	SiO ₂	Al ₂ O ₃	CaO	Na ₂ O	K ₂ O	SO ₃	Cl	Others
MK	58.5	33.6	3.25	1.17	0.88	–	–	2.60
FGD	0.51	0.17	45.63	1.23	0.41	38.28	8.44	4.33

Table 2 Compositions studied

Composition (%)	MK	FGD	Sand	Sodium hydroxide	Sodium silicate	Water
0	535.80	0.00	535.80	140.71	7.01	316.47
10	482.22	53.58	535.80	140.71	7.01	316.47
20	428.64	107.16	535.80	140.71	7.01	316.47

Materials and Methods

The materials used in the production of geopolymer tiles are MK, a commercial precursor with high aluminosilicate content, as seen in Table 1. FGD was also used as a supplemental precursor. This material has high levels of calcium, but it also has appreciable amounts of sulfates, which can harm the geopolymerization process, as shown in Table 1.

The other materials used were sodium hydroxide in microbeads, with 99% purity, and sodium silicate with a silica modulus of 3.50. The compositions used presented a SiO₂/Al₂O₃ molar ratio fixed at 3.00, varying the FGD content by 0, 10, and 20%, replacing the MK contents, as shown in Table 2.

The specimens were produced through molding using prismatic geometry 120 × 30 × 20 mm³. The geopolymers were cured at room temperature at 25 °C (normal) and through thermal curing in an oven at 65 °C (thermal). The specimens were kept in this curing condition for 7 days, being subsequently tested for mass density, linear shrinkage, water absorption by immersion, and tensile strength in bending. The procedures followed the recommendation of NBR 15310 [12].

Results and Discussion

Figure 1 shows the results of flexural strength. It is observed that thermal curing favors an increase in the material's strength, which is associated with an increase in molecular agitation during thermal curing. The geopolymerization reaction requires contact between the components that form the final product [2, 6]. Therefore, increasing the degree of agitation increases the degree of contact between the materials, which promotes an increase in strength.

Furthermore, it is possible to observe the increase in resistance as the percentage of FGD utilization increases. This is related to the type of reaction that occurs in

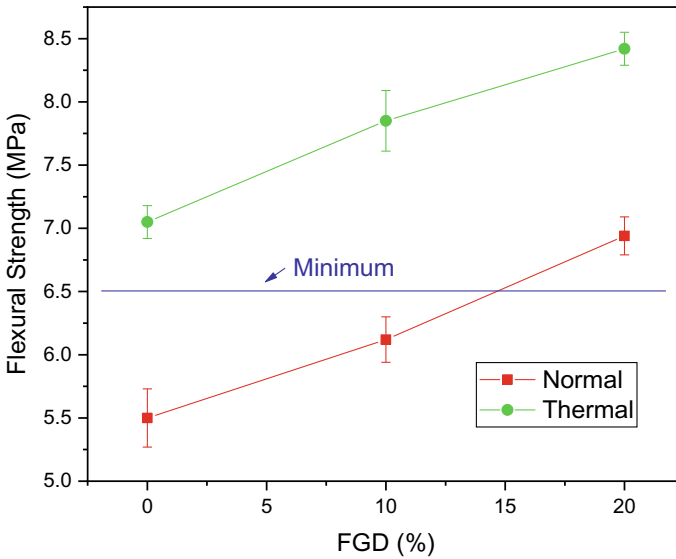


Fig. 1 Flexural strength of geopolymers tiles

the alkaline activation of FGD, a calcium-rich precursor. This type of precursor forms complementary products to those formed during the geopolymerization of MK, consequently generating a network stronger than the 0% composition. Some publications recommend a minimum strength of 6.5 MPa for flexural strength in tile applications [13, 14]. It is observed that the normal 20% composition meets this requirement and that all thermal compositions also meet this requirement.

Figure 2 shows the water absorption results obtained for the geopolymer tiles. It is observed that the compositions evaluated in thermal cure present greater water absorption, due to the loss of constitution water promoted by this type of cure. Furthermore, it is observed that the use of FGD reduces water absorption, which is directly related to the reduction of porosity promoted by waste, due to the formation of more compact networks. All compositions present water absorption below 20%, recommended by the Brazilian standard and other publications in the area [14, 15].

Figure 3 presents the linear shrinkage results, while Fig. 4 presents the mass density results. It is observed that the linear shrinkage of geopolymer tiles is very low, less than 0.30%, different from what occurs in the production of ceramic tiles. This is because ceramic tiles are obtained through the formation of a liquid phase, which promotes large geometric changes in the material produced [16, 17]. Geopolymer tiles, on the other hand, are obtained through a process that promotes minor changes in the material's geometry. In addition, the use of sand helps to control shrinkage, indicating a great feasibility of applying the studied tiles. In the case of density, it is observed that the results are compatible with the values obtained for water absorption, where the denser compositions are those with less water absorption, consequently being less porous.

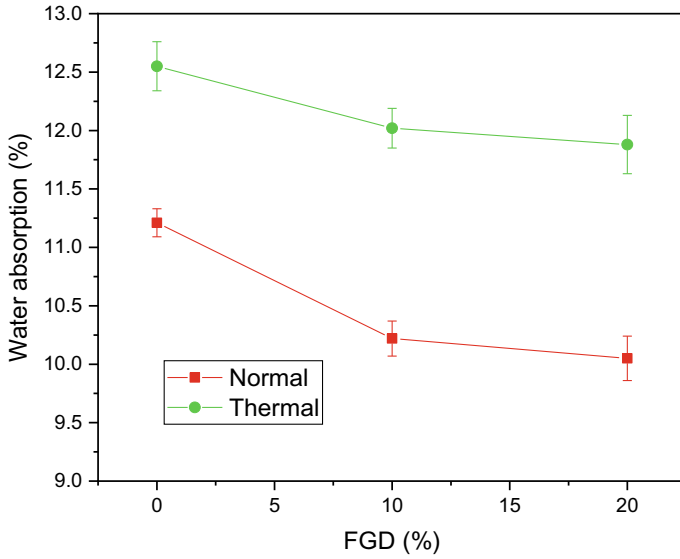


Fig. 2 Water absorption of geopolymers tiles

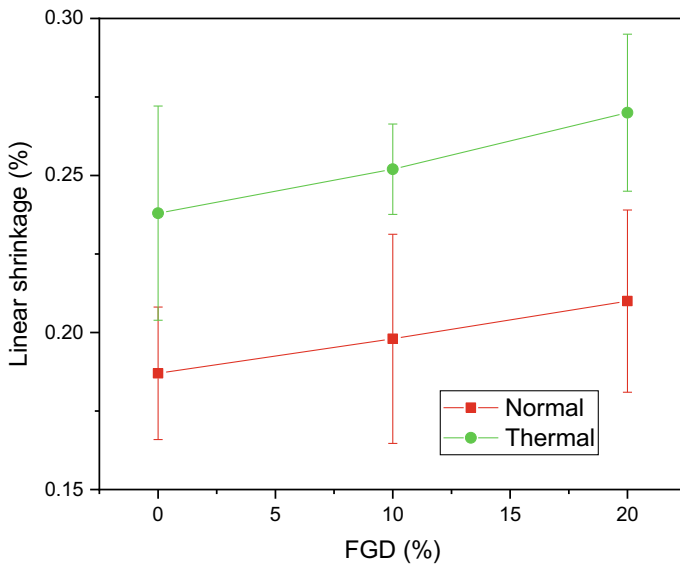


Fig. 3 Linear shrinkage of geopolymers tiles

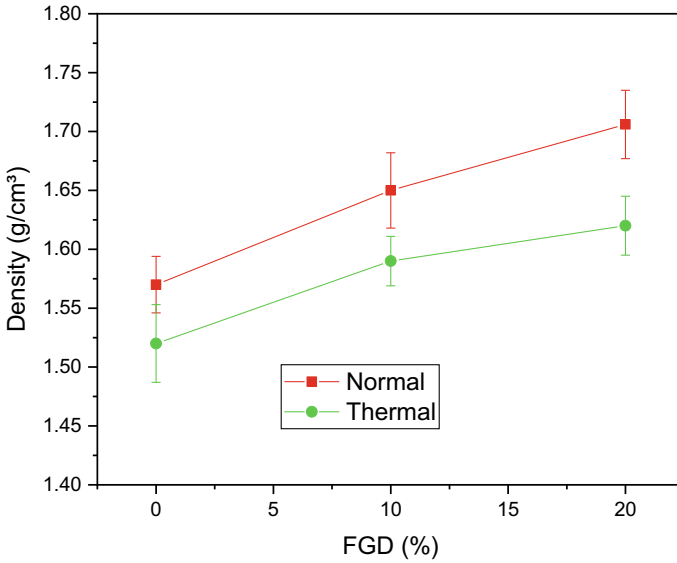


Fig. 4 Density of geopolymer tiles

Figure 5 illustrates the appearance of specimens with 20% FGD, cured in normal and thermal cure. It is observed that the lower part of the composition in normal cure has a darker phase, indicating that the geopolymerization happened only superficially. In the case of the thermally cured composition, the appearance of the specimen is more uniform, which suggests that the geopolymerization was more intense, and not just superficial. Therefore, this figure proves the pattern that was observed in Fig. 1, where the results of flexural strength are presented.



Fig. 5 Illustration of geopolymer tile specimens with 20% FGD

Conclusion

After the results, it can be concluded that:

- The use of 20% FGD as a supplemental precursor to MK is indicated for the production of geopolymer tiles, because it promotes an increase in flexural strength and a reduction in water absorption.
- The increase in properties observed with the use of FGD is attributed to the formation of a more complex, resistant, and less porous network, because the alkaline activation of FGD, a calcium-rich precursor, is different from the geopolymerization of MK, forming complementary products.
- Thermal curing increases the degree of molecular agitation and promotes increased geopolymerization of the tiles, improving flexural strength, but also promoting increased water absorption, at values compatible with the proposed application.
- Density and linear shrinkage values obtained are compatible with the application proposed in this study and enable the use of FGD as a supplemental precursor to MK in geopolymeric tiles.

Acknowledgements The authors thank the Brazilian agencies: CNPq, CAPES, and FAPERJ for the support provided to this investigation.

References

1. Palomo A, Krivenko P, Garcia-Lodeiro I, Kavalerova E, Maltseva O, Fernández-Jiménez A (2014) A review on alkaline activation: new analytical perspectives. *Mater Const* 64:e022
2. Marvila MT, Azevedo ARG, Vieira CMF (2021) Reaction mechanisms of alkali-activated materials. *Rev IBRACON Estruturas Mater* 14(3):1–26
3. Marvila MT, Azevedo ARG, Matos PR, Monteiro SN, Vieira CMF (2021) Rheological and the fresh state properties of Alkali-activated mortars by blast furnace slag. *Materials (Basel)* 14:2069
4. Azevedo ARG, Vieira CMF, Ferreira WM, Faria KCP, Pedroti LG, Mendes CB (2020) Potential use of ceramic waste as precursor in the geopolymerization reaction for the production of ceramic roof tiles. *J Build Eng* 29:101156
5. Marvila MT, Azevedo ARG, Matos PR, Monteiro SN, Vieira CMF (2021) Materials for production of high and ultra-high performance concrete: review and perspective of possible novel materials. *Materials (Basel)* 14:4304
6. Marvila MT, Azevedo ARG, Delaqua CGC, Mendes BC, Pedroti LG, Vieira CMF (2021) Performance of geopolymer tiles in high temperature and saturation conditions. *Constr Build Mater* 286:122994
7. Xia M, Muhammad F, Zeng L, Li S, Huang X, Jiao B, Shiao YC, Li D (2019) Solidification/stabilization of lead-zinc smelting slag in composite based geopolymer. *J Clean Prod* 209:1206–1215
8. Lahoti M, Tan KH, Yang EH (2019) A critical review of geopolymer properties for structural fire-resistance applications. *Constr Build Mater* 221(2019):514–526

9. Rozek P, Krol M, Mozgawa W (2019) Geopolymer-zeolite composites: a review. *J Clean Prod* 230(2019):557–579
10. Azevedo ARG, Marvila MT, Rocha HA, Cruz LR, Vieira CMF (2020) Use of glass polishing waste in the development of ecological ceramic roof tiles by the geopolymerization process. *Int J Appl Ceram Technol*. <https://doi.org/10.1111/ijac.13585>
11. Azevedo ARG, Marvila MT, Oliveira LB, Ferreira WM, Colorado H, Teixeira SR, Vieira CMF (2021) Circular economy and durability in geopolymers ceramics pieces obtained from glass polishing waste. *Int J Appl Ceram Technol*. <https://doi.org/10.1111/ijac.13780>
12. NBR 15310 (2005) Componentes cerâmicos, Telhas, Terminologia, requisitos e métodos de ensaio
13. Marvila MT, Azevedo ARG, Alexandre J, Zanelato EB, Azerede NG, Simonassi NT, Monteiro SN (2019) Correlation between the properties of structural clay blocks obtained by destructive tests and ultrasonic pulse tests. *J Build Eng* 26(1):100869
14. Girondi GD, Marvila MT, Azevedo ARG, Souza CC, Souza D, Brito J, Vieira CMF (2020) Recycling potential of powdered cigarette waste in the development of ceramic materials. *J Mater Cycles Waste Manag* 22(2020):1672–1681
15. Girondi GD, Marvila MT, Souza D, Sanchez Rodriguez RJ, Colorado HA, Vieira CMF (2020) Evaluation of the application of macrophyte biomass *Salvinia auriculata* Aublet in red ceramics. *J Environ Manag* 275:111253
16. Marvila MT, Azevedo ARG, Alexandre J, Vieira CMF, Zanelato EB, Delaqua GCG, Xavier GC, Monteiro SN (2020) Study of the compressive strength of mortars as a function of material composition, workability, and specimen geometry. *Model Simul Eng* 2020:1–6
17. Azevedo ARG, França BR, Alexandre J, Marvila MT, Zanelato EB, Xavier GC (2018) Influence of sintering temperature of a ceramic substrate in mortar adhesion for civil construction. *J Build Eng* 19(2018):342–348

Lowering the Presence of Heavy Metals in Textured Coat Using Recycled Post Consumer Glass



A. O. Adejo, A. D. Garkida, C. M. Gonah, and E. V. Opoku

Abstract Four extender batches of 95.7% recycled post consumer glass, 0.25% colourant, and 4% acrylic binder each were processed into extenders of yellow, blue, red, and black separately. Textured coat batches of 20.1% solvent, 12.0% binder, 67.0% extender, 0.2% natrosol, 0.2% texanol, 0.2% biocides, and 0.1% ammonia were developed and characterized using atomic absorption spectroscopy (ASTM D3335). Results showed that yellow coat has concentration of 170.65 ± 0.031 ppm lead (Pb), 3.40 ± 0.025 ppm cobalt (Co), and 24.25 ± 0.08 ppm cadmium (Cd); red coat has concentration of 27.25 ± 0.015 ppm lead, 0.30 ± 0.045 ppm cobalt, and 9.85 ± 0.065 ppm cadmium; blue coat has concentration of 115.15 ± 0.125 ppm Pb, 0.30 ± 0.01 ppm Co, and 9.85 ± 0.065 ppm Cd while black coat has concentration of 33.10 ± 0.37 ppm Pb, 1.70 ± 0.01 ppm Co, and 0.30 ± 0.02 ppm Cd. This study shows that recycled post consumer glass can be employed to produce textured coats with lower concentrations of heavy metals for buildings as compared to contemporary textured coats whose concentrations are greater than 90 ppm for Pb, 100 ppm for Cd, and 100 ppm for Co.

Keywords Heavy metals · Recycled post consumer glass · Textured coat

Introduction

Coating also known as paint is a generic name that describes any material which when applied to the surface of an object (substrate) leaves behind a thin layer of the

A. O. Adejo (✉)

Department of Glass and Silicate Technology, Federal University of Lafia, Lafia, Nasarawa State, Nigeria

A. D. Garkida · C. M. Gonah

Department of Glass and Silicate Technology, Ahmadu Bello University, Kaduna, Nigeria

E. V. Opoku

Department of Industrial Design, Ahmadu Bello University, Kaduna, Nigeria

© The Minerals, Metals & Materials Society 2022

M. Zhang et al. (eds.), *Characterization of Minerals, Metals, and Materials 2022*,

The Minerals, Metals & Materials Series,

https://doi.org/10.1007/978-3-030-92373-0_5

film upon drying and has decorative, functional qualities, or both [1]; this construction material is basically used on structures and buildings and they are applied using spray, trowel, rollers, brush, or any other desired equipment as the need arise. Textured coat is a kind of coating material with special effect upon their substrate of application; this kind of coatings has a heavy consistency and consists of grains of sand and/or gypsum which are bound by a water-thinned binder and are characterised by a rough effect upon application. This property of the coat (heavy consistency and thickness) accounts for its wide range of usage which ranges from covering of joints in drywall, painting drywall without priming to mention but a few [2]; this kind of coat can exist in different degrees of roughness such as smooth texture paint, sand texture paint, premixed sand texture paint, self(post)-mixing texture paint, knockdown texture paint, popcorn texture paint, orange peel texture paint, splatter knockdown texture, hawk and trowel, skip trowel, slap brush texture, and so on.

Paint or coating is one of the outstanding sources of heavy metals in the environment [3]. Recycled post consumer glass or Post consumer recycled glass is a category of post consumer waste that is composed of glass that has been discarded as waste by the consumer, and they are also referred to as cullet when they exist in granular form as a result of crushing [4]. With the use of lead-based additives during its manufacturing, it serves as the major contributor of metal such as lead in the coat [5]. However, the additives used in paint and coat manufacturing contain not only lead but also other heavy metals [6]. Though, Lead has attracted a considerable number of studies due to its pronounced negative effects on children in particular [7]. Exposure to the heavy metals occurs after the material drywall becomes susceptible to peeling off [3] due to contact with any object unintended or intended as during renovations [8] or construction work [9]. As such, heavy metals enter the environment by the natural and anthropogenic means [10], and they are absorbed into the human body through inhalation, ingestion, and skin absorption leading to accumulations, though gradual, and over a period of time, they are faster than the body tissue can detoxify thereby leading to build up of toxins within the human system which leads to the severe pulmonary and gastrointestinal irritant, causing damages to the central nervous system, kidney, liver, and reproductive system [11].

In the study of Ogilo et al. [11], it was found that heavy metals are present in both dust and paint chip samples from residential houses which is a source of concern as most of the coats in the study exhibit the presence of heavy metals that are above the World Health organization standard (WHO). Apanpa-Qasim et al. [12] examined the presence of Lead and Cadmium in Water-based Paints Marketed in Nigeria, specifically sold in Lagos and Ibadan, regardless of the type of paint result shows that the coats contain a high presence of heavy metals that is beyond the permissible limits of 100 and 90 ppm as stipulated by European Union (EU), United States (US) Consumer Product Safety Commission and also the Standards Organization of Nigeria (SON) [13]. Owing to the various studies conducted on the presence of heavy metals in coats, there is a need to mitigate the presence of heavy metals in coats through the introduction of recycled post consumer glass in developing textured coats with the view to lowering the presence of heavy metals so as to achieve a safe

coat that has no heavy metals or amounts that are within the acceptable limits as stipulated by acceptable standards.

Methodology

Using the mass colouration technique [14], Samples of beneficiated recycled post consumer glass (RPCG) was processed into four coloured extenders of black, blue, red, and yellow in a composition of 4 g of styrene-acrylic binder, 0.25 g of pigments (i.e., each of carbon black, copper-phthalocyanine, metalize azo red, and monoarylide yellow), and 91.75 g of RPCG. This was mixed thoroughly for 20 min in a plastic container until the RPCG is completely covered with the colourant and finally subjected to drying for 3 h at room temperature.

A textured coat from the developed extenders was produced using a composition of 20.1 g of water and 0.5 g of hydroxyl ethyl cellulose (natrosol) and was mixed for 5 min until no lump was found. Also, 0.4 g each of biocides and texanol was added to the composition, 18.0 g of styrene-acrylic and 0.2 g of ammonia were also added to the composition, and they were all uniformly mixed for 10 min to form a gelatinous solution. Finally, 60.0 g of the extender was added to the composition, mixed for another 20 min, and the coat was produced. These procedures were carried out separately on each of the developed extenders to produce a textured coat of colours yellow, red, blue, and black, respectively.

The developed coat was subjected to a viscosity test in order to determine the workability of the coat according to American Standard for Testing Material (ASTM) D4741-13 [15]. 40 g of the produced RPCG coat was measured and filled into a viscometer cup of model-35 viscometer, the spindle was inserted into the cup filled with the coat in it and it was allowed to spin until it reached a stoppage point, and the result was recorded. This procedure was conducted separately for the different types of the developed coats (i.e., yellow, red, blue, and black). Specific gravity test was conducted in line with ASTM D854-14 [16] to determine the density of the coat, empty specific gravity cup was weighed and recorded, it was filled with water and the weight was recorded separately, again the empty bottle was filled with the produced coat and it was recorded, and finally, the weight of the bottle, produced coat, and water was determined and recorded; this procedure was repeated for the various colours of coats developed.

The atomic absorption spectroscopy (AAS) analysis was conducted to determine the presence of heavy metals in the coat as stipulated by ASTM D3335 [17], dried coat samples were digested as follows, 0.6 g of the dry sample of coat was weighed and transferred into 200 ml crucible, and 7.5 ml of nitric acid (HNO_3) and 2.5 ml of sulfuric acid (H_2SO_4) were weighed and poured into the crucible, respectively. The sample was placed on a heating mantle and it was heated at a temperature range of 100–200 °C for 30 min to allow complete digestion of sample, the mixture was filtered into a 100 ml volumetric flask, and distilled water was added to the distillate to make up 30 ml of the concentration. The Agilent 280FS AAS equipment was

used to investigate the presence of Pb in the coat, and the AAS instrumentation was calibrated using distilled water and set to standard using 10, 20, and 30 ml of Pb concentration part per million (Conc. ppm) after which the sample was analysed. In the case of Co, like Pb, the equipment was calibrated using distilled water and it was set to standard using 2, 4, and 6 ml of Cobalt Conc. ppm, and the sample was analysed to check for the presence of Co. The same procedure was carried out for Cd at a set standard 1, 2, and 3 ml of Cd Conc. ppm, and the sample was analysed to check for the presence of Cd in the developed coat.

Results and Discussion

Treatment of Recycled Post Consumer Glass (RPCG) with Colourants

The study explored the colouration of RPCG with pigments that are composed of primary colours and carbon black; this was done in a bid to create coloured granules of extenders for the textured coat production. Results from the study show that using the mass colouration technique, an excellent yield of colouration shade on RPCG was achieved with light and wet fastness [18] (Figs. 1, 2, 3 and 4).

Fig. 1 Treated RPCG with monoarylide yellow pigment (azo yellow) (Color figure online)

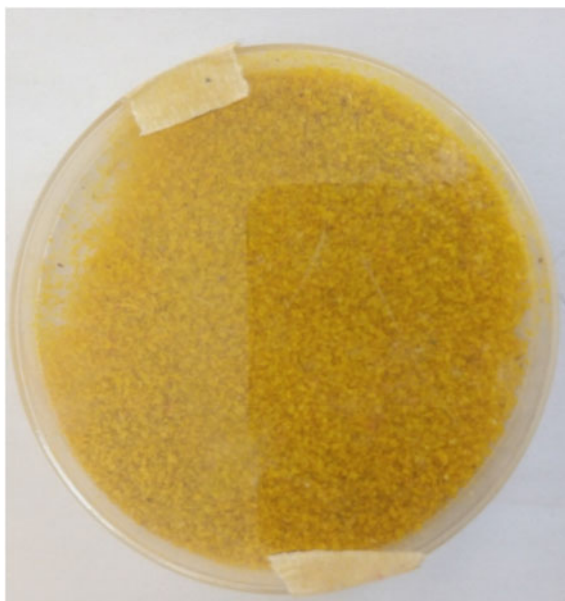


Fig. 2 Treated RPCG with metallic azo red pigment (azo red) (Color figure online)

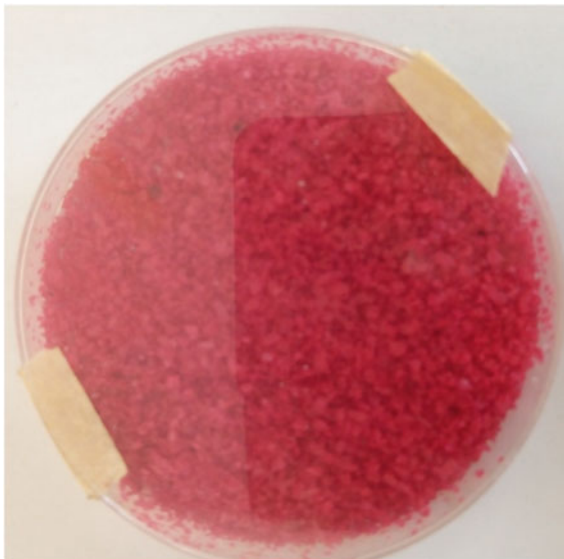
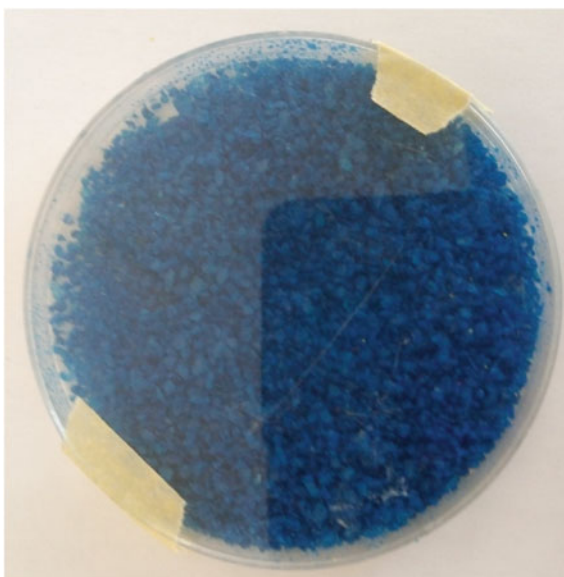


Fig. 3 Treated RPCG with copper phthalocyanine blue pigment (Color figure online)



Textured Coat Produced Using Recycled Post Consumer Glass

Using coat-making raw materials with the processed RPCG, a batch for glass coat was formed and the production of building coat was possible into the desired colouration (see Figs. 5, 6, 7 and 8). An exploration of the coverage rate shows that 100 g of the

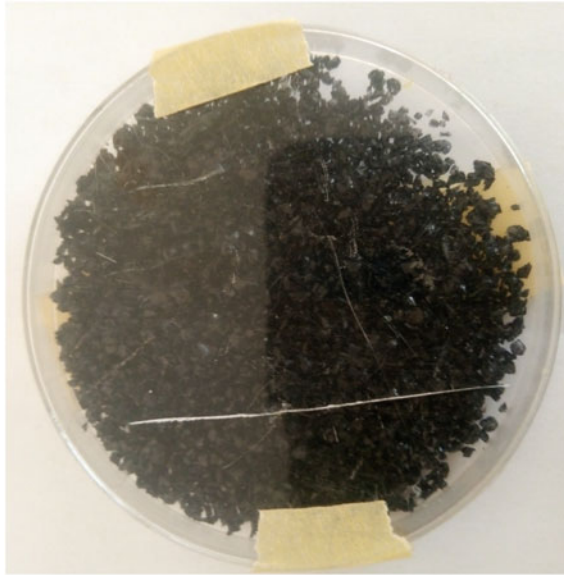


Fig. 4 Treated flint PCG with carbon black pigment



Fig. 5 Sample of yellow glass coat produced from RPCG (Color figure online)



Fig. 6 Sample of red glass coat produced from RPCG (Color figure online)

produced coat has the ability to cover a space of 28.0 cm by 7.2 cm (i.e., 201.6 cm²) with an excellent coverage rate regardless of its colour, thereby establishing the fact that glass, like other extending materials, is a suitable material to produce glass coat of any kind and colour [19–21].



Fig. 7 Sample of blue glass coat produced from RPCG (Color figure online)



Fig. 8 Sample of black glass coat produced from RPCG

Viscosity Test

This study shows the level of fluidity of the coat viz-a-viz its workability and orange peeling upon drying, irrespective of the type of parent material (i.e., RPCG) or the processed raw material that was used in the production of the coat. The study shows a uniform result of viscosity value as seen in Table 1, implicating that the produced coat's workability falls within the standard level of 40 ± 5 poise. Also, since the extender used is not fluid absorbing, an excellent binding ability that does not accommodate orange peel effects upon drying was observed. This is in line with the view of Ajayi et al. [19] study that states that, for any material to be used as coating and finish, it must have a viscosity that is not more than 40 ± 5 poise [22] as supported by the ASTM D4741-13 [15] and Nigerian Industrial Standard ICS: 87.040 [23].

Table 1 Viscosity rate of produced coat

S/N	Sample of RPCG coat	Viscosity (centi poise)
1	Yellow coat	36
2	Red coat	36
3	Blue coat	36
4	Black coat	36

Table 2 Specific gravity of produced coat

S/N	Sample	Specific gravity
1	Yellow coat	1.27
2	Red coat	1.27
3	Blue coat	1.27
4	Black coat	1.27

Specific Gravity Test

Considering the result of the specific gravity test carried out on the coat (see Table 2), the study shows that irrespective of the coat type (interior and exterior) and colour, the produced coat has a specific gravity that falls within the 1–1.5 standard range as ascertained by ASTM. This means that the coats produced are less dense and have the tendency of giving out water through the process of evaporation when applied on the desired surfaces [24].

Atomic Absorption Spectroscopy (AAS) Analysis on Produced Post Consumer Glass Coat

The result of the AAS analyses (see Table 3) conducted show that the produced coats from recycled RPCG regardless of their colour contain some amounts of heavy metals with variations in the quantity of the presence of the heavy metal. The presence of Pb in the coat falls within the range of 33.10–170.65 ppm, Co falls within the range of 1.70–3.40 ppm while that of Cd also falls within the range of 0.30–24.25 ppm, respectively. Based on colour classification of the produced coats, the yellow coat both for interior and exterior use has the highest presence of heavy metals; the red coat has the lowest value of Pb and Co while the black coat has the lowest presence of Cd in the entire produced coats. In comparison with the permissible limits of heavy metals (Pb, Co, and Cd) [1, 12, 25–27], red and black coats fall within the permissible limit of Pb presence in coat of 90 ppm; yellow, red, blue, and black coats fall within the permissible limit of Cd in coat of 100 ppm; and yellow, red, blue, and black coat falls within the permissible limit of Co presence in coat of 100 ppm.

Table 3 Atomic absorption spectroscopy of the coat

S/N	Coat in colouration	Lead (Pb) (ppm \pm SD)	Cobalt (Co) (ppm \pm SD)	Cadmium (Cd) (ppm \pm SD)
1	Yellow	170.65 \pm 0.31	3.40 \pm 0.025	24.25 \pm 0.08
2	Red	27.25 \pm 0.015	0.30 \pm 0.045	9.85 \pm 0.065
3	Blue	115.15 \pm 0.125	0.30 \pm 0.01	20.35 \pm 0.005
4	Black	33.10 \pm 0.37	1.70 \pm 0.01	–0.30 \pm 0.02

Conclusion

In conclusion, this study established that recycled post consumer glass can be employed as a suitable extender material for the development of textured coat based on the result of the viscosity of 35 poise and specific gravity analysis of 1.27. Also, that the developed coat exhibits lower concentrations of heavy metals for buildings as compared to contemporary textured coats whose concentrations are greater than 90 ppm for Pb, 100 ppm for Cd, and 100 ppm for Co.

References

1. World Health Organization (WHO) (2010) Global Alert and response. Nigeria: mass lead poisoning from mining activities, Zamfara state. www.who.int/csr/don/2010_07_07/en/index.html. Accessed 18 Aug 2020
2. Howarth GA, Manock HL (1997) Water-borne polyurethane dispersions and their use in functional coatings. *Surf Coat Int* 80(7):324–328. <https://doi.org/10.1007/bf02692680>. ISSN: 1356-0751
3. Dixon SL, Gaitens JM, Jacobs DE, Strauss W, Nagaraja J, Pivetz T et al (2009) Exposure of U.S. children to residential dust lead, 1999–2004: II. The contribution of lead contaminated dust to children's blood lead levels. *Environ Health Perspect* 117(3):468–474
4. Dhanashri (2017) Different types of texture paints techniques-how to paint. <https://aapkapainter.com/blog/what-is-texture-painting-and-types/>. Accessed 25 Aug 2021
5. Gaitens JM, Dixon SL, Jacobs DE, Nagaraja J, Strauss W, Wilson JW et al (2009) Exposure of U.S. children to residential dust lead, 1999–2004: I. Housing and demographic factors. *Environ Health Perspect* 117(3):461–467
6. Brokbarold M, Wischermann M, Marschner B (2012) Plant availability and uptake of lead, zinc, and cadmium in soils contaminated with anti-corrosion paint from pylons in comparison to heavy metal contaminated urban soils. *Water Air Soil Pollut* 223:199–213
7. Gupta A, Gauri SK (2013) Determination of optimal quantities of different types of driers for addition in the batches of paint formulation. *Int J Eng Sci Technol* 5(4):1–13
8. Jacobs DE, Clickner RP, Zhou JY, Viet SM, Marker DA, Rogers JW et al (2002) The prevalence of lead-based paint hazards in U.S. housing. *Environ Health Perspect* 110(10):599–606
9. Spanier AJ, Wilson S, Ho M, Hornung R, Lanphear BP (2013) The contribution of housing renovation to children's blood lead levels: a cohort study. *Environmental health: a global access science source. Environ Health* 12:72–80
10. Ming-Ho Y (2005) *Environmental toxicology: biological and health effects of pollutants*, 2nd edn. Chap. 12. CRC Press LLC, Boca Raton, USA. ISBN 1-56670-670-2
11. Ogilo JK, Onditi AO, Salim AM, Yusuf AO (2017) Assessment of levels of heavy metals in paints from interior walls and indoor dust from residential houses in Nairobi City County, Kenya. *Chem Sci Int J* 21(1):1–7. Article no. CSIJ.37392, ISSN: 2456-706X
12. Apanpa-Qasim AFI, Adebola AA, Sandeep MN, Karthik R, Prasant T (2016) Examination of lead and cadmium in water-based paints marketed in Nigeria. *J Health Pollut* 6(12):43–49
13. Pruss-Ustun A, Corvalan C (2016) Preventing disease through healthy environments: towards an estimate of the environmental burden of disease [Internet], Geneva, Switzerland: World Health Organization. www.who.int/quantifying_ehimpacts/publications/preventingdisease.pdf
14. Janalta Interactive (2018) Post-consumer waste. <https://www.safeopedia.com/definition/2347/post-consumer-waste>

15. ASTM D4741-13 (2013) Standard test method for measuring viscosity at high temperature and high shear rate by tapered-plug viscometer, ASTM International, West Conshohocken, PA. www.astm.org
16. ASTM D854-14 (2014) Standard test methods for specific gravity of soil solids by water pycnometer, ASTM International, West Conshohocken, PA. www.astm.org
17. ASTM D3335-85a (2014) Standard test method for low concentrations of lead, cadmium, and cobalt in paint by atomic absorption spectroscopy, ASTM International, West Conshohocken, PA. www.astm.org
18. Asim K, Choudhury R (2017) Sustainable chemical technologies for textile production. Sustainable Fibres and Textiles. <https://doi.org/10.1016/B978-0-08-102041-8.00010-X>, IKPS Institute of Polytechnic, Belmuri, West Bengal, India; 2Ex-professor, Government College of Engineering and Textile Technology, Serampore, West Bengal, India
19. Ajayi O, Ajekwene KK, Keren C (2015) DN Mayer raw material specification according to standard organization of Nigeria (SON). Oregon Lagos
20. Nwuzor IC, Igwe IO (2016) Extender properties of some Nigerian clays. *J Miner Mater Charact* 04(05):279–291. <https://doi.org/10.4236/jmmce.2016.45025>
21. Umunakwe IJ, Umunakwe R, Nwigwe US, Popoola VA, Oyeturji A (2020) Properties evaluation of interior decorative emulsion paint produced using local extenders obtained from Akure, Ondo State, Nigeria. *Eur J Mater Sci Eng* 05(01):17–22. <https://doi.org/10.36868/ejmse.2020.05.01.017>
22. Akinterinwa A, Osemeahon SA, Nkafamiya II, Dass PM (2015) Formulation of emulsion paint from a copolymer composite of dimethylol urea/polystyrene. *Chem Mater Res* 7(7):20–26
23. Standards Organisation of Nigeria (2008) Specifications for emulsion paints for decorative purposes. Nigerian Industrial Standard ICS: 87.040
24. Arewa JA, Alor EO, Akpoguma (2018) Extration of soya bean oil for the formulation of oil and emulsion paint. *Sci Res J*. <https://doi.org/10.313364/SCRJ/v6.i12.2018.P1218596>
25. United State Consumer Product Safety Commission (US CPSC) (2009) FAQs: lead in paint (and other surface coatings). <https://www.cpsc.gov/en/Business-Manufacturing/Business-Education/Lead/FAQs-Lead-In-Paint-And-Other-Surface-Coatings>
26. European Union (2016) Specifies restriction limit for cadmium in certain paints. SGS, Geneva, Switzerland. <http://www.sgs.com/en/news/2016/02/safeguards-04316-eu-specifies-restriction-limit-for-cadmium-in-certain-paints-under-reach>
27. Standard Organization of Nigeria (SON) (2016) Stakeholders partner on lead reduction in paints Lagos, Nigeria. <http://son.gov.ng/son-stakeholders-partner-on-lead-reduction-in-paints>

Microstructural Characterisation of AA5083 in AA5083/SiC Co-Continuous Ceramic Composites (C4) Fabricated by Gravity and Gas Pressure Infiltration



Georgia Warren, Jianshen Wang, Krishna Shankar, V. Krishnaraj,
A. S. Prasanth, R. Ramesh, and Juan Pablo Escobedo-Diaz

Abstract The microstructures of AA5083 in AA5083/SiC co-continuous ceramic composites (C4) fabricated by gas pressure infiltration with 10 and 20 PPI SiC foams and by gravity infiltration with 10 PPI SiC foam were characterized. The porosity and hardness were evaluated through optical microscopy and Vickers hardness testing. This paper examines the effects of pressure and SiC foam pore size on the microstructural properties of AA5083 in these composites. AA5083 in the 10 PPI composite fabricated by gas pressure infiltration had a smaller average grain size, higher average hardness, and lower average porosity than in the 10 PPI composite fabricated by gravity infiltration. It also had a larger average grain size and higher average hardness and porosity than in the 20 PPI composite fabricated by gas pressure infiltration. Hardness was observed to increase with decreasing distance from areas of SiC within each composite.

Keywords Co-continuous ceramic composites (C4) · Gas pressure infiltration · Liquid–metal infiltration · AA5083 · SiC foam

G. Warren · J. Wang · K. Shankar · J. P. Escobedo-Diaz (✉)
School of Engineering and Information Technology, University of New South Wales, Canberra,
Australia
e-mail: j.escobedo-diaz@unsw.edu.au

V. Krishnaraj · A. S. Prasanth
Department of Production Engineering, PSG College of Technology, Coimbatore, India

R. Ramesh
Department of Mechanical Engineering, PSG Institute of Technology and Applied Research,
Coimbatore, India

Introduction

There has been a significant investigation into the use of ceramic/metal interpenetrating composites for wear applications in recent years due to their high strength, toughness, stiffness, and resistance to wear, distortion, corrosion, and thermal shock [1–3].

Ceramic/metal interpenetration also has applications in the aerospace and armour domains in which weight reduction while retaining strength and dimensional stability is a major concern. In armour, the crack bridging properties and interlocking microstructural features of ceramic/metal composites may reduce the need for both a front and backing face plate to retard the striking force and absorb the residual kinetic energy of a projectile. This would in turn reduce both weight and processing complexities and increase the ability of ballistic protection systems to withstand multiple impacts [4].

Aluminium appears to be the preferred metal for ceramic/metal interpenetrating composites and SiC the preferred ceramic when compared with B_4C , Si_3N_4 , TiB_2 , and TiC in terms of both mechanical properties and ease and cost of manufacture [4, 5]. Co-continuous ceramic composites are also preferred over particle-reinforced composites as they allow for a higher proportion of ceramic [6, 7]. SiC/Al–Cu particle-reinforced and SiC/Al co-continuous ceramic composites have been used to produce brake discs where the latter exhibited better wear resistance with half the density of cast iron and steel [8, 9].

Gravity infiltration has been reported as an effective method of fabricating Al/SiC co-continuous ceramic composites [10, 11] though volumetric contraction of the alloy during solidification can reduce the quality of interfacial bonding between metal and ceramic. Gas pressure infiltration is therefore suggested as the preferred method of fabricating metal/ceramic co-continuous ceramic composites to enhance interfacial bonding [12].

Vijayan et al. [13] discuss a novel approach to the fabrication of AA5083/SiC co-continuous ceramic composite by gas pressure infiltration and analyse the composite's synthesis, microstructural properties, and mechanical behaviour in comparison with SiC foam. The AA5083/SiC co-continuous ceramic composite was fabricated in a custom-made Ar gas-based pressure chamber in which SiC foam was preheated to 750 °C before the addition of AA5083 ingot slices for melting. Upon addition of the AA5083, the melt was then superheated to 795 °C, atmospheric air was evacuated from the chamber, and Ar gas was purged to the sealed pressure chamber to a pressure of 4 bars for gas pressure infiltration and 1 bar for gravity infiltration. The results of the study by Vijayan et al. [13] included successful fabrication of the AA5083/SiC co-continuous ceramic composite, analysis of the chemical composition of the SiC foams and AA5083 alloy, microstructural and metallographic analysis of the 10 and 20 PPI SiC foams and composite samples, and macroscopic failure analysis of the composite samples.

The aim of this study is to characterise and compare the microstructural properties and mechanical behaviour of the AA5083 alloy in samples of AA5083/SiC co-continuous ceramic composite fabricated by gas pressure infiltration with 10 and 20 PPI SiC foams and by gravity infiltration with 10 PPI SiC foam. To this end, porosity measurements, microstructural examination, and hardness testing of the AA5083 alloy in each of the three groups of composite samples were carried out to determine the effects of both pressure and SiC foam pore size on the microstructural properties of the AA5083 in each group.

Materials and Methods

Materials

Co-Continuous SiC Foams

Co-continuous SiC foams were used as the ceramic preforms in both gravity and gas pressure infiltration to fabricate the AA5083/SiC co-continuous ceramic composites investigated in this study. The composites fabricated by gas pressure infiltration used two different foam pore sizes of 10 and 20 pores per inch. Only 10 PPI SiC foam was used in the composite fabricated by gravity infiltration.

The average densities of the 10 and 20 PPI SiC foams were calculated by measuring their masses and volumes, respectively. The 10 PPI SiC foams prior to infiltration had an average density of 443.399 kg/m³ while the 20 PPI SiC foams prior to infiltration had an average density of 468.865 kg/m³. According to this data, the 20 PPI SiC foams had a higher average density than the 10 PPI SiC foams by 25.466 kg/m³.

Aluminium Alloy

During both gravity and gas pressure infiltration, SiC foams were infiltrated with AA5083. The chemical composition of this alloy is shown in Table 1. Samples of AA5083 following heat treatment were subjected to both optical microscopy and Vickers hardness testing in this study.

Co-Continuous Ceramic Composite

Samples of the AA5083 co-continuous ceramic composite investigated in this study were fabricated using both gravity and gas pressure infiltration. The aims of the

Table 1 Chemical composition of AA5083 aluminium alloy [13]

Element	Mg	Mn	Fe	Si	Cr	Ti	Cu	Zn	Al
Percent composition (%)	4.43	0.55	0.24	0.13	0.094	0.058	0.02	0.02	Balance [94.458]

study were to compare the two fabrication methods and identify any differences in the composite caused by using 10 and 20 PPI SiC foams for gas pressure infiltration.

Metallographic Sample Preparation

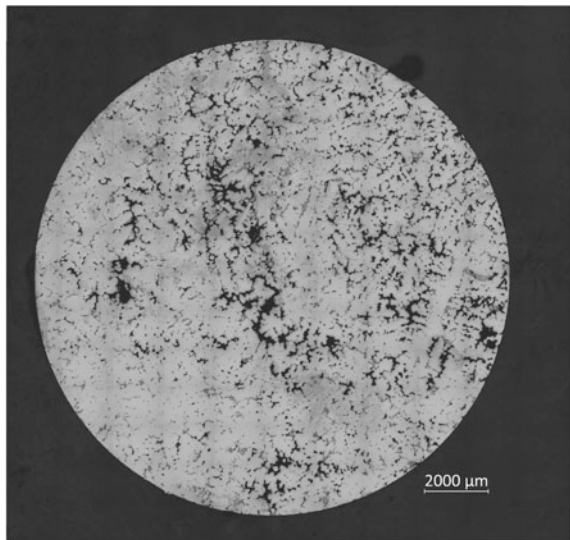
Both the AA5083 and AA5083/SiC co-continuous ceramic composite samples were cut with a Buehler IsoMet Low Speed Saw using a 102 mm IsoCut CBN LC Wafering Blade and IsoCut Fluid as the coolant. All samples were ground and polished on a Struers Tegramin-25 before being automatically cleaned in a Struers Lavamin. The samples were further polished in a Buehler VibroMet 2 Vibratory Polisher Machine set to an amplitude of 30% for 240 min. They were then rinsed with distilled water followed by ethanol and lightly dried with compressed air. Finally, all samples were individually submerged in a beaker of distilled water and cleaned in an ultrasonic cleaner for 3 min each.

Microstructural and Mechanical Property Analysis

Optical Microscopy

All AA5083 and A5083/SiC co-continuous ceramic composites were examined (Figs. 1, 2, 3 and 4) on a ZEISS Axio Imager 2.M2m. Images were captured with a ZEISS AxioCam MRc digital camera for optical microscopy using ZEISS ZEN 3.2

Fig. 1 AA5083 sample after heating without infiltration



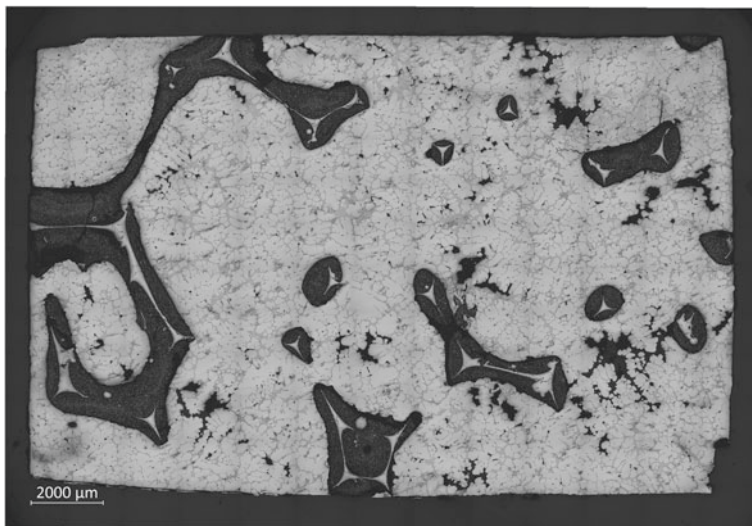


Fig. 2 10 PPI AA5083/SiC co-continuous ceramic composite sample fabricated by gas pressure infiltration

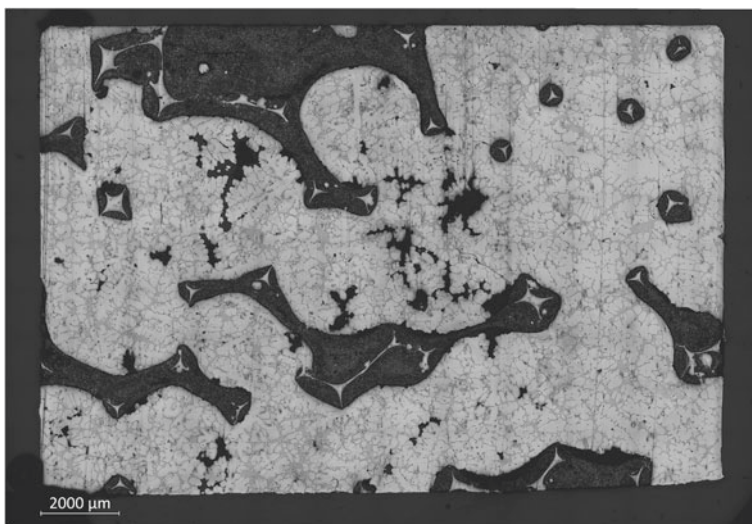
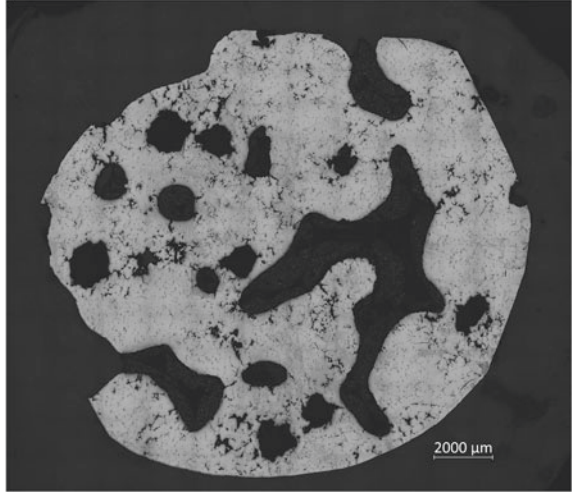


Fig. 3 20 PPI AA5083/SiC co-continuous ceramic composite sample fabricated by gas pressure infiltration

Fig. 4 10 PPI AA5083/SiC co-continuous ceramic composite sample fabricated by gravity infiltration



(ZEN pro) microscope software. Area fraction measurement was performed on each sample using ImageJ software to determine the area fractions of SiC and AA5083 present in each sample.

Vickers Hardness Testing

Vickers hardness testing was performed on all AA5083 and AA5083/SiC co-continuous ceramic composite samples using a Shimadzu HMV-G21 Micro Vickers Hardness Tester. Indentation hardness measurements were recorded approximately every 2 mm along both the horizontal and vertical axes of the samples with care taken to avoid direct contact of the indenter with SiC.

Results

Area Fraction Measurement

SiC Area Fraction

The highest average area fraction of SiC was in the 20 PPI composite with an average area fraction of 31.3% followed by the 10 PPI composite fabricated by gravity infiltration with an average area fraction of 30.4%. The lowest average area fraction of SiC was in the 10 PPI composite fabricated by gas pressure infiltration with an average area fraction of 26.2%.

Comparing the 10 and 20 PPI composite samples fabricated by gas pressure infiltration, the 20 PPI sample had a higher average area fraction of SiC than the 10 PPI sample by 5.1%. Comparing the 10 PPI composite samples, the composite fabricated by gravity infiltration had a higher average area fraction of SiC than the sample fabricated by gas pressure infiltration by 4.3%.

Porosity

The AA5083 alloy samples after heating without infiltration had an average porosity of 8.6%. Both gravity and gas pressure infiltration of SiC foam with AA5083 alloy caused a reduction in average porosity from that of the AA5083 alloy. The greatest reduction in average porosity was in the 20 PPI composite with a reduction of 5.9% or 68.2% of the alloy's original porosity followed by the 10 PPI composite fabricated by gas pressure infiltration with a reduction of 5.6% or 65.6% of the alloy's original porosity. The least reduction in average hardness was in the 10 PPI composite fabricated by gravity infiltration with a reduction of 5.0% or 58.1% of the alloy's original porosity.

Comparing the 10 and 20 PPI composite samples fabricated by gas pressure infiltration, the AA5083 in the 20 PPI sample had a lower average porosity than the 10 PPI sample by 0.22%. Comparing the 10 PPI composite samples, the AA5083 in the sample fabricated by gas pressure infiltration had a lower average porosity than the sample fabricated by gravity infiltration by 0.65%.

Mechanical Property Analysis

Hardness

The AA5083 alloy samples after heating without infiltration had an average hardness of 79 HV. Both gravity and gas pressure infiltration of SiC foam with AA5083 alloy caused a reduction in average hardness from that of the AA5083 alloy. The greatest reduction in average hardness was in the 20 PPI composite with a reduction of 15.6 HV or 19.7% followed by the 10 PPI composite fabricated by gravity infiltration with a reduction of 6.6 HV or 8.3%. The least reduction in average hardness was in the 10 PPI composite fabricated by gas pressure infiltration with a reduction of 5.3 HV or 6.7%.

Comparing the 10 and 20 PPI composite samples fabricated by gas pressure infiltration, the AA5083 in the 10 PPI sample had a higher average hardness than the 20 PPI sample by 14.7 HV. Comparing the 10 PPI composite samples, the AA5083 in the sample fabricated by gas pressure infiltration had a higher average hardness than the sample fabricated by gravity infiltration by 1.3 HV.

Discussion

In this study, four main quantitative properties were investigated to inform the discussion as to the effects of pressure and SiC foam size on the microstructural properties of AA5083 in AA5083/SiC co-continuous ceramic composites. These properties were SiC foam density, SiC area fraction, AA5083 porosity, and AA5083 hardness. The average values of these properties for each sample group are ranked in Table 2 for ease of comparison. Observations were also made as to the grain sizes of AA5083 in each sample group and AA5083 hardness approaching and moving further away from areas of SiC in each sample.

In all sample groups, infiltration of SiC foam with AA5083 alloy resulted in a decrease in average porosity and hardness of the AA5083 alloy. The greatest reduction in average porosity was in the 20 PPI composite fabricated by gas pressure infiltration with a reduction of 68.2% of the alloy's original porosity, followed by the 10 PPI composite fabricated by gas pressure infiltration with a reduction of 65.62% and the 10 PPI composite fabricated by gravity infiltration with a reduction of 58.1%. The greatest reduction in average hardness was in the 20 PPI composite fabricated by gas pressure infiltration with a reduction of 19.7% of the alloy's original average hardness followed by the 10 PPI composite fabricated by gravity infiltration with a reduction of 8.3% and the 10 PPI composite fabricated by gas pressure infiltration with a reduction of 6.7%.

The decrease in porosity of the AA5083 during infiltration can be attributed to the stresses the alloy experiences as it moves through the SiC foam which cause the collapse of pores within the alloy. These stresses are particularly pronounced with the additional application of pressure to the alloy in gas pressure infiltration resulting in further decreases in porosity. The decrease in hardness can then be attributed to the alloy being divided into smaller conglomerated volumes during infiltration. These smaller individual volumes are less compacted than one large volume of aluminium due to there being less force due to gravity on each individual volume which causes a decrease in hardness.

Table 2 Ranked average microstructural properties of each AA5083/SiC co-continuous ceramic composite. #1 represents the highest and #3 the lowest values

	20 PPI gas pressure infiltration	10 PPI gas pressure infiltration	10 PPI gravity infiltration
SiC foam density	#1 468.865 kg/m ³	#2 443.399 kg/m ³	#2 443.399 kg/m ³
SiC area fraction	#1 31.287%	#3 26.162%	#2 30.443%
AA5083 porosity	#3 2.737%	#2 2.960%	#1 3.607%
AA5083 hardness	#3 63.5 HV	#1 73.8 HV	#2 72.5 HV
AA5083 grain size	#3	#2	#1

Foam Density and SiC Area Fraction

In all sample groups, there was a direct correlation between SiC foam density and SiC area fraction. The 20 PPI samples had the highest average foam density and SiC area fraction while the 10 PPI samples had the lowest. This is to be expected as a higher average foam density will directly correspond to a larger presence of SiC. It should be noted that the 20 PPI SiC foams have smaller pore sizes and more pores than the 10 PPI SiC foams.

Pressure

Examining the 10 PPI composites fabricated by both gas pressure and gravity infiltration, an inversely proportional relationship was observed between porosity and hardness of the AA5083. This is to be expected as AA5083 with a higher proportion of pores will collapse more readily and thus exhibit lower hardness than AA5083 with a lower proportion of pores [14].

The AA5083 in the 10 PPI composite fabricated by gas pressure infiltration had a higher average hardness (73.8 HV) and lower average porosity (2.960%) than in the 10 PPI composite fabricated by gravity infiltration (72.5 HV, 3.607%) by 1.3 HV and 0.65%. The effect of increasing the pressure of infiltration is thus an increase in hardness and decrease in porosity of the AA5083. This is also to be expected as the application of pressure will cause further collapse of pores within the alloy and thereby decrease porosity and increase hardness [14, 15].

An inversely proportional relationship between grain size and hardness was also observed as the AA5083 in the 10 PPI composite fabricated by gas pressure infiltration had a smaller average grain size and higher average hardness than in the 10 PPI composite fabricated by gravity infiltration. This inverse proportionality can be attributed to the application of pressure during gas pressure infiltration which compacts and reduces the size of grains within the alloy while also collapsing AA5083 pores to decrease porosity and increase hardness [14–16].

Pore Size

Examining the 10 and 20 PPI composites fabricated by gas pressure infiltration, an unexpectedly proportional relationship was observed between porosity and hardness. The AA5083 in the 10 PPI composite fabricated by gas pressure infiltration had a higher average hardness (73.8 HV) and higher average porosity (2.96%) than in the 20 PPI composite fabricated by gas pressure infiltration (63.5 HV, 2.74%) by 14.7 HV and 0.22%. The effect of decreasing the SiC foam density and consequently increasing pore size is thus a decrease in hardness and porosity of the AA5083.

An unexpectedly proportional relationship between grain size and hardness was also observed as the AA5083 in the 20 PPI composite fabricated by gas pressure infiltration had a smaller average grain size and lower average hardness than in the 10 PPI composite fabricated by gas pressure infiltration. The smaller grain size of the 20 PPI composite can be attributed to a faster cooling rate [17] as smaller conglomerated areas of aluminium like those present in the 20 PPI composite will take less time to cool and thus form smaller grains. In AA5083, smaller grain size is generally associated with lower porosity [18] as is the case in the 20 PPI composite fabricated by gas pressure infiltration.

The proposed cause of increasing hardness with increasing SiC foam pore size in this study is the compaction caused by having larger quantities of AA5083 conglomerating in a single volume within larger pores. The 10 PPI composite fabricated by gas pressure infiltration in this study had larger pores than the 20 PPI composite allowing more AA5083 to seep into each pore and resulting in larger conglomerated volumes of AA5083. In a conglomerated volume of AA5083, AA5083 particles entering the volume push the outer AA5083 particles against the SiC and the outer particles push back on the inner particles in response, resulting in compaction of the AA5083 (Fig. 5). The presence of more AA5083 in each pore causes there to be more particles pushing against the outer AA5083 and consequently more force pushing back on the inner AA5083 particles which results in greater compaction of the alloy as a whole and higher average hardness.

This hypothesis was supported by the qualitative observation that the hardness of AA5083 increased with decreasing distance from the interface between AA5083 and SiC in each sample. This observation was made by determining the location and corresponding magnitude of each hardness measurement on the optical microscopy

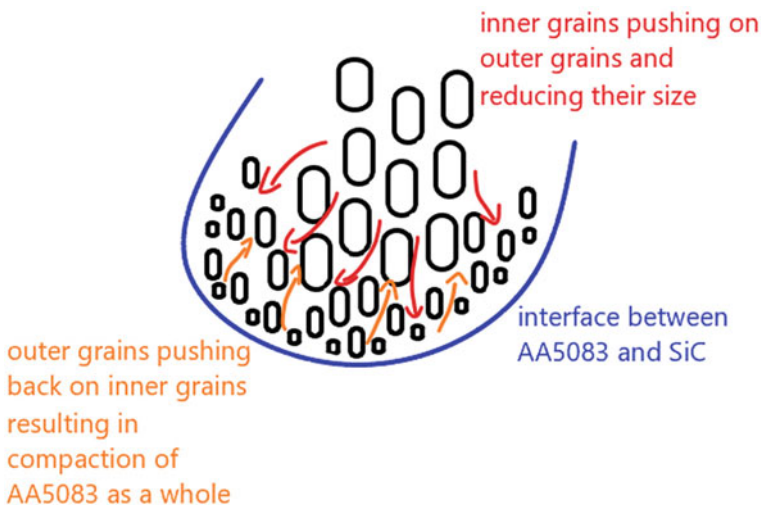


Fig. 5 Compaction of AA5083 within SiC foam pores

images. The outermost AA5083 had the most pressure applied to it when forced against the SiC by the collective AA5083 within the pore and thus appeared to generally contain higher hardness measurements.

Other potential contributing factors to the increase in AA5083 hardness nearing the interface between AA5083 and SiC include a faster rate of cooling of the outermost AA5083 within each pore [19] or the formation of a SiC precipitate as small portions of loose SiC may have been displaced by the AA5083 near the interface. There is some evidence of AA5083 grain size reducing along some of the interfaces within each sample which could be caused by both the pressure of the inner AA5083 in each pore pushing outward [15, 16] and the faster cooling rate of the outer AA5083 near the interface [17, 19]. Further investigation is required to confirm the cause of this phenomenon which could include scanning electron microscopy (SEM), electron backscatter diffraction (EBSD), and energy-dispersive X-ray spectroscopy (EDS) of the samples.

Conclusions

This study sought to characterise the microstructures of AA5083 in AA5083/SiC co-continuous ceramic composites (C4) fabricated by gas pressure infiltration with 10 and 20 PPI SiC foams, respectively, and by gravity infiltration with 10 PPI SiC foam.

The following conclusions were drawn from the results of the study:

1. Both gas and gravity infiltration of SiC foams with AA5083 resulted in lower AA5083 hardness and porosity than heating the AA5083 without infiltration under the same conditions.
2. Gas pressure infiltration resulted in higher AA5083 hardness and lower AA5083 porosity than gravity infiltration.
3. Lower SiC foam density and consequently larger SiC foam pore size resulted in higher AA5083 hardness and porosity.
4. AA5083 hardness increased with decreasing distance from SiC within each of the AA5083/SiC co-continuous ceramic composites.

Ongoing research into the influence of SiC foam pore size on the microstructural properties of AA5083 in AA5083/SiC co-continuous ceramic composites is focused on the determination of the cause of increased hardness nearer to the interface between AA5083 and SiC and the correlation of this phenomenon with pore size.

References

1. Travitzky NA, Shlayan A (1998) Microstructure and mechanical properties of Al_2O_3 : Cu-O

- composites fabricated by pressureless infiltration technique. *Mater Sci Eng A* 244:154–160
2. Lu Y, Yang J, Lu W et al (2010) The mechanical properties of co-continuous $\text{Si}_3\text{N}_4/\text{Al}$ composites manufactured by squeeze casting. *Mater Sci Eng A* 527:6289–6299
 3. Jimoh A, Sigalas I, Hermann M (2012) In situ synthesis of titanium matrix composite (Ti-TiB-TiC) through sintering of $\text{TiH}_2\text{-B}_4\text{C}$. *Mater Sci Appl* 3:30–35
 4. Chang H, Higginson R, Binner J (2010) Microstructure and property characterization of 3–3 Al(Mg)/ Al_2O_3 interpenetrating composites produced by a pressureless infiltration technique. *J Mater Sci* 45:662–668
 5. Meti VKV, Shirur S, Nampoothiri J et al (2018) Synthesis, characterization and mechanical properties of AA7075 based MMCs reinforced with TiB_2 particles processed through ultrasound assisted in-situ casting technique. *Trans Indian Inst Met* 71:841–848
 6. Daehn GS, Breslin MC (2006) Co-continuous composite materials for friction and braking applications. *JOM* 58:87–91
 7. Jiang L, Jiang YL, Yu L et al (2012) Experimental study and numerical analysis on dry friction and wear performance of co-continuous SiC/Fe-40Cr against SiC/2618 Al alloy composites. *Trans Nonferrous Met Soc China* 22:2913–2924
 8. Nong XD, Jiang YL, Fang M et al (2017) Numerical analysis of novel SiC 3D/Al alloy co-continuous composites ventilated brake disc. *Int J Heat Mass Transf* 108:1374–1382
 9. Maleque MA, Dyuti S, Rahman MM (2010) Material selection method in design of automotive brake disc. In: *Proceedings of the world congress on engineering 2010*, London, UK, 30 June–2 July 2010
 10. Prasanth AS, Ramesh R, Gopalakrishnan P et al (2019) Multi-response optimization of end milling parameters for Al-Zn-Mg/SiC co-continuous composite using response, surface methodology. *Mater Sci* 25:471–477
 11. Prasanth AS, Ramesh R, Gopalakrishnan P (2018) Taguchi Grey relational analysis for multi response optimization of wear in co-continuous composite. *Materials* 11(1743):1–17
 12. Zhang Q, Dong S, Ma S et al (2020) Microstructure and compressive behavior of lamellar $\text{Al}_2\text{O}_3/\text{Al}$ composite prepared by freeze-drying and mechanical-pressure infiltration method. *Sci Eng Compos Mater* 27:1–9
 13. Vijayan K, Ramalingam S, Sadik MRA et al (2021) Fabrication of co-continuous ceramic composite (C4) through gas pressure infiltration technique. *Mater Today Proc* 46(2):1013–1016
 14. Boileau J, Allison JE (2001) The effect of porosity size on the fatigue properties in a cast 319 aluminium alloy. *SAE Tech Pap* 110:648–659
 15. Jahangiri A, Marashi SPH, Mohammadaliha M et al (2017) The effect of pressure and pouring temperature on the porosity, microstructure, hardness and yield stress of AA2024 aluminium alloy during the squeeze casting process. *J Mater Process Technol* 245:1–6
 16. Obiekea K, Aku SY, Yawas DS (2012) Influence of pressure on the mechanical properties and grain refinement of die cast aluminium Al350 alloy. *Adv Appl Sci Res* 3(6):3663–3673
 17. Liang G, Ali Y, You G et al (2018) Effect of cooling rate on grain refinement of cast aluminium alloys. *Materialia* 3:113–121
 18. Jia Y, Wang S, Shu D (2020) Grain size prediction and investigation of 7055 aluminium alloy inoculated by Al-5Ti-1B master alloy. *J Alloys Compd* 821:153504
 19. Xu Z, Wang S, Wang H et al (2020) Effect of cooling rate on microstructure and properties of twin-roll casting 6061 aluminium alloy sheet. *Metals* 10(9):1168

Part IV
Metallurgical Processing Analysis
and Characterization

Study on the Degradation Behavior of Organic Humic Acid from the Wastewater by Refractory High-Titanium Slag After Metallurgical Transformation



Yubi Wang, Shengpeng Su, Bingbing Liu, Guihong Han, and Yanfang Huang

Abstract Vanadium-titanium magnetite and ilmenite are recognized as one type of the most refractory mineral resources. Conventional carbothermal reduction smelting to extract Fe and Ti from vanadium-titanium magnetite and ilmenite is based on the natural resource attribute. After reduction smelting, abundant refractory high-titanium slag was obtained. In this work, according to the environmental material attribute, an alternative utilization for degradation of organic humic acid from the wastewater by high-titanium slag after metallurgical transformation was conducted via the ultraviolet absorption and degradation experiments. After metallurgical transformation at 1200 °C for 120 min, the high-titanium slag was transformed to titanate with spinel-type structure and photocatalytic property in the manganese titanates. The degradation efficiency of humic by the manganese titanate was over 48% as the fine-grained manganese titanate was with a dosage of 1.5 g/L and humic acid concentration was 10 mg/L. This work provided a high-value treatment of high-titanium slag for environmental remediation.

Keywords High-titanium slag · Metallurgical transformation · Titanate · Humic acid · Photocatalytic degradation

Introduction

Vanadium-titanium magnetite and ilmenite are recognized as one type of the most refractory mineral resources and it is widely distributed in the Panzhihua, Chendei, and Hanzhong of China [1]. In recent years, ilmenite has become the main mineral resource of the titanium industry with the massive consumption of global rutile resources [2]. About 95% of titanium resources are used to produce titanium dioxide pigments [3]. There are two traditional processes for the production of titanium dioxide pigment, including the sulfate process and chloride process. Compared with the sulfate process, the chloride process requires high-grade titanium resources [4].

Y. Wang · S. Su · B. Liu (✉) · G. Han · Y. Huang
School of Chemical Engineering, Zhengzhou University, Zhengzhou 450001, Henan, P.R. China
e-mail: liubingbing@zzu.edu.cn

© The Minerals, Metals & Materials Society 2022
M. Zhang et al. (eds.), *Characterization of Minerals, Metals, and Materials 2022*,
The Minerals, Metals & Materials Series,
https://doi.org/10.1007/978-3-030-92373-0_7

The high-titanium slag, as a raw material for the chloride process, is a high-grade titanium resource obtained by treating the ilmenite through electric furnace smelting.

The process of producing titanium dioxide and metallic titanium from high-titanium slag consumes high energy and generates a large amount of wastes [5]. As a high-quality raw material for the production of titanium dioxide, the content of titanium dioxide in high-titanium slag is higher than that of ilmenite, while the content of iron oxide is lower than that of ilmenite. Titanium dioxide has been used in various fields such as pigment, semiconductor reagent, and photocatalyst. In order to reduce costs, high-titanium slag has been developed as a photocatalyst to degrade organics in wastewater [6]. The rare metals were used as additives to increase the degradation rate [7]. These processes for pure titanates production are characterized by high energy consumption, environmental pollution, and low efficiency. Therefore, it is of scientific value and practical significance to prepare titanates directly through short physical or chemical treatment of high-titanium slag. For example, the high-titanium slag was used as a precursor to prepare TiC and KNaTiO_3 functional materials [8, 9].

Humic acid as part of natural organic matter accounts for 90% of the dissolved organic matter in surface water. Humic acid, as a pollutant of drinking water resources, can be removed by activated carbon adsorption, ultrafiltration membrane filtration, photocatalytic degradation, and other technologies. Photocatalytic degradation of humic acid has become a popular research topic. BaTiO_3 as a photocatalyst has an excellent degradation effect on humic acid [10].

Manganese titanate is used as a photocatalyst to degrade organic matter and can be obtained by solid phase calcination [11–13]. In consideration of the expensive price of pure titanium dioxide, in this work, we will use high-titanium slag as a raw material to compose manganese titanate. Titanate is widely used in the photocatalytic degradation of organic matter. The photocatalytic degradation of humic acid by the as-prepared manganese titanate was evaluated. In addition, the degradation effect of manganese titanate synthesized from the high-titanium slag was compared with the manganese titanate synthesized by pure materials.

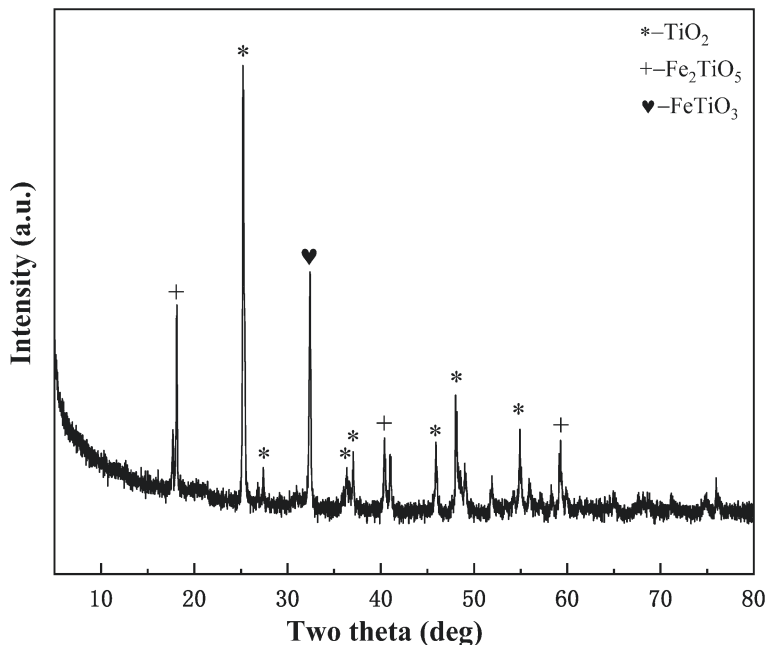
Experimental

Materials

The high-titanium slag used in this work was obtained from ilmenite smelted by an electric furnace. The main components of high-titanium slag are TiO_2 and Fe_2O_3 with 79.635 wt% and 9.078 wt%, respectively (as shown in Table 1). The main impurities included 2.103 wt% Na_2O , 2.584 wt% SiO_2 , 1.188 wt% Al_2O_3 , and 0.923 wt% MgO . The X-ray diffraction (XRD) patterns of the high-titanium slag are presented in Fig. 1. The main phases in the high-titanium slag were ilmenite (FeTiO_3), iron titanate (Fe_2TiO_5), and titanium dioxide (TiO_2). Pure MnO_2 (Aladdin Reagent (Shanghai))

Table 1 Composition of high-titanium slag (wt %)

Na ₂ O	MgO	Al ₂ O ₃	SiO ₂	P ₂ O ₅	SO ₃	Cl	K ₂ O	CaO	TiO ₂	Cr ₂ O ₃	MnO ₂	Fe ₂ O ₃
2.013	0.923	1.188	2.584	0.061	0.194	1.483	0.023	0.247	79.635	0.237	1.909	9.078

**Fig. 1** XRD diagram of high-titanium slag ore

Co., LTD.) with purity of 99.5 wt% was used in the present work. In this work, the high-titanium slag was ground and sieved to 100 wt% by being passed through a 0.074 mm sieve in advance. The chemically pure TiO₂ powders also were used as raw materials in the cause of investigating the reaction mechanism.

Oxidization Roasting Process

Figure 2 shows the experimental flowsheet for the preparation of titanate. Before the briquetting and oxidization roasting, the high-titanium slag and MnO₂ were mixed with an agate mortar. The mass ratio of high-titanium slag and manganese dioxide is variable. Then the mixture added with 10 wt% moisture was briquetted by mold into a cylindrical briquette with a diameter of 10 mm and height of 20 mm at a pressure of 50 MPa, and then the cylindrical briquette was dried at 60 °C for 24 h. The oxidization roasting experiment on the waterless briquettes was carried out in a muffle furnace

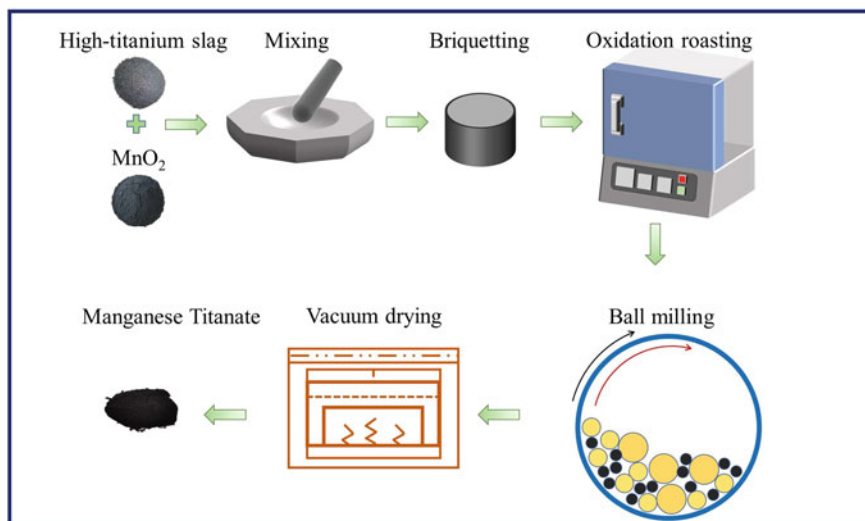


Fig. 2 Schematic diagram of the experimental process

at 1200 °C for 2 h under an air atmosphere. Subsequently, the manganese titanate was wet-milled in a ceramic ball mill for 12 h and dried at 60 °C for 12 h to obtain titanate with uniform particles. The chemically pure TiO₂ and MnO₂ reacted in the same way as the process in Fig. 2 with a mass ratio of 1:1 to prepare pure manganese titanate.

Characterization of Material

The main phase identification of the manganese titanate was investigated by XRD (RIGAKU D/Max 2500, Japan) under the following conditions: Cu K α , tube current, and voltage: 250 mA, 40 kV, scanning range: 10°–80° (2 θ), and scanning speed: 5°/min. The microstructure of the roasted samples was observed using optical microscopy (LEICA DM1750M, Germany). The particle size distribution of the manganese titanate was examined by Malvern Laser Particle Size Analyzer (Mastersizer, 2000; Britain).

Photocatalytic Degradation of Humic Acid

The photocatalytic degradation of humic acid by the manganese titanate was carried out in a multi-channel photochemical reaction apparatus (PL-SX100A). The photocatalytic experiment was conducted in a cylindrical quartz glass reactor with an

effective vessel volume of 30 mL. A 200 W UV lamp ($\lambda = 365$ nm) acted as a light source. The photocatalytic degradation experiment was carried out at a stirring speed of 100 r/min for 120 min. During the photocatalytic reaction, the manganese titanate suspension was kept at 25 °C by cooling water. After the photocatalytic reaction, the suspension was taken out and centrifuged at 8000 r/min for 10 min to obtain a clear HA solution. The concentration of HA in a clear solution was measured by a Dual-beam UV-Vis Spectrophotometer (TU-1902) at 204 nm. The degradation rate of HA can be calculated by the following formula:

$$R = \frac{C_0 - C}{C_0} \times 100\% \quad (1)$$

where R is the degradation rate of HA; C_0 is the initial concentration of HA, mg/L; and C is the concentration of HA after reacting 120 min, mg/L.

Results and Discussion

Characterization of Titanate

XRD is used to analyze the phase compositions of the high-titanium slag and MnO_2 roasted at 1200 °C for 2 h. As exhibited in Fig. 3, the main phase in the roasted products from chemically pure TiO_2 and MnO_2 is MnTiO_3 (PDF#77-1858). As for the titanate synthesis from slag, manganese titanate is generated in the roasted production from the high-titanium slag with the addition of MnO_2 . As the contents of MnO_2 increase, the peak intensity of MnTiO_3 enhances sharply, whereas the peak intensities of TiO_2 and $\text{Fe}_2\text{MnTi}_3\text{O}_{10}$ decrease. The TiO_2 and $\text{Fe}_2\text{MnTi}_3\text{O}_{10}$ in the roasted products disappear when the content of MnO_2 additions is 50% and 100%, respectively. The main phase transforms to pure manganese titanate as the MnO_2 dosage is over 100%. In the following work, the manganese titanate synthesized from the high-titanium slag is marked as MTS, whereas the manganese titanate synthesized from the pure chemicals is called MTC.

The phase distribution of the MTS and MTC were observed by optical microscopy. As shown in Fig. 4a, the TiO_2 was uniformly distributed in the high-titanium slag with massive form. In the MTS, many MnTiO_3 are formed and there are massive holes around the MnTiO_3 (Fig. 4b), which are produced from the MnO_2 deoxidation at high temperature. It can be seen that the MnTiO_3 in MTC is homogeneous (Fig. 4c).

Figure 5 illustrates the particle size distribution of the MTS and MTC after wet grinding. It can be seen the particle size distributions of the MTS and MTC are uniform and concentrated. The average particle size $D_{(50)}$ of the MTS is 1.883 μm , whereas the average particle size $D_{(50)}$ of MTC is 1.61 μm . The particle size of MTC is smaller than that of the MTS. The main reason is that the high-titanium slag

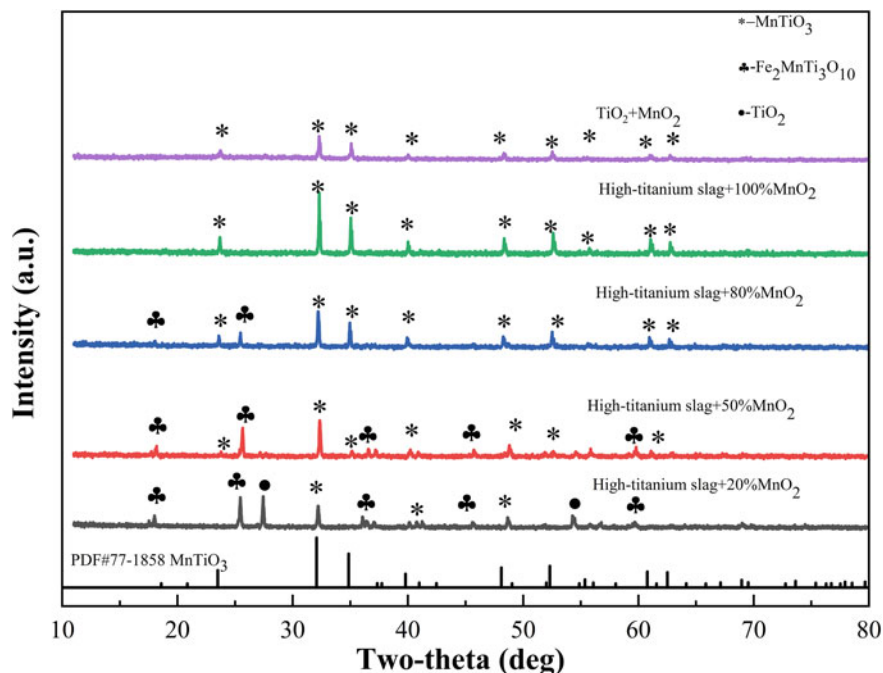


Fig. 3 XRD patterns of products from the high-titanium slag and MnO_2 roasted at $1200\text{ }^\circ\text{C}$ for 2 h

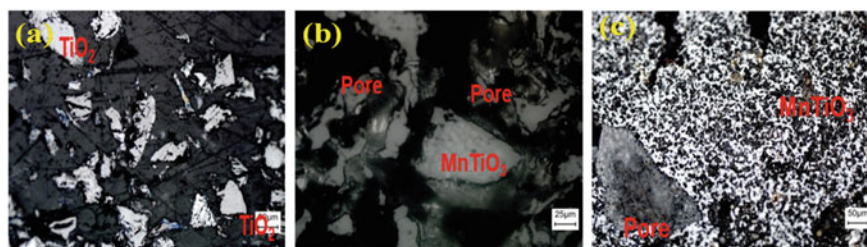


Fig. 4 Optical microscopy images of samples **a** high-titanium slag; **b** MTS; **c** MTC

contains other metal ions, which can react with manganese dioxide to form some substance that is difficult to grind.

Photocatalytic Degradation of Humic Acid Experiment

The effects of MTS and MTC on the degradation rate of humic acid with 10 mg/L are displayed in Fig. 6. When the HA degradation was conducted by MTC or MTS with

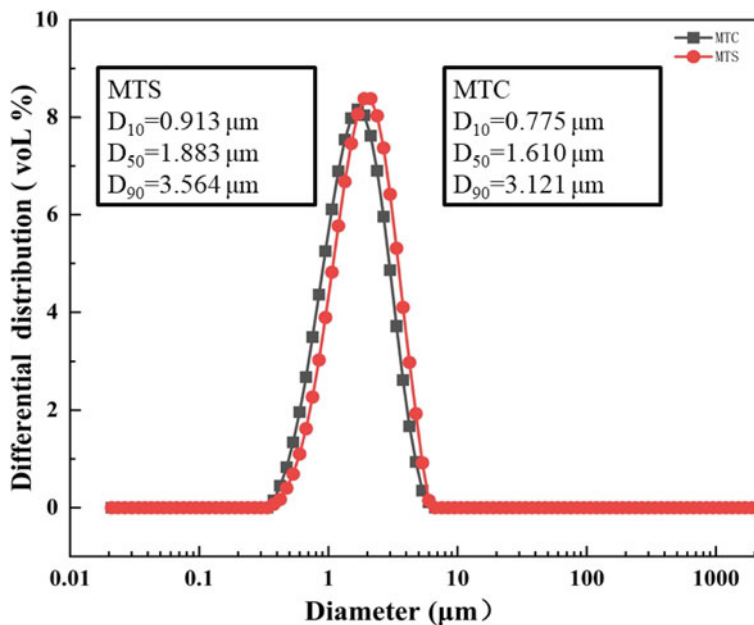


Fig. 5 Particle size distributions of MTS and MTC

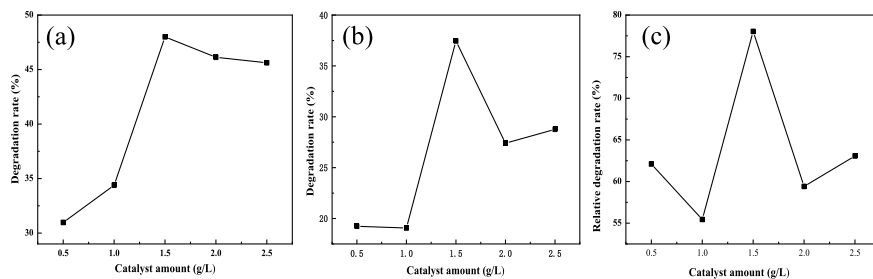


Fig. 6 Degradation rates of humic acid. **a** MTC; **b** MTS; **c** degradation ratio of MTS to MTC

a concentration of 1.5 g/L, it is observed from Fig. 6 that the highest degradation rate of humic acid by MTC and MTS are 48% and 37%, respectively. As can be seen from Fig. 6c, the relative degradation rates of MTS to MTC are all above 50%, and the highest relative degradation rate of 78% is achieved at an MTS addition of 1.5 g/L.

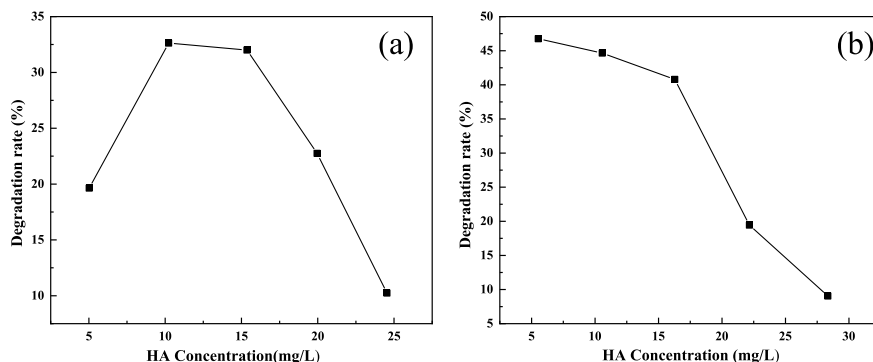


Fig. 7 Effect of HA concentrations on the photocatalytic degradation of humic acid. **a** MTC; **b** MTS

Figure 7 shows the effect of humic acid concentration on the photocatalytic degradation rate with MTC or MTS of 1.5 g/L. It can be seen from Fig. 7a that the degradation rate of humic acid by MTS first increases and then decreases with the increase of humic acid concentration and reaches the maximum of 33% at the humic acid concentration of 10 mg/L. It can be seen from Fig. 7b that the degradation rate of humic acid by MTC decreases with increasing humic acid concentration, and the maximum degradation rate is 47%. Compared with MTS, the degradation rate of humic acid by MTC is higher at the concentration of humic acid below 20 mg/L.

The comparison between photolysis, adsorption, and photocatalysis of MTC and MTS with a concentration of 1.5 g/L and humic acid concentration of 10 mg/L is presented in Fig. 8. As observed, the humic acid degradation is in this order: photocatalysis > adsorption > photolysis. The photocatalytic degradation rate of MTC is 30% and the adsorption degradation rate is 23%, while the photocatalytic and adsorption degradation rates of MTS are marginally lower than that of MTC. Although the degradation efficiency of MTS is slightly lower than that of MTC,

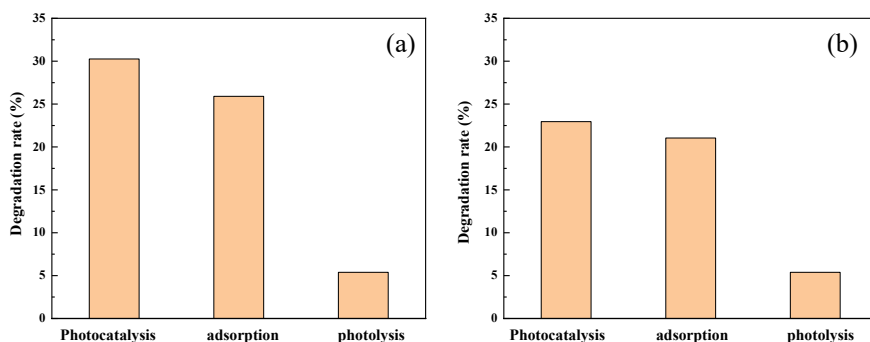


Fig. 8 Comparison of photolysis, adsorption, and photocatalysis. **a** MTC; **b** MTS

we can enhance the degradation effect of MTS by some strengthening technologies, such as mechanical activation, alkali leaching activation, rare metals doping, and so on. We will report this part of the work in the future.

Conclusion

High-titanium slag and MnO_2 were roasted at 1200 °C for 2 h to prepare the manganese titanate, and it was used to degrade the humic acid from the wastewater. Compared with the manganese titanate prepared from the pure chemicals, the maximum humic acid degradation rate by the titanate synthesized from high-titanium slag was 37% when the humic acid concentration was 10 mg/L and the addition of catalyst addition was 1.5 g/L, accounting for 78% of the degradation effect of pure titanate. This work provided a high-value treatment of high-titanium slag for environmental remediation. Although the degradation efficiency of manganese titanate prepared from the high-titanium has a relative degradation effect compared with the pure manganese titanate, some strengthening approaches such as mechanical activation, alkali leaching activation, and rare metals doping, can be applied to enhance the performance of the titanate materials prepared from the high-titanium slag directly.

Acknowledgements The authors wish to express their thanks to the National Natural Science Foundation of China (No. 51904273, U2004215), the China Postdoctoral Science Foundation (No. 2019M660174, 2019TQ0289), and the Special Support Program for High-Level Talents in Henan Province (No. ZYQR201912182) for the financial support.

References

1. Chong X, Luan W et al (2020) Overview of global titanium resources status and titanium consumption trends in China. *Miner Conserv Util* 40(2):162–170
2. Du Y, Meng Q et al (2020) Study on the flotation behavior and mechanism of ilmenite and titaugite with sodium oleate. *Miner Eng* 152:106366
3. Gázquez MJ, Bolívar JP et al (2014) A review of the production cycle of titanium dioxide pigment. *Mater Sci Appl* 5:441–458
4. Nguyen TH, Lee MS (2019) A review on the recovery of titanium dioxide from Ilmenite ores by direct leaching technologies. *Miner Process Extr Metall Rev* 40(4):231–247
5. Huaxin (2014) Introduction to non-ferrous metallurgy. Metallurgical Industry Press, Beijing, China
6. Kang Y, Xue X et al (2009) Characterization of titanium-containing slag and catalytic degradation of nitrobenzene-containing wastewater under the action of ultrasonic waves. *Silic Bull* 28(02):229–234
7. Liu D, Bai L et al (2010) Effect of rare earth element doping on the photocatalytic performance of high titanium slag and titanium concentrate. *Chin J Rare Earths* 28:313–315
8. Zhou Z, Zhang Y et al (2018) Electrolytic synthesis of TiC/SiC nanocomposites from high titanium slag in molten salt. *Ceram Int* 44(4):3596–3605

9. Fan W, Gao W et al (2021) Scalable synthesis of KNaTiO_3 -based high-temperature CO_2 capture material from high titanium slag: CO_2 uptake, kinetics, regenerability and mechanism study. *J CO₂ Util* 49:101578
10. Wang P, Fan C et al (2013) A dual chelating sol-gel synthesis of BaTiO_3 nanoparticles with effective photocatalytic activity for removing humic acid from water. *Mater Res Bull* 48:869–877
11. Sharma YK, Kharkwal M et al (2009) Synthesis and characterization of titanates of the formula MTiO_3 ($M = \text{Mn, Fe Co, Ni and Cd}$) by co-precipitation of mixed metal oxalates. *Polyhedron* 28:579–585
12. Song Z, Wang S et al (2004) Synthesis of manganese titanate MnTiO_3 powders by a sol-gel-hydrothermal method. *Mater Sci Eng B* 113:121–124
13. Alkaykh S, Mbarek A et al (2020) Photocatalytic degradation of methylene blue dye in aqueous solution by MnTiO_3 nanoparticles under sunlight irradiation. *Heliyon* 6(4):e03663

Adsorption of Iron, Copper, Lead, Chromium, and Cadmium in Cobalt Sulfate Solution by Goethite



Sujun Lu, Jiang Cao, Yuanyuan Li, Guoju Chen, Jesika, and Guanwen Luo

Abstract Battery level cobalt sulfate is an important raw material for the production of cathode materials for lithium-ion batteries. Crude cobalt sulfate solution often contains a variety of impurities. The existence of these impurities will affect the performance of cathode materials, so it needs deep purification and impurity removal. In this project, we used goethite for adsorption and impurity removal of Fe, Cu, Pb, Cd, Cr, and other impurity elements in cobalt sulfate solution. The result shows that the order of goethite adsorbing heavy metal ions is chromium, cadmium/nickel, and cobalt. And we used the direct oxidation adsorption method to remove iron and adsorb chromium and copper ions from the solution. Under the conditions of pH value 4.0 and temperature 60 °C, the removal rate of iron ions in the solution can reach 89%, which provides guidance for the study of adsorption and impurity removal of cobalt sulfate solution in the future.

Keywords Goethite adsorption · Adsorption sequence · Influence of temperature and pH

Introduction

As an important strategic metal resource, cobalt and nickel are widely used in aerospace, chemical industry, pigment, electroplating, battery, daily life, and other fields [1, 2] At the same time, the waste containing cobalt includes scrap alloy materials, scrap catalysts, scrap battery materials, metallurgical slag, etc. [3]. It

Sujun Lu and Jiang Cao contributed equally to this work.

S. Lu · G. Chen

State Key Laboratory of Nickel and Cobalt Resources Comprehensive Utilization, Jinchang 737100, China

J. Cao · Y. Li · Jesika · G. Luo (✉)

School of Metallurgy and Environment, Central South University, Changsha 410083, China

J. Cao

e-mail: xdxcaojiang@163.com

© The Minerals, Metals & Materials Society 2022

M. Zhang et al. (eds.), *Characterization of Minerals, Metals, and Materials 2022*,

The Minerals, Metals & Materials Series,

https://doi.org/10.1007/978-3-030-92373-0_8

also contains many heavy metal impurities. Without reasonable treatment, these secondary resources of cobalt and nickel will be lost in vain and the heavy metals contained will cause great damage to the environment.

At present, natural ores and secondary resources are mainly resources of cobalt and nickel. The treatment process of cobalt and nickel secondary resources includes pyrometallurgy, hydrometallurgy, biological process, direct regeneration process, and so on [4]. The waste battery materials of nickel cobalt secondary resources are often treated by hydrometallurgy. For the cobalt nickel solution obtained from the leaching step in the hydrometallurgy process, the current impurity removal methods mainly include neutralization method, sulfide precipitation method, solvent extraction, ion purification, and so on [5–7]. A large number of scholars have explored the removal of some metal ions in nickel cobalt solution. Liu Bo et al. [8] used oxidation hydrolysis method to remove iron from ferric cobalt sulfate solution. When the iron removal rate reached 99.68%, the loss rate of cobalt in the solution was 2.87%. But the corresponding experimental conditions were harsh. Lin et al. [9] used amorphous vulcanizing agents MnS and FeS as copper removal agents. It is found that MNS and FES have good copper removal effect. The copper ion concentration in the solution after copper removal is less than 3 mg/L. Fuliang [10] and others used P204 to extract and remove copper from nickel electrolyte. Under the conditions that the volume concentration of P₂₀₄ was 15% and the ratio was 1:2, the primary extraction rate of copper in the solution was 81.33%. Qixiu et al. [11] used a new silicone polyamine composite resin to deeply purify and remove copper from cobalt chloride solution. Through experiments, it was found that the effect was the best when the pH value of the feed solution was 4, the contact time was 30 min, and the temperature was 60 °C. Gang et al. [12] introduced dithiocarboxyl into polyethyleneimine matrix to synthesize a new PEX, which has a good impurity removal effect on mixed heavy metal ions. When 360 mg/l pex was used, the removal rates of copper ion, lead ion, zinc ion, and cadmium ion were 100%, 100%, 78.2%, and 99.4%, respectively. We can see that there are multiple ways to remove some metal impurity ions in the solution. In terms of operation difficulty and economic benefit., it is unreasonable to remove different impurity elements in the secondary nickel cobalt resource leaching solution with multiple ways.

In summary, we propose to remove iron, copper, lead, and other impurity elements initially in cobalt sulfate solution by goethite adsorption. Also, we can explore its adsorption sequence of impurity elements and consider the effects of dry or wet goethite, different pH, and temperature.

Experiment

The reagents used in this experiment include NiSO₄ · 6H₂O, CoSO₄ · 7H₂O, CuSO₄ · 5H₂O, PbCl₂, CdCl₂ · 2.5H₂O, CrCl₃ · 6H₂O, FeSO₄ · 7H₂O, NiCl₂ · 6H₂O, CoCl₂ · 6H₂O, NaOH, and Na₂CO₃. In this experiment, the main components of the feed

solution (simulated feed solution) are Ni, Co, Fe, Cu, Cr, Pb, and Cd which are 0.02 g/L and Fe is 1.5 g/L.

Firstly, prepare the goethite. We used ferrous sulfate heptahydrate as the iron source and prepared 2500 ml solution containing 0.1 mol/l iron. With the air blown in and the speed adjusted, we adjusted the pH value of the solution to about 7 slowly by adding in 2 mol/L sodium hydroxide. We kept the pH value unchanged. After the color of the solution turned brown, we filtered the solution by suction. Then the wet goethite was successfully prepared. The steps to prepare dry goethite are the same in the first part. After preparing wet goethite, we put it into the oven for 5 h at 50 °C, and then grinded it to get dry goethite powder.

Secondly, we prepared 1L of solution containing Ni, Co, Cd, and Cr with a concentration of 0.005 mol/l. We weighed 1.14 g cadmium chloride, 2.5 g water, 1.33 g chromium chloride hexahydrate, 1.11 g cobalt chloride hexahydrate, and 1.21 g nickel chloride hexahydrate. Then we dissolved them, transferred the solution, washed them, and metered volume. We made the molar ratio of dry and wet goethite to impurities 10:1, 20:1, 60:1, and 80:1 with 200 ml of the above-prepared solution for each one. Then we took the corresponding quantity dry and wet goethite to complete the reactions with PH 4.5 at 25 °C for 10 h.

Thirdly, we controlled pH value at 3.0, 3.5, 4.0, 4.5, and 5.0 with 200 ml of the above-prepared solution for each one to complete the reactions with injecting air, stirring at a rate of 10 r/min at 60 °C for 1.5 h. Lastly, we controlled temperature at 50, 60, 70, 80, and 90 °C with 200 ml of the above-prepared solution for each one to complete the reactions with injecting air, stirring at a rate of 10 r/min at pH value 4.0 for 1.5 h.

The main equipment used to test the experimental results are X-ray diffractometer and ICP-AES. XRD uses the specific diffraction pattern of each crystal to analyze and detect the composition and content of compounds in the sample; ICP detection uses the linear relationship between the characteristic spectral intensity and concentration of the element standard solution to detect the spectral intensity of unknown samples, and then convert it into the concentration of elements in the solution.

Results and Discussion

Impurity Removal by Goethite Method

We tested the prepared goethite samples by XRD after drying and grinding. Comparing the obtained sample with the goethite standard PDF card (PDF#81-0463), the results are as follows.

It can be seen from Fig. 1 that all diffraction peaks of the prepared goethite are in good agreement. It is determined that the prepared sample is goethite and there are no other impurity peaks. It indicates that there is no third phase. Meanwhile,

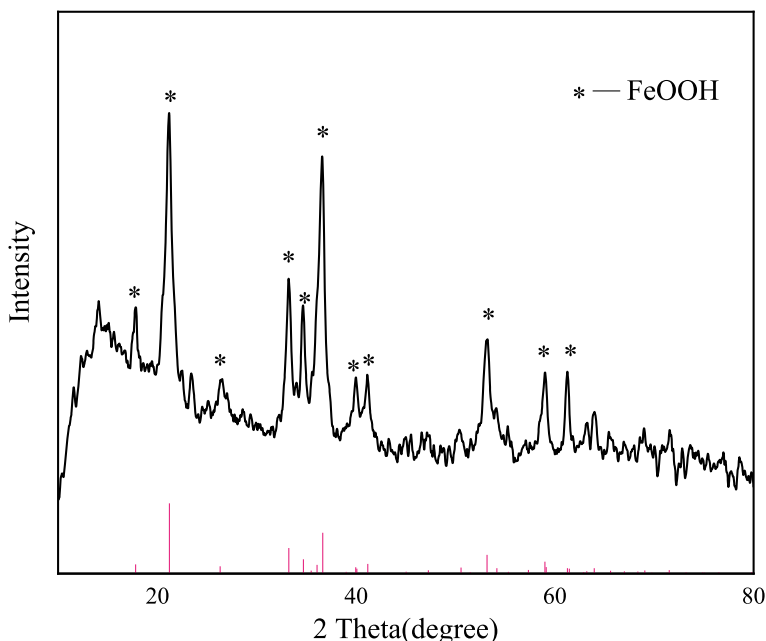


Fig. 1 Diffraction pattern of goethite

the poor diffraction peak type is due to the low crystallinity of goethite obtained by hydrothermal method without heat treatment.

In next section, we compared the adsorption effects of dry and wet goethite. Then we studied the adsorption sequence and adsorption effect of goethite on impurities such as lead, chromium, and cadmium under different molar ratios.

To compare the adsorption effects of dry and wet goethite, we controlled the molar ratio of dry and wet goethite to impurities to 20:1 to complete reaction at 25 °C with initial pH value 4.0 and stirring for 10 h. Then we tested it by ICP after diluting the original solution and posting reaction solution by corresponding multiple. The results are as follows.

It can be seen from Table 1 that both dry and wet goethite can adsorb Cd, Cr, Ni, and Co. But through the comparison between dry and wet goethite, we can see that the adsorption rate to the main metal nickel and cobalt is relatively low by wet

Table 1 Comparison of adsorption rates of dry and wet goethite

Goethite	Adsorption rate of each element/%			
	Cd	Cr	Ni	Co
Dry	39.65	56.80	39.63	40.03
Wet	22.99	54.45	23.30	23.02

goethite. It also resulted in less loss of nickel and cobalt. Therefore, the adsorption effect of wet goethite is better. So that we used wet goethite in subsequent tests.

To explore the influence of the amount of wet goethite on the adsorption effect, we controlled the molar ratio of goethite to impurities to 10:1, 20:1, 40:1, 60:1, and 80:1, respectively, to complete reaction at 25 °C with initial pH value 4.5 and stirring for 10 h. Then we tested it by ICP after diluting the original solution and posting reaction solution by corresponding multiple. The results are as follows.

It can be seen from Fig. 2 that with the increase in molar ratio of goethite and impurity, the removal rate of chromium and cadmium ions increases as a whole. The adsorption order is chromium, cadmium/nickel, and cobalt. The removal rate of cadmium is low about 22% and fluctuates little. Compared with dry adsorption, the removal effect of impurities by wet adsorption is better, but there is no obvious difference.

For the main metal nickel and cobalt, with the increase in molar ratio of goethite and impurity, the loss of nickel and cobalt increases firstly and then decreases. When the molar ratio is 40:1, the loss of nickel and cobalt is the largest about 24%, basically the same as that of dry adsorption. On the whole, the loss rate of nickel and cobalt is between 20 and 25%, and the loss is large.

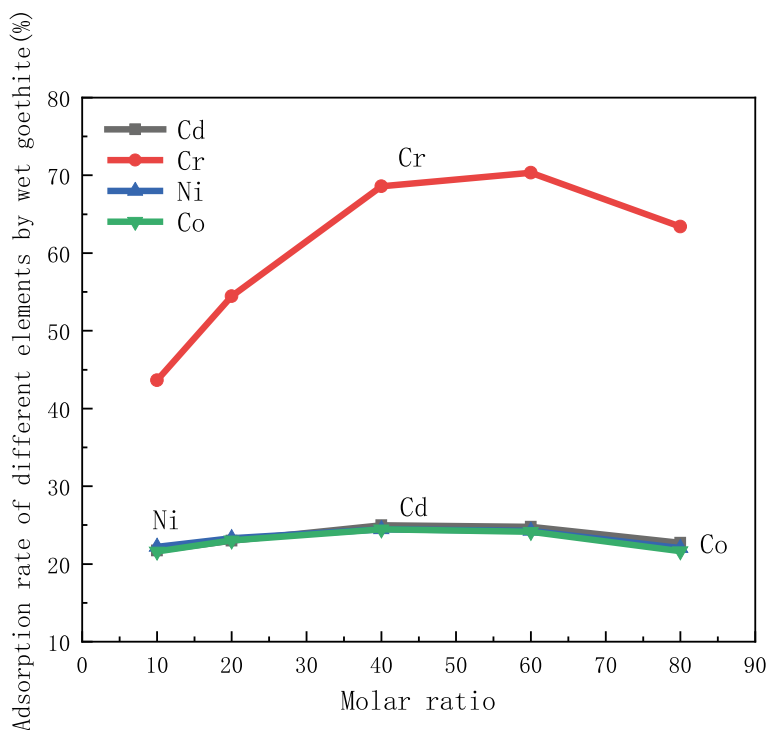


Fig. 2 Adsorption effect of wet goethite on various elements

With the increase of goethite addition, the number of adsorbents increases. The adsorption and impurity removal effect of goethite on various elements is enhanced. So the adsorption rate of various elements in Fig. 2 shows an increasing trend. On the whole, the wet goethite has good adsorption effect. But at the same time, the loss of nickel and cobalt is also large. We speculated that the wet goethite was more active and easier to adsorb nickel and cobalt than the dry goethite. So the loss of nickel and cobalt is also large. From Fig. 2, the order of goethite adsorption and impurity removal is chromium, cadmium/nickel, and cobalt.

Direct Oxidation Adsorption Impurity Removal

In this section, we used direct oxidation adsorption method for impurity removal. We used ferrous sulfate as the iron source to generate goethite to remove Fe^{2+} in the solution with injecting air, changing the reaction temperature and pH value and regulating the oxidation of Fe^{2+} . And we investigated the effects of temperature and pH value on iron removal.

To explore the influence of pH value on adsorption effect, we controlled pH value at 3.0, 3.5, 4.0, 4.5, and 5.0, respectively, to complete the reactions with injecting air, stirring at a rate of 10 r/min at 60 °C for 1.5 h. Then we tested it by ICP after diluting the original solution and posting reaction solution 50 times. The results are as follows.

It can be seen from Fig. 3 that with the increase of pH value, the removal rate of iron has been increasing. When the pH value is 4.5, the iron precipitation rate is as high as 99.9%. The iron has been basically removed. There are some differences between copper and iron removal effect. With the increase of pH, the copper removal effect increases significantly at first. When the pH is about 4.0, the copper removal effect is the best about 99%. With the increase of pH value, the copper removal effect decreases. When the pH is about 5.0, the copper removal rate is 80%.

Within the range of series pH value experiments, the effect of cadmium removal is better, more than 85%. The chromium removal rate is more than 99% when $\text{pH} \geq 3.5$. With the increase of pH value, the cadmium removal rate decreased slightly, and then increased slowly. When pH value is 5.0, the cadmium removal effect is the best about 37.6%. Generally speaking, the lead removal rate is not high. When the pH reaches 5.0, the lead removal effect is the best about 47.5%.

The loss rate of main metal increases with the increase of pH. For metal nickel, the loss effect is not obvious when the pH is lower than 3.5. When the pH is 4.0, the loss rate is 4%. When the pH is higher than 4.0, the loss rate increases significantly. When the pH is about 5.0, the loss rate of nickel is as high as 73%. The loss trend of metal cobalt is similar to that of metal nickel, but its loss rate is always higher than that of metal nickel. When pH is 5.0, cobalt loss is the most serious, and the loss rate is as high as 76%. In general, the experimental conditions with pH 4.0 are the best.



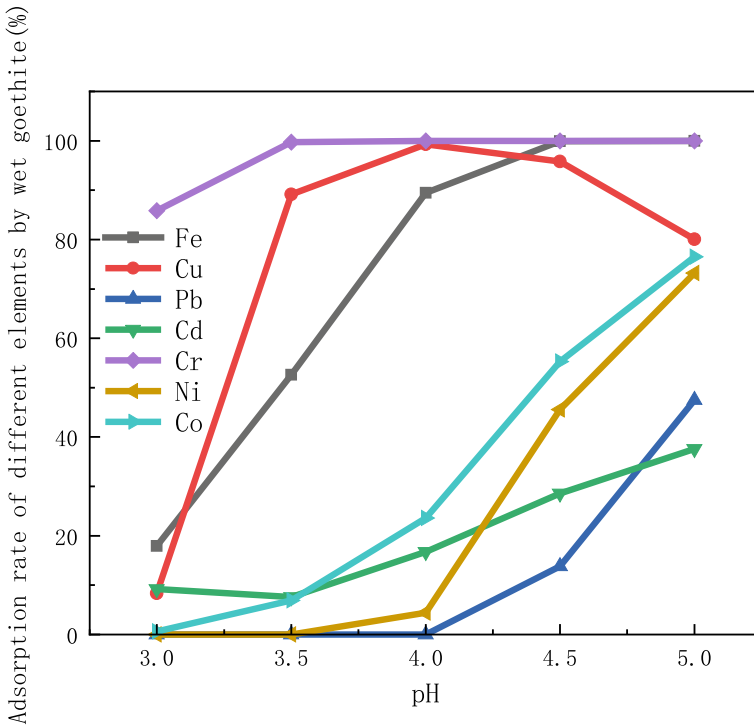


Fig. 3 Effect of pH on impurity removal

It can be seen from this formula that with the increase of pH value, the more hydrogen ions consumed by hydroxide ions, promoting the positive movement of the reaction, the more goethite has been generated. The iron removal rate is increased. And the more goethite is generated, the better adsorption effect on impurity elements is. So the removal rate of each element is increasing as a whole.

To explore the influence of temperature on adsorption effect, we controlled temperature at 50, 60, 70, 80, and 90 °C to complete the reactions with injecting air, stirring at a rate of 10 r/min and pH value 4.0 for 1.5 h. Then we tested it by ICP after diluting the original solution and posting reaction solution 50 times. The results are as follows.

It can be seen from Fig. 4 that with the increase of temperature, the removal rates of iron and copper show an overall growth trend. When the temperature increases from 70 to 80 °C, the iron and copper removal effects increase significantly. At 80 °C, the removal rates of iron and copper are the highest about 63.12% and 90.77%, respectively. When the temperature continues to increase, the removal rates of iron and copper effects decrease, but the change is not obvious.

In the range of series temperature experiments, the removal effect of chromium changes little, and the chromium removal rate is high. For the removal of lead and

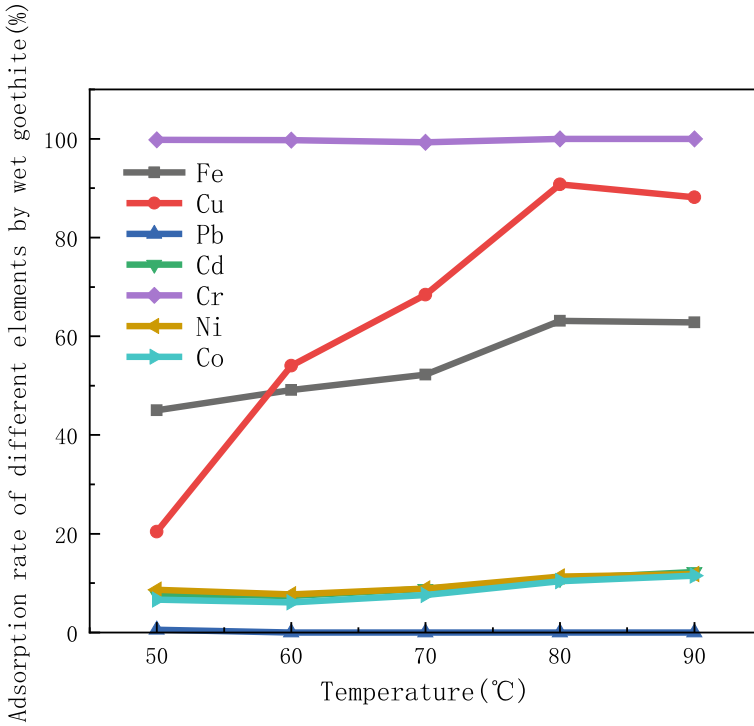


Fig. 4 Effect of temperature on impurity removal

cadmium, the effect is not particularly obvious. The removal rate of cadmium is stable between 8 and 15%. It has little effect on the removal of lead.

The loss rate of nickel and cobalt is basically between 5 and 10% with little fluctuation. The loss rate is the lowest at 60 °C, about 7.75% and 6.12%, respectively.

Overall, the removal effect of chromium, copper, and iron is good, and the loss of nickel and cobalt is low at 80 °C. Therefore, 80 °C is a good experimental condition.

Conclusions

- (1) The adsorption order of goethite to chromium and cadmium is chromium and cadmium. The direct oxidation adsorption method can remove iron ions, copper ions, and chromium ions in the solution. It can remove some nickel and cobalt ions by adsorbing.
- (2) In the experiment of direct oxidation adsorption impurity removal, the temperature of 80 °C and pH value of 4 are the best experimental conditions.

References

1. Qiang L (2020) Ore body characteristics and resource potential evaluation of yinte nickel cobalt deposit in Subei County Gansu Province. *World Nonferrous Met* 08:108–109
2. Lingyu Y, Anjian W (2016) Analysis on supply and demand pattern of global nickel resources. *Chin Min Mag* 25(04):1–5
3. Huanzheng D, Jiqing B, Jie X (2013) Study on current situation and development countermeasures of secondary resource recovery and utilization of cobalt and nickel. *Renew Resour Circu Econ* 6(02):33–39
4. Weihui Y, Jingang Y (2016) Current situation and development of recovery and utilization of cobalt nickel secondary resources. *Chem Enterp Manag* (29):312
5. Xiaozhong X, Jianming Y (2016) Study on extraction and purification of cobalt sulfate from cobalt sulfate waste liquid. *World Nonferrous Met* 2016(11):57–60
6. Xuebin P, Lin T, Zhongbiao Z, Tao Q, Gang X, Yongnian D (2018) Experimental study on Extraction and separation of nickel and cobalt from cobalt sulfate solution by Cyanex 272. *Min Eng* 38(06):127–130
7. Longzhao W, Xiaodong S, Yuanhui Z, Haixia Z, Yan C (2020) Experimental study on treatment of cobalt sulfate solution containing heavy metal by vulcanization. *Chem Enterp Manag* (23):171–172
8. Bo L, Qiusheng Z, Xiaobin L, Zhihong P, Guihua L, Tiangui Q (2020) Oxidation hydrolysis of cobalt sulfate solution for iron removal and hydrothermal treatment of iron removal slag. *Chin J Nonferrous Met* 30(11):2672–2683
9. Lin L (2014) Study on deep copper removal from anode solution of nickel electrolysis by amorphous metal sulfide. Central South University
10. Yanshuang M, Zhufuliang, Feng Z, Yaohua F (2007) Copper removal from nickel electrolyte by P204 extraction. *Nonferrous Met (Smelting Part)* 2007(06):7–9
11. Junjie W, Qixiu Z, Guiqing Z, Liping Z (2008) Deep purification and removal of copper from cobalt chloride electrolyte by new silica gel polyamine resin. *Ion Exch Adsorp* 2008(03):254–259
12. Gang W (2013) Preparation and properties of heavy metal flocculant sodium polyimide xanthate. Lanzhou Jiaotong University

Study on Efficient Burdening for Preparation of Fused Calcium Magnesium Phosphate Fertilizer from Low-Grade Phosphate Ores



Tingting Wang, Luyi Li, Cuihong Hou, Haobin Wang, Shouyu Gu, and Jie Wang

Abstract Acidification and trace elements lack in the soil deteriorates the healthy planting of crops in China. One effective approach to relieving soil acidification and infertility is to use alkaline-fused calcium magnesium phosphate fertilizer (FMP). As a carrier of many micronutrients, low-grade phosphate ore was used as the raw materials to prepare the alkaline FMP in this work. An efficient burdening for preparation of FMP based on the glass structure factors (O_b/Y_b) was briefly introduced, and then the fusion characteristic of the low-grade phosphate ore with various O_b/Y_b values was characterized. Melting experiments show that the increase of melting temperature and time can dramatically enhance the effective conversion of nutrient elements in phosphate ore. After melting at 1450 °C for 10 min with O_b/Y_b of 3.06, 94.87% P_2O_5 , 91.68% CaO, 93.69% MgO, and 92.46% SiO_2 are activated in the alkaline FMP, which can be readily absorbed by the crop root system.

Keywords Fused calcium magnesium phosphate fertilizer · Melting temperature · Melting time · Effective conversion

Introduction

In recent decades, with the large-scale application of NPK fertilizers and the improvement of crop yield in the process of crop plantation, the phenomenon of soil acidification and the deficiency, and imbalance of trace elements in soil and crops have become increasingly severe, which have become the limiting factors for the sustainable improvement of crop yield and quality. According to the data estimated by the National Agricultural Technology Extension Center of the Ministry of rural of the Ministry of agriculture in 2014, Chinese soil cultivated land areas with the content

T. Wang · L. Li · C. Hou (✉) · H. Wang · S. Gu · J. Wang
School of Chemical Engineering, National Center for Research & Popularization of Calcium, Magnesium, Phosphate and Compound Fertilizer Technology, Engineering Research Center of Advanced Functional Material Manufacturing of Ministry of Education, Zhengzhou University, Zhengzhou 450001, Henan, People's Republic of China
e-mail: hch92@zzu.edu.cn

of trace elements such as Ca, Mg, S, Fe, Mn, Cu, Zn, B, and Mo below the critical values which has reached 63%, 53%, 40%, 31%, 48%, 25%, 42%, 84%, and 59%, respectively [1, 2]. Therefore, it is urgent to study and prepare alkaline fertilizer with a reasonable proportion and rich nutrient elements.

Chinese phosphate ore resources are abundant but not rich, of which 70% are P_2O_5 15–25% middle-low-grade collophane ore containing high silicon and magnesium. Due to its small mineral grain size, densely embedded, and many harmful impurities, it makes beneficiation difficult largely, and a considerable amount of phosphorus will be lost during the beneficiation process [3, 4]. In addition, 4t tailings were accumulated at least when 1t high-grade phosphate ore with P_2O_5 30% was beneficiated, which has a significant impact on the environment [5, 6]. Fused calcium magnesium phosphate fertilizer (FMP) can directly use middle-low-grade phosphate rock and the ore flux containing magnesium and silicon as raw materials, which are melted at high temperature and quenched with water to form glassy fragments with low chemical stability. Xu Xiucheng [7] invented the glass structure factor (O_b/Y_b) batching method to guide the production of FMP. O_b/Y_b is a significant parameter reflecting the size of FMP glass network. If O_b/Y_b has a large value, the glass network is too small to prevent the growth of crystal and obtain a complete vitreous body, resulting in the inferior of citric solubility, whereas the glass network has a small O_b/Y_b value, which will stabilize the glass structure and hinder the dissolution of nutrient elements. Therefore, it is of crucial importance to produce FMP to control the burdening range within a suitable O_b/Y_b range.

FMP prepared with low-grade phosphate rock contains essential elements (P_2O_5 , MgO, CaO, SiO_2 , K_2O , FeO, MnO, etc.) for plant growth, which can effectively alleviate soil acidification, nutrient deficiency, and imbalance of trace elements in crops. Meanwhile, the direct utilization of low-grade phosphate rock can avoid the high cost and phosphorus loss caused by beneficiation, as well as environmental risks caused by tailings [8]. In this paper, the efficient burdening and preparation process of FMP from low-grade phosphate ore were studied, aiming to find an appropriate O_b/Y_b value. The influence of melting temperature and time on the effective conversion of various nutrient elements in phosphate ore under this O_b/Y_b was studied, which can provide support for preparing multifunctional FMP from low-grade phosphate ore resources.

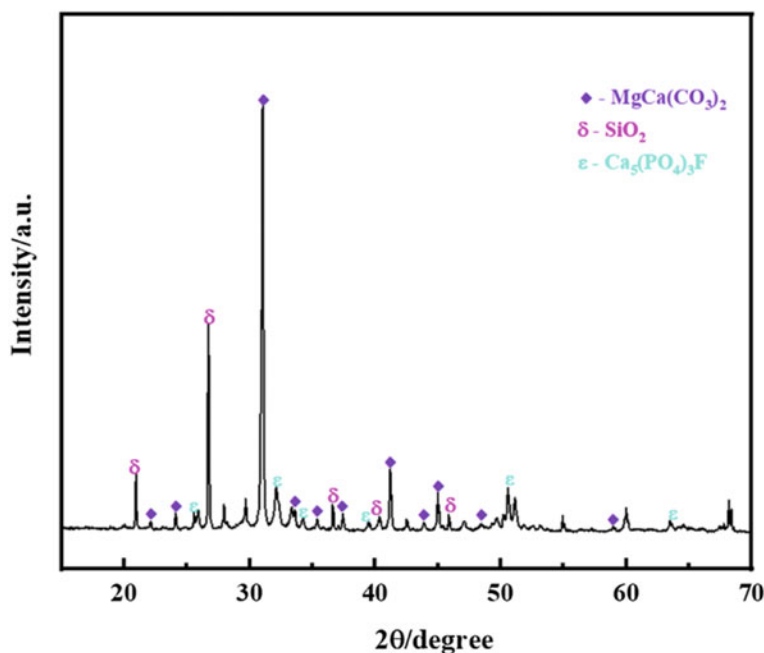
Experimental

Raw Materials

Phosphate ore and dolomite used in the experiment were taken from Guizhou, China. Raw materials were dried at 120 °C for 3 h, and then ground to 100% passing 0.125 mm standard sieve. Their chemical compositions are presented in Table 1. From the main chemical compositions in Table 1, the sample was characterized

Table 1 Chemical compositions of the phosphate ore and dolomite (mass fraction, wt%)

Composition	P ₂ O ₅	CaO	MgO	SiO ₂	Fe ₂ O ₃	Al ₂ O ₃
Phosphate ore	18.10	27.47	2.21	35.72	1.71	2.91
Dolomite	–	29.01	17.00	–	–	1.16

**Fig. 1** XRD patterns of phosphate ore

by a low-grade phosphorus ore with P₂O₅ grade of 18.10%. XRD patterns of the phosphate ore shown in Fig. 1 which reveals that phosphate ore mainly consists of fluorapatite, quartz, and dolomite.

Characterization

Based on the theory of O_b/Y_b prepared by fertilizer [9], four formulations of O_b/Y_b values were designed, respectively, and the batching schemes were shown in Table 2. In terms of characteristic fusion temperatures, the phosphate ore and dolomite with various O_b/Y_b values were tested to determine the suitable temperatures for the melting process. The mixtures were placed in a mold into pyramids with a bottom side length of 8 mm and a vertical height of 18 mm. The pyramids were then roasted in a microcomputer grey melting point tester with a heating rate of 5 °C/min in

Table 2 Design of raw material compositions under different O_b/Y_b values

O_b/Y_b	Raw material compositions (mass fraction, wt%)					
	P_2O_5	CaO	MgO	SiO_2	Fe_2O_3	Al_2O_3
2.89	15.58	35.60	8.66	31.38	0.68	2.91
2.97	15.09	36.20	9.40	30.38	0.65	2.99
3.03	14.69	36.68	9.99	29.58	0.64	2.97
3.06	14.43	36.98	10.37	29.06	0.63	2.95

an air atmosphere. The characteristic temperatures were identified according to: (1) deformation temperature (T_D), determined by the temperature at which the tip of the pyramid becomes spherical or curved; (2) sphere temperature (T_S), determined by the temperature at which the whole pyramid deforms to be hemispheric; and (3) flow temperature (T_F), determined by the temperature at which the pyramid melts until the vertical height is less than 1.5 mm [10, 11].

Melting Process

Before oxidation melting experiments, the raw materials consisted of phosphate ore and dolomite with various O_b/Y_b values were evenly mixed, and then the mixtures were put into a cylindrical heat-resistant graphite crucible with a diameter of 80 mm and height of 80 mm. The graphite crucible was loaded into the high-temperature industrial electric furnace and isothermally melted in the air atmosphere at given temperatures and time periods. After that, melted products were quenched into the cool water to obtain glassy fragments. These fragments were dried and ground into pulverous samples for further characterization and analysis.

Determination of the Activities of Nutrients

In order to determine the effect of different O_b/Y_b values, melting temperature and time on the effective conversion of nutrients in the molten pulverous sample were measured with reference to the Chinese standard (GB/T 201,412-2006), and the total content of various nutrients was measured according to the Chinese standards (GB/T 1871.1-1995, GB/T 1871.4-1995, GB/T 1871.5-1995, and GB/T 1873-1995). The effective conversion of the nutrients was calculated using Eq. (1):

$$\eta = \frac{c}{T} \times 100\% \quad (1)$$

where η is the effective conversion of the nutrients, %; C and T are the content of effective nutrient and total nutrient, respectively, %.

Results and Discussion

Effect of Various O_b/Y_b Values

Generally, the operation temperature of FMP is tentatively set at $T_F + 150$ °C in order to discharge products smoothly during the industrial production process [12]. The characteristic fusion temperatures of mixtures under different O_b/Y_b values are measured, as shown in Fig. 2. It can be seen that the T_D and T_S first decrease and then increase, and the temperature changes slightly. The T_F first decreases and then tends to be stable with the gradual increase of O_b/Y_b .

As a macronutrient contained in FMP, phosphorus is very important for plant growth. The effective conversion of P_2O_5 is used as the evaluation index. In this paper, the influence of various O_b/Y_b values on the effective conversion of P_2O_5 is studied at $T_F + 150$ °C for 3, 5, and 10 min. It can be seen from Fig. 3 that the effective conversion of P_2O_5 is generally lower at about 50% under the reaction time of 3, 5 min. When the reaction time is 10 min, the effective conversion of P_2O_5 decreases slowly and then increases with the increase of O_b/Y_b , and the conversion rate reaches 94.87% at O_b/Y_b of 3.06. Hence, the suitable O_b/Y_b is in the range of

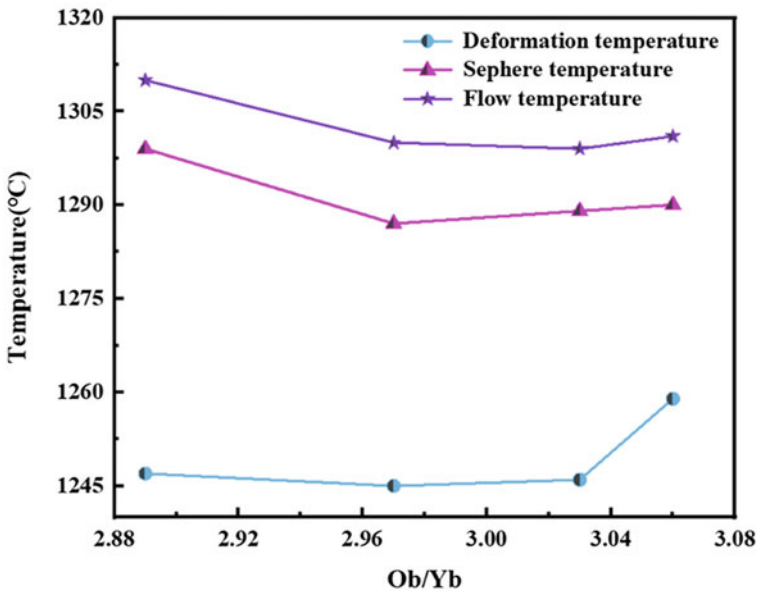


Fig. 2 Effect of various O_b/Y_b values on characteristic fusion temperatures of materials

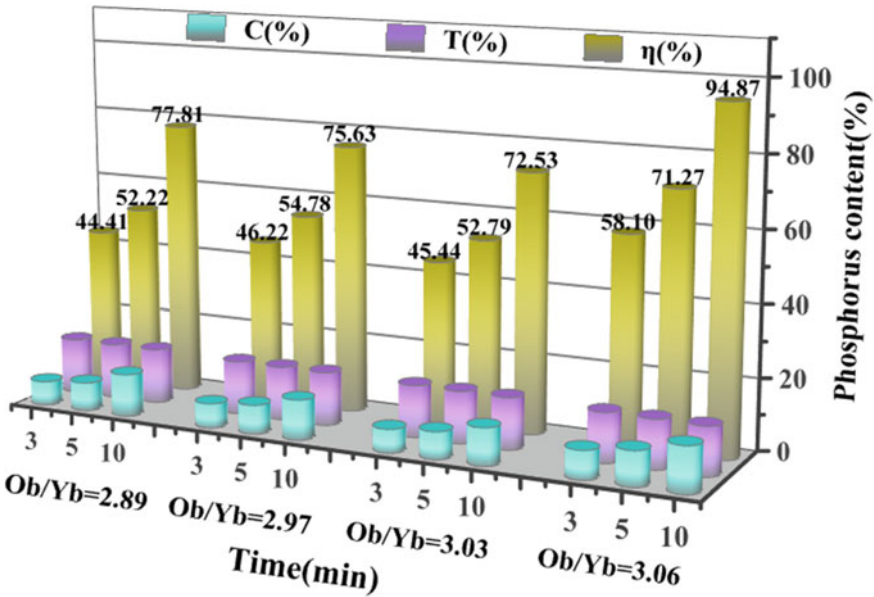


Fig. 3 Effect of various O_b/Y_b values on the effective conversion of P_2O_5

2.87–3.07. It is favorable to form a suitable size glass network, which can not only prevent the growth of crystal and the precipitation of $Ca_5F[PO_4]_3$ crystal but also can facilitate the dissolution of nutrient element $[PO_4]^{3-}$ and improve the effective conversion of nutrient elements.

Effect of Temperature

The kinetic energy of the thermal movement of molecules in phosphate ore increases and the material changes from crystal phase to amorphous phase when the temperature rises. Therefore, the melting of phosphate ore is a strong endothermic process, the change of temperature has a significant effect on the melting of phosphate ore [13]. The effect of temperature on effective conversion of P_2O_5 , SiO_2 , CaO , and MgO is investigated when the O_b/Y_b is 3.06 and the reaction time is 10 min. The results are shown in Fig. 4.

Figure 4a, b displays that the effective conversion rates of P_2O_5 and SiO_2 are 10.62% and 13.49%, respectively, at a sintering temperature ($T_D-100\text{ }^\circ\text{C}$) of 1160 $^\circ\text{C}$. As the temperature increases, the elements of phosphorus and silicon are continuously activated, and the effective conversion increases accordingly. Within the temperature scope of T_F (1300 $^\circ\text{C}$) – $T_F + 150\text{ }^\circ\text{C}$ (1450 $^\circ\text{C}$), the effective conversion rates of P_2O_5 and SiO_2 increase rapidly from 31.08% and 50.78% to 94.87% and 92.46%, increasing by 63.79% and 41.68%, respectively.

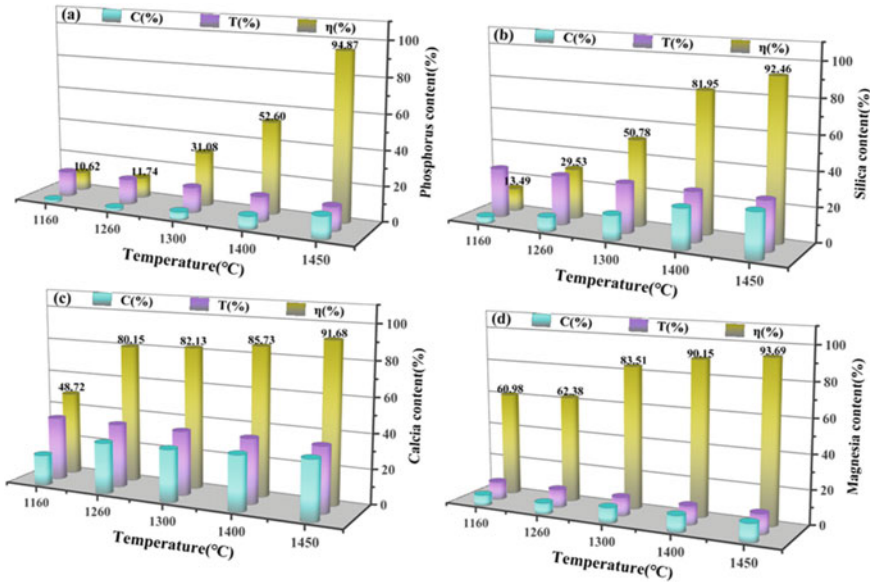


Fig. 4 Effect of temperature on effective conversion of nutrient elements **a** P₂O₅; **b** SiO₂; **c** CaO; **d** MgO

As can be viewed in Fig. 4c, d, the effective conversion of CaO and MgO increases rapidly with the temperature from T_D-100 °C to T_F, and the effective conversion of CaO and MgO is above 80% at T_F. After that, with the increase of temperature, the increase of effective conversion of CaO and MgO begins to slow down, and the effective conversion reaches 91.68% and 93.69%, respectively, at T_F + 150 °C. Thus, this shows that temperature has a remarkable effect on the effective conversion of nutrient elements. According to O_b/Y_b theory, the higher the melting temperature, the more fluorapatite in the mineral can dissociate into dispersed ions during the melting of minerals. Due to adding a certain amount of dolomite, the dispersed ions combine with Ca²⁺ and Mg²⁺ to form a distorted chain network, which can disperse F-Ca-PO₄ crystals and block them from growing up inside the network. Consequently, it is recommended to choose T_F + 150 °C as the suitable melting temperature.

Effect of Time

Figure 5 shows the influence of time on the effective conversion effect of nutrient elements under the condition of O_b/Y_b of 3.06. Figure 5a illustrates the time has a significant effect on the effective conversion of P₂O₅, and the effective conversion rate is relatively lower with an effective conversion of 58.10% at 3 min. When the time ranges from 3 to 10 min, the effective conversion increases rapidly and reaches

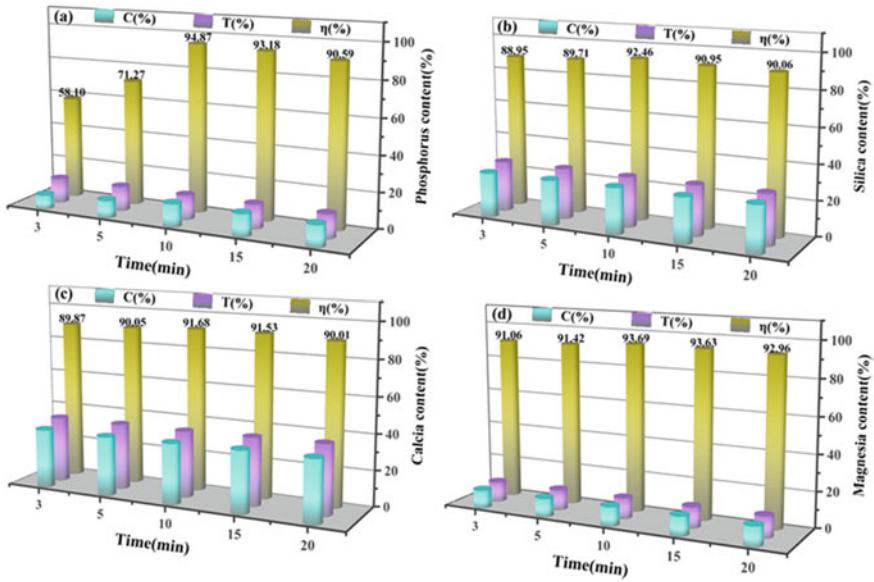
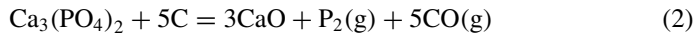


Fig. 5 Effect of time on effective conversion of nutrient elements a P₂O₅; b SiO₂; c CaO; d MgO

the highest value of 94.87% at 10 min. However, the effective conversion of P₂O₅ decreases slightly to 90.59% with the extension of time to 20 min, which reduces by 4.28% compared with the maximum. This may be since more and more dispersed ions are dissociated from fluorapatite in phosphate ore, and the reaction is sufficient for the well-contact between materials with the increase of time in the initial stage of the reaction. However, a long reaction time would result in partial phosphorus volatilization according to Formulas (2)–(3). As seen from Fig. 5b–d, the smelting time has no obvious effect on the effective conversion of SiO₂, CaO, and MgO, in which all the effective conversion of nutrient elements are about 90%. Eventually, 10 min is recommended as the melting time.



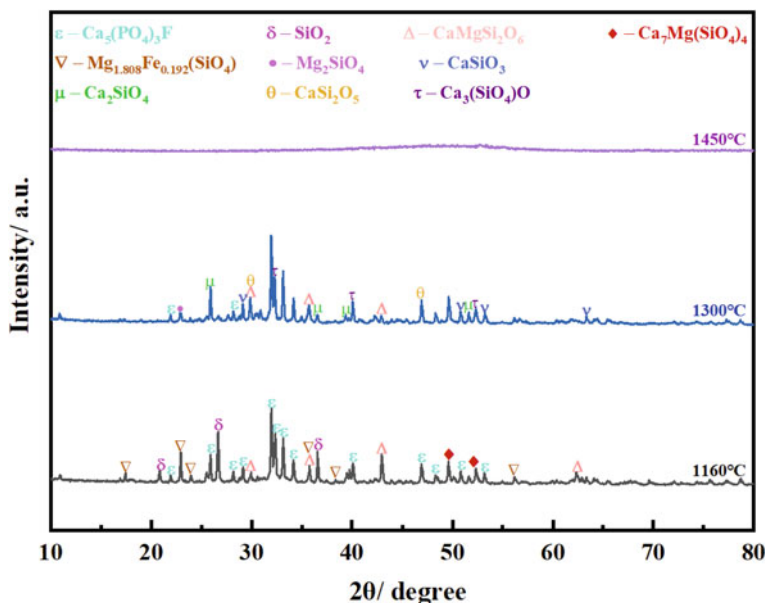


Fig. 6 XRD patterns of the FMP obtained at different temperatures after water quenching

Phase Analysis

Figure 6 reveals the XRD patterns of FMP obtained at different melting temperatures for 10 min with O_b/Y_b of 3.06 after water quenching. It can be seen that the main phases are fluorapatite, quartz, and forsterite. In this case, the phosphate rock is not fully melted, while only part of the fluorapatite is dissociated, and the phase changes under the condition of the low temperature of 1160 °C. Moreover, the characteristic peaks of fluorapatite and quartz gradually weaken, and the crystal form gradually disappears. Some new substances are constantly formed with the increase in temperature. However, the water-quenched FMP still shows characteristic peaks of different crystals and fails to show the glassy structure in the range of 1160–1400 °C. As the temperature increases to 1450 °C, there is no obviously sharp characteristic diffraction peak in the XRD pattern, and it basically shows wide range and slowly changing diffraction peaks, indicating that the FMP prepared at this temperature is in a glassy state, and it is beneficial to the release of nutrient elements.

Conclusions

In this paper, an efficient batching for the preparation of FMP from low-grade phosphate ore and dolomite was studied. The influence of melting temperature and time on the effective conversion of nutrient elements in phosphate ore was explored, and

the process conditions were optimized to find out suitable conditions. The results indicated that a higher O_b/Y_b burden was more likely to form a suitable size glass network. The melting temperature and time have a significant influence on the effective conversion of nutrient elements. The effective conversion of nutrients increased with the increase of temperature since the higher melting temperature, the more fluorapatite in the mineral can dissociate into dispersed ions, according to O_b/Y_b theory. After melting at 1450 °C for 10 min with O_b/Y_b of 3.06, 94.87% P_2O_5 , 91.68% CaO, 93.69% MgO, and 92.46% SiO_2 are activated in the alkaline FMP, which can be readily absorbed by the crop root system.

Acknowledgements The authors wish to express their thanks to the National Key Research and Development Program of China (No. 2018YFC1900201, 2018YFC1900200), the Program for Innovative Research Team (in Science and Technology) in the University of Henan Province (No. 19IRTSTHN028), and the Special Support Program for High-Level Talents in Henan Province (No. ZYQR201912182) for the financial support.

References

1. Zhao YF, Yin YW (2015) Key scientific problems on establishing green fertilizer insurance system. *Chin Sci Bull* 60(36):3527–3534
2. Hou CH, Miao JY, Gu SY, Wang HB (2019) Innovation of fused calcium magnesium phosphate products to promote industry development. *J Plant Nutr Fert* 25(12):2162–2169
3. Abouzeid AZM (2008) Physical and thermal treatment of phosphate ores—an overview. *Int J Miner Process* 85(4):59–84
4. Liu BB, Xue YB, Han GH, Zhang L, Huang YF, Hou CH, Cao YJ (2021) An alternative and clean utilisation of refractory high-phosphorus oolitic hematite: P for crop fertiliser and Fe for ferrite ceramic. *J Clean Prod* 299:126889
5. Hou CH, Xu XC, Miao JY (2017) Sustainable utilization of various grades of phosphorus resources in China. *J Wuhan Inst Technol* 39(06):629–632
6. Liu YC (2013) Analysis of the present state and prospects of comprehensive utilization technology of mineral resources in China. *Multipurp Util Miner Resour* 06:1–3
7. Xu XC (1982) Glass structure theory of fused magnesium phosphate and its application. *J Zhengzhou Univ* 2:1–10
8. Cooper J, Lombardi R, Boardman D I (2011) The future distribution and production of global phosphate rock reserves. *Resour Conserv Recy* 57:78–86
9. Xu XC (1983) Fused magnesium phosphate using the burden method of the glass structure factor. *Henan Chem Indus* 2:7–11
10. Luo J, Li G, Rao M, Zhang Y, Peng Z, Zhi Q, Jiang T (2015) Evaluation of sintering behaviors of saprolitic nickeliferous laterite based on quaternary basicity. *JOM* 67(9):1966–1974
11. Liu BB, Li RJ, Su SP, Zhang YB (2020) Characterization on the behaviors of Ca and Si constituents during the consolidation of ferruginous manganese ores. In: TMS characterization of minerals, metals, and materials, pp 126–135
12. Hou CH, Li LY, Hou LS, Liu BB, Gu SY, Yao Y, Wang HB (2021) Sustainable and clean utilization of Yellow Phosphorus Slag (YPS): activation and preparation of granular rice fertilizer. *Materials* 14(8):2080
13. Hu B (2014) Study on process optimization and mechanism of phosphate ore melting reduction. M.D. thesis, Wu Han Institute of Technology

Characterization of Nano-crystalline Metallurgical-Grade Silicon Prepared from Rice Husk Ash



B. O. Ayomanor, C. Iyen, I. S. Iyen, V. Mbah, D. I. Anyaogu, D. N. Dawuk, S. D. Ndiriza, S. O. Aniko, and M. Omonokhua

Abstract Rice husk (RH), an agricultural waste product, contains a large proportion of silicate minerals, making it a potential source of low-cost metallurgical-grade silicon (MG-Si) suitable as a solar-grade silicon material. Processing rice husk ash into MG-Si requires careful control of temperature and time during the initial ash-making procedure and subsequent refinement to remove impurities. In this work, silica of between 95.24 and 98.03% has been prepared from RHA (ash made at 700, 800, 900, and 1000 °C for 6 h). Furthermore, the silica value was boosted by use of hydrometallurgical purification process. The improved purification processes yielded between 99.18 and 99.51% of silica. The metallic trace impurities were significantly reduced beyond detection of the X-ray Fluorescence (XRF) after the final processing step. Metallothermic reduction of pulverized Mg and SiO₂ mixture at ratio 1:1 g was post hydrometallurgical purified to further eliminate all soluble impurity. XRF showed silicon powder with purity >98% and the X-ray Diffraction (XRD) showed that Rice Husk Ash (RHA) transformation from amorphous to crystalline material depends on temperature and time. Transmission Emission Microscopy (TEM) investigation shows that derived silicon consists of agglomerate polycrystalline materials with grain sizes of 20–67.08 nm.

Keywords Rice husk ash · Anneal · Carbothermal · Metallothermic · Leaching

B. O. Ayomanor (✉) · V. Mbah · D. I. Anyaogu · D. N. Dawuk · S. D. Ndiriza · S. O. Aniko · M. Omonokhua

Department of Science Laboratory Technology, School of Applied Sciences, Federal Polytechnic Nasarawa, Nasarawa, Nigeria

C. Iyen

Department of Pure and Applied Physics, Federal University Wukari, Wukari, Nigeria

I. S. Iyen

Department of Chemical Sciences, Federal University Wukari, Wukari, Nigeria

© The Minerals, Metals & Materials Society 2022

M. Zhang et al. (eds.), *Characterization of Minerals, Metals, and Materials 2022*,

The Minerals, Metals & Materials Series,

https://doi.org/10.1007/978-3-030-92373-0_10

Introduction

MG-Si is a semi-conductor, which has a wide range of industrial applications which include the production of electronic-grade silicon used in the production of solar cells. It is the least category within the quality ranges of different silicon products [1]. MG-Si with a purity of 98% was prepared by carbothermal reduction of quartz (SiO_2) in electric-arc furnace at high temperature of about 1900 °C [2]. For economic purpose, rice husk known to have a high ash (silica) content at low temperature is used as alternative starting material for silicon [3]. Globally, approximately 706.2 million tonnes of rice paddy were produced in 2012, with Nigeria producing 4.2 million tonnes [4]. Rice husk (RH), an agricultural waste, constitutes between 14 and 27% of the rice paddy [5]. The major constituents of RH are cellulose, hemicellulose, lignin, and ash [6]. On the average, 20% of rice husk ash (RHA) is produced from combusted RH yielding 80–95% useful silica content [7]. Meaning, that Nigeria alone could produce as much as 170,000 tonnes of silica per year from its rice production. Silica dominates RHA with other trace amount of oxides [8]. The nature of this silica depends on its burning temperature and time; by carefully controlling the combustion of the RH, a reactive silica can be achieved [9]. The presence of amorphous silica, crystalline silica, or both in RHA depends on the temperature of heating used. Previous work has shown that RHA obtained at about 1000 °C contains certain amount of tridymite and cristobalite [10–12]. International Agency for Research on Cancer (IARC), a part of World Health Organization (WHO), strongly points that crystalline silica particles belong to group 1 that has carcinogenic risk to humans [12]. RHA with its high proportion of silica and a relatively low proportion and narrow range of metallic impurities could be an attractive renewable source of raw material for high-purity silicon production [13]. Quartzite rocks used as a source material for conventional carbothermic metallurgical-grade silicon yield smaller proportion of silica and many more impurity elements [13]. Therefore, effort has considerably been put to optimize the production of silicon from RHA [14–17]. RHA is a highly porous and fibrous material with high surface area and a microstructure of a honeycomb as indicated by Scanning Electron Microscopy (SEM) images, and these properties makes the removal of impurities through leaching easier [18]. The primary objective of this study is to produce a nano-crystalline metallurgical-grade silicon material from high-level purity silica feasibly acceptable as a starting material for solar-grade silicon.

Materials and Method

Rice husk, a by-product of rice paddy collected from Nasarawa Local Government Area in Nasarawa state of Nigeria, was used as source of raw materials for preparation of rice husk silica. Raw rice husk (RRH) is a RH as obtained from a rice milling industry dumping site, which, as such, contains some very small particles of rice and

dirt from the rice husk dumping site. Figure 1a shows the representation of RRH thoroughly washed with distilled water and sun dried at above 30 °C for 12 h. 30 g sun-dried RRH were placed in four different crucibles and introduced into a furnace for pyrolysis treatment at 700, 800, 900, and 1000 °C for 6 h as shown in Fig. 1b. The obtained annealed RHA samples in Fig. 1c were analyzed with XRF, XRD, SEM, TGA (thermal gravimetric analysis), and Attenuated Total Reflectance-Fourier Transform Infrared (ATR-FTIR) spectroscopy.

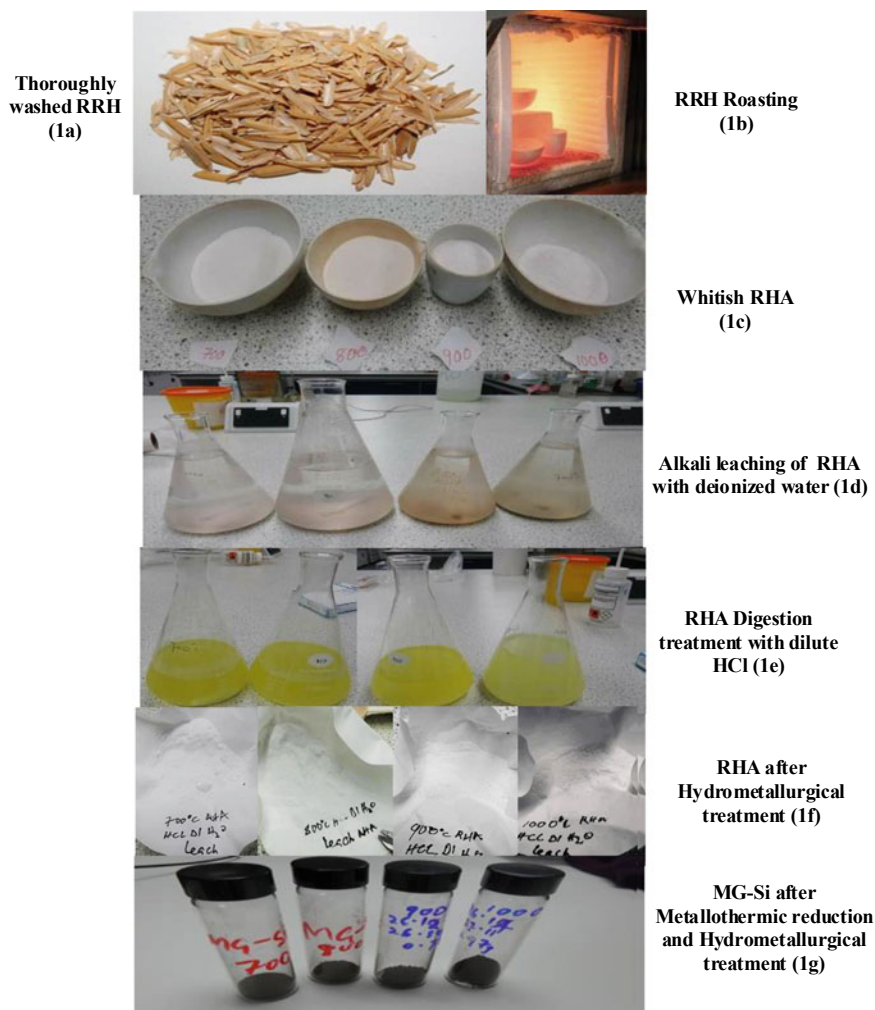


Fig. 1 The appearances and processes from Raw Rice Husk (RRH) to RHA (silica) to MG-Si. **a** RRH thoroughly washed with deionized water. **b** Thoroughly washed RRH roasting at different temperatures for 6 h. **c** Whitish RHA derived from roasting. **d** Alkali leaching of RHA with deionized water. **e** RHA treatment with hot diluted HCl. **f** High purity RHA after hydrometallurgical treatment. **g** Derived MG-Si after metallurgical reduction and hydrometallurgical treatment

Preparation of High-Purity Silica (RHA)

Rice husk ash samples containing chemical compositions were subjected to upgradation/purification by carrying out induced oxidation of RHA carbon to CO_2 to improve the silica content. 15 g of each RHA were added to 0.8 cm^3 of 16 M HNO_3 , and heated in an electric furnace at $700 \text{ }^\circ\text{C}$ for 1 h. The coarse particles of all RHA specimens were seen to have pulverized, and particle sizes reduced on cooling to room temperature. 13 g of each oxidant-treated RHA were boiled in 500 ml deionized water for 1 h so as to leach out the sodium and potassium impurities that are soluble in boiling water as shown in Fig. 1d. The residues were dried at $100 \text{ }^\circ\text{C}$ in an oven till constant weights were obtained. Exactly 11 g of RHA specimens from alkali leach RHA were digested in 500 ml of 5 M hydrochloric acid on hot plate for 120 min at $95 \text{ }^\circ\text{C}$, giving constant agitation of 300 rpm by magnetic stirrer. The solution was then left to cool to room temperature as shown in Fig. 1e. The residues of digested samples were filtered using Whitman paper and then dried in an oven for 1 h at $110 \text{ }^\circ\text{C}$. 9.5 g of each sample was added to conical flask containing 1000 ml deionized water with magnetic stirrer for continuous stir at 300 rpm. The flasks were transferred to hot plates to heat up for 1 h at $85 \text{ }^\circ\text{C}$ before dropping to cool down for 12 h. The acidic solution was decanted carefully with the solution temperature and pH reading taken. The process was repeated this time for 2 h settling time before decanting of solution after dropping from the hot plate until acidic solution was observed to have a pH = 7.0–7.4 before final filtering and oven drying. The obtained samples shown in Fig. 1f were analyzed by XRD, SEM, and XRF.

Production of Silicon

The treated RHA samples derived after various solid–liquid extraction were pulverized and thoroughly mixed with magnesium powder in a mortar at a ratio of RHA: Mg (1.0 g: 1.0 g) to form magnesium and silica mixture. 4.0 g of each sample were transferred from the mortar to alumina crucibles for heating in an electric furnace with controlled atmosphere at $800 \text{ }^\circ\text{C}$ for 5 h. By heating the mixture, the magnesium reduces the silica to elemental metallurgical-grade silicon.



The reduced samples were treated with an oxidant (HNO_3), digested in dilute HCl, and digested solution neutralized to a pH of about 7.0 with enough deionize water. The solution was finally filtered and oven dried; the products in Fig. 1g were obtained and analyzed by XRD, XRF, SEM, TEM, and Raman spectroscopy.

Results and Discussion

In order to obtain high-purity RHA (silica), thoroughly washed raw rice husk (RRH) has to undergo pyrolysis and various hydrometallurgical processes as shown in Fig. 1. Samples of rice husk (both as-produced and ground) underwent thermogravimetric (TG) analysis using a TGA/DSC1 Gas Controller GC100 Mettler Teledo at heating rate of 10 °C/min. Two starting states were used to investigate the effect of initial particle size on the ash-making process. In all samples, volatile organic substances (cellulose, hemicellulose, and lignin) contained in the RH started to be driven off at 40 °C; the process was completed at 117 °C, as shown in Fig. 2. It was seen that 4.60% and 4.98% (0.50 mg and 0.66 mg) of the substance lost in the process for “raw” rice husk and ground rice husk, respectively. Carbonization occurs between 117 and 300 °C to yield black rice husk ash with very little loss in mass. Decarbonization occurs rapidly between 300 and 500 °C with very high percentage weight lost up to 63% (7.06 mg) and 56% (7.47 mg) for “raw” RH and ground RH, respectively.

These results show that a greater proportion of carbon and volatile organic substances are removed from the “raw rice husk. It is postulated that this impact is due to the release of some volatile organic compounds as a result of increase in exposed surface from grinding. The settling of the finer particles may also reduce the penetration of oxygen to some of the sample resulting in incomplete combustion. The final product mainly contains silica [19]. The secondary electron images obtained using FEI Nova Nano SEM 200 reveal in Fig. 3 some selected forms and microstructures of RHA independent of temperature and time. It was observed from Fig. 3a that undamaged RH after ash-making between 700 and 1000 °C possesses a finger-like shape made up of inner honeycombed structure as shown in Fig. 3b and a thick outer surface skin-like well-organized corrugated structure in nature as shown in the micrographs of Fig. 3c surface morphology. These observations are in

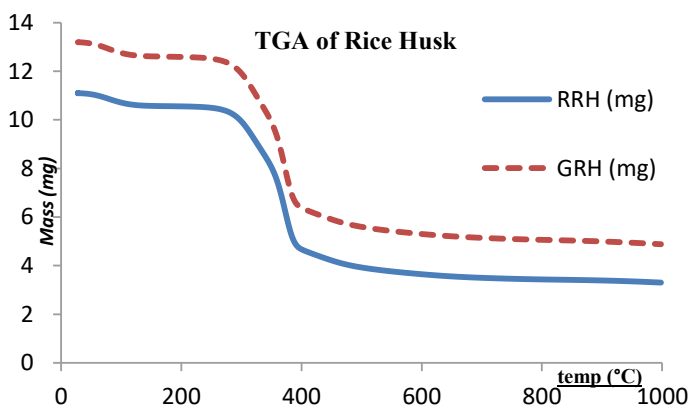


Fig. 2 Thermogravimetric analysis offset curves of raw rice husk (RRH) and ground rice husk (GRH)

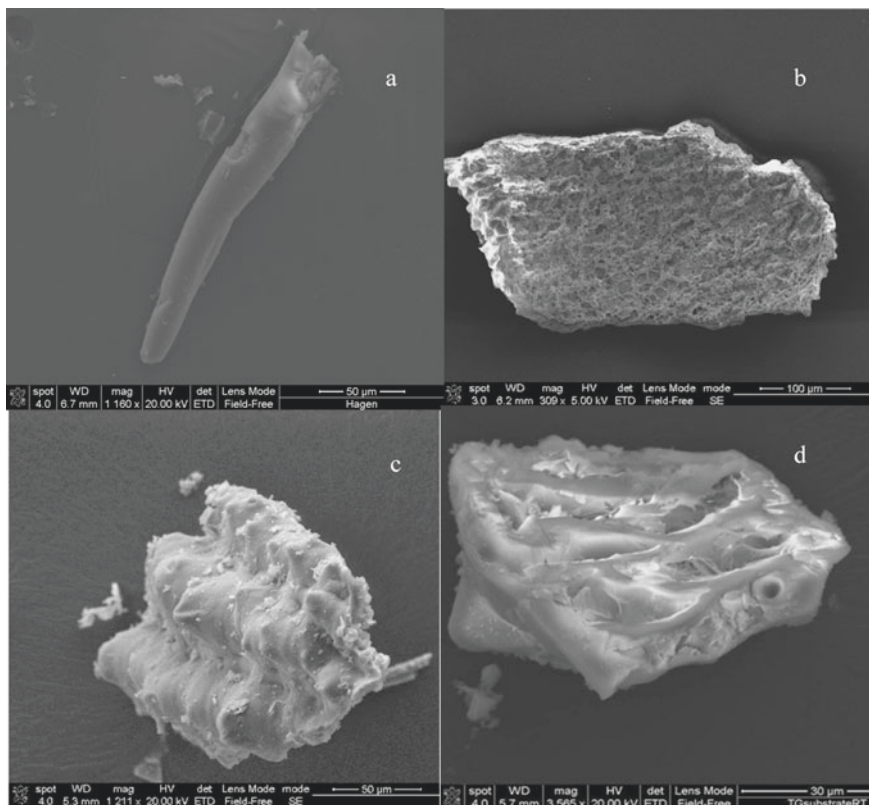


Fig. 3 Typical micrograph of 900 °C for 5 h **a** RHA undamaged finger-like structure, **b** porous, honeycomb-like structure, **c** well-organized outer corrugated structure, **d** the structure with many residual pores of large internal surface area

agreement with those made by Ikram and Akhter [20]. The porosity shown in Fig. 3d with honeycombed structure of the RHA is responsible for its high specific surface area; the increased reactivity that is a consequence of the high specific surface area reduces the time needed for leaching process to be effective and highly suitable for hydrometallurgical purification.

Samples of rice husk and rice husk ash underwent attenuated total reflection Fourier transform infrared (ATR-FTIR) analysis using a single reflection diamond ATR cell (Graseby Specac, UK), which has the trade name “Golden gate”. Samples of RH and RHA were pressed on top of the diamond ATR crystal and their spectra were collected. To collect and analyse the spectra, OMNIC software (version 7.3) was used. Figure 4 shows the resulting ATR spectra for the samples of raw RH (lowest peak and intensity) and the ash silica heated at 700, 800, 900, and 1000 °C (in order to see the differences, spectra were offset).

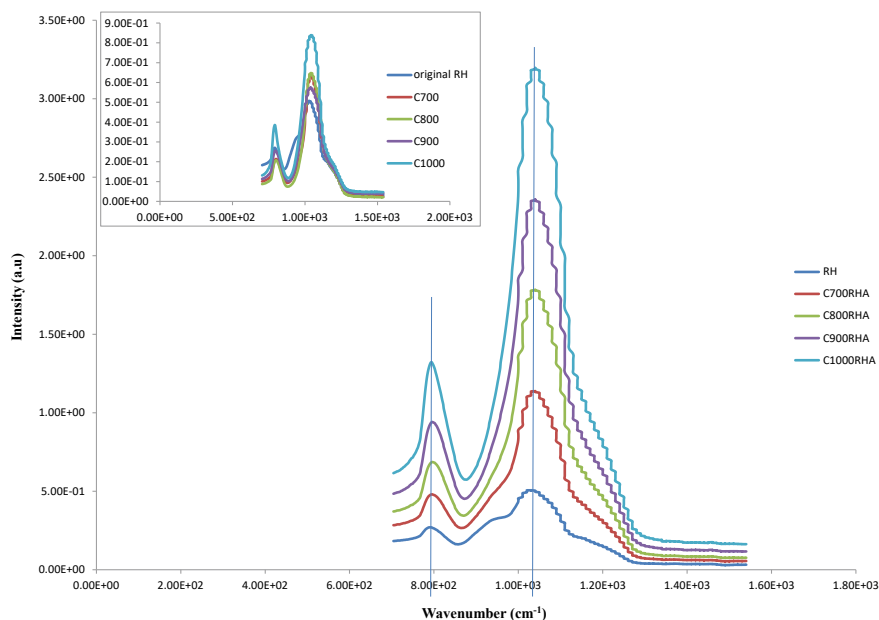


Fig. 4 ATR spectrogram of RH and RHA. **a** original spectra, **b** offset spectra

As can be seen, there are strong absorption peaks at ~ 789 and 1040 cm^{-1} , just as those from commercial-grade silica, indicating the presence of silica which slightly varied from that of the rice husk with 789 and 1030 cm^{-1} . For the various heating rates, the ATR spectrum shows no significant changes in the peak position. However, the intensity of the peaks for 700 and $800 \text{ }^\circ\text{C}$ (amorphous silica) just above the RH was higher and almost of same intensity compared to that of crystalline silica ($900 \text{ }^\circ\text{C}$), indicating that the amorphous silica yield decreased with increasing heating rate above $800 \text{ }^\circ\text{C}$. The intensity later increased with increased heating to $1000 \text{ }^\circ\text{C}$ (highest peak) which is consistent with the results of reaction characteristic analysis, as indicated by some XRD diffractogram. This inferred that the sample is almost entirely crystalline in nature. Figure 5 shows the diffractogram of the purified silicon derived compared to a standard silicon. The XRD pattern showed the typical phases identified in the MG-Si derived from metallothermic process of rice husk silica reduced with magnesium powder and some by-products other than silicon. The reaction products observed apart from silicon are magnesium silicide (Mg_2Si) and spinel (MgAl_2O_4). These by-products irrespective of their amounts presented in the phases of diffractogram spectra have detrimental effect on silicon yield. Grinding of RHA before reduction and acid leaching increases the exposed surface of derived RHA MG-Si. This helps in enhancing material purification.

The micrograph of Fig. 6a shows that the RHA MG-Si is in agglomerate of tiny flakes up to $0.5 \text{ }\mu\text{m}$ in diameter. The ring diffraction from Fig. 6b shows that the RHA MG-Si consists of fine polycrystalline material with no obvious texture.

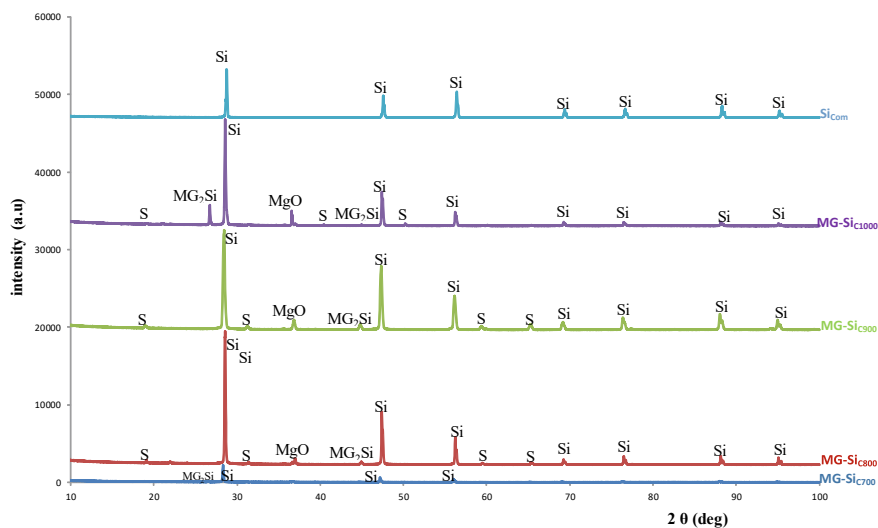


Fig. 5 Offset X-Ray diffractograms for RHA reduced with magnesium and a commercial-grade MG-Si (symbols Si, Mg₂Si, MgO and S: Peak positions of silicon, silicide, Magnesium oxide, and spinel, respectively)

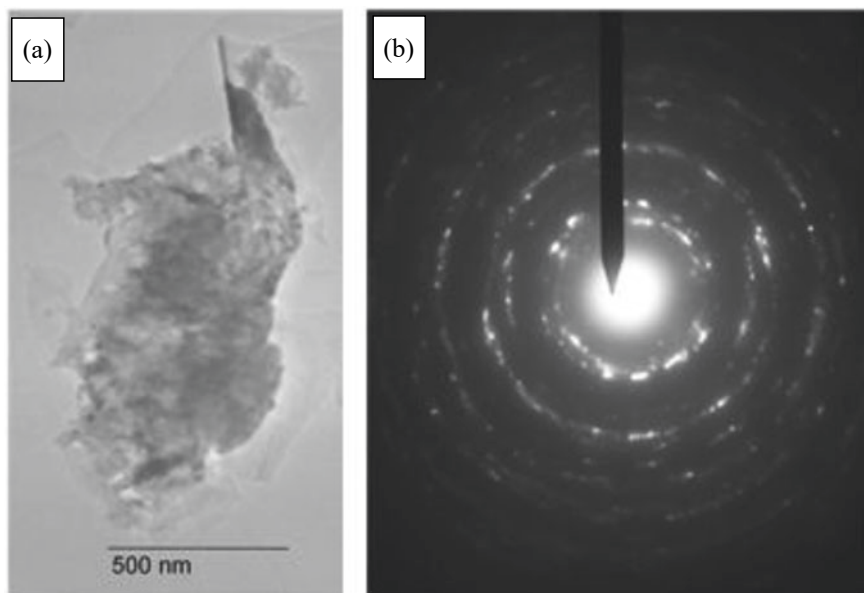


Fig. 6 **a** Bright-field TEM micrograph of a particle of RHA-derived silicon. **b** Ring diffraction pattern obtained from selected area of particles of RHA-derived silicon

Table 1 Crystallite size of MG-Si derived from RH roasted at different temperatures

S/N	Temp (°C)	Crystallite size (nm)	(hkl)
1	700	54.46	(111)
2	800	54.49	(111)
3	900	61.32	(111)
4	1000	50.29	(111)

Some of the crystallites within the RHA MG-Si are as small as 20 nm in diameter, which is in agreement with the calculated results in Table 1 showing obtained nano-particle sizes of the derived MG-Si by evaluation of their XRD parameters using Scherrer's equation [21]

$$D = \frac{0.9\lambda}{\beta \cos\theta} \quad (2)$$

where D is the crystallite size; λ is the standard X-ray wavelength of Cu $K\alpha$ line; and β is the broadening of diffraction line measured at half of its maximum intensity (rad). Meaning conversion of Full Width at Half Maximum (FWHM) to radian.

Figure 7 shows a set of representative Raman spectra run under same conditions for all samples of silicon produced under different temperatures. The Raman instrument used is Thermo Scientific, DXR2 Raman Microscope, USA product. It was observed that 700 and 800 silicon powder shift farther away from the frequency of single crystal silicon value 520 cm^{-1} toward amorphous silicon of lower frequency value 480 cm^{-1} and become more broaden than the crystalline silicon. The line that passes through 700 and 800 of the spectra peak occurs at frequency value 505 cm^{-1} indicating 900 and 1000 with frequency value 513.5 are more crystalline in nature than the latter. The downshift of frequency and spectral broadening are indicative of small crystallite size smaller than $\sim 300 \text{ \AA}$. These observations are in agreement with those made by Campbell and Fauchet [22] and Iqbal et al. [23].

Conclusion

The results from characterization of annealed and treated RHA, show that over 99% clean RHA silica were derived via leaching purification process. The results of derived RHA silica reduced with magnesium and further purified confirmed that a nano-polycrystalline silicon of above 98% purity containing agglomerate of tiny flakes up to $0.5 \text{ }\mu\text{m}$ and crystallites as small as 20 nm in diameter can be produced from an agricultural by-product via an inexpensive process. The nano-crystalline sizes were further determined using Scherer's formula on obtained MG-Si XRD plots, the evaluation confirmed the nano-crystalline nature of derived silicon. Results of Raman revealed that the crystalline nature of the material depends on temperature and time. This observation is in agreement with that made by Chopra et al. [24].

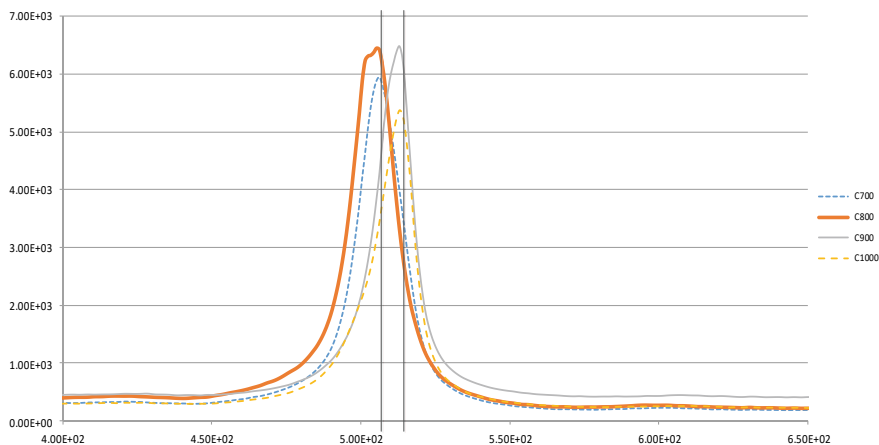


Fig. 7 Raman spectra of polycrystalline silicon derived from RHA at different temperatures. Using laser power of 5mW and wavelength of 532 nm

References

1. Van Overstraeten R, Palz W (eds) (1979) 2nd EC photovoltaic solar energy conference: proceedings of the international conference, held at Berlin (West), 23–26 April 1979. D. Reidel
2. O'Mara C, Herring B, Hont P (1990) Handbook of semiconductor silicon technology. Publications Park Ridge, New Jersey, USA
3. Houston DF (1972) Rice hulls. In: Rice chemistry and technology American Association of Cereal Chemists, Inc. St. Paul, MN, pp 301–352
4. Kapur T, Kandpal TC, Garg HP (1996) Electrical generation from rice husk in Indian rice mills: potential and financial viability. Biomass Bioenergy 10:393–403
5. Govinda Rao VMH (1980) J Sci Indus Res 39(1980):496–501
6. Larbi KK, Roy R, Barati M, Lakshmanan VI, Sridhar R, Mclean A (2012) use of rice husk for emission neutral energy generation and synthesis of solar-grade silicon feedstock. Biomass Conv Bioref 2:149–157
7. Agrawal BM (1989) Utilization of rice husk ash. Glass Ceram Bull 36:1–2
8. Farooque KN, Zaman M, Halim E, Islam S, Hossain M, Mollah YA, Mahmood AJ (2009) Characterization and utilization of Rice Husk Ash (RHA) from rice mill of Bangladesh. Bangladesh J Sci Ind Res 44(2):157–162
9. Nakata Y, Suzuki M, Okutani T, Kikuchi M, Akiyama T (1989) Preparation and properties of SiO₂ from rice hulls. J Ceram Soc Jpn 97:842–849
10. Real C, Alcalá MC, Criado JM (1996) Preparation of silica from rice husks. J Am Ceram Soc 79:2012–2016
11. Hara N (1988) Utilization of rice husk ash for calcium silicate lightweight building materials. J Miner Soc Jpn 18:405–415
12. IARC Monographs on the evaluation of carcinogenic risks to humans, 58(1993):41–61
13. Zemnukhova L, Egorov A, Fedorishcheva G, Barinov N, Sokol' -mitskaya T, Botsul A (2006) Properties of amorphous silica produced from rice and oak processing waste. Inorg Mater 42(2006):24–29
14. Banerjee HD, Sen S, Acharya HN (1982) investigation on the production of silicon from rice husks by the magnesium method. J Mater Sci Eng 52:173–179
15. DN Bose, PA Govindacharyulu (1984) Progress in solar-grade silicon from rice husk ash. Pergamonpress, Perth, pp 2735–2781

16. Ikram N, Akhter M (1988) X-ray diffraction analysis of silicon prepared from rice husk ash. *J Mater Sci* 23:2379–2381
17. Ayomanor BO, Vernon-Parry K (2016) Potential synthesis of solar-grade silicon from rice husk ash, gettering and defect engineering technology XVI, solid state phenomena, vol 242. Trans Tech Publication, Switzerland, pp 41–47
18. Zhang MH, Malhotra VM (1996) High performance concrete incorporating rice husk ash as a supplementary cementing material. *J ACI Mat* 93(6):629–636
19. Liou TH (2004) Preparation and characterization of nano-structured silica from rice husk. *Mater Sci Eng A* 364:313–323
20. Ikram N, Akhter M (1988) X-ray diffraction analysis of silicon prepared from rice husk ash. *J Mater Sci* 23(7):2379–2381
21. Sarangi M, Nayak P, Tiwari TN (2011) Effect of temperature on nano-crystalline silica and carbon composites obtained from rice husk ash. *Comp Part B Eng* 42(7):1994–1998
22. Campbell IH, Fauchet PM (1986) The effects of microcrystal size and shape on the one phonon Raman spectra of crystalline semiconductors. *Solid State Commun* 58(10):739–741
23. Iqbal Z, Vepřek S, Webb AP, Capezzuto P (1981) Raman scattering from small particle size polycrystalline silicon. *Solid State Commun* 37(12):993–996
24. Chopra SK, Ahluwalia SC, Laxmi S (1981) Technology and manufacture of rice-husk ash masonry (RHAM) cement. In: Proceedings of ESCAP/RCTT workshop on rice-husk ash cement, New Delhi

Separation of Nickel and Cobalt from Nickel and Cobalt Solution by Cyanex272



Ganggang Yan, Zibiao Wang, Dinghao Le, Xijun Zhang, Xintao Sun, and Dalin Chen

Abstract The physical chemistry of nickel and cobalt is similar. In this paper, Cyanex272 was employed to extraction and separation of nickel and cobalt. Acetic acid solution was used to reverse extract cobalt from the organic phase, and the cobalt acetate obtained was used as the cobalt source for the preparation of graphene @Co₃O₄ absorbing material. The optimal extraction conditions for maximizing the extraction of cobalt and minimizing the extraction of nickel were researched as follows: extraction ratio (O/A) 1:1, initial pH 5.5, reaction temperature 25 °C, and reaction time 10 min. Under the above conditions, the extraction ratio of single stage cobalt can reach about 96%. The three-stage extraction ratio of cobalt can reach more than 99%, according to the equilibrium diagram of cobalt extraction. Cobalt in organic phase can be easily extracted by acetic acid, and the extraction rate can reach more than 99%. The cobalt acetate obtained by reverse extraction can be used to prepare graphene @Co₃O₄, which can improve the comprehensive utilization of cobalt.

Keywords Nickel–cobalt · Extraction separation · Cyanex272 · Acetic acid

Introduction

Cobalt is often associated with nickel sulfide ore because of the very similar physical and chemical properties of nickel and cobalt. It is very important to separate and recover cobalt from nickel smelting since cobalt resources are scarce. At present, the separation methods of nickel and cobalt are mainly listed as follows: chemical precipitation method, ion exchange method, membrane separation method, solvent

Ganggang Yan and Zibiao Wang contributed equally to this work.

G. Yan · X. Zhang · D. Chen
State Key Laboratory of Nickel and Cobalt Resources Comprehensive Utilization, Jinchang 737100, China

Z. Wang (✉) · D. Le · X. Sun
School of Metallurgy and Environment, Central South University, Changsha 410083, China

extraction method, etc. [1–7]. Solvent extraction technology has become the main method for cobalt–nickel separation due to its advantages of high selectivity, high direct yield, simple process, continuous operation, and easy automation [8].

At present, P507 and Cyanex272 are commonly used extractants for separating cobalt and nickel in industry [9]. P507 is a non-volatile colorless transparent oily liquid. Its chemical name is 2-ethylhexylphosphonic acid mono(2-ethylhexyl) ester, and its molecular formula is $(C_8H_{17})_2OPOOH$. The order of extraction capacity for different metals in the sulfate system is as follows: $Fe^{3+} > Zn^{2+} > Cu^{2+} \approx Mn^{2+} \approx Ca^{2+} > Co^{2+} > Mg^{2+} > Ni^{2+}$. The equilibrium pH values of Ni and Co are so different that they can be separated. However, calcium, manganese, and aluminum can be extracted together during the separation of nickel and cobalt [10]. Cyanex272 is a yellow or colorless oily liquid. Its chemical name is bis(2,4,4-trimethyl) pentyl phosphoric acid, and its molecular formula is $(C_8H_{17})_2POOH$. The separation effect of nickel and cobalt in the solution with HCl is better than that with H_2SO_4 . Cyanex272 is highly selective for nickel and cobalt. Calcium, manganese, and other elements will not be extracted in the nickel–cobalt extraction process [11, 12].

In recent years, many studies have shown that cobalt still has good hysteresis after magnetization, which can be used in the preparation of absorbing materials [13, 14]. Sun et al. [15] have developed a heterostructure material of cobalt sulfide with strong absorption, wide frequency band, thin thickness, and low density. Wang et al. [16] have doped cobalt acetate into graphene through ultrasonic synthesis. It is found that the electrical properties of the composite material were greatly improved. Chen [17] has loaded cobalt on the surface of graphene. It is proved that cobalt does exist on graphene through XRD, Raman, and other detection methods. It is found that compared with graphene with other metal elements, graphene with cobalt composite had better electromagnetic properties.

In this paper, Cyanex272 is used to extract the nickel and cobalt solution from a smelter in China. The pH, phase ratio, reaction time, and reaction temperature of the solution were researched for the optimum extraction conditions. Cobalt acetate is obtained by back extraction of cobalt with acetic acid.

Experimental

Materials and Instruments

The nickel–cobalt solution came from some kind of nickel–cobalt solution of a nickel plant in Jinchang, China. The concentrations of Ni^{2+} and Co^{2+} were 9.6 g/L and 2.6 g/L, respectively. Cyanex272 and sulfonated kerosene used were industrial grade. Other reagents included glacial acetic acid, sodium hydroxide, and hydrochloric acid.

The main instruments included pH meter, water bath thermostatic oscillator, thermostatic magnetic stirrer, dispensing funnel, ICP-OES, etc.

Methods

According to the concentration fraction of 10%, a certain volume of Cyanex272 extractant was evenly mixed with sulfonated kerosene to obtain Cyanex272 organic phase. Cyanex272 organic phase was saponified by adding NaOH solution according to 45–60% saponification ratio. The saponified Cyanex272 and P204 raffinate are added to the separating funnel, and then placed in a shaking table for shaking extraction for a period of time. After standing, the layered organic phase and aqueous phase were poured out from the upper mouth and discharged from the lower mouth, respectively. The discharged raffinate was filtered and detected by ICP to detect the ion concentration of cobalt and nickel. The prepared glacial acetic acid solution and the extracted organic phase were added to the separation funnel. The separating funnel was put into the shaking table to vibrate and react for a certain time and then stand. After the organic phase and aqueous phase were layered, the raffinate was filtered and detected by ICP.

The extraction ratio was calculated according to the concentration test results of ICP. The calculation formula of extraction rate was shown in Formula (1):

$$E = \frac{C_0 V_0}{(C_w V_w + C_0 C_0)} \times 100\% \quad (1)$$

where C_0 is the target element concentration in the organic phase, C_w is the target element concentration in the aqueous phase, V_0 is the volume of organic phase, and V_w is the volume of aqueous phase.

Results and Discussion

Effect of Extraction Phase Ratio (O/A) on Extraction Rate of Nickel and Cobalt

The effect of extraction phase ratio (O/A) from 3:1 to 5:1 on extraction rate was studied. The results are shown in Fig. 1. It can be seen that the extraction rate of nickel and cobalt by Cyanex272 increases significantly with the increase of extraction phase ratio. The extraction rate of cobalt increased from 28.38 to 100% and that of nickel increased from 0 to 15.36%. When the extraction phase ratio is lower than 1:1, cobalt's extraction rate begins to decrease significantly. But the extraction rate of nickel also decreases to 0 when the extraction phase ratio is lower than 1:1. Cyanex272 exists as dimer under acidic conditions and monomer after saponification. Cyanex272 (HA) in the organic phase existed in the form of monomer and dimer at the same time when the saponification rate of Cyanex272 was 45–60%. The reaction of Cyanex272 with nickel and cobalt is shown in Formula (2)–(5). HA and A^- increase in the reaction

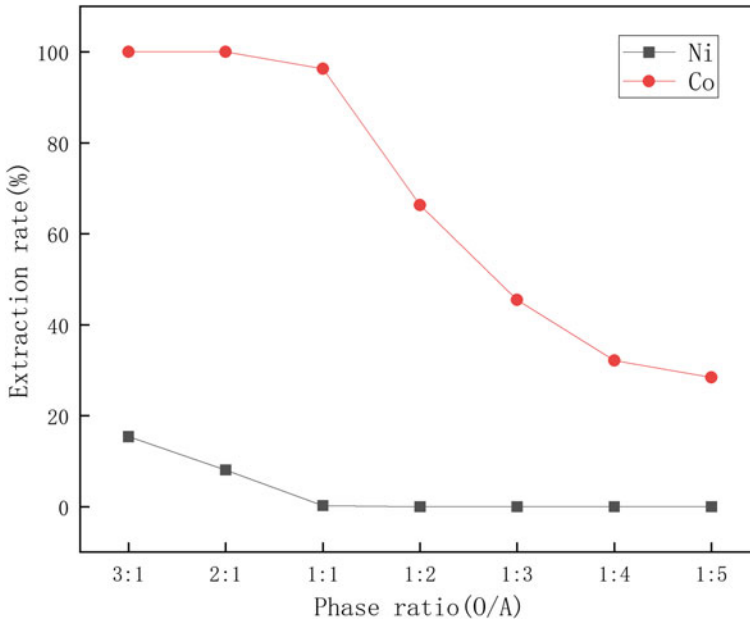
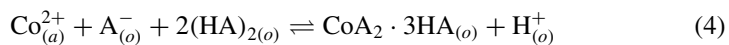
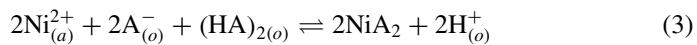
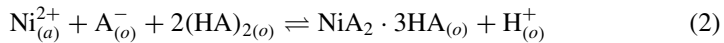


Fig. 1 Effect of extraction phase ratio (O/A) on extraction rate of nickel and cobalt. Reaction conditions: reaction temperature 25 °C, reaction time 15 min, initial pH 5.5

process with the extraction ratio increasing. It can be seen from Formula (2)–(5) that the reaction proceeds in the forward direction and the extraction rate will increase.



$$D = \frac{C_0}{C_w} \quad (6)$$

$$\beta = \frac{D_A}{D_B} \quad (7)$$

In order to control the effective separation of nickel and cobalt, their separation coefficient is calculated according to Formula (7). It is found that the maximum separation coefficient of nickel and cobalt is 1.2×10^4 at the extraction ratio of 1:1.

Under this extraction ratio, the more extraction amount of cobalt, the less extraction amount of nickel. It realizes the effective separation of nickel and cobalt. Therefore, the best extraction phase ratio is regarded as 1:1.

Effect of Initial pH of Nickel and Cobalt Solution on Extraction Rate of Nickel and Cobalt

Figure 2 shows the effect of initial pH of nickel and cobalt solution on nickel and cobalt extraction rate. It can be seen that the extraction rate of cobalt increases from 93.5% to more than 96% with the increase of the initial pH value of nickel and cobalt solution. The extraction rate of nickel also increases from 0 to about 0.3%. The extraction rate of nickel increases less. It can be seen from Formula (2)–(5) that the H^+ concentration decreases in the reaction process with initial pH increasing. It is conducive to the positive progress of the reaction. The extraction rate of nickel and cobalt increases with the increase of pH of nickel and cobalt solution. When the extraction pH is less than 6, the extraction rate of Cyanex272 for nickel is low. The change of pH has little effect on the extraction rate of nickel. When the pH of nickel and cobalt solution is 5–6, the extraction rate of nickel is low but that of cobalt is high (about 96%). The pH value of the nickel and cobalt solution provided is about

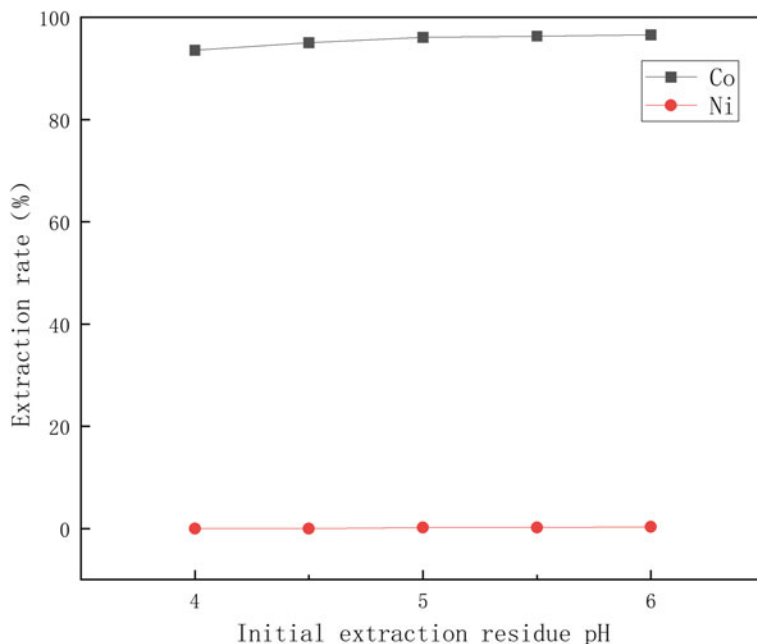


Fig. 2 Effect of initial pH of nickel and cobalt solution on extraction rate of nickel and cobalt. Reaction conditions: reaction temperature 25 °C, reaction time 15 min, extraction phase ratio 1:1

5.5. The pH value is also the optimal pH range. Therefore, the optimal initial pH condition for extraction is 5.5, shortening the experimental process and avoiding to adjust the pH of the solution.

Effect of Reaction Time on Extraction Rate of Nickel and Cobalt

Figure 3 gives the effect of reaction time on the extraction rate of nickel and cobalt under the conditions of 1, 5, 10, 15, and 20 min. It can be seen that the extraction rate of cobalt increases with the increase of reaction time. The extraction rate of nickel hardly changes. The extraction reaction speed of cobalt is very fast. When the reaction time is 1 min, the extraction rate of cobalt can reach about 73%. When the reaction time is 5 min, the extraction reaction is basically completed. In the whole extraction process, the extraction rate of nickel is low (about 0.2%). Considering the separation of nickel and cobalt, only the reaction time with high cobalt extraction rate needs to be selected. When the reaction time is from 10 to 20 min, the extraction rate of cobalt changes little. In order to save time and energy, the optimal extraction reaction time is considered as 10 min.

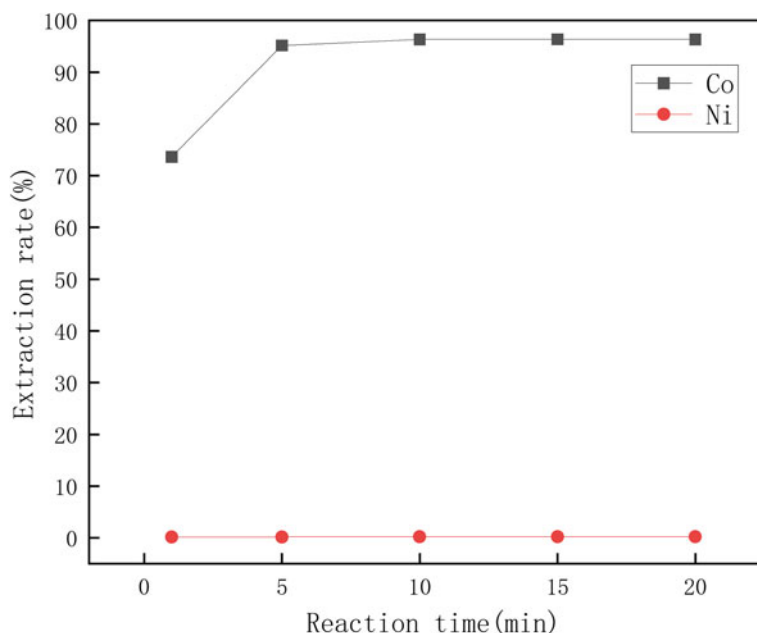


Fig. 3 Effect of reaction time on extraction rate of nickel and cobalt. Reaction conditions: reaction temperature 25 °C, initial pH 5.5, extraction phase ratio 1:1

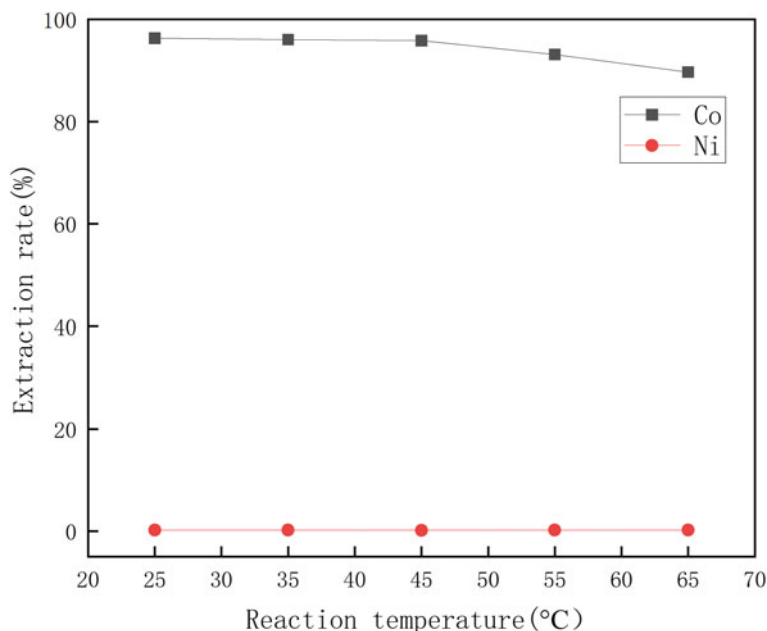


Fig. 4 Effect of reaction temperature on extraction rate of nickel and cobalt. Reaction conditions: reaction time 10 min, initial pH 5.5, extraction phase ratio 1:1

Effect of Reaction Temperature on Extraction Rate of Nickel and Cobalt

Figure 4 indicates the effect of reaction temperature on the extraction rate of nickel and cobalt. It can be seen that the extraction rate of cobalt decreases to 89.69% at 65 °C with the increase of reaction temperature. The extraction rate of nickel is almost unaffected by temperature. The extraction rate has been stable at about 0.2%. According to the above data and production practice, the best extraction separation effect can be achieved by controlling the extraction temperature to 25 °C. Therefore, the best extraction temperature for nickel–cobalt separation and extraction is 25 °C.

Extraction Equilibrium Isotherm of Cobalt

The isothermal diagram of extraction equilibrium of cobalt is shown in Fig. 5. The McCabe-Thiele diagram and operation line are drawn on the phase ratio (O/A) of 1:1.2 according to the extraction equilibrium drawing method and the principle of countercurrent extraction. It can be seen from the operation line in Fig. 5 that the cobalt ion concentration in the aqueous phase can be reduced to 0.03 g/L through

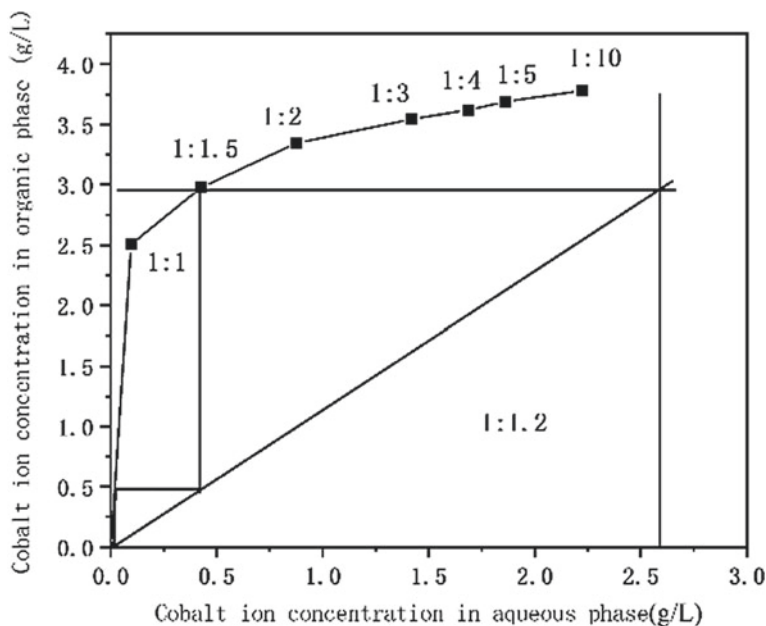


Fig. 5 Extraction equilibrium isotherm of Cyanex272 for cobalt extraction

theoretical two-stage extraction. The extraction rate of cobalt can reach more than 98.85% according to Formula 1. Under the experimental conditions, the extraction rate of cobalt can reach more than 99% by three-stage extraction. Therefore, three-stage extraction should be selected to extract and separate nickel and cobalt.

Acetic Acid Stripping of Negative Cobalt Organic Phase

The Cyanex272 containing cobalt 2.6 g/L and nickel 0.02 g/L was extracted by glacial acetic acid. The reverse extraction conditions are as follows: reaction time 10 min, stripping ratio 1:1, stripping temperature 25 °C, and stripping agent acetic acid concentration 2 mol/L. The results show that the stripping rate of cobalt can reach more than 99%. The organic phase changes from blue black to orange yellow while the aqueous phase also changes to pink. The results of the validation experiment are shown in Table 1. It can be seen from Table 1 that nickel and cobalt in the supported organic phase can be nearly 100% stripping by acetic acid. The effect of nickel can be ignored after dilution of cobalt acetate solution in subsequent material preparation. It can achieve the requirements of preparing high-quality cobalt acetate.

Table 1 Nickel and cobalt content in acetic acid solution

Unit (mg/L)	1	2	3	4	5	6	7	8	9	10
Co	2596	2597	2598	2597	2596	2598	2599	2600	2592	2598
Ni	19.23	19.43	19.12	18.86	18.95	18.88	20.02	20.03	18.96	19.43

Conclusion

The nickel and cobalt in P204 raffinate were separated by Cyanex272 and the organic phase was back extracted by extraction. The conclusions were obtained in the following:

- (1) The optimum extraction conditions of P204 nickel–cobalt raffinate by Cyanex272 extraction are as follows: the initial pH of P204 raffinate 5.5, the extraction phase ratio (O/A) 1:1, the extraction time 10 min, and the extraction temperature 25 °C. Under the above conditions, the extraction rate of cobalt is more than 96% and that of nickel is only about 0.21%.
- (2) The extraction equilibrium isotherm of cobalt was drawn. It is found that when two-stage extraction is used, the extraction rate of cobalt can reach more than 98.85%. When three-stage extraction is used, the extraction rate of cobalt can reach more than 99%. Therefore, three-stage countercurrent extraction should be used in the actual production operation.
- (3) The results show that cobalt in the organic phase can be completely stripping. The extraction rate is close to 100%. The high-quality cobalt acetate is generated. This provides guidance for the connection between nickel production system and composite preparation.

References

1. Dai MY, Zhang YR, Zhang K, Zhao YB (2019) Recovery of cobalt nickel lithium from cathode materials of waste lithium ion batteries by solvent extraction precipitation method. *Hydrometallurgy* 38(04):276–282
2. Zhu AL (2012) Nickel solution purification method research. *J hydrometallurgy* 31(02):71–75. <https://doi.org/10.13355/j.carolcarrollnkisfyj.2012.02.006>
3. Dai MS, Yang HB, Zhang FD (1989) Yellow sodium iron vitriol in addition to the production of nickel sulfate, tiefa coal industry group. *J Chem Indus Shaanxi* 1989(6):52. <https://doi.org/10.16581/j.carolcarrollnkiissn1671-3206.1989.06.029>
4. Li XY (2019) Study on the recovery process of nickel, cobalt and manganese from waste ternary battery cathode materials. Harbin University of Technology
5. Liu FQ, Zhong LD, Liu ZC, Li AM (2018) Characteristics and mechanism of selective separation of nickel and cobalt from strong acid high iron solution by a new pyridine based chelating resin. *Ion Exch Adsorpt* 34(05):390–400
6. Bobrowski A et al (2014) A novel screen-printed electrode modified with lead film for adsorptive stripping voltammetric determination of cobalt and nickel. *Sens Actuators B Chem* 191:291–297

7. Panigrahi S et al (2009) Processing of manganese nodule leach liquor for the separation of cobalt and nickel using PC 88A. *Miner Metall Process* 26(3):133–140
8. Cao MX (2016) Synthesis of a new phosphoramidate extractant and its extraction and separation of rare earth, cobalt and nickel plasma. Yanshan University
9. Qin L (2016) Synthesis and properties of high purity organic phosphonic acid extractant. China University of Petroleum (Beijing)
10. Zhao YC (2017) Study on preparation process of high purity cobalt. Henan University of Science and Technology
11. Peng XB, Tian Lin, Zhai ZB, Qu Tao, Xie Gang, Dai YN (2018) Experimental study on extraction and separation of nickel and cobalt from cobalt sulfate solution by Cyanex272. *Min Metall Eng* 38(06):127–130
12. Lei Z, Liu DX (2012) Study on anode liquid purification process in high copper nickel sulfide anode electrolysis process. *Nonferrous Metals (smelting part)* 2012 (10):7–9
13. Ning Z, Chen BT, Yong L (2009) Preparation and properties of spherical lithium cobalt oxide. *Tianjin Sci Technol* 36(04):17–19
14. Zhao DL, Jin YH, Luo Xi et al (2021) Preparation methods and research progress of nano ferrite based core-shell composite microwave absorbing materials. *J Jilin Univ (2nd edn)* 59(02):397–407
15. Sun H (2020) Preparation and microwave absorbing properties of cobalt sulfide/manganese sulfate micro nano heterostructures. Harbin Engineering University
16. Wang WZ, Wang GF, Ye SL, Jiang S (2017) Preparation of graphene/cobalt doped ZnO quasi shell core nano materials. *J Hangzhou Univ Electron Sci Technol (Natural Science Edition)* 37(06):14–17
17. Chen YH (2017) Study on nickel and cobalt doped lithium manganate/reduced graphene oxide composites and their lithium battery properties. Zhengzhou University

Low-Temperature Preparation and Mechanism Study of Vanadium Nitride



Yongjie Liu, Qingqing Hu, Donglai Ma, Yue Wang, and Zhixiong You

Abstract In this study, VN was successfully prepared in an ammonia atmosphere using V_2O_5 as a raw material at 600 °C. The gas composition of the reaction process was analyzed by Factsage 8.0 software. At the same time, based on the first principles of density functional theory, the adsorption model of NH_3 on the V_2O_5 (001) surface is established. Through the analysis of the structure changes of the adsorption model and the size of the adsorption energy, the mechanism of the adsorption reaction of ammonia and V_2O_5 was revealed. Through thermodynamic calculations and the first-principles calculations method of density functional theory (DFT), the microscopic mechanism of the reaction between ammonia and V_2O_5 is revealed, which is of great significance to the determination of process parameters in the actual reaction.

Keywords Vanadium nitride · Ammonia · V_2O_5 · DFT

Introduction

In recent years, transition metal nitrides have received extensive attention due to their superior chemical and physical properties, such as high toughness, high-temperature stability, excellent corrosion resistance, extreme hardness, excellent catalytic performance, and electrical conductivity [1–3]. Among transition metal nitrides, vanadium nitride (VN) has attracted much attention due to its excellent physical and chemical properties [4–6]. Thus, it has many applications in the field of structural materials, electrochemistry, and catalysis [7, 8].

Traditionally, the conventional preparation method of vanadium nitride has high temperature (above 1000 °C) and long reaction time due to the diffusion rate of solid–solid reaction related to temperature, such as carbothermal reduction of vanadium

Y. Liu · Q. Hu · D. Ma · Y. Wang · Z. You (✉)

College of Materials Science and Engineering, Chongqing University, Chongqing 400044, China
e-mail: youzx@cqu.edu.cn

Z. You

Laboratory of Vanadium–Titanium Metallurgy and New Materials, Chongqing University, Chongqing 400044, China

© The Minerals, Metals & Materials Society 2022

M. Zhang et al. (eds.), *Characterization of Minerals, Metals, and Materials 2022*,

The Minerals, Metals & Materials Series,

https://doi.org/10.1007/978-3-030-92373-0_12

oxide or direct nitridation of pure metal vanadium [5, 9]. In order to find a method of low temperature, short time, and low cost, ammonia reduction-nitridation is widely studied as a low-cost and efficient method for the preparation of vanadium nitride [10–12]. Mosavati et al. [10] prepared vanadium-based precursor by hydrothermal method for 24 h, and then synthesized VN nanopowders having an average particle diameter of 47 nm under NH_3 atmosphere at 800 °C. Panda et al. [11] reported that nano-sized vanadium nitride was prepared by sol–gel synthesis of V_2O_5 precursor in the atmosphere of ammonia gas. Qin et al. [12] reported using ultra-fast (within 1 min) solution combustion to synthesize vanadium dioxide (VO_2) precursor in an ammonia atmosphere to prepare nano-vanadium nitride powder. The above studies have shown that the nanostructure and high activity of the nanostructure and high activity prepared by the method of hydrothermal method, sol–gel method, and solution combustion synthesis method are used to successfully synthesize the VN nano-powder. During the preparation process of VN, the vanadium-based precursor phase changes to: $\text{V}_2\text{O}_5 \rightarrow \text{VO}_2 \rightarrow \text{V}_2\text{O}_3 \rightarrow \text{VN}$. However, there are few theoretical studies on the microscopic mechanism of vanadium nitride formation at the surface of vanadium oxide in ammonia atmosphere.

In this study, VN was successfully prepared by using micron- V_2O_5 as raw material in ammonia atmosphere at 600 °C. Through thermodynamic calculation, the variation of gas and solid in gas–solid reaction process was analyzed by FactSage 8.0. In order to further analyze the change of the surface microstructure of V_2O_5 in the ammonia atmosphere, we use the first-principles calculations method of density functional theory (DFT) to study the structural change of the surface adsorption of V_2O_5 (001), providing a deeper theoretical basis for the further study of the ammonia reduction-nitridation of V_2O_5 .

Experimental and Computational Methods

Experimental Procedure

The solid powder raw material for preparing vanadium nitride (VN) is vanadium pentoxide (V_2O_5 , >99.9 wt.%). For preparing vanadium nitride, V_2O_5 was placed in an alumina crucible and put into the constant-temperature zone of a horizontal resistance furnace. Initially, at the heating stage, a flow of Ar gas (99.999%) was introduced into the furnace tube to get rid of O_2 and H_2O . The flow rate of Ar gas was kept at about 300 ml/min. When the furnace was heated to the desired temperature (400–600 °C) at the rate of 10 °C min^{-1} , the nitridation reaction of the raw materials was performed in a tube furnace at a constant heating temperature of flowing ammonia (NH_3 , 99.999%) gas at the flow rate of 500 ml/min. After holding at the desired temperature for 1 h, the tube furnace was cooled down under flowing

Ar gas. After reaction and nitridation, the obtained products were examined by X-ray powder diffraction (PANalytical D/max 2500). Scanning electron microscope (Quattro S, ThermoFisher) was carried out to monitor overall morphology.

Computational Details

All structural optimizations and corresponding total energy calculations were performed using density functional theory (DFT) with the VASP package by the plane wave basis sets [13]. The exchange correlation function used is the generalized gradient approximation of the Perdew–Burke–Ernzerhof (PBE). The plane wave base cutoff energy of 500 eV is used to ensure good accuracy. The structure of vanadium oxide is geometrically optimized by the conjugate gradient method. The maximum force of each atom in the system is less than 0.03 eV/Å and the total energy is less than 10⁻⁵ eV. In order to eliminate the influence of radical-containing systems, we considered spin polarization in our calculations. The V₂O₅(001) surface was modeled with the slab supercell approach including a 15 Å vacuum region, as shown in Fig. 1. There are two kinds of vanadium (V^a and V^b) and three kinds of lattice oxygen active sites on the surface [14, 15]. Among them, V^a is vanadium-based oxygen (V^a = O) located outside the surface and vanadium-based oxygen (V^b = O) located inside the surface. Lattice oxygen includes single-coordinated terminal oxygen O(1),

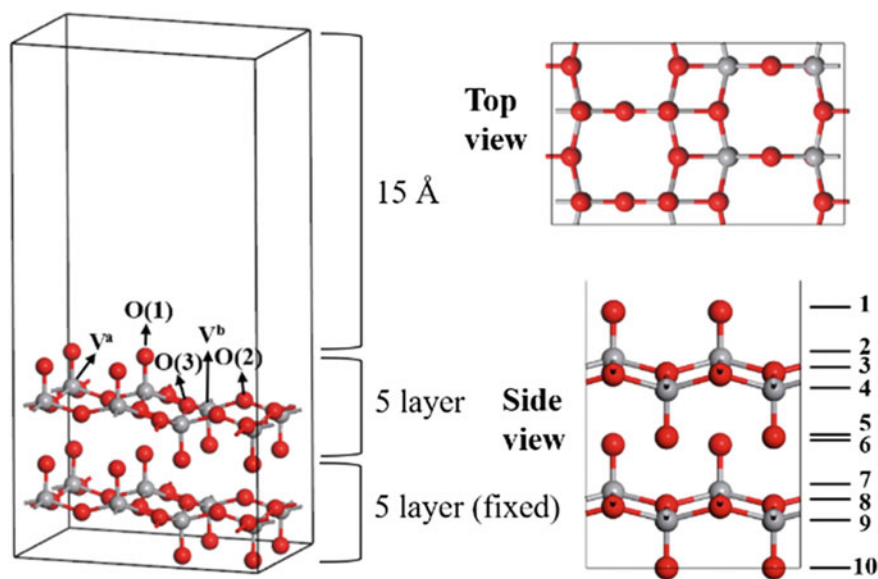


Fig. 1 Configuration of vanadium oxide (V₂O₅) slab model

namely, vanadium-based oxygen ($V = O$), double-coordinated oxygen O(2), and tri-coordinated oxygen O(3). It is worth noting that from the structural position of O(1), O(1) is the most prone to adsorption reaction site [16], and O(1) is also the research site of this article. We used a (1×2) supercell containing a ten-layer slab in which the bottom five layers were fixed and all the other atoms are allowed to relax freely. A $3 \times 4 \times 1$ k-point grid that has been tested for convergence is used to ensure that the interface has sufficient accuracy. Since the zero-point correction has a small effect on the adsorption energy, the relative energy reported does not include the zero-point energy and thermal correction.

The adsorption energy (E_{ad}) is calculated according to Formula (1).

$$E_{ad} = E_{NH_3+V_2O_5} - (E_{NH_3} + E_{V_2O_5}) \quad (1)$$

where $E_{NH_3+V_2O_5}$ is the surface energy of NH_3 adsorbed on the V_2O_5 surface, E_{NH_3} is the energy of NH_3 , and $E_{V_2O_5}$ is the energy of the V_2O_5 clean surface.

Results and Discussion

Thermodynamic Analysis

As shown in Table 1, the main reactions and their standard Gibbs free energies during reduction-nitridation process were calculated by FactSage 8.0. From the products of Eqs. 3 and 4, it can be seen that there are two possible ways for V_2O_5 to react with NH_3 . The products of the two different pathways are N_2 and NO , respectively. It can be seen from Eq. 2 that NO easily reacts with NH_3 , indicating that it is difficult

Table 1 Main reactions and their standard Gibbs free energies

Eq.	Chemical equation	$\Delta_r G^\ominus$ (J/mol)	Starting reaction temperature ($^\circ C$)
1	$NH_3 = 1/2N_2 + 1/3H_2$	21,562.34–114.50 T	188
2	$NH_3 + 3/2NO = 5/4N_2 + 3/2H_2O$	–455,952.62–15.85 T	–
3	$V_2O_5 + 2/3NH_3 = 2VO_2 + 1/3N_2 + H_2O$	–112,843.32–123.41 T	–
4	$V_2O_5 + 2/5NH_3 = 2VO_2 + 2/5NO + 3/5H_2O$	8719.67–119.12 T	73
5	$VO_2 + 1/3NH_3 = 1/2V_2O_3 + 1/6N_2 + 1/2H_2O$	–18,870.21–45.52 T	–
6	$VO_2 + 1/5NH_3 = 1/2V_2O_3 + 1/5NO + 3/10H_2O$	41,922.70–43.41 T	966
7	$V_2O_3 + 2NH_3 = 2VN + 3H_2O$	105,711.36–149.15 T	709
8	$V_2O_5 + H_2 = 2VO_2 + H_2O$	–127,002.18–47.65 T	–
9	$VO_2 + H_2 = V_2O_3 + H_2O$	–26,057.75–7.35 T	–

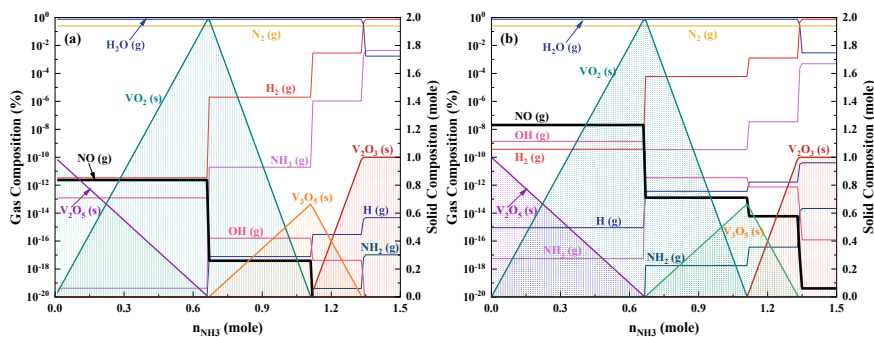


Fig. 2 Equilibrium composition of solid and gas products in the $\text{NH}_3\text{-V}_2\text{O}_5$ (1.0 mol V_2O_5) system at different temperatures: **a** 400 °C **b** 600 °C

to detect the formation of NO during the actual reaction process. Meanwhile, the reaction pathway of VO_2 is similar to that of V_2O_5 . However, it can be seen from Eq. 6 that the initial temperature of NO generation is 966 °C under standard condition, indicating that the reaction between VO_2 and NH_3 is dominated by Eq. 5. In addition, the temperature required to generate VN under standard conditions is 703 °C, under standard condition by Eq. 7. Equations 8 and 9 show that H_2 can reduce V_2O_5 to V_2O_3 . This indicates that H_2 decomposed from ammonia gas also participates in the reaction.

In order to further illustrate the $\text{NH}_3\text{-V}_2\text{O}_5$ system changes during the reaction, the solid and gas phase composition was calculated as a function of input NH_3 under standard condition. Figure 2 shows the equilibrium of the gas–solid composition of the product with the increase of ammonia at 400 and 600 °C. As shown in Fig. 2, the solid phase changes to: $\text{V}_2\text{O}_5 \rightarrow \text{VO}_2 \rightarrow \text{V}_3\text{O}_5 \rightarrow \text{V}_2\text{O}_3$. In our previous study, with the further increase of ammonia, V_2O_3 would eventually change to VN [17]. In the gas product, its main components are H_2O and N_2 . As the reaction progresses, the content of H_2 and NH_3 will gradually increase. It is worth mentioning that the black line is the change of NO gas. When V_2O_5 is gradually transformed into V_2O_3 , the NO gas content also drops by orders of magnitude. Meanwhile, when the temperature increases from 400° to 600° °C, the content of NO gas increases by several orders of magnitude, while the content of ammonia decreases by several orders of magnitude, indicating that the increase of temperature is beneficial to the reaction. In addition, it can be seen from Eq. 2 that NO and NH_3 will react, resulting in a small amount of NO compared to the content of N_2 .

Phase Transformation Analysis

The phase transformation during the preparation of VN was shown in Fig. 3a. As shown in Fig. 3a, after reacting at 400 °C for 1 h, the sample consisted of VO_2 , V_2O_3 ,

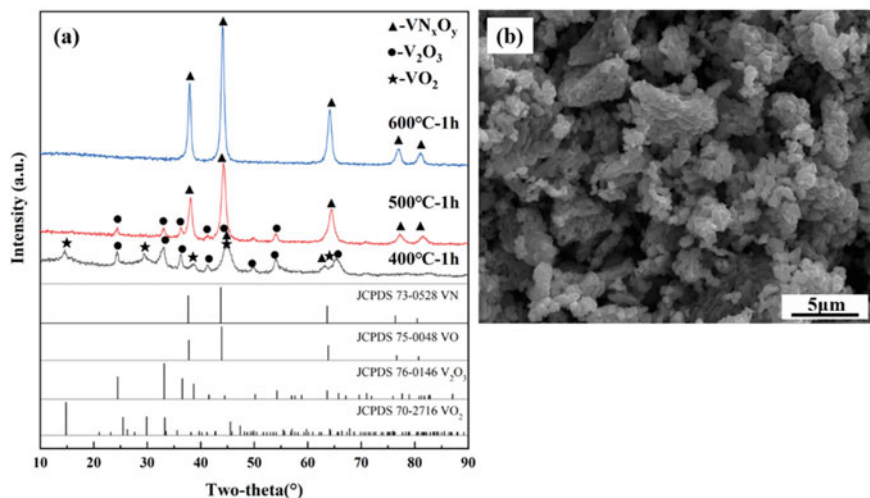


Fig. 3 The phase and SEM images of the reaction products: **a** XRD patterns of the products; **b** SEM image of the V_2O_5 at 600 °C after reacting for 1 h

and VN. It can be concluded that, in this case, the reaction time was not sufficient to completely reduce vanadium oxides. With the increase of temperature to 500 °C, the diffraction peak of VO_2 disappeared leaving only the diffraction peaks of V_2O_3 and VN. When the temperature was 600 °C, all diffraction peaks were assigned to VN. In addition, the lattice parameters and structure of VO and VN are similar. Therefore, the VN produced by the reaction is a solid solution of VN_xO_y ($x < 1$, $y < 1$). It is worth noting that the above thermodynamic calculation shows that the initial temperature of VN generation in the standard state is 709 °C, while the actual experimental reaction temperature is lower than the theoretical temperature, which is due to dynamics and other factors. Figure 3b shows a scanning electron micrograph (SEM) of the product reacted at 600 °C for 1 h. The product is micron-sized particles composed of many small cubes.

DFT Analysis

In order to further study the reaction of adsorbed gas on the microscopic surface of V_2O_5 under ammonia atmosphere, we used DFT to calculate the structural changes and adsorption energy of NH_3 , H_2 , N_2 , H, and N adsorbed on the surface of V_2O_5 (001), as shown in Fig. 4. On the surface of V_2O_5 , the structural position of O(1) site shows that O(1) is most likely to adsorb gas. Meanwhile, Fu et al. [16] also found that O(1) and H combined to form H_2O would leave the solid surface, thus changing the structure of V_2O_5 . From Fig. 4a–c, it can be seen that the adsorption energy ($E_{ad} = -0.15$ eV) of NH_3 adsorbed on the surface of V_2O_5 (001) is

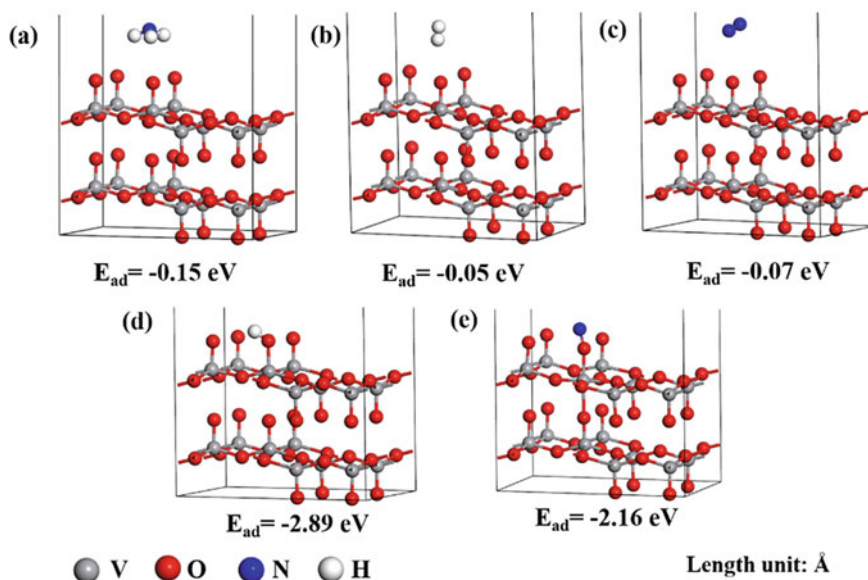


Fig. 4 Adsorption structures of **a** NH_3 , **b** H_2 , **c** N_2 , **d** H, **e** N on the surface of V_2O_5 (001)

the largest, indicating that in the actual reaction process, ammonia is most easily adsorbed on the surface of the reactant and reacts with V_2O_5 . In addition, NH_3 and H_2 are easily decomposed to obtain active N atoms and H atoms. In the actual reaction process, there are active N atoms and H atoms in the ammonia atmosphere. Therefore, we calculate the adsorption of H and N atom on the V_2O_5 (001) surface, as shown in Fig. 4d, e. The adsorption energies of the H and N atom are -2.89 eV and -2.16 eV, respectively, indicating that H and N atoms can react spontaneously with O(1). Meanwhile, the bond length between O(1) and V atom becomes longer, and O(1) has a tendency to desorb on the V_2O_5 (001) surface.

Conclusions

VN was successfully prepared in ammonia atmosphere using V_2O_5 as a raw material at 600 °C for 1 h. Through thermodynamic calculation, the gas–solid change in the reaction process was analyzed. The formation of NO gas was found at the initial stage of the reaction. NO gas will react with NH_3 , resulting in a very low NO content in the product gas. Meanwhile, through DFT study, it was found that NH_3 was easily adsorbed on V_2O_5 (001) surface compared with N_2 and H_2 . The active N and H atoms obtained from the decomposition of NH_3 and H_2 are easily adsorbed on the surface of V_2O_5 (001) and bind to O(1). Meanwhile, O(1) has a tendency to detach

from the V_2O_5 (001) surface, which shows the change process of the microscopic reaction process.

Acknowledgements The authors wish to express their thanks to the National Natural Science Foundation of China (U2003215 and 51974053), the Fundamental and Frontier Research Project of Chongqing, China (cstc2020jcyj–msxmX0515), and the Fundamental Research Funds for the Central Universities (2020CDJ–LHZZ–083) for the financial support of this research.

References

1. Chen L, Korányi TI, Hensen EJ (2016) Transition metal (Ti, Mo, Nb, W) nitride catalysts for lignin depolymerisation. *Chem Commun* 52(60):9375–9378
2. Huang HH, Hon MH (2002) Effect of N_2 addition on growth and properties of titanium nitride films obtained by atmospheric pressure chemical vapor deposition. *Thin Solid Films* 416(1–2):54–61
3. Li Q, Chen Y, Zhang J, Tian W, Wang L, Ren Z, Li X, Gao B, Peng X, Chu PK, Huo K (2018) Spatially confined synthesis of vanadium nitride nanodots intercalated carbon nanosheets with ultrahigh volumetric capacitance and long life for flexible supercapacitors. *Nano Energy* 51:128–136
4. Jiang X, Lu W, Yu Y, Yang M, Liu X, Xing Y (2019) Ultra-small Ni–VN nanoparticles co-embedded in N-doped carbons as an effective electrode material for energy storage. *Electrochim Acta* 302:385–393
5. Roldan MA, Lopez-Flores V, Alcalá MD, Ortega A, Real C (2010) Mechanochemical synthesis of vanadium nitride. *J Eur Ceram Soc* 30(10):2099–2107
6. Zhang L, Holt CM, Luber EJ, Olsen BC, Wang H, Danaie M, Cui X, Tan X, Lui VW, Kalisvaart P, Mitlin D (2011) High rate electrochemical capacitors from three-dimensional arrays of vanadium nitride functionalized carbon nanotubes. *J Phys Chem C* 115(49):24381–24393
7. Zhou P, Xing D, Liu Y, Wang Z, Wang P, Zheng Z, Qin X, Zhang X, Dai Y, Huang B (2019) Accelerated electrocatalytic hydrogen evolution on non-noble metal containing trinickel nitride by introduction of vanadium nitride. *J Mater Chem A* 7(10):5513–5521
8. Ningthoujam RS, Gajbhiye NS (2015) Synthesis, electron transport properties of transition metal nitrides and applications. *Prog Mater Sci* 70:50–154
9. Sansan YU, Nianxin FU, Feng GAO, Zhitong SUI (2009) Synthesis of vanadium nitride by a one step method. *J Mater Sci Technol* 23(01):43–46
10. Mosavati N, Salley SO, Ng KS (2017) Characterization and electrochemical activities of nanostructured transition metal nitrides as cathode materials for lithium sulfur batteries. *J Power Sour* 340:210–216
11. Mishra PP, Theerthagiri J, Panda RN (2014) Mesoporous vanadium nitride synthesized by chemical routes. *Adsorpt Sci Technol* 32(6):465–474
12. Qin M, Wu H, Cao Z, Zhang D, Jia B, Qu X (2019) A novel method to synthesize vanadium nitride nanopowders by ammonia reduction from combustion precursors. *J Alloy Compd* 772:808–813
13. Perdew JP, Burke K, Ernzerhof M (1996) Generalized gradient approximation made simple. *Phys Rev Lett* 77(18):3865
14. Yao H, Chen Y, Wei Y, Zhao Z, Liu Z, Xu C (2012) A periodic DFT study of ammonia adsorption on the V_2O_5 (001), V_2O_5 (010) and V_2O_5 (100) surfaces: Lewis versus Brønsted acid sites. *Surf Sci* 606(21–22):1739–1748
15. Yao H, Chen Y, Zhao Z, Wei Y, Liu Z, Zhai D, Liu B, Xu C (2013) Periodic DFT study on mechanism of selective catalytic reduction of NO via NH_3 and O_2 over the V_2O_5 (0 0 1) surface: competitive sites and pathways. *J Catal* 305:67–75

16. Fu H, Liu ZP, Li ZH, Wang WN, Fan KN (2006) Periodic density functional theory study of propane oxidative dehydrogenation over V_2O_5 (001) surface. *J Am Chem Soc* 128(34):11114–11123
17. Liu Y, Wang Y, You Z, Lv X (2020) Reduction and nitridation of iron/vanadium oxides by ammonia gas: mechanism and preparation of FeV45N alloy. *Metals* 10(3):356

Part V
Mineralogical Analysis and Process
Improvement

Leaching Cobalt from a Nickel-Containing Copper-Cobalt Zebesha Ore



Foibe D. L. Uahengo, Yotamu R. S. Hara, Rainford Hara,
Nachikonde Fumpa, Alexander Old, and Golden Kaluba

Abstract Two copper-cobalt ore samples with varying amounts of nickel, manganese, and iron from Zebesha Mine in Zambia were leached under different conditions with the purpose of understanding leaching characteristics. Leach tests were conducted at different conditions such as pH, temperature, and varying amount of reductant (sodium metabisulphite). The as-received materials and leach residues were analyzed by scanning electron microscopy and atomic absorption techniques. Copper and manganese selectively leached from the material in the absence of SMBS thereby leaving out cobalt, nickel, and iron. However, all elements, (Cu, Co, Ni, Mn, and Fe) leached out in the presence of SMBS. The overall recoveries of copper, cobalt, nickel, manganese, and iron were dependent on pH and amount of sodium metabisulphite.

Keywords Cobalt · Nickel · Leaching · Recoveries · Reductant · SMBS

Introduction

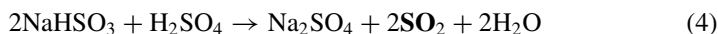
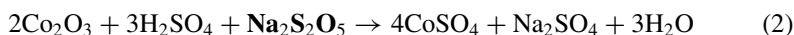
Zebesha mine in Zambia hosts a heterogenite oxide cobalt ore ($\text{CoO} \cdot 2\text{Co}_2\text{O}_3 \cdot 6\text{H}_2\text{O}$) which contains both Co^{2+} and Co^{3+} valences. The cobalt ore deposit contains nickel which is caused by atomic substitution. Cobalt oxide deposits are difficult to dissolve especially in tetravalent form (e.g. Co_2O_3) since Co^{3+} becomes soluble only after converted to Co^{2+} [2, 6, 8]. Upon contact with an acid (H_2SO_4), the Co^{2+} would dissolve (Eq. 1) leaving Co^{3+} unreactive. Co^{3+} requires a reducing agent to convert it to the acid-soluble Co^{2+} as shown in Eq. 2, with the sodium meta-bi-sulphate (SMBS) being the commonly used reductant among others [1, 5, 6 12–14]. The SMBS generates SO_2 that then reduces Co^{3+} to Co^{2+} as given in Eqs. 3 and 5.



F. D. L. Uahengo · Y. R. S. Hara (✉) · R. Hara · N. Fumpa · A. Old · G. Kaluba
Cham, Switzerland

Table 1 Chemical analysis of as-received Zebesha materials in weight %

Sample ID	Cu	Co	Ni	Mn	Fe
Z02	2.28	0.73	0.09	0.15	3.16
BCo	2.06	3.57	0.50	0.28	3.49



In order to understand the effect of SMBS addition, two samples with similar copper content but varying contents of cobalt, nickel, and manganese were leached out. The samples were leaching under different conditions such as SMBS dosing, pH and temperature.

Materials and Methods

Materials

Two samples, namely, Z02 and BCo were collected from Zebesha Mine Limited in Mwinilunga District of the Western Province Zambia. The chemical analysis is shown in Table 1 from which it can be observed that the two samples have similar content of copper and iron. However, BCo sample has more cobalt and nickel content than Z02 sample.

Leach Tests

The purpose of leach tests was to understand the dissolution of the valuable elements in the material. The as-received ore samples were crushed and milled down to particle size of less 150 μm . Each sample was leached at 33% solids and for a period of 1.5 h in sulphuric acid media. pH of the solution during leaching was controlled via addition of sulphuric acid. Leach was carried out either at room temperature or high temperature (about 70 $^\circ\text{C}$) and the aim was to understand the effect of temperature.

The slurry was stirred at a speed of 400 revolutions per minute. At the end of the leach experiment, the slurry was filtered off and the residue was washed with fresh water and dried.

Analysis

The dried leach residues were analysed for copper, cobalt, nickel, manganese, and iron using atomic absorption spectrometer (AAS). The respective recovery was calculated based on the metal content in the feed and residue. For mineralogical examination, a portion of the sample was screened on sieve size 1.7 mm at 100% passing and a 90° transverse epoxy block was made and re-casted in epoxy for analysis on the TESCAN Integrated Mineral Analyser (TIMA). The TIMA is an automated mineralogy system for fast quantitative analysis of samples such as rocks, ores, concentrates, tailings, leach residues, or smelter products. TIMA combines BSE and EDX analysis to identify minerals and create mineral images that are analysed to determine mineral concentrations, element distributions, and mineral texture properties such as grain size, association, liberation, and locking parameters.

Results and Discussion

Mineralogy Examination

Mineralogical examination was done using TESCAN Integrated Mineral Analyser (TIMA). TIMA is an automated mineralogy system for fast quantitative analysis of samples such as rocks, ores, concentrates, and tailings. It combines backscattered electron and energy dispersive X-ray analysis to identify minerals and create mineral images that are analyzed to determine mineral concentrations, element distributions, and mineral texture properties such as grain size, association, liberation, and locking parameters.

Mineralogical data for the as-received samples is shown in Table 2. It can be observed from Table 2 that cobalt is contained in the heterogenite mineral. Copper is predominantly contained in the malachite mineral in the BCo sample (2.06 weight % malachite). However, Z02 sample only has 0.03 weigh % malachite. It is clear from the mineralogical data from Table 2 that the main gangue phases in both samples are quartz, biotite, muscovite, talc, chlorite, and schorl.

Several parameters such as temperature, pH, sodium meta-bisulphate concentration, and acid consumption were studied.

Table 2 Mineralogical data for the as-received samples in weight %

Phase name	Z02	BCo
Quartz	34.57	31.11
Biotite	20.83	18.33
Talc	12.86	10.93
Muscovite	0.95	0.86
Chlorite Co Cu Mn	9.96	9.46
Fe oxides (Hematite)	7.10	6.53
Chlorite with Fe Cu (chrysocolla)like	7.33	6.89
Schorl	2.52	2.37
Malachite	0.03	2.06
Heterogenite	1.48	9.37
Alumosilicate	0.80	0.63
K-feldspar	0.10	0.08
Rutile	0.35	0.17
Kaolinite	0.05	0.08
Plagioclase	0.06	0.01
Chrysocolla	0.08	0.02
Fe Mn Cu Co oxide	0.09	0.01
Fe O Si Al K phases	0.02	0.03

Effect of Temperature and pH

The effect of pH was studied at room temperature and elevated temperature (70 °C). The results showing the effect of pH at different temperatures for BCo and Z02 samples are shown in Fig. 1a and 1b, respectively. The main observations in Figs. 1 and 2 are as follows:

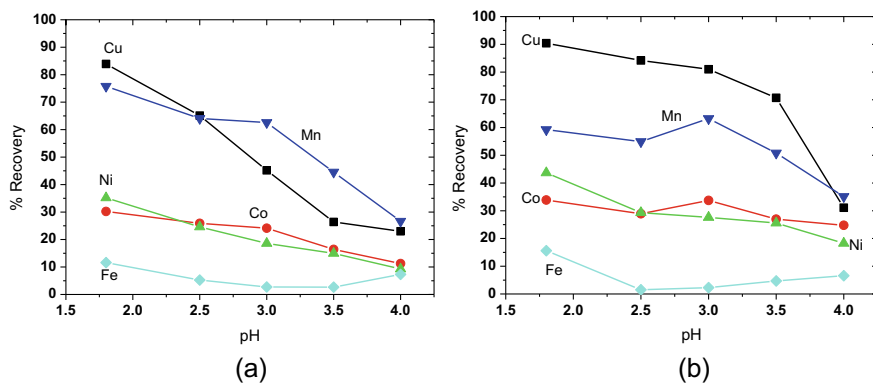


Fig. 1 Effect of pH at: **a** room temperature and **b** at 70 °C for BCo sample. The amount of SMBS added was 1.2 weight %

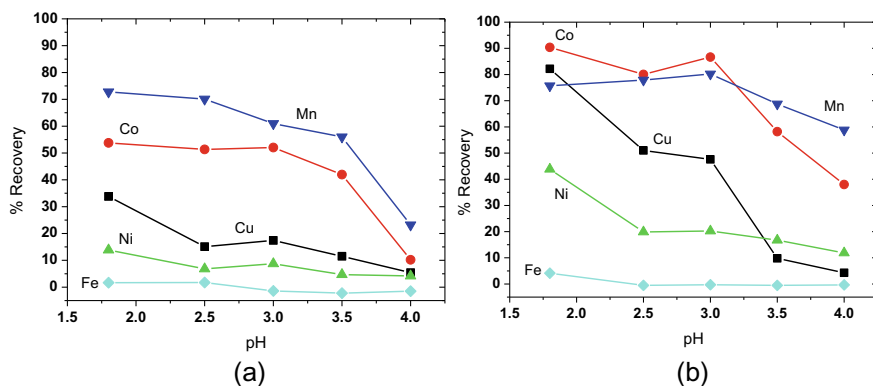


Fig. 2 Effect of pH at: **a** room temperature and **b** at 70 °C for Z02 sample. The amount of SMBS added was 1.2 weight % of the weight of the ore

- Recovery of iron is extremely low and similar for both samples (BCo and Z02) at both room temperature and elevated temperature.
- The recoveries of Cu, Co, Ni, and Mn decrease with increase in pH.
- The overall recoveries for all elements are similar at room temperature and higher temperature (70 °C) for BCo.
- The recoveries of Cu, Co, Ni, and Mn are higher at 70 °C than at room temperature for the Z02 sample.
- The recovery of copper is higher in the BCo sample than Z02 sample and this is due to the presence of malachite in the former (BCo).
- The recovery of cobalt is higher in the Z02 sample compared to the BCo. This is due to the fact that Z02 has less heterogenite content and hence has less cobalt which then requires less reductant.

The recoveries of Cu, Co, Ni, and Mn are not sensitive to temperature in the BCo sample and this is due to the presence of malachite which acts as a catalyst. However, there is no malachite in Z02 sample and hence recoveries of Cu, Co, Ni, and Mn are more sensitive to temperature.

Effect of Sodium Metabisulphite Concentration During Leaching

Effect of sodium meta-bisulphate addition was studied by leaching the sample at pH of 1.8 and 4.0 at room temperature. The samples were leached out at different dosing of SMBS and results are shown in Fig. 3a, b. It can be observed from Fig. 3a that the recoveries of Cu and Mn are higher than for Co, Ni, and Fe. The results in Fig. 3a further show that recoveries of Co, Ni, and Mn increase with increase in SMBS addition. It is worth noting that Co, Ni, and Mn exist in the heterogenite mineral

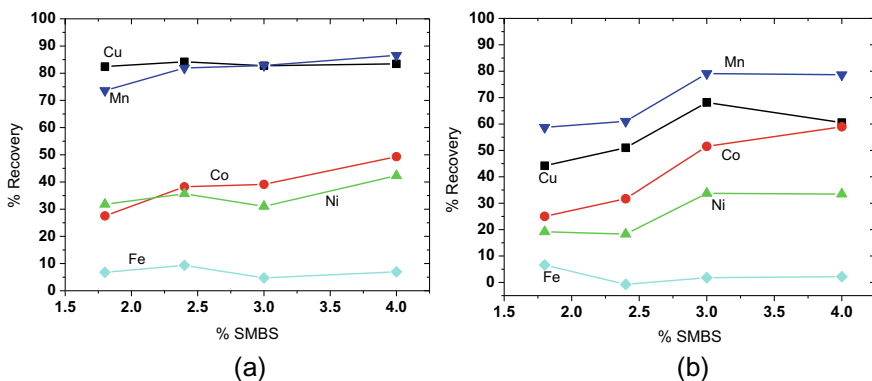


Fig. 3 Effect of SMBS addition on % recovery for the BCo sample at **a** pH 1.8 and **b** pH 4.0, at room temperature

which requires a reductant to dissolve and hence recoveries were increasing with increase in SMBS addition. Comparing the results in Fig. 3a, b, it can be observed that the recoveries of Co, Ni, and Mn were similar at pH of 1.8 and 4.0 and this is because these elements are soluble even at pH of 6.0. By comparison, the recovery of Cu decreased significantly at pH of 4.0 and this is due to decreased solubility. Based on the results in Fig. 1a it can be concluded that it is possible to preferentially leach out copper and manganese while leaving out Co and Ni which can be leached in a second stage.

With a view of maximising the recoveries of Co and Ni, SMBS was added up to 12 weight % at leaching pH of 1.8 and the results are shown in Fig. 4a. It is evident from Fig. 4a that further increase of SMBS to 10 weight % yielded a sharp increase in the recoveries for Co, Ni, and Fe. On the other hand, the recoveries of all elements

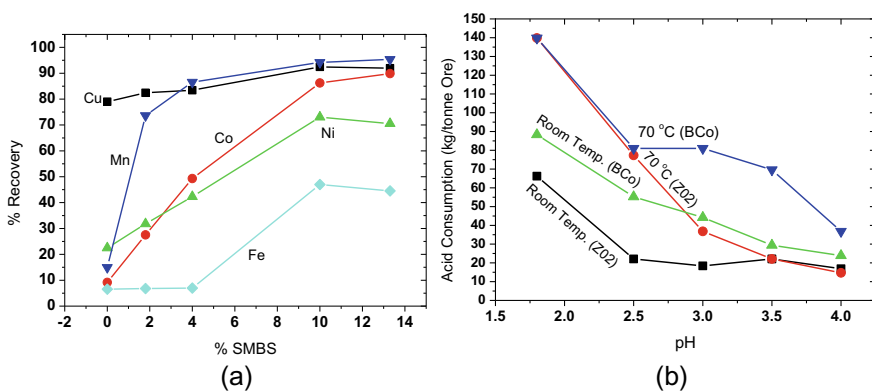


Fig. 4 **a** Metal recovery as function of SMBS addition for BCo material at room temperature and **b** acid function as a function of pH

did not significantly change as SMBS was increased from 10 to 12 weight %. Based on the results in Fig. 4a, it can be concluded that the optimal addition of SMBS is 10 weight % which is comparable to the overall content for Cu, Co, Ni, Mn, and Fe. It can be observed from Fig. 4a that the recovery of iron was the lowest and this is due to the fact that some of it is present in hematite/magnetite minerals.

The plot of acid consumption against pH is shown in Figs. 4b from which the following observations can be made:

- Acid consumption reaches a steady state as pH extends beyond 2.5 at room temperature for the Z02 sample.
- Acid consumption is higher at 70 °C than at room temperature and this is due to lack of selectivity at higher temperature. Other elements such as Al, Mg, and Ca dissolve at higher temperature thereby leading to increased acid consumption.
- Acid consumption is higher for the BCo sample than Z02 sample at room temperature. The higher consumption of acid at room temperature for the BCo sample is caused by the higher dissolution of Cu, Co, Ni, and Mn.

Conclusions

Based on the mineralogical examination, test works carried out, and experimental data obtained, the following conclusions were made:

- The main copper-cobalt-bearing minerals in the samples are malachite and heterogenite. Some of the copper and cobalt are dissolved in the chlorite and chrysocolla minerals.
- The recoveries of Cu, Co, Ni, and Mn are higher at 70 °C than at room temperature for the Z02 sample meaning that the reactions are temperature dependent. However, temperature did not have effect on recoveries of Cu, Co, Ni, and Mn on the BCo which contains malachite.
- The experimental data shows that it possible to preferentially leach out copper and manganese from the sample thereby leaving cobalt and nickel which can be leached in a second stage and precipitated together for production of cobalt-nickel alloy.
- Acid consumption decreases with increase in leach pH of the solution at both room temperature and 70 °C. Acid consumption for both samples is 20–140 kg/ton of ore.
- The optimum amount of SMBS is 10% of the weight of the feed for BCo sample and this is equivalent to the Cu, Co, Ni, Mn, and Fe content.

Acknowledgements This work and the publication thereof are funded by the Copperbelt University Africa Centre for Sustainable Mining (CBU-ACESM).

References

1. Abreu CMR et al (2012) Inorganic sulfites: efficient reducing agents and supplemental activators for atom transfer radical polymerization. *ACS Macro Lett Am Chem Soc* 1(11):1308–1311. <https://doi.org/10.1021/mz300458x>
2. Greenwood NN, Earnshaw A (1997) *Chemistry of elements*. Second Edi. Linacre House, Jordan Hill. Butterworth-Heinemann, Oxford
3. Havlik T et al (2019) Considering the influence of calcium on EAF dust acid leaching. *Physicochem Probl Min Proc* 55(2):528–536. <https://doi.org/10.5277/ppmp18164>
4. IAEA (2001) *Manual of acid In Situ Leach uranium mining technology*. International Atomic Energy Agency (IAEA), Vienna, (August), p 294 (71). https://www-pub.iaea.org/MTCD/Publications/PDF/te_1239_prn.pdf.
5. Kafumbila J (2018) Dissolution of cobalt (III) using simultaneously ferrous and sulfur dioxide as reducing reagents performed in open agitated tank: kinetic model
6. Mwema MD, Mpoyo M, Kafumbila K (2002) Use of sulphur dioxide as reducing agent in cobalt leaching at Shituru hydrometallurgical plant. *J S Afr Inst Min Metall* 102(1):1–4
7. Ntengwe F (2010) The leaching of dolomitic-copper ore using sulphuric acid under controlled conditions. *Open Min Proc J* 3(1):60–67. <https://doi.org/10.2174/1874841401003010060>
8. Pourret O, Faucon M-P (2018) Cobalt: encyclopedia of geochemistry, encyclopedia of geochemistry. In: White WM (ed) *Encyclopedia of earth sciences series*. Springer International Publishing, Cham. <https://doi.org/10.1007/978-3-319-39193-9>.
9. Pretorius PJ (2019) Atmospheric acid leaching of oxidised and mixed copper cobalt ores mined in the Democratic Republic of the Congo by or (April)
10. Sole KC (2018) The evolution of cobalt–nickel separation and purification technologies: fifty years of solvent extraction and ion exchange, pp 1167–1191. https://doi.org/10.1007/978-3-319-95022-8_95
11. Sole KC et al (2019) Flowsheet options for cobalt recovery in African Copper–cobalt hydrometallurgy circuits. *Min Proc Extr Metall Rev* 40(3):194–206. Taylor & Francis. <https://doi.org/10.1080/08827508.2018.1514301>
12. Stuurman S, Ndlovu S, Sibanda V (2014) Comparing the extent of the dissolution of copper-cobalt ores from the DRC region. *J South Afr Inst Min Metall* 114(4):347–353
13. Sutcliffe ML, Johnson GM, Welham NJ (2011) Method for leaching cobalt from oxidised cobalt ores
14. Tshipeng SY, TshamalaKaniki A, Kime MB (2017) Effects of the addition points of reducing agents on the extraction of copper and cobalt from oxidized copper–cobalt ores. *J Sustain Metall* 3(4):823–828. Springer. <https://doi.org/10.1007/s40831-017-0149-x>

Interaction Between Iron Ore and Magnesium Additives During Pellet Roasting Process



Lian-Da Zhao, Hong-Su, Qing-Guo Xue, and Jing-Song Wang

Abstract To study the interaction between iron ore and magnesium additives, several types of interaction couples were prepared and SEM–EDS was used to measure the diffusion distance of Mg^{2+} . Results showed that prolonging the roasting time was beneficial to the diffusion of Mg^{2+} in the iron ore. When the basicity (CaO/SiO_2) of iron ore increased from 0.2 to 1.0, the diffusion distance of Mg^{2+} increased from 15 to 35 μm . Among three magnesium additives, the diffusion distance of Mg^{2+} in dolomite was the longest, while that in serpentine was the shortest. Serpentine contains a large amount of SiO_2 , which can hinder the contact between MgO and Fe_2O_3 , thus reducing the diffusion distance of Mg^{2+} . The roasting experiment of high-magnesium pellets was further carried out to study the influence of basicity on the compressive strength of pellets. Result shows that the compressive strength of pellets decreased from 2701 to 2556 N when 2% dolomite was added. The basicity of high-magnesium pellets was adjusted by adding CaO into the pellets. The compressive strength of pellets with basicity of 1.2 was 2629 N. The compressive strength of pellets with basicity of 1.5 was 2654 N. Adding CaO to high-magnesium pellets can improve the compressive strength.

Keywords Interaction couple · Compressive strength · Diffusion performance · MgO additives

Introduction

As China plans to reach a carbon peak by 2030, using a high proportion of pellets to produce iron is an important measure for the metallurgical industry to reduce energy consumption and reduce carbon dioxide emissions. Traditional acid pellets have the disadvantages of poor reducibility and high reductive swelling index. It has

L.-D. Zhao · Hong-Su · Q.-G. Xue · J.-S. Wang (✉)
State Key Laboratory of Advanced Metallurgy, University of Science and Technology Beijing,
Beijing 100083, China
e-mail: wangjingsong@ustb.edu.cn

been shown that the composition of pellet has an important effect on its metallurgical properties. Therefore, improving pellet composition is an important method to increase the proportion of pellet into furnace [1–3]. It is an important method to add fluxes and adjust the composition of gangue under the existing pellet production conditions [4].

Adding MgO is an effective method to improve the metallurgical properties of pellets [5]. Dwarapudi et al. [6] studied the effect of MgO content on the quality and microstructure of hematite pellets, and they found that addition of MgO to both acid and limestone fluxed pellets considerably reduced their swelling tendency. Fan studied the influence of magnesium additives on iron ore oxidized pellets. When adding magnesium additives, the compressive strength of pellets decreases because of the oxidation of magnetite retarded by MgO [7]. For pellets containing high content of MgO, Wang found that increasing the content of CaO was helpful to reduce the influence of MgO on the compressive strength of pellets [8]. Yang et al. [9] pointed out that alkaline pellet with high-MgO content has better softening-melting characteristic and reduction swelling index. However, in the actual production, it is found that the higher compressive strength of magnesium-containing pellets often requires a more stringent roasting system [10]. The metallurgical properties of pellets can be significantly improved by adding magnesium-containing additives. But the residual MgO in pellets hinders the continuous crystallization of Fe_2O_3 and reduces the compressive strength of pellets. Therefore, accelerating the diffusion of Mg^{2+} between iron ores is of great significance for improving the compressive strength of high-magnesium pellets. It is necessary to explore the consolidation mechanism of pellets containing magnesium additives. The diffusion of Mg^{2+} in the pellets has a very important effect on the performance of the pellets [11].

In our study, the interaction couple method was used to study the effects of roasting time, basicity, and magnesium additives on the diffusion rate of Mg^{2+} . First, the diffusion distance of Mg^{2+} was measured under different experimental conditions. Next, the basicity of pellets was changed by adding dolomite and CaO, and the compressive strength of pellets was tested. Combined with the mineral phase analysis of pellets, the reasons affecting the change of compressive strength of pellets were explored. At the same time, SEM–EDS was used to measure the diffusion distance of Mg^{2+} and observe the mineral phase of pellet. This investigation is helpful in understanding the interaction between the mineral phases of iron ores and magnesium additive (dolomite, serpentine).

Experimental

Raw Materials

The raw materials used to prepare pellets in the present work, including magnetite, dolomite, and serpentine, were acquired from an iron and steel enterprise in China.

Table 1 Main chemical compositions of raw materials (wt%)

Raw materials	TFe	FeO	CaO	SiO ₂	Al ₂ O ₃	MgO
Magnetite	69.07	29.28	0.38	1.62	0.35	0.73
MgO (a. r.)						99.00
Dolomite	0.36		31.78	2.57	0.55	
Serpentine	1.03		1.82	35.68	0.08	47.18
CaO (a. r.)			99.00			

Table 2 Chemical compositions of bentonite (wt%)

Al ₂ O ₃	Fe ₂ O ₃	Na ₂ O	CaO	MgO	Water
12.00	1.60	0.56	2.01	2.00	2.00

Table 3 Physical characteristics of bentonite

Colloid index/ (mL (15 g) ⁻¹)	Expansion volume/(mL (2 g) ⁻¹)	Montmorillonite content/wt%	Water absorption (2 h)/%	Content of methylene blue adsorbed (mL (100 g) ⁻¹)
100	25	80	420	35.36

The chemical composition of the raw materials is listed in Table 1. Both MgO and CaO used in the experiment were analytical reagents with a purity of 99%. Bentonite was added to the pellets at a content of 1 wt%. The composition and bonding properties of bentonite are shown in Tables 2 and 3.

Interaction Couple Experiments

Preparation of Interaction Couples

The method of interaction couples was adopted to explore the diffusion of Mg²⁺ in high-magnesium pellets. The mineral powder or the mineral powder-containing additives and the magnesium-containing reagent were pressed separately under 2 MPa. In order to ensure that the pellets would not be broken in the experiment, the pellets were roasted at 600 °C for 3 h (protected by N₂). After roasting, the pellets were annealed, and the two pellets were made into interaction couples by close contact, as shown in Fig. 1.

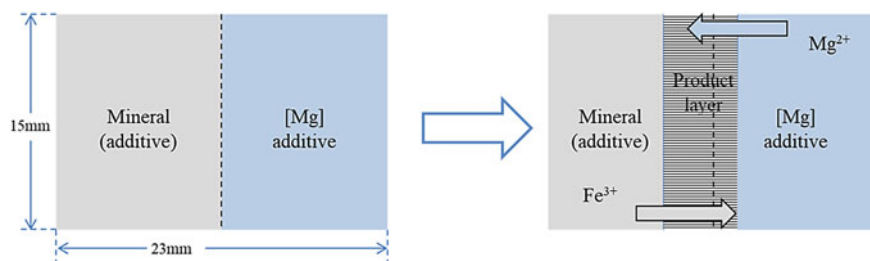


Fig. 1 Diagram of ion diffusion in interaction couples

Roasting of Interaction Couples

In order to simulate the actual roasting process of pellet as much as possible, the interaction couples were roasted by three-stage roasting method. The temperatures of the three sections of the electric furnace was set to 500 °C (eliminating crystal water), 950 °C (preheating), and 1 250 °C (roasting). The duration of the first two stages was 15 min.

Microscopic Observation of Interaction Couples

After roasting, the couples were sliced along the diffusion direction, and the sections were polished and inserted. The product layer was observed by electron microscope and the diffusion distance of Mg^{2+} was measured. In our study, the effects of roasting time, basicity of pellets (CaO/SiO_2), and magnesia-containing additives on the diffusion distance of magnesium were studied. Experimental conditions are shown in Table 4.

Table 4 Experimental conditions

Basicity of the minerals (CaO/SiO_2)	Magnesia additive	The roasting time (min)
0.20	MgO	15
		25
		35
0.20	MgO	15
	Dolomite	
	Serpentine	
0.20	MgO	15
0.50		
1.00		

Table 5 Compositions of the pelletizing mixtures

CaO/SiO ₂	Magnetite/wt%	Dolomite/wt%	CaO/wt%	Bentonite/wt%
0.2	100	0	0	1
0.6	100	2	0	1
1.2	100	2	0.9	1
1.5	100	2	1.3	1

Pellet Roasting Experiments

In order to explore the effect of basicity (CaO/SiO₂) on the compressive strength of magnesium oxide pellets in the actual production process, the experiment was carried out to produce magnesium-containing pellets by briquetting. In our study, dolomite was used as magnesium additive, and the basicity of the pellets was changed by adding different contents of CaO to the pellets.

The specific experimental scheme is shown in Table 5, and the pellets were placed in each area for 15 min.

Results and Analysis

Effect of Roasting Time on Diffusion of Mg²⁺

The microstructure and Mg²⁺ distribution of the interaction couples during different roasting times are shown in Fig. 2. It can be seen from the SEM image that Mg²⁺ diffused into the iron ore and produced magnesium ferrite in solid phase reaction with Fe₂O₃ during the roasting process. In the SEM picture, the outer boundary of diffusion layer is defined by the distribution of magnesium dots varying greatly, and it has been marked in the picture. According to the contact length in the diffusion couple and the area of the defined diffusion region, the diffusion distance is approximately calculated.

In Fig. 2, the diffusion distance of Mg²⁺ increases with the increase of roasting time. In the interaction couple roasted for 15 min, the diffusion distance of Mg²⁺ was 15 μm. For the interaction couple with a roasting time of 25 min, the diffusion distance was 20 μm. When the roasting time was increased to 35 min, the diffusion distance of Mg²⁺ increased to 31 μm. The ratio of diffusion distance of Mg²⁺ to calcination time reflects the diffusion rate of Mg²⁺. In our study, the average diffusion rate of Mg²⁺ was 0.9 μm/min. This indicates that the diffusion rate of Mg²⁺ is relatively stable under certain roasting conditions. Increasing the roasting time significantly increases the diffusion distance of Mg²⁺.

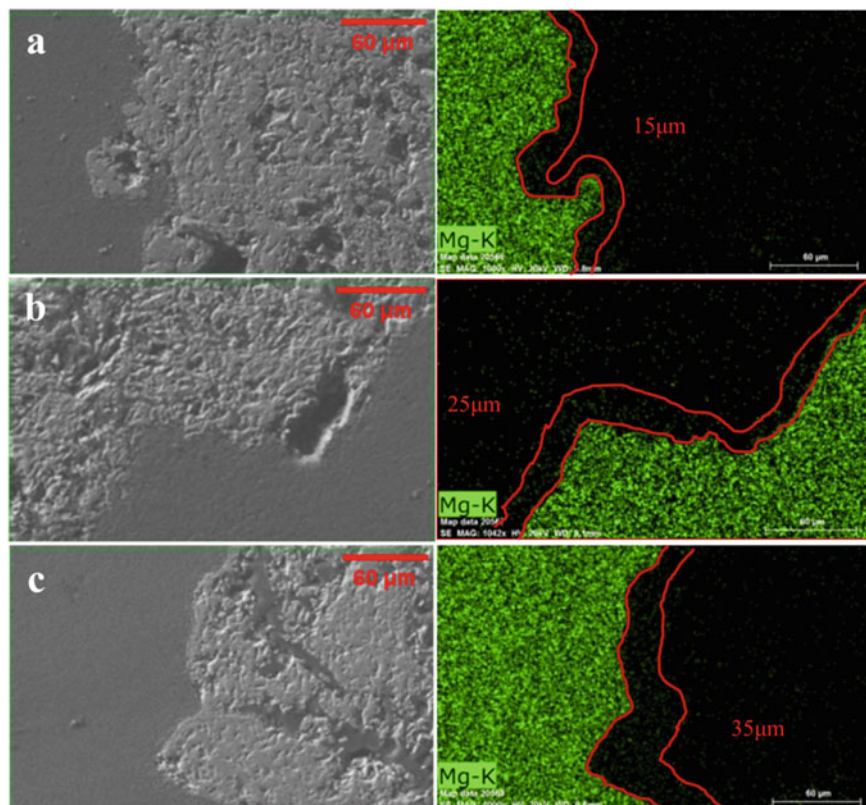


Fig. 2 SEM image of interaction couples of different roasting times. **a** 15 min; **b** 25 min; **c** 35 min

Effect of Chemical Composition on Diffusion of Mg^{2+}

In order to explore the influence of chemical composition on Mg^{2+} diffusion, two research methods were adopted according to the actual production situation. One was to change the basicity of magnetite by adding CaO to it. The other was to change the type of magnesium additives. Analytical reagents MgO, dolomite, and serpentine were adopted in our study.

Figure 3 shows the SEM images of interaction couples with different basicity. Mg^{2+} has different diffusion distance in interaction couple with different basicity of magnetite. It can be seen from Fig. 3 that the diffusion distance of Mg^{2+} was 19 μm in the couple in which the basicity was 0.5. When the basicity increased to 1, the diffusion distance increased to 35 μm .

In actual production, there are many sources of magnesium flux, such as dolomite, magnesite, and serpentine. Figure 4 shows SEM image of interaction couples containing different kinds of magnesium additives. It is found that different kinds of

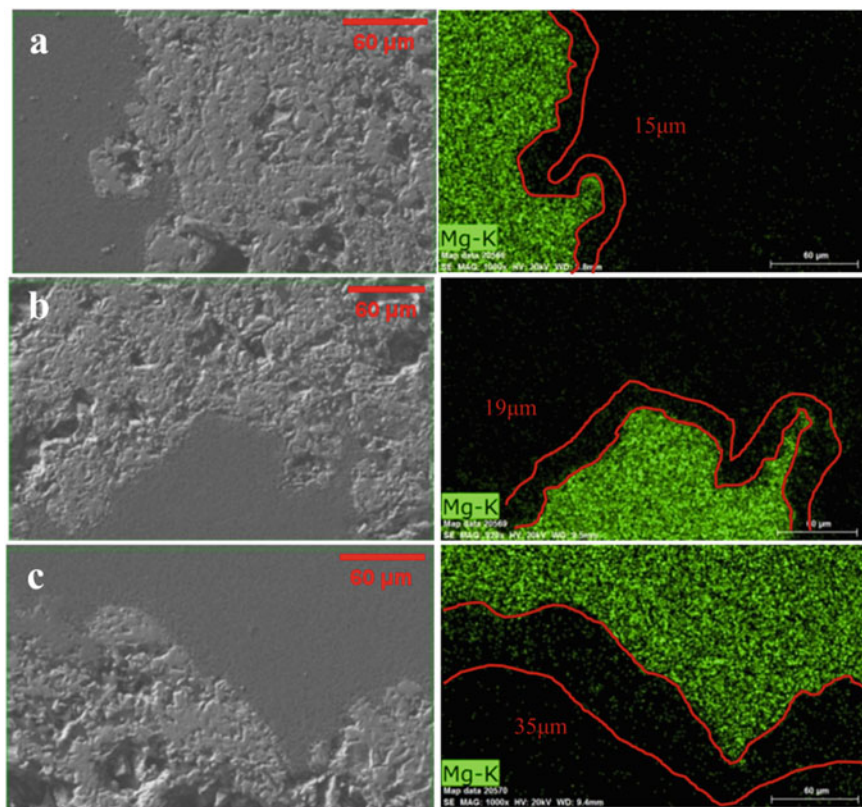


Fig. 3 SEM image of interaction couples of magnetite with different basicity. **a** $R = 0.2$; **b** $R = 0.5$; **c** $R = 1$

reagents containing MgO have different diffusion distances in interaction couples. The diffusion distance of Mg^{2+} in MgO-magnetite interaction couple was 15 μm . The diffusion distance of Mg^{2+} in the serpentine-magnetite interaction couple was reduced to 11 μm . The diffusion distance of Mg^{2+} in the dolomite-magnetite interaction was the longest, which was 25 μm .

The chemical composition of magnesium additives had an important effect on the diffusion distance of Mg^{2+} in interaction couples. The main chemical compositions of serpentine are SiO_2 and MgO. Dolomite contains a large amount of CaO and MgO after roasting. For serpentine-magnetite diffusion couples, there was a large amount of SiO_2 at the contact interface. In the oxidizing atmosphere, SiO_2 does not react with Fe_2O_3 . The solid-state SiO_2 was filled between MgO and Fe_2O_3 , which prevented MgO from contact with Fe_2O_3 and inhibited the formation of magnesium ferrite. This situation resulted in the short diffusion distance of Mg^{2+} . Dolomite is rich in Mg and Ca. CaO and Fe_2O_3 preferentially form calcium ferrite during calcination. Calcium ferrite has a very low melting point and forms a large liquid phase at the

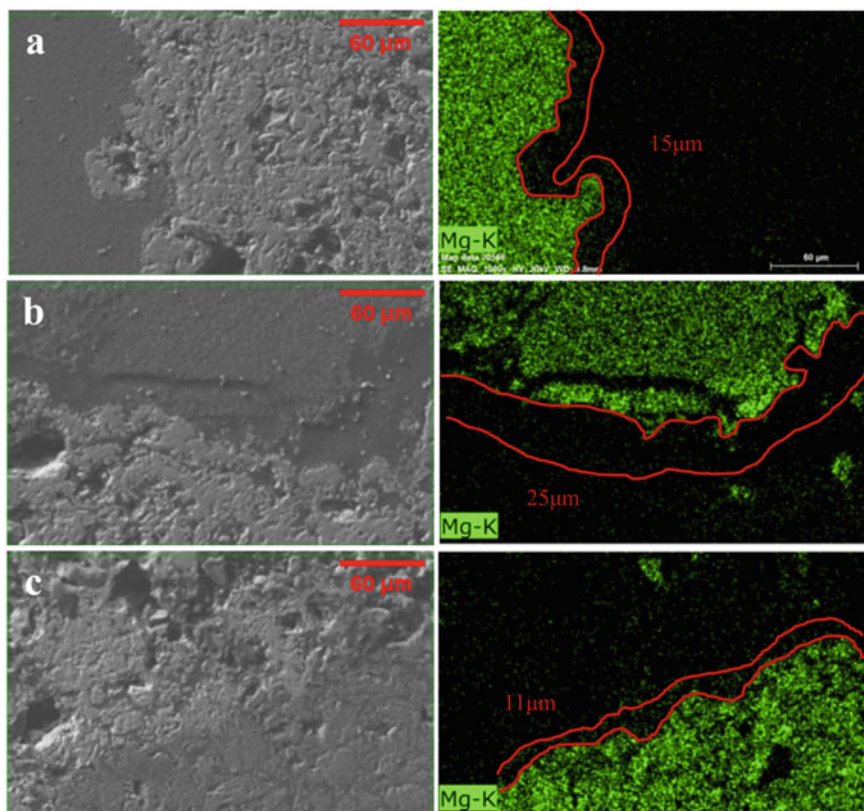


Fig. 4 SEM image of interaction couples of different types of magnesium additives. **a** Analytical reagent MgO; **b** dolomite; **c** serpentine

experimental temperature. The liquid phase calcium ferrite produced in the roasting process acted as a bond between Fe_2O_3 crystals and accelerated the reaction between MgO and Fe_2O_3 . The diffusion rate of Mg^{2+} was accelerated, and the formation rate of magnesium ferrite was greatly improved [12].

Effect of Basicity on Minerals Phase and Compressive Strength of Pellets with High-MgO Content

It has shown that appropriate roasting time, magnesia additives, and basicity can promote the diffusion of Mg^{2+} and accelerate the reaction between MgO and Fe_2O_3 . In our study, the behavior of high-magnesium pellets during roasting was characterized by X-ray Diffraction (XRD) and SEM-EDS. The compressive strength of the pellets was measured using a pressure test machine.

The compressive strength of pellets with different basicity is shown in Fig. 5. When the pellets did not contain dolomite, the basicity was 0.2, and the compressive strength was 2701 N. The basicity of pellets with 2% dolomite was 0.6, and the compressive strength dropped to 2556 N. Different proportions of CaO were added to pellet to change the basicity of pellet. When the basicity was 1.2, the compressive strength increased to 2629 N, and when the basicity was 1.5, the compressive strength was 2654 N.

Figure 6 shows the microscopic mineral phases of pellets with different basicity. XRD spectra of roasting products are shown in Fig. 7. The reaction rate of MgO and Fe₂O₃ was very slow when dolomite was added to pellet. When the pellet roasting was finished, the MgO that did not participate in the reaction still remained in the pellet. Because the residual MgO hinders the Fe₂O₃ crystal connection, it can reduce

Fig. 5 Effect of basicity on compressive strength of high-MgO pellets

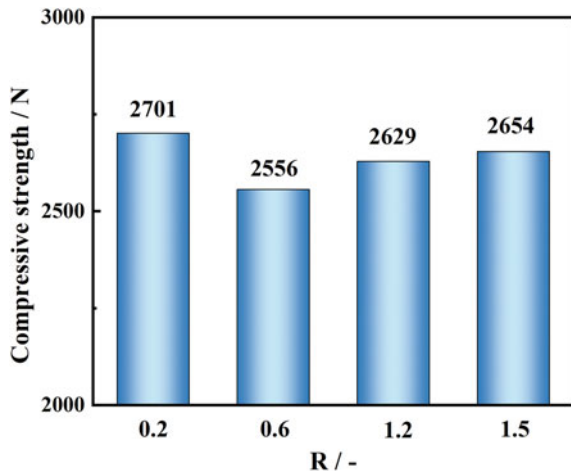
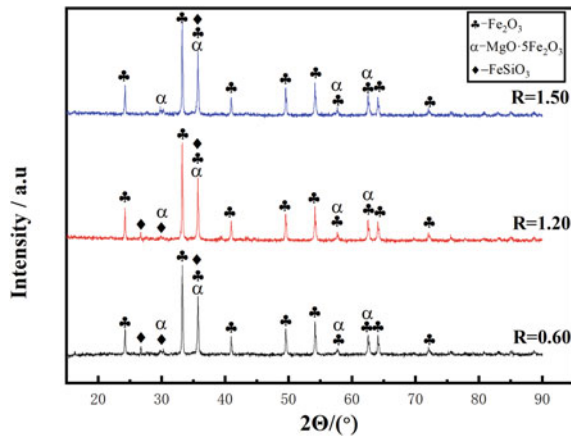


Fig. 6 XRD spectra of high-MgO pellets under different basicity



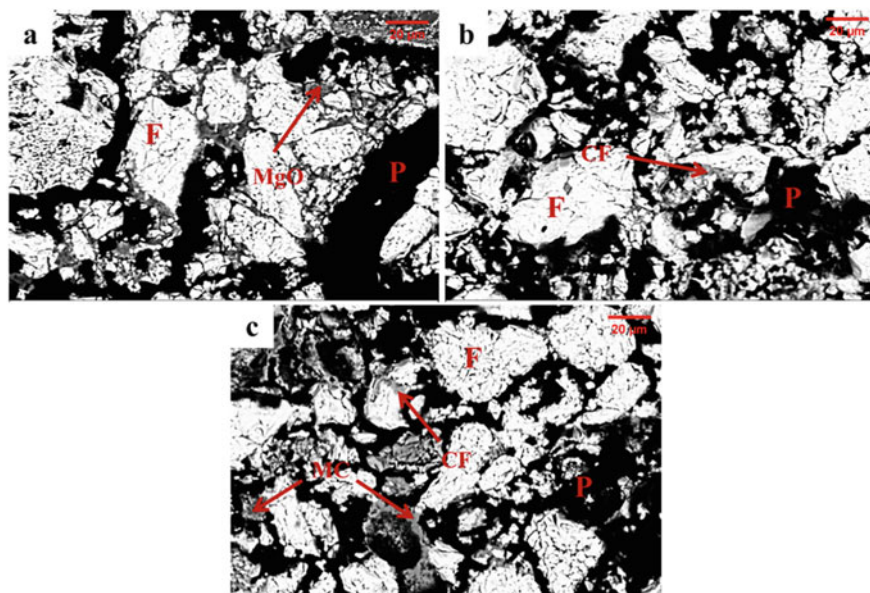


Fig. 7 SEM image of the pellets with different basicity. **a** 2% dolomite; **b** 2% dolomite + 0.9% CaO; **c** 2% dolomite + 1.3%CaO. F-Fe₂O₃; P-pore; CF-calcium ferrite; MC-monticellite

the compressive strength of the pellets. The content of calcium ferrite and monticellite in pellets increased with the increase of basicity and CaO content in pellets. On the one hand, this kind of low melting point material melted in the process of pellet roasting, and then filled in between Fe₂O₃ crystals, which plays a connection role between crystals. This behavior reduced the porosity of pellets. On the other hand, liquid calcium ferrite and monticellite can accelerate the reaction rate of MgO and Fe₂O₃, so that the distribution of MgO in pellet was more uniform. Therefore, for high-magnesium pellet, increasing CaO content in pellet can optimize the mineral phase of pellet and increase the compressive strength of pellet. From the XRD results of different basicity pellets, it can be seen that the main composition of pellets is Fe₂O₃. When the basicity of pellets increased, the content of FeSiO₃ decreased, and there was almost no FeSiO₃ in the pellets with basicity of 1.5. The change of gangue phase in the pellets has a great influence on the compressive strength of the pellets [13, 14].

Conclusions

In this study, magnetite, dolomite, serpentine, and analytically pure reagent CaO and MgO were used to study the diffusion behaviors of Mg²⁺ in iron ore during roasting. Simulating the actual pellet production process, the mineral phases and

the influencing factors of compressive strength of high-Mg content pellets under different basicity were explored. Results are shown below:

- (1) The diffusion distance of Mg^{2+} was positively correlated with the roasting time. The diffusion distance of Mg^{2+} increased from 15 to 31 μm when roasting time increased from 15 to 35 min.
- (2) For different kinds of magnesium additives, under the same roasting conditions, the diffusion distance of Mg^{2+} in dolomite was the farthest, which was 25 μm . The diffusion distance of Mg^{2+} in serpentine was 11 μm . The basicity has a great influence on the diffusion distance of Mg^{2+} . When the basicity increased from 0.2 to 1, the diffusion distance of Mg^{2+} increased from 15 to 35 μm . In the presence of dolomite additives and high basicity, there was a large amount of CaO in the interaction couple. During the roasting process, CaO reacts with Fe_2O_3 in preference to generate calcium ferrite. Due to the low melting point of calcium ferrite, liquid phase was formed during the roasting process, and the presence of liquid phase increases the contact area between Mg^{2+} and Fe_2O_3 . This behavior accelerated the diffusion of Mg^{2+} .
- (3) MgO in pellet affects the consolidation of ore phase. Residual MgO in ore phase reduces the compressive strength of pellets. Increasing the basicity of pellets can improve the situation. When the content of CaO in pellet increases, the chemical composition of gangue changes. A large amount of liquid phase accelerated the diffusion of Mg^{2+} and reduced the content of MgO in the pellet that did not participate in the reaction. At the same time, increasing basicity can reduce the porosity of pellet. For high-magnesium pellets, the basicity of pellets needs to be increased in order to obtain higher compressive strength.

References

1. Tang J, Chu MS, Li F (2020) Development and progress on hydrogen metallurgy. *Int J Miner Metall Mater* 27(6):713–723
2. Zhao P, Dong PL (2018) Carbon emission cannot be ignored in future of Chinese steel industry. *Iron Steel* 53(8):1–7 (in Chinese)
3. Petrus HTBM, Putera ADP, Sugiarto E, Perdana I, Warmada IW, Nurjaman F (2019) Kinetics on roasting reduction of limonitic laterite ore using coconut-charcoal and anthracite reductants. *Miner Eng* 132:126–133
4. Pal J, Arunkumar C, Rajshekhkar Y (2014) Development on iron ore pelletization using calcined lime and Mgo combined flux replacing limestone and bentonite. *ISIJ Int* 54(10):2169–2178
5. Bai KK, Liu LC, Pan YZ, Zuo HB, Xue QG (2021) A review: research progress of flux pellets and their application in china. *Ironmak Steelmak*: 1–16
6. Srinivas D, Tamal KG, Amitabh S, Vilas T, Bhattacharjee D, Venugopal R (2011) Effect of pellet basicity and MgO content on the quality and microstructure of hematite pellets. *Int J Miner Process* 99(1–4):43–53
7. Fan XH, Gan M, Jiang T, Yang LS, Chen XL (2010) Influence of flux additives on iron ore oxidized pellets. *J Cent South Univ Technol* 4:732–737
8. Wang RR, Zhang JL, Liu ZJ, Li Y, Xu CY (2021) Effect of CaO and MgO additives on the compressive strength of pellets: exploration on the decisive stage during induration. *Powder Technol* 390:496–503

9. Yang ZC, Liu ZG, Chu MS, Gao LH, Tang J (2021) Effect of basicity on metallurgical properties of fluxed pellets with high MgO content. *ISIJ Int* 61(5):1431–1438
10. El-Geassy AA (1999) Influence of doping with CaO and/or MgO on stepwise reduction of pure hematite compacts. *Ironmak Steelmak* 26(1):41–52
11. Dwarapudi S, Ghosh TK, Tathavadkar V (2012) Effect of MgO in the form of magnesite on the quality and microstructure of hematite pellets. *Int J Miner Process* 112–113:55–62
12. Wang RR, Zhang JL, Liu ZJ (2020) Effects of magnesium olivine on the mineral structure and compressive strength of pellets. *Ironmak Steelmak* 47(2):100–105
13. Guo H, Jiang X, Shen FM, Zheng HY, Gao QJ, Zhang X (2019) Influence of SiO₂ on the compressive strength and reduction-melting of pellets. *Metals* 9(8):852–870
14. Lu JG, Lan CC, Qing LY, Zhang SH, Sun JN (2021) Effects of SiO₂ on the preparation and metallurgical properties of acid oxidized pellets. *Int J Miner Metall Mater* 28(4):629–636

Chemical Analysis of Mineral Surfaces Using Digital Image Processing



Juan C. González-Islas, Abdon R. Aparicio-Durán,
Gildardo Godínez-Garrido, Karime A. González-García,
and Mizraim U. Flores-Guerrero

Abstract Quantitative and qualitative chemical analyses are of great importance in the characterization of materials and in mineralogy, in order to determine the content of elements present in minerals; the equipment used for this kind of analysis is very expensive and sophisticated. Image segmentation can provide a semi-quantitative analysis of the elemental content of the mineral surface. In the present work, the semi-quantitative analysis of purple fluorite was carried out using atomic absorption spectrophotometry, X-ray dispersive energy spectrometry and the comparison with image segmentation was made, matching the percentages of calcium and fluorine in the three methods. The analysis of the images was based on the intensity of the colors to determine the content of each element present in the mineral, subsequently the method of functional approximation and interpolation was used so that it can be an economic form, precise, and easy to use for determining semi-quantitative composition of mineral surfaces.

Keywords Semi-quantitative analysis · Image segmentation · Purple fluorite · Atomic absorption spectrophotometry

Introduction

Image segmentation is the process of partitioning or segregating an image into parts or regions. Often, such splitting is based on the pixel properties of an image, for

J. C. González-Islas · A. R. Aparicio-Durán · G. Godínez-Garrido · M. U. Flores-Guerrero (✉)
Área Electromecánica Industrial, Universidad Tecnológica de Tulancingo, 43645 Tulancingo,
Hidalgo, México
e-mail: mflores@utectulancingo.edu.mx

J. C. González-Islas · G. Godínez-Garrido
Área Académica de Computación Y Electrónica, Universidad Autónoma del Estado de Hidalgo,
42184 Pachuca, Hidalgo, México

K. A. González-García
Tecnológico Nacional de México, Instituto Tecnológico de Saltillo, 25280 Saltillo, Coahuila,
México

example, abrupt discontinuities typically represent edges, in addition, segmentation can also be done by color, texture, and gradient, among others [1]. Color segmentation facilitates the separation of space-spectral attributes. This technique is predominantly used as a pre-processing step to annotate, improve, analyze, classify, or summarize image information. In general, there are many segmentation applications in image processing, artificial vision, and pattern recognition, including image rendering, compression, security, graphics, biomedical imaging, and agricultural product quality inspection, among others [2–4]. Another less common application has been used to monitor the health and well-being of livestock by implementing novel non-invasive techniques based on the monitoring of face characteristics taken from images of livestock [5]. One of the first works related to image processing in terms of chemical analysis was presented in [6]. It focuses on the quantification of images of ionic mass spectrometries produced by a microscope, using micro-photodensitometry and digital image processing based on feature analysis and cross correlation using the Fourier fast transform. One of the most common methods is the semi-quantitative characterization through SEM and TEM microscopy, this through the spectroscopy of X-ray dispersive energies (EDS). The EDS technique detects the X-rays emitted by the sample during bombardment by an electron beam to characterize the elemental composition of the analyzed volume. The EDS X-ray detector measures the relative abundance of X-rays emitted versus their energy. The detector is typically a solid-state lithium-derived silicon device. When an incident X-ray hits the detector, it creates a charge pulse that is proportional to the X-ray's energy. The X-ray energy spectrum versus counts is evaluated to determine the elemental composition of the sampled volume [7]. For quantitative analysis, Atomic Absorption Spectrometry (AAS) is used, a technique in which free gaseous atoms absorb electromagnetic radiation at a specific wavelength to produce a measurable signal. The absorption signal is proportional to the concentration of those free absorption atoms in the optical path. Therefore, for AAS measurements, the analyte must first be converted into gaseous atoms, usually by applying heat to a cell called an atomizer [8, 9]). Therefore, in this work, a semi-quantitative chemical analysis of surfaces is done to determine the percentages of calcium and fluorine present in a purple fluorite (CaF_2). The results have been verified by unsupervised machine learning for image segmentation and are verified by X-ray scattering energy spectroscopy, which is a semi-quantitative analysis. Furthermore, likewise, the samples are analyzed by atomic absorption spectrometry which is a quantitative technique which will analyze the calcium content present in the purple fluorite samples.

Materials and Methods

For the present study, a sample of purple fluorite from “La Sabina” mine, located in the state of Coahuila, México between the municipalities of Melchor Múzquiz and Ocampo, was used. A quantitative chemical analysis using Atomic Absorption Spectrophotometry (The AAnalyst™ 200 spectrometer) was performed to determine

the calcium content present in the purple fluorite sample. Three shades of mineral were analyzed, one that is completely transparent, one with the presence of light purple, and one that has an intense purple. The purple fluorite samples were dissolved with hydrochloric acid in a 1:1 ratio with bi-distilled water to be able to analyze them by Atomic Absorption Spectrophotometry (AAS). The sample was vaporized and the element of interest (calcium) atomized at high temperatures. The concentration of calcium is determined by the attenuation or absorption by the atoms of the analyte of a characteristic wavelength emitted by a light source. The light source has been a hollow cathode lamp containing calcium in the filament. An air-acetylene flame (2300 °C) was used to determine calcium. In order to quantify fluorine, it had to be done by means of X-ray dispersive energy spectroscopy, with the help of a Scanning Electron Microscope, with field emission (JEOL JSM-6701F, Tokyo, Japan).

The determination of the chemical elements in the mineral of the purple fluorite sample by digital image processing is done by two stages, the first focuses on the segmentation of images to isolate the rock that has the mineral of interest and the second is to determine the amount of the chemical elements present. In stage 1, the starting point is the acquisition of images with a resolution of 720×1280 . The images are then pre-processed using a medium filter. The unsupervised learning model used for the segmentation task of the region of interest is k-nearest neighbors, one of the most used in the statistical classification, standing out for being accurate and not depending on any distributional assumption [10].

Figure 1 shows the starting point of the algorithm as the segmented image. Subsequently, this image of the red, green, blue (RGB) color space is converted to Hue, Saturation, Value (HSV), since, unlike the first, the second simplifies the execution of color adjustments. In the next step, the linear regression parameters are entered, which consist of the predictors for the $x \in \mathbb{R}$ domain and the estimated values of the element in the codomain $y \in \mathbb{R}$, which consist of the predictors and the estimated values. Then select in the image the point of interest related to the study mineral, enter the threshold for the tone values, saturation and brightness around the point of interest, and with this the present amount of the chemical element is determined by a previously trained linear regression model.

Results and Discussion

The analysis performed by Atomic Absorption Spectrophotometry shows that the amount of calcium decreases when the purple fluorite hue becomes a darker purple and vice versa, when the purple fluorite becomes light the calcium content increases, which is shown in Table 1 where the content of this element is in the samples and the clearer the tone of the mineral becomes the greater the amount of calcium that presents within its structure.

The EDS spectra confirm what was observed with the AAS analysis, where the concentrations of calcium present in the sample and its distribution are confirmed. Figure 2a shows an EDS spectrum of the most intense purple fluorite sample where

Fig. 1 Flow diagram for the determination of the amount present of the chemical element in the ore of interest

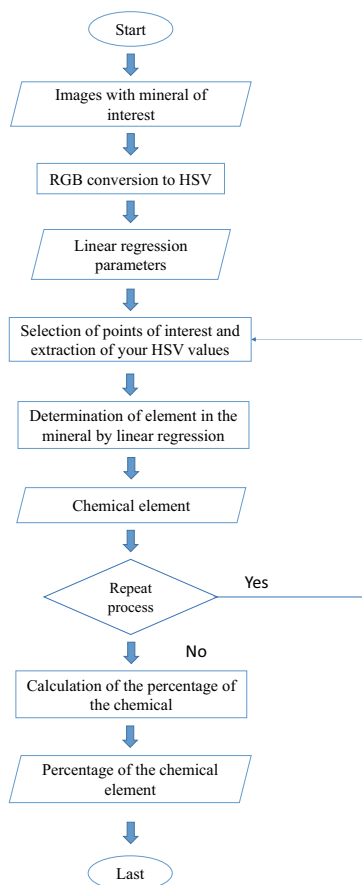


Table 1 Analysis of calcium content in the different purple fluorite samples

Sample type	Calcium concentration sample 1 (ppm)	Calcium concentration sample 2 (ppm)	Calcium concentration sample 3 (ppm)
Intense purple sample	9.17	10.03	10.26
Faint purple sample	18.73	19.73	18.86
Transparent sample	26.29	28.15	26.12

calcium peaks are lower than fluorine. Figure 2b shows an EDS from the analysis of the faint purple sample, showing that calcium peaks have increased and the fluorine peak has decreased in intensity, so it is consistent with the analyses performed by the atomic absorption spectrometer. Finally, the most transparent part of the mineral sample was analyzed, and it was observed that calcium peaks increased considerably following the trend of the analyses performed by AAS. This is seen in Fig. 3c where the fluorine peaks are of lower intensity.

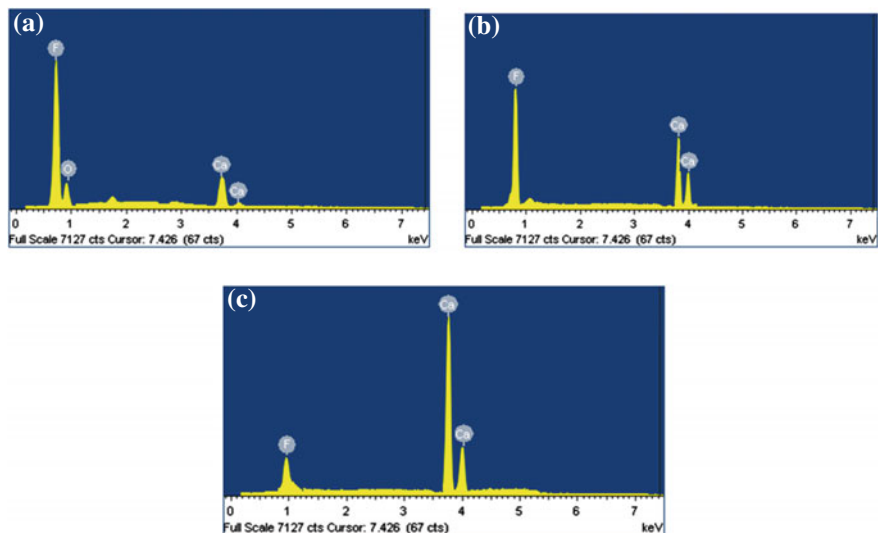


Fig. 2 a EDS analysis performed on the intense purple sample, b EDS analysis performed on the faint purple sample, c EDS analysis performed on the clear sample (Color figure online)

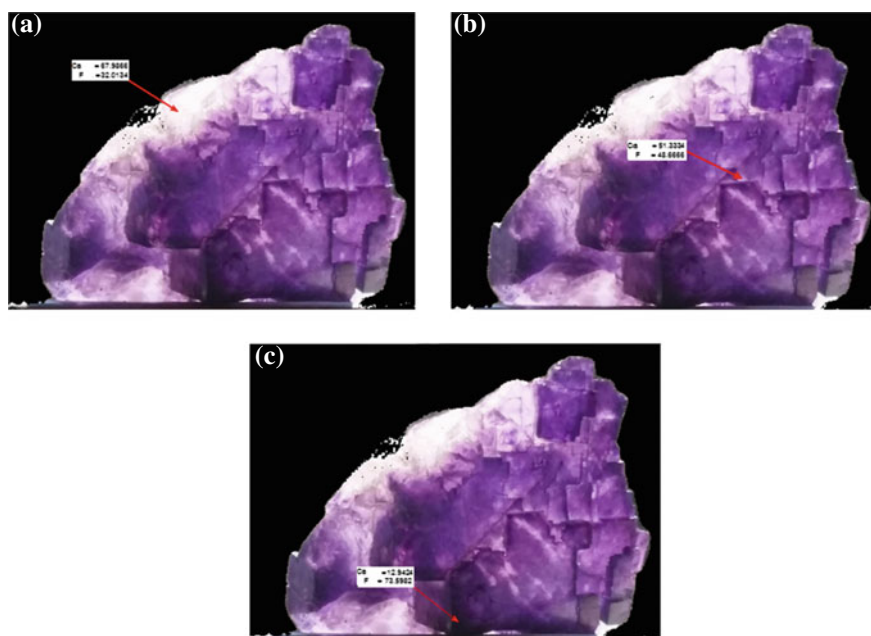


Fig. 3 a Calcium and fluorine concentrations present in the clear, b in the light purple, c and in the dark purple part of the mineral (Color figure online)

Functional Approximation and Interpolation

For digital image processing an Eq. 1 was used, which is given by the function $p(x)$ defined in an interval $[a,b]$ approximates a function $f(x)$ in the same interval if

$$p(x) \cong f(x) \tag{1}$$

For the functional approach method to be fully described, two fundamental ingredients are necessary. The function space where the approximation $p(x)$ is chosen has to be defined. That is, choose the type of approach. The approach criterion is then defined.

Approximation functions are obtained by linear combinations of elements of families of functions called elementary functions, which in general have the form of Eq. (2).

$$a_0g_0(x) + a_1g_1(x) + \dots + a_n(x) \tag{2}$$

where a_i , $0 \leq i \leq n$, are constant to be determined and $g_i(x)$, $0 \leq i \leq n$ functions of a particular family. Monomials in x (x^0, x, x^2, \dots) constitute the most commonly employed family or group, whose general combinations polynomial type approximations, according to Eq. (3).

$$p(x) = \sum_{i=0}^n a_i x^i \tag{3}$$

Is a tabular function $f(x)$ (Table 2).

In this case, the exact setting will be used, which will pass the function through all the points within the table. Once the approximation polynomial has been obtained, it can be used to obtain additional points to those existing in Table 3.

The procedure for calculating the element percentage is described in Table 3.

Table 2 Tabular function $f(x)$

Points	0	1	2	...	N
X	X_0	X_1	X_2	...	x_n
$f(x)$	$f(X_0)$	$f(X_1)$	$f(X_2)$...	$f(X_n)$

Table 3 Data for statistical analysis

Points	0	1	2
X	0.7443	0.7834	0.9833
$y(f)$	70.7071	52.4887	13.6882
$Y(c)$	17.6768	47.5113	86.3118

In Table 3, there are two functions, one for fluorine $y(f)$ and one for calcium $y(c)$ and then an example is made to obtain a function and then perform an interpolation.

Suppose you want to know the value you will have $y(f)$ when $x = 0.8$.

One way to solve this problem is to replace points (1) and (2) in the straight line equation $p(x) = a_0 + a_1x$, such that they result in two equations with two unknowns that are a_0 y a_1 . With the system solution, a first degree approximation is achieved, allowing linear interpolations to be made, that is, the points (1) and (2) are replaced on the straight line and the result is (Eq. 4)

$$\begin{bmatrix} a_0 & 0.7834a_1 \\ a_0 & 0.9833a_1 \end{bmatrix} = \begin{bmatrix} 52.4887 \\ 13.6882 \end{bmatrix} \quad (4)$$

Solving the system of equations yields

$$a_0 = 204.5463 \quad a_1 = -194.0995$$

The results generate the following Eq. (5):

$$p(x) = 204.5463 - 194.0995x \quad (5)$$

By replacing 0.8, the value of fluorine is 49.27% of concentration.

Analysis of the Images

The first selection was made in the white part of the mineral, in this part it is expected to have lower fluorine content and more calcium. Figure 3a shows the selected part of the mineral. Figure 3b shows the concentration of calcium and fluorine present in the clear part of the mineral. The following test shows the selected area, in this case a part is selected where the concentrations of the mineral are expected to be similar. Figure 3c shows the mineral analysis in the dark purple part.

Conclusions

Analysis by scanning electron microscopy in conjunction with spectroscopy analysis of X-ray dispersive energies shows that a mineral with high calcium content and low fluorine is present. The analyses performed by atomic absorption spectrometry coincide with the approximate percentages of the EDS analyses and the method based on digital image processing presented in this paper because as the purple color becomes dim the content of fluorine decreases. The percentage approximation of

elements in a mineral, employing digital image processing in conjunction with linear regression presents an efficient tool for mineral analysis with low computational cost.

References

1. Jordan MI, Mitchell TM (2015) Machine learning: trends, perspectives, and prospects. *Science* 349(6245):255–260
2. Sabliov C, Boldor D, Keener K, Farkas B (2002) Image processing method to determine surface area and volume of axi-symmetric agricultural products. *Int J Food Prop* 5(3):641–653
3. Vantaram SR, Saber E, (2012) Survey of contemporary trends in color image segmentation. *J Electron Imaging* 21(4):040901
4. Noordam JC, Van Den Broek WHAM (2007) Clustering and classification in multispectral imaging for quality inspection of postharvest products. In: *Techniques and applications of hyperspectral image analysis*, pp 43–67. <https://doi.org/10.1002/9780470010884.ch3>
5. Jorquera-Chavez M, Fuentes S, Dunshea FR, Warner RD, Poblete T, Jongman EC (2019) Modelling and validation of computer vision techniques to assess heart rate, eye temperature, ear-base temperature and respiration rate in cattle. *Animals* 9(12):1089
6. Fassett J, Roth J, Morrison G (1977) Quantitation of secondary ion mass spectrometric images by microphotodensitometry and digital image processing. *Anal Chem* 49(14):2322–2329
7. Martínez A (2010) Microanálisis por dispersión de energías de rayos-X (XEDS), Servicio de Microscopía Electrónica. SCAI, Universidad de Málaga
8. Slavin M (1978) *Atomic absorption spectroscopy*. Wiley, New York
9. Van Loon JC (1980) *Analytical atomic absorption spectroscopy*. Academic Press, New York
10. Patiño CV, Covarrubias CC (2016) Condensación controlada en k-NN y su aplicación para la identificación del color en tiempo real. *Revista de Matemática: Teoría y Aplicaciones* 23(1):143–154

Degradation of Structure and Properties of Coke in Blast Furnace: Effect of High-Temperature Heat Treatment



Jingbo Chen, Wei Ren, Yan Guo, and Shengfu Zhang

Abstract Coke, as one of the main raw materials for blast furnace iron-making, is consumed in large quantities in the iron and steel industry. Coke performance is deteriorated by thermal stress, carbon loss reaction, molten slag, iron erosion, and alkali metal catalytic erosion. Therefore, the degradation of coke properties is very complicated in blast furnace. The deterioration of coke properties is also closely related to structural changes. To clarify the relationship between coke properties and carbon matrix structure during high temperature in the blast furnace, metallurgical coke obtained by blending was subjected to heat treatment under N_2 at 1100–1600 °C (corresponding from the lumpy zone to the dropping zone). I-type drum, universal material testing machine, X-ray diffraction, and optical microscope were used to characterize the change of coke properties and carbon matrix structure. The results showed that the compressive strength and particle size of coke will regularly decrease after heat treatment. The degradation of coke structure and properties is low below 1100 °C and becomes serious rapidly at 1300–1600 °C. The main reason for the decrease of coke compressive strength and pulverization is the increase of graphitization and enlargement of porosity, respectively.

J. Chen · Y. Guo · S. Zhang (✉)

College of Material Science and Engineering, Chongqing University, Chongqing 400044, China
e-mail: zhangsf@cqu.edu.cn

J. Chen

e-mail: chenjingbo@cqu.edu.cn

Y. Guo

e-mail: 295580031@qq.com

W. Ren

Technical Centre, Angang Steel Company Limited, Anshan 114021, Liaoning, China
e-mail: 36805841@qq.com

S. Zhang

Chongqing Key Laboratory of Vanadium-Titanium Metallurgy & Advanced Materials, Chongqing University, Chongqing 400044, China

© The Minerals, Metals & Materials Society 2022

M. Zhang et al. (eds.), *Characterization of Minerals, Metals, and Materials 2022*,

The Minerals, Metals & Materials Series,

https://doi.org/10.1007/978-3-030-92373-0_16

Keywords Coke performance · Heat treatment · Microstructure · Compressive strength

Introduction

Coke is an indispensable material in the blast furnace (BF) iron-making, playing a crucial role in providing heat for the blast furnace operation, providing carbon monoxide for reduction, carburizing to the iron, and supporting the furnace stack to keep it permeable [1–4]. Then the degradation and fines generation of coke is carried out at the same time.

Many factors contribute to the degradation of coke, thermal shock impact by high temperature, the mechanical stress, the carbon solution loss reaction, the alkaline attack, and shock impact by high-speed blast [5–7]. However, the existing evaluation index of coke quality in industrial production seriously simplifies the environment of BF, and only the effect of carbon solution loss reaction was taken into account. In order to propose an evaluation index that is more consistent with the actual operation of the blast furnace, the mechanism of coke degradation in the blast furnace needs to be deepened.

In the upper part of the lumpy zone and the lower part of the cohesive and dripping zone, the degree of carbon solution loss reaction is low. The high-temperature thermal stress is the main reason for coke degradation in these parts. The effect of high temperature on coke is mainly concentrated in the following aspects: (1) crystal structure evolution of coke. In the process of heat treatment, the structure of amorphous carbon in coke gradually tends to a regular graphite structure. Graphitization of coke leads to the reduced reactivity of coke and the increased strength after reaction [8, 9]. (2) Further removal of volatile and decomposition of inorganic components. With the increase of temperature, the residual volatiles in coke will become gas and escape. Meanwhile, some minerals such as kaolin and quartz will decompose at high temperatures. These will increase micro-pores and the specific surface area of coke, resulting in an increase in the porosity of coke and a decrease in strength, thereby promoting the degradation and fines generation of coke [10, 11]. (3) Thermal stress effect. At high temperatures, the thermal stress will further expand the coke, and a temperature gradient will be generated on the coke surface and inside. At the same time, the difference in thermal expansion coefficient between coke and minerals will lead to stress concentration. This will cause coke cracking and promote the degradation and fines generation of coke [12–14].

In recent years, with the development of large BF, an increase of pulverized coal injection rate, and degradation of iron ore grade, coke as the only solid material remaining throughout the BF is believed to display an accelerated degree of degradation and fines generation [15]. High-temperature thermal shock is considered to be the main factor affecting coke strength decline and pulverization [16–18]. In order to degrade these indicators of coke, the effect of high temperature on coke properties and structure has been widely studied. The strength of coke will continuously

decrease in a BF, which is the same as when it is affected by high temperature only in the experiment [19–21]. However, some researchers point out that the compressive strength of coke will be greatly improved at high temperatures, which is not consistent with the deterioration of coke in BF. Strength is only a macroscopic representation of microstructures [22, 23]. Figuring out what happens to the microstructures of coke is the key to understand the change of strength. Hilding et al. [24] have found that the average stack height (L_c) increased linearly with the increase of temperature. Xing et al. [25] carried out the effect of temperature on porosity and pore geometry in the temperature range from 700 to 1500 °C under nitrogen or carbon dioxide atmosphere. It was found that heat treatment had a marginal effect on the pore shape of coke, enlarged pore size, and decreased pore density. Though there is much research about the effects of temperature on coke properties and structure, the relationship between coke properties like coke strength and structure is still unclear. In addition, quantitative analysis of these indicators is still lacking. Degradation priorities and interactions between different properties have not been investigated.

In this study, coke samples obtained by blending were treated at different temperatures, and those samples were comprehensively characterized to reveal the evolution of coke properties and structure. Through particle size measurement, compressive strength testing, pore structure analysis, and XRD analysis, the effect of heat treatment temperature on the properties and structure of coke was found. Furthermore, the relationship between coke properties and structure during heat treatment is revealed.

Experiment

Sample Preparation

Four kinds of Chinese coal samples, coking coal (ZJ), 1/3 coking coal (1/3ZJ), fat coal (FM), and lean coal (SM), were selected for study, and their properties are given in Table 1. The particle size of the selected coal samples ranged from 0.5 to 3.0 mm. After dried at 110 °C for 2 h in a laboratory oven, the coal samples were mixed and homogenized in a laboratory mixer according to the composition of 30% ZJ, 40% 1/3ZJ, 20% FM, and 10% SM.

Table 1 Proximate and elemental analysis of four coal samples^a

Coal	Proximate analysis (wt%)				Elements analysis (wt%)				
	M _{ad}	A _d	V _d	FC _d	C _d	H _d	N _d	O _d	S _d
ZJ	2.30	7.52	20.57	71.90	81.35	4.58	1.45	4.73	0.37
1/3ZJ	2.34	7.12	31.95	60.94	78.30	5.25	0.94	8.24	0.15
FM	1.74	9.61	28.67	61.72	77.27	4.61	1.36	5.68	1.47
SM	1.70	13.92	15.78	70.30	76.44	3.89	1.25	4.50	1.06

^a M: moisture, V: volatile, FC: fixed carbon, A: ash, ad: air-dry basis, d: dry basis

Carbonization of Blending Coal

Carbonization of the prepared samples was carried out in a 2-kg electric furnace with a dimension of $\Phi 100 \text{ mm} \times 500 \text{ mm}$. The charge bulk density was 850 kg/m^3 (dry basis). The moisture was controlled at about 10%. On reaching $800 \text{ }^\circ\text{C}$ at the center of the charge, the reactor (containing the sample) was transferred to the isothermal zone of the electric furnace, and a heating rate of $10 \text{ }^\circ\text{C/min}$ was used to raise its temperature to $1050 \text{ }^\circ\text{C}$. In total, the sample is kept in the furnace for approximately 6 h. At the end of the carbonization, the reactor was removed from the furnace and cooled to a temperature below $100 \text{ }^\circ\text{C}$ in the air within 40 min.

Method of High-Temperature Heat Treatment to Coke

A 20 g sample of coke (+10–15 mm particle size range) was contained in a graphite crucible and then heat-treated through a specific heating system (Fig. 1) in a silicon molybdenum furnace (Fig. 2). The furnace was heated at a variable heating rate to the target temperature and kept at a constant temperature for 2 h under the N_2 (99.99%) atmosphere with a flow rate of 5 L/min . In order to simulate the temperature from lumpy zone to cohesive and dripping zone in a blast furnace, the target

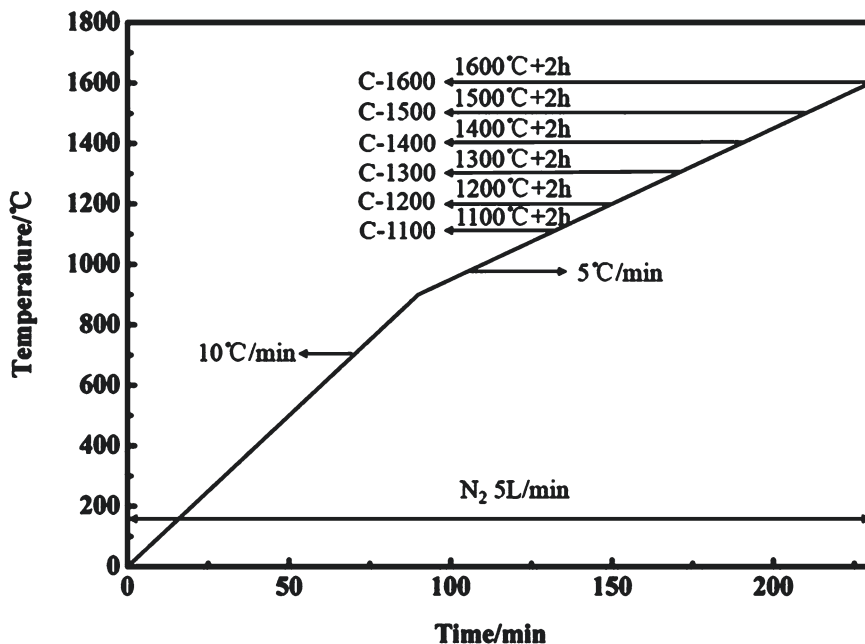


Fig. 1 Schematic diagram of the heat treatment system

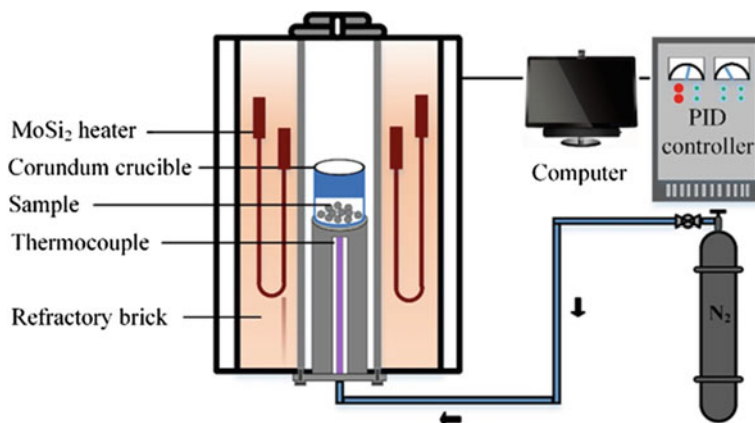


Fig. 2 Schematic diagram of Si-Mo furnace used to heat treatment of coke samples

temperature was adopted to 1100 °C, 1200 °C, 1300 °C, 1400 °C, 1500 °C, and 1600 °C, respectively. The weight losses of the sample were measured by weighing the samples before and after heat treatment. The prepared coke sample was named raw coke and other coke samples annealed at different temperatures were labeled as C-1100, C-1200, C-1300, C-1400, C-1500, and C-1600, respectively.

Particle Size Measurement

In order to simulate the destruction of the mechanical effect on coke in the blast furnace, the drum method proposed by Nippon Steel was used. The coke samples heated at different temperatures were taken out for an I-type drum and rotated (20 rotations/min for 100 rotations). Then, the treated samples were sieved by different screens (15, 10, 5, 1, 0.5, 0.074 mm) to obtain the particle size distribution. Each coke sample was sieved twice to ensure the accuracy of the data.

Compressive Strength of Coke

The compressive strength of coke was measured through tensile testing on a universal material testing machine (Tinisolsen CMT7000) at a loading rate of 1 mm/min. Cylindrical coke samples with a diameter of 10 and a height of 10 were prepared by wire-electrode cutting. A dynamic compression load was applied across the diameter of the coke cylinder until the fracture. As shown in Eq. (1), the tensile strength was calculated from the applied load at breakage and the dimensions of the cylinder sample.

$$C = \frac{4p}{\pi d^2} \quad (1)$$

where p is the largest load and d is the diameter of coke samples.

Pore Structure Analysis

The method for measuring the pore structure of coke refers to Xing et al. [26]. A Leica DM4 M microscope with Nikon digital camera was used to observe the pore structure of coke samples. Images were taken from 10 different lumps of samples to ensure the representativeness of the analysis. The variations in coke macro-pores were focused on. Therefore, a low power objective (magnification five times) was used. Image J, an image analysis software developed by NIH, was used to binarize the captured images. The porosity of the samples was calculated from the processed images.

XRD Analysis

Carbon structure has an essential influence on the properties of coke. An XRD analyzer (Escalab 250Xi powder diffractometer) with a monochromator and a copper $K\alpha$ X-ray source was used to evaluate carbon structure parameters. The accelerating voltage and current were 60 kV and 60 mA, respectively. In addition, the samples were scanned at 4°/min over an angular range of 10° to 90° with a scanning interval of 4°/step. The broad peak of 2θ ranging from 15° to 50° was fitted by three Gaussian peaks among 21°, 26°, and 43°, representing the γ -band, π -band(002 peak), and 100 peaks, respectively [27, 28]. From that, the resultant peak position, intensity, area, and full width at half maximum (FWHM) were determined. In this work, the inter-layer spacing (d_{002}) and the average stacking height (L_c) and lateral size (L_a) of the crystallite were calculated using the classical Scherer equations:

$$d_{002} = \lambda/2 \sin \theta_{002} \quad (2)$$

$$L_c = 0.89\lambda/\beta_{002} \cos \theta_{002} \quad (3)$$

$$L_a = 1.84\lambda/\beta_{100} \cos \theta_{100} \quad (4)$$

$$g = \left(\frac{3.8 - d_{(002)A}}{3.8 - 3.354} \right)^2 \quad (5)$$

where λ is the wavelength of the X-ray, β is the FWHM, and θ is the corresponding scattering angle.

Results and Discussion

Effect of Heat Treatment Temperature on Coke Properties

Effect of High Temperature on the Particle Size of a Coke

Fine materials in a BF (material <6 mm) impede gas flow which causes channeling and uneven heat transfer, reducing process efficiency [29–32]. Therefore, the number of fines in a BF should be strictly controlled. Fines can be generated in different regions of the BF, and the primary source of them is coke. Current understanding of coke degradation and fines generation mechanisms can be summarized as being due to: (1) mechanical stress and high-impact abrasion; (2) solution loss reaction; (3) thermo-mechanical impact; and (4) high-temperature chemical attack including recirculating alkalis.

In the process of coke degradation and fines generation, thermal effects play a crucial role. Coke under high temperature will lead to secondary carbonization, which causes lattice structure changes, resulting in coke breakage. Due to different temperatures in different parts of the blast furnace, the pulverization rate of coke will be significantly different as a function of carbonization.

The particle size distribution of heated coke samples after treatment in the I-type drum is shown in Fig. 3. It can be clearly seen that the amount of coke whose

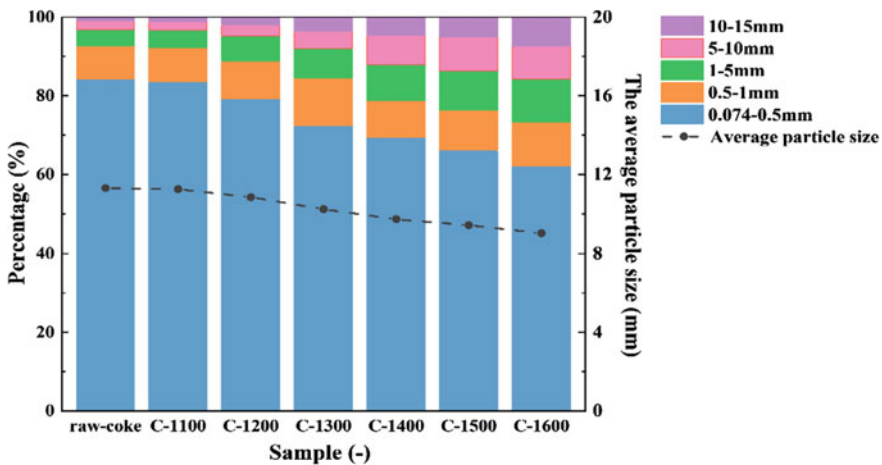


Fig. 3 Particle size distribution of coke after heat treatment at different temperatures

particle size is located in 0.074–0.5, 0.5–1, and 1–5 mm increase with the increase of temperature, while the amount of coke whose particle size is located in 10–15 mm decreases. No significant changes have been observed for the coke, whose particle size is located in 5–10 mm. These phenomena can prove that high temperatures can cause coke fines generation. The average coke particle diameter was calculated and compared with that of the coke sample by tuyere. The average coke particle diameter from blast furnace inlet to tuyere is approximately decreased by 50–60% [13, 14]. It can be seen that the particle diameter of coke decreased by 20.27% at most affected by thermal stress. In a blast furnace, the coke diameter degradation is also affected by varieties of factors like carbon melting and alkali metals.

Effect of High Temperature on the Compressive Strength of Coke

The compressive strength of coke can effectively characterize its supporting effect on the material column in the blast furnace. The tensile testing results of coke samples at different heat treatment temperatures are shown in Fig. 4. The p - d curve is used to reflect the macroscopic deformation process of different coke samples which is caused by pressure. The p - d curve shows that the initial deformation pressure increases rapidly, and the initial deformation pressure tends to decrease as the annealing temperature increases. Data in Fig. 4 showed that with the increase of temperature, the compressive strength decreases obviously. However, when the temperature is lower than 1200 °C, the annealing has no significant impact on the compressive strength. When the temperature is higher than 1300 °C, the compressive strength of coke decreases significantly. When the temperature rises to 1600 °C, the

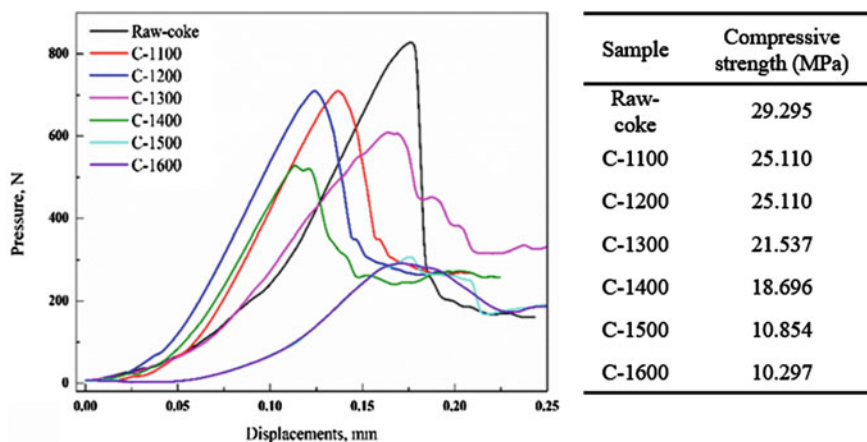


Fig. 4 The compressive strength and p - d curve of coke after different heat treatment temperatures

compressive strength decreases by about 65%, with a value of 10.297 MPa. Therefore, the influence of the decrease of compressive strength on coke should mainly occur in the lower part.

Effect of Heat Treatment Temperature on Coke Structure

Effect of High Temperature on the Pore Structure of Coke

Previous studies have proved that the optical microscope can be used to analyze the pore structure of coke. The analysis method put forward by Xing et al. [26] is used to analyze the pore size distribution, porosity, equivalent diameter, and perimeter of different coke samples.

Figure 5 shows the optical images of different samples. It can be observed that most pores in raw coke are micro-pore. The pore walls of raw coke seem stronger than the samples after annealing. Compared with raw coke, the pore size of the samples after annealing becomes bigger with the increase of temperature, indicating that the pore walls disappear at high temperature resulting in micro-pores interconnecting to form macro-pores. When the temperature increases up to 1400 °C or 1500 °C, cracks

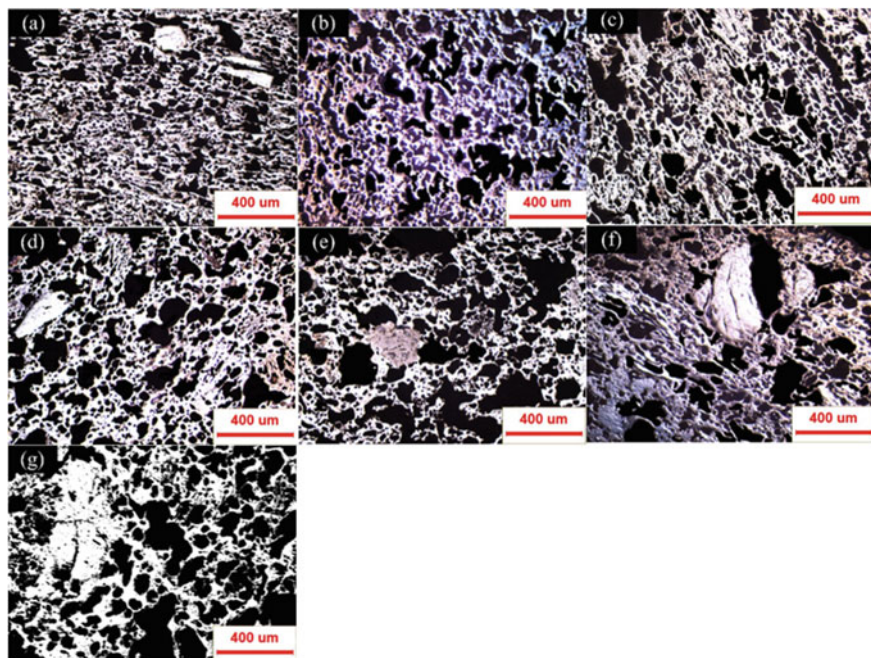
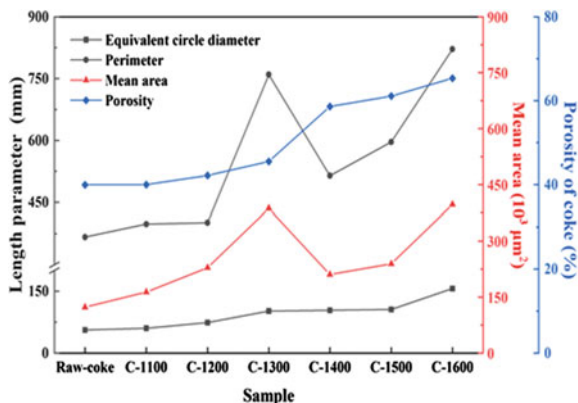


Fig. 5 Optical images of samples after different heat treatment temperatures. **a** raw coke; **b** C-1100; **c** C-1200; **d** C-1300; **e** C-1400; **f** C-1500; **g** C-1600

Fig. 6 Pore geometry parameters of coke after different heat treatment temperatures



can be clearly seen in Fig. 5f, g. Combined with the trend of compressive strength, the reason for the decrease of compressive strength is the increase of macro-pores and cracks.

To better understand, the effect of temperature on coke pore structure, porosity, pore mean area, perimeter, and equivalent circle on diameter of different samples was calculated automatically by Image J program, as shown in Fig. 6. The porosity increases with increasing temperature. Originally, the raw coke has the lowest porosity of 39.94%. From 1100 to 1300 °C, the porosity has minor increase. However, after 1300 °C, the porosity rises up rapidly to 65.31%, which is nearly twice of raw coke. Meanwhile, the equivalent circle diameter has a similar trend to the porosity, indicating that high temperature is causing the pore formation regularly. Pore structure has a strong influence on mechanical properties. The increase of coke pores and the thinning of the pore wall are bound to lead to a decline in compressive strength. The rapid decline in the compressive strength of between 1300 and 1600 °C also coincided with the degradation of pore structure.

Effect of High Temperature on the Crystalline Structure of Coke

The microcrystalline structure of coke can broadly reflect the state of the carbon matrix. X-ray diffraction was used to analyze the trend of the microcrystalline structure after heat treatment.

The XRD curves (Fig. 7) of different samples are similar. Two obvious diffraction characteristics, 002 and 100, exist in the XRD curves. With the increase of temperature, the peak type of peak 002 became sharper, and the acromion became narrower, indicating that the crystalline structure of coke changed after heat treatment. Furthermore, the graphitization degree (ρ) and characteristic parameters (d_{002} , L_c , L_a) were calculated to study the change of crystalline structure. The results in Fig. 8 clearly show that both L_c and L_a significantly increased with the increase of temperature, indicating that carbon structure becomes increasingly ordered and graphitized with

Fig. 7 X-ray diffraction spectra of coke after different heat treatment temperatures

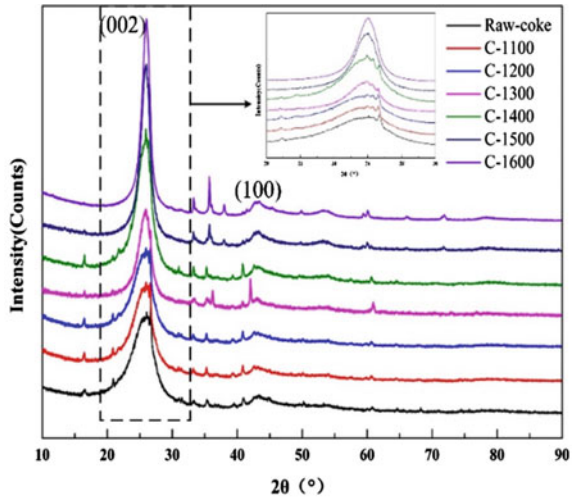
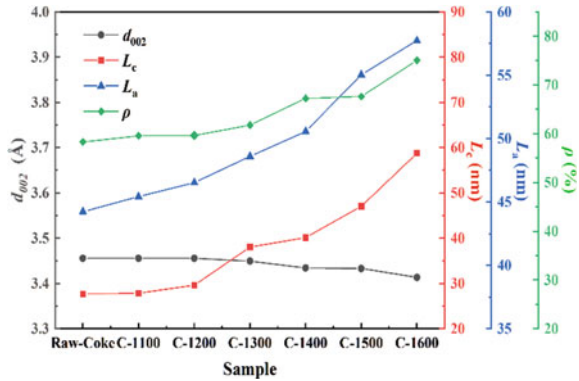


Fig. 8 Structural parameters obtained from curve-fitting XRD spectra



increasing temperature. Graphitization of coke at high temperatures begins at the coke surface. The same phenomenon is found in the pulverization of coke, indicating that the microcrystalline structure evolution mainly effect on the generation of coke fines. Moreover, the ρ value increased rapidly and reached 21.48% from 1300 to 1600 °C, which is very similar to the law of coke powder formation. It is more confirmed that the graphitization evolution of coke is the main reason for the formation of fine powder at high temperatures.

Conclusion

In this work, proximate analysis, universal material testing machine, and mechanical screening were used to analyze the change of coke properties (physicochemical properties, compressive strength, and granularity) and structure (microcrystalline structure, and pore structure) after heat treatment. In order to further explore the causes of these phenomena, an optical microscope and X-ray diffraction were used to analyze the relationship between properties and structure. The significant findings are as follows:

- (1) The compressive strength and particle size of coke will regularly decrease after heat treatment. Concurrently, high temperature can destroy the pore walls resulting in micro-pores interconnecting to form macro-pores. Furthermore, the graphitization degree of coke will increase, which means the carbon matrix will be more ordered.
- (2) The graphitization evolution of coke is the main reason for the formation of fine powder at high temperatures. The evolution of the coke pore structure is the main reason for the decrease of coke compressive strength.
- (3) The degradation of coke properties and structure is low below 1100 °C. From 1100 to 1300 °C, the compressive strength decreases a little, the porosity has a slight increase, and a certain amount of coke fines is generated. From 1300 to 1600 °C, the compressive strength decreases a lot, the porosity decreases rapidly, and a lot of coke fines are generated.

Acknowledgements This work was supported by the National Natural Science Foundation of China (Grant No. 52074055 and 52104323).

References

1. Gudenau HW, Senk D, Babich A et al (2004) Sustainable development in Iron and steel research, CO₂, and wastes. *ISIJ Int* 44(9):1469–1479
2. Wang W, Wang J, Xu RS et al (2017) Influence mechanism of zinc on the solution loss reaction of coke used in blast furnace. *Fuel Process Technol* 159:118–127
3. Longbottom RJ, Monaghan BJ, Chowdhury AA (eds) (2016) Effect of mineral matter on the reactivity of coke and its replication in a coke analogue. *ISIJ Int* 56(9):1553–1558
4. Yamaoka H, Suyama S, Nakano K (2003) Development of a size degradation model of coke particles at the drum test and inside the blast furnace. *ISIJ Int* 43(1):44–53
5. Díez MA, Alvarez R, Barriocanal C (2002) Coal for metallurgical coke production: predictions of coke quality and future requirements for cokemaking. *Int J Coal Geol* 50:389–412
6. Wang W (1995) Iron catalysed graphitisation in the blast furnace. *Carbon* 33(11):1525–1535
7. Gornostayev SS, Hrkki JJ (2007) Graphite crystals in blast furnace coke. *Carbon* 45(6):1145–1151
8. Gupta S, Ye Z, Kim B (eds) (2013) Coke graphitization and degradation across the tuyere regions in a blast furnace. *Fuel* 113:77–85

9. Kawakami M, Kanba H, Sato K (eds) (2006) Characterization of thermal annealing effects on the evolution of coke carbon structure using raman spectroscopy and x-ray diffraction. *ISIJ Int* 46(8):1165–1170
10. Shen F, Gupta S, Liu Y (eds) (2013) Effect of reaction conditions on coke tumbling strength, carbon structure and mineralogy. *Fuel* 111: 223–228
11. Gornostayev SS, Harkki JJ (2006) Mechanism of physical transformations of mineral matter in the blast furnace coke with reference to its reactivity and strength. *Energy Fuels* 20(6):2632–2635
12. Li KJ, Zhang JL, Sun MM (eds) (2018) Existence state and structures of extracted coke and accompanied samples from tuyere zone of a large-scale blast furnace. *Fuel* 225:299–310
13. Grigore M, Sakurovs R, French D (eds) (2006) Influence of mineral matter on coke reactivity with carbon dioxide. *ISIJ Int* 46(4):503–512
14. Li K, Zhang J, Barai M (eds) (2015) Influence of alkaline (Na, K) vapors on carbon and mineral behavior in blast furnace cokes. *Fuel* 145:202–213
15. Aizawa S, Uebo K, Yoshida S (2010) Mechanism of fine coke generation under drum test. *Tetsu to Hagane* 95(5):337–343
16. Tang HQ, Liu SH, Rong T (2019) Preparation of high-carbon metallic briquette for blast furnace application. *ISIJ Int* 59(1):22–30
17. Chen Z.Y, Zeilstra C, Vanderstel J (eds) (2020) Thermal decomposition reaction kinetics of hematite ore. *ISIJ Int* 60(1):65–72
18. Cheng A (2002) Coke quality requirements for blast furnace. Part V. *Fuel Energy Abstr* 43(4):239–240
19. Qiu SX, Zhang SF, Zhu RJ (eds) (2018) Influence of TiO₂ addition on the structure and metallurgical properties of coke. *Int J Coal Prep Util* 3(1):1–7
20. Hideyuki Y, Shinichi S, Kaoru N (2003) Development of a size degradation model of coke particles at the drum test and inside the blast furnace. *ISIJ Int* 43(1):44–53
21. Grant MGK, Chaklader ACD, Price JT (1991) Factors affecting the strength of blast-furnace coke. *Fuel* 70(2):181–188
22. Zhang SF, Peng HJ, Zhang X (eds) (2015) Structure characterization and metallurgical properties of the chars formed by devolatilization of lump coals. *Fuel Process Technol* 129:174–182
23. Haapakangas J, Uusitalo J, Mattila O (eds) (2013) A method for evaluating coke hot strength. *Steel Res Int* 84(1):65–71
24. Hilding T, Gupta S, Sahajwalla V, Bjoerkman B (eds) (2005) Degradation behaviour of a high CSR coke in an experimental blast furnace: effect of carbon structure and alkali reactions. *ISIJ Int* 45(7):1041–1050
25. Xing X, Zhang G, Mark Dell' Amico (eds) (2013) Effect of annealing on properties of carbonaceous materials. Part ii: porosity and pore geometry. *Metall Mater Trans B-Process Metall Mater Process Sci* 44(4):862–869
26. Xing X, Zhang G, Dell' Amico M (eds) (2013) Effect of annealing on properties of carbonaceous materials. Part iii: macro and microstrengths. *Metall Mater Trans B-Process Metall Mater Process Sci* 44(4):870–877
27. Qiu SX, Zhang SF, Suo GS (eds) (2020) Effects of Fe₂O₃ addition on the thermoplasticity and structure of coking coal matrix during thermoplastic stage of pyrolysis. *Fuel* 206:1–9
28. Iwanaga Y (1991) Disintegration of coke by mechanical impact under gasification reaction. *ISIJ Int* 31(1):32–39
29. Nogami H, Pintowantoro S, Yagi JI (2005) Numerical analysis on behavior of unburned char and fine coke in blast furnace. *ISIJ Int* 45(10):1489–1495
30. Fu LC, Bi XG, Xiong W, Zhou GF (2008) Observation and analysis of fluidisation and flooding phenomena in lower blast furnace by model experiments. *Ironman. Steelmak* 35(6):430–435
31. Hutny WP, Lee GK, Price JT (1991) Fundamentals of coal combustion during injection into a blast-furnace. *Prog. Energ. Combust* 17(4):373–395
32. Xing X, Rogers H, Zhang G (eds) (2016) Coke degradation under simulated blast furnace conditions. *ISIJ Int* 56(5):786–793

Coking Coal Macromolecular Structural Characteristic and Its Correlations with the Compressive Strength of CaO-Containing Carbon Pellets



Xiaomin You, Xuefeng She, Jingsong Wang, and Qingguo Xue

Abstract CaO-containing carbon pellets (CCCP) preparing from well-mixed coking coal (CC) and calcium oxide (CaO) were roasted at different pyrolysis temperatures (400–800 °C). To investigate the effect of roasted temperature on the compressive strength of CCCP, Raman spectroscopy and X-ray diffraction were adopted to characterized macromolecular structure changes of CC in CCCP. The results showed that the compressive strength of CCCP increased with the increase in temperature. The compressive strength of CCCP was negatively correlated with the peak intensity ratio (I_{D1}/I_G) value and positively correlated with the peak intensity ratio (I_G/I_{All}) value. A linear relationship between the compressive strength of CCCP and the carbon layer spacing of CC was established. As the temperature increased, the structural defects and imperfections of carbon crystallites were gradually decreased. The aromatic carbon layers were more closely packed, which formed high-order CC. As a result, the compressive strength of CCCP increased.

Keywords CaO-containing carbon pellets · Coal macromolecular · Raman spectroscopy · X-ray diffraction · Compressive strength

Introduction

China is the largest producer and consumer of calcium carbide. The annual production of calcium carbide in China increased in the past decade to approximately 42 million tons in 2018. Currently, the electrothermal calcium carbide manufacturing process is used in China as the primary process to produce acetylene [1]. The electrothermal calcium carbide manufacturing process is characterized by poor kinetic conditions because of the limited contact area between bulky CaO and char, resulting in a higher reaction temperature (2000–2200 °C) and high energy consumption (approximately 3000–3500 kW·h/t to obtain 80% calcium carbide yield) [2–6]. The use of new raw

X. You · X. She (✉) · J. Wang · Q. Xue
State Key Laboratory of Advanced Metallurgy, University of Science and Technology Beijing,
Beijing 100083, China
e-mail: shexuefeng@ustb.edu.cn

© The Minerals, Metals & Materials Society 2022
M. Zhang et al. (eds.), *Characterization of Minerals, Metals, and Materials 2022*,
The Minerals, Metals & Materials Series,
https://doi.org/10.1007/978-3-030-92373-0_17

materials and processes will be essential for calcium carbide production, considering processes that require lower energy consumption and material efficiency during this process.

The complete contact of the two materials will improve the mass transfer rate of CaO and reduce reaction temperature. Several studies have addressed calcium carbide formation from pellets obtained through well-mixed powder feeds [7–10]. Yin et al. [11] proposed a new process of calcium carbide production which included a two-step process. Firstly, the CaO-containing carbon pellets (CCCP) by using mixed lime powder and coal powder were pyrolyzed in a prepyrolysis furnace. Then the CCCP was placed in the arc furnace for the production of calcium carbide. In a two-step calcium carbide production process, the pyrolysis process of CCCP determined the compressive strength of CCCP. Some studies have shown that the pyrolysis temperature and the coal content have significant impacts on the thermal strength of the calcium coke [12]. Some studies think that the change in CCCP compressive strength during the preheating pyrolysis stage could be attributed to the structural changes in the CC itself [13]. However, only a few pieces of literature have been found regarding the effect of coal structures on CCCP compressive strength. Therefore, establishing a relationship between macromolecular structures of coal and CCCP compressive strength is necessary.

Coal is an organic, porous, and heterogeneous sedimentary rock containing complex physical and chemical structures. Thus, the fundamental understanding of the physical, chemical, and structural properties of coal remains paramount and challenging to coal researchers [14–16]. Fortunately, Raman spectroscopy [17, 18], X-ray diffraction (XRD) [19, 20], Fourier transform infrared spectroscopy (FTIR) [21, 22], and solid-state ^{13}C nuclear magnetic [23, 24] have been employed for quantitative evaluation of macromolecular structures of coal with varying degrees of success [25, 26]. Raman spectroscopy can explore not only the functional groups but also the carbon skeleton in coals since its broad determination range. It can also offer a higher resolution for coal macromolecular structure and is more sensitive to the change of coal structure than other analytical techniques [27, 28]. This enables a better understanding of coal macromolecular structure. XRD is basically a non-destructive and one of the most useful techniques to study the crystal arrangement. This technique has been adopted extensively to analyze the physical structure of amorphous substances [29]. The XRD can not only retrieve half of the coal but also calculate the geometric parameters of the basic structural unit of the carbon atom in coal [30].

In this study, CaO-containing carbon pellets (CCCP) preparing from well-mixed coking coal (CC) and calcium oxide (CaO) were roasted at different pyrolysis temperatures (400–800 °C). The compressive strength change of roasted CCCP at different pyrolysis temperatures was analyzed. Raman spectroscopy and X-ray diffraction were adopted to characterized macromolecular structure changes of CC in CCCP. The relationship between macromolecular structure changes and compressive strength was established.

Table 1 Results of proximate and elemental analysis of coking coal wt%

Proximate analysis					Ultimate analysis				
Coking coal	M _{ad}	A _{ad}	V _{ad}	FC _{ad}	C _{ad}	H _{ad}	O _{diff}	N _{ad}	S _{ad}
	9.85	8.19	17.18	64.78	70.40	3.69	4.07	1.09	0.78

Note Ad-air dry basis; diff: difference; FC-fix carbon; A-ash; V-volatile matter; M-moisture

Table 2 Chemical composition of ash from coking coal wt%

Material	CaO	SiO ₂	Al ₂ O ₃	TiO ₂	Fe ₂ O ₃	P ₂ O ₅	Other
Ash	1.01	51.4	38.6	1.23	2.81	0.69	4.26

Sample Preparation and Experiments

Materials

Analytical grade CaO (AR, > 9.0%) and CC were collected from a Chinese steel plant. They were further dried at 80 °C for 6 h under vacuum and placed in sealed bags. The chemical composition of the CC is presented in Table 1. The ash obtained from coal oxidation was characterized by X-ray fluorescence (AXIOS, Holland), as shown in Table 2.

CCCP Preparation and Roasting of CCCP

The coking coal powder (80 μm) was homogeneously mixed with the CaO powder (80 μm) at a C/Ca molar ratio of 3.5:1. The mixtures were placed in a stainless-steel mold and pressed uniaxially using an embedding sample machine (XQ-5, China) under a pressure of 20 MPa for 2 min. Thus, 3.5 g of the CCCP sample with a diameter of 20 mm was prepared.

As shown in Fig. 1, a rapid heating tube furnace with controllable cooling speed was used to heat CCCP. The tube of the furnace is a rigid jade tube with a diameter of 42 cm, and the thermostatic region is effective in 10 cm. Before conducting the experiments, the temperature was increased to the target temperature (400, 500, 600, 700, or 800 °C) at a rate of 10 °C/min. The CCCP samples were placed in a corundum crucible. Following this, the corundum crucible was placed in a constant temperature zone of the furnace and maintained in an Ar atmosphere for 30 min. After roasting, the sample was cooled to 100 °C at a rate of 22 °C/min and kept at that temperature for 5 min under an Ar atmosphere. The pellets were removed from the furnace at 20 °C. The CCCP can be divided into five categories based on the roasting temperature (400–800 °C). The results of the elemental analyses of the roasted CCCPs are shown in Table 3.

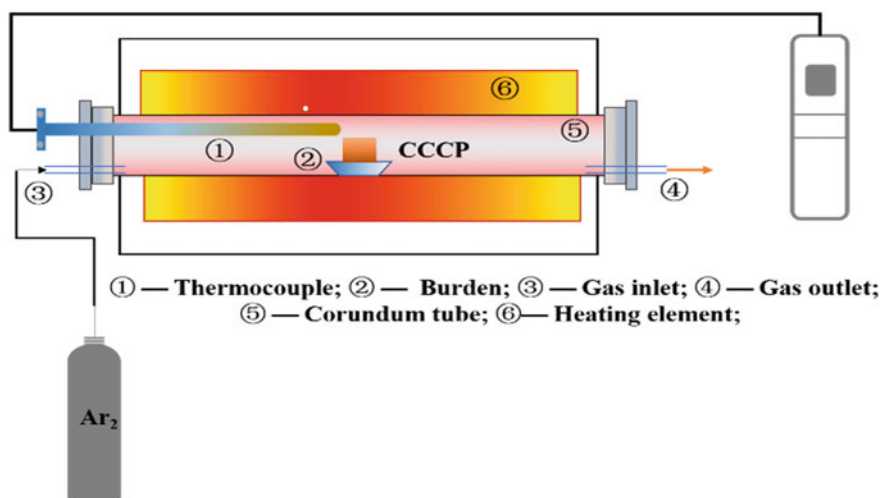


Fig. 1 Schematic diagram of the CCCP pyrolysis preheating device

Table 3 Results of the elemental analysis of CCCP at different pyrolysis temperatures

Sample	Ultimate analysis (ad) /wt%					Atomic ratio	
	N	C	S	H	O _{diff}	H/C	O/C
CCCP-400 °C	0.89	40.39	0.22	2.71	5.66	0.40	0.10
CCCP-500 °C	0.81	36.35	0.24	2.11	7.33	0.34	0.15
CCCP-600 °C	0.80	36.01	0.19	1.86	8.22	0.30	0.17
CCCP-700 °C	0.74	35.83	0.09	1.62	9.07	0.27	0.19
CCCP-800 °C	0.79	36.84	0.11	1.25	8.84	0.20	0.18

Note: ad-air dry basis; diff: difference

Measurement of the CCCP Strength Index

The compressive strength of roasted CCCP at different temperatures is tested in accordance with MT/T748-2004 [11]. The compressive strength of five groups of roasted CCCP was measured using a pressure test machine. Each group selected 12 pellets for measurement and calculated the average value after discarding the maximum and minimum values of the data group.

Characterization Experiments of CCCP

Raman spectroscopy was used to analyze the carbon structural changes in the CC of CCCP. The experiments were performed on a LabRAM HR Raman spectrometer (Horiba, Japan) with an irradiation power of 1 mW and a measurement wavelength of 532 nm in the scanning range of 800–1800 cm^{-1} . X-ray diffraction (XRD; M21XVHF22, MAC Science Co. Ltd., Japan) was used to detect the phase composition of the CCCP and the variations in the carbon structure of the CC in CCCP. The diffractometer employed Cu $K\alpha$ radiation, and the measurements were conducted in the 2θ range of 10–90° with the step scan mode.

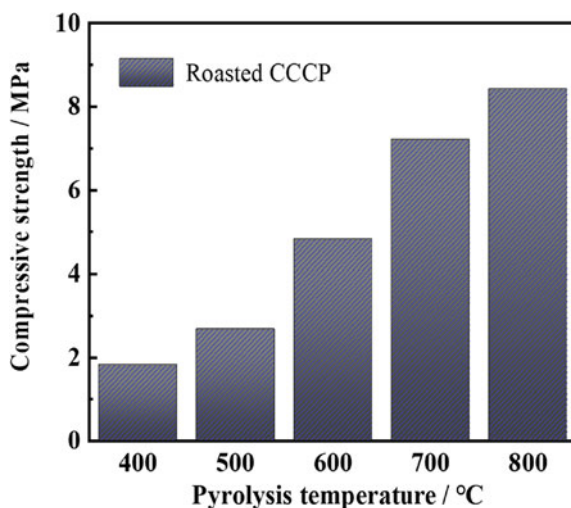
Results and Discussion

The Change of Compressive Strength of Roasted CCCP at Different Pyrolysis Temperatures

To avoid disintegration in calcium carbide furnace, the severe cold and thermal strengths of roasted CCCP are needed to ensure the CO and other gases travel through the bed material evenly [10]. Therefore, it is of great significance to study the strength change of roasted CCCP during the preheating pyrolysis process. Prior to compressive strength evaluation, the CCCP samples were roasted at different temperatures (400, 500, 600, 700, or 800 °C) for 30 min.

The compressive strength change of CCCP at different roasting temperatures is shown in Fig. 2. As the pyrolysis temperature increased, the compressive strength

Fig. 2 Compressive strengths of the CCCP samples roasted at different temperatures



values of roasted CCCP were increased. When the pyrolysis temperature reached 800 °C, the compressive strength of the roasted CCCP reached a maximum of 8.42 MPa. During the preheating pyrolysis process, with the temperature increase, CC gradually undergoes pyrolysis reaction to form colloids and solidifies and shrinks into semi-coke. The process is accompanied by a change of coal macromolecular structures. It is inferred that more organized coal structures are formed with the increase of temperature, bringing about the addition of CCCP compressive strength, which will be inspected next.

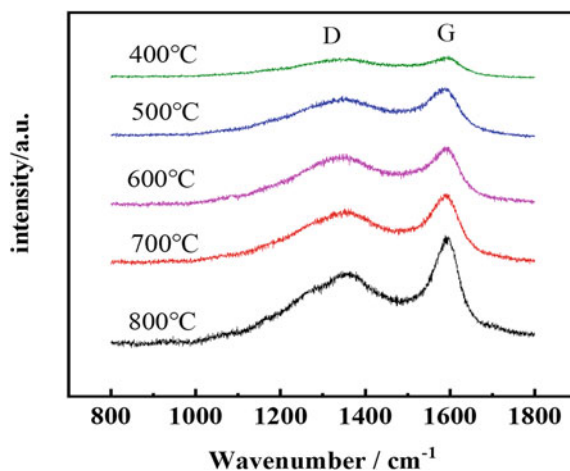
The Macromolecular Structure Variation of CC in CCCP at Different Pyrolysis Temperatures

Raman spectroscopy and X-ray diffraction were adopted to characterized macromolecular structure changes of CC in CCCP at different pyrolysis temperatures. We analyzed the changes of Raman and XRD structural parameters of CC in CCCP at different pyrolysis temperatures, respectively.

Raman Characteristics of CC in CCCP

Figure 3 shows the Raman spectral curves of studied samples. Clearly, two obvious peaks at 1350 and 1590 cm^{-1} are found, corresponding to the D band and G band, respectively. D band results from the disordered structure or in-plane defects between the basic structural units in coal, and the G band is related to the breathing of aromatic rings for amorphous carbonaceous materials [31]. However, the only use of D and G bands from Raman spectra can lead to the loss of information about coal

Fig. 3 Raman spectra of CC in CCCP



macrostructure due to the overlapped area between these two bands [32]. Therefore, the curve fitting was adopted for the decomposition of Raman spectra. The detailed instructions about the curve-fitting procedure are described in the literature 800–2000 cm^{-1} (first-order region) using the Peak Fitting Module of Origin Pro 9.1.0 software (OriginLab Corporation, USA). The goodness of fit is measured by the maximum values of R_2 . After the linear baseline subtraction was performed, a combination of four Lorentzian/Gaussian bands, with D_1 , D_2 , D_3 , D_4 , G at around 1350, 1720, 1450–1540, 1200–1350, 1580 cm^{-1} , respectively, were interpreted for this curve-fitting procedure, shown in Fig. 4. The detailed band assignment for Raman spectra in coal is displayed in Table 4.

In general, the ratio of the D_1 peak intensity (I_{D_1}) to the G peak intensity (I_G), and the ratio of the G peak intensity (I_G) to all peak intensities (I_{all}) were chosen because they are sensitive to coal maturation [33]. Thus, these two Raman parameters were analyzed in this study. I_{D_1}/I_G represents the order degree or imperfections of aromatic macromolecular in coal, and its decrease of I_{D_1}/I_G means the growth of aromatic rings. I_G/I_{all} represents the order degree of aromatic macromolecular in coal, and its increase also means the growth of aromatic rings.

The structural parameters of CC in the CCCP samples are shown in Table 5. As the temperature increased, the values of I_{D_1}/I_G for the coal in CCCP gradually decreased, which indicated that the proportion of the D band representative of structural defects and the G band representing the ordered structure decreased as the temperature increases. However, the values of I_G/I_{all} for the CC in CCCP significantly increased when the roasting temperature increased. This revealed that an increase in the proportion of ordered structure as the roasting temperature increased.

Therefore, it can be concluded that the different defects and imperfections in the carbon crystallite structures generally decrease, and the highly ordered structure is produced as the temperature increases.

XRD Characteristics of CC in CCCP

In order to extract the structural parameters of the CC characteristic (002) peak, we select a map of 16–33° in XRD to make a curve fitting. The Gaussian fitting method in the Origin software was used to fit the XRD pattern, and the results of curve fitting are as shown in Fig. 5. The spectra of XRD were smoothed firstly, and then the background was subtracted, fitted to two Gaussian peaks named γ -band between 20 and 22° and band (002) between 24 and 26°. Diffraction outlines designate an obvious asymmetric band (002) prevalence around that suggests the presence of a second (γ) band towards the left. In many other studies, the γ -band was reported and was assigned to the existence of a saturated structure like an aliphatic side chain, which is adhered with a border of coal crystallites [34]. The band (002) was attributed to the aromatic ring layers spacing. The sharp peaks represent minerals.

Some of the structural parameters used to characterize the CC include layer spacing (d_{002} , nm), stack height (L_c , nm). The layer spacing can be calculated using the Bragg equation and the stack height can be calculated by the half-width of the

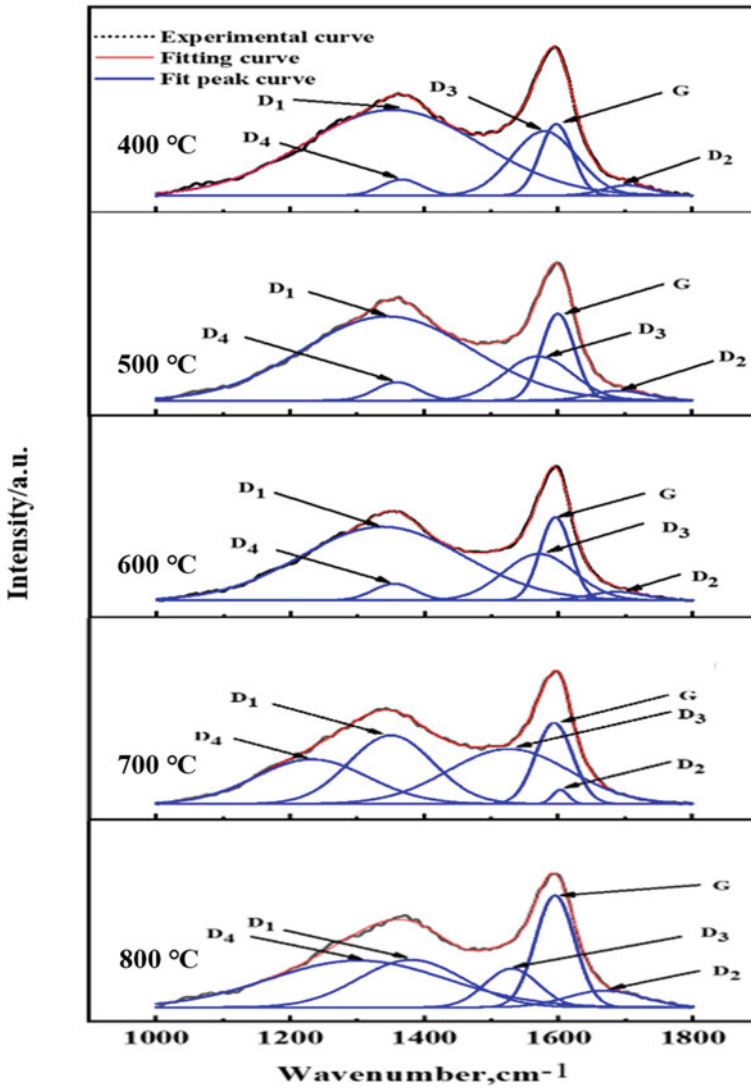


Fig. 4 Curve fitting of Raman spectrum for CC in CCCP

band (002) [35], respectively. The formulas for calculating the structural parameters are as follows:

$$d_{002} = \frac{\lambda}{2\sin\theta_{002}} \quad (1)$$

$$L_c = \frac{0.89\lambda}{B\cos\theta_{002}} \quad (2)$$

Table 4 Summary of band/peak assignment in coals

Band name	Band position, cm ⁻¹	Vibration mode	Bond type
G	1580	E _{2g} symmetry stretching vibration in the aromatic layers of graphite crystalline	sp ²
D ₁	1350	A _{1g} symmetry graphitic lattice vibration	sp ²
D ₂	1720	Disordered graphite lattice structure	sp ²
D ₃	1450–1540	Semicircle breathing of aromatic rings; amorphous carbon structure	sp ² , sp ³
D ₄	1200–1350	Aryl–alkyl ether; para-aromatics	sp ² , sp ³

Table 5 Structural parameters derived from Raman of coals in CCCP

Temperature (°C)	I _{D1} /I _G	I _G /I _{all}
400	1.20	0.28
500	0.97	0.30
600	0.69	0.35
700	0.50	0.36
800	0.42	0.42

where λ (nm) is the wavelength of the X-ray used, θ (°) is the corresponding scattering angle, and B (°) is the FWHM of the 002 peak.

The peak position (2θ), interlayer space (d_{002}), and stacking height (L_C) of coal samples are outlined in Table 6. As can be seen from Table 6, the positions of the (002) peaks of the five investigated pulverized coals were substantially similar. The layer spacings of the crystals of the investigated five coals were 0.36 nm; the difference is not large. Compared with the layer spacing of pure graphite crystals of 0.3354 nm, the larger spacing of the pulverized coals crystals and the more relatively open is their crystal structures. Moreover, the L_C values gradually increased as the roasting temperature increased. This result is consistent with literature results on the structural evolution of char using other techniques [36, 37], which means that coal structure is more ordered with an increased temperature.

Relationship Between Macromolecular Structure and Compressive Strength

It is generally accepted that the compressive strength of CCCP is determined by the properties of the macromolecular structure of cc in CCCP to a large extent [12, 13]. Therefore, we established a relationship between macromolecular structure and compressive strength.

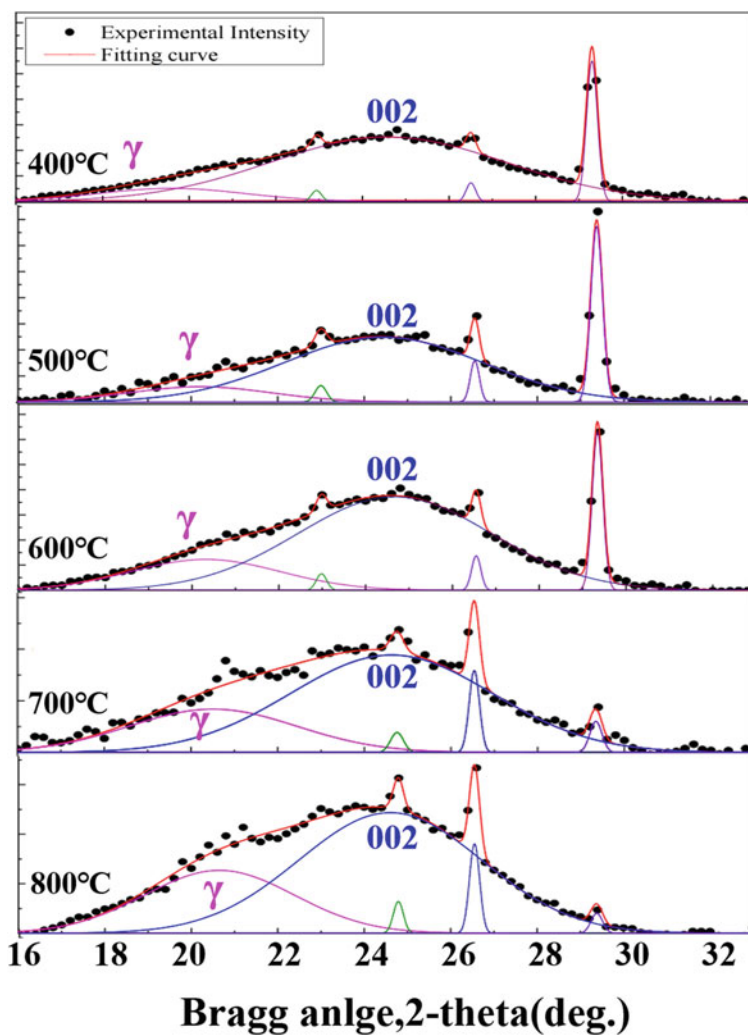


Fig. 5 Curve fitting of XRD for CC in CCCP

Table 6 Structural parameters of coal-derived from the XRD patterns of the CC in CCCP

Temperature/ $^{\circ}\text{C}$	$2\theta_{002}/(^{\circ})$	d_{002}/nm	L_c/nm
400	24.99	0.36	1.55
500	24.88	0.36	1.61
600	24.78	0.36	1.75
700	24.60	0.36	1.87
800	24.51	0.36	1.96

Relationship Between Raman Structural Parameters and Compressive Strength

The relationship between Raman structural parameters and the compressive strength is presented in Fig. 6. From Fig. 6a, the compressive strength and I_D/I_G display a power functional relation. The compressive strength values decline with increasing I_D/I_G . This means that the compressive strength of roasted CCCP was negatively correlated with the peak intensity ratio (I_D/I_G) value.

A power functional relationship can be observed between the compressive strength and I_G/I_{all} , as shown in Fig. 7b. However, the compressive strength values increase with increasing I_G/I_{all} . This means that the compressive strength of roasted CCCP was negatively correlated with the peak intensity ratio (I_G/I_{all}) value.

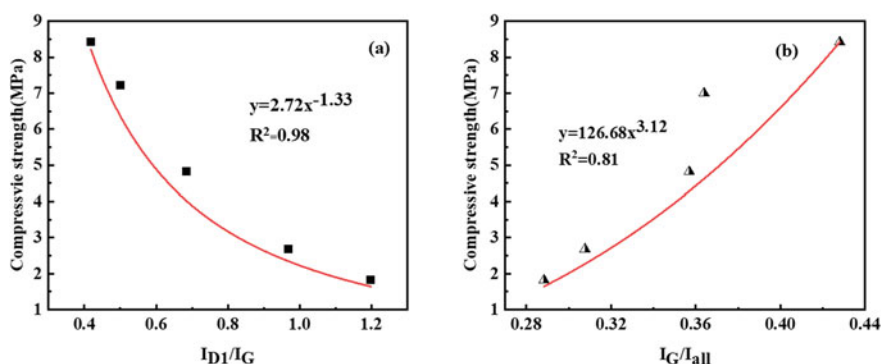
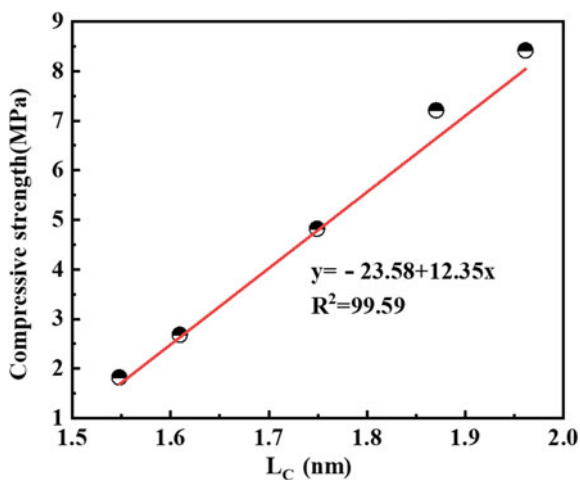


Fig. 6 Relationship between compressive strength and Raman structural parameters: **a** I_D/I_G ; **b** I_G/I_{all}

Fig. 7 Relationship between compressive strength and XRD structural parameters (L_C)



In the process of pyrolysis, as pyrolysis temperature rises a rapid change occurs within coal macromolecular. The decrease of I_D/I_G and the increase of I_G/I_{all} mean that the noncrystalline structure in coal gradually becomes structurally stable and ordered with the decrease of structural defects after condensation polymerization. The constant increase in the degree of crystallization enables CCCP to contain higher compressive strength, which is also supported by a previous study [13].

Relationship Between XRD Structural Parameter and Compressive Strength

A linear relationship can be observed between the compressive strength and the stacking height (L_C), as shown in Fig. 7, where the best-fit line was $y = 12.35x - 23.58$ ($R_2 = 0.99$). The compressive strength values increase linearly with increasing L_C value.

In the process of pyrolysis, the aromatic carbon arrangement of coal macromolecular is accompanied by the change of the stacking height (L_C), further affecting compressive strength. As mentioned earlier, a temperature increase resulted in the increase of L_C values. According to graphitization theory, crystalline carbon with a large L_C value is generally considered an ordered structure [35]. The increase of graphitization degree can trigger the compaction of coal macromolecular, and the aromatic carbon layers are more closely packed, which improves the degradation resistance of CCCP to external forces [38]. As a result, the compressive strength of CCCP increased. According to some researchers [38, 39], the L_C of the microcrystalline coke structure is linearly related to the cold strength of coke. Similarly, the coal stacking height (L_C) of CC could be employed to predict the compressive strength of CCCP in the pyrolysis process.

Conclusions

To investigate the effect of roasted temperature on the compressive strength of CCCP, macromolecular structural characteristics including chemical and physical structures were studied for coking coal in CCCP. The Raman structural parameters were obtained from the curve-fitted spectrum. The XRD structural parameters were obtained from the curve-fitted spectrum and formula calculation. The effect of coking coal macromolecular structure on CCCP compressive strength was also analyzed, and the following conclusions are obtained:

1. The compressive strength of roasting CCCP increased with the increase of temperature during the 400–800 °C range.
2. On increasing the roasting temperature, the I_{D1}/I_G values gradually decreased and the I_G/I_{all} values increased. The various structural defects and imperfections

- in the carbon crystallites were gradually eliminated and more organized char structures were formed.
3. The L_C values gradually increased as the roasting temperature increased, which means that the coal structure was more ordered.
 4. The compressive strength of CCCP was negatively correlated with the peak intensity ratio (I_{D1}/I_G) value and positively correlated with the peak intensity ratio (I_G/I_{All}) value.
 5. A linear relationship between the compressive strength of the CCCP and the L_C of CC was obtained, as expressed by the linear equation $y = 12.35x - 23.58$ ($R^2 = 0.99$). The compressive strength values increase linearly with increasing L_C value.

Acknowledgements This work was financially supported by the National Key R&D Program of China (No. 2018YFB0605900).

References

1. Mi Y, Zheng DX, Guo J, Chen XH, Jin P (2014) Assessment of energy use and carbon footprint for low-rank coal-based oxygen-thermal and electro-thermal calcium carbide manufacturing processes. *Fuel Process Technol* 119:305
2. Xin CF, Qian XR (1994) Reviews on technical routes for chemicals production from carbide acetylene. *Prog Chem* 6(1):62
3. Li GD, Liu QY, Liu ZY (2013) Kinetic behaviors of CaC_2 production from coke and CaO. *Ind Eng Chem Res* 52(16):5587
4. Mu JJ, Hard RA (1987) A rotary kiln process for making calcium carbide. *Ind Eng Chem Res* 26(10):2063
5. Zhang JQ, Wang ZS, Li T, Wang Z, Zhang S, Zhong M, Liu YE, Gong XZ (2019) Preparation of CaO-containing carbon pellet from recycling of carbide slag: effects of temperature and H_3PO_4 . *Waste Manage* 84:64
6. Xie KC, Li WY, Zhao W (2010) Coal chemical industry and its sustainable development in China. *Energy* 35(11):4349–4355
7. Zhang S, Gong XZ, Wang Z, Cao JW, Guo ZC (2014) Preparation of block CaO from carbide slag and its compressive strength improved by H_3PO_4 . *Int J Miner Process* 129:6–11
8. Wang RX, Liu ZY, Ji LM, Guo XJ, Lin X, Wu JF, Liu QY (2016) Reaction kinetics of CaC_2 formation from powder and compressed feeds. *Front Chem Sci Eng* 10(4):517
9. Li ZK, Liu ZY, Wang RX, Guo XJ, Liu QY (2018) Conversion of bio-char to CaC_2 at low temperatures-morphology and kinetics. *Chem Eng Sci* 192:516–525
10. Xu Q, Li YS, Deng SP, He YL, Li L, Yu HJ (2019) Modeling of multiprocess behavior for feedstock-mixed porous pellet: Heat and mass transfer, chemical reaction, and phase change. *ACS Sustain Chem Eng* 7(14):12510
11. Yin SW, Wang HY, Wang L, Liu CP, Tong LG (2021) Influencing factors and evaluation system for Carbon-Calcium pellet performance in a pyrolysis furnace. *Energy* 214:118991
12. Gong XZ, Zhang JQ, Wang Z, Wang D, Liu JH, Jing XD, Qian GY, Wang C (2021) Development of calcium coke for CaC_2 production using calcium carbide slag and coking coal. *Int J Miner Metall Mater* 28(1):76–87
13. You XM, She XF, Wang JS, Xue QG, Jiang ZY (2021) Preparation of CaO-containing carbon pellets from coking coal and calcium oxide: effects of temperature, pore distribution and carbon

- structure on compressive strength in pyrolysis furnace. *Int J Miner Metall Mater* 28(7):1153–1163
14. Gupta R (2007) Advanced coal characterization: a review. *Energy Fuels* 21(2):451–460
 15. Liu XF, Nie BS (2016) Fractal characteristics of coal samples utilizing image analysis and gas adsorption. *Fuel* 182:314–322
 16. Rybicki M, Marynowski L, Misz-Kennan M, Simoneit BRT (2016) Molecular tracers preserved in Lower Jurassic “Blanowice brown coals” from southern Poland at the onset of coalification: organic geochemical and petrological characteristics. *Org Geochem* 102:77–92
 17. Schmidt JS, Hinrichs R, Araujo CV (2017) Maturity estimation of phytoclasts in strew mounts by micro-Raman spectroscopy. *Int J Coal Geol* 173:1–8
 18. Mumm AS, İnan S (2016) Microscale organic maturity determination of graptolites using Raman spectroscopy. *Int J Coal Geol* 162:96–107
 19. Baysal M, Yürüm A, Yıldız B, Yürüm Y (2016) Structure of some western Anatolia coals investigated by FTIR, Raman, ¹³C solid state NMR spectroscopy and X-ray diffraction. *Int J Coal Geol* 163:166–176
 20. Wertz DL, Bissell M (1994) Relating the nonideal diffraction from the graphene layer stacking peak to the aliphatic carbon abundance in bituminous coals. *Energy Fuels* 8(3):613–617
 21. Giroux L, Charland JP, MacPhee JA (2006) Application of thermogravimetric Fourier transform infrared spectroscopy (TG–FTIR) to the analysis of oxygen functional groups in coal. *Energy Fuels* 20(5):1988–1996
 22. Zhang J, Zheng N, Wang J (2016) Two-stage hydrogasification of different rank coals with a focus on relationships between yields of products and coal properties or structures. *Appl Energy* 173:438–447
 23. Strydom CA, Bunt JR, Schobert HH, Raghoob M (2011) Changes to the organic functional groups of an inertinite rich medium rank bituminous coal during acid treatment processes. *Fuel Process Technol* 92(4):764–770
 24. Ouyang ZQ, Liu DM, Cai YD, Yao YB (2016) Fractal analysis on heterogeneity of pore-fractures in middle-high rank coals with NMR. *Energy Fuels* 30(7):5449–5458
 25. Wang X, Gai GS, Yang YF (2008) Preparation of natural microcrystalline graphite with high sphericity and narrow size distribution. *Powder Technol* 181(1):51–56
 26. Li Q, Lin B, Wang K, Zhao MZ, Ruan ML (2015) Surface properties of pulverized coal and its effects on coal mine methane adsorption behaviors under ambient conditions. *Powder Technol* 270:278–286
 27. Morga R (2011) Micro-Raman spectroscopy of carbonized semifusinite and fusinite. *Int J Coal Geol* 87(3–4):253–267
 28. Ferrari AC, Basko DM (2013) Raman spectroscopy as a versatile tool for studying the properties of graphene. *Nat Nanotechnol* 8(4):235–246
 29. Manoj B, Kunjomana AG (2012) Structural characterization of selected Indian coals by X-ray diffraction and spectroscopic techniques. *Trends Appl Sci Res* 7(6):434–444
 30. Wu D, Liu GJ, Sun RY, Xiang F (2013) Investigation of structural characteristics of thermally metamorphosed coal by FTIR spectroscopy and X-ray diffraction. *Energy Fuels* 27(10):5823–5830
 31. Potgieter-Vermaak S, Maledi N, Wagner N, Van Heerden JHP, Van Grieken R, Potgieter JH (2011) Raman spectroscopy for the analysis of coal: a review. *J Raman Spectrosc* 42(2):123–129
 32. Schito A, Romano C, Corrado S, Grigo D, Poe B (2017) Diagenetic thermal evolution of organic matter by Raman spectroscopy. *Org Geochem* 106:57–67
 33. Sheng CD (2007) Char structure characterised by Raman spectroscopy and its correlations with combustion reactivity. *Fuel* 86(15):2316–2324
 34. Ullah H, Chen BL, Shahab A, Naseem F, Rashid A, Lun L, Yousaf B, Khan S (2020) Influence of hydrothermal treatment on selenium emission-reduction and transformation from low-ranked coal. *J Clean Prod* 267: 122070
 35. Liu HY, Xu L, Jin Y, Fan BG, Qiao XL, Yang YX (2015) Effect of coal rank on structure and dielectric properties of chars. *Fuel* 153:249–256

36. Li XJ, Hayashi JI, Li CZ (2006) FT-Raman spectroscopic study of the evolution of char structure during the pyrolysis of a Victorian brown coal. *Fuel* 85(12–13):1700–1707
37. Shim HS, Hurt RH, Yang NYC (2000) A methodology for analysis of 002 lattice fringe images and its application to combustion-derived carbons. *Carbon* 38(1):29–45
38. Song TF, Zhang JL, Wang GW, Wang HY, Xu RS, Pang QH (2018) Influence mechanism of lignite and lignite semi-coke addition on drum strength of coke. *ISIJ Int* 58(2):253–258
39. Zhao J, Zuo HB, Wang GW, Wang JS, Xue QG (2020) Improving the coke property through adding HPC extracted from the mixture of low-rank coal and biomass. *Energy Fuels* 34(2):1802–1810

Part VI
Poster Session

An Investigation of the Relationship Between Raw Coal Caking Characteristics and Its Petrographic Properties



Yucen Kuang, Wei Ren, Lechi Zhang, and Shengfu Zhang

Abstract In industry, the coking characteristics of coal are mainly based on investigating the traditional coal chemical indicators, and the coal petrology theory can better reflect the intrinsic properties of coal, so it is necessary to explore these two aspects. The relationship between the caking parameters and maceral properties of coal was obtained by testing and analysis. The results show that the formation of colloids in coal is mainly related to the vitrinite composition and the Audibert–Arnu dilatation and caking index are closely related to the average maximum vitrinite reflectance. According to the softening temperature, the caking property of blending coal can be improved under the condition of ensuring the formation of colloids without temperature fault during the process. Since the parameters of macerals have an obvious effect on caking characteristics, it is of great significance to introduce the related indexes of macerals into the auxiliary production.

Keywords Plastic layer · Macerals of coal · Arnu–Audibert’s dilatometer · Caking index

Introduction

Coke has a pivotal role in the iron and steel industry, which is formed by the high-temperature carbonization of coal. With the development of extensive research by

Y. Kuang · L. Zhang · S. Zhang (✉)
College of Material Science and Engineering, Chongqing University, Chongqing 400044, China
e-mail: zhangsf@cqu.edu.cn

Y. Kuang
e-mail: yucenkuang@foxmail.com

S. Zhang
Chongqing Key Laboratory of Vanadium-Titanium Metallurgy & Advanced Materials, Chongqing University, Chongqing 400044, China

W. Ren
Technical Centre, Angang Steel Company Limited, Anshan, Liaoning 114021, China

scholars from all over the world, the coking mechanism can be summarized as the cohesive substance produced by coal during the heating process, which solidifies coal particles to form coke [1–5]. Therefore, the cohesive substance is a crucial factor in determining the quality of coke.

Testing the caking property, in terms of the production index reflected in practice, is one of the important links required by coking. Traditionally, corresponding indexes in coal chemistry that index of plastic layer, Arnu–Audibert’s dilatometer, and caking index have characterized caking and coking properties of coal. Conversely, studies related to the introduction of coal petrology into the coal coking process have gradually emerged in recent years. Many researchers generally believe that the existing coal chemical indexes are almost the external performance of coal’s internal properties. Briefly speaking, the corresponding factor of cohesion is related to the essential attribute of coal [6–8]. Consequently, it is beneficial to reveal external caking properties by mechanism level after clarifying the relationship between traditional coal chemical and petrology indexes.

According to many reported results, coal macerals parameters would have an impact on the caking process of coal to coke transformation. Andrew et al. [9] took advantage of attenuated total reflectance fourier transform infrared (ATR-FTIR) to study the pyrolysis process of coals with different vitrinite reflectance at 450–700 °C and found that binding substances were produced with pyrolysis and condensation at 350–500 °C. Furthermore, Qin et al. [10] investigated the source of cohesive substance by a solvent method. Two kinds of coal were extracted and back-extracted, the separated strong binding components derived from the same group even if coal metamorphism had a different degree. Soonho et al. [11] conducted micro-computed tomography (micro-CT) and ATR-FTIR research on properties of the plastic layer and concluded that with the increases content of vitrinite in coal, the total mass of plastic matter increases. To sum up, all the results investigated the coal’s caking component and the behavior of coal macerals components are closely related during the coking process, especially in the relationship of vitrinite quantity and reflectivity to the caking characteristics. Nevertheless, the specific relationship between the existing cohesiveness indexes and the characteristics of the coal itself has not yet been investigated.

Thus, the aim of this paper is to clarify the linkages between the coking indexes and coal macerals properties of different coal types by caking characteristics testing and maceral parameter analysis. We selected four typical coals to determine the index of plastic layer, Arnu–Audibert’s dilatometer and caking index, established relations between theoretical analysis of macerals and experimental information.

Experiment

The whole process of the experiment is shown in Fig. 1. The main steps are followed. Firstly, the basic properties were analyzed after the samples were prepared and then measured caking index. Finally, the relationship between the macerals parameters and the caking characteristics was constructed.

Coal Materials

Four types of on-site coal from a Chinese steel plant, labeled with coking coal (ZJ), 1/3 coking coal (1/3ZJ), fat coal (FM), and lean coal (SM). Samples preparation were carried out in GBT 474-2008 standard procedure. The proximate and ultimate analysis were tested by SJGFY-5000 proximate analyzer and Unicube-Elementar ultimate analyzer according to GBT 212-2008 and GBT 31391-2015 standard procedure respectively.

Coal Maceral Analysis

We analyzed the content of exinite (E), vitrinite (V), inertinite, and mineral matters. Especially the total amount of inertinite components (I) included the inertinite and the mineral group. The classification standards for coal maceral, micro-mineralization,

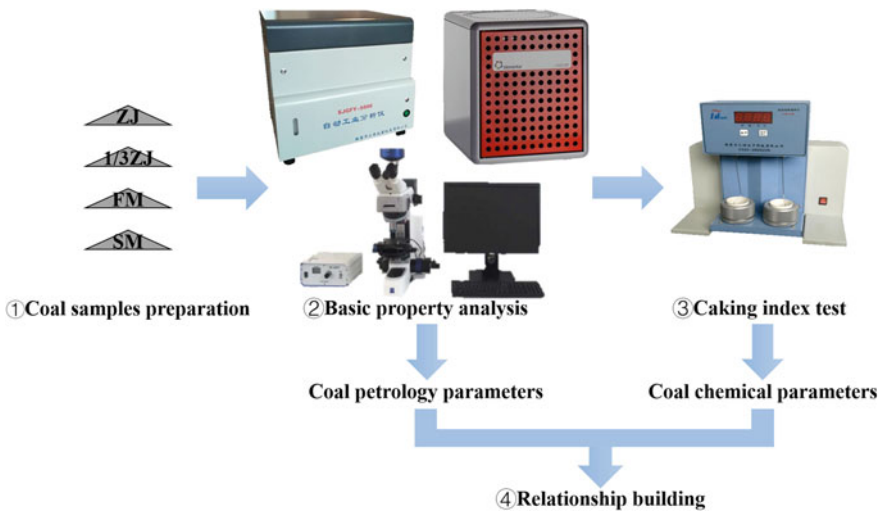


Fig. 1 Illustration of the experimental process

and micro-mineral types were implemented in accordance with GBT 15589-1995 standard procedure. The average maximum reflectance of vitrinite group and the determination of microscopic composition and minerals were determined following GBT 694-2008 and GBT 8899-1998 standard procedure. The experiment was performed using the Axio-Scope A1 fully automatic digital macerals analyzer to characterize the maceral composition of the coal sample.

Caking Characteristics Test

The measurement of the plastic layer index and Arnu–Audibert’s dilatometer was carried out by Chongqing research institute of China Coal Technology Engineering Group. The most well-known method for the index of plastic layer testing is a one-sided heating measurement, which uses the probe to measure the maximum thickness Y of the plastic layer, and the final shrinkage X according to the volume curve recorded in the experiment [12]. Many researchers have utilized related parameters of Arnu–Audibert’s dilatometer to measure the same way which takes the effective distance of the expansion rod and the corresponding temperature as the relevant parameters [12–14]. The caking index was measured according to GBT 5447-1997 standard procedure and the experimental machine was performed using the TJNJ-6JB adhesion index tester. The method of determining caking index used the abrasion strength of the coal sample’s rapid coke formation to indicate the cohesiveness of the experimental coal sample [15, 16].

Results and Discussion

Table 1 presents the foundational properties of proximate and ultimate analysis of four coal samples on a dry ash-free basis.

Table 1 Raw coal properties analysis

Coal	Proximate analysis (%)				Ultimate analysis (%)				
	M_{ad}	V_{ad}	A_{ad}	FC_{ad}	C	H	O	N	S
ZJ	2.26	20.11	7.35	70.28	76.99	4.58	4.73	2.16	0.76
1/3ZJ	2.28	31.22	6.96	59.55	77.27	4.61	1.34	5.68	1.47
FM	1.61	29.25	6.59	62.54	78.51	4.80	5.68	1.44	0.46
SM	1.62	15.53	13.69	69.13	79.03	4.10	4.50	1.31	1.74

M: moisture, V: volatile, A: ash, FC: fixed carbon, ad: dry ash-free basis

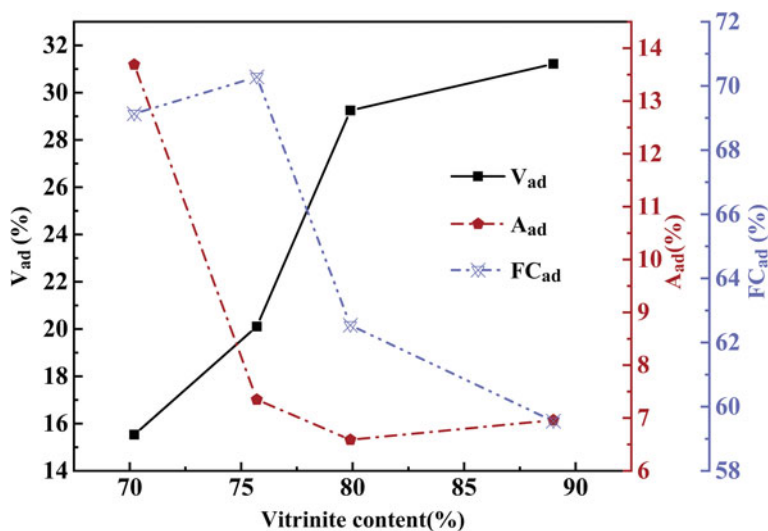


Fig. 2 Variation of proximate analysis with vitrinite content

Composition Analysis

It can be seen from Table 1 that all the samples contain higher proportions of fixed carbon and carbon element. Among them, ZJ has the highest fixed carbon, 1/3ZJ has the highest content of volatile matter and nitrogen, and SM contains the highest ash and harmful element sulfur. Figure 2 describes details of the variation in proximate compositions with vitrinite contents in different coal types, which can find that volatile matter, ash content, and fixed carbon in coal have obvious variety with the change of vitrinite content. The higher the vitrinite content in coal, the higher its volatile content, and the ash and fixed carbon content decrease in the general trend. Hence, it is confirmed that the industrial indicators concerned with actual production are associated with the content of macerals components.

Coal Macerals Analysis

The maceral analysis is shown in Fig. 3. The four kinds of samples are commonly used coal with vitrinite as the main part. Additionally, the average maximum reflectance of vitrinite in oil (R_{\max}) varies from 0.85 to 1.71%. From the order of the R_{\max} , it is demonstrated that the coal rank is SM (1.71) > ZJ (1.23) > FM (1.01) > 1/3ZJ (0.85), which same as confirmed by the order of volatile content in proximate analysis. Also, it shows that as the coal rank increases, the vitrinite content gradually decreases, and the inertinite content gradually increases.

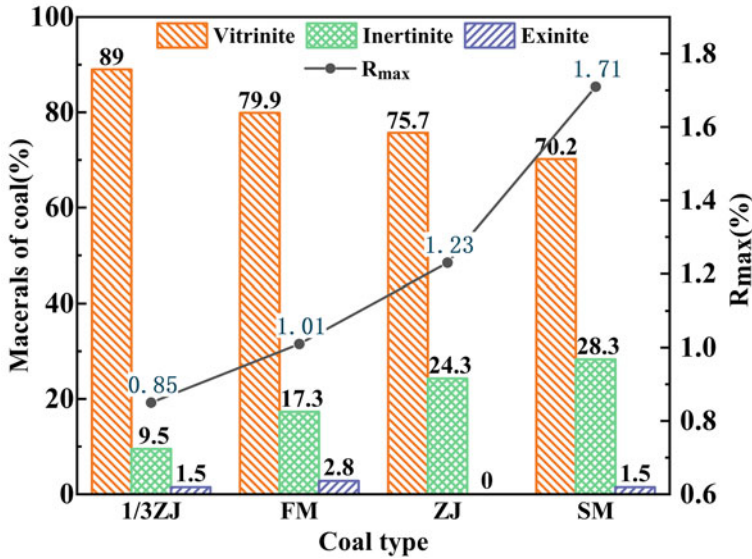


Fig. 3 Macerals content distribution of raw coal

Coking Characteristics of Raw Coal

The test results of the raw coal’s coking characteristic indexes are shown in Table 2.

(1) Index of plastic layer

Y stands for the maximum thickness of the plastic layer, which evaluates the cohesive ability of the coal type through the colloid amount. The larger the value of *Y* is, the stronger the cohesive ability. *X* means the final shrinkage and reflects the amount of colloid escaping after coking, to judge the coke cake properties and the impact on the coke pushing process. The larger the *X* value is, the stronger the coke cake shrinkage. From Table 2, we can see that the order of the cohesive capacity of raw coal reflected by the index of plastic layer is 1/3ZJ > FM > ZJ > SM. The coke produced by 1/3ZJ and FM has strong coke cake shrinkage, small coke lumps and many cracks, but it

Table 2 Test results of cohesiveness of raw coal

Coal	Index of plastic layer		Arnu–Audibert’s dilatometer						Caking index
	<i>X</i> /mm	<i>Y</i> /mm	<i>b</i> /%	<i>a</i> /%	<i>T</i> ₁ /°C	<i>T</i> ₂ /°C	<i>T</i> ₃ /°C	Δ <i>T</i> /°C	
1/3ZJ	8.0	48.0	Shrink only	38.0	339	–	452	113	80
FM	22.5	45.0	73.0	33.0	362	–	474	112	74
ZJ	7.0	35.0	Shrink only	13.0	423	–	501	78	70
SM	7.0	26.0	Shrink only	9.0	453	–	504	51	40

is beneficial for pushing coke. The characteristics of ZJ and SM are opposite to the above two.

(2) Arnu–Audibert’s dilatometer

The degree of expansion b is mainly influenced by the airtightness of the coal sample after heating and the rate of gas evolution during plasticity. Therefore, the higher the b value is, the better the colloid fluidity, the thermal stability and the uniformity of the resulting coke. The degree of shrinkage a is mainly used to evaluate the cohesive ability by the number of colloids. The larger the a value is, the stronger the cohesive ability. T_1 reflects the starting temperature of colloid formation, T_2 represents the starting temperature of colloidal solidification (because only FM shows expansion in the experimental coal samples, T_2 is not discussed in this experiment), T_3 indicates the formation temperature of semi-coke, ΔT ($\Delta T = T_3 - T_1$) shows the size of the temperature interval for colloid formation. All the kinds of temperature indexes indicate the length of the residence time of coal in the colloidal state. The longer the temperature interval is, the longer the residence time in the colloidal state and more conducive to the full caking of coal particles during the coking process.

As shown in Table 2, the order of the cohesive capacity of the raw coal measured by Arnu–Audibert’s dilatometer is $1/3ZJ > FM > ZJ > SM$, which is the same as the measurement of the plastic layer index. The temperature order of T_1 and T_3 are $SM > ZJ > FM > 1/3ZJ$, indicate the weaker caking ability and the higher temperature is required for the precipitation and curing of colloid. From the perspective of coal types, the overall fluidity of FM colloids is better, but a larger amount of FM addition will increase coke cracks. $1/3ZJ$ not only produces more colloids but also produces a longer range of colloids, and the colloid has a strong caking ability after curing, ZJ and SM were the opposite.

In particular, Fig. 4 is obtained by analyzing the softening interval of each coal type. The softening interval of the experimental coal samples is distributed between

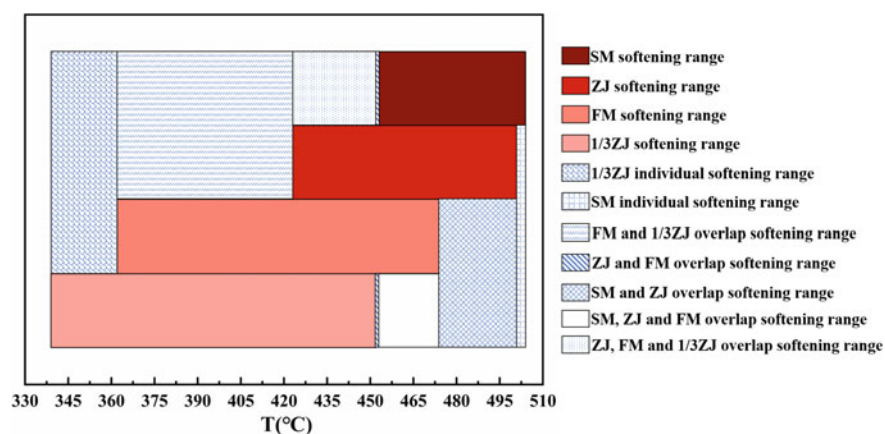


Fig. 4 Distribution of softening interval of various coals

339 and 504 °C, but the specific softening interval of each coal type is different. According to the colloidal layer overlapping coal blending theory, during the coking process, the blended coals have a longer temperature range, the more benefits to improving the coke quality. The softening interval of single coal is narrow, but the softening intervals of different coal types have overlapping areas. Therefore, coking with coal blending can be used to ensure that the coal can be in a long plasticity range without temperature breaks of colloids, thereby improving the caking process.

(3) Caking index

The determination of the caking index test requires adding the anthracite. And it needs to be bonded with the coal samples. The result of the index was $1/3ZJ > FM > ZJ > SM$ can be seen from Table 2, which is consistent with the order of colloid volume and consolidation capacity determined by the above two indicators. Although G is a comprehensive index, compared with the index of plastic layer and Arnu–Audibert’s dilatometer, it is not helpful to evaluate the shrinkage capacity, cracks, and the size of the coke cake. G needs to be used in conjunction with other indicators.

The Relationship Between Macerals Components and Coking-Related Index of Raw Coal

As mentioned above, the Y in the colloidal layer test experiment reflects the amount of colloid. The a in Arnu–Audibert’s dilatometer is similar to the Y , which reflects the amount of colloid. According to previous studies [17–20], the macerals of vitrinite and exinite affect the formation of active melt, also the inertinite group mainly affects the formation of the coke framework during the coking process. Hence, it could conceivably be hypothesized that the value of Y and a are mainly related to the content of macerals. Figure 5 is obtained from a mapping of the value of Y and a , and the content of coal macerals. We can see that the higher vitrinite content, the

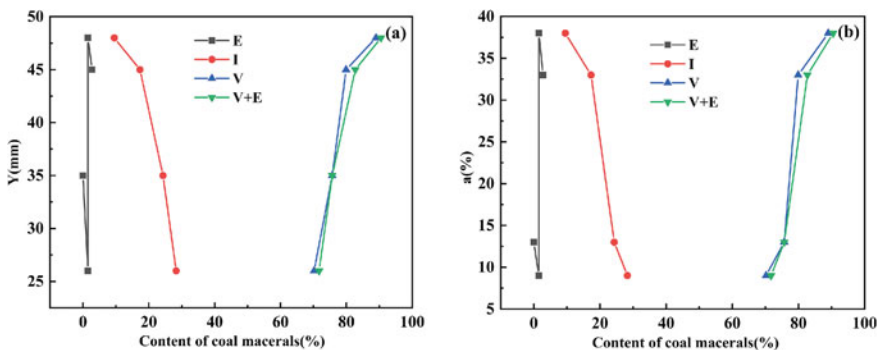


Fig. 5 Variation of colloid related parameters with coal macerals: (a) Relationship between Y and content of coal macerals; (b) Relationship between a and content of coal macerals

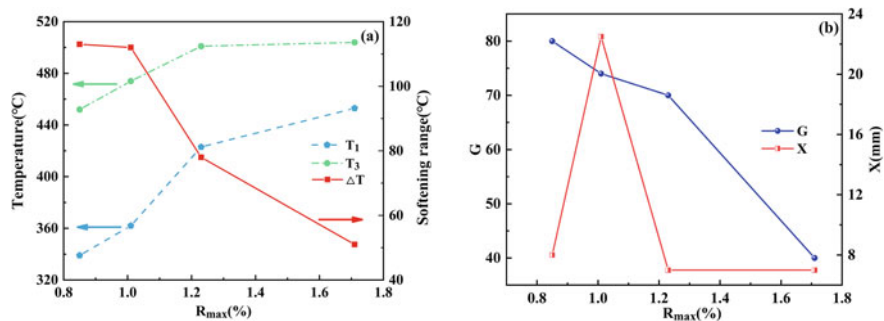


Fig. 6 Variation of vitrinite reflectance with coking performance: (a) Relationship between T_1 , T_3 , ΔT , and R_{max} ; (b) Relationship between G , X , and R_{max}

larger is the value of Y and a . This result further supports the idea that the more vitrinite content, the more colloidal body is produced. However, due to the low inertinite content, it cannot distinguish the individual effects of inertinite group.

On the other hand, the values of X , b , T_1 , T_3 , ΔT , and G in the cohesive property index all characterize the quality of colloid, and the coal maceral indicators that affect colloid quality should be mainly coal rank. Owing to three of the four coal samples showing the only shrinkage, temporarily consider the relationship between the remaining indicators except for b and R_{max} are plotted in Fig. 6. It can be seen that as the coal rank increases, T_1 increases which means the solidification temperature of colloid moves back, T_3 also increases which proves the temperature of colloid formation in the solid state shifts back, and the decrease of ΔT indicates that the range of colloidal plastic state is shortened. From the decreases in G , it can be known that the cohesiveness of colloid has decreased. However, the trend variation of X has increased firstly and then decreased with the rise of coal rank. A possible explanation for this may be that X characterizes the amount of colloid escaped after coking, which is related to the internal evolution of coal molecules.

Taken together, these results suggest that although the current indicators include airtightness, total amount, and cohesiveness of colloids have been delineated, there is no indicator to fully reflect the properties of colloids, and it is impossible to directly determine whether the coking process of colloids is good or not for a coal type. However, the artificially prescribed coking evaluation index and its coal macerals properties have a clear connection. These relationships may be explained by the coking evaluation index is a macroscopic representation of coal macerals properties. Therefore, it is a scientific and effective evaluation method to consider introducing maceral indicators instead of the traditional coking indicators to evaluate the coking capacity of coal.

Conclusion

The objective of this work was to examine the relationship between coal's caking properties and coal petrological parameters. It has been clearly by testing four coal caking property indexes and coal macerals parameter analysis. The main conclusions drawn from this work are as follows:

- (1) As the coal rank increases, the volatile content gradually decreases, and similarly, the vitrinite content gradually decreases, but the inertite content gradually rises. The more vitrinite content, the more colloids are produced, and the coal index affects the colloid quality is mainly coal rank.
- (2) There are overlapping regions in the colloid generation interval of each coal type. Coking with many kinds of coal can expand the colloid layer generation interval and regulate the amount of colloid formation and volatilization under the condition of ensuring that there is no temperature fault in the formation of colloids.
- (3) The indicators that characterize the amount of colloidal mass, such as the maximum thickness of the colloidal layer Y and the degree of shrinkage a , are mainly affected by the content of the microscopic components of macerals. The indexes that characterize colloidal physique, such as final shrinkage X , softening temperature T_1 , curing temperature T_3 , and cohesiveness index G , are mainly affected by coal rank. Therefore, it is feasible to introduce maceral indexes to replace the traditional coking indexes to evaluate the coking capacity of coal.

Acknowledgements This work was supported by the National Natural Science Foundation of China (Grant No. 52074055 & 52104323).

References

1. The general committee of China metallurgical encyclopedia (1992) China metallurgical encyclopedia: coking and chemical industry. Metallurgical Industry Press, Beijing
2. Yao ZZ, Zheng MD (2005) The science of coking. Metallurgical Industry Press, Beijing
3. Yu JL, Lucas JA, Wall TF (2007) Formation of the structure of chars during devolatilization of pulverized coal and its thermoproperties: a review. Prog Energy Combust Sci 33(2):135–170
4. Chen P, Zhang XH, Xiang R (2015) Analysis of the behavior of coal coking process. Shandong Chem Ind 44(23):20–21
5. Chen YX, Lee S, Tahmasebi A et al (2020) A review of the state-of-the-art research on carbon structure evolution during the coking process: from plastic layer chemistry to 3D carbon structure establishment. Fuel 271:117657
6. Shui HF, Zhao WJ, Shan CJ et al (2014) Caking and coking properties of the thermal dissolution soluble fraction of a fat coal. Fuel Process Technol 118:64–68
7. Qin ZH, Li X, Sun H et al (2016) Caking property and active components of coal based on group component separation. Int J Min Sci Technol 26(04):571–575

8. Li X, Qin ZH, Bu LH et al (2016) Structural analysis of functional group and mechanism investigation of caking property of coking coal. *Journal of Fuel Chemistry and Technology* 44(04):385–393
9. Odeh AO (2015) Qualitative and quantitative ATR-FTIR analysis and its application to coal char of different ranks. *J Fuel Chem Technol* 43(02):129–137
10. Qin ZH, Li XS, Chen J et al (2010) Origin and formation mechanism of coal caking property. *J China Univ Min Technol* 39(01):64–69
11. Lee S, Yu JL, Mahoney M et al (2018) A study on the structural transition in the plastic layer during coking of Australian coking coals using synchrotron micro-CT and ATR-FTIR. *Fuel* 233:877–884
12. China Coking Industry Association (2017) Innovation and development of china coking industry. Metallurgical Industry Press, Beijing
13. Liu LR, Wang PZ (1992) Metallurgical charge handbook. Metallurgical Industry Press, Beijing
14. Yang HX (1990) Coal chemistry and coal quality evaluation. China University of Geosciences Press, Wuhan
15. Wang WL, Li HT (2007) Research of factors for determination of caking index of bituminous coal with high caking property. *Clean Coal Technol* 6:77–78+101
16. Qiu B (2010) Study on factors of effecting accurate determination of caking index. *Clean Coal Technol* 16(03):94–95
17. Morga R (2010) Chemical structure of semifusinite and fusinite of steam and coking coal from the Upper Silesian Coal Basin (Poland) and its changes during heating as inferred from micro-FTIR analysis. *Int J Coal Geol* 84(1):1–15
18. Miao ZY, Wu GG, Li P et al (2012) Investigation into co-pyrolysis characteristics of oil shale and coal. *Int J Min Sci Technol* 22(02):245–249
19. Zhang L, Liu WL, Men DP (2014) Preparation and coking properties of coal maceral concentrates. *Int J Min Sci Technol* 24(01):93–98
20. Ren XY, Zhang DL, Wang K et al (2016) Study on Vitrinite Properties of Different Rank Coking Coals. *J Anhui Univ Technol (Nat Sci)* 33(01):38–43

Application of Grinding, Pyrometallurgical Pretreatment, and Silver Leaching of Mineral Tailings from the State of Morelos, Mexico



Jesús Iván Martínez Soto, Aislinn M. Teja-Ruiz, Martin Reyes-Perez, Miguel Pérez-Labra, Víctor Esteban Reyes-Cruz, José A. Cobos-Murcía, Gustavo Urbano-Reyes, and Julio Cesar Juárez-Tapia

Abstract The study of the benefit of noble metals is of utmost importance at an industrial level, when dealing with a mining-metallurgical waste the complexity of the process increases due to factors such as the characteristic refractoriness of these wastes. As an alternative to try to achieve the highest silver dissolutions, a chemical granulometric analysis was performed where it was determined that 40.61% of silver contained in the tailings sample is below 325 mesh (44 μm). Also, grinding tests were carried out in periods of 20–40 min to determine the operating parameter in the leaching. The leaching experiments were carried out in times of 24, 48, and 72 h, to samples of the whole tail, with grinding of 40 min and with pyrometallurgical pretreatment (roasting), using a constant concentration of cyanide of 0.1% and calcium oxide at the 0.2% reaching a maximum silver dissolution of 69.19%.

Keywords Grinding · Roasting pretreatment · Leaching

J. I. M. Soto · A. M. Teja-Ruiz · M. Reyes-Perez · M. Pérez-Labra · V. E. Reyes-Cruz · J. A. Cobos-Murcía · G. Urbano-Reyes · J. C. Juárez-Tapia (✉)
Autonomous University of the State of Hidalgo, Academic Area of Earth Sciences and Materials,
Road Pachuca-Tulancingo Kilometer 4.5 Mineral de la Reforma, Hidalgo 42180, México
e-mail: jcjuarez@uaeh.edu.mx

J. I. M. Soto
e-mail: ivan_kai@outlook.es

A. M. Teja-Ruiz
e-mail: aislinn_teja@uaeh.edu.mx

M. Reyes-Perez
e-mail: mreyes@uaeh.edu.mx

G. Urbano-Reyes
e-mail: Gustavo_urbano@uaeh.edu.mx

Introduction

At present, Mexico is not exempt from the adverse international outlook, the mining sector has been affected in the activity of exploration as it is unable to reduce pre-operating expenses in this area, which has generated a decrease in investment capital [1]. In addition, there is a deficit to satisfy the demand for precious metals from simple minerals, due to the massive exploitation of gold, silver, copper, and zinc deposits, which has led to the search for alternatives to recover these metals [2]. Currently, there are options, such as recycling and the recovery of mining waste by leaching with pretreatments [3, 4].

This last alternative of metal recovery represents an important source, based on the fact that there is a large amount of waste with significant gold and silver values. That is, these metals remain in the tailings, because the minerals benefited through conventional metallurgical processes did not achieve a complete release of said values [5, 6]. An additional benefit provided by this research is an alternative for remediation of affected sites where metallurgical mining waste has been deposited when reprocessing and removing this waste due to its negative impact on the environment [7, 8].

Today, it is possible to achieve a profitable recovery of these precious metals, using alternative metallurgical processes, capable of extracting a significant percentage of the metallic content. However, the re-processing of these residues still represents a challenge for metallurgy, since the noble metals are related to other elements or encapsulated in more complex mineral species [9].

Regarding this has been reported in previous works the silver dissolution contained in mining waste with concentrations of 71 g Ag ton^{-1} , reaching maximum dissolutions of 97% [10].

On the other hand, Coronado et al., in 2012 managed to obtain refractory concentrates difficult to leach from the processing of heavy minerals with high pyrite content, for which they used the roasting method to oxidize a refractory concentrate of gold and silver and thus make it more susceptible to cyanidation. The optimal recovery result was achieved by roasting the concentrate for 4 h at a temperature of $600 \text{ }^\circ\text{C}$, after a cyanidation of 20 h, where the consumption of lime to raise the pH (11.3) increased notably to 25 kg m^3 [11].

Unlike the previous work, Wei et al., in 2016 carried out the extraction of silver from a refractory mineral with low Au–Ag grade through a cyanidation process and a reductive leaching pretreatment in the presence of copper, in alkaline solution of ammonium and sulfate of ammonium, with concentrations of 2 mol L^{-1} and 1 mol L^{-1} , respectively, 4 g of copper wire and using a stirring speed of 300 min^{-1} for a period of 4 h, thus obtaining, a recovery of 78.96% [12].

In turn, Celep et al., in 2019 through a mineral release analysis and a diagnostic leaching, subjected an extremely complex arsenical silver mineral to an ultra-fine grinding of up to $8 \text{ }\mu\text{m}$, taking the cyanide leaching of a 71–84% of recovery [13].

The purpose of this study was to determine the optimal operating conditions for the benefit of tailings from the state of Morelos by applying grinding and conducting

conventional leaching experiments with the addition of a roasting pyrometallurgical pretreatment and achieve the maximum dissolution of gold and silver values.

Experimental Methodology

The tests were carried out for particle reduction by using a ball mill, where the variables of time and granulometry were analyzed. For this process, a kilogram of sample was introduced, using a volume of water of 8 L, at a speed of 17.65 min^{-1} and 30% of the volume in a ball bed. The milling times studied were 20, 30, and 40 min to carry out the elaboration of the granulometric and graphical analysis of the K_{80} , corresponding to each time tested.

For the pyrometallurgical pretreatment, the roasting was applied to a 1 kg of sample with operating parameters of 60 min at $800 \text{ }^\circ\text{C}$ with an air pressure of 8 L min^{-1} – 10 min^{-1} , by using a rotary reactor with oxygen injection, model Carbolite LP/ME-12, which has the ability to heat and stir the material through a 315° angle rotation system in both directions and a speed changer of 1 – 10 min^{-1} .

The tailings leaching experiments from the state of Morelos were carried out in times of 24, 48, and 72 h, with 0.1 and 0.2% concentration of cyanide and calcium oxide, respectively, these values were maintained throughout the experiment, carrying out samplings and titrations in periods of 6 h, compensating the amounts of cyanide and calcium oxide required by the process.

Four different leaching experiments were carried out, the first was carried out with the sample all one, the second experiment was carried out with a 40-min grinding and the pyrometallurgic pretreatment, the third was carried out with a 40-min grinding and the pyrometallurgic pretreatment. Finally, the fourth experiment, unlike the previous ones, an increase of 0.05% in the cyanide concentration was applied with the ground sample for 40 min and with a roasting pyrometallurgical pretreatment, the foregoing in order to determine whether there is a significant increase in the dissolution of silver or gold.

Results

Following are presented the results of the leaching experiments with grinding and roasting pyrometallurgical pretreatment carried out on tailings from the State of Morelos, Mexico.

Grinding

Figure 1 shows the grinding results for the tested times of 20, 30, and 40 min, obtaining as a result a K_{80} of $66.31 \mu\text{m}$ in a period of 20 min which is insufficient to release the silver values, the following period studied was 30 min, achieving a K_{80} of $63.84 \mu\text{m}$, however, to achieve the highest release of silver values, the mechanical reduction of the mineral sample to $44 \mu\text{m}$ is recommended, the above with the objective that the leaching solution enters greater contact with the solid. Finally, the grinding was carried out at 40 min, achieving a particle size of $43.59 \mu\text{m}$, for this reason the grinding time was stopped in 40 min, since reducing the particle size too much favors the formation of agglomerates, creating a layer liquid around the powders of the sample, which avoids the contact of the solution with the solid particle [14].

According to the results obtained from the grinding process, it was determined to use the mining metallurgic waste obtained after a 40-min grinding for the leaching experiments with a percentage of 74.63 below the 325 mesh and a particle size of $44 \mu\text{m}$ as shown in Table 1.

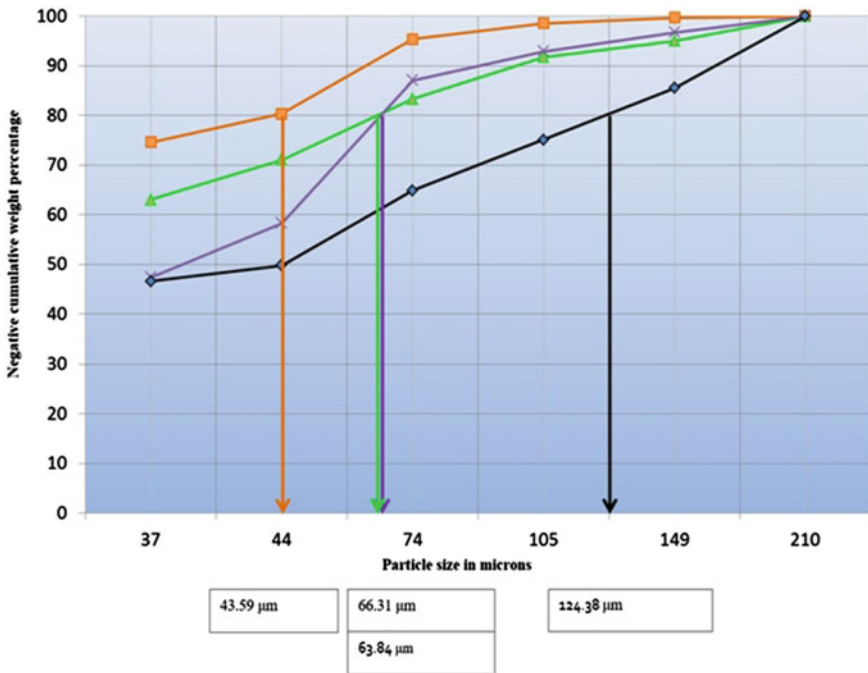


Fig. 1 Behavior of grinding at different times and determination of K_{80}

Table 1 40-min grinding mining waste from Morelos

Grinding at				
Product	Opening	%	%	40 min
Mesh	mm	Weight	Cumulate (+)	Cumulate (–)
+65 #	210	0.0	100.00	0.0
–65 + 100 #	149	0.25	99.75	0.25
–100 + 150 #	105	1.20	98.55	1.45
–150 + 200 #	74	3.15	95.40	4.60
–200 + 325 #	44	15.08	80.32	19.68
–325 + 400 #	37	5.69	74.63	25.37
–400 #		74.63	0.00	100

Leaching Tests

Cyanide Leaching

Table 2 shows the results obtained from three direct leaching to the tailings, without grinding or pyrometallurgical pretreatment, the reaction times were 24, 48, and 72 h, reaching 38.84%, 41.70%, and 44.30% of silver dissolution and 16.67%, 33.33%, and 41.67% for gold, respectively. From the above, it is highlight Table 2 at the dissolution process of the precious metals Au and Ag had different behaviors, since as can be seen in Table 2; for the same reaction times, different percentages dissolution were achieved, mainly in the first 48 h, in the case of gold, it had a progressive increase as the reaction time increased, however, for silver, the onset of the reaction was faster the first 24 h with respect to gold and later it becomes slow increasing only 5.5% of silver in the dissolution liquors in the following 48 h of reaction.

Cyanide Leaching and Grinding for 40 min

Three leaching was carried out with the ground tailings for 40 min, without previous roasting treatment, obtaining 47.41%, 49.91%, and 54.29% of dissolution for silver and 25%, 41.67%, and 50% for gold, in times of 24, 48, and 72 h, respectively, as shown in Table 3.

When comparing the percentages of silver dissolution from the unmilled tailings sample with respect to the dissolution percentages obtained with the tailings sample subjected to the milling process, an increase of 10% of leached silver is observed, suggesting that the grinding process has no significant effect, because the mineral species that contains the silver is a complex sulfide, as had been reported in a previous study [15].

Table 2 Cyanide leaching tests, sample of mining waste from Morelos all one

Samples	Head law		% Solid	Time	Solid waste cyanidation		Cyanidation dissolution		Reactive consumption	
	Ag g Ton ⁻¹	Au			Ag g Ton ⁻¹	Au	Ag %	Au	NaCN (kg Ton ⁻¹)	CaO (kg Ton ⁻¹)
Mining wastes Morelos	104.00	0.12	30	h	63.61	0.10	38.84	16.67	0.466	3.724
Sample without pretreat (49.80% – 325#) (64.86% – 200#)				48	60.63	0.08	41.70	33.33	0.676	3.771
				72	58.97	0.07	44.30	41.67	0.816	3.817

Table 3 Cyanide leaching tests, sample of mining waste from Morelos with 40-min grinding

Samples	Head law		% Solid	Time h	Solid waste cyanidation		Cyanidation dissolution		Reactive consumption	
	Ag	Au			Ag	Au	Ag	Au	NaCN	CaO
	g Ton ⁻¹				g Ton ⁻¹		%		(kg Ton ⁻¹)	
Mining wastes Morelos	104.000	0.12	30	24	54.69	0.09	47.41	25.00	0.613	3.817
Grinding to 40 min				48	52.09	0.07	49.91	41.67	0.752	3.864
(80.32% - 325#) (95.40% - 200#)				72	47.54	0.60	54.29	50.00	0.885	3.911

Cyanide Leaching, Sample with Roasting Pretreatment and 40 min of Grinding

Subsequently, the leaching of tailings previously roasted was carried out, in order to achieve the conversion of complex sulfides to simpler sulfides, reaching 55.74, 60.20, and 69.19% dissolution for silver and 42.11, 52.63, and 68.42% for gold, the results of these tests are presented in Table 4. A considerable increase in silver and gold dissolution is highlighted compared to the test without the roasting pretreatment, leading to a 54.29% silver and gold dissolution up to 69.19% and 50%–68.42%, respectively, in a 72-h leaching time.

Cyanide Leaching, 40-min Grinding, Roasting Pretreatment, and Increase in Cyanide Concentration to 0.15%

In this phase of the experimentation, the test was carried out by increasing the cyanide concentration to 0.15% with the ground tailings and the roasting pretreatment. The following results were obtained 58.57, 64.45, and 68.48% of dissolution for silver and 42.11, 52.63, and 68.42% for gold, as shown in Table 5.

This showed that there is no significant increase in the dissolution of the precious metals Ag and Au, when increasing the cyanide concentration. This also reveals that the system was saturated with cyanide, so it is recommended not to increase the cyanide concentration [16].

Conclusion

The performance of the grinding process did not have a significant impact on the dissolution of the metallic values of silver and gold, it revealed that the particle size is not of great relevance for the experiments carried out in this research, the above due to the fact that we have a complex sulfide as a mineral species which contains the silver. Additionally, since it deals with the benefit of a complex mineral, the pyrometallurgical pretreatment proposal favored the dissolution of silver and gold, going from 44.30 and 41.67% in leaching tests of the sample all one to 69.19 and 68.42% in the leaching tests with roasting pretreatment, respectively, revealing an increase in the dissolution percentage of 24.89% in the case of silver and 26.75% for gold.

Table 4 Cyanide leaching, sample of mining waste from Morelos with pretreatment of roasting and grinding of 40 min

Samples	Head law		% Solid	Time h	Solid waste cyanidation		Cyanidation dissolution		Reactive consumption	
	Ag g Ton ⁻¹	Au			Ag g Ton ⁻¹	Au	Ag %	Au	NaCN (kg Ton ⁻¹)	CaO (kg Ton ⁻¹)
Mining wastes Morelos	102.00	0.11	30	24	47.19	0.06	55.74	42.11	0.558	3.914
Sample without pretreat				48	40.60	0.05	60.20	52.63	0.698	3.961
(80.32% - 325#)				72	31.43	0.03	69.19	68.42	0.916	4.206

Table 5 Leaching tests, sample of mining waste from Morelos with roasting treatment, grinding for 40 min and 0.15% [CN⁻]

Samples	Head law		% Solid	Time h	Solid waste cyanidation		Cyanidation dissolution		Reactive consumption	
	Ag g Ton ⁻¹	Au			Ag g Ton ⁻¹	Au	Ag %	Au	NaCN (kg Ton ⁻¹)	CaO g Ton ⁻¹
Mining wastes Morelos	104.00	0.12	30	24	42.26	0.06	58.57	42.11	0.625	3.715
Grinding to 40 min (80.32% - 32.5#)				48	36.26	0.05	64.45	52.63	0.742	3.961
				72	32.15	0.03	68.48	68.42	0.916	4.310

References

1. Jiménez L (2019) Panorama de la Minería en México. FINGUACH. Revista de Investigación Científica y Tecnológica de la Facultad de Ingeniería de la Universidad Autónoma de Chihuahua 4(13):6–7. <https://148.229.0.27/index.php/finguach/article/view/319>
2. López C (2014) México: Política en Materia Minera. (Diálogo Unión Europea-América Latina Sobre Materias Primas). europa.eu/geninfo/query/index.do?queryText=plata&query_source=GROWTH&summary=summary&more_options_source=restricted&more_options_date=* &more_options_date_from=&more_options_date_to=&more_options_language=es&more_options_f_formats=* &swlang=en. Accessed 14 July 2018
3. Celep O, Alp I, Deveci H (2011) Extracción mejorada de oro y plata de un mineral de antimonio refractario mediante pretratamiento con lixiviación de sulfuro alcalino. Departamento de Ingeniería Minera. Universidad Técnica Karadeniz 105(3–4):234–239 <https://doi.org/10.1016/j.hydromet.2010.10.005>
4. Murciego A, Alvarez E, Aldana S, Sanz A, Medina J, Rull F, Villar P (2019) Characterization of secondary products in arsenopyrite-bearing mine wastes: Influence of cementation on arsenic attenuation. J Hazard Mater 373:425–436. <https://doi.org/10.1016/j.jhazmat.2019.03.086>
5. Parga J, Carrillo F (1996) Avances en los métodos de recuperación de oro y plata de minerales refractarios. Revista de Metalurgia 32(4):254–261. <https://doi.org/10.3989/revmetalm.1996.v32.i4.907>
6. Alp I, Celep O, Paktunç D, Thibault Y (2014) Influence of potassium hydroxide pretreatment on the extraction of gold and silver from a refractory ore. Hydrometallurgy 146:64–71. <https://doi.org/10.1016/j.hydromet.2014.03.007>
7. Jamieson H, Walker S, Parsons M (2015) Mineralogical characterization of mine waste. Appl Geochem 57:85–105. <https://doi.org/10.1016/j.apgeochem.2014.12.0140883-2927>
8. Mosco J, González M, López L, Barrera J, Durán M (2011). Estudio del efecto de una cubierta de calcita en la solubilización selectiva de metales en jales mineros a escala de laboratorio Ciencia Ed. (IMIQ) vol. Tec. Ciencia Ed. (IMIQ). 26(2):92–102. ISSN: 0186-6036
9. Teja Ruiz A, Juarez Tapia J, Reyes Pérez M (eds) (2017) Characterization and leaching proposal of Ag(I) from a Zn Concentrate in an S₂O₃²⁻-O₂ Medium. In: Characterization of minerals, metals, and materials. Springer, Cham, Switzerland, vol 146, pp 567–575. https://doi.org/10.1007/978-3-319-51382-9_62
10. Juarez J, Patiño F, Roca A, Teja A (eds) (2018) Determination rates Of Ag contained in metallurgical and mining residues in the S₂O₃²⁻-O₂-Cu²⁺ system: kinetic analysis. Minerals 8(7):309. <https://doi.org/10.3390/min8070309>
11. Coronado J, Encinas M, Leyva J, Valenzuela L, Valenzuela A, Munive G (2012) Tostación de un concentrado refractario de oro y plata. Revista de Metalurgia 48(3):165–174. <https://doi.org/10.3989/revmetalm.1102>
12. Li W, Liu Z, Huang Q, Tang Y, Qiu X (2016) Extraction of low-grade silver from a refractory Au-Ag ore in cyanidation by pretreatment with reductive alkaline leaching. Hydrometallurgy 164:257–264. <https://doi.org/10.1016/j.hydromet.2016.06.021>
13. Celep O, Yazici E, Altinkaya P, Deveci H (2019) Characterization of a refractory arsenical silver ore by mineral liberation analysis (MLA) and diagnostic leaching. Hydrometallurgy 189:105–106. <https://doi.org/10.1016/j.hydromet.2019.105106>
14. Guarniz O, Lescano E, Antonio M (2015) Proceso de lixiviación a nivel artesanal para la obtención de los parámetros óptimos en la recuperación de plata y oro en el distrito de Simbron de la provincia de gran chimú. Universidad Nacional de Trujillo. Facultad de Ingeniería Química. <http://dspace.unitru.edu.pe/handle/UNITRU/3633>

15. Martínez J, Teja A, Reyes M (eds) (2020) Chemical characterization and mineralogical analysis of mining-metallurgical tailing from the state of Morelos. Characterization of minerals, metals and materials 2020. Springer, Cham, pp 501–510. https://doi.org/10.1007/978-3-030-36628-5_49
16. Álvarez R (2005) Aplicación de sistemas pasivos para el tratamiento de soluciones residuales de procesos de cianuración en minería de oro. Universidad de Oviedo. Departamento de Explotación y Prospección de Minas. ISBN: 9788469078532

Application of Subnanosecond-Pulsed Dielectric Barrier Discharge in Air to Structural and Technological Properties Modification of Natural Minerals



Igor Zh. Bunin, Natalia E. Anashkina, Irina A. Khabarova,
and Maria V. Ryazantseva

Abstract The application of the high-energy impacts is a promising approach to effectively disintegrate fine-disseminated mineral complexes, and modifying the surface structure and technological properties of geomaterials (minerals, rocks, and ores). In this paper, the main results of the experimental studies on the directional modification of the surface morphology and phase composition as well as the physicochemical properties of semiconducting ore minerals and quartz under subnanosecond-pulsed dielectric barrier discharge in air at atmospheric pressure are presented. The rational parameters of discharge initiating electromagnetic impulses are recommended: $t_{\text{imp}} = 10 \mu\text{s}$ is the pulse duration, $t_{\text{fr}} = 250\text{--}300 \text{ ns}$ is the duration of the leading edge of the pulse, $U = 20 \text{ kV}$ is the amplitude of pulse, and $f = 15 \text{ kHz}$ is the pulse repetition rate. We used scanning electron microscopy, microhardness testing, wetting angle determination, electrode potential measurements, and other methods. The results are compared with those obtained from method of the high-power nanosecond electromagnetic pulses minerals irradiation.

Keywords Sulfide minerals · Quartz · Dielectric barrier discharge · High-power nanosecond pulses · Scanning electron microscopy · Surface morphology · Microhardness · Electrode potential · Flotation

Introduction

In Russia and in the world, the extensive studies have been performed using such energy impacts as radiation, ultrasonic, mechanochemical, electrochemical, pulsed-power energy, and plasma treatment for selective disintegration of fine-disseminated mineral complexes, directional change in the surface properties of minerals and an

I. Zh. Bunin (✉) · N. E. Anashkina · I. A. Khabarova · M. V. Ryazantseva
Mel'nikov Institute of the Comprehensive Exploitation of Mineral Resources, Russian Academy
of Science (IPKON RAS), Moscow 111020, Russia
e-mail: bunin_i@mail.ru

increase in the contrast between their structural–chemical and technological (flotation) properties [1–3]. Recent years, the growth of interest in low-temperature atmospheric plasma (LTP), which is a quasi-neutral medium that contains positively and negatively charged particles, radicals, and ultraviolet radiation, have seen [4].

LTP is a source of strong oxidizers in an oxide-containing medium (e.g., O, OH, HO₂, H₂O₂, and O₃). Chemically active plasma allows us to conduct selective chemical reactions at extremely high rates [4, 5]. The nonequilibrium low-temperature plasma of dielectric-barrier discharge (DBD [6, 7]) is characterized by high electron temperatures and low temperatures of the working gas. LT-plasma of dielectric barrier discharge in air at atmospheric pressure is considered as the safest, most precise technological tool for modifying the composition, structure, and surface properties of different materials, including geological materials (minerals, rocks, and ores) [8–10].

In this paper, we report the results of experimental investigations on the effect of low-temperature plasma from a DBD at atmospheric pressure and other effective factors resulting from a discharge have on the surface morphology (SEM), hydrophobicity (contact angle of wetting), microhardness (Vickers), and flotation activity of semiconductor ore minerals (e.g., sulfides: galena PbS, pyrrhotite Fe_nS_{n+1}, chalcopyrite CuFeS₂, arsenopyrite FeAsS, pyrite FeS₂, and sphalerite ZnS) and natural dielectric mineral quartz SiO₂. Additional studies were performed using polished sections of eudialyte (ideal formula of eudialyte itself, Na₁₅Ca₆Fe₃Zr₃Si₂₆O₇₂(O, OH)₂Cl₂ [11]). The results are compared with those obtained from method of the high-power nanosecond electromagnetic pulses (HPEMP, [12, 13]) minerals irradiation.

Experimental

Minerals

We performed our studies using monomineral fractions (particle size, 63–100 μm, arsenopyrite, pyrite) and plane-parallel polished sections of galena, pyrrhotite, chalcopyrite, sphalerite, veined milk-white quartz, and eudialyte 10 × 10 × 4.5 mm in size. The total contents of elements in the mineral samples of sulfides (Table 1) were determined via inductively coupled plasma atomic emission spectroscopy using a Varian Vista CCD Simultaneous ICP–AES unit. The detailed chemical composition of arsenopyrite and pyrite specimens and impurity content in them are summarized in our previous paper [14].

The chemical composition and contents of impurities in a quartz sample (wt %: SiO₂, 99.11; Al₂O₃, 0.61; C, 0.08; K₂O, 0.07; Na₂O, 0.05; TiO₂, 0.03; Fe₂O₃, 0.03; CaO, 0.03) were found via X-ray fluorescence analysis using an ARL ADVANT’X X-ray fluorescence spectrometer. Also, we used samples of eudialyte (Lovozero deposit, Russia; eudialyte is a complex ring silicate of zirconium, iron, manganese with triple and ninefold rings; chemical formula of eudialyte samples, Na₁₅Ca₆(Fe²⁺, Mn²⁺)₃Zr₃[Si₂₅O₇₃](O, OH, H₂O)₃(OH, Cl)₂).

Table 1 Chemical composition of sulfide mineral samples (wt%)

Sample	Fe	S	As	Cu	Pb	Zn	Sb	Ni	Ca	Si	Total
PbS	1.40	15.60	0.45	0.10	56.70	8.75	–	–	0.24	16.76	100
Fe _n S _{n+1}	59.80	39.20	–	0.04	–	–	–	0.03	0.55	0.38	100
CuFeS ₂	27.53	29.20	0.01	28.55	3.20	1.91	0.1	–	0.70	8.80	100
ZnS	4.08	29.30	0.2	0.28	6.61	59.32	0.01	–	0.20	–	100
FeAsS	30.79	19.60	40.30	0.02	0.01	–	0.04	–	–	–	[14]
FeS ₂	40.61	49.89	0.69	1.29	0.88	0.28	1.17	–	–	–	[14]

Impulse Generators

We treated mineral samples under normal conditions of a pulsed (subnanosecond) dielectric barrier discharge in air at atmospheric pressure on an experimental laboratory setup at the IPKON RAS (Moscow) and NPP FON (Ryazan). In this work, we established the rational parameters of pulses that initiate a discharge at which the greatest changes in the structure-sensitive properties of minerals are observed: the length of the leading edge of a pulse is 250–300 ns, the length of pulse is 10 μ s, the electrode voltage in the barrier discharge cell is 20 kV, and the frequency of pulse repetition is 15 kHz. The range of change in the duration of the sample LTP-treatment is $t_{\text{treat}} = 10\text{--}150$ s. The flow of a discharge current in a discharge cell was limited by one dielectric layer, and the length of the inter-electrode space is ~ 5 mm.

Additional research on the processing of minerals with high-power nanosecond electromagnetic pulses (HPEMP) was carried out using a special nanosecond pulse generator. The generator operates at a frequency of 100 Hz (pulse repetition rate), the output pulse amplitude is ~ 25 kV, the duration of the leading edge of the pulse varies from pulse to pulse within 2–5 ns, and the pulse duration varies within 4–10 ns. Video pulses of a bipolar shape are generated, pulse energy ~ 0.1 J, electric field strength in the inter-electrode gap is $(0.5\text{--}1) \times 10^7$ V \times m⁻¹, time range of the minerals pulsed treatment is $t_{\text{treat}} = 10\text{--}150$ s.

Analysis Methods

The morphological features of the surface of minerals were studied on thin polished sections using scanning electron microscopy on a LEO 1420VP SEM–EDX microscope equipped with an INCA Oxford 350 analyzer, and a scanning electron microscope Hitachi Tabletop Microscope TM 4000 Plus. The microhardness of the minerals was determined according to Vickers (HV , MPa) using a PMT-3 M (LOMO, Russia) microhardness tester. The load on the indenter was 50–100 g for sulfides and 200 g for quartz and eudialyte; the period of loading was 10–15 s. The contact angle of wetting (Θ°) of the initial surfaces and the surfaces altered via plasma treatment of

the polished mineral sections was measured using drops of distilled water with diameters of ~2–3 mm resting on them using a digital optical microscope and the ImageJ, DropSnake, and LB-ADSA programs [15]. The electrokinetic potential (ζ -potential, mV) of the ground eudialyte samples (particle size, <50 μm) was measured on a Microtrac ZETA-Check Zeta Potential Analyzer.

The flotation of arsenopyrite, pyrite, and sphalerite (before and after plasma treatment) was conducted using weighed quantities of minerals of 1.0 g on a laboratory flotation setup with a chamber volume of 20 mL. The consumption of potassium ethyl xanthate (PEX) was 200 g/t for arsenopyrite and pyrite and 50 g/t for sphalerite; pH 9.5 (CaO).

We measured the electrode potential (E , mV) of pyrrhotite by potentiometric titration with simultaneous monitoring of the potential of the mineral and the pH of the medium (pH 5–12). The effect of HPEMP-irradiation on the flotation activity of pyrrhotite was assessed by the yield of minerals into the foam product in the presence of the following flotation reagents: butyl xanthate 50 mg/L, sodium dimethyldithiocarbamate 150 mg/L, and methyl isobutyl carbinol at pH 10.5. Flotation experiments were carried out in a laboratory flotation machine with a 20-ml chamber on weighed portions of 1 g of minerals with $-100 + 63 \mu\text{m}$ in size. The agitation time with the reagents was 1 min and the flotation time was 2.5 min.

Results and Discussion

During the low-temperature plasma treatment of mineral samples, the temperature of the gas (ionized air) did not exceed that of the dielectric barrier in the working zone of the discharge cell of the dielectric barrier discharge and remained around room temperature at $t_{\text{treat}} = 10\text{--}60$ s.

Polished sections of the minerals were placed in a discharge so that the working (controlled) surfaces of the samples were located on the surface of the dielectric barrier. The mineral surfaces were treated in a strong electric field under conditions of DBD radiation, an ion wind, the transfer of electric charge to the samples surfaces, an elevated temperature of the dielectric barrier, and a high concentration of chemically active particles.

As a result of the impact of the electric field, microdischarges in the DBD cell, and the ozone formed in electric discharges, we observed a number of changes in the surface morphology, microhardness, and hydrophobicity of the minerals. Regular defects formed on the galena surface (Fig. 1a), due to the removal of microcrystal fragments, and mineral microhardness HV falling from ~120 MPa (in the untreated state) to 92 MPa ($t_{\text{treat}} = 50$ s); the relative change (drop) in microhardness was $\Delta HV \approx 23\%$. Regular and irregular defects formed on the chalcopyrite surface (Fig. 1b), and micropaths of dielectric breakdown on the surface of sphalerite were enclosed in a sintered material of (presumably) oxide (hydroxide) micro- and nanophases (Fig. 1c), which reduced the microhardness of chalcopyrite by ~30% (from 490 to 345 MPa) and that of sphalerite by ~18% (from 315 to 260 MPa).

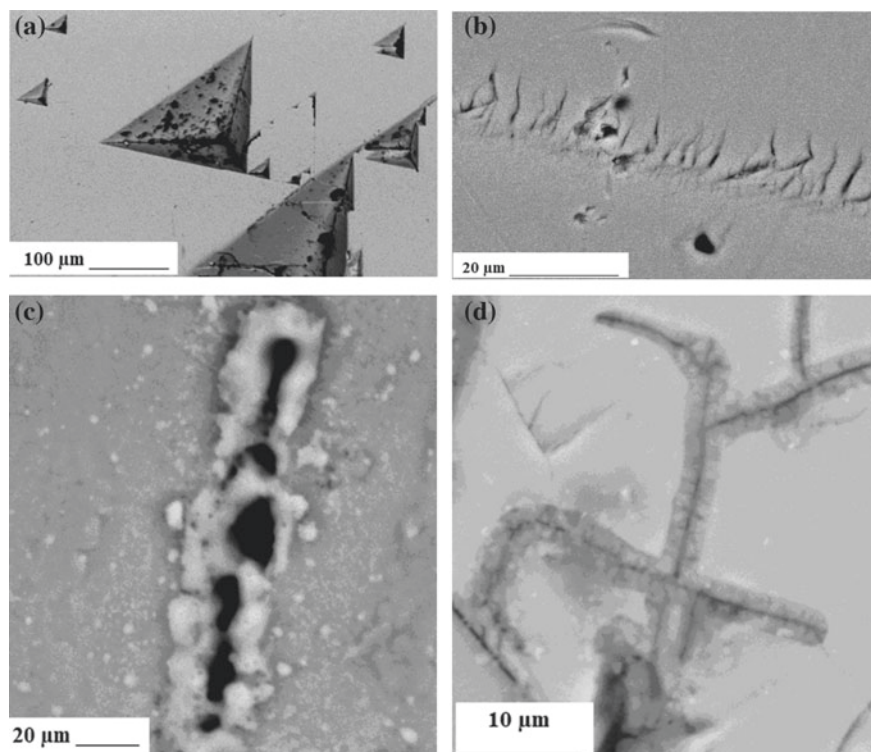


Fig. 1 SEM micrographs of **a** galena, **b** chalcopyrite, **c** sphalerite, and **d** pyrrhotite surfaces after exposure to a dielectric barrier discharge ($t_{\text{treat.}} = 10\text{--}30$ s)

Mineral particles of the crushed sulfides samples were separated from the dielectric barrier by a small air gap, allowing the particles to move freely (hang) over the barrier during a discharge. In this case, the particles were affected by the high-intensity pulsed electric field, ion wind, and such chemically active compounds as ozone and nitrogen oxides [16]. The flotation activity of the sulfide minerals changed as a result of $t_{\text{treat.}} = 10\text{--}30$ s of preliminary plasma treatment of our arsenopyrite, pyrite, and sphalerite samples: the flotation of sphalerite rose by 6% (from 45 to 51%), and in contrast, the recovery of arsenopyrite and pyrite into foamy products of flotation fell by 5% (from 12 to 7%) and 22% (from 37 to 15%), respectively.

The effect of dielectric barrier discharge caused an effective changes in the surface morphology (Fig. 1d) and electrode potential of pyrrhotite: in the range of pH 9.5–12, the largest changes in the electrode potential were established for the mode of short-term ($t_{\text{treat.}} = 10$ s) treatment of the mineral. The shift of the electrode potential to the region of negative values ($E = -60$ mV) occurred, which caused the effect of a decrease in the sorption and flotation activity of pyrrhotite.

As a result of short-term ($t_{\text{treat.}} = 10$ s) treatment of pyrrhotite samples by high-power nanosecond electromagnetic pulses (HPEMP), a shift of the electrode potential

of the mineral in the direction of negative values occurred. The maximum difference in the values of the electrode potential before and after the electric pulse treatment was achieved in an alkaline medium at pH 10. The minimum sorption of the flotation reagent butyl xanthate (decrease by 17%) on the surface of pyrrhotite was also found under a short-term pulse treatment ($t_{\text{treat}} = 10$ s). Thus, a sharp shift in E of pyrrhotite to the region of negative values caused a decrease in the sorption of the anionic collector on the mineral. Preliminary electric pulse treatment of pyrrhotite during $t_{\text{treat}} = 10$ s caused a decrease in the hydrophobicity of the surface and floatability of the mineral in the presence of a flotation reagent (dimethyldithiocarbamate), which corresponds to the data on the highest content of oxidized ferric iron on the mineral surface [17, 18]. Thus, the advantages of using the short-term ($t_{\text{treat}} = 10\text{--}30$ s) energy impacts for structural and chemical modification of the surface and physicochemical properties of sulfide minerals are shown.

Irregular microdefects ≤ 3 μm in size formed upon increasing the duration of LTP treatment of quartz polished sections. The surface roughness was smoothed, which slightly lowered the corresponding roughness parameters (R_a and R_q). This microstructural changes in surface of quartz (Mohs hardness 7) caused by the impact of LTP ($t_{\text{treat}} = 10\text{--}150$ s) effectively softened and consistently reduced the mineral's microhardness during plasma treatment, from ~ 1420 to 1320 MPa in the initial and altered states at $t_{\text{treat}} = 150$ s, respectively; the maximum relative change in microhardness was $\Delta HV_{\text{max}} \sim 7\%$.

As a result of the nonthermal impact of high-power (high-voltage) nanosecond electromagnetic pulses (HPEMP) on our samples of quartz, ΔHV_{max} was $\sim 29\%$ (from 1425 to 1015 MPa at $t_{\text{treat}} = 150$ s). For sphalerite, however, the drop in microhardness under the impact of HPEMP was smaller than that of LTP treatment: $\sim 5\%$ (from 315 to 300 MPa at $t_{\text{treat}} = 50$ s). The contact angle of the water wetting of quartz surfaces changed nonlinearly (nonmonotonically) upon increasing the duration of LT-plasma treatment: at brief impacts ($t_{\text{treat}} = 10\text{--}30$ s), Θ rose from 44° to 53° ($\Delta\Theta_{\text{max}} \sim 20\%$), indicating an increase in the hydrophobicity of the mineral's surface. The value of Θ then fell to 48° at $t_{\text{treat}} = 150$ s, corresponding to the behavior of Θ under the impact of HPEMP.

According to SEM-EDX data, the plasma treatment of eudialyte resulted in the formation of numerous defects (microcracks and microcraters of electrical breakdown (Fig. 2a, b)) and the appearance of fragmented coatings (Fig. 2c) on the surfaces

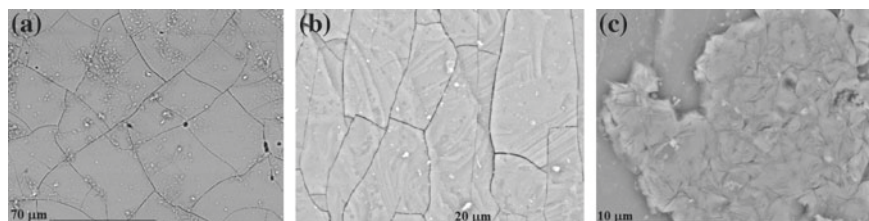


Fig. 2 SEM micrographs of eudialyte surface as a result of LTP of DBD exposure ($t_{\text{treat}} = 50$ s)

of mineral samples. The formation of this new surface phase is apparently associated with the destruction of minerals associated with eudialyte (possibly aegirine with nepheline, or lamprophyllite with nepheline), and the transfer of elements and their redeposition on the eudialyte surface.

The microhardness of eudialyte fell monotonically as the period of plasma treatment grew ($t_{\text{treat}} = 10\text{--}150$ s): from ~ 780 MPa (the average HV values of samples in the initial state) to ~ 420 MPa after 150 s of LTP treatment. The maximum relative change (drop) in microhardness ΔHV_{max} was $\sim 46\%$.

As a result of brief plasma treatment of eudialyte particles, the negative electrokinetic potential (ζ -potential) values grew from -96 mV in the initial state to -110 mV at $t_{\text{treat}} = 10$ s, apparently raising the hydrophobicity of the surface particles. At longer periods of LTP exposure ($t_{\text{treat}} = 30\text{--}150$ s), the negative ζ -potential fell to around -82.5 mV. In the $t_{\text{treat}} = 10\text{--}150$ s range of variation, the contact angle of wetting (Θ°) a eudialyte surface with water also changed nonlinearly (non-monotonically). At $t_{\text{treat}} = 10\text{--}30$ s, there was an increase in the hydrophobicity of the mineral's surface, with Θ rising from 57° to $73^\circ\text{--}78^\circ$, which, presumably, can cause an increasing the mineral's sorption and flotation activity. At $t_{\text{treat}} = 50\text{--}150$ s, Θ gradually fell from 68° to 55° .

These results indicate it is possible in principle to use the impacts of pulsed-power energy to raise the efficiency of the disintegration and flotation separation of sulfides and rockforming minerals, particularly quartz extraction (purification). Our results also demonstrate the fundamental possibility of using low-temperature atmospheric-pressure plasma to softening and modifying the physicochemical and technological properties of rare-metal minerals.

Conclusions

Our results demonstrate the fundamental possibility of using a dielectric barrier discharge in air at atmospheric pressure, in which a low-temperature plasma is generated and other effective processes are implemented, to improve the technological properties of natural minerals (geological materials). We indicated experimentally, that it is possible in principle to use the impact of pulsed-power energy to raise the efficiency of the disintegration and flotation separation of sulfides and rockforming minerals, particularly quartz (purification) and eudialyte extraction.

The obtained results testify to practicability and potential of using comparatively brief ($t_{\text{treat}} = 10\text{--}30$ s) electromagnetic pulse treatment (DBD, HPMP) in air under standard conditions for the structural chemical modification of surfaces and physicochemical properties of sulfide minerals, quartz and REE-bearing minerals in order to improve efficiency of complex refractory ores processing.

Acknowledgements This work supported in part by the President of the Russian Federation under contract number NSh-7608.2016.5 (Academician V.A. Chanturiya's scientific school). The authors

are grateful to Cand. Sci. (Geol.-Mineral.) E.V. Koporulina of Moscow State University for her help with the experiments.

References

1. Bunin IZh, Ryazantseva MV, Samusev AL, Khabarova IA (2017) Composite physicochemical and energy action on geomaterials and aqueous slurries: theory and practice. *Gornyi Zhurnal (Mining Journal)* 11:77–83. <https://doi.org/10.17580/gzh.2017.11.14>
2. Chanturiya VA, Bunin IZh, Ryazantseva MV (2019) XPS study of sulfide minerals surface oxidation under high-voltage nanosecond pulses. *Miner Eng* 143(11):105939. <https://doi.org/10.1016/j.mineng.2019.105939>
3. Huang W, Chen Y (2021) The application of high voltage pulses in the mineral processing industry. *Powder Technol* 393(11):116–130. <https://doi.org/10.1016/j.powtec.2021.07.003>
4. Keudell AV, Gathen VSV (2017) Foundations of low-temperature plasma physics—an introduction. *Plasma Sources Sci Technol* 26(11):113001. <https://doi.org/10.1088/1361-6595/aa8d4c>
5. Rusanov VD, Fridman AA, Sholin GV (1981) The physics of a chemically active plasma with nonequilibrium vibrational excitation of molecules. *Soviet Physics Uspekhi* 24(6):447–474. <https://doi.org/10.1070/PU1981v024n06ABEH004884>
6. Avtaeva SV (2011) Barrier discharge. Lambert Academic Publishing, Saarbrücken. Research and Application
7. Brandenburg R (2017) Dielectric barrier discharges: progress on plasma sources and on the understanding of regimes and single filaments. *Plasma Sourc Sci Tech* 26(5):053001. <https://doi.org/10.1088/1361-6595/aa6426>
8. May F, Hamann S, Quade A, Bruser V (2017) Froth flotation improvement by plasma pretreatment of sulfide minerals. *Miner Eng* 113(11):95–101. <https://doi.org/10.1016/j.mineng.2017.08.009>
9. Ran J, Qiu X, Hu Z, Liu Q, Song B (2018) Selective flotation of pyrite from arsenopyrite by low temperature oxygen plasma pre-treatment. *Minerals* 8(12):568. <https://doi.org/10.3390/min8120568>
10. Ran J, Qiu X, Hu Z, Liu Q, Song B, Yao Y (2019) Enhance flotation separation of arsenopyrite and pyrite by low-temperature oxygen plasma surface modification. *Appl Surf Sci* 480(6):1136–1146. <https://doi.org/10.1016/j.apsusc.2019.02.172>
11. Rastsvetaeva RK, Chukanov NV, Aksenov SM (2012) Mineraly gruppy evdialita: kristal-lokhimiya, svoistva, genezis (Minerals of the eudialyte group: crystal, chemistry, properties, genesis). Nizhnenovgorod Gos Univ, Publishing, Nizhny Novgorod
12. Bunin IZh, Bunina NA, Vdovin VA, Voronov PS (eds) (2001) Experimental studies of non-thermal effect of high-power electromagnetic pulses on rebellious gold-bearing raw materials. *Bull Russ Acad Sci: Phys* 65(12):1788–1792
13. Chanturiya VA, Bunin IZh, Ryazantseva MV, Filippov LO (2011) Theory and applications of high-power nanosecond pulses to processing of mineral complexes. *Miner Process Extr Metall Rev* 32(2):105–136. <https://doi.org/10.1080/08827508.2010.530722>
14. Ryazantseva MV, Bogachev VI (2009) Influence of nanosecond electromagnetic pulses on electrophysical properties of pyrite and arsenopyrite. *J Min Sci* 45(5):499–505
15. Stalder AF, Melchior T, Müller M, Saged D, Bluc T, Unser M (2010) Low-bond axisymmetric drop shape analysis for surface tension and contact angle measurements of sessile drops. *Colloids Surf A* 364(1):72–81
16. Lazukin AV, Grabel'nykh OI, Serdyukov YA (eds) (2019) The effect of surface barrier discharge plasma products on the germination of cereals. *Tech Phys Lett* 45(1):16–19. <https://doi.org/10.1134/S1063785019010292>

17. Ivanova TA, Bunin IZh, Khabarova IA (2008) On the characteristic properties of oxidation of sulfide minerals exposed to nanosecond electromagnetic pulses. *Bull Russ Acad Sci: Phys* 72(10):1326–1329
18. Bunin, IZh, Chanturiya VA, Ryazantseva MV (eds) (2016) Structural modification of sulfide minerals irradiated by high-power nanosecond pulses. In: Parinov IA (eds) *Advanced materials. Manufacturing, physics, mechanics and applications 2016*. Springer Proceedings in Physics vol 175, Heidelberg; Springer, New York, pp 3–21. https://doi.org/10.1007/978-3-319-26324-3_1

Characterization and Stain Analysis in Natural and Artificial Rocks



M. G. S. Freitas, E. D. F. Castilho, A. R. G. Azevedo, J. A. T. Linhares júnior,
M. T. Marvila, and S. N. Monteiro

Abstract Technological characterization tests have an important influence on the evaluation of rocks, for an assertive choice of use. In this context, this work aims to evaluate the resistance that various types of natural and artificial rocks have to staining by everyday substances, through the ABNT-NBR 13818:1997 standard, annex G. During the tests, changes in the brightness of the rocks were also evaluated. After the tests, it was observed that 25% of the artificial rocks had permanent spots and in the group of natural rocks 39.29%. In general, most of the samples tested underwent some kind of change in visual appearance and final brightness. It is concluded that the artificial rocks presented greater resistance to the attack of staining agents. The group of artificial rocks presented a performance about 15% higher than that of natural rocks in terms of the presence of permanent spots.

Keywords Ornamental rock · Staining · Artificial rock

M. G. S. Freitas · E. D. F. Castilho

FIFES—Federal Institute of Espírito Santo, Rodovia Engenheiro Fabiano Vivácqua 1568,
Cachoeiro de Itapemirim, Espírito Santo 29322-000, Brazil
e-mail: freitas@uol.com.br

E. D. F. Castilho

e-mail: evanizis@ifes.edu.br

A. R. G. Azevedo (✉)

UENF—State University of the Northern Rio de Janeiro, LECIV—Civil Engineering Laboratory,
Av. Alberto Lamego 2000, Campos dos Goytacazes, Rio de Janeiro 28013-602, Brazil

J. A. T. L. júnior · M. T. Marvila

UENF—State University of the Northern Rio de Janeiro, LAMAV—Advanced Materials
Laboratory, Av. Alberto Lamego 2000, Campos dos Goytacazes, Rio de Janeiro 28013-602, Brazil

S. N. Monteiro

IME - Military Institute of Engineering, Department of Materials Science, Square General
Tibúrcio 80, Rio de Janeiro 22290-270, Brazil

© The Minerals, Metals & Materials Society 2022

M. Zhang et al. (eds.), *Characterization of Minerals, Metals, and Materials 2022*,

The Minerals, Metals & Materials Series,

https://doi.org/10.1007/978-3-030-92373-0_21

Introduction

Rocks have been used by man since ancient times as a structure and masonry for the construction of different types of buildings. With the expansion of construction techniques, the attribution of rocks was directed towards finishing and coatings as well as ornamentation. According to the Brazilian Association of Technical Standards—ABNT, ornamental rock is defined as a natural rock material that is subjected to different degrees or types of processing to perform an aesthetic function. Coating rock, then, is the natural rock that, after undergoing processing processes, can be used in surface finishing, especially on floors, walls, and facades of civil constructions [1].

Dimension stones have gained considerable market relevance in a world context. Used both in finishes and coatings as well as in decoration and furniture pieces, their demand has grown in the country and the variety of available products has increased. The ornamental stone sector moves the country's economy since in 2018 they totaled US\$ 992.5 million in Brazilian exports [2].

The state of Espírito Santo is a world reference in the sector of ornamental stones with the extraction of marble and granite. The state stands out as the largest exporter of ornamental stones in the country, having moved around US\$ 791.36 million dollars in 2018. According to available data, it is estimated that there are approximately 63.0 billion tons in reserves and 9.3 billion mineable tons of ornamental rocks in Espírito Santo. As a result, the sector has become one of the most important in generating jobs and income in the state. In 2017, this activity employed 17,551 workers in 1,350 establishments in Espírito Santo [3].

Dimensional stones are commercially qualified through their aesthetic characteristics, highlighting the chromatic pattern, design, grain, and texture. When the variability of this parameter is very accentuated in a deposit, the commercial typification and the category are compromised [4].

In the same way that aesthetic appearance is important in the choice of ornamental and coating stones, the technological characteristics that reflect the physical–mechanical behavior of the rocks under the conditions of use, allow the detection of aesthetic problems arising from the inadequate selection and application of the material. For correct assignment of functions to natural and artificial rock materials, technological characterization is recommended. The tests predict the behavior of the rocks in the face of the required demands, anticipating the resistance of the material for consumers [5]. Even the most resistant rocks are not immune to physical–mechanical and chemical hostilities from the different environments in which they are inserted.

The main coating pathologies refer to stains, efflorescences, cracks, and abrasive wear, externalized both by contact with cleaning products, foods, beverages, cosmetics, paints, oils, greases, etc., as well as by atmospheric pollution, for example, acid rain. This work aims to compare the reaction of rocks when exposed to substances used in everyday life through visual analysis and brightness measurement, in order to examine the reaction of each rock lithotype to exposure to a specific staining agent.

Materials and Methods

The staining test of ornamental rocks and the cleaning evaluation do not have a specific standard. For this reason, an adaptation of the standard for the ceramic industry ABNT-NBR 13,818, described in the book *Technological Characterization of Dimension Stones: laboratory practices*, which describes how to carry out the staining test, is used [6]. This standard for tests on ceramic materials establishes the specification of staining agents and cleaning agents, the equipment used, the preparation of specimens, the procedure for applying staining agents, the stain removal attempts, and the classification regarding the cleanability of the stained surfaces. The need to adapt the standard is due to the difference between ceramic materials and ornamental stones.

The natural rocks chosen for this work are described in the *Characterization, Application, Use and Maintenance Manual of the Main Commercial Rocks of Espírito Santo* presented in Fig. 1 [7].

A second group of ornamental rocks of artificial origin shown in Fig. 2 was selected.

To carry out the test, specimens with different dimensions can be used as long as the area is larger than the diameter of the disposable cup that will be used. Eight specimens were prepared per lithotype with dimensions of: 14 cm high \times 7 cm wide \times 0.5 cm thick for the artificial ones, and 7 cm high \times 7 cm wide \times 2 cm thick for the natural ones, totaling 64 specimens. Initially, it is necessary that the specimens are

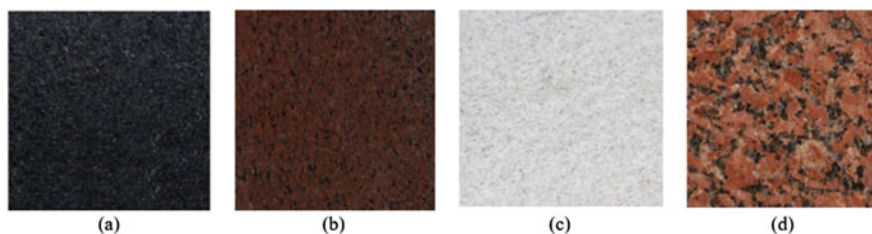


Fig. 1 Natural ornamental rocks. **a** Black saint gabriel. **b** Tobacco brown. **c** Siena white. **d** Brasilia red (Color figure online)

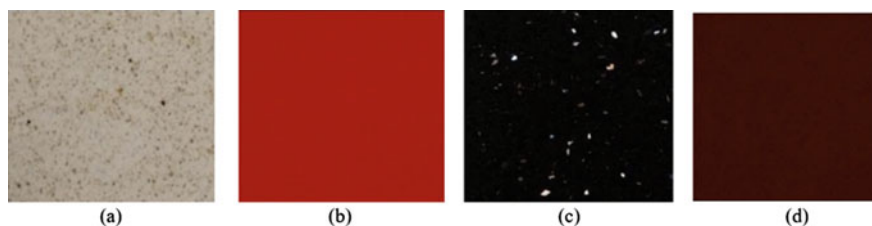


Fig. 2 Artificial ornamental rocks. **a** Absolute beige. **b** Absolute red. **c** Stellar black. **d** Absolute brown (Color figure online)

Table 1 Identification of lithotypes

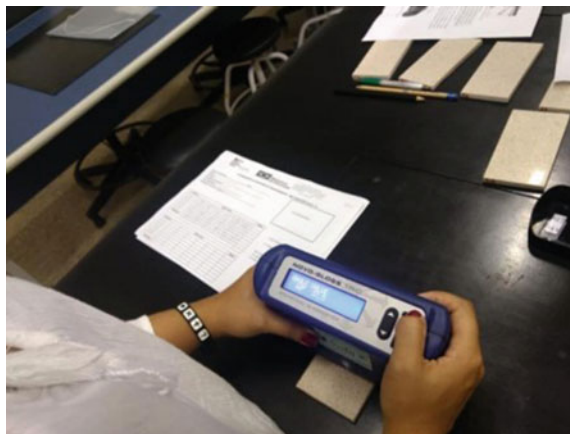
Lithotype	Lithotype identification	Lithotype	Lithotype identification
Absolute red (artificial)	A1 a A7	Siena white (natural)	F1 a F7
Absolute brown (artificial)	B1 a B7	Brasilia red (natural)	G1 a G7
Stellar black (artificial)	C1 a C7	Black saint gabriel (natural)	I1 a I7
Absolute beige (artificial)	E1 a E7	Tobacco brown (natural)	H1 a H7

clean and dry. For this, the specimens were washed with running water and placed to dry at room temperature, for at least 24 h.

The next step was the identification of the specimens. For the test, eight lithotypes were used, (four of natural rocks and four of artificial rocks) and eight specimens for each one. Each lithotype had one specimen chosen as a reference sample, to serve as a comparison of samples that passed through the staining agents. The specimens were identified according to Table 1.

After the identification step, the brightness of the surface of each specimen was measured using the Gloss meter device. Each measurement is performed in the center of the material, in the region that will be exposed to the staining agent Fig. 3.

For better accuracy of the values, six gloss measurements were performed on each specimen and the average between these values was taken to obtain a more representative result of the gloss of each material. The reference angle obtained by

Fig. 3 Measurements of surface gloss of specimens

the geometry test that was adopted during the brightness unit measurements was set at 60° for all studied lithotypes, both natural and artificial rocks.

The next step was to expose the rock surface to the staining agent. For this, one third of the volume of the 50-ml plastic cup was filled. To facilitate the application, the specimens were organized in trays according to the staining agent that would be applied, thus, each tray received a rock lithotype in which the same staining agent was applied.

After organizing the trays, the plastic cup containing the selected staining agent was centered and placed in contact with the face of each specimen. The rock was exposed to the staining agent for a period of 24 h.

The specimens identified with number 1 were exposed to soybean oil, those with number 2 to neutral detergent and the specimens ending in 3, 4, 5, 6, and 7 were, respectively, subjected to coffee, steel wool with detergent and water, degreasing, sanitary water, and lemon juice.

At the end of the 24-h exposure time, the cleaning process began. Excess staining agent was removed and the specimen was cleaned with running water. After 24 h of cleaning with running water, it was possible to carry out a visual analysis of stains. After this period, new brightness measurements were performed on the surface of the specimens and data collection. Afterwards, the stain removal procedure was started.

For the first cleaning attempt, warm water was used. For this, the specimens were placed in trays filled with warm water until they remained submerged. The specimens were kept submerged for 5 min, then, using a paper towel to remove excess water, they were placed to dry naturally at room temperature for 24 h.

The second cleaning step involved the application of a cleaning product (in this case, neutral detergent). The surface of the specimens was subjected to cleaning with a soft sponge and neutral detergent for about 1 min. After this step, the specimens were washed in running water and the excess water was removed with a paper towel. Then they were placed to dry naturally at room temperature.

In the third cleaning step, the previous procedure was repeated, but the cleaning agent used was the multipurpose paste and a soft sponge. Again, after 24 h of natural drying, new gloss measurements were performed on the specimens.

Results and Discussion

Regarding staining agents, regarding the formation of permanent stains, it is worth noting that for natural rocks, soybean oil was the agent that provided the largest number of these stains, whereas for artificial rocks, bleach was responsible for causing the greatest number of spots in the lithotypes.

Another factor existing in relation to staining agents, regarding stain removal, is that, for natural rocks, neutral detergent was the only staining agent that allowed the total removal of stains for all analyzed lithotypes, after the cleaning steps. The high concentration of sodium perborate in the detergent is a positive factor in terms of the potential for removing stains, which has already been verified in a study

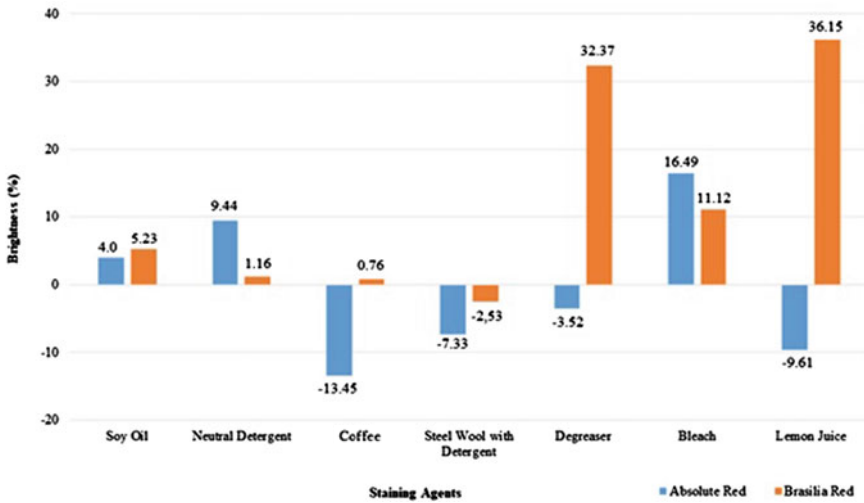


Fig. 4 Brightness of the absolute red (artificial rock) and Brasília red (natural rock) lithotypes according to the staining agents (Color figure online)

in the literature, which indicated a 30% improvement in the cleaning efficiency of this product [8]. The analysis also found that, for artificial rocks, the agents: soy oil, neutral detergent, and coffee were the only staining agents that did not have permanent stains.

It can also be highlighted regarding the brightness analysis, that the average loss of brightness for natural rocks was 21.45% and, for artificial rocks, it was 11.51%. And in the aspect of average loss of brightness, natural rocks showed 9.94% more loss of brightness compared to artificial rocks [7]. Thus, Fig. 4 presents the results of the brightness variation in the Absolute Red (artificial rock) and Brasília Red (natural rock) lithotypes after completion of the cleaning steps. Positive values correspond to loss of brightness and negative values to gain in brightness [5].

It was possible to observe that in the Brasília Red natural rock, the lemon juice caused a greater loss of shine and with the use of coffee a lesser loss of shine. In the Red Absolute artificial rock, the greatest loss of shine was with the bleach agent and the smallest loss with soy oil. The constituent acid from the lemon acted as a degrading agent of the surface minerals existing in the natural rock, a phenomenon that was the opposite in artificial rocks, because according to a study, the artificial rocks use neutralizing components that inhibit the effect of the acid in the lemon [9].

Figure 5 presents the results of the brightness variation in the Brown Absolute (artificial rock) and Brown Tobacco (natural rock) lithotypes after completion of the cleaning steps. It is verified that in the natural rock Brown Tobacco the degreaser provided the greatest loss of shine and the soybean oil the least loss of shine. In the Absolute Brown artificial rock, the only loss of shine registered was with the degreasing agent, in the other agents there was an increase in shine. The steel wool

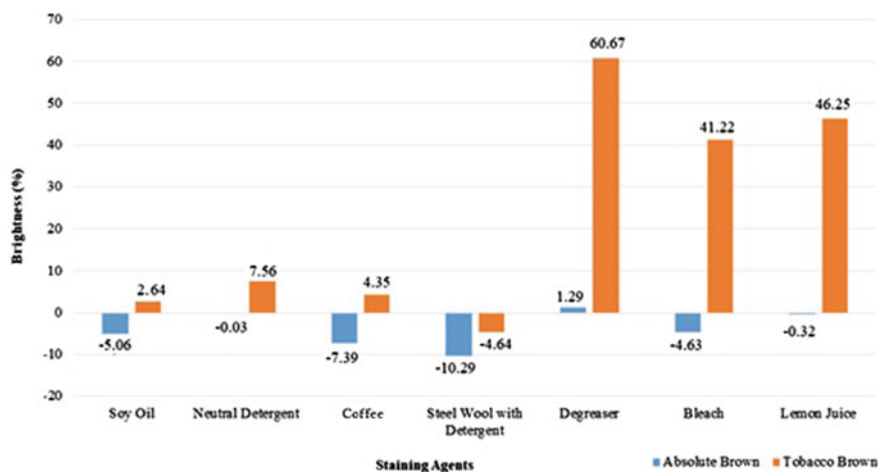


Fig. 5 Brightness of the absolute brown (artificial rock) and tobacco brown (natural rock) lithotypes according to the staining agents (Color figure online)

with detergent enabled the greatest increase in brightness for the studied lithotypes [10].

The results obtained in Fig. 5 corroborate studies in the literature, in which the use of degreaser, bleach, and lemon juice on natural rocks tend to facilitate the loss of shine due to the action of acidic products that act on the deterioration of natural constituents, behavior totally opposite to artificial rocks, and that its use is a positive factor [8, 9]. Figure 6 compares the results of brightness variation in Black Stellar (artificial rock) and Preto São Gabriel (natural rock) lithotypes after completion of the cleaning steps. It was observed that in the Preto São Gabriel natural rock, the lemon juice provided the greatest loss of shine and the coffee the least loss of shine. On the other hand, in the Preto Stellar artificial rock, bleach provided the greatest loss of shine and the degreasing agent the least loss [11].

Figure 7 shows the results of brightness variation in Beige Absolute (artificial rock) and White Siena (natural rock) lithotypes after completion of the cleaning steps.

It is also verified that in White Siena the lemon juice and degreaser showed high values of loss of shine and the smallest loss of shine was registered by the exposure to steel wool with detergent. In the Beige Absolute artificial rock, the greatest loss of shine occurred with bleach and the smallest loss with neutral detergent [7]. In this specific case, the use of bleach on natural rock had a different effect from that seen previously, as the white pigmentation was an active agent throughout the process, which even justifies its higher cost in general in the market [6].

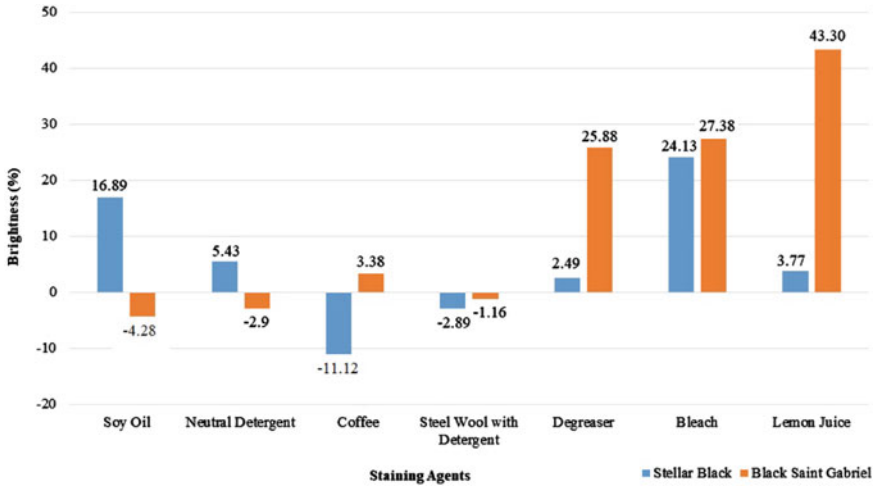


Fig. 6 Brightness of the stellar black (artificial rock) and black saint gabriel (natural rock) lithotypes according to the staining agents

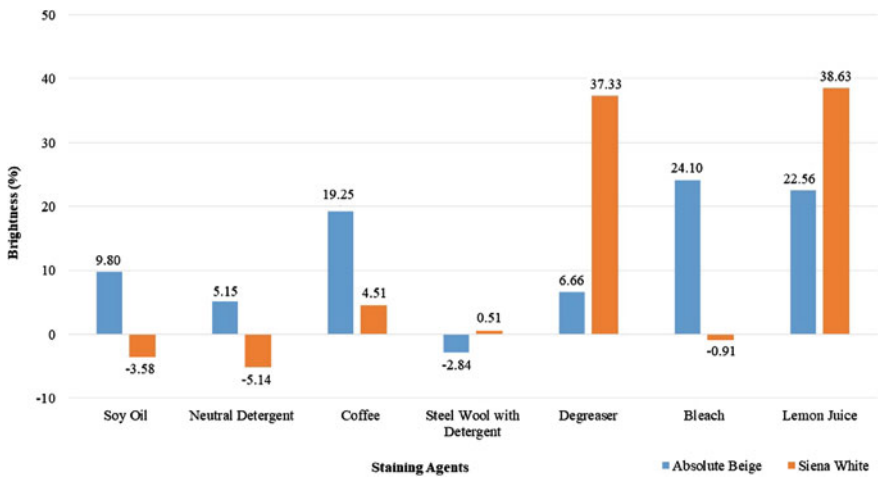


Fig. 7 Brightness of the absolute beige (artificial rock) and siena white (natural rock) lithotypes according to the staining agents

Conclusion

After the results, it can be concluded that:

- In general, most of the samples tested underwent some kind of change, either in the visual aspect or in the final shine, confirming the action of culinary and

household cleaning products as the cause of these changes, in addition to the sample cleaning steps;

- According to the results obtained, it is concluded that the rocks of an artificial nature presented greater resistance regarding the attack of the proposed staining agents, in the formation of permanent stains and in the average loss of brightness of the samples submitted to the tests;
- The group of artificial rocks presented a performance about 15% higher than that of natural rocks in the aspect of the presence of permanent spots and in the aspect of average loss of brightness, the natural rocks showed 9.94% more loss of brightness in relation to the artificial rocks.

References

1. Brazilian Association of Technical Norms (2003) NBR 15012. Rocks for building coatings, Rio de Janeiro (In Portuguese)
2. Brazilian Association of Dimension Stone Industry—ABIROCHAS. Balance of Brazilian exports and imports of ornamental stones in 2018. Inform 01/2019. Brasília, 2019 (In Portuguese)
3. Mozer T, Machado J (2019) Espírito Santo economic factor. Espírito Santo educational and industrial development institute. Year 3. n. 3 (In Portuguese)
4. Chiodi Filho C (1995) Technical and economic aspects of the dimension stones sector - studies and documents series, 18–28 (In Portuguese)
5. Chiodi Filho C, Rodrigues EP (2009) Guide for applying rocks in coatings. Package Insert—ABIROCHAS, pp 16–25 (In Portuguese)
6. Castilho EDF (2018) Technological characterization of dimension stones: laboratory practices—Edifes (In Portuguese)
7. Alencar CRA, Instituto Euvaldo Lodi (2013) Manual for the characterization, application, use and maintenance of the main commercial rocks in Espírito Santo: ornamental—IEL (In Portuguese)
8. Barbosa MZ, de Oliveira Dias J, Marvila MT, de Azevedo ARG (2021) Life cycle approach applied to the production of ceramic materials incorporated with ornamental stone wastes. *Environ Sci Pollut Res*. <https://doi.org/10.1007/s11356-021-16386-w>
9. Costa KOB, Xavier GC, Marvila MT (eds) (2021) Influence of high temperatures on physical properties and microstructure of gneiss. *Bul Eng Geo Env* 80(9):7069–7081. <https://doi.org/10.1007/s10064-021-02362-8>
10. Marvila MT, Azevedo ARG, Cecchin D (eds) (2020) Durability of coating mortars containing açafí fibers. *Case Studies Con Mat* 13. <https://doi.org/10.1016/j.cscm.2020.e00406>
11. Neuba LM, Pereira Junio RF, Ribeiro MP (eds) (2020) Promising mechanical, thermal, and ballistic properties of novel epoxy composites reinforced with cyperus malaccensis sedge fiber. *Polymers* 12(8). <https://doi.org/10.3390/polym12081776>

Characterization of Blast Furnace Slag for Preparing Activated Alkali Cements



M. T. Marvila, A. R. G. Azevedo, E. B. Zanelato, S. N. Monteiro,
and C. M. F. Vieira

Abstract Blast furnace slag (BFS) activated alkali cements are an alternative to the use of Portland cement. The objective of this work was to characterize a BFS for potential application as an activated alkali cement. Characterizations were performed using SEM, particle size, physical parameter analysis, chemical composition, XRD, FTIR, and ATD. The mechanical strength of activated alkali cement, compared to Ordinary Portland cement (OPC), was also evaluated. The results demonstrate the feasibility of applying BFS as an alternative and eco-friendly cement, due to the characterization parameters being within the recommended range and due to the superior compressive strength of the OPC composition.

Keywords Ceramics · Mechanical properties · Activated alkali cements

Introduction

Blast furnace slag (BFS) is a by-product resulting from the fusion of iron ore into pig iron, in a process carried out in industrial units called blast furnaces, where the oxides contained in the iron minerals are reduced and the impurities that accompany them are separated [1]. Slag is formed by the melting of impurities from iron ore

M. T. Marvila (✉) · C. M. F. Vieira

LAMAV—Advanced Materials Laboratory, UENF—State University of the Northern Rio de Janeiro, Av. Alberto Lamego, 2000, Campos dos Goytacazes, Rio De Janeiro 28013-602, Brazil

C. M. F. Vieira

e-mail: vieira@uenf.br

A. R. G. Azevedo · E. B. Zanelato

LECIV—Civil Engineering Laboratory, UENF—State University of the Northern Rio de Janeiro, Av. Alberto Lamego, 2000, Campos dos Goytacazes, Rio De Janeiro 28013-602, Brazil

S. N. Monteiro

Department of Materials Science, IME—Military Institute of Engineering, Square General Tibúrcio, 80, Rio de Janeiro 22290-270, Brazil

© The Minerals, Metals & Materials Society 2022

M. Zhang et al. (eds.), *Characterization of Minerals, Metals, and Materials 2022*,

The Minerals, Metals & Materials Series,

https://doi.org/10.1007/978-3-030-92373-0_22

after the addition of molten materials such as limestone and dolomite, and coke ash [2].

The molten slag is a mass that, due to its insolubility and low density when compared to pig iron, is transported by channels to the cooling place. This cooling operation can occur in two ways: to atmospheric air, where crystallized slag is formed [3]; or abruptly by means of jets of water under high pressure, forming the granular slag [4]. The main differences between these two processes are that crystallized slag, as it is crystalline, does not acquire binding power, and can only be used as an aggregate or replacing stone materials, while granulated slag, as it is mineralogically amorphous, has a high hydraulic potential, hardening when finely ground and in contact with water. Granulated slag is used in the production of Portland cement as a substitute for clinker, but it is not a pozzolanic material [5]. In this context, the objective of this work is to evaluate the potential of application of BFS in AAC, aiming to totally replace the Portland cement by an ecological one, obtained by the alkaline activation of the slag.

Materials and Methods

The materials used in this research were blast furnace slag from an industry located in Serra, ES, Brazil. The BFS was characterized using scanning electron microscopy (SEM) in a Jeol model JSM 6460 LV microscope and using a Tecnival confocal optical microscope (OM). The characterization of the physical parameters was carried out through granulometry and distribution of grain sizes, specific mass, natural moisture content, and degree of vitrification. Specific surface area analysis was also performed using the Blaine method.

The mineralogical characterization was carried out using X-ray diffraction spectrometry (XRD), using a Shimadzu model 6000 diffractometer, operating with copper radiation (Cu-K α), voltage of 40 kV and 2θ scan ranging from 10° at 60°. Fourier transform infrared spectroscopy (FTIR) was also performed using a model 4500a infrared spectrometer from Agilent Technologies. Next, an energy-dispersive X-ray fluorescence (FRX) test was carried out in an Axios Max model equipment manufactured by Malvern Panalytical. Thermal characterization was performed by thermogravimetric analysis (TGA) using a TA instruments thermal analyzer, model SDT-Q600 with a heating rate of 10°C/min and a maximum temperature of 1100°C.

Finally, the analysis of important properties of cements was performed, compressive strength, at ages of 7 and 28 days of thermal cure, at a temperature of 65 °C. A composition based on AAC in the ratio 1:2:0.45 (cement: sand: water) was used, using blast furnace slag activated by an alkaline solution with 10% sodium, extracted from other works. A 1:2:0.45 (cement: sand: water) composition, based on Ordinary Portland cement (OPC), was also used for comparison.

Results and Discussion

Figure 1 shows the characterization by SEM of the studied slag. It is observed that the morphology of the material is irregular, an indication of its amorphism, as is the morphology of Portland cement [6] and any other material in the form of powder used as a precursor. This is the case of metakaolin and fly ash [7].

Figure 2 shows the BFS optical microscopy before and after ball milling. There is an increase in the surface area of the residue with this treatment. This operation is essential for the alkaline activation reaction to be effective, since the specific surface area is a parameter that directly interferes with the resistance of the AAC [8].

Figure 3 shows the BFS granulometry before and after grinding in a ball mill. Through the figure it is possible to observe that the treatment performed is efficient

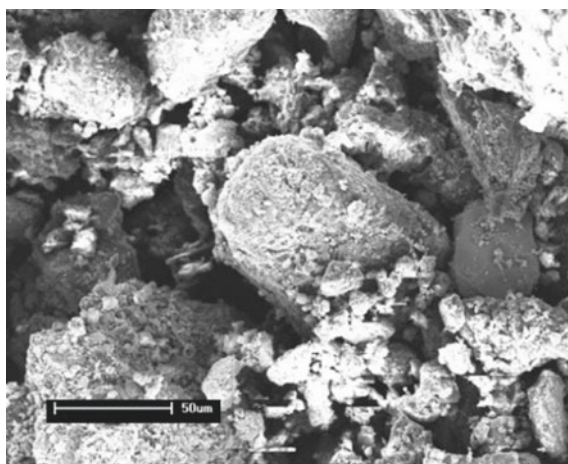


Fig. 1 SEM image of BFS

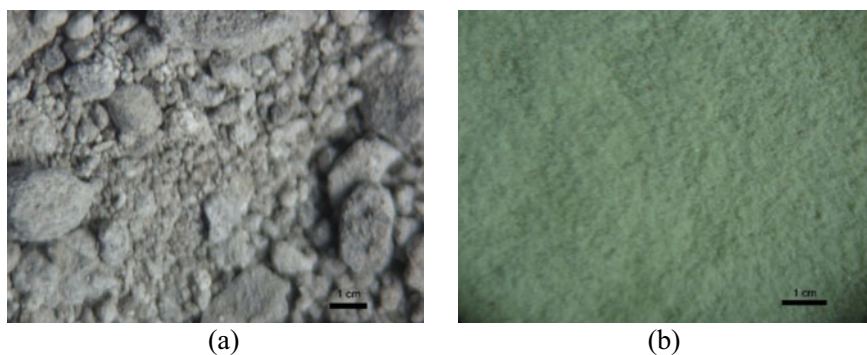
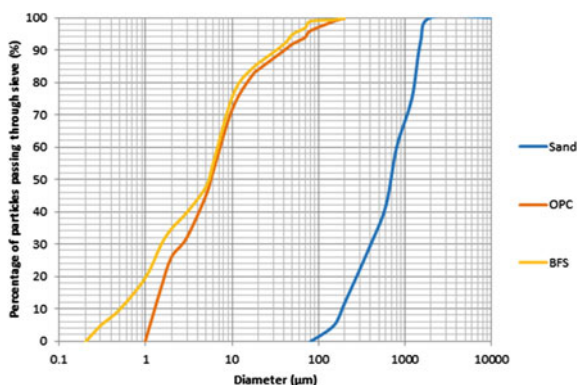


Fig. 2 OM image of BFS: **a** natural; **b** ground

Fig. 3 Particle size curve of the BFS



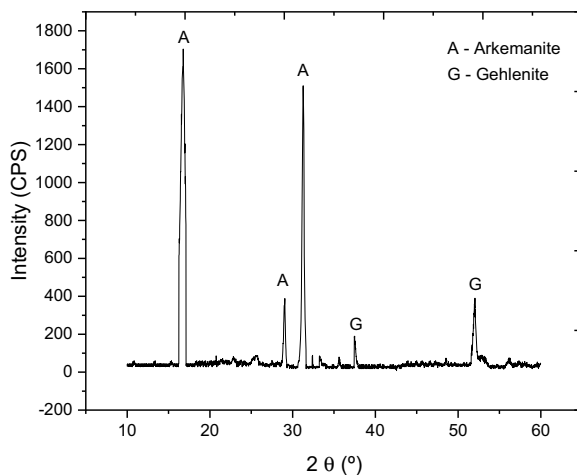
in the sense of reducing the waste particles. This becomes clear when evaluating the equivalent diameters D_{10} and D_{90} , which for waste in its natural form are 200 and 1800 mm, respectively. The residue in ground form has $D_{10} = 0.6$ mm and $D_{90} = 70$ mm, a considerable reduction in the size of particles of the material that enables the occurrence of the alkaline activation reaction.

The main physical parameters of the BTS are detailed below: the specific mass is around 1.27 g/cm^3 , natural moisture content is approximately 4.8%, and the degree of vitrification is 98%. The degree of vitrification is essential for the alkaline activation reaction to occur as it is related to the amorphism of the material. Furthermore, it is observed that the specific surface area by the Blaine method obtained after grinding for 6 h was $4520 \text{ cm}^2/\text{g}$. Saedi et al. [8] concluded that the use of precursors with specific surface area by the Blaine method of $4200 \text{ cm}^2/\text{g}$ is sufficient for the alkaline activation to occur with satisfactory resistance values. Wang et al. [9] obtained satisfactory results using precursors with specific surface area by the Blaine method of $4260 \text{ cm}^2/\text{g}$. Thus, it is verified that the specific surface area by the Blaine method obtained by the slag after 6 h of grinding is compatible with other researches with AAC.

Table 1 shows the chemical composition of BFS. It is observed that the major oxides are CaO (47.49%), SiO_2 (33.00%), Al_2O_3 (9.69%), and MgO (5.96%). Furthermore, regarding the classification of the precursor that takes into account the $\text{CaO}/(\text{SiO}_2 + \text{Al}_2\text{O}_3)$ ratio, it is observed that the value obtained is 1.12, above 1 [10, 11]. Therefore, the material is classified as rich in calcium, not forming polysialate networks typical of geopolymers in high amounts. In the alkaline activation reaction, the formation of tobermorite is expected, with structures like C-A-S-H.

Table 1 Chemical composition of blast furnace slag

Composition	CaO	SiO_2	Al_2O_3	MgO	SO_3	TiO_2	Others
(%)	47.49	33.00	9.69	5.96	0.95	0.86	2.05

Fig. 4 XRD of BFS

With regard to classification, the BFS studied for being classified as basic, since the hydraulicity modulus is greater than 1, according to NBR 5753 [12]. Furthermore, the MgO contents are less than 6%. This is an indication that few secondary phases will form due to magnesium interference. Thus, the studied blast furnace slag has a high calcium content, which indicates that the precursor can be activated alone.

Figure 4 presents the mineralogical composition. The presence of a considerable amorphous region is observed between 2θ from 10 to 15°, from 18 to 28°, from 32 to 38°, and from 40 to 52°, approximately. Furthermore, it is possible to detect the presence of minerals of akermanite whose theoretical formula is $\text{Ca}_2\text{Mg}(\text{Si}_2\text{O}_7)$, and gehlenite with theoretical formula $\text{Ca}_2\text{Al}_2\text{SiO}_7$. The mineralogical composition is in agreement with other authors who studied BFS, such as Jamil et al. [13] and Aziz et al. [14]. It is expected that there will be an increase in the peaks of detected minerals, and that there will be a change of phases from akermanite and gehlenite to tobermorite and hydrotalcite after the BFS alkaline activation reaction.

Figure 5 shows the results of the FTIR analysis. The following events are observed: around 3750 cm^{-1} a peak occurs due to O–H bonds, indicating the presence of water in the composition of the evaluated slag [15]. It is noteworthy that in the compounds formed through the alkaline activation of the slag, these peaks are expected to be reduced, due to the formation of resistant compounds. Another interesting event occurs at 1750 cm^{-1} , related to C–Na bonds [16]. This peak occurs more intensely in compositions where efflorescence occurred. Finally, events formed at approximately 1500 , 1000 , and 750 cm^{-1} are observed, related to Si–O–Ca, Si–O–Al, and Si–O–Si bonds, respectively. These peaks are characteristic of the formation of tobermorite and hydrotalcite, which are the main compounds resistant to formation in the alkaline activation of calcium-rich precursors. These peaks are expected to be intensified during the alkaline activation of BFS.

Figure 6 shows the thermal analysis of the blast furnace slag. There are two very characteristic events in the behavior of the slag. An event at a temperature of

Fig. 5 FTIR of BFS

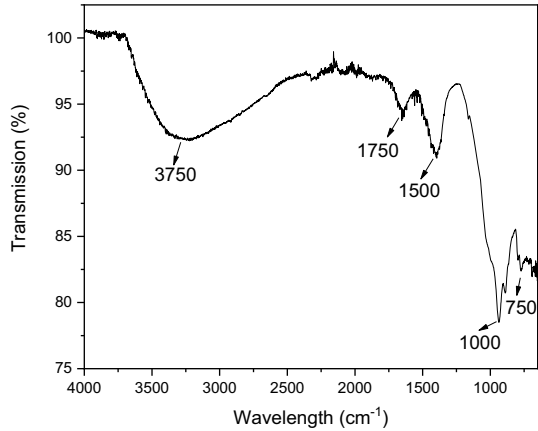
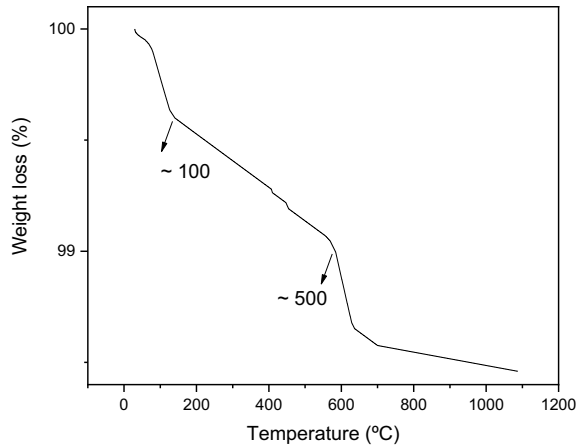
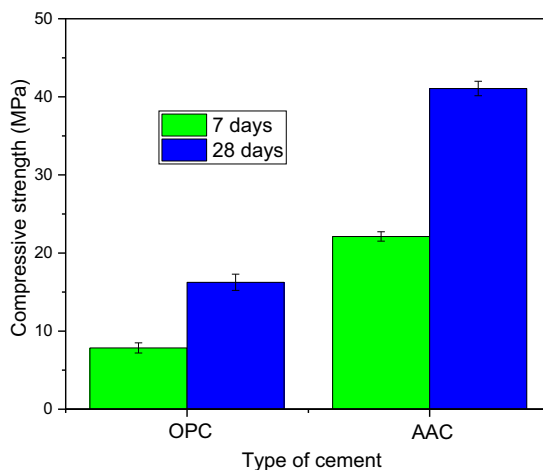


Fig. 6 TGA of BFS



approximately 100 °C, related to the loss of free moisture from the BFS [17]. In the case of activated alkali compounds, this same temperature range is associated with the decomposition of portlandite, which has bound hydroxyls [18]. It is expected that the percentage of mass lost at this temperature is not potentiated after alkaline activation, as the presence of portlandite is an indication of a low AA reaction. In the temperature range of approximately 500–600 °C, another definite event is observed, related to the dehydration of the slag and molecular rearrangement, that is, the crystallization of the glass present in the composition of the slag [13, 17]. This characteristic is beneficial because it highlights the amorphous composition of the material, which is essential for the efficiency of alkaline activation. In the case of AA compounds, hydrotalcite decomposes in this same temperature range. No event is observed associated with approximately 400 °C, related to tobermorite decomposition (C–A–S–H) or to C–S–H. It is expected that the loss of mass at this

Fig. 7 Compressive strength depending on the type of cement



temperature occurs after alkaline activation, since the more intense this event is in the AAC, the greater the amount of tobermorite formed [1, 19].

Figure 7 shows the results of compressive strength at 7 and 28 days of activated alkali cement based on BFS and another based on OPC. It is observed that the composition based on AAC presented superior compressive strength values both at 7 and at 28 days, proving its possibility of application as a substitute cement for OPC. The strength values are higher than OPC cement due to the formation of tobermorite (C–A–S–H), a phase more resistant than the C–S–H formed in the hydration of OPC [10, 11].

Conclusion

After the results, it can be concluded that: the physical characterization of the blast furnace slag indicates that the material has a high specific surface area, proven by particle size and Blaine's method. This proves the feasibility of alkaline activation of the material. Chemical characterization proves that BFS is a calcium-rich precursor, while mineralogical and thermal characterization indicates that the material presents parameters compatible with other works published in the area. Finally, the compressive strength values observed for AAC cement are higher than the values observed for OPC, at 7 and 28 days, due to the formation of more resistant phases, such as tobermorite.

Acknowledgements The authors thank the Brazilian agencies: CNPq, CAPES, and FAPERJ for the support provided to this investigation.

References

1. Marvila MT, Azevedo ARG, Matos PR, Monteiro SN, Vieira CMF (2021) Rheological and the fresh state properties of alkali-activated mortars by blast furnace slag. *Materials (Basel)* 14:2069
2. Isnugroho K, Birawidha DC (2018) The production of pig iron from crushing plant waste using hot blast cupola. *Alexandria Eng J* 57:427–433
3. Schupsky JP, Wu G, Guo M, Müller M (2020) Crystallisation characteristics and crystal phase quantification of a synthetic lignite gasifier slag system. *Fuel Process Technol* 201:106345
4. Srivastava U, Kawatra SK, Eisele TC (2013) Production of pig iron by utilizing biomass as a reducing agent. *Int J Miner Process* 119:51–57
5. Shen D, Jiao Y, Gao Y, Zhu S, Jiang G (2020) Influence of ground granulated blast furnace slag on cracking potential of high-performance concrete at early age. *Constr Build Mater* 241:117839
6. Jo BW, Chakraborty S, Kim KH, Lee YS (2014) Effectiveness of the top-down nanotechnology in the production of ultrafine cement (~220 nm). *J Nanomater* 2014:1–9
7. Wulandari KD, Ekaputri JJ, Triwulan JJ, Kurniawan SB, Primaningtyas WE, Abdullah SRS, Ismail NI, Imron MF (2021) Effect of microbes addition on the properties and surface morphology of fly ash-based geopolymer paste. *J Build Eng* 33:101596
8. Saedi M, Behfarnia K, Soltanian H (2019) The effect of the blaine fineness on the mechanical properties of the alkali-activated slag cement. *J Build Eng* 26:100897
9. Wang XY (2020) Analysis of hydration kinetics and strength progress in cement–slag binary composites. *J Build Eng* 35:101810
10. Marvila MT, Azevedo ARG, Vieira CMF (2021) Reaction mechanisms of alkali-activated materials. *Rev IBRACON Estruturas e Mater* 14:1–26
11. Marvila MT, Azevedo ARG, Delaqua GCG, Mendes BC, Pedroti LG, Vieira CMF (2021) Performance of geopolymer tiles in high temperature and saturation conditions. *Constr Build Mater* 286:122994
12. Associação Brasileira de Normas Técnicas, NBR 5753—Cimento Portland—Ensaio de pozolanicidade para cimento Portland pozolânico, Assoc. Bras. Normas Técnicas (2016)
13. Jamil NH, Abdullah MMAB, Pa C, Mohamad FH, Ibrahim WM, Chairapa AWJ (2020) Influences of SiO₂, Al₂O₃, CaO and MgO in phase transformation of sintered kaolin-ground granulated blast furnace slag geopolymer. *J Mater Res Technol* 9:14922–14932
14. Aziz IH, Abdullah MMAB, Mohd Salleh MAA, Yoriya S, Chairapa J, Rojviriyia C, Li LY (2020) Microstructure and porosity evolution of alkali activated slag at various heating temperatures. *J Mater Res Technol* 9:15894–15907
15. Hakem I, Mustafa M, Bakri A, Salleh MAAM, Aizat E, Chairapa J, Victor A (2020) Strength development of solely ground granulated blast furnace slag geopolymers. *Constr Build Mater* 250:118720
16. Nikolić I, Đurović D, Marković S, Veselinović L, Janković-Častvan I, Radmilović VV, Radmilović VR (2020) Alkali activated slag cement doped with Zn-rich electric arc furnace dust. *J Mater Res Technol* 9(2020):12783–12794
17. Singh R, Gorai AK, Segaran RG (2013) Characterisation of LD slag of Bokaro steel plant and its feasibility study of manufacturing commercial “fly ash-LD slag” bricks. *Int J Environ Technol Manag* 16:129
18. Azevedo ARG, Marvila MT, Rocha HA., Cruz LR, Vieira CMF (2020) Use of glass polishing waste in the development of ecological ceramic roof tiles by the geopolymerization process. *Int J Appl Ceram Technol* 17(6):2649–2658
19. Marvila MT, Azevedo ARG, Alexandre J, Colorado H, Antunes MLP (2021) Vieira CMF (2021) circular economy in cementitious ceramics: Replacement of hydrated lime with a stoichiometric balanced combination of clay and marble waste. *Int J Appl Ceram Technol* 18:192–202

Characterization of Mortar in Fresh State with the Addition of Açai Fiber



A. R. G. Azevedo, D. L. Rocha, T. E. S. Lima, M. T. Marvila, E. B. Zanelato, J. Alexandre, S. N. Monteiro, and H. Colorado

Abstract The natural fiber from açai (*Euterpe oleracea Mart.*) is an example of agro-industrial waste generated in large quantities in Brazil. The objective of this work is to evaluate the technological characteristics of mortars in their fresh state, reinforced with the addition of natural açai fiber, submitted to a type of surface treatment, such as immersion in NaOH, KOH and Ca(OH)₂ in the concentration of 10%. The mixtures have a ratio of 1:3 (cement: sand) with additions of 0 (reference), 1.5, 3.0, and 4.5% of the açai fiber, in relation to the cement mass. Tests were carried out to determine the consistency index, mass density in the fresh state, incorporated air content, and water retention. The results showed that the 4.5% mixture treated with KOH was the one that showed the best results due to its lower density and one of the highest water retentions.

Keywords Açai · Fiber · Mortar · Characterization

A. R. G. Azevedo (✉) · J. Alexandre
LECV—Civil Engineering Laboratory, UENF—State University of the Northern Rio de Janeiro,
Av. Alberto Lamego, 2000, Campos dos Goytacazes, Rio De Janeiro 28013-602, Brazil

J. Alexandre
e-mail: jonas@uenf.br

D. L. Rocha · T. E. S. Lima · M. T. Marvila · E. B. Zanelato
LAMAV—Advanced Materials Laboratory, UENF—State University of the Northern Rio de
Janeiro, Av. Alberto Lamego, 2000, Campos dos Goytacazes, Rio De Janeiro 28013-602, Brazil

S. N. Monteiro
Department of Materials Science, IME—Military Institute of Engineering, Praça General
Tibúrcio, 80, Rio de Janeiro 22290-270, Brazil

H. Colorado
CCCComposites Laboratory, University of Antioquia UdeA, Medellín, Colombia
e-mail: henry.colorado@udea.edu.co

Introduction

Natural products have significantly increased their use in recent years. Among these products, fibers of vegetable origin stand out, which can be used as reinforcement in cementitious composites [1]. The use of natural fibers indicates a potential for strengthening Portland cement-based materials, which can improve the properties of the mortar, when compared to them without the addition of any element [2].

The functionality of the natural fiber depends on its interaction as a binder in the cementitious matrix, and also on its dispersion inside the mixture, these two characteristics form a composite material with good characteristics [3]. The vegetable fibers used are lignocellulosic materials, which can be considered as composites of cellulose fibrils held together by a matrix consisting of lignin and hemicellulose, whose function is to act as a natural barrier to microbial degradation and serve as mechanical protection [4, 5]. Natural fibers are good materials for many applications as they provide very low-cost reinforcing properties, low density, good strength and stiffness, tensile elongation, toughness, and impact resistance [6, 7]. Another important characteristic of natural fibers in a cementitious composite is to neutralize hydraulic shrinkage, characteristic of the mortar during the hardening process [8]. The fiber prevents the formation of cracks inside and on the surface of the plaster. This characteristic makes it suitable to work as a structure reinforcement mortar [9].

In Brazil, there is enormous potential for the extraction of different natural fibers [10]. Açai fiber, for example, is still almost unexplored in the literature, especially when evaluating the conditions of its characteristics in the fresh state in different scenarios of surface treatments [11].

Recent researches have observed an increase in flexural and compressive strengths in composites reinforced with açai fibers, when superficially treated with hydroxides [12]. The fiber used in natura, that is, without any type of treatment ends up being harmful to the composite due to the degradation, it can suffer due to its presence in environments with high alkalinity [13, 14]. The surface treatment increases the proportion of cellulose in the açai fiber, making it stronger and more rigid [15]. Thus, the treatment increases the crystalline cellulose content rate and, consequently, increases the mechanical properties of the composite [16].

Therefore, the present work used açai fibers in different proportions, after its surface treatment with different types of hydroxides (NaOH, Ca(OH)₂ and KOH), thus evaluating the changes in the technological properties in the fresh state of the mortars. All tests were carried out following the standard Brazilian standard for mortars for coating walls and ceilings.

Materials and Methods

The materials used in this research were: Açai fibers and fine aggregates for the production of mortar: natural sand and Ordinary Portland Cement (OPC) type CP

II-E-32. The açai fibers were collected in the city of Rio Novo do Sul—ES—Brazil, in an agroindustry that produces ice cream. The natural sand was collected in the bed of the Paraíba do Sul River, located in the city of Campos dos Goytacazes—RJ. The sand was uniformed in a 24-mm mesh sieve.

- The research methodology of this study was developed as follows:
- Fiber processing and processing methods: Surface treatments were carried out on the açai fibers, in the proportions of 10% hydroxide in relation to the total mass of water, with sodium, potassium, and calcium hydroxides;
- Preparation of mortar with a mixture 1:3:0.75 (cement: sand: water) with a ratio of 0; 1.5; 3.0; and 4.5% of açai fiber added in relation to the cement mass;
- Carrying out technological tests on fresh mortar.

The fiber was collected and cleaned with distilled water. After that, it was dried in an oven at a temperature of 60 °C for 24 h. The surface treatment by hydroxides aims to observe the behavior of the fibrous reinforcement for more than one type of alkaline medium [10]. To formulate the alkaline solution, an amount of 10% by mass of hydroxide in relation to the mass of water was used. For every 1000 g of water, 100 g of alkaline material were mixed [13]. The use of proportions greater than 10% is prohibited because, from this proportion, there is the degradation of the fiber of vegetable origin, due to the destruction of the cellulose crystals contained in the lignin matrix of the fiber [16].

While the solution was being prepared, the fibers were weighed and placed in a separate container. After the solution was ready, it was poured into the container with the fibers, where they were immersed in the solution for a period of 30 min, while they were being stirred, to ensure that all the fibers were exposed to the solution. Subsequently, the fibers are washed with a solution that mixes 300 g of chlorine with 1000 g of water. Cleaning allows you to remove excess hydroxide still contained in the fiber. Afterwards, the fibers were dried in ovens for a period of 24 h. This procedure was stipulated by [13].

The next step consisted of making the mortar. The mixture of 1:3:0.75 (cement: sand: water) is one of the most used in the literature for reinforcement mortars. The mortar was made in accordance with the Brazilian standard [17], which, among other things, specifies the preparation of mortars dosed in the laboratory using a mortar.

Then, the fresh state tests were performed, firstly, the determination of the consistency index [17]. This test consisted of determining the mortar spread on a densification table, after performing 30 consecutive strokes on the mortar. This test is strictly important as it will measure the amount of water used in each mixture. A high percentage of water makes the mortar spread more, and a low percentage makes it little flow. It is worth noting that to maintain a standard in all fiber proportions used, the amount of water from the reference mixture was fixed, i.e., 0% addition of açai fiber. As the value of 0.75 in relation to the cement mass was within the norm, this same value was used in the following tests, although the mortars with fibers had less spread due to the water absorption characteristic of the vegetable fibers.

The determination of mass density and air content of the mortar in its fresh state are standardized by the Brazilian standard [18]. The determination of the incorporated air content was carried out using the pressureometric method. The mortar water retention parameter was obtained using the Brazilian standard [19]. The test procedure consisted of the mortar suction through a funnel, using a vacuum pump, which is a widely used methodology [13].

Results and Discussion

Table 1 shows the results of the consistency tests. It was evident that the greater the proportion of fiber, the greater the absorption of water and therefore the workability of the mortar reduces, as occurred in the works [23, 24].

The alkaline treatment carried out on the reference mixture, the one that does not have added fiber in the mixture, was 260 mm. With the increase in fibers, the workability was reduced, proportionally to the greater proportion of fibers. The treatment with NaOH proved to be the one that absorbed the most water, obtaining the lowest workability, while the treatment with KOH proved to be the most water repellent, with higher workability's, in the proportions of 1.5 and 3%. Such results were also found by [20], who noted that samples treated with KOH gave better water repellency results compared to samples treated with NaOH for coconut fibers. At 4.5%, their workability was close. As [21] noted that, in general, samples treated with NaOH gave moderate results in terms of water repellent property. In relation to $\text{Ca}(\text{OH})_2$, [22] observed that when subjected to this treatment, there is a drop in the water adsorption capacity, to a certain extent. However, the adsorption is still lower than the treatment with NaOH, which is based on the fact that the treatment with NaOH is the most aggressive to fiber, as demonstrated by [23, 24]. Analyzing Table 1, it was concluded that the workability was lower in the treatment with NaOH, followed by $\text{Ca}(\text{OH})_2$, and finally KOH, with a small variation for the proportion of 4.5%.

In the fresh mass density test (Fig. 1), a decrease in the density value was observed in all mixtures that used fiber in their matrix, this can be attributed to a decrease in the density of the mortar, associated with an increase in its porosity [10], or due to adsorption of water by the greater amount of vegetable fibers [27].

Note that treatments with hydroxides that showed lower workability also showed lower density. The lower density is an important characteristic for the materials used as mortar for reinforcement, as they can guarantee greater mechanical strength to

Table 1 Consistency test results

Alkaline Treatment	0%	1.5%	3.0%	4.5%
NaOH	260 mm	254 mm	252 mm	251 mm
$\text{Ca}(\text{OH})_2$		257 mm	255 mm	240 mm
KOH		260 mm	255 mm	226 mm

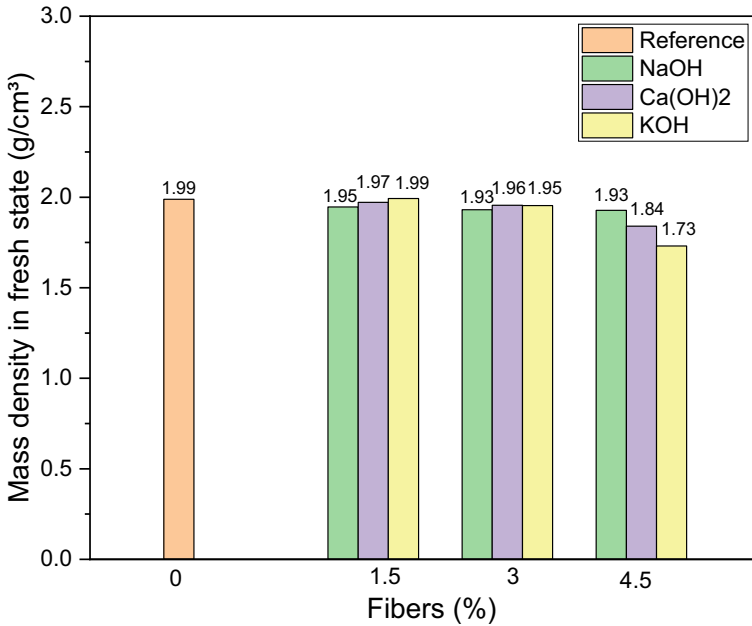


Fig. 1 Result of the density test in the fresh state of mortars

compression, generating a lower weight for the system. The research results observed that in the proportions of 1.5 and 3% the lowest density is obtained in composites reinforced with fibers treated with NaOH. Possibly due to the high adsorption of water occurring in these fibers.

Meanwhile, at 4.5%, the situation is reversed. The densities of mortars with fibers treated with Ca(OH)₂ and KOH were lower than those treated with NaOH, with values of 1.84 and 1.73 g/cm³, respectively. It is assumed that, in this proportion, it is not the adsorption of water that explains the low density, but the large amount of voids, as demonstrated [7]. The incorporated air content test can be used to analyze the void ratio.

In the embedded air content test, it was observed that all mortars are within the limits of the embedded air values proposed in the standard literature [6], which is from 7 to 17% for reinforcement applications. The addition of natural fiber increases the air content incorporated into the product. As the percentage of fiber addition increases, due to additions of reinforcing materials the surface contact area between the matrix and the reinforcement also increases. Therefore, observing Fig. 2, it can be seen that the low density of the mortar reinforced with 4.5% of fiber treated with KOH is due to its high content of incorporated air.

In the other proportions, such as 1.5%, there were no variations between treatments, while in the proportion of 3%, we observed an incorporated air content slightly higher in the proportion of NaOH, but not enough to cause such significant density variations.

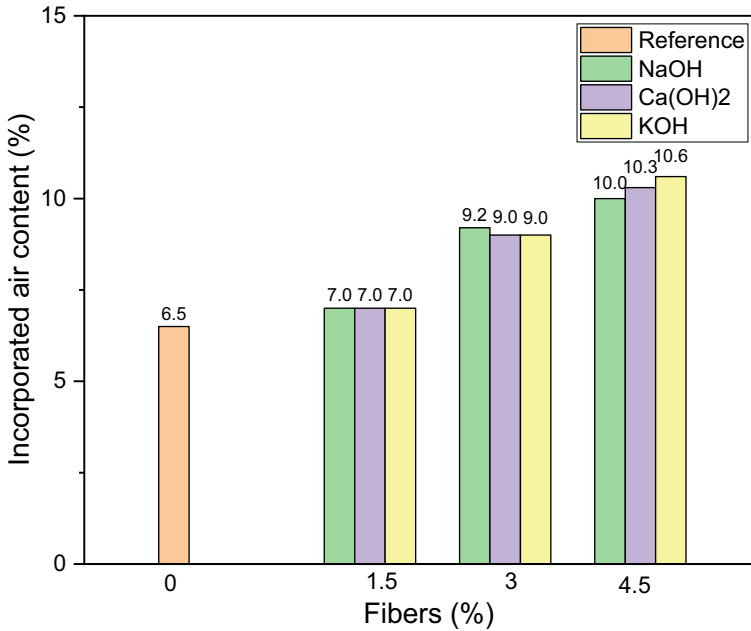


Fig. 2 Result of the incorporated air content test

Finally, Fig. 3 shows the results of the water retention test. Water retention is a property directly linked to the ability of the mortar to maintain its workability properties when subjected to water loss. Natural fibers, due to their hydrophilic character, have a high-water retention capacity, as previously mentioned [5]. Note that the higher the percentage of fibers, the greater the capacity to retain water, as these are trapped inside the fibers. However, this water trapped inside the fiber greatly reduces the consistency values of the mortar, as shown in Table 1. Once inserted into the mortar, the fibers remove the water from the mixture. Therefore, the water retention test little reduced the proportion of water in the mortars, since these are already retained in the fibers at the time of manufacture. The same was observed by [9] who found that the retained water is impregnated in the fibers and not in its free form, not contributing to the hydration of the mortar.

In this trial it was noted that no treatment stood out more than the other, as they had very similar results. Varying the percentage value of its retention for each proportion increase the insertion of the açai fiber. Note that all mortars were within the norm [21–23] with a water retention greater than 97%

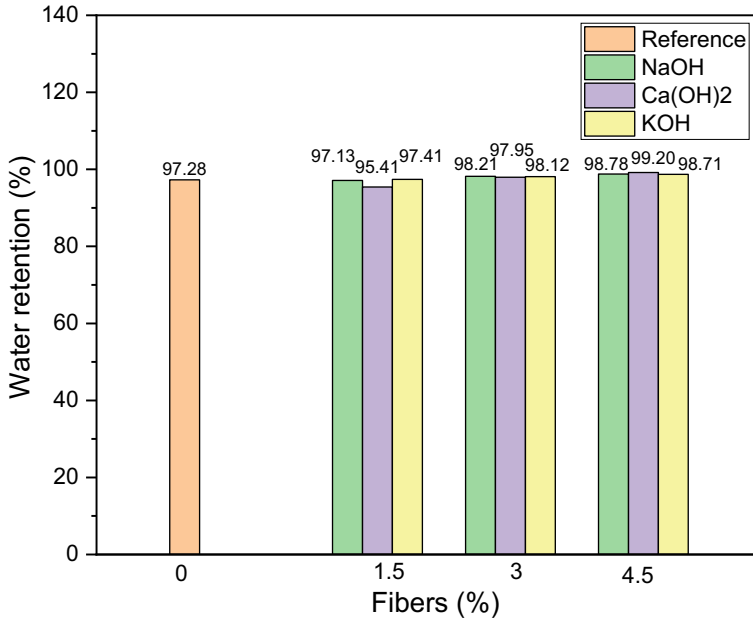


Fig. 3 Result of the water retention test

Conclusion

It can be concluded from this research that the mixtures of mortar with natural açai fibers treated with different hydroxides resulted in changes in their technological properties in the fresh state of the mortars. If, on the one hand, the workability dropped drastically due to the greater insertion of the natural fiber, on the other hand, there was a reduction in density, which is positive as it allows the system to work with lighter materials.

The treated fibers greatly increase the consistency of the mortar, however, after that, even when it is subjected to suction, it varies little in relation to its water retention. As for the incorporated air content, it was noticed that the fibers increased the number of voids inside the mortar in the regions between the fiber and the matrix. These larger spaces are filled with air. It was noted that the mixture that had the highest air retention was the 4.5% mixture treated with KOH, it also had the lowest density and one of the highest water retentions. In other words, this mixture was the one that absorbed the most water, becoming less dense and increasing the space for the air inside the matrix.

Acknowledgements The authors thank the Brazilian agencies: CNPq, CAPES, and FAPERJ for the support provided to this investigation.

References

1. Kareche A, Agoudjil B, Haba B, Boudenne A (2020) Study on the durability of new construction materials based on mortar reinforced with date palm fibers wastes. *Waste Biomass Valorization* 11(7):3801–3809. <https://doi.org/10.1007/s12649-019-00669-y>
2. Bayapureddy Y, Muniraj K, Mutukuru MRG (2020) Sugarcane bagasse ash as supplementary cementitious material in cement composites: strength, durability, and microstructural analysis. *J Korean Ceram Soc* 57(5):513–519. <https://doi.org/10.1007/s43207-020-00055-8>
3. De Azevedo, ARG, Alexandre, J, Marvila, MT, Xavier, GC, Monteiro, SN, Pedroti LG (2020) Technological and environmental comparative of the processing of primary sludge waste from paper industry for mortar. *J Clean Prod* 32
4. Covino C, Sorrentino AD, Pierro P, Roscigno G, Vece AP, Masi P (2020) Lignocellulosic fibres from enzyme-treated tomato plants: characterisation and application in paperboard manufacturing. *Int J Biol Macromol* 161:787–796. <https://doi.org/10.1016/j.ijbiomac.2020.06.077>
5. Cherief M, Belaadi A, Bouakba M, Bourchak M, Meddour I (2020) Behaviour of lignocellulosic fibre-reinforced cellular core under low-velocity impact loading: Taguchi method. *Int J Adv Manuf Technol* 108(1–2):223–233. <https://doi.org/10.1007/s00170-020-05393-9>
6. Azevedo A, De Matos P, Marvila M, Sakata R, Silvestro L, Gleize P, De Brito J (2021) Rheology, hydration, and microstructure of portland cement pastes produced with ground açai fibers. *Appl Sci (Switzerland)* 11(7):15–26
7. Rocha DL, Azevedo ARG, Marvila MT, Cecchin D, Alexandre J, Carmo DF, Rossi G (2021) Influence of different methods of treating natural açai fibre for mortar in rural construction. *Agronomy Res* 19(Special Issue 1):910–921. <https://doi.org/10.15159/AR.21.062>
8. Azevedo ARG, Marvila MT, Zanelato EB, Lima TES, Cecchin D, Souza JS, Xavier GC (2021) Evaluation of different methods of surface treatment of natural açai fiber added in cementitious composites. https://doi.org/10.1007/978-3-030-65493-1_37
9. de Azevedo ARG, Marvila MT, Antunes MLP, Rangel EC, Fediuk R (2021) Technological perspective for use the natural pineapple fiber in mortar to repair structures. *Waste Biomass Valorization*. <https://doi.org/10.1007/s12649-021-01374-5>
10. Marvila MT, Azevedo ARG, Cecchin D, Costa JM, Xavier GC, de Fátima do Carmo D, Monteiro SN (2020) Durability of coating mortars containing açai fibers. *Case Stud Constr Mater* 13. <https://doi.org/10.1016/j.cscm.2020.e00406>
11. Neuba LM, Pereira Junio RF, Ribeiro MP, Souza AT, Lima ES, Filho FCG, Azevedo ARG, Monteiro SN (2020) Promising mechanical, thermal, and ballistic properties of novel epoxy composites reinforced with cyperus malaccensis sedge fiber. *Polymers* 12(8). <https://doi.org/10.3390/polym12081776>
12. Deb S, Mitra N, Maitra S, Basu Majumdar S (2020) Comparison of mechanical performance and life cycle cost of natural and synthetic fiber-reinforced cementitious composites. *J Mater Civil Eng* 32(6). [https://doi.org/10.1061/\(ASCE\)MT.1943-5533.0003219](https://doi.org/10.1061/(ASCE)MT.1943-5533.0003219)
13. de Azevedo ARG, Marvila MT, Tayeh BA, Cecchin D, Pereira AC, Monteiro SN (2021) Technological performance of açai natural fibre reinforced cement-based mortars. *J Build Eng* 33. <https://doi.org/10.1016/j.jobe.2020.101675>
14. Selen L, Panthi KK, Vistnes G (2020) An analysis on the slaking and disintegration extent of weak rock mass of the water tunnels for hydropower project using modified slake durability test. *Bull Eng Geol Env* 79(4):1919–1937. <https://doi.org/10.1007/s10064-019-01656-2>
15. Wei J, Meyer C (2015) Degradation mechanisms of natural fiber in the matrix of cement composites. *Cem Concr Res* 73:1–16. <https://doi.org/10.1016/j.cemconres.2015.02.019>
16. Tatleri M, Sailer N, Ulven CA, Wiesenborn DP, Tostenson K, Polansky P, Krog A (2006) Vegetable oil-based epoxy resin for structural composite material manufacturing. In: Paper presented at the American society for composites—21st technical conference of the American society for composites 2006, vol 2, pp 851–861
17. Brazilian Association of Technical Standards (2016) NBR 13276: Mortar for laying and coating walls and ceilings—determination of consistency index. ABNT, Rio de Janeiro (in Portuguese)

18. Brazilian Association of Technical Standards (2005) NBR 13278: Mortar for laying and coating walls and ceilings—determination of mass density and incorporated air content. ABNT, Rio de Janeiro (in Portuguese)
19. Brazilian Association of Technical Standards (2005) NBR 13277: Mortar for laying and coating walls and ceilings—determination of water retention. ABNT, Rio de Janeiro (in Portuguese)
20. David AO, Chukwuemeka IS, Osther EE, Salihu GN (2021) Development and characterization of hybrid coconut/glass fibers reinforced low density polyethylene composites for bumper application. *Metall Mater Eng* 27(1):89–104. <https://doi.org/10.30544/453>
21. Sang Y, Zhao JR (2015) Reduction of water absorption capacity of cellulose fibres for its application in cementitious materials. *J Compos Mater* 49(22):2757–2763. <https://doi.org/10.1177/0021998314554123>
22. Sari NH, Padang YA (2019) The characterization tensile and thermal properties of hibiscus tiliaceus cellulose fibers. In: Paper presented at the IOP conference series: materials science and engineering, vol 539, no 1. <https://doi.org/10.1088/1757-899X/539/1/012031>
23. Azevedo ARG, Cecchin D, Carmo DF, Silva FC, Campos CMO, Shtrucka TG, Mavila MT, Monteiro SN (2020) Analysis of the compactness and properties of the hardened state of mortars with recycling of construction and demolition waste (CDW). *J Mater Res Technol* 9(3):5942–5952. <https://doi.org/10.1016/j.jmrt.2020.03.122>

Characterization of Slag and Growth of Ferronickel Grains During Smelting of Nickel Laterite Ore



Donglai Ma, Jianbo Zhao, Hanghang Zhou, and Zhixiong You

Abstract The growth of ferronickel particles and separation of metal fraction from slag fraction are essential during the pyrometallurgical smelting nickel laterite ore. Thus, many measures were adopted to regulate the properties of slag and metal fractions. In this study, Na_2S , Na_2CO_3 , and FeO were used to regulate the properties of a basic slag (64 wt.% SiO_2 –9 wt.% Al_2O_3 –3 wt.% CaO –24 wt.% MgO). The liquid phase content and melting temperature of different slag compositions were determined from the view of thermodynamics. Then, growth behaviors of ferronickel particles in the presence of different additives were investigated. The experimental results indicated that the average diameter of ferronickel particles increased from $<10\ \mu\text{m}$ to larger than $35\ \mu\text{m}$ when 3.3% Na_2S was added, comparing to an average diameter less than $30\ \mu\text{m}$ by adding the other two additives. The effect of Na_2S was proved to be the most efficient.

Keywords Nickel laterite ore · Direct reduction · Metal growth · Metal–slag separation

Introduction

The demand for nickel resources has soared with the increase in global consumption of stainless steel [1]. The main sources of nickel are nickel sulfide and laterite nickel ores [2]. With the depletion of nickel sulfide ore, the efficient utilization of laterite nickel ore accounting for approximately 72% of global nickel resources has become more attractive [3]. Many techniques have been used to extract nickel from laterite ore, which are classified as pyrometallurgical, hydrometallurgical, and pyro–hydrometallurgy processes. Pyrometallurgical processes gradually hit the mainstream for saprolite-type ore, including rotary kiln–electric furnace (RKEF), sintering–blast furnace smelting, Krupp–Renn (Nippon Yakin Oheyama), and direct reduction–magnetic separation processes [4–6]. In recent years, many scholars have

D. Ma · J. Zhao · H. Zhou · Z. You (✉)

College of Materials Science and Engineering, Chongqing University, Chongqing 400044, China
e-mail: youzx@cqu.edu.cn

© The Minerals, Metals & Materials Society 2022

M. Zhang et al. (eds.), *Characterization of Minerals, Metals, and Materials 2022*,

The Minerals, Metals & Materials Series,

https://doi.org/10.1007/978-3-030-92373-0_24

conducted a lot of research on the direct reduction–magnetic separation process. Since the reduction procedure is carried out at a relatively low temperature, the energy consumption can be saved [7].

However, in order to promote the magnetic separation of ferronickel, it is necessary to enhance the reduction process as well as the growth of ferronickel grains. Formation of regional liquid phase has been proved to be effective for metal growth and preliminary metal–slag separation. Metal and slag represent the magnetic fraction (ferronickel) and nonmagnetic fractions, respectively. The method of generating regional liquid phase during the direct reduction process is classified as adjusting the properties of slag or metal fractions by using different additives. The slag will melt locally into the liquid phase when the temperature rises to a certain level during the laterite nickel smelting process [8]. The liquid phase can promote the growth of ferronickel particles and the slag–metal separation obviously, because it can act as a carrier for the movement of ferronickel grains [9]. Hence, the high-temperature properties of the slag need to be taken into consideration.

In general, a rise in temperature is conducive to the formation of more liquid, but it will also cause more problems in terms of energy consumption [10]. Additives such as CaSO_4 , Na_2SO_4 , and Na_2CO_3 can change the phase composition of the slag and reduce the melting temperature of the slag phase, thus saving much energy [11–13]. At the same time, additives can affect viscosity, wettability, and other high-temperature properties of the slag, so as to improve the fluidity of the slag liquid phase [14–16].

In this study, the effects of Na_2S , Na_2CO_3 , and FeO on the liquid content and melting temperature of the slag were investigated. The variation of the slag liquid phase content and melting temperature with additives was determined by thermodynamic calculation. Then, the effects of different additives on the growth of ferronickel grains were investigated. Finally, the onset temperature of metal–slag separation was determined by using high-temperature confocal scanning laser microscopy (CSLM).

Experimental

Materials

Chemical reagents, including SiO_2 , Al_2O_3 , CaO , and MgO (purity greater than 99.99%) were used to synthesize a primary slag. These reagents were proportioned at 64 wt.% SiO_2 –9 wt.% Al_2O_3 –3 wt.% CaO –24 wt.% MgO and pre-melted. Ferronickel mixture contained 10 wt.% Ni and 90 wt.% Fe was uniformly mixed and used as the metal fraction. The mixture was milled to less than 10 μm with a high-energy ball mill. Other reagents including Na_2S , Na_2CO_3 , and FeO (purity greater than 99.99%) were employed to regulate the properties of slag.

Table 1 The mass fraction of different additives

	Mass fraction/%			
Na ₂ S	0	1.10	2.20	3.30
Na ₂ CO ₃	0	1.49	2.98	4.47
FeO	0	2.00	4.00	6.00

Methods

Firstly, the synthetic slag was milled to less than 10 μm by using a high-energy ball mill. The slag–metal sample was obtained by mixing the synthetic slag with ferronickel mixture at a mass ratio of 73.56: 26.44. Then, the additives were weighed according to Table 1, and mixed into the slag–metal sample. In Table 1, the mass fraction of Na₂S and Na₂CO₃ is determined by keeping moles of Na consistent. The mass fraction of FeO is determined by referring to the actual production process.

The mixture of ferronickel, slag, and additives were pressed into pellets with a diameter of 30 mm under a pressure of 15 Mpa and roasted at 1300°C for 60 min. Optical microscope was used to observe the microstructure of samples after roasting, and the image processing software of ImageJ Pro was used to count the area and number of metallic particles in the micrograph. The average area (S) of the particles can be obtained when the total area and number of the particles were known. The average diameter (d) of the particles was calculated by the formula of $d = 2\sqrt{S/\pi}$. In Situ observation using confocal scanning laser microscopy (CSLM) was carried out to observe the metal–slag separation behavior. The schematic diagram of CSLM is shown in Fig. 1.

Results and Discussion

Effects of Additives on Liquid Phase Content

The effect of different additives on liquid slag content was calculated, and the results are presented in Fig. 2. The additives have a positive effect on the formation of liquid phase, and it can be found that the liquid slag contents increased obviously after adding additives. Within the experimental additive content, the liquid slag content in the presence of Na₂S was significantly higher than that with Na₂CO₃ and FeO at 1300 °C. The liquid phase content reached 47.86% as the Na₂S content was increased to 3.3%. It is inferred that the sequence of additive content affecting the liquid slag content was determined as follows: Na₂S > Na₂CO₃ > FeO.

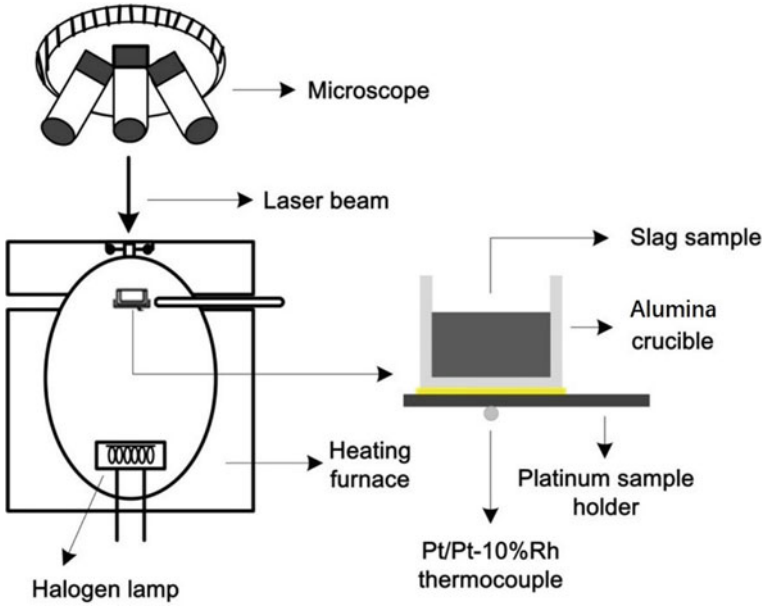
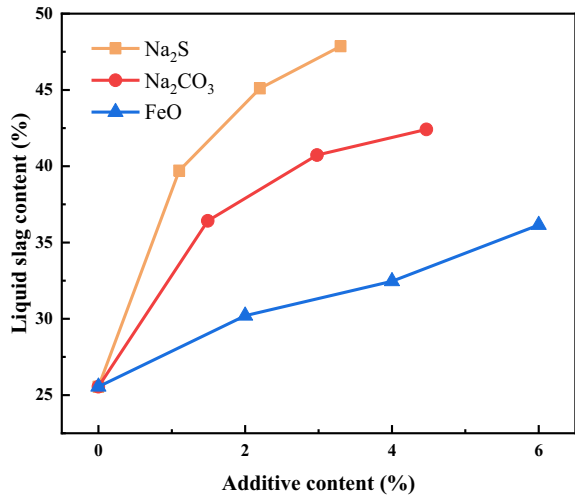


Fig. 1 Schematic diagram of confocal scanning laser microscopy

Fig. 2 Effect of additives on the liquid slag content



Effects of Additives on Melting Temperature

Slag (nonmagnetic fraction in direct reduction of nickel laterite ore) is a mixture having no fixed melting point, whose melting temperature was the range between

the initial melting temperature and the complete melting temperature. The effect of additives on the initial melting temperature and the complete melting temperature was calculated, and the results are shown in Figs. 3 and 4. It can be seen that the initial melting temperature and the complete melting temperature gradually decreased with the increase of additive content. When 3.3% Na_2S was added, the initial melting temperature and complete melting temperature decreased to 1075.51 °C and 1376.18 °C, respectively. At the same time, the melting temperatures were 1107.34 °C and 1390.46 °C under 4.47% Na_2CO_3 . By adding 6% FeO , the initial and complete melting temperatures decreased to 1197.76 °C and 1397.77 °C. Thus, it can be concluded that the most effective additive in decreasing the melting temperature of slag is Na_2S , and followed by Na_2CO_3 , FeO .

Fig. 3 Effect of additive content on initial melting temperature

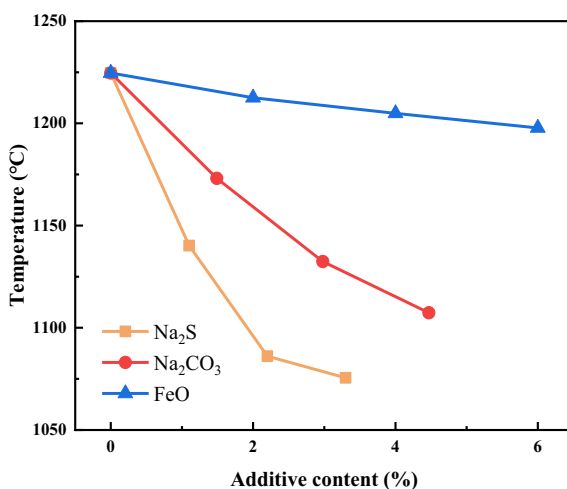


Fig. 4 Effect of additive content on complete melting temperature

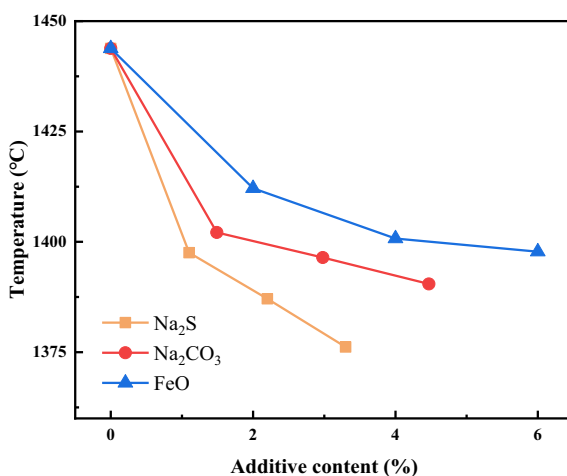
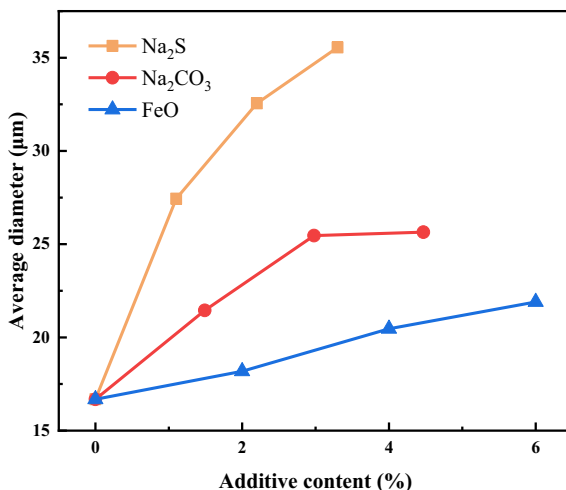


Fig. 5 Effect of additives content on ferronickel growth



Effects of Additives on Ferronickel Growth and Metal–Slag Separation

In order to investigate the influence of additives on the growth of ferronickel grains, the average diameter of ferronickel particles in the presence of different additives was measured. The experiments were carried out at 1300 °C. The results in Fig. 5 indicate that the average diameter increased from 16.68 μm to more than 20 μm with the addition of Na₂S, Na₂CO₃, and FeO. When 3.3% of Na₂S was added, the diameter of ferronickel increased to 35.55 μm. It was noteworthy that the average diameter was almost unchanged when Na₂CO₃ was 2.98–4.47%, but the liquid content increased by 1.68% (as shown in Fig. 2). It could be inferred that the liquid phase content was not the only factor that promotes the growth of metal particles. The high-temperature properties of the slag phase were also worth consideration.

It is concluded that the effect of Na₂S content on the average diameter of ferronickel particles was the most remarkable. Microstructure of roasting pellets with different Na₂S content were studied by optical microscope analysis in order to understand the growth of ferronickel grains varying the Na₂S content from 0 to 3.3%. The results are plotted in Fig. 6, in which bright areas represented ferronickel. It can be seen that with the increase of Na₂S content, the amount of small-size ferronickel particles decreased gradually, and the amount of big-size particles gradually increased. Ferronickel particles were mostly flaky. It can be concluded that the small ferronickel particles were irregularly distributed throughout the pellets in the absence of additive. With increase in the Na₂S content, the small ferronickel particles gradually began to gather to the larger ones. Finally, flake ferronickel particles were formed.

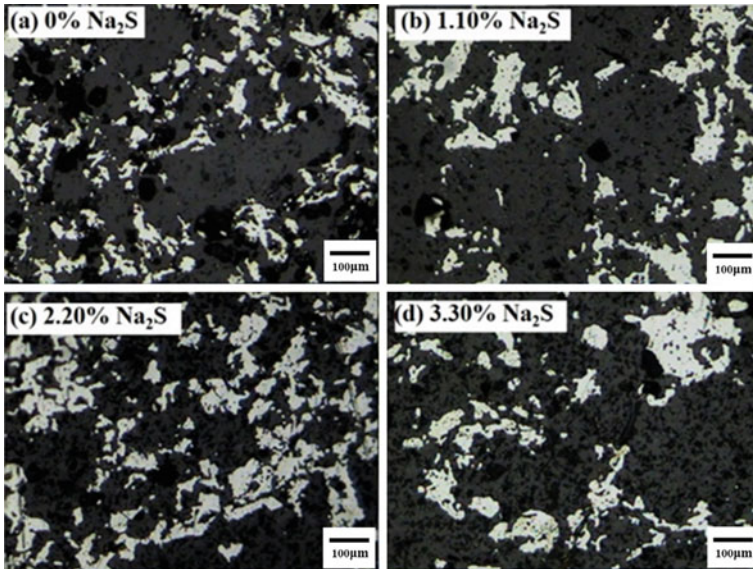


Fig. 6 Microstructures of roasting pellets with different Na_2S content (Bright area: ferronickel)

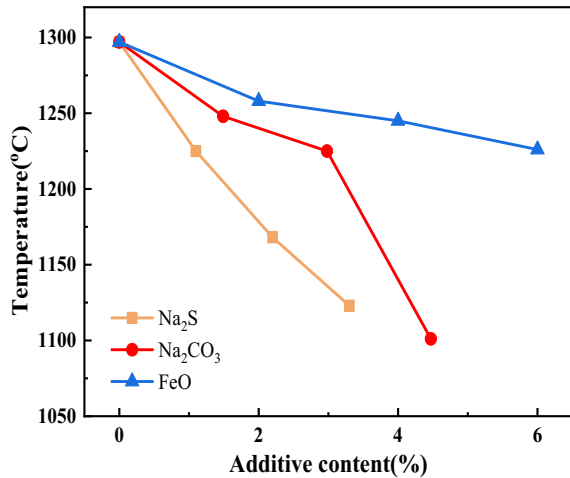
To investigate the temperature at which the slag or metal fractions begin to gather, a metal–slag separation start temperature was defined as being defocused temperature due to the start of liquid slag or iron droplets coalescence [17, 18]. Slag–metal separation is the starting point for the growth of ferronickel grains, which is of great significance to the study of the growth and subsequent separation of ferronickel particles from nonmagnetic fraction. In situ observation carried out by CSLM was used to investigate the metal–slag separation behavior. the onset temperature of metal–slag separation under different additives was determined, and the results are shown in Fig. 7.

As shown in Fig. 7, the lowest onset temperature of metal–slag separation was 1101 °C with 4.47% Na_2CO_3 . The temperature decreased from 1297 to 1123 °C with increase of Na_2S content from 0 to 3.3%, and it dropped from 1297 to 1126 °C with 0–6% FeO. Compared with the results in Fig. 3, the temperature was higher than the initial melting temperature and lower than the complete melting temperature, which meant slag–metal separation occurs after existing a certain amount of liquid phase.

Conclusions

The additives of Na_2S , Na_2CO_3 , and FeO were effective fluxing agents that can promote the formation of liquid phase that was beneficial to the growth of ferronickel grains. In the experimental range of additives, Na_2S was the most effective than other

Fig. 7 Effect of additives on the the onset temperature of metal–slag separation



additives ($\text{Na}_2\text{S} > \text{Na}_2\text{CO}_3 > \text{FeO}$). As the Na_2S content increased from 0 to 3.30%, the liquid phase content reached the maximum of 47.86%, and the average diameter increased from 16.68 to 35.55 μm . These additives were also capable of decreasing the initial, complete melting temperatures and the onset temperature of metal–slag separation. The onset temperature of metal–slag separation decreased from 1297 to 1101 °C after adding 4.47% Na_2CO_3 . In most cases, the onset temperature of metal–slag separation was within the range of melting temperature, indicating that certain liquid phase content provides a material basis for the beginning of metal–slag separation.

Acknowledgements The authors are grateful to the National Natural Science Foundation of China (51904047), the Fundamental and Frontier Research Project of Chongqing, China, (cstc2020jcyj–msxmX0515) and the State Key Laboratory of Complex Nonferrous Metal Resources Clean Utilization for the financial support of this research.

References

1. Zeng X, Xu M, Li J (2018) Examining the sustainability of China’s nickel supply: 1950–2050. *Resour Conserv Recy* 139:188–193
2. Zhang B, Liu G, Liu Y et al (2020) Analysis of world nickel ore resources and market. *China Resour Compr Util* 38(7):94–98
3. Janelle ZK, Nawshad H, Sankar B (2017) Process simulation and exergy analysis of two nickel laterite processing technologies. *Int J Miner Process* 161:83–93
4. Li G, Wang J, Rao M et al (2020) Coprocessing of stainless-steel pickling sludge with laterite ore via rotary kiln–electric furnace route: enhanced desulfurization and metal recovery. *Process Saf Environ* 142:92–98
5. Lv X, Bai C, He S et al (2010) Mineral change of Philippine and Indonesia nickel lateritic ore during sintering and mineralogy of their sinter. *ISIJ Int* 50(3):380–385

6. Gao L, Liu Z, Pan Y et al (2019) Separation and recovery of iron and nickel from low-grade laterite nickel ore using reduction roasting at rotary kiln followed by magnetic separation technique. *Mining Metall Explor* 36:375–384
7. Ciftci H, Atik S, Gurbuz F (2018) Biocatalytic and chemical leaching of a low-grade nickel laterite ore. *Metall Res Technol* 115(3):305
8. Yuan S, Zhou W, Li Y et al (2020) Efficient enrichment of nickel and iron in laterite nickel ore by deep reduction and magnetic separation. *T Nonfer Metal Soc* 30(3):812–822
9. Silveira RF, Fernandez OJ, Luz PT et al (2020) Thermal transformations of the nickel laterite agglomerate phases and their metallurgical influence. *Mater Sci Forum* 6122:337–342
10. Zhang Y, Cui K, Wang J et al (2020) Effects of direct reduction process on the microstructure and reduction characteristics of carbon-bearing nickel laterite ore pellets. *Powder Technol* 376:496–506
11. Tian H, Jian P, Zhu D et al (2020) Improved beneficiation of nickel and iron from a low-grade saprolite laterite by addition of limonitic laterite ore and CaCO_3 . *J Mater Res Technol* 9:2578–2589
12. Zulfiadi Z, Windu S (2021) Evolution of ferronickel particles during the reduction of low-grade saprolitic laterite nickel ore by coal in the temperature range of 900–1250 °C with the addition of CaO – CaF_2 – H_3BO_3 . *Int J Min Met Mater* 28(4):612–620
13. Yayat IS, Iqbal HS, Sudibyo (2019) Preliminary study of smelting of Indonesian nickel laterite ore using an electric arc furnace. *Mater Today: Proc* 13:127–131
14. Liu Y, Lv X, You Z et al (2020) Kinetics study on non-isothermal carbothermic reduction of nickel laterite ore in presence of Na_2SO_4 . *Powder Technol* 362:486–492
15. Pedro PM, Reiner N, Iranildes DS et al (2019) Nickel carriers in laterite ores and their influence on the mechanism of nickel extraction by sulfation-roasting-leaching process. *Miner Eng* 131:90–97
16. Yang J, Zhang G, Oleg O et al (2019) Selective reduction of an Australian garnieritic laterite ore. *Miner Eng* 131:79–89. <https://doi.org/10.1016/j.mineng.2018.10.018>
17. Kim HS, Kang Y, Jang G et al (2011) The role of iron oxide bearing molten slag in iron melting process for the direct contact carburization. *ISIJ Int* 51(1):166–168
18. Minsoo S, Soonki M, Joonho L et al (2012) In-Situ observation of the carburization of solid iron by graphite. *Met Mater Int* 18:1041–1047

Characterization of Soil from Areas Degraded by Mining Activity in Campos dos Goytacazes-RJ, Brazil



A. R. G. Azevedo, J. G. F. Brainer, M. T. Marvila, G. C. Xavier,
and S. N. Monteiro

Abstract The clay mineral extraction activity for the production of ceramic artifacts generates huge problems related to the degraded areas. The objective of this research was a physical, chemical, and mineralogical characterization of different soils from regions degraded by the mining activity, located in the municipality of Campos dos Goytacazes, RJ, Brazil. Five soil samples were collected (1 and 2: soil located in São Sebastião—Campos dos Goytacazes—Brazil; 3, 4, and 5: soil located in Saturnino Braga—Campos dos Goytacazes—Brazil) and characterized according to their technological and environmental parameters in order to compare their results by the literature and the Brazilian standard, and to verify the potential environmental problem that occurred. The results showed that samples 1 and 2 were contaminated by organic fuel, possibly from leaks from trucks that extract the still active deposit. The sample 3, on the other hand, presented itself as rich in iron, being a factor to be considered in the remediation technique to be used in this area.

Keywords Characterization · Areas degraded · Mining Activity

A. R. G. Azevedo (✉) · J. G. F. Brainer · G. C. Xavier
LECIV—Civil Engineering Laboratory, UENF—State University of the Northern Rio de Janeiro,
Av. Alberto Lamego, 2000, Campos dos Goytacazes, Rio De Janeiro 28013-602, Brazil

G. C. Xavier
e-mail: gxavier@uenf.br

M. T. Marvila
LAMAV—Advanced Materials Laboratory, UENF—State University of the Northern Rio de
Janeiro, Av. Alberto Lamego, 2000, Campos dos Goytacazes, Rio De Janeiro 28013-602, Brazil

S. N. Monteiro
Department of Materials Science, IME—Military Institute of Engineering, Square General
Tibúrcio, 80, Rio de Janeiro 22290-270, Brazil

Introduction

The recovery of degraded areas is a legal duty guaranteed by the Brazilian Constitution of 1981 after the reformulation of Law number 6.938/81 (National Policy on the Environment) and the promulgation of the Federal Constitution of 1988, where National Council for the Environment (CONAMA) is responsible for submitting forms and assisting guidelines aimed at environmental quality [1, 2]. It is undeniable that the mining activity contributes to great impacts on the environment, since the practice of mineral extraction often implies the suppression of vegetation, thus exposing the soil to physical, chemical and biological weathering processes [3].

Thus, the greatest socio-economic and environmental losses of mining come from environmental degradation by anthropic action, as there is a loss of CO₂ capture, loss of forest products, and ultimately the loss of livelihoods of the population that directly uses the resources of the forest. It is evident, therefore, a negative interference of the consequences of mining in people's lives, but that this problem often goes unnoticed [4].

In Brazil, the mining activity has great extractive potential and consequently economic, thus the country focused on national development, aims to promote and encourage through public policies and legislation the practice of mineral exploration [5]. Since the proportion of incentive to mineral exploration and recovery of degraded areas is unbalanced, due to the prioritization of the economic pillar at the expense of the ecological one, there is a need for sustainability.

Clay mining aims to obtain clayey sediments, the classification is given by very fine grains, below 1/256 mm (4 μm) in diameter. They can be formed by only one clay mineral, but the most common is to be formed by a mixture of them, with a predominance of one mineral. Such product from sedimentary rocks is associated with oxides that will confer tone and properties [6, 7].

Given the ancient importance of clay, with ceramic material (clay and/or pure oxides) being one of the main materials used in civil construction [8], the city of Campos dos Goytacazes located in the North of the State of Rio de Janeiro, Brazil, where there is an abundance of clay mineral, there is an exploration and with it the degradation of such areas. Therefore, the objective of this research was a physical, chemical, and mineralogical characterization of five different soils from regions degraded by the mining activity, located in the municipality of Campos dos Goytacazes, RJ, Brazil. In view of the objective, revegetation and the conduction of natural regeneration provide the recovery of fauna and flora, affirming biodiversity and ensuring environmental, social and economic balance [9, 10].

Materials and Methods

The Campos dos Goytacazes region (Fig. 1) is located in the north of the state of Rio de Janeiro, being crossed by the Rio Paraíba do Sul. The soil in this region comes

Fig. 1 Location of the soil collection region [12]



from a sedimentary basin that, in the case of some regions, is widely used for mineral extraction activities for the ceramic industry [11].

For this research, five soil sample collection points were selected for characterization. The criteria for choosing these deposits were the depth of extraction, location, whether or not they are in mining activity, occupation of the area after the mining process and occupation of the area before mining, as shown in Table 1.

Table 1 Criteria for choosing the soil collection areas

Sample	Extraction depth (m)	Localization	Whether or not you are in mining activity	Occupation of the area after the mining process	Occupation of the area before mining
01	0.90	São Sebastião—Campos dos Goytacazes—Brazil	Yes	—	Animal pasture area
02	1.20	São Sebastião—Campos dos Goytacazes—Brazil	Yes	—	Animal pasture area
03	1.35	Saturnino Braga—Campos dos Goytacazes—Brazil	No	Degraded area unused	Animal pasture area
04	1.10	Saturnino Braga—Campos dos Goytacazes—Brazil	No	Degraded area unused	Animal pasture area
05	0.95	Saturnino Braga—Campos dos Goytacazes—Brazil	No	Degraded area unused	Animal pasture area

For soil collection, a standard procedure was performed on all samples, where the surface layer of soil was first removed by scraping the A horizon, which has an accumulation of organic matter mixed with surface mineral material. Layer may be contaminated with other transient elements in the system, defrauding the results obtained [13, 14]. After removing the surface layer, the site was excavated with manual instruments to a depth determined in Table 1, which was delimited according to local conditions, such as potential exposure of the water table in some cases. Each sample was collected in triplicate, being properly identified and transported to the characterization laboratory.

The physical characterization of the soil samples was performed with particle size analysis, according to the prescription of ABNT NBR 7181:1984 [15], which consists of a combination of sieving and material sedimentation. In addition, part of the sample was collected to verify the hygroscopic moisture and actual grain density of each of the samples, according to the prescription of ABNT NBR 6508:1984 [16].

For the chemical characterization of the samples, the X-Ray Energy-Dispersive Spectroscopy (EDX) technique was used in an equipment (Shimadzu, EDX700, Japan), under a two-channel vacuum adjustment condition with the very fine powder material placed in a sample holder. In the mineralogical characterization, the X-ray diffraction (XRD) technique was used to identify the clay minerals and minerals present in each of the collected samples. The equipment Shimadzu, XRD700, Japan, with Cu-K α radiation, with 40 kV and 30 mA, was used. The scan was carried out with θ varying between the angles of 5–55° with a sweep speed of 2°/minute. The results were observed in a comparative way with other data in the literature [17–19]

Result

Table 2 shows the results of the particle size analysis of the different soil samples collected.

The results presented in Table 2 indicate that all the soil samples collected present a predominance of clay in their constitution, in contents above 55% in all cases. According to the literature [20–22], a soil with a predominance of clay has a range corresponding to particles with an equivalent spherical diameter <2 μm . This reduced diameter of these particles favors the process of increasing the potential transport of

Table 2 Particle size analysis of different soil samples collected from degraded areas

Particle size classification		Sample 01 (%)	Sample 02 (%)	Sample 03 (%)	Sample 04 (%)	Sample 05 (%)
Sand	Bulky	1.70	1.80	2.60	2.90	2.40
	Average	7.70	6.50	5.40	5.80	6.10
	Fine	11.10	11.80	10.80	10.20	11.50
Silt		20.70	21.10	22.50	22.30	22.40
Clay		58.80	58.80	58.70	58.80	57.60

pollutants through the soil, which can be harmful in degraded areas [23]. On the other hand, samples 03, 04, and 05 have higher percentages of sand, mainly in the bulky sand fraction, which can counterbalance the clay effect [22]. Figures 2 and 3 show the compiled results of hygroscopic moisture and actual grain density, respectively.

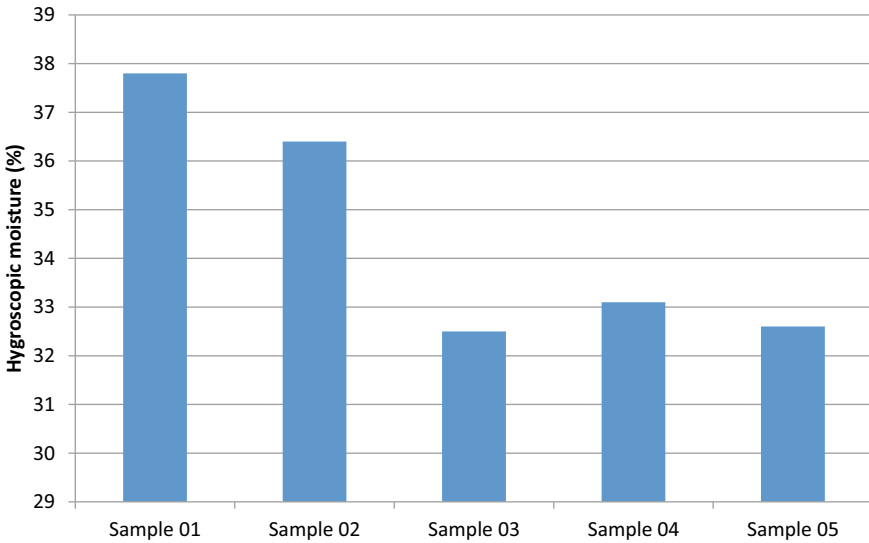


Fig. 2 Results of hygroscopic moisture to all samples

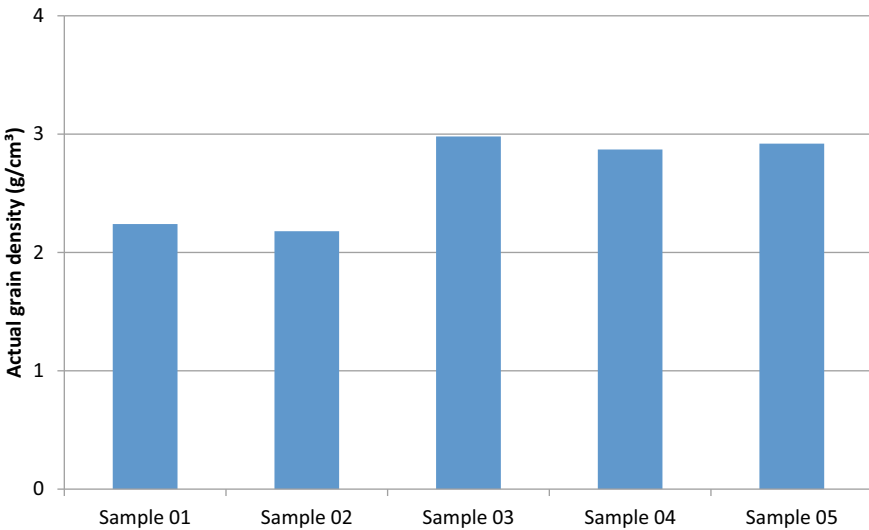


Fig. 3 Results of actual grain density to all samples

The result shown in Fig. 2 shows that samples 01 and 02 have hygroscopic humidity of 37.8% and 36.40%, respectively, these values being higher than those found in the other samples. The higher humidity found can be attributed to the concentration relative to the sand and silt fraction of these samples and also because they are areas with a still active degradation stage, unlike the other samples that are degraded areas already consolidated [13]. Figure 3 shows the actual grain density, in which samples 01 and 02 have lower values due to the smaller proportion of coarse sand fraction, while the results generally show similarity and compatibility with other data in the literature [24]. Table 3 below shows the results of the chemical analysis obtained from the different soil samples collected.

The results shown in Table 3 indicate that in all samples there is a high concentration of SiO_2 and Al_2O_3 which together are above 77% in all conditions evaluated. This high concentration is typical of soil with kaolinitic predominance, found in the study region and discussed in other works in the literature [23, 24]. The results obtained in the mineralogical analysis of the different samples, available in Fig. 4 below, corroborate the other analyzes of this preliminary study.

It is observed in Fig. 4 the presence of kaolinite, quartz, and mica peaks, predominantly. In samples 1 and 2, however, there is a clear reduction in the peaks associated with the kaolinite mineral (swept at 12.5 and 25°). This indicates that these two compositions have leached from this type of mineral, extremely important for the production of ceramic artifacts and essential for the environmental balance of the soil, especially with regard to pH and fertility characteristics for agricultural applications to areas to be occupied after recovery [23]. Mica and quartz minerals do not suffer a reduction in the amount of peaks, as these two minerals are denser and more difficult to carry [13].

Another relevant aspect that deserves to be highlighted in samples 1 and 2 is the presence of peaks of organic material, which are not observed in the other compositions (scan at 33 and 42°). This suggests that something different happened on the ground in these compositions, as the same peaks were not observed in compositions 3–5. It is a strong indication of the contamination of these soils by organic fuel, coming from vehicles that extract the raw material for ceramic production [21]. Another relevant issue is the presence of hematite peaks, which are more accentuated in composition 3, indicating that this composition is rich in iron. This indicates that this soil is made of red clay, widely used in ceramic artifacts to obtain the typical

Table 3 Chemical composition of oxides, in %

Sample	SiO_2	Al_2O_3	Fe_2O_3	TiO_2	K_2O	Na_2O	CaO	MgO	Others
01	55.89	22.30	3.80	1.19	0.50	0.55	0.48	0.22	15.07
02	56.47	21.80	4.20	1.09	0.95	0.69	0.34	0.34	14.12
03	62.25	20.00	8.50	1.05	1.85	0.76	0.67	0.29	4.63
04	60.70	22.58	4.42	0.97	1.26	0.64	0.54	0.19	8.70
05	61.05	23.25	4.79	0.80	1.76	0.75	0.61	0.21	6.78

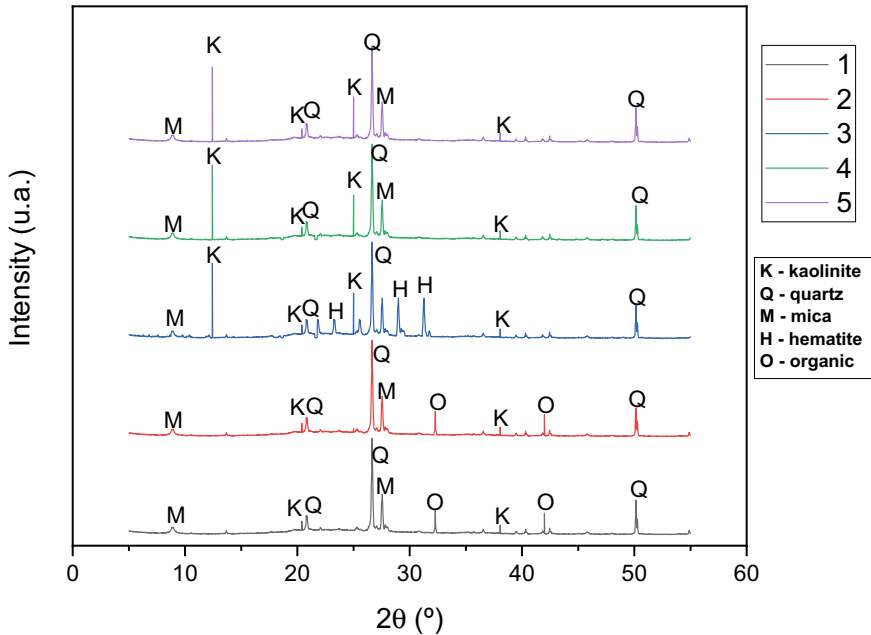


Fig. 4 Result of the mineralogical analysis of the different samples evaluated

coloration, accentuated after burning. The high iron content can be harmful to the recovery activities of these degraded areas, mainly due to the restriction of plantations in this area.

Conclusion

The soils from samples 1 and 2, coming from areas that are still in the initial stage of degradation and highly exposed, are highly susceptible to the degrading process, showing traces of fuel spillage from the process of transporting the soil to the local ceramic industries. This potential contamination hinders the future recovery process of these degraded areas, in addition to making it compatible with other physical parameters evaluated in this research.

The soil from sample 3 showed a higher concentration of iron, corroborated by hematite peaks observed in the mineralogical composition. This condition will certainly hinder the recovery process of this area, which is already degraded and exposed, with potential contaminants permeating through the soil. A potential solution for this case is the revegetation of this area for its recovery, however, this will be harmed by the conditions found.

In all evaluated conditions, the soil proved to be a kaolinitic clay typical of the study region, which presents physical, chemical, and mineralogical conditions that must be monitored and followed up to predict the potential for recovery of these degraded areas and their impacts on the local environment.

Acknowledgements The authors thank the Brazilian agencies: CNPq, CAPES, and FAPERJ for the support provided to this investigation.

References

1. Brazil Constitution (1981) Constitution of the Federative Republic of Brazil (in Portuguese)
2. Brazil Constitution (1988) Constitution of the Federative Republic of Brazil. Brasília (in Portuguese)
3. Mechi A, Sanches DL (2010) Environmental impacts of mining in the state of São Paulo. *Adv Stud* 24(68):209–220. Available at: <http://hdl.handle.net/11449/71822>
4. Daily GC (1997) Nature's services: societal dependence on natural ecosystems. In: Daily GC (ed) Island Press, Washington, DC, pp 200–392. ISBN 1-55963-476-6
5. Sánchez LE (2010) Planning and management of the degraded areas recovery. *Adv Stud* 22(67) 100–140. Available at: <http://hdl.handle.net/11449/71822>
6. White PM (2008) Dictionary of mineralogy and gemology: texts workshop
7. Kulaif Y (2012) DNPM-SP/ DDM National Department of Mineral Production: Clay production in Brazil (in Portuguese)
8. Mulinari M (2000) Analysis of the production process for the extraction of precious stones aiming at profitable and environmentally efficient alternatives. *Extr Ind Soc* 6(4)
9. Center for Mineral Technology (2015) Technological Trends Brazil 2015: Geosciences and Mineral Technology (in Portuguese)
10. Areias IOR, Vieira CMF, Colorado HA, Delaqua GCG, Monteiro SN, Azevedo ARG (2020) Could city sewage sludge be directly used into clay bricks for building construction? A comprehensive case study from Brazil. *J Build Eng* 31. <https://doi.org/10.1016/j.jobbe.2020.101374>
11. Brazilian Institute of Geography and Statistics (IBGE). <https://biblioteca.ibge.gov.br/visualizacao/livros/liv101712.pdf> Accessed 2 Aug 2021 (in Portuguese)
12. Azevedo ARG, Klyuev SV, Klimenko VA, Marvila MT, Fediuk R (2021) Characterization of different Brazilian soils for the production of ceramic artifacts. *Mater Sci Forum*. <https://doi.org/10.4028/www.scientific.net/MSF.1017.123>
13. Lousada LL, Freitas SP, Marciano CR, Esteves BS, Muniz RA, Siqueira DP (2013) Correlation of soil properties with weed occurrence in sugarcane areas. *Planta Daninha* 31(4):765–775. <https://doi.org/10.1590/S0100-83582013000400002>. (In Portuguese)
14. Brazilian Association of Technical Standards (1984) Soil—Method for granulometric analysis of soils, performed by sieving or by a combination of sedimentation and sieving: NBR 7181:1984. 1988. Rio de Janeiro, RJ, 1984 (in Portuguese)
15. Brazilian Association of Technical Standards (1984) Soil—Method for determining the specific mass of soil grains that pass through a 4.8 mm sieve: NBR 6508. Rio de Janeiro, RJ, 1984 (in Portuguese)
16. Anderson JD, Ingran JSI (1993) Tropical soil biology and fertility: a handbook of methods. 2. ed. Wallingford: UK CAB International, 171p
17. Vitti GC (1989) Assessment and interpretation of sulfur in soil and plant. Jaboticabal: FCAV/FUNEP, 37p (in Portuguese)
18. EMBRAPA (1997) Manual of soil analysis methods. 2. ed. Rio de Janeiro: National Soil Research Center—Embrapa Solos, 210p (in Portuguese)

19. Huaraca-Meza F, Custodio M, Peñaloza R, Alvarado-Ibañez J, Paredes R, De la Cruz H, Lazarte-Pariona F (2022) Bacterial diversity in high andean grassland soils disturbed with lepidium meyenii crops evaluated by metagenomics. *Braz J Biol* 82. <https://doi.org/10.1590/1519-6984.240184>
20. Prodana M, Bastos AC, Silva ARR, Morgado RG, Frankenbach S, Serôdio J, Loureiro S (2021) Soil functional assessment under biochar, organic amendments and fertilizers applications in small-scale terrestrial ecosystem models. *Appl Soil Ecol* 168. <https://doi.org/10.1016/j.apsoil.2021.104157>
21. Takagi T, Shin K, Jige M, Hoshino M, Tsukimura K (2021) Microbial nitrification and acidification of lacustrine sediments deduced from the nature of a sedimentary kaolin deposit in central japan. *Sci Rep* 11(1). <https://doi.org/10.1038/s41598-021-81627-4>
22. El-Mehalawy N, Awaad M, Turkey GM, Ali-Bik MW, Abd El Rahim SH, Naga SM (2021) Self-glazing dielectric ceramic bodies fabricated from egyptian rhyodacite and kaolin. *Mater Chem Phys* 270. <https://doi.org/10.1016/j.matchemphys.2021.124785>
23. Vieira CMF, Sánchez R, Monteiro SN (2008) Characteristics of clays and properties of building ceramics in the state of rio de janeiro, brazil. *Constr Build Mater* 22(5):781–787. <https://doi.org/10.1016/j.conbuildmat.2007.01.006>
24. Vieira CMF, Soares TM, Sánchez R, Monteiro SN (2004) Incorporation of granite waste in red ceramics. *Mater Sci Eng, A* 373(1–2):115–121. <https://doi.org/10.1016/j.msea.2003.12.038>

Comparative Study of Staining Resistance for Polished and Resined Silicatic Ornamental Rocks



S. Rocha, E. D. F. Castilho, A. R. G. Azevedo, L. R. Cruz, M. T. Marvila, and S. N. Monteiro

Abstract The consumption of ornamental stones has become expressive in the world and has spread widely as a coating material. Therefore, in order to overcome the problems observed in relation to mechanical strength associated with rocks, an epoxy-based resin was developed to waterproof them and maintain their strength. Therefore, in addition to verifying whether the resin promotes resistance gains, the possibility that it offers stain resistance was evaluated. To carry out the tests, four types were chosen whose commercial names are Ornamental Yellow, Corumbazinho Gray, Ocher Itabira, and Labrador Green, divided into polished and resined. After the test, lemon juice and steel wool were the staining agents that caused the most visible changes. In addition, it was observed that some resin materials had a greater loss of gloss compared to polished ones, making it clear that the resin did not waterproof the rock in terms of loss of gloss.

Keywords Dimension stone · Resin · Staining

S. Rocha · E. D. F. Castilho

Science and Technology of Espírito Santo, IFES—Federal Institute of Education, Rodovia Engenheiro Fabiano Vivacqua, 1568, Cachoeiro do Itapemirim, Espírito Santo 29322-000, Brazil
e-mail: evanizis@ifes.edu.br

A. R. G. Azevedo (✉) · L. R. Cruz

LECIV—Civil Engineering Laboratory, UENF—State University of the Northern Rio de Janeiro, Av. Alberto Lamego, 2000, Campos dos Goytacazes, Rio De Janeiro 28013-602, Brazil

M. T. Marvila

LAMAV—Advanced Materials Laboratory, UENF—State University of the Northern Rio de Janeiro, Av. Alberto Lamego, 2000, Campos dos Goytacazes, Rio De Janeiro 28013-602, Brazil

S. N. Monteiro

Department of Materials Science, IME—Military Institute of Engineering, Square General Tibúrcio, 80, Rio de Janeiro 22290-270, Brazil

© The Minerals, Metals & Materials Society 2022

M. Zhang et al. (eds.), *Characterization of Minerals, Metals, and Materials 2022*,

The Minerals, Metals & Materials Series,

https://doi.org/10.1007/978-3-030-92373-0_26

Introduction

Ornamental stones have more and more attention due to variety of lithotypes, their aesthetic beauty, versatility, among other aspects. The characteristics that add value to the rock such as brightness, texture, color, and homogeneity, for example, are given to the rock during its formation due to geological and environmental factors that gave rise to it. Thus, the ornamental stone production chain tends to occupy more and more space in the Brazilian economic scenario, generating thousands of jobs directly or indirectly [1].

According to data from the Brazilian Association of Dimension Stones Industry (ABIROCHAS), Brazil is highly active in the field of exports and ranks among the five largest stone exporters in the world. In 2016, the country exported rocks to over 120 countries and the United States of America (USA) was again its main customer. Sales to these three destinations (USA, China, and Italy) together accounted for 80.6% of total external rock sales. The state of Espírito Santo is the country's largest producer of ornamental stones, around 50%, and responsible for 75% of the physical volume of exports [2].

Once the importance of the sector is shown, attention should be paid to the application of the rocks. The most varied lithological types found in nature have their own characteristics and react in different ways when exposed to bad weather and chemical substances [1]. Even rocks with high mechanical resistance are susceptible to staining of the material, which can be caused by inappropriate use of products and/or maintenance of wrong procedures. The sum of these factors can cause permanent or temporary changes in the rock's feature [3].

Changes in the rock surface occur when a substance penetrates the rock, which can cause the blemish, change in color, or loss of brightness, altering its original visual form. In order to minimize such occurrences, the industry has developed resins that increase the mechanical strength of rocks, creating a protective layer that prevents direct contact of external agents with the rock surface [4].

Thus, seeking to contribute to studies related to staining of stone materials by everyday products, this work aims to compare the behavior of polished and resined rock against exposure to everyday substances and correlate them with the cleaning steps, brightness measurements, and visual analysis, in order to verify the particularities of the behavior of polished and resined materials throughout the experiment, in addition to making adaptations of standardized staining tests for ceramic plates, which is applied to ornamental stones.

Materials and Methods

The work followed a methodology (Fig. 1) that can be seen in more detail in the flowchart below, enabling a better understanding of each step performed during the work and the tests performed.

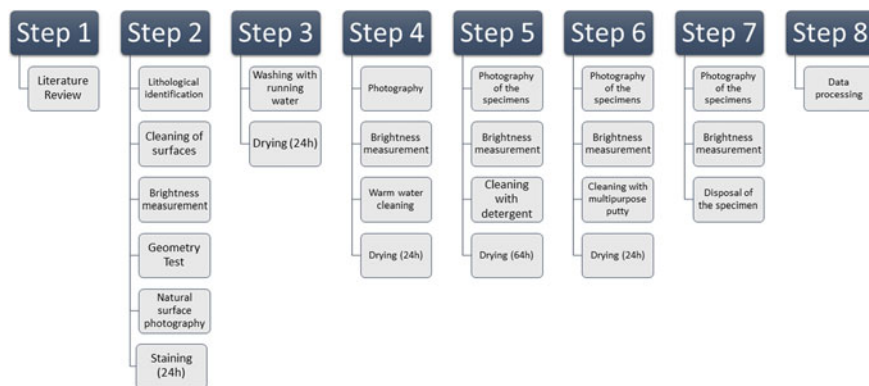


Fig. 1 Flowchart of the steps developed

Four types of lithotypes were chosen to carry out the tests, namely: Amarelo Ornamental, Cinza Ortognaisse/Corumbazinho, Ocre Itabira, and Verde Labrador. All were produced and processed in the state of Espírito Santo, being among the most sold in the domestic market due to its aesthetic standard, its varied colors, and its commercial value. From this, 16 specimens were prepared for each type of lithotype, 8 resined and 8 polished with surface dimensions $(7.5 \times 7.5 \text{ cm})$, totaling 64 specimens, which were divided into one group of polished rock and the other of resined polished rock [5].

A staining agent is understood to be a product that, in contact with the rock surface for a certain time, is capable of producing temporary or permanent stains that alter visual characteristics such as color and surface shine of the rock. Thus, to carry out the staining test, the criteria for choosing staining agents were products that are used in everyday life. Being divided into culinary and cleaning products that are often products used in daily life in domestic environments, especially in kitchens (sinks and countertops), since the standard does not specify which agents should be adopted [6].

The cleaning agents for stain removal are chosen in accordance with the standard of ABNT NBR 13,818 [3] annex G. To carry out the first attempt to remove the stain, warm water was used as an agent. For the second and third attempts to remove the stain, two cleaning agents were chosen, a weak one with a pH between 6.5 and 7.5 and a strong one with a pH between 9.5 and 10.5, respectively, according to Fassarela, in his studies found neutral detergent as a weak pH agent, while multipurpose paste as a strong pH agent [4].

The standard specifies test procedures. To do the same, the following substances were used as staining agents: lemon juice, grape juice, vinegar, Coca-Cola, washing powder, detergent, bleach and steel wool with water, and the cleaning agents that are standardized were warm water, detergent, and multipurpose paste. The device used for the brightness measurements was the Gloss meter. The specimens were selected and prepared, the stone plates were placed in contact with the staining agents and



Fig. 2 Specimens separated into polished and resined

then attempts were made to remove the stains [7]. To start the test, the specimens must be clean and dry. For this, the specimens were washed with running water and left to dry at room temperature, around 25 °C, for a minimum of 24 h. The next step was the identification of the specimens. For this test, there were 16 specimens per lithotype, divided into 8 polished and 8 resined, as shown in Fig. 2.

At the end of this step, the specimens were cleaned with the aid of a flannel and then the gloss measurements were carried out on the surface of the specimens with the aid of the Gloss meter device. Gloss measurements were randomly performed in the center of the specimen, a region that was exposed to staining agents. The device was programmed to perform the collection of 40 points of brightness measurement in each specimen, at the end of the 40 measurements the device presents an average on its display. At the end of this step, a total of 2560 brightness measurements were collected [8].

After the 24-h period that the rock was exposed to the staining agent, the rock was cleaned with running water to remove excess surface agent and 24 h were allowed for a visual analysis of the stone plates and new brightness measurements were performed. Then began the process of trying to remove the stains. In the first cleaning attempt, the agent used was warm water [9]. The remaining specimens were placed in trays filled with warm water at a temperature of approximately 66.1 °C until they were submerged. They were kept that way for approximately 5 min. With the aid of a paper towel, excess water was removed and the specimens were placed to dry at room temperature for a period of 24 h. After this period, a new gloss measurement was performed on the surface of the specimens.

The second cleaning step consists of applying cleaning agent 2, which is the neutral detergent, scrubbing for about 2 min with the aid of a sponge. After this procedure, the surface was washed with running tap water and then the bodies were left to dry at room temperature for a minimum period of 24 h. After this period, new gloss measurements were performed on the surface of the specimens.

The third cleaning attempt was to wash the rock with the aid of a sponge, but the cleaning agent used was the multipurpose paste. And again, new gloss measurements were performed on the surface of the specimens.

Results and Discussion

The results will be arranged and discussed according to: in relation to visual changes after staining, change in brightness after exposure to staining agents and change in brightness after cleaning steps in each of the rocks.

1. Assessment of visual change after staining:

1.1 Amarelo Ornamental: after exposure to staining agents, the Amarelo Ornamental that was exposed to grape juice, detergent, and bleach showed visual changes. The grape juice caused purple stains on the rock, both in the polished material and in the resin, but in the resin, the stains had a milder change. The detergent and bleach, on the other hand, caused the material to fade, the rock became lighter in both materials. With the other staining agents, they showed no apparent visual changes [10].

1.2 Cinza Ortognaisse/Corumbazinho: after exposure to staining agents, the samples that were exposed to grape juice, Coca-Cola, washing powder, and steel wool showed visual changes. The grape juice made the light minerals in the material acquire a yellowish color, both in the polished and resined material. The same fact was verified with Coca-Cola. Powder soap made the rock appear darker, in the polished material, staining was more intense. The steel wool oxidized, with it, the exposed rock turned yellowish. The other agent's lemon juice, vinegar, detergent, and bleach did not cause visual changes. Grape Juice was the staining agent that caused the most visual changes in both polished and resined plates.

1.3 Ocre Itabira: in this material, only the steel wool caused a visual change in the rock, the area that was exposed to this staining agent acquired a yellow color, characteristic of the oxidation of steel wool, both in the polished and resined material. The other staining agents did not cause visual changes in the materials [11].

1.4 Verde Labrador: after exposure to staining agents the samples that were exposed to lemon juice, vinegar, bleach, and steel wool showed visual changes. The lemon juice acted under the rock making it look "faded". In the polished material, this happened more intensely than in the resin. The rock exposed to vinegar turned white. In resined samples, this happened in a milder way. The same fact was verified for bleach. With steel wool the material became darker, the green became a darker and more intense green. The other staining agents, grape juice, Coca-Cola, washing powder, and detergent did not cause visual changes in the materials. The bruising agent that caused the most visual alteration in this material was the lemon juice in the polished material.

2. Change in post-staining brightness:

Equation (1) is used for brightness variation:

$$\Delta B = [(B_i - B_f)/B_i] \times 100 \quad (1)$$

where

B_i = Initial brightness

B_f = Final brightness

If $\Delta B > 0$ the material had a loss of brightness;

If $\Delta B < 0$ the material has a gain in brightness.

2.1 Amarelo Ornamental: after contact with staining substances, almost all materials lost their shine, with the exception of the grape juice in the polished material, which gained in shine. Juice generated a greater loss of brightness in polished rock when compared to resined ones. The stone slabs stained with vinegar, Coca-Cola, washing powder, detergent, and bleach all lost their shine, but the resin ones had a greater loss. With steel wool the polished rock had no change in brightness and the resin lost. The staining agent responsible for the greatest variation in brightness in this material was the bleach in the resined rock and the one that showed the least change was the steel wool in the polished one [12].

2.2 Cinza Corumbazinho/Ortognaisse: after the test, most of the samples lost shine, with the exception of the polished rock whose staining agent was steel wool, and showed a gain in shine. The staining agent's lemon juice, vinegar, Coca-Cola, detergent, and bleach caused a loss of shine, but in the resinous material, there was a greater loss than in the polished one. Grape juice and soap powder also provided a decrease in the percentage of gloss; however, polished materials had a greater loss of gloss compared to resin materials. Again, the staining agent responsible for the greatest variation in brightness was the bleach on the resined rock and the one that showed the least change was the detergent on the polished rock.

2.3 Ocre Itabira: almost all staining agents caused a loss of shine, with the exception of detergent and steel wool, which provided a gain in shine, both in the polished and in the resin. With the staining agent's lemon juice, grape juice, Coca-Cola, washing powder, and bleach, the stone slabs showed the same loss of shine for the same staining agent in both polished and resined ones. With vinegar, the polished material showed a greater loss of shine. Ocre Itabira was the material that showed more uniform results after staining. Showing equal or close values for polished and resined materials [13]. Again, the staining agent responsible for the greatest variation in brightness was bleach in both the resined and polished rocks, and the one that showed the least change was the detergent in the resined material.

2.4 Verde Labrador: from the data of brightness measurements obtained, it can be observed that after coloring almost all coloring agents caused loss of brightness, with the exception of the polished stone stained with grape juice, which showed gain. The dyes lemon juice, vinegar, detergent, bleach, and steel wool caused a loss of shine, but the polished rock showed a greater reduction. With washing powder and Coca-Cola, the resins showed a greater drop compared to polished ones after measurements with the gloss meter. The staining agent responsible for the greatest

variation in brightness in this material was the lemon juice on the polished stone and the one that showed the least change was the grape juice on the polished material.

3. Evaluation of change in brightness after cleaning steps:

3.1 Amarelo Ornamental: after cleaning step 1, that is, after warm water, some materials stained with: lemon juice, washing powder, detergent, and bleach on the polished plates and those exposed to vinegar and washing powder agents in resins showed a gain in brightness, the other plates had a loss of brightness. Then, after cleaning step 2, which the cleaning agent was detergent, only resin stains stained with powdered soap and bleach showed a brightness gain, the other materials had a loss of brightness. In cleaning step 3, in which the multipurpose paste was used, all materials showed a loss of shine [14]. This was due to the fact that the paste is abrasive, promoting wear on the rock surface. In many cases, as can be seen, materials with resin showed a greater loss of gloss. In general, all slabs were purchased from sound rock and after all cleaning attempts they lost their shine. At the end of the cleaning attempts, the resin-based rock stained with bleach showed the greatest loss of shine and the one with the least variation was with powdered soap on the polished rock.

3.2 Cinza Ortognaisse: after cleaning step 1 (warm water) most materials showed a gain in brightness, with the exception of the polished rock stained with grape juice and detergent and the resin exposed to the agents of grape juice and bleach. Then, after cleaning steps 2 (detergent) and cleaning process 3 (multipurpose paste), all materials, both polished and resined, lost their shine. In general, comparing the healthy rock with it after the test and all cleaning attempts, the materials showed a loss of gloss and the resinous materials were the ones with the greatest loss of surface gloss. At the end of the cleaning attempts, the resinous rock stained with Coca-Cola showed the greatest loss of shine and the one with the least variation was with powdered soap on the polished rock.

3.3 Ocre Itabira: after the first cleaning step (warm water), the materials stained with lemon juice, soap powder, bleach and steel wool showed a gain in brightness, both in polished and resined ones. On the other hand, rocks exposed to grape juice, vinegar, Coca-Cola and detergent had a loss of shine after cleaning step 1. After cleaning step 2 (detergent), almost all materials showed loss of shine, except for stained materials with washing powder and detergent. Gloss measurements, after cleaning process 3 (multi-purpose paste) of all materials with the exception of the resin-based rock stained with bleach, had a loss of gloss [15]. During the test, Ocre Itabira was the material that presented the most uniformity of values considering the same staining agent for the polished and resined material. In general, comparing the healthy rock with it after the test and all cleaning attempts, the materials showed a loss of gloss and the resinous materials were the ones with the greatest loss of surface gloss. After all cleaning attempts, the polished rock stained with grape juice showed the greatest loss of shine and the one with the least variation was with steel wool in the resin material.

3.4 Verde Labrador: after the first cleaning step, almost all materials showed loss of shine, with the exception of the polished rock exposed to grape juice and vinegar

and the resinous stone plates stained with lemon juice, grape juice, vinegar and steel wool, which had gained of shine. After cleaning step 2, most materials showed a gain in brightness. Polished rocks whose staining agents were lemon juice, Coca-Cola and water, and resinous materials that were tested with vinegar and steel wool had a loss of shine [8]. After cleaning step 3, all polished and resined rocks have lost their shine. In general, comparing the healthy rock with it after the test and all cleaning attempts, the materials showed a loss of gloss, however resinous materials were the ones with the greatest loss of surface gloss. At the end of the cleaning attempts, the resinous rock stained with lemon juice showed greater loss of shine and the one that had the least variation was with powder soap on the polished material [16].

Conclusion

Visual analysis and measurements of brightness after staining and after cleaning steps brought unprecedented results regarding the use of the resin. The importance of this work is given by the possibility of verifying the materials that suffered staining, which staining agents caused the most changes in the rock and also those in which visual changes were not observed, although with the aid of the Gloss Meter, changes in brightness were presented. Once the rock surface is exposed, it can show visible and irreversible damage, as was the case with some materials. By quantifying the changes through brightness measurements, an important tool in the prevention of pathologies due to the use of ornamental stones in environments with high exposure to a range of chemical substances, such as in sinks and kitchen countertops, is obtained.

In general, all materials showed a loss of gloss at the end of the test, in some cases during the test or in some cleaning steps the material gained gloss, but after the last cleaning step, there was a loss of gloss, mainly associated with the use of the multipurpose paste, which caused abrasive wear on the rock.

Resin materials in many cases showed greater loss of shine than polished rocks, however, they visually had less visual alteration, a fact that can be verified in the Verde Labrador stained with lemon juice, which was the material that had the most visual alterations. However, what could be observed is that the polished and resined materials in general would not follow a pattern throughout the tests, varying randomly, but at the end of the tests, all had a loss of shine as a result.

After the staining step, the material that showed the most variation in brightness was the resinous Cinza Ortognaisse stained with bleach, on the other hand, the one with the least variation was the Amarelo Ornamental polished with the steel wool agent. The visual and brightness changes, in most cases, could not be reversed during the cleaning steps, however, in many cases they were mitigated as in the Amarelo Ornamental stained with grape juice, detergent, and bleach and in the Cinza Corumbazinho stained with the steel wool. Finally, the methodology used proved to be efficient for stone materials and the staining analysis carried out visually and by the quantitative method of verification of brightness measurements allows the adoption of criteria and establishing limits for a qualitative classification.

Acknowledgements The authors thank the Brazilian agencies: CNPq, CAPES, and FAPERJ for the support provided to this investigation.

References

1. Chiodi Filho C (2017) Balance of Brazilian exports and imports of dimension stones in 2017. ABIROCHAS, 2017, São Paulo. 13 p. (Report n.01/2017)
2. Alencar CRA (2013) Euvaldo Lodi Institute. Manual for the characterization, application, use and maintenance of the main commercial rocks in Espírito Santo, Cachoeiro de Itapemirim/ES, IEL
3. Brazilian Association of Technical Standards—ABNT (1997) Ceramic tile for coating—specification and test methods. NBR 13818 attachment G. Rio de Janeiro
4. Fassarella MD (2016) Colorimetric and gloss evaluations applied to ornamental rocks subjected to stain testing. Monograph (graduation)—Federal Institute of Espírito Santo, Engineering Coordination of Minas, Engineering Course of Minas
5. Marvila MT, Azevedo ARG, Cecchin D, Costa JM, Xavier GC, de Fátima do Carmo D, Monteiro SN (2020) Durability of coating mortars containing açaí fibers. *Case Stud Constr Mater* 13. <https://doi.org/10.1016/j.cscm.2020.e00406>
6. Neuba LM, Pereira Junio RF, Ribeiro MP, Souza AT, Lima ES, Filho FCG, Azevedo ARG, Monteiro SN (2020) Promising mechanical, thermal, and ballistic properties of novel epoxy composites reinforced with cyperus malaccensis sedge fiber. *Polymers* 12(8). <https://doi.org/10.3390/polym12081776>
7. de Azevedo ARG, Marvila MT, Tayeh BA, Cecchin D, Pereira AC, Monteiro SN (2021) Technological performance of açaí natural fibre reinforced cement-based mortars. *J Build Eng* 33. <https://doi.org/10.1016/j.jobe.2020.101675>
8. de Azevedo ARG, Marvila MT, Antunes MLP, Rangel EC, Fediuk R (2021) Technological perspective for use the natural pineapple fiber in mortar to repair structures. *Waste Biomass Valorization*. <https://doi.org/10.1007/s12649-021-01374-5>
9. Azevedo A, De Matos P, Marvila M, Sakata R, Silvestro L, Gleize P, De Brito J (2021) Rheology, hydration, and microstructure of portland cement pastes produced with ground açaí fibers. *Appl Sci (Switzerland)* 11(7):15–26
10. Azevedo ARG et al (2019) Assessing the potential of sludge generated by the pulp and paper industry in assembling locking blocks. *J Build Eng* 23:334–340. <https://doi.org/10.1016/j.jobe.2019.02.012>
11. Marvila MT et al (2019) Evaluation of the use of marble waste in hydrated lime cement mortar based. *J Mater Cycles Waste Manage* 21(5):1250–1261. <https://doi.org/10.1007/s10163-019-00878-6>
12. França BR et al (2018) Durability of soil-cement blocks with the incorporation of limestone residues from the processing of marble. *Mater Res* 21(1). <https://doi.org/10.1590/1980-5373-mr-2017-1118>
13. Azevedo ARG et al (2020) Potential use of ceramic waste as precursor in the geopolymerization reaction for the production of ceramic roof tiles. *J Build Eng* 29. <https://doi.org/10.1016/j.jobe.2019.101156>
14. Marvila MT et al (2019) Correlation between the properties of structural clay blocks obtained by destructive tests and ultrasonic pulse tests. *J Build Eng* 26. <https://doi.org/10.1016/j.jobe.2019.100869>

15. Azevedo ARG et al (2015) Addition of paper sludge waste into lime for mortar production. *Mater Sci Forum* 820:609–614. <https://doi.org/10.4028/www.scientific.net/MSF.820.609>
16. Azevedo ARG, Cecchin D, Carmo DF, Silva FC, Campos CMO, Shtruck TG, Mavila MT, Monteiro SN (2020) Analysis of the compactness and properties of the hardened state of mortars with recycling of construction and demolition waste (CDW). *J Mater Res Technol* 9(3):5942–5952. <https://doi.org/10.1016/j.jmrt.2020.03.122>

Comparative Study of the Flexural Strength of Rock Materials for Applications in Civil Construction



L. M. Campos, E. D. F. Castilho, A. R. G. Azevedo, T. R. Silva,
M. T. Marvila, E. B. Zanelato, and S. N. Monteiro

Abstract The sector of ornamental rocks has been enabling the insertion of more sustainable technologies in industrial activities and extraction, thus, seeking better use of rock materials for cladding in the construction industry. This study aimed to evaluate the flexural strength of rock materials when submitted to shingling and resin coating techniques. The work quantified the modulus of rupture from bending stresses at four points, according to Brazilian standard. The materials analyzed were Vicenza, Romanix, and Nevasca, in their raw state and after being submitted to epoxy-based shingling and resin coating. The results showed that after the strengthening processes of the materials evaluated, there was an increase in flexural strength in four points for both materials when compared to NBR 15.844, except the material Nevasca (raw state), which did not show a satisfactory value. Thus, most of the materials could be considered suitable for cladding in civil construction applications.

Keywords Technological characterization · Construction cladding · Mechanical properties

L. M. Campos · E. D. F. Castilho

IFES—Federal Institute of Espírito Santo, Rodovia ES-482 Fazenda Morro Grande, Campus Cachoeiro de Itapemirim, Espírito Santo 29311-970, Brazil

e-mail: evanizis@ifes.edu.br

A. R. G. Azevedo (✉) · E. B. Zanelato

LECIV—Civil Engineering Laboratory, UENF—State University of the Northern Rio de Janeiro, Av. Alberto Lamego, 2000, Campos dos Goytacazes, Rio De Janeiro 28013-602, Brazil

E. D. F. Castilho · A. R. G. Azevedo · T. R. Silva · M. T. Marvila

LAMAV—Advanced Materials Laboratory, UENF—State University of the Northern Rio de Janeiro, Av. Alberto Lamego, 2000, Campos dos Goytacazes, Rio De Janeiro 28013-602, Brazil

S. N. Monteiro

Department of Materials Science, IME—Military Institute of Engineering, Square General Tibúrcio, 80, Rio de Janeiro 22290-270, Brazil

© The Minerals, Metals & Materials Society 2022

M. Zhang et al. (eds.), *Characterization of Minerals, Metals, and Materials 2022*,

The Minerals, Metals & Materials Series,

https://doi.org/10.1007/978-3-030-92373-0_27

Introduction

The stone industry represents a global powerhouse market and drives major economies around the world [1]. Brazil can be considered one of the protagonists in the production and commercialization of ornamental stones, corresponding to a production of 8 million tons, and can be considered among the five largest producers in the world with a global participation of 5.4% [2, 3].

Ornamental stones can be processed and finished for ornamental and cladding purposes, thus occupying a large space in the construction sector and representing more than 70% of the total produced [2, 4]. The use of these stones is constantly being valued from a more environmental perspective, because the methods for extracting natural stone are quite aggressive [3, 5]. The processing of ornamental stones generates about 30%–40% of losses in the form of debris throughout the various stages of the industrial process, from extraction to the finishing stage [6]. Thus, its use in civil construction, besides mitigating environmental impacts, potentiates the benefits regarding physical and mechanical properties, durability, as well as the importance of the technological characterizations performed on the stones, with more focus on their applications and better performances [7, 8].

Natural stone is used as a building material because of its aesthetic, mechanical, and durable properties. Often, some stones have weaknesses that are mechanically critical because they can restrict their processing. Therefore, epoxy resin treatment has become widely used due to its good performance and good finishing properties [9].

Besides this treatment, some types of stones are directly associated with the development of reinforcement techniques, better known as shingling. The shingling process aims to give the ornamental stones an increase in resistance to bending efforts and consists in the fixation of a glass fiber mesh, with the help of a resin, generally epoxy, on the back of the rock slab. With this, this technique seeks to attenuate the appearance of cracks or breaks during the finishing and transportation of the stones [10]. Moreover, the resin when used on the rock surface can also be related as a strengthening technique, because it has the ability to percolate the fractures and micro-cracks of the material, filling the preferential areas of breakage and increasing the resistance efforts [9].

The ornamental stones are usually heterogeneous materials, with variations in petrographic characteristics due to their formation in the geological environment, but with high added value. However, this heterogeneity directly influences the mechanical properties of the material, especially the bending strength. This problem may also be associated with the fact that the reinforcement process does not follow a precise methodology, affecting the quality and performance of rock materials [10].

In this context, knowing that the use of strengthening techniques allows the improvement of the performance of stone materials, as well as considering the mineralogical and textural factors of the material in these processes, the present study sought to evaluate the flexural strength of stone materials (Vicenza, Romanix, and

Nevasca) when subjected to shingling and resin treatment, thus allowing a comparative relationship between the interference of these treatments in relation to the materials in natura.

Materials and Methods

Three materials of polished lithotypes with distinct petrographies named Vicenza (Fig. 1a), Romanix (Fig. 1b), and Nevasca (Fig. 1c) were selected, in their raw state, subjected to the treatments of shingling and resin (epoxy), according to NBR 15,845-7 [11]. Initially, petrographic analysis of each type of material (macroscopic and mineralogical) were performed in order to characterize the stones.

To perform the resin treatment of the materials shingled with fiberglass with a basis weight of 80 g/m^2 and $4 \times 4 \text{ mm}$ mesh, the combination of epoxy resin (epichlorohydrin and bisphenol-A base) and a catalyst were used to cure the material at 37% for 48 h, totaling 6 g of mixture composed of resin and catalyst. These parameters were stipulated by the manufacturer and should be adopted for the chemical compound to react properly. Samples with dimensions of $30 \times 100 \times 400 \text{ mm}$ were selected for each test, cut parallel to their structure. Before the resin coating process of the shingled materials, the samples were submitted to a washing process in order to remove impurities that could compromise the adhesion between the resin and the surface of the material. After complete washing, the samples were sent to the oven in order to remove the humidity from the stones for 48 h.

After removing the samples from the oven, they were cooled, followed by the resin weighing step, which was done individually for each shingled sample. For this, a precision scale was used, adding in a plastic container the proportions of resin and catalyst previously established, mixing them using a glass rod. The resin was applied and spread for 8 min uniformly throughout the top layer of the samples with the help of a plastic spatula so that the product permeates all possible voids and fractures in the stone.

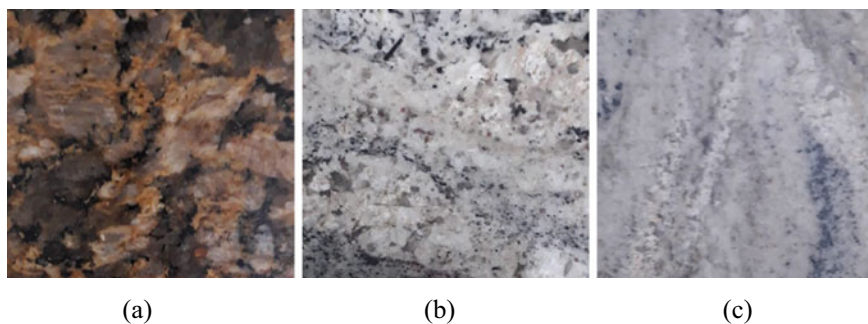


Fig. 1 Evaluated stones. **a** Vicenza; **b** Romanix; **c** Nevasca

Subsequently, the samples were dried at room temperature for 48 h, meeting the curing time of the mixture and ensuring the necessary adherence to avoid interference in the rupture stage of the materials. After this step, four width measurements and eight thickness measurements were made in different points of the specimens with the aid of a pachymeter. Afterwards, the specimens were again placed in an oven at 70 °C for 48 h, avoiding the probable humidity from the previous stages.

In order to establish a comparison related to the changes in the mechanical performance of the evaluated rocks, the 4-point bending test was performed according to NBR 15,845–7 [11] with reinforced and unreinforced specimens, using an EMIC hydraulic press with a minimum capacity of 100 kN.

Results and Discussion

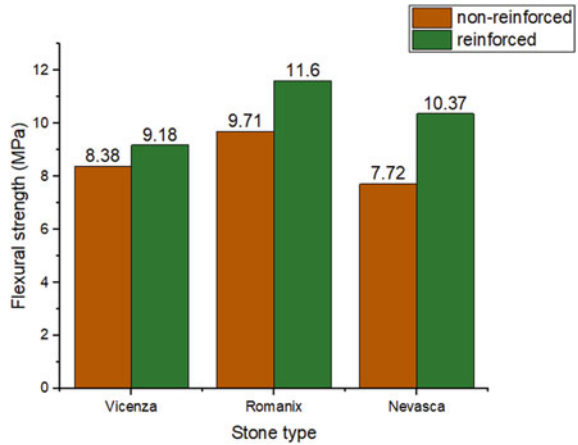
The results obtained from the petrographic analysis of the evaluated stones (macroscopic and mineralogical) according to NBR 15,845–2 [12] showed for each stone type (Table 1).

According to the analysis performed, it can be stated that the flexural strength is very dependent on the mineral structure and texture of the stone since this influences the different planes of weakness by which the stones can break. With this, it was possible to observe that the samples have the same main minerals, due to the proximity of the stone conditions, but there are quantitative variations that should be considered, because they influence mainly the mechanical behavior of the stones [3]. As for the results regarding the flexural strength of the samples, the data are shown in Fig. 2.

Table 1 Macroscopic and mineralogical characteristics of stones

Stone type	Macroscopic characteristics	Mineralogical characteristics
Vicenza	Very coarse-grained stone with yellow feldspar phenocrysts	85% microcline, 5% quartz, 4% plagioclase, <1% alanite and 5% biotite
Romanix	Stone in the sound state, white colored, massive, dense, heterogeneous, inequigranular, and with fine to medium-grained minerals	35% plagioclase, 25% alkali feldspar, 25% quartz, 10% biotite, and 5% muscovite
Nevasca	Cohesive, dense stone, slightly foliated, with heterogeneous aspect, formed by crystals of feldspars and quartz of whitish to slightly pinkish color, with millimeters and centimeters dimensions, detached in a matrix where these minerals are associated with biotite and muscovite vanes and dispersed crystals of red garnet and tourmaline	45% microcline, 25% quartz, 15% plagioclase, 8% tourmaline, 4% muscovite, 3% garnet

Fig. 2 Flexural strength by four points bending



Through the data obtained, it was possible to verify that the Vicenza stone, after the reinforced techniques, showed an increase of 9.53% in flexural strength at four points when compared to the unreinforced form, while the Romanix rock showed an increase of 19.41% compared to the unreinforced material. The Nevasca stone, on the other hand, showed a significant increase in flexural strength in four points, corresponding to 34.31% when compared to the unreinforced.

For the Vicenza and Romanix types, it was also found that their average tension, regardless of the condition of the stone (reinforced and unreinforced), was higher than the value of 8 MPa (Fig. 3) stipulated by NBR 15.844 [13].

As for the Nevasca type, it was noted that this material in its raw state showed flexural strength lower than the value stipulated by the standard (Fig. 4). This may occur due to this type of stone being inferior to the others evaluated in natura, since

Fig. 3 Increased flexural strength compared to NBR 15.844

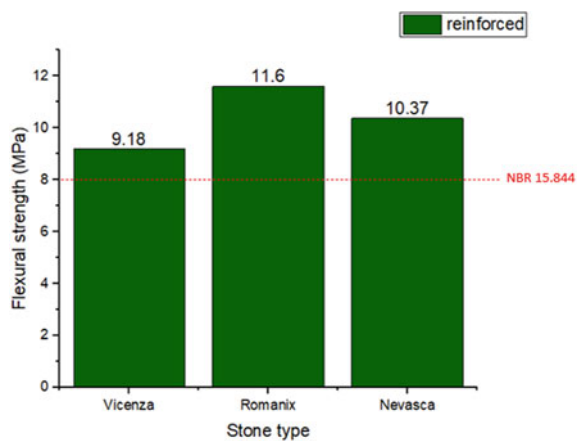
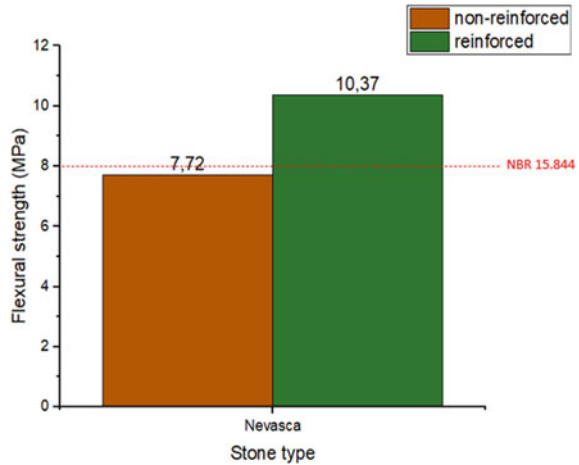


Fig. 4 Flexural strength lower than the value established by NBR 15.844 for Nevasca in raw state



the raw stone usually shows characteristics of weakness, which can be verified from the mechanical point of view [9].

Thus, comparing the stones evaluated after being submitted to the treatments of shingling and resin coating, with regard to the four-point bending strength, it can be stated that the Romanix-type stone is the most suitable for application as cladding in civil construction, followed by the Nevasca-type stone, and then the Vicenza type. In addition, study [14] affirm that using the four-point bending technique collaborates to the effective evaluation of the stones that demand better geometric dimensioning in their applications.

Conclusion

It was possible to verify with the present study that the technological characterization for cladding materials is quite relevant, since the petrographic characteristics provide the most significant mechanical performance of the evaluated rocks. The resistance to bending in four points was analyzed for the three rocks named Vicenza, Nevasca, and Romanix, in natura and after submitted to the treatments of shingling and resin coating, showing a significant increase for each of 9.53%, 19.41%, and 34.31%, respectively. Thus, concluding that the materials evaluated are suitable for civil construction cladding according to Brazilian standards. Thus, this study showed that using reinforcement techniques contributes to increasing the performance of the types of stones evaluated, as well as the choice of technique for evaluating their technological properties.

References

1. Galetakis M, Soultana A (2016) A review on the utilisation of quarry and ornamental stone industry fine by-products in the construction sector. *Constr Build Mater* 102:769–781. <https://doi.org/10.1016/j.conbuildmat.2015.10.204>
2. Montani C (2019) Marble and rock in the world report 2019—Dossier Brazil 2019. ABIROCHAS, Brazil, 86p
3. Almada BS, Melo LS, Dutra JB, Bubani LC, Silva GJB, Santos WJ, Aguiar MTP (2020) Influence of the heterogeneity of waste from wet processing of ornamental stones on the performance of Portland cement composites. *Constr Build Mater* 262:120036. <https://doi.org/10.1016/j.conbuildmat.2020.120036>
4. Vianna Bahiense A, Alexandre J, Castro Xavier G, de Azevedo ARG, Monteiro SN (2021) Dosage of interlocking paving with ornamental rock waste: an experimental design approach, particle packing and polluting potential. *Case Stud Constr Mater* 15:e00596. <https://doi.org/10.1016/j.cscm.2021.e00596>
5. Carvalho EAS, Vilela NF, Monteiro SN, Vieira CMF, Silva LC (2018) Novel artificial ornamental stone developed with quarry waste in epoxy composite. *Mater Res* 21:1–6. <https://doi.org/10.1590/1980-5373-MR-2017-1104>
6. Marvila MT, Alexandre J, Azevedo ARG, Zanelato EB (2019) Evaluation of the use of marble waste in hydrated lime cement mortar based. *J Mater Cycles Waste Manage* 21:1250–1261. <https://doi.org/10.1007/s10163-019-00878-6>
7. Zulução R, Calmon JL, Rebello TA, Vieira DR (2020) Life cycle assessment of the ornamental stone processing waste use in cement-based building materials. *Constr Build Mater* 257:19523. <https://doi.org/10.1016/j.conbuildmat.2020.119523>
8. Azevedo ARG, Marvila MT, Barroso LS, Zanelato EB, Alexandre J, Xavier GC, Monteiro SN (2019) Effect of granite residue incorporation on the behavior of mortars. *Materials* 12. <https://doi.org/10.3390/ma12091449>
9. López-Buendía AM, Guillem C, Cuevas JM, Mateos F, Montoto M (2013) Natural stone reinforcement of discontinuities with resin for industrial processing. *Eng Geol* 166:39–51. <https://doi.org/10.1016/j.enggeo.2013.09.004>
10. Pazeto AA, Amaral PM, Arcanjo RL (2020) A performance analysis of conventional reinforcement methods for ‘exotic’ building stones according to the current technical requirements. *Int J Rock Mech Min Sci* 135:104507. <https://doi.org/10.1016/j.ijrmms.2020.104507>
11. Brazilian Association of Technical Standards—ABNT (2015) NBR 15845–7 Rocks for cladding Part 7: determination of flexural strength by four points bending; ABNT, Rio de Janeiro, Brazil, pp 1–5 (in Portuguese)
12. Brazilian Association of Technical Standards—ABNT (2015) NBR 15845–2 Rocks for cladding Part 2: determination of bulk density, apparent porosity and water absorption; ABNT, Rio de Janeiro, Brazil, pp 1–4 (in Portuguese)
13. Brazilian Association of Technical Standards—ABNT (2015) NBR 15844 Rocks for cladding—requirements for granite; ABNT, Rio de Janeiro, Brazil, pp 1–3
14. Guzmán C, Torres D, Hucailuk C, Filipussi D (2015) Analysis of the acoustic emission in a reinforced concrete beam using a four points bending test. *Procedia Mater Sci* 8:148–154. <https://doi.org/10.1016/j.mspro.2015.04.058>

Comparison of Ceramic Blocks Incorporated with Ornamental Rock Waste in Hoffman and Caieira Furnace



E. B. Zanelato, A. R. G. Azevedo, M. T. Marvila, J. Alexandre, and S. N. Monteiro

Abstract The production of ceramic materials for the construction industry consists of different processes, among which burning can be highlighted. The burning process is primarily responsible for the final properties of the ceramic piece. As it is a gradual process of increasing the temperature, the environment provided by the furnace is essential for the burning to occur in a homogeneous way. Considering the trend of incorporation of waste in ceramics, the objective of this work is to compare the performance of two different furnaces, Hoffman and Caieira, in the production of ceramic pieces incorporated with ornamental rock waste. Physical and chemical characterization tests of the residue and clays were carried out. To evaluate the performance of the pieces burned in each furnace, mechanical resistance, water absorption, and linear variation tests were carried out. The results indicated that the pieces burned in the Hoffman furnace have superior properties to the Caieira furnace.

Keywords Ceramic · Residue · Furnace

Introduction

The red ceramic and ornamental stone industries are responsible for a considerable part of the economy in several places in Brazil and in the world. There is a high demand for ceramic pieces for civil construction works, becoming a basic segment in several places where there is expansion and modernization of urban centers. The ornamental stone industry, where the location of the poles is more restricted to places

E. B. Zanelato (✉)

IFF—Federal Institute Fluminense, Rua Cel. Valter Kramer, 357 - Parque Vera Cruz, Campos dos Goytacazes, Rio de Janeiro 28080-565, Brazil

A. R. G. Azevedo · M. T. Marvila · J. Alexandre

LECIV—Civil Engineering Laboratory, UENF—State University of the Northern Rio de Janeiro, Av. Alberto Lamago, 2000, Campos dos Goytacazes, Rio de Janeiro 28013-602, Brazil

S. N. Monteiro

Department of Materials Science, IME—Military Institute of Engineering, Square General Tibúrcio, 80, Rio de Janeiro 22290-270, Brazil

© The Minerals, Metals & Materials Society 2022

M. Zhang et al. (eds.), *Characterization of Minerals, Metals, and Materials 2022*,

The Minerals, Metals & Materials Series,

https://doi.org/10.1007/978-3-030-92373-0_28

close to the rock extraction, also have high demand in different industries, including civil construction.

The production of red ceramics still presents very rudimentary aspects, both in the materials used and, in the processes, and equipment. Studies carried out within this area are fundamental for the advances of the red ceramic industry and, consequently, for the improvement of the performance of its products.

Analyzing the manufacturing process of ceramic pieces, it can be seen that the firing step stands out as one of the main steps. The firing process, in general, is similar in all local ceramics, where the procedure is given by the gradual heating of the furnace for long periods and the final rise in temperature to the firing level, however, due to the use of different furnace, the efficiency with which each furnace performs the firing is different.

The verification of the efficiency of different types of furnace is recurrent, works such as Viera [1] that among the furnace used is the Hoffman, or de Moraes [2] that among the furnace used is the Caieira, in addition to the report produced by INT [3] which presented comparative data between different furnaces. It is also worth mentioning the studies carried out with the objective of individually evaluating each stage of the manufacturing process for each type of furnace such as the one in Azevedo [4].

In addition to the type of furnace used, another variable that directly influences the properties of manufactured ceramic pieces is their composition, that is, the dosage of raw materials for the production of ceramics.

In addition to clay, several residues have been used with the objective of combining performance and reducing the environmental impact, where the ornamental rock residue can be highlighted.

Several studies have already pointed out the ornamental rock waste as a solution to reduce the production cost, the environmental impact, in addition to increasing the performance of materials such as: concrete [5], mortar [6], and ceramic blocks [7].

The use of ornamental rock waste in red ceramics reduces the environmental impact in two different ways: (1) Replacement of clay, raw material removed from deposits for use in industry and (2) Appropriate destination for a waste that would be discarded in landfills [7].

The objective of this work is to evaluate the performance of ceramic pieces manufactured with different levels of incorporation of ornamental rock waste burned in Hoffman and Caieira furnace.

Materials and Methods

The clay used in the work was collected directly from the ceramic sector, being a material used for making ceramic masses.

Dimension stone residue was collected in settling deposits in the ornamental rock industry. The residue was collected in the form of sludge and placed to dry in the environment and later in a furnace.

The particle size analysis was performed following the standards of the NBR 7181 [8]. The fraction of the material retained in the 0.074 mm opening sieve (ABNT #200), the samples were classified by sieving. The passing fraction of material in the same sieve was classified by sedimentation. To carry out the sedimentation test, the substance sodium hexametaphosphate, a material with deflocculating action, was used. To classify the soil, the standard of Casagrande (1942)—Unified Soil Classification System was used. Classification is also used by the U.S. Army Corps of Engineers (Airports) and U.S. Bureau of Reclamation (Dams).

The material used in the Atterberg limits was ground and passed through a 0.42-mm aperture sieve (ABNT #40). The plasticity limit test was performed according to NBR 7180 [9], while the liquidity limit was performed according to NBR 6459 [10].

The determination of the real grain density was performed according to NBR 6457 [11] and NBR6458 [12], using a pycnometer.

The chemical composition was obtained through Energy-Dispersive X-Ray Spectroscopy (EDX), in the SHIMADZU EDX 700 equipment. With the test, it was possible to identify the amounts of each of the chemical elements present in the clay.

Five formulations were made to make the ceramic. The reference using only clay, in addition to replacements of 5%, 10%, 15%, and 20% of the clay mass per residue. the masses were

The ceramic formulations were molded by extrusion in the laboratory and fired at two temperatures, 750° and 900° in Caieira and Hoffman furnaces.

The Hoffman furnace has the following dimensions: 12.90 m (width) × 91.40 m (length) × 3.50 m (height). The volumetric capacity of the furnace is 10.60 m³ in each of the 15 ranges for filling with ceramic pieces. Figure 1 illustrates the morphology of the furnaces.

The Caieira furnace has the following dimensions: 4.45 m (width) × 5.50 m (length) × 4.30 m (height). The furnace's volumetric capacity is 56.89 m³ for filling with ceramic pieces. Figure 2 illustrates the morphology of Caieira furnace.

After firing, mechanical resistance, water absorption and linear variation tests were performed.

Results

Figure 3 shows the particle size distribution obtained by the residues and the clay used in the work to make the ceramics.

It can be seen from the figure that clay has a finer particle size than the residue, having up to 40% more fines volume below 2 μm. Only at 65 μm do the curves approach and the residue has a slight superiority in the volume of the passing material.

Table 1 presents the results of Atterberg limits and real grain density.



Fig. 1 Side view of the Hoffman furnace

Fig. 2 Caieira furnace



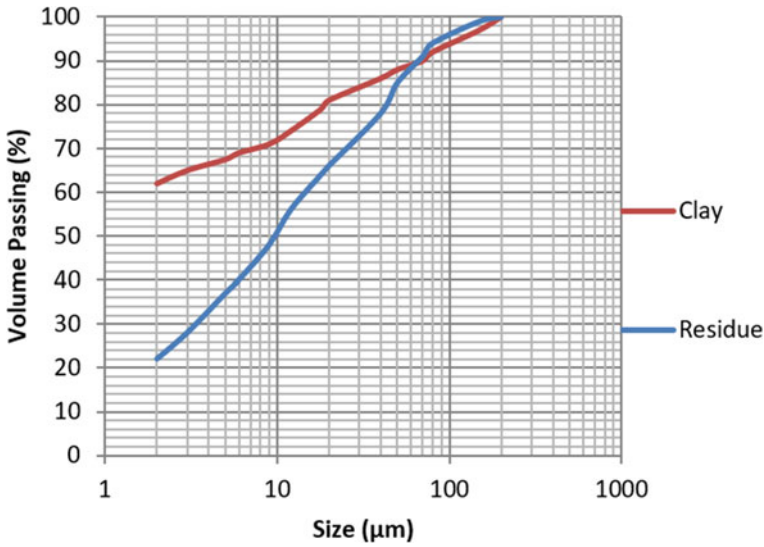


Fig. 3 Particle grain size

Table 1 Real grain density and Atterberg indices

	Clay	Residue
LL	47,8	–
LP	19,8	–
IP	28,0	–
Yg	2,83	2,67
USCS	CH	SM

The real density of the grains of the different waste granulometries obtained very similar results, and they present some similarity with clay. It was not possible to perform the Atterberg limits test with the ornamental rock residue as it does not have sufficient plasticity for the test.

Table 2 presents the results of the chemical analysis of the residue and clay.

The clay has an expressive composition of silicon oxide and aluminum, indicating a strong indication of the presence of clay minerals such as kaolinite ($Al_2O_3 \cdot 2SiO_2 \cdot 2H_2O$), a clay mineral commonly found in the region where the clay

Table 2 Chemical composition

Sample	Elements (%)								
	SiO ₂	Al ₂ O ₃	Fe ₂ O ₃	K ₂ O	TiO ₂	SO ₃	CaO	BaO	Outros
Clay	44,18	41,23	7,02	2,03	1,75	1,59	1,29	–	0,91
Residue	61,2	19,98	5,22	6,74	0,65	1,11	3,59	0,52	0,99

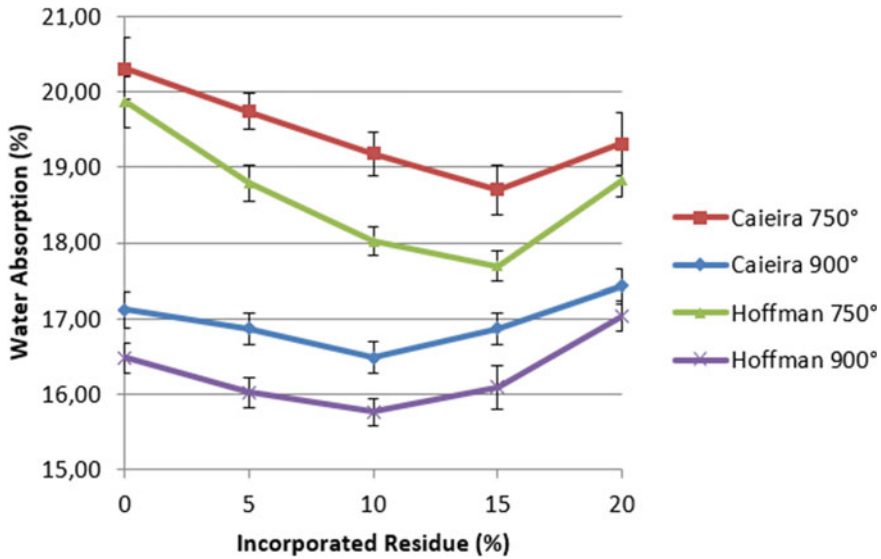


Fig. 4 Water absorption

was collected. The ornamental rock residue, on the other hand, has a predominance of Silica, a common element in granite.

The results obtained by the ceramic in the immersion absorption test are illustrated in Fig. 4.

It can be seen from the figure that the results show that the absorption of water by immersion varies according to the level of incorporation, the firing temperature, and the type of furnace used.

The firing temperature was the variable with the greatest influence on the performance of ceramic pieces. Calcination at higher temperatures causes greater densification of the structure and, consequently, less porosity.

The use of the Hoffman furnace presented better performance than the Caieira furnace. For both firing temperatures, the Hoffman furnace showed decreased absorption by immersion at all levels of ornamental waste incorporation.

The incorporation of residue was effective up to 10% incorporation with the Hoffman furnace and 15% with the Caieira furnace, where the best performances were obtained. After these levels of incorporation, absorption goes back up.

Figure 5 presents the results of linear variation.

Part of the trends verified in the water absorption test are verified in the linear variation test.

The firing temperature promotes an increase in linear variation, mainly due to greater densification promoted by chemical reactions at higher temperatures in the ceramic mass.

As in the absorption test, the use of the Hoffman furnace shows a similar tendency to increase in temperature, that is, to greater densification. However, the effect of the

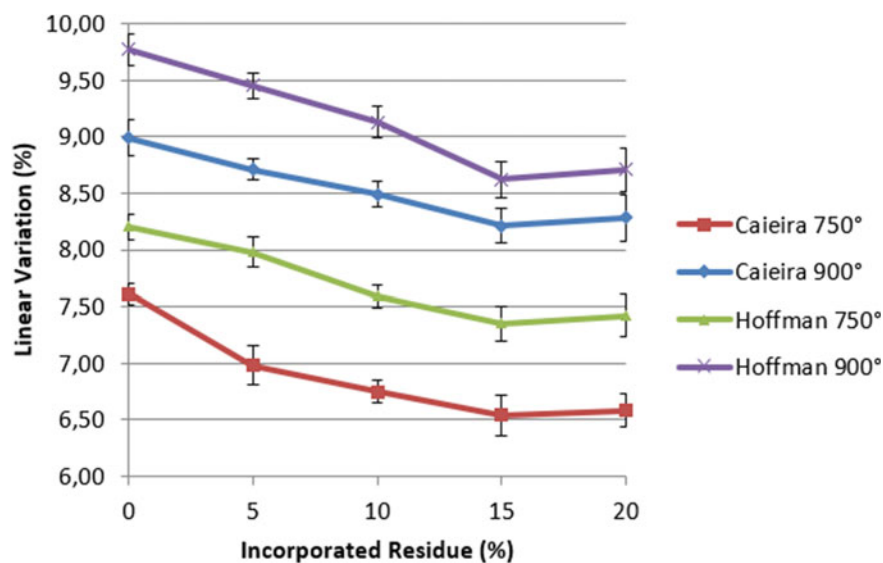


Fig. 5 Linear variation

furnace change impacts less on the linear variation performance than the temperature change.

Different from the behavior in the absorption test, the increase in the incorporation of ornamental rock residue has an inverse effect on the increase in the firing temperature and the use of the Hoffman furnace. The presence of the residue promotes a decrease in linear variation resulting from the decrease in chemical reactions at high temperatures occurring in clay.

The linear variation tends to stabilize with the incorporation of ornamental rock above 15% for both temperatures and furnace.

Figure 6 shows the results of the mechanical strength test.

The results obtained in the mechanical strength test have trends with great similarity to those obtained in the water absorption test.

The increase in the firing temperature is the variable with the greatest impact on mechanical strength, promoting a significant increase in strength as the temperature rises from 750 to 900 °C.

Changing the furnace from Caieira to Hoffman also significantly increases the mechanical resistance of the ceramic masses, as expected due to the greater densification of the ceramic, verified in previous tests.

The increase in the incorporation of ornamental rock residue follows the trend observed in the water absorption test and differs from the linear variation. The increase in the incorporation of ornamental rock promotes greater mechanical resistance, as well as the increase in temperature and the use of the Hoffman furnace.

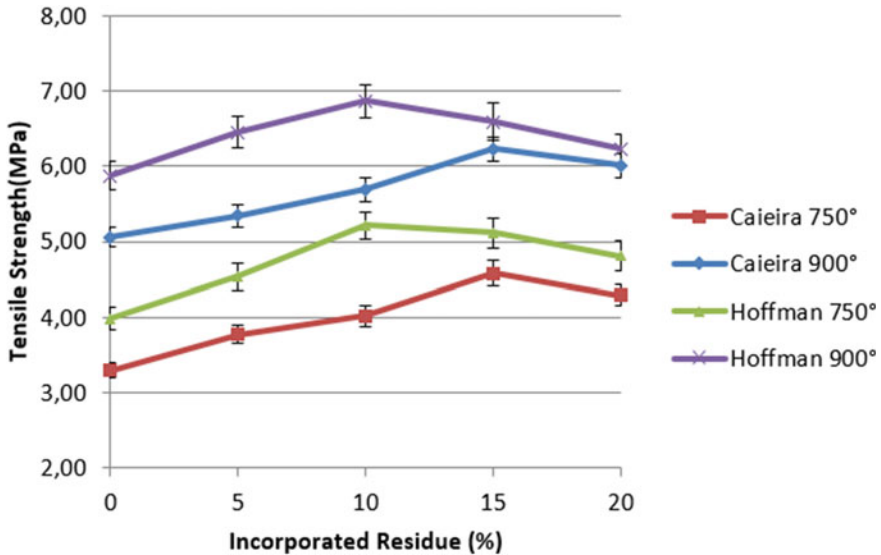


Fig. 6 Mechanical strength

The incorporation of ornamental stone residue obtains the best performance with 10% in the Hoffman furnace and 15% in the Caieira furnace. Above these levels of incorporation, the mechanical strength tends to decrease.

Conclusion

In this work, it was verified the influence that the firing temperature, the type of furnace and the incorporation of the ornamental rock residue have on the performance of ceramic pieces by the tests of water absorption by immersion, linear variation, and mechanical resistance. The following conclusions can be made with the analysis of the results:

- The firing temperature is the variable that most influences the performance of ceramic pieces. The increase in temperature promotes greater densification of ceramic pieces, verified by the decrease in water absorption, increase in linear variation, and increase in mechanical strength.
- The use of Hoffman furnace also showed greater capacity for densifying the ceramic mass as verified by the decrease in water absorption, increase in linear variation, and increase in mechanical strength.
- The incorporation of ornamental rock waste, despite promoting less impact than the other two variables, also influences the densification and reduction of chemical reactions at high temperatures of the ceramic mass. The incorporation of the

residue makes the ceramic pieces more stable during firing, reducing the linear variation. In addition, the incorporation of waste increases the density of the pieces, presenting less absorption and greater mechanical resistance.

- For the Hoffman furnace, incorporation of 10% achieved the best performance. Even with lower performance than the Hoffman furnace, the Caieira furnace achieves maximum performance with 15% residue incorporation.

Acknowledgements The authors thank the Brazilian agencies CNPq, CAPES, and FAPERJ for the support provided to this investigation.

References

1. Vieira CMF, Soares TM, Monteiro SN (2003) Ceramic mass for tiles: characteristics and firing behavior. *Cerâmica* 49:245–250 (in Portuguese)
2. Moraes DSG, Mendes JUL, Silva RM, Filho MOT, Cavalcante MAV (2010) Comparative analysis of heat loss between the Caieira furnace and vaulted furnace with insulation. VI Congresso Nacional de Engenharia Mecânica. Campina Grande—PB (in Portuguese)
3. Instituto Nacional de Tecnologia—INT (2011). Evaluation of the ceramic sector in the Northern region of the State of Pará—abaetetuba regions, Igarapé-Miri e São Miguel do Guamá. Rio de Janeiro—RJ (in Portuguese)
4. Azevedo ARG, de Alexandre JIS, Zanelato E, Marvila MT, Cerqueira N (2017) Influence of the burning temperature on red ceramic articles, pp 258–263. <https://doi.org/10.5151/1516-392X-30162> (in Portuguese)
5. Singh M, Choudhary K, Srivastava A, Sangwan KS, Bhunia D (2017) A study on environmental and economic impacts of using waste marble powder in concrete. *J Build Eng* 13:87–95
6. Singh Y, Vyas AK, Kabeer KISA (2017) Compressive strength evaluation of mortars containing ISF slag and marble powder. *Mater Today: Proc* 4(9):9635–9639
7. Munir MJ, Kazmi SMS, Wu Y, Hanif A, Khan MUA (2018) Thermally efficient fired clay bricks incorporating waste marble sludge: an industrial-scale study. *J Clean Prod* 174:1122–1135
8. Associação Brasileira de Normas Técnicas (2016) ABNT NBR 7181. Soil—grain size analysis
9. Associação Brasileira de Normas Técnicas (2016) ABNT NBR 7180. Soil—plasticity limit determination. Rio de Janeiro
10. Associação Brasileira de Normas Técnicas (2016) ABNT NBR 6459. Soil—liquid limit determination
11. Associação Brasileira de Normas Técnicas (2016) ABNT NBR 6457. Soil samples—preparation for compactation and characterization tests
12. Associação Brasileira de Normas Técnicas (2016) ABNT NBR 6458. Gravel grains retained on the 4,8 mm mesh sieve—determination of the bulk specific gravity, of the apparent specific gravity and of water absorption

Cooling Rate and Roughness Dependence of the Undercooling for One Single Sn Droplet with Si Thin Film Substrate by Nanocalorimetry



Shun Li, Li Zhang, Bingge Zhao, Kai Ding, and Yulai Gao

Abstract Nanocalorimetry has been developed and used to study the nucleation behavior of one single metallic droplet, especially the solidification undercooling. For heterogeneous nucleation, cooling rate and nucleation substrate are deemed as significant factors to affect the solidification undercooling. In this paper, the roles of cooling rate and substrate roughness in undercooling for the Sn droplet were comparatively studied. The Si thin film substrate was prepared by magnetron sputtering deposition technique with the deposition rate about 10 nm/min. Increasing the cooling rate from 50 to 10^4 K/s, the undercooling of the Sn droplet on the substrate was increased, followed by a gradually slow increment and then kept stable at high cooling rate. Besides, a roughness dependence of undercooling could also be observed at low cooling rate. The undercooling was increased with decreasing the roughness of the Si substrate, reflecting the nucleation acceleration by the large roughness for its favorable heat transfer.

Keywords Nanocalorimetry · Undercooling · Substrate · Si thin film · Cooling rate · Roughness

S. Li · L. Zhang · B. Zhao · K. Ding · Y. Gao (✉)

Center for Advanced Solidification Technology (CAST), School of Materials Science and Engineering, Shanghai University, Shanghai 200444, P.R. China
e-mail: ylgao@shu.edu.cn

B. Zhao · K. Ding · Y. Gao

State Key Laboratory of Advanced Special Steel, Shanghai University, Shanghai 200444, P.R. China

Y. Gao

Shanghai Engineering Research Center for Metal Parts Green Remanufacture, Shanghai 200444, P.R. China

© The Minerals, Metals & Materials Society 2022

M. Zhang et al. (eds.), *Characterization of Minerals, Metals, and Materials 2022*,

The Minerals, Metals & Materials Series,

https://doi.org/10.1007/978-3-030-92373-0_29

Introduction

The solidification undercooling is of significance theoretically and experimentally. It is generally accepted that unique properties like grain refinement [1, 2] and heterogeneous mechanism transition [3] will occur when metallic materials are solidified with large undercooling. The undercooling, as a crucial factor for the solidification process, is related not only to the overheating [4, 5], droplet size [6], and heterogeneous nucleation interface [7, 8] but also to the cooling rate [9, 10]. Some studies have been carried out on the cooling rate dependence of undercooling [11–13]. However, in many cases, the liquid–solid transition of metallic materials could not be investigated directly because of the limitation of the equipment and the high-temperature conditions during this kind of transition. Generally speaking, the undercooling is always measured by conventional thermal analysis devices like differential scanning calorimeter (DSC) and differential thermal analyzer (DTA), which can only operate at the cooling rate below 500 K/min [14, 15]. For higher cooling rate, computer simulation techniques, and theoretical calculation are more frequently employed [16] because of the limitation of the conventional calorimetry.

Attributing to the technique development in the study of solidification process of micro-sized droplets, some solidification behavior such as undercooling and enthalpy can be successfully measured at high scanning rate by nanocalorimeter. This analysis device allows a scanning rate from 1 to 10^6 K/s with the sensitivity of nJ/K. With the help of nanocalorimeter, two exothermic peaks of Sn droplets embedded in the Al matrix were traced in our previous study [17]. In addition, it was reported that different structure in amorphous $\text{Ce}_{68}\text{Al}_{10}\text{Cu}_{20}\text{Co}_2$ (at. %) in situ prepared by nanocalorimetry were obtained at the quenching rates from 100 to 50,000 K/s [18]. In particular, early stage nucleation of Ag_3Sn phase under rapid solidification was detected [19].

Generally, heterogeneous nucleation is dominant in the solidification process. For film substrates, roughness is one of the main features that can possibly affect the nucleation behavior. Large roughness of Si substrate could slow down the nucleation of c-BN, indicated by Chan et al. [20]. Utilizing the magnetron sputtering deposition technique, the thin film Si substrate was prepared and cut to some piece small enough to be moved to the measurement zone of the nanocalorimeter. In the present study, the undercooling of one single Sn droplet was measured with scanning rate from 50 to 10^4 K/s by nanocalorimetry. The Si thin film was prepared as the nucleation substrate. Besides, its roughness dependence of the undercooling was discussed.

Experiment

The spherical Sn (99.999 wt.%) droplets used in this investigation were prepared by the self-developed consumable-electrode direct current arc (CDCA) technique [21], and Si thin films were prepared by employing a magnetron sputtering deposition technique (JGP-560, SKY Technology Development) with a base pressure of $4 \times$

Table 1 Preparation parameters of Si thin films

Film	Sputtering time, h	Sputtering power, W	Sputtering pressure, Pa	Base pressure, Pa
Film #1	0.5	120	0.6	4×10^{-4}
Film #2	1.0	120	0.6	4×10^{-4}
Film #3	2.0	120	0.6	4×10^{-4}

10^{-4} Pa, deposited on the silica glass substrates. In addition, polycrystalline silicon (99.999 wt.%) was used as the sputtering target with the dimension of 50 mm and 4 mm in thickness. The sputtering time was chosen as 0.5 h, 1.0 h, and 2.0 h, respectively. To confirm that the Si thin film is small enough to be positioned in the measurement zone, the film was cut to the infinitesimal piece and moved by a thin Cu wire (with the diameter of 30 μm). More details of the preparation parameters of Si thin films are listed in Table 1.

After being cleaned by anhydrous alcohol and deionized water, a Si thin film and one Sn droplet with a diameter of 12.5 μm were placed exactly on the measurement zone of the nanocalorimetric sensor with the help of copper wire and optical microscopy (OM, Olympus SZ61). Then the undercooling of this single Sn droplet was measured by nanocalorimetry. The microstructure of the Si thin films was observed by scanning electron microscopy (SEM, Phenom ProX) and atomic force microscopy (AFM, Nanonavi SPA-400).

Results and Discussion

The appearance of the different Si thin films is shown in Fig. 1. The bright part with irregular shape is the above-mentioned sputtered thin film, while the square and transparent silica glass substrate is on the bottom. Clearly, the sputtered Si thin films are flat and smooth, reflecting the successful preparation for the substrate.

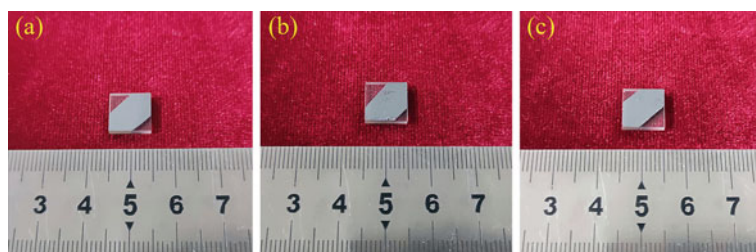


Fig. 1 Images of the Si thin films that prepared by magnetron sputtering technique: **a** film #1, **b** film #2, and **c** film #3

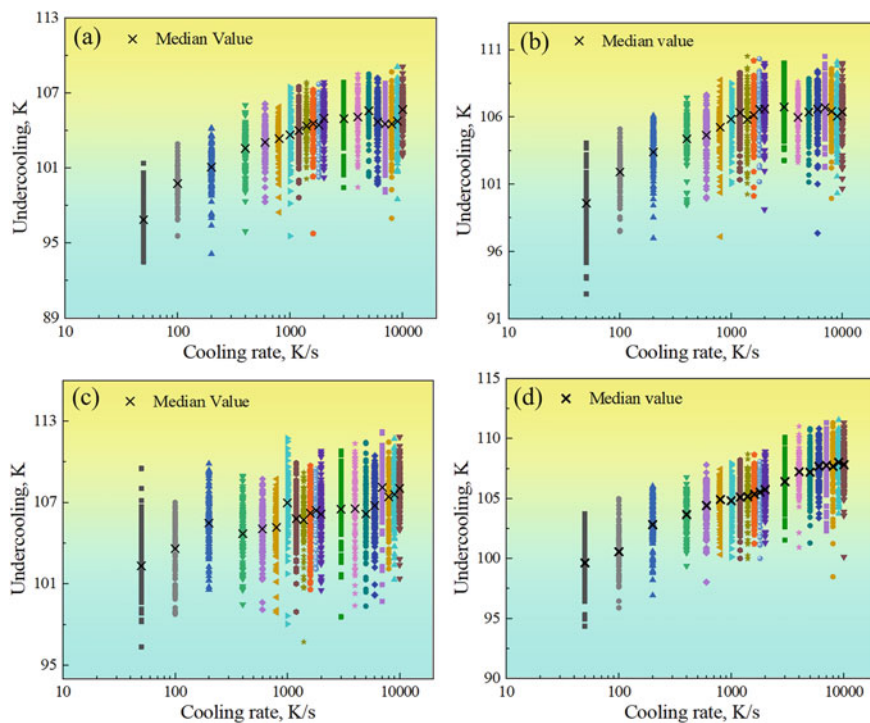
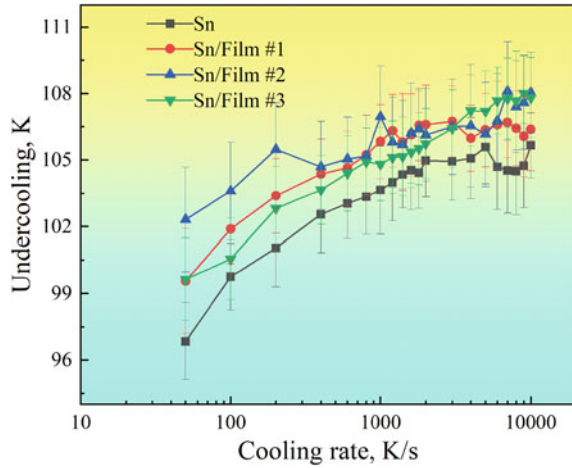


Fig. 2 Undercooling of single Sn droplet with various substrates and cooling rate conditions: **a** without film substrate, **b** film #1, **c** film #2, and **d** film #3

Only one same Sn droplet was used in the nanocalorimetric experiments. As shown in Fig. 2, a total of 20 cooling rates in the range from 50 to 10^4 K/s are chosen, and 100 cycle measurements are repeated for each cooling rate. It should be noticed that the undercooling varies in a range of temperatures because of the random nature of nucleation. The median value of undercooling is obtained by calculation so that the general trend could be predicted. Compared to the undercooling obtained at low cooling rate, high cooling rate scanning can result in larger undercooling, as indicated in Fig. 2a. A similar trend is found in the experiments with various Si thin film substrates. Increasing the cooling rate from 50 to 10^4 K/s, the undercooling increases, followed by a gradually slow increment and then keeps stable at high cooling rate, as shown in Fig. 2b–d. According to the results from Yang et al. [22], the undercooling of an Al–Si₁₂ particle increased with increasing cooling rate as well.

To investigate the undercooling change of one single Sn droplet on various substrates, the median value of undercooling is put together, as presented in Fig. 3. Increasing the cooling rate from 50 to 10^4 K/s, the measurement without Si thin film substrate reveals the lowest median value of undercooling. In addition, the increase

Fig. 3 Comparison of undercooling change of one single Sn droplet on various substrates



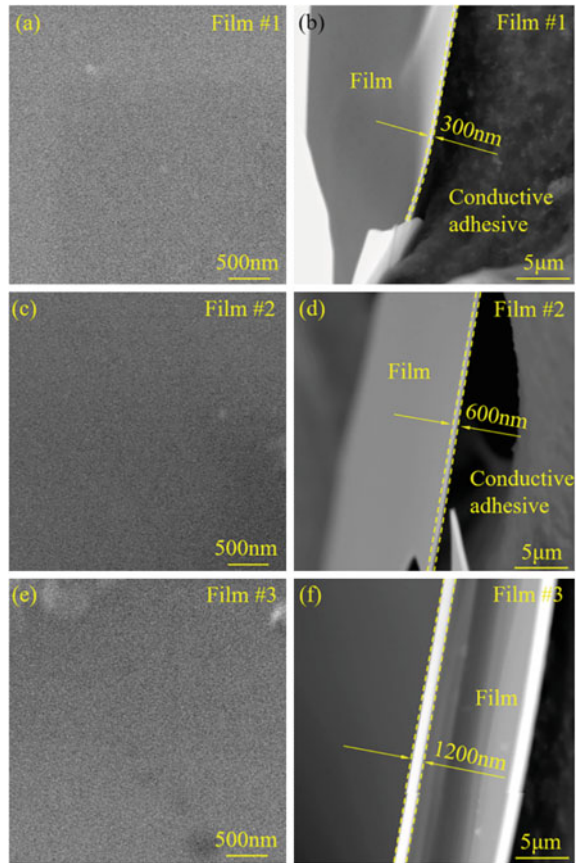
of undercooling with the addition of Si thin films indicates the inhibition of Si thin films on the nucleation of Sn droplets.

For the cooling rate range from 50 to 1,000 K/s, the undercooling increases in a stable way. In particular, it can be observed that with the substrate of film #2 the median value of undercooling is always the largest at each rate, while the lowest undercooling is obtained by using the substrate of film #3. In order to illustrate the effect of various film substrates on the undercooling, the SEM analysis was performed.

The top surface and cross-sectional images of Si thin films are observed by SEM, as exhibited in Fig. 4. It is found that for all three kinds of films, the top surfaces are flat and smooth. According to our previous study and the result by Marquez et al. [23], the Si thin films were fully amorphous. The Si thin film substrate prepared by the magnetron sputtering deposition technique can be easily divided into several parts owing to its brittleness. The Si thin film was placed on the side face of the cylindrical objective table (Cu) with the help of the conductive adhesive. Thus, the cross section of the Si thin films can be clearly observed by SEM, and the Si thin film can be confirmed by observing the position of the conductive adhesive, as shown in Fig. 4b, d, and f. The thickness of films #1–#3 is 300, 600, and 1200 nm, respectively. The deposition rate is about 10 nm/min, and obviously the increase of sputtering time can induce larger thickness. It should be noticed that the thickness of Si thin films was controlled at the microscale, and the film details should be further accurately measured.

The AFM images of various Si thin film substrates are exhibited in Fig. 5. It can be observed from 2D images that the surface is relatively flat and more details about the feature of films are shown in Fig. 5b, d, and f. The root mean square (RMS) roughness of film #1 to #3 is 0.67, 0.60, and 0.70 nm, respectively. With the increase of sputtering time, the roughness decreased first and then increased again. Clearly, the undercooling is increased with decreasing the roughness of the Si

Fig. 4 Scanning electron microscope images of the prepared Si thin films: **a**, **c**, and **e** top surface of films #1, #2, and #3, respectively, and **b**, **d**, and **f** cross section of films #1, #2, and #3, respectively



thin film substrate at low cooling rate. As previously mentioned, the heterogeneous nucleation surfaces were controlled by the applied Si thin film substrates, which could correspondingly influence the undercooling. In an early study by Glicksman et al. [24], the undercooling of liquid Sn which is in contact with various substrates was measured. The metallic substrate may lead to a lower undercooling than the others, but the effect of substrate roughness was not explained. The relationship between undercooling and substrate roughness can be further elucidated by nanocalorimetry combined with AFM. In this case, the median value of undercooling changes in a range of about 2 K in the condition of the film substrates RMS roughness mentioned above.

Based on the above facts, a schematic is established to explain the influence of the cooling rate and surface roughness on the undercooling for the solidified Sn droplet, as shown in Fig. 6. On one hand, the undercooling of one single Sn droplet is clearly affected by the surface roughness at lower cooling rates. As for the small roughness, a large number of Sn atoms concentrate on the Si thin film substrate, yet the heat transfer process is limited because of the less contact between the liquid Sn atoms and the cooling substrate, as indicated in Fig. 6a. On the contrary, for the large

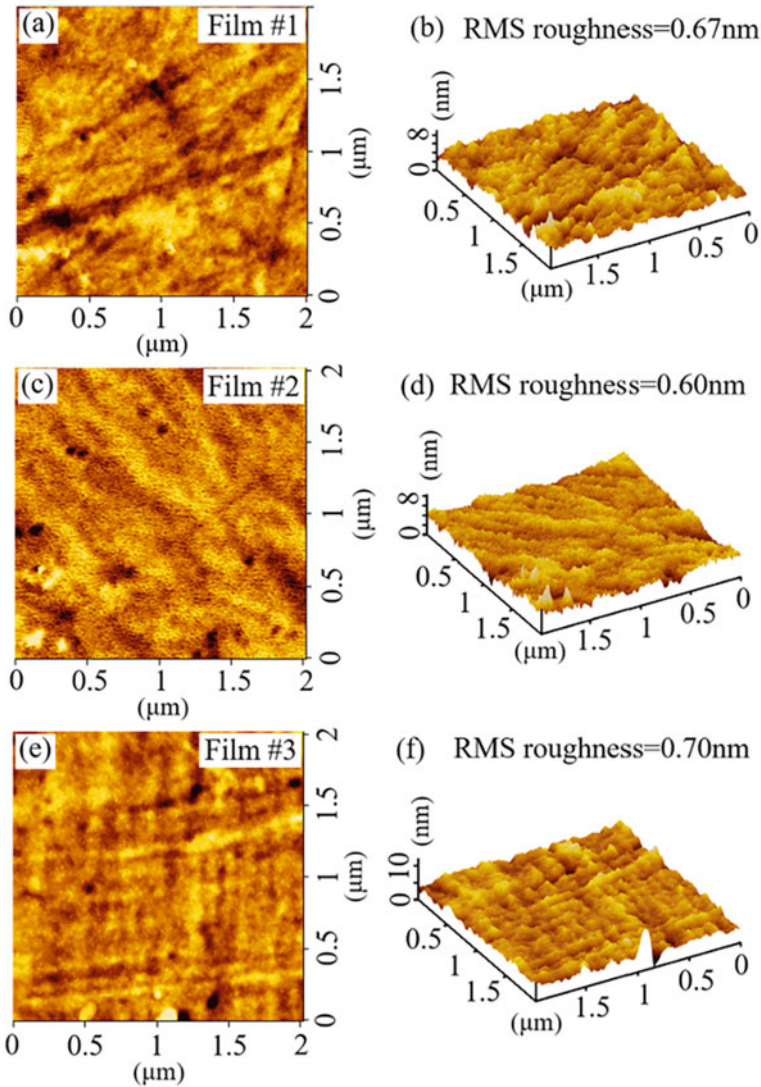


Fig. 5 Atomic force microscope images of Si thin films: **a**, **c**, and **e** 2D images of the surface morphology, and **b**, **d**, and **f** 3D images of the surface morphology

roughness substrate the liquid Sn atoms can concentrate in the “cavities” existed in the rough surface and gain better heat transfer, promoting their nucleation (namely decreasing the undercooling), as illustrated in Fig. 6b. Continuously increase the cooling rate, the high-temperature atoms can be frozen as rapidly as possible. That is to say, the cooling rate is increased rapid enough and dominates the nucleation

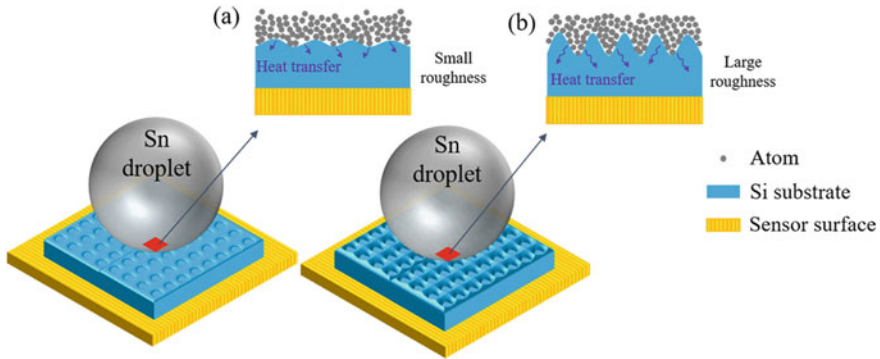


Fig. 6 Schematic of the nucleation of Sn droplet on various substrates: **a** small roughness, **b** large roughness. The red rectangles indicate the zones where droplet and Si thin film substrate contact and the heat transfer are indicated by the arrows, and the length of the arrows reflect the heat-transfer intensity (Color figure online)

process. In this case, the variety of the substrate roughness becomes unimportant, though the undercooling still increases based at higher cooling rates.

Conclusions

The undercooling of metallic materials was significantly influenced by cooling rate and nucleation substrate. Attributing to the nanocalorimetry, the undercooling of one single Sn droplet was obtained with a cooling rate ranging from 50 to 10^4 K/s. A significant increase in the undercooling was observed, followed by a slow increment and then a stable undercooling occurred at a high cooling rate. Si thin films were selected as nucleation substrates, which were prepared with different sputtering time at the deposition rate of about 10 nm/min. The RMS roughness of Si thin films was 0.67, 0.60, and 0.70 nm, respectively. The undercooling decreased with increasing the surface roughness of Si thin films because of the “cavities” that existed in the surface with large roughness and their promotion effect on the heat transfer.

Acknowledgements This work is supported by the National Natural Science Foundation of China (Grant no. 52071193).

References

1. Ma K, Zhao YH, Xu XL, Hou H (2019) The effect of undercooling on growth velocity and microstructure of Ni95Cu5 alloys. *J Cryst Growth* 513:30–37

2. Xu XL, Zhao YH, Hou H (2019) Observation of dendrite growth velocity and microstructure transition in highly undercooled single phase alloys. *Mater Charact* 155:109793
3. Yang B, Gao YL, Zou CD, Zhai QJ, Abyzov AS, Zhuravlev E, Schmelzer JWP, Schick C (2010) Cooling rate dependence of undercooling of pure Sn single drop by fast scanning calorimetry. *Appl Phys A Mater Sci Process* 104(1):189–196
4. Minakov A, Morikawa J, Ryu M, Zhuravlev E, Schick C (2021) Variations of interfacial thermal conductance at melting and crystallization of an indium micro-particle in contact with a solid. *Mater Des* 201:109475
5. Yang B, Perepezko JH, Schmelzer JW, Gao YL, Schick C (2014) Dependence of crystal nucleation on prior liquid overheating by differential fast scanning calorimeter. *J Chem Phys* 140(10):104513
6. Qian M (2007) Heterogeneous nucleation on potent spherical substrates during solidification. *Acta Mater* 55(3):943–953
7. Sun J, Wang DP, Zhang YH, Sheng C, Dargusch M, Wang G, John D, Zhai QJ (2018) Heterogeneous nucleation of pure Al on MgO single crystal substrate accompanied by a MgAl₂O₄ buffer layer. *J Alloys Compd* 753:543–550
8. Ma ZL, Gourlay CM (2017) Nucleation, grain orientations, and microstructure of Sn-3Ag-0.5Cu soldered on cobalt substrates. *J Alloys Compd* 706:596–608
9. Gao YL, Zhuravlev E, Zou CD, Yang B, Zhai QJ, Schick C (2009) Calorimetric measurements of undercooling in single micron sized SnAgCu particles in a wide range of cooling rates. *Thermochim Acta* 482(1–2):1–7
10. Wang DP, Chang W, Sun J, Sheng C, Zhang YH, Zhai QJ (2018) Heterogeneous nucleation of Au on Al₂O₃ substrate under the impact of droplet size and cooling rate. *IOP Conf Ser: Mater Sci Eng* 381:012058
11. Gao YL, Zhao BG, Vlassak JJ, Schick C (2019) Nanocalorimetry: Door opened for in situ material characterization under extreme non-equilibrium conditions. *Prog Mater Sci* 104:53–137
12. Guo EJ, Wang L, Feng YC, Wang LP, Chen YH (2018) Effect of cooling rate on the microstructure and solidification parameters of Mg-3Al-3Nd alloy. *J Therm Anal Calorim* 135(4):2001–2008
13. Sheng C, Sun J, Wang DP, Zhang YH, Li LJ, Chen XR, Zhong HG, Zhai QJ (2017) Heterogeneous nucleation of pure gold on highly smooth ceramic substrates and the influence of lattice misfit and cooling rate. *J Mater Sci* 53(6):4612–4622
14. Mizoguchi T, Perepezko JH (1997) Nucleation behavior during solidification of cast iron at high undercooling. *J Mater Sci Eng A* 226–228:813–817
15. Mueller BA, Perepezko JH (1991) The undercooling of aluminum. *Metall Trans A* 18:1143–1150
16. Xu Jf, Xiang M, Dang B, Jian ZY (2017) Relation of cooling rate, undercooling and structure for rapid solidification of iron melt. *Comput Mater Sci* 128:98–102
17. Zhang WP et al (2013) Application of fast scanning calorimetry in the rapid solidification of Tin particles embedded in Al matrix. Paper presented at the 142nd TMS annual meeting, San Antonio, Texas, 3–7 Mar 2013, pp 477–484
18. Zhao BG, Yang B, Abyzov AS, Schmelzer JWP, Rodriguez-Viejo J, Zhai QJ, Schick C, Gao YL (2017) Beating homogeneous nucleation and tuning atomic ordering in glass-forming metals by nanocalorimetry. *Nano Lett* 17(12):7751–7760
19. Zhao BG et al (2014) Structure characterization of Sn-based and Ce-based alloys treated by ultrafast scanning. Paper presented at the 143rd TMS annual meeting, San Diego, California, 16–20 Feb 2014, pp 227–234
20. Chan CY, Eyhusen S, Meng XM, Bello I, Lee ST, Ronning C, Hofsass H (2006) The effect of substrate surface roughness on the nucleation of cubic boron nitride films. *Diamond Relat Mater* 15(1):55–60
21. Zhao J, Gao YL, Zhang WP, Zhao BG (2012) Observation of the solidification microstructure of Sn_{3.5}Ag droplets prepared by CDCA technique. *J Mater Sci Mater Electron* 23(12): 2221–2228

22. Yang B, Peng Q, Milkereit B, Springer A, Liu D, Rettenmayr M, Schick C, Kessler O (2021) Nucleation behaviour and microstructure of single Al-Si₁₂ powder particles rapidly solidified in a fast scanning calorimeter. *J Mater Sci* 56(22):12881–12897
23. Marquez E, Saugar E, Diaz JM, Garcia-Vazquez C, Fernandez-Ruano SM, Blanco E, Ruiz-Perez JJ, Minkov DA (2019) The influence of Ar pressure on the structure and optical properties of non-hydrogenated a-Si thin films grown by rf magnetron sputtering onto room-temperature glass substrates. *J Non-Cryst Solids* 517:32–43
24. Glicksman ME, Childs WJ (1962) Nucleation catalysis in supercooled liquid tin. *Acta Metall* 10(10):925–933

Determination of Strength to the Hard Body Impact of Raw, Resinate, and Screened Ornamental Rocks



A. C. Hilário, E. D. F. Castilho, A. R. G. Azevedo, T. E. S. Lima,
M. T. Marvila, and S. N. Monteiro

Abstract Ornamental rocks applied to civil construction are subject to the appearance of cracks and ruptures. Some processes provide the rock with greater resistance to bending efforts: The resin coating method consists of applying a mixture of resin and catalyst on the surface to be used, while meshing is the process of fixing a fiberglass mesh on the unfinished face of the rock. This work shows the results achieved in hard body impact resistance tests, aiming to define and scale the increase in resistance using resin and screen in materials with a thickness of 0.03 m. The rocks used in this work are commercially known as Vicenza, Romanix, and Nevasca. The research results indicate the effectiveness of the application of resin and mesh provided by the significant increase in strength. However, the raw materials also achieved satisfactory results, especially the Nevasca material, which obtained the highest average of rupture heights.

Keywords Hard body impact · Raw · Resinate · Screened · Ornamental rock

A. C. Hilário · E. D. F. Castilho

IFES—Espírito Santo Federal Institute, Department of Mining Engineering, Eng. Fabiano Vivácqua Highway, 1.568, Cachoeiro de Itapemirim 29322-000, Brazil
e-mail: andrea@ifes.edu.br

E. D. F. Castilho

e-mail: evanizis@ifes.edu.br

A. R. G. Azevedo (✉)

UENF—State University of the Northern Rio de Janeiro, LECIV—Civil Engineering Laboratory, Av. Alberto Lamego, 2000, Campos dos Goytacazes, Rio de Janeiro 28013-602, Brazil

T. E. S. Lima · M. T. Marvila

UENF—State University of the Northern Rio de Janeiro, LAMAV—Advanced Materials Laboratory, Av. Alberto Lamego, 2000, Campos dos Goytacazes, Rio de Janeiro 28013-602, Brazil

S. N. Monteiro

IME—Military Institute of Engineering, Department of Materials Science, Square General Tibúrcio, 80, Rio de Janeiro 22290-270, Brazil

© The Minerals, Metals & Materials Society 2022

M. Zhang et al. (eds.), *Characterization of Minerals, Metals, and Materials 2022*,
The Minerals, Metals & Materials Series,
https://doi.org/10.1007/978-3-030-92373-0_30

Introduction

Buildings in general receive finishing or coating layers on the walls, floors, and facades, of which the purpose is both aesthetic, for the purpose of decorating the environments and buildings, and functional for protecting the structure of the buildings from the weather, the attack of chemicals contained in cleaning products and others. Within this context, the materials commonly used in civil construction are rocks, ceramics, and glass [1–3].

The rocks are a differential constantly cited by engineers and architects in the planning of the work because they are a natural material, with a huge range of textures, patterns, and exclusive colors. Similar to other construction materials, rocks have their own peculiarities, of which their definition and understanding are fundamental for their specification and correct use [4].

The characterization of ornamental stones aims to obtain physical, chemical, mechanical, and petrographic parameters through laboratory tests, which guide the correct choice, application, and use of these materials in civil construction. From these tests, pathologies are identified in these rocks, such as a tendency to spots, granular degradation, among others, which can be recovered or avoided. According to Frascá et al. [4], the knowledge and correct handling of technological information, ensure the safety in the selection and specification of rocks for various coating projects.

Ornamental rocks that are used as coatings, floors, and benches are susceptible to breakage due to the fall of the most diverse types of objects, as well as cracks and cracking during processes subsequent to unfolding, such as polishing and/or transport. In order to increase the flexural strength of these materials, the meshing process is used, which consists of applying the fiberglass mesh together with the epoxy system (resin/catalyst) on the part that will not be polished. The epoxy system promotes the fixation of the mesh and fills the micro-cracks [5].

The test to determine the hard body impact strength, carried out following the Brazilian standard NBR 15,845–8:2015 [6], is the recommended method for determining the hard body impact strength of finished rock products intended for use as building cladding materials.

Given the growing demand from the domestic and foreign market for ornamental rocks, technical criteria are sought to determine the best use and application for them. Therefore, this work aims to perform the technological characterization of rock materials used for coatings by determining the hard body impact strength in raw, resins, and screens materials.

Materials and Methods

The specimens used in the test belong to the large group of granites and were identified as Vicenza, Romanix, and Nevasca.

Thirty specimens were used, 10 for each type of material, 5 raw, and 5 resined and screened measuring $0.2 \times 0.2 \times 0.03$ m.

The samples were placed in the oven for drying. This moisture removal step is important for the specimens to absorb the resin well. The samples remained for 48 h in an oven at a temperature of 70°C and, at the end of this period, they were resined. The resin used was of the epoxy type and the catalyst had a cure time of 48 h. The catalyst used was 37%, that is, for 100 g of resin, 37 g of catalyst should be used. Considering that each sample had an area of 0.04 m^2 , 6 g of the mixture were applied.

To resin the screened samples, the mixture was spread over the unfinished face for approximately 8 min until the rock completely absorbed the compound. After applying the resin, the 15 samples were left to dry at room temperature for 48 h. For the screening process, a fiberglass screen weighing 80 g/m^2 and a 4×4 mm mesh was used.

After curing, markings and measurements of the lengths and thicknesses of all faces of the specimens were made. After measuring all specimens, the samples were taken to the hard body impact equipment. The specimens were placed on the sand mattress with the finishing side facing upwards. Subsequently, the specimen was accommodated so that the sphere reached its center. The samples were leveled with the aid of a spirit level. From the height of 20 cm, the ball was released in free fall according to [6]. In the intervals between falls, the specimens were cleaned with the aid of a brush so that the sand would not interfere with the friction between the samples. After the initial fall, the procedures were repeated, increasing the interval by 5 cm until the specimen ruptured.

Results and Discussion

The results of the hard body impact strength tests for each group of granites are shown in Table 1 in raw, resin, and screen materials in a thickness of 0.03 m. The results of the average rupture height in meters, rupture energy in joules (J), the standard deviations of each test, and the average deviation of each specimen are displayed.

The rupture of a plate caused by the amount of energy released by the impact of a body is important for materials in their many applications. Thus, the smaller the result of the experiment, the lower the impact strength of the material, making it essential to take care in terms of transport, storage, and placement [7]. Among the samples, the raw materials obtained the result of lower energy of rupture compared to the resins and screens, thus suggesting greater care in handling these materials.

Figures 1, 2, and 3 demonstrate the increase in the average breakage heights of raw materials in relation to resin and screen. The normative parameter used to verify the results obtained in the tests is the reference standard for granites ABNT NBR 15,844:2010 [8], which corresponds to a minimum average height of 0.3 m.

As can be seen, all materials in raw or resined and screened form meet the reference standard for granites NBR 15,844:2010, which determines the value of 0.3 m as the minimum average height of rupture of the specimens [9]. The Vicenza material

Table 1 Hard body impact strength test results in different types of specimens

	Granite type Vicenza		Granite type Romanix		Granite type Nevasca	
	Raw specimens	Resined and screened specimens	Raw specimens	Resined and screened specimens	Raw specimens	Resined and screened specimens
Average break height (m)	0.59	0.92	0.62	0.88	0.63	0.92
Standard deviation ^a	0.042	0.057	0.045	0.084	0.057	0.148
Breaking energy (J)	5.786	9.022	6.080	8.629	6.178	9.022
Mean deviation ^b	0.049		0.064		0.103	

^a For five specimens^b For ten specimens

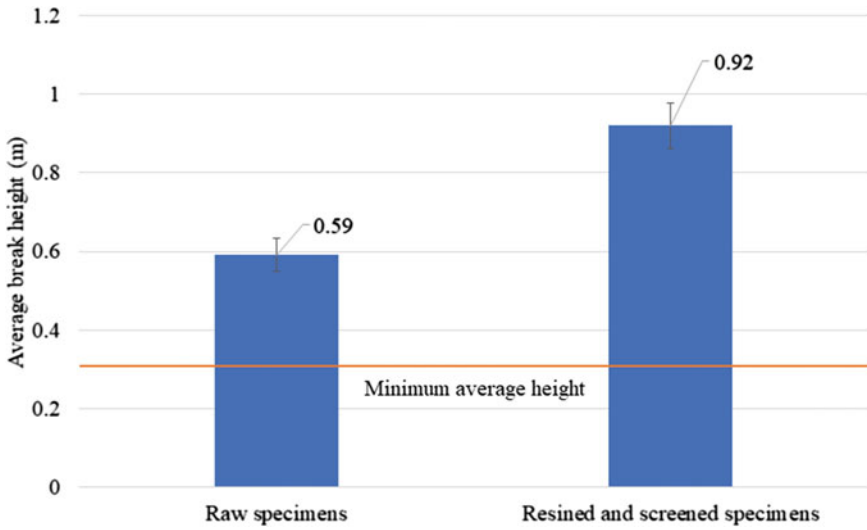


Fig. 1 Results of Granite type Vicenza breakage heights average (m)

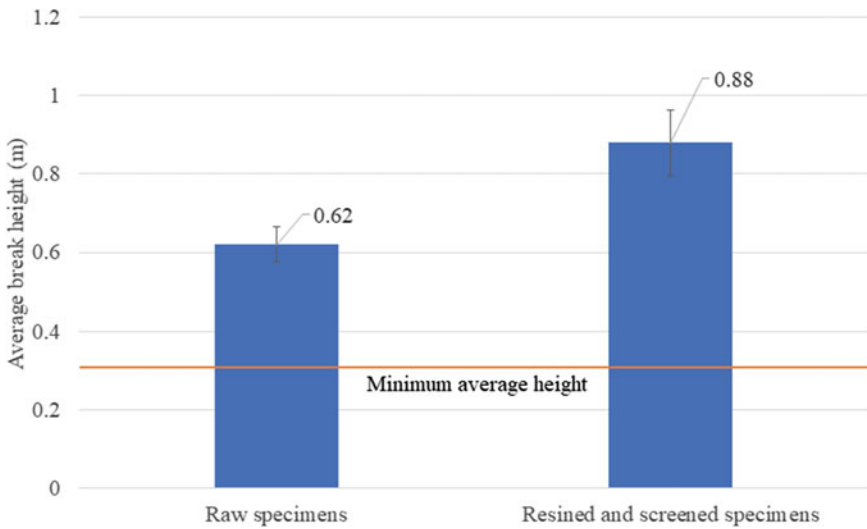


Fig. 2 Results of Granite type Romanix breakage heights average (m)

obtained an increase of 0.33 m in the average breakage heights with the application of resin and screen, while the raw Romanix material reached 0.26 m of increase in the average of the breakage heights with the use of resin and screen. Finally, the Nevasca material obtained an increase of 0.29 m in the average rupture heights [10].

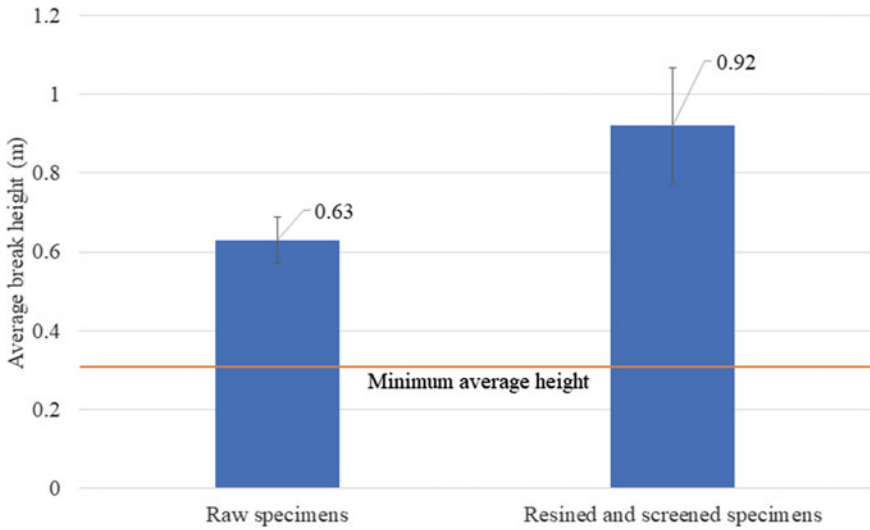


Fig. 3 Results of Granite type Nevasca breakage heights average (m)

It is observed that the use of resin and mesh in these materials resulted in a considerable gain in strength. The Nevasca material presented resistance slightly higher than the other raw samples. For resins and screens, Vicenza and Nevasca materials resulted in the same average breakage heights [11].

Figure 4 compares the percent increase in impact strength of resined and screened samples.

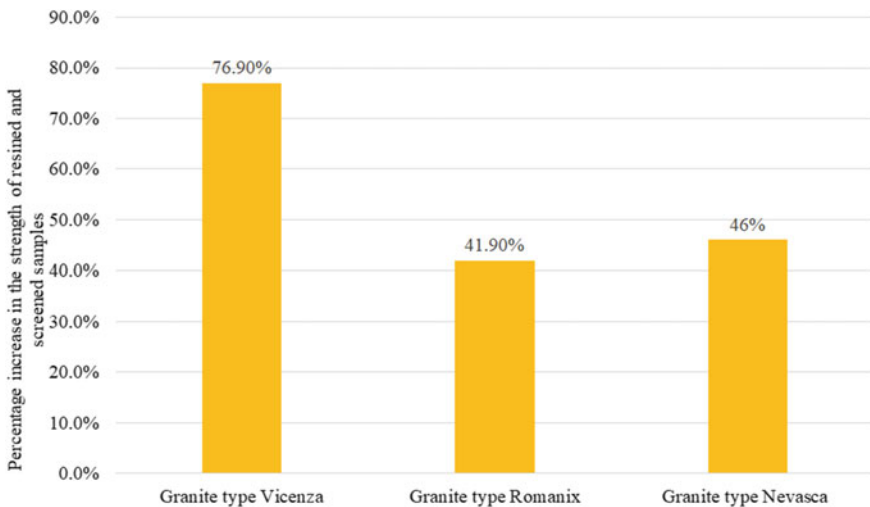


Fig. 4 Percentage increase in the strength of resined and screened samples

The results demonstrate that the application of resin and mesh led to an increase in mechanical strength in the samples. Among the specimens studied, the Vicenza material stood out for presenting an increase of almost 80% in strength, while the samples Romanix and Nevasca showed percentage increases in strength of 41.93 and 46.03%, respectively, with the application of the resin and screen [12].

In relation to the hard body impact strength in ornamental rocks, all samples presented the satisfactory value, thus, being above the parameters stipulated by ABNT NBR 15,844:2010 [8], which allows these samples with a thickness of 0.03 m to be used in the most diverse applications such as floors, thresholds, steps, counters, and sinks [13, 14].

Conclusion

After the results, it was concluded that the use of resin and screen in ornamental rocks with a thickness of 0.03 m were able to generate a considerable increase in resistance in relation to falling objects. Resining and screening improved the strength of materials in the same thickness by at least 40%. Likewise, the raw samples presented satisfactory results, meeting the requirements of the ABNT NBR 15,844:2010 [8] standard, which determines the minimum value for the hard body impact strength test of 0.3 m.

The values obtained attest that the analyzed rock samples present a good resistance to shock and can be used for coatings on floors, steps, tables, counters, and sinks. Among the samples, the granite type Vicenza achieved the best result with the use of resin and mesh and the granite type Nevasca sample stood out among the raw materials, obtaining the highest average of the rupture heights.

The application of the mesh, in addition to adding mechanical flexural strength, recovers materials with cracks and fissures, in addition to visually hiding the resin cracks, fissures and structurally restoring the plate and enhancing the color.

Acknowledgements The authors thank the Brazilian agencies: CNPq, CAPES, and FAPERJ for the support provided to this investigation.

References

1. Amaral LF, Delaqua GCG, Nicolite M, Marvila MT, Azevedo ARG, Alexandre J, Vieira CMF, Monteiro SN (2020) Eco-friendly mortars with addition of ornamental stone waste—a mathematical model approach for granulometric optimization. *J Clean Prod* 248:119283
2. Bahiense AV, Alexandre J, Xavier GC, Azevedo ARG, Monteiro SN (2021) Dosage of interlocking paving with ornamental rock waste: an experimental design approach, particle packing and polluting potential. *Case Stud Const Mater* 15:e 00596

3. Marvila MT, Azevedo ARG, Barroso LS, Barbosa MZ, Brito J (2020) Gypsum plaster using rock waste: a proposal to repair the renderings of historical buildings in Brazil. *Const Build Mater* 250:118786
4. Frascá, MHBO, Rodrigues, EP (2019) Technological characterization of coating rocks. In: Collection of technical documents Academia das Rochas Project. <http://cms.academiadasrochas.com.br/wpcontent/uploads/2019/05/5cdd4b7e232df.pdf>. Accessed 31 March 2020 (in Portuguese)
5. SILVEIRALLL et al (2014) Processing of ornamental stones. In: Cetem. http://mineralis.cetem.gov.br/bitstream/handle/cetem/1736/CCL00050014_CAPITULO_07_opt.pdf. Accessed 10 Feb 2020 (in Portuguese)
6. NBR 15845–8, Coating rocks Part 8: Determination of impact strength of hard body, Brazilian Association of Technical Standards (2015) (in Portuguese)
7. Iamaguti APS (2001) Manual of Dimension Stones for Architects. Masters' dissertation, State University of São Paulo Júlio de Mesquita Filho (in Portuguese)
8. NBR 15844, Rocks for coatings—requirements for granites, Brazilian Association of Technical Standards (2010) (in Portuguese)
9. Marvila MT, Azevedo ARG, Cecchin D, Costa JM, Xavier GC, de Fátima do Carmo D, Monteiro SN (2020) Durability of coating mortars containing açai fibers. *Case Stud Const Mater* 13. <https://doi.org/10.1016/j.cscm.2020.e00406>
10. Neuba LM, Pereira Junio RF, Ribeiro MP, Souza AT, Lima ES, Filho FCG, Azevedo ARG, Monteiro SN (2020) Promising mechanical, thermal, and ballistic properties of novel epoxy composites reinforced with cyperus malaccensis sedge fiber. *Polymers* 12(8). <https://doi.org/10.3390/polym12081776>
11. de Azevedo ARG, Marvila MT, Tayeh BA, Cecchin D, Pereira AC, Monteiro SN (2021) Technological performance of açai natural fibre reinforced cement-based mortars. *J Build Engin* 33. <https://doi.org/10.1016/j.job.2020.101675>
12. de Azevedo ARG, Marvila MT, Antunes MLP, Rangel EC, Fediuk R (2021) Technological perspective for use the natural pineapple fiber in mortar to repair structures. *Waste Biom Valoriz.* <https://doi.org/10.1007/s12649-021-01374-5>
13. Azevedo A, De Matos P, Marvila M, Sakata R, Silvestro L, Gleize P, De Brito J (2021) Rheology, hydration, and microstructure of portland cement pastes produced with ground açai fibers. *Appl Sci (Switzerland)* 11(7):15–26
14. Carvalho A, Xavier GC, Alexandre J, Pedroti LG, de Azevedo ARG, Vieira CMF, Monteiro SN (2014) Environmental durability of soil-cement block incorporated with ornamental stone waste. *Mater Sci Forum* 20(3):25–39. <https://doi.org/10.4028/www.scientific.net/MSF.798-799.548>

Development of Metakaolin-Based Geopolymer Mortar and the Flue Gas Desulfurization (FGD) Waste



L. B. Oliveira, A. R. G. Azevedo, M. T. Marvila, C. M. Vieira,
N. A. Cerqueira, and S. N. Monteiro

Abstract It is estimated that the cement industry is responsible for 5–7% of all CO₂ generated in the world. However, alternatives to Portland cement have been researched, with emphasis on geopolymers, which are materials obtained through the reaction of a source rich in aluminosilicate, together with an alkaline activator. The aim of this study is the development of metakaolin-based geopolymer mortar and the flue gas desulfurization (FGD) waste, alkali activated with hydroxide and sodium silicate for structural reinforcement. Samples of geopolymers, with different dosages, were prepared and tested in compression after curing at ambient temperature and 90 °C for 14 days. The results showed that the geopolymer made from 90% metakaolin and 10% FGD waste obtained the highest compressive strength of 19.39 MPa. This preliminary data revealed that this geopolymer could serve as a potential material for civil construction due to its availability, affordability, compressive strength values, and environmental sustainability.

Keywords Geopolymer · Mortar · Metakaolin · FGD

Introduction

Portland cement is one of the most widely used building materials in roads, buildings, bridges, and all these infrastructural projects around the globe have made the demand and production of Portland cement to increase progressively year after year [1, 2]. However, the cement production causes significant greenhouse gas (GHG) emissions

L. B. Oliveira · M. T. Marvila · C. M. Vieira · N. A. Cerqueira
UENF—State University of the Northern Rio de Janeiro, LAMAV—Advanced Materials Laboratory, Av. Alberto Lamego, 2000, Campos dos Goytacazes, Rio de Janeiro 28013-602, Brazil

A. R. G. Azevedo (✉)
UENF—State University of the Northern Rio de Janeiro, LECIV—Civil Engineering Laboratory, Av. Alberto Lamego, 2000, Campos dos Goytacazes, Rio de Janeiro 28013-602, Brazil

S. N. Monteiro
IME—Military Institute of Engineering, Department of Materials Science, Praça General Tibúrcio, 80, Rio de Janeiro 22290-270, Brazil

and energy waste. Nearly 810 kg of carbon dioxide (CO₂), 1.0 kg of sulfur dioxide (SO₂), and 2.0 kg of oxides of nitrogen (NO_x) are produced in the manufacturing process of each ton of cement. Furthermore, approximately, 3.2 GJ energy per ton need be consumed in the production process of Portland cement, involving raw material mining, transporting, clinker calcination, and finish grinding [3]. The cement industry accounts for 5–7% of worldwide CO₂ emission [4]. Due to these reasons, there is the need to develop alternate binders to support the construction industry [1].

In recent years, several alternatives to Portland cement have been researched. Alkali-activated binders have attracted the attention of the construction and research sectors because their production substantially reduces the carbon footprint as it involves naturally occurring materials or industrial by-products [5]. Alkali-activated binders, including geopolymers, are produced through the reaction of an aluminosilicate, normally supplied in powder form as an industrial by-product or other inexpensive material, with an alkaline activator, which is usually a concentrated aqueous solution of alkali hydroxide or silicate [6].

According to the reaction chemistry, alkaline binders are mainly divided into two major categories: geopolymers and alkali-activated materials (AAMs). These two different alkaline binders are mainly classified by the unique chemical reaction series and the reacted end products [7].

Geopolymers contain precursors rich in Si and Al with low or no calcium content, such as metakaolin and fly ash. The products from the geopolymerization process are three-dimensional structures of silico-aluminates amorphous gels, called by some authors N-A-S-H (hydrated sodium aluminosilicate), while the crystalline or semi-crystalline phases are called zeolites [8, 9].

In relation to alkali-activated materials, the precursor is primarily composed of Si, Al, and high Ca, such as blast furnace slag. The products of the reaction between calcium-rich slags and alkaline hydroxides or silicates are hydrated sodium/potassium aluminum silicate gel (N(K)-A-S-H) and hydrated calcium aluminum silicate gel (C-A-S-H), giving rise to minerals known as tobermorites. The C-A-S-H has a structure similar to the resulting gel from the hydration of Portland cement (C-S-H), but with lower amounts of Ca and more amounts of Al in tetrahedral locations [8, 9].

These materials have been of great interest because of their excellent properties such as high temperature resistance, low permeability, good durability, excellent resistance to chemical corrosion, in addition to the sustainability [3, 10].

The aim of this work is the development of metakaolin and residue FGD-based geopolymer mortar, alkali activated with hydroxide and sodium silicate for structural reinforcement.

The use of metakaolin is justified for two reasons: The first is that aluminosilicate minerals in general contain very little carbonates, and their combustion entails scanty any CO₂ emissions (in Portland cement, 60% of the CO₂ emitted is attributable to limestone calcination). The second is that the thermal treatment required to dehydroxylate a clay is of low to medium intensity (500–800 °C) and is also much lower than needed to manufacture clinker (1400–1500 °C) [11, 12].

In relation to the other waste, the most used process for SO_2 removal is the FGD process—flue gas desulfurization, where SO_x gases are removed by adsorption in alkaline media and the main product generated is mainly composed of gypsum. A total of about 33 million tons of FGD gypsum was produced by utilities in the United States in 2015 [13]. In China, production reaches the mark of 80 million tons per year [14]. Thus, due to its characteristics and availability, this waste presents a great possibility of being used in civil construction. The aim of the work is to evaluate the partial replacement of metakaolin by FGD waste by the compressive strength test in the based geopolymer mortar, with different molarities and curing temperatures.

Materials and Methods

A number of starting materials were used in the formulation of the geopolymer that was examined for mechanical performance: sodium hydroxide (NaOH) pellets, powdered sodium silicate (Na_2SiO_3), metakaolin, FGD waste, fine aggregate, and water.

Metacaulim HP ULTRA was used by the company Metacaulim do Brazil. This material has in its chemical composition alumina (Al_2O_3) and silica (SiO_2), with approximate 39.2% of alumina and 52.2% of silica, in a total of 91.4% in mass according to data from the company [15].

Another precursor is the FGD waste, in powder form, generated in the gas treatment of coking ovens (coal treatment), where a hydrated lime solution is injected to mix with the gas and combine with SO_2 . Then, the calcium reacts with the sulfur to produce calcium sulfate, which is physically removed from the scrubber as a powder [16]. The generating unit is ArcelorMittal Tubarão, located in Vitória-ES and this waste is rich in calcium oxide with approximate 45.63% of CaO , 0.51% of silica, and 0.17% of alumina.

The sand used in this research was collected from the natural type, extracted from the Paraíba do Sul River, in the city of Campos dos Goytacazes, RJ. The alkaline solution was sodium hydroxide pellets (99% purity) by Nox and powdered sodium silicate by Lader Química [15].

The dosage of the geopolymeric mixtures was based on the chemical composition of the materials and in the study of Davidovits [17]. The molar ratios were the same for all FGD waste replacement percentages (0, 10 and 20%) as shown in Table 1. A constant sand to precursor ratio of 1.5–1 was used.

Table 1 Molar ratio of based geopolymer mortar

Molar ratio	
$\text{SiO}_2/\text{Al}_2\text{O}_3$	2.50
$\text{Na}_2\text{O}/\text{SiO}_2$	0.40
$\text{Na}_2\text{O}/\text{Al}_2\text{O}_3$	1.00
$\text{H}_2\text{O}/\text{Na}_2\text{O}$	12.00

In the preparation of the geopolymer mortar, the sodium hydroxide and silicate solutions were prepared 24 h beforehand in a magnetic mixer. Later, all materials (metakaolin, waste FGD, sand e solution) were mechanically mixed with a planetary mixer [15]. Then, geopolymer samples were cast in cylindrical molds measuring 50 mm in diameter and 100 mm in height. The procedure was carried out through the application of three layers of mortar, being compacted with 25 strokes for each layer. A total of 18 geopolymeric paste specimens were produced. The division was as follows: 3 specimens for each of the three compositions that were performed with replacement of 0, 10, and 20 wt.% of FGD waste in relation to metakaolin. Thus, nine samples were cured at room temperature and nine samples in a curing at 90 °C and later tested in compression at 14 days of age [18]. The compressive strengths of samples were calculated using Eq. 1 [19].

$$\sigma = \frac{P}{A} \quad (1)$$

where σ is the compressive strength measured in N/mm² or MPa, P is the Load applied (N), and A corresponds to the sample pressed area (mm²).

Molar ratios of 2.26 and 3 were adopted for of SiO₂/Al₂O₃. For each one, 18 specimens were produced, divided between reference geopolymers and the best composition. In this new procedure, thermal curing at 90 °C for 7 days and mixed thermal curing with 1 day in the oven at 90 °C and 6 days at external temperature were adopted. [20]. Subsequently, the samples were tested for compression strength.

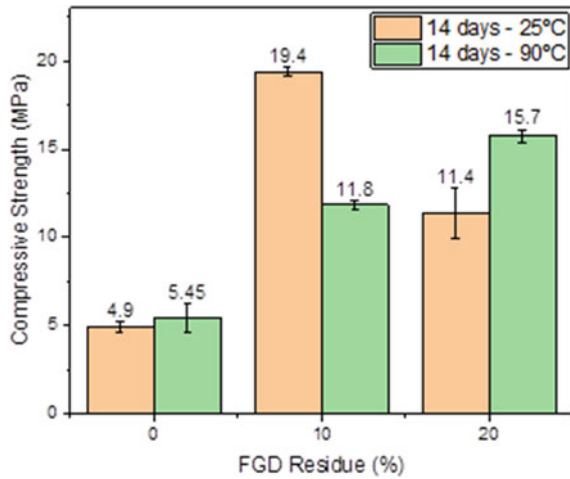
Results and Discussion

Figure 1 summarizes the results of the effect of curing temperature on the compressive strength of metakaolin-based geopolymer mortar with partial replacement by FGD waste with molar ratio of 2.5.

The initial results indicate that showed that the geopolymer made from 90% metakaolin and 10% FGD waste obtained the best compressive strength, reaching a strength of 19.39 MPa in ambient cure with 14 days. Thus, the strength gain may be linked to several factors, such as the fineness of the FGD powder and its surface area, the alkali activation process of a material rich in calcium replacing a material rich in silica and alumina, among others [21, 22].

Thermal cure at 90 °C did not show a significant increase in strength and had a considerable drop in the percentage of 10%. This can be explained by two factors: First, oven curing deserves special attention, as prolonged curing times distort the reactions, causing partial evaporation of water with the formation of microcavities that lead to cracking of the samples [23]. The second is that at high temperatures,

Fig. 1 Effect of FGD waste addition and curing temperature on 2.5 molar ratio metakaolin-based geopolymer mortars



alkaline activation is impaired, as the samples have insufficient moisture. This accelerated water loss leads to carbonation and delays the activation of precursors. In this situation, the final product is granular, porous, and with low mechanical strength [8].

After that, the compression test was performed for 0 and 10% FGD waste with mixed thermal cure. Figure 2 shows the results of the effect of mixed curing temperature on the compressive strength of metakaolin-based geopolymer mortar with partial replacement by FGD waste with molar ratio of 2.26.

The molar ratio of 2.26 was made so that the use of sodium silicate was not necessary, as this material has a high cost. In thermal curing at 90 °C for 7 days, the values exceeded 9 MPa. The increase in resistance in thermal cure for a few days

Fig. 2 Effect of FGD waste addition and curing temperature on 2.26 molar ratio metakaolin-based geopolymer mortars

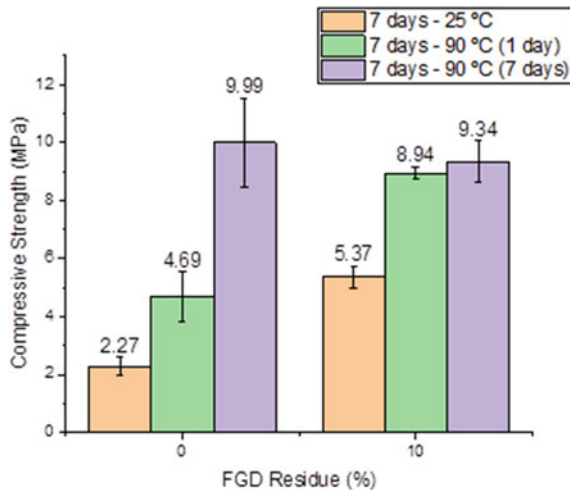
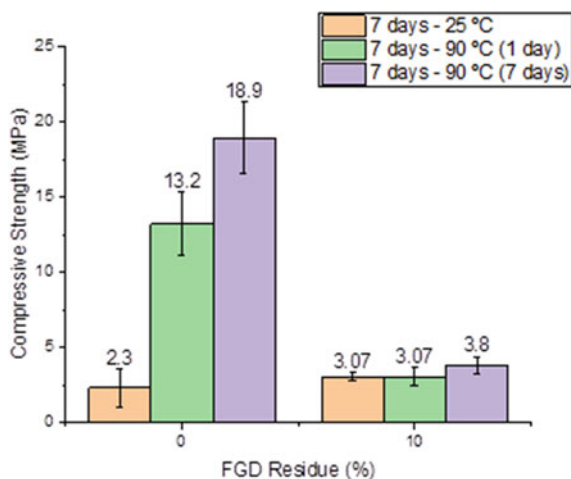


Fig. 3 Effect of FGD waste addition and curing temperature on 3.0 molar ratio metakaolin-based geopolymer mortars



was already expected according to some authors [24]. Nasir et al. [25] observed that curing at a temperature of 60 °C for 6 h was ideal as it presented a high strength of 38 MPa within 3 days and used blast furnace slag, a precursor with many published studies. The use of FGD residue as a precursor with metakaolin as a geopolymeric mortar is still scarce in the literature and its unprecedented results are important for the analysis of the potential of these materials.

Finally, the same parameters were used for a different molar ratio. Figure 3 shows the results of the effect of mixed curing temperature on the compressive strength of metakaolin-based geopolymer mortar with partial replacement by FGD waste with molar ratio of 3.00.

The results show the highest compressive strength value for the reference geopolymeric mortar 18.9 MPa with a thermal cure at 90 °C for 7 days. For most authors, increasing Si is known to improve the mechanical properties of the geopolymer [15;26]. In addition, metakaolin is considered one of the main precursors of geopolymers due to its high reactivity [3]. Mechanical strength gain with increasing temperature was also expected. Muñiz-Villarreal et al. [27] used metakaolin at an oven temperature and obtained property gains. This can be explained because temperature increases the reaction kinetics and consequently favors the gain of mechanical strength, because it increases the dissolution of reactive species, such as silica and alumina. However, the addition of FGD for this molar ratio of 3 was not effective [28, 29].

All graphics refer to materials classified as ceramic. These materials are rigid, have fragile ruptures and work practically in an elastic regime with low tenacity. In the axial compression tests of geopolymer materials, in some situations cracks and section losses with stress drops were observed. Subsequently, the materials increased stress until failure.

Conclusion

This work carried out investigations of the addition of FGD waste in a geopolymer mortar with different percentages, temperatures, and curing times. The molar variation of the samples was also performed. After the compression tests, it can be concluded that:

- The addition of FGD waste was effective for a molar ratio of 2.5, with a compressive strength of 19.4 MPa. However, with greater molarity, the values did not exceed 3.80 MPa;
- Thermal cure at 90 °C for seven days with the use of only metakaolin obtained strength gains, reaching a value of 18.4 MPa;
- The thermal cure mixed with geopolymer mortar in the oven for 1 day achieved significant gains, but smaller when compared to the geopolymer for 7 days in the oven;
- There is a good number of publications related to geopolymers with precursors known as metakaolin, blast furnace slag, and fly ash. However, the use of FGD residue with metakaolin is initial and needs further study related to resistance, thermal cure, and durability.
- These preliminary data revealed that metakaolin-based geopolymers with partial FGD replacement can serve as a potential material for civil construction due to their availability, accessibility, compressive strength, and sustainability.

Acknowledgements The authors thank the Brazilian agencies: CNPq, CAPES, and FAPERJ for the support provided to this investigation.

References

1. Ayeni O, Onwualu AP, Boakye E (2021) Characterization and mechanical performance of metakaolin-based geopolymer for sustainable building applications. *Const Build Mater* 272:121938
2. Van den Heede P, De Belie N (2012) Environmental impact and life cycle assessment (LCA) of traditional and 'green' concretes: literature review and theoretical calculations. *Cement Concr Compos* 34:431–444
3. Wu Y, Lu B, Bai T, Wang H, Du F, Zhang Y, Cai L, Can J, Wang W (2019) Geopolymer, green alkali activated cementitious material: synthesis, applications and challenges. *Constr Build Mater* 224:930–949
4. Rashad A (2013) Alkali-activated metakaolin: a short guide for civil engineer—an overview. *Constr Build Mater* 41:751–765
5. Azevedo ARG, Cruz ASA, Marvila MT, Oliveira LB, Monteiro SN, Vieira CMF, Fediuk R, Timokhin R, Vatin N, Daironas M (2021) Natural fibers as an alternative to synthetic fibers in reinforcement of geopolymer matrices: a comparative review. *Polymers* 13:2493
6. Provis JL (2014) Geopolymers and other alkali activated materials: why, how, and what? *Mater Struct* 47:11–25

7. Samarakoon MH, Ranjith PG, Rathnaweera TD, Perera MSA (2019) Recent advances in alkaline cement binders: a review. *J Clean Prod* 227:70–87
8. Marvila MT, Azevedo ARG, Vieira CMF (2021) Reaction mechanisms of alkali-activated materials. *Rev IBRACON Estrut Mater* 14:3
9. Mendes BC, Pedroti LG, Vieira CMF, Marvila M, Azevedo ARG, Carvalho JMF, Ribeiro JCL (2021) Application of eco-friendly alternative activators in álcali-activated materials: a review. *J Build Eng* 35:102010
10. Duxson P, Provis JL, Luckey GC, Van Deventer JSJ (2007) The role of inorganic polymer technology in the development of 'green concrete.' *Cem Concr Res* 25:1471–1477
11. Chaves GLD, Siman RR, Ribeiro GM, Chang NB (2021) Synergizing environmental, social, and economic sustainability factors for refuse derived fuel use in cement industry: a case study in Espirito Santo, Brazil. *J Environ Manag* 288:112401
12. Zang ZH, Zhu HJ, Zhou CH, Wang H (2016) Geopolymer from kaolin in China: an overview. *Appl Clay Sci* 119:31–41
13. Walia M, Dick WA (2018) Selected soil physical properties and aggregate-associated carbon and nitrogen as influenced by gypsum, crop waste, and glucose. *Geoderma* 320:67–73
14. Wenyi T, Suping G, Wei X, Youxu L, Zixin Z (2018) Feature changes of mercury during the carbonation of FGD gypsum from different sources. *Fuel* 212(19–26):7
15. Azevedo ARG, Marvila MT, Oliveira LB, Ferreira WM, Colorado H, Teixeira SR, Vieira CMF (2021) Circular economy and durability in geopolymers ceramics pieces obtained from glass polishing waste. *Int J Appl Ceram Technol* 00:1–10
16. Mathieu Y, Tzani L, Soulard M, Patarin J, Vierling M, Molière M (2013) Adsorption of SO_x by oxide materials: a review. *Fuel Process Technol* 114:81–100
17. Davidovits J (1994) Properties of geopolymeric cements. In *Proceedings of the first international conference on Alkaline cements and concretes*, pp 131–149
18. ABNT, NBR 7215—Portland cement—Determination of compressive strength of cylindrical specimens, Brazilian Association of Technical Standards (2019) (in Portuguese)
19. ABNT, NBR 5739—Concrete—Compression Test of Cylindric Specimens, Brazilian Association of Technical Standards (2007) (in Portuguese)
20. Azevedo ARG, Vieira CMF, Ferreira WM, Faria KCP, Pedroti LG, Mendes BC (2020) Potential use of ceramic waste as precursor in the geopolymerization reaction for the production of ceramic roof tiles. *J Build Eng* 29(1):101–156
21. Kaur M, Singh J, Kaur M (2018) Microstructure and strength development of fly ash-based geopolymer mortar: role of nano-metakaolin. *Constr Build Mater* 190:672–679
22. Guo X, Dick WA (2013) Utilization of thermally treated flue gas desulfurization (FGD) gypsum and class-C Fly Ash (CFA) to prepare CFA-based geopolymer. *J Wuhan Univer Technol Mater Sci* 28:132–138
23. Kovalchuk G, Fernández-Jiménez A, Palomo A (2007) Alkali-activated fly ash: effect of thermal curing conditions on mechanical and microstructural development—Part II. *Fuel* 86:315–322
24. Provis JL, Bernal SA (2014) Geopolymers and related Alkali-activated materials. *Annu Rev Mater* 44:299–327
25. Nasir M, Johari MAM, Maslehuddin M, Yusuf MO, Al-Harathi MA (2020) Influence of heat curing period and temperature on the strength of silico-manganese fume-blast furnace slag-based alkali-activated mortar. *Const Build Mater* 251:118961
26. Shi C, Fernández Jiménez A, Palomo A (2011) New cements for the 21st century: the pursuit of an alternative to Portland cement. *Cem Concr Res* 41:750–763
27. Muñiz-Villarreal MS, Manzano-Ramírez A, Sampieri-Bulbarela S, Gasca-Tirado JR, Reyes-Araiza JL, Rubio-Ávalos JC, Pérez-Bueno JJ, Apatiga LM, Zaldivar-Cadena A, Amigó-Borrás V (2011) The effect of temperature on the geopolymerization process of a metakaolin-based geopolymer. *Mater Lett* 65:9995–9998
28. Marvila MT, Azevedo ARG, Cecchin D, Costa JM, Xavier GC, de Fátima do Carmo D, Monteiro SN (2020) Durability of coating mortars containing açáí fibers. *Case Stud Const Mater* 13. <https://doi.org/10.1016/j.cscm.2020.e00406>

29. Neuba LM, Pereira Junio RF, Ribeiro MP, Souza AT, Lima ES, Filho FCG, Azevedo ARG, Monteiro SN (2020) Promising mechanical, thermal, and ballistic properties of novel epoxy composites reinforced with cyperus malaccensis sedge fiber. *Polymers* 12(8). <https://doi.org/10.3390/polym12081776>
30. Callister WD, Rethwisch DG (2008) *Fundamentals of materials science and engineering: an integrated approach*. Hoboken, NJ, John Wiley & Sons

Effects of Natural Aging on Fique Fabric-Reinforced Epoxy Composites: An Analysis by Charpy Impact Energy



Michelle Souza Oliveira, Fernanda Santos da Luz, Artur Camposo Pereira, Fabio da Costa Garcia Filho, Noan Tonini Simonassi, Lucio Fabio Cassiano Nascimento, and Sergio Neves Monteiro

Abstract The interest in the use of composites reinforced with natural fibers is growing and this great interest in their use makes it necessary to know the mechanical knowledge of materials under the most varied conditions of structural application. Among these, the application of these materials can be highlighted in situations that suffer the action of different conditions, and in this case, the studies of mechanical properties in addition to the fracture mechanism against natural aging are extremely necessary. The present work presents results of the behavior under Charpy impact energy of epoxy composites reinforced with 40 vol% of fique fabric aged in a natural environment for 90 days. The absorbed energy reduced around 47%.

Keywords Mechanical performance · Epoxy resin · Fique fabric · Aging materials

Introduction

The use of ecological materials, aiming to minimize environmental problems, has become quite common in recent years and is a major concern of the scientific community [1]. The new paradigm of economic development is aimed at improving the quality of life of future generations, incorporating fewer polluting modes of production in its conception [2]. The use of lignocellulosic fibers as substitutes for various synthetic reinforcements in polymer composites has shown great potential for technological application, showing significant advantages, such as low cost and low density [3, 4]. In addition, natural fibers are biodegradable, are not toxic or polluting, come from renewable sources and are available all over the world, reducing environmental problems. The search for new materials has led researchers to develop composites using these types of fibers as reinforcement. Charpy and Izod impact energy studies, Fig. 1, have been carried out with other natural fibers like sugarcane bagasse [5], jute [6], mallow [7, 8], hemp [9], PALF [10], coir [10], curaua [11], and fique [12, 13].

M. S. Oliveira (✉) · F. S. da Luz · A. C. Pereira · F. da Costa Garcia Filho · N. T. Simonassi · L. F. C. Nascimento · S. N. Monteiro
Military Institute of Engineering, IME, Rio de Janeiro, Brazil
e-mail: oliveirasmichelle@ime.eb.br

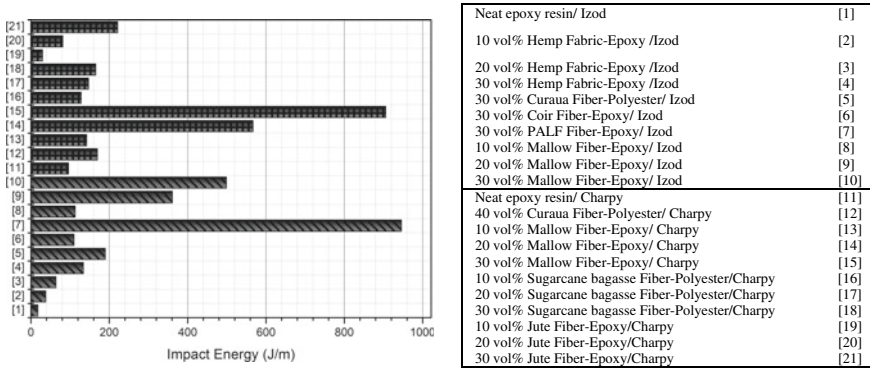


Fig. 1 Sergio Monteiro' laboratory studies in Charpy and Izod impact energy

Results of the above studies carried out in this laboratory by Sergio Monteiro and coworkers have shown natural fiber to be an effective reinforcement in polymers. The applicability and the potential for composites fabricated with natural reinforcement relies on the economy of the country, with particular applications in the ballistic panels in which the reliability, weight reduction, cost reduction, and material sources are critical points for evaluation [1, 12].

Composites reinforced with fique fabric are currently being investigated as possible advanced engineering materials. Charpy notched impact of epoxy resin matrix reinforced with a multilayer natural fique fiber in a bi-directional commercial fabric configuration was analyzed by Rua et al. [12] and Oliveira et al. [13]. The last one, compared the Charpy and Izod impact energies and noted that a proportional increase with the volume fraction of fique fabric layers incorporated into the epoxy matrix up to 40 vol%. These natural fibers reinforcing polymer materials would either be exposed to natural weathering (e.g., heat, humidity, rain, frost, atmospheric pollutants, wind gusting, sand abrasion, sunshine) [14]. Natural weathering encompasses the effects of most types of degradation phenomena and usually involves the combined effect of the polymer's mechanical properties, leading to embrittlement or catastrophic failure, i.e., cracking, of the material [14, 15]. It is of fundamental importance to study the behavior in relation to the degradation mechanisms of the composite, in a view of possible applications in external environments, under the action of solar radiation, rainfall, temperature, and humidity. Therefore, the objective of the present work was to evaluate the impact resistance of epoxy matrix composites reinforced with 40 vol% of fique fabric weathering aged.

Materials and Methods

Fique fabric commercially available in Medellin, Colombia, was purchased from a local commercial outlet. The polymer used as the material of the composite plate

Fig. 2 Sample holder apparatus placed on the roof of a building in Rio de Janeiro/Brazil



matrix was a commercial epoxy resin diglycidyl ether type of bisphenol A (DGEBA) cured with triethylenetetramine (TETA), using the phr of 13 parts of hardener to 100 parts of resin. In sequence, the resin, still liquid, was poured over the figue fabric inside the mold. The composite formed was allowed to cure for 24 h at room temperature.

The natural weathering experiment was performed in Rio de Janeiro/Brazil. Each sample was placed on the roof of a building in the center of the city and was exposed to natural weathering for 2160 h (90 days: 05/10/2020–05/01/2021). The sample holder apparatus, Fig. 2, was placed on the roof to the south direction at an angle of elevation of 45°. The geographic coordinate of the weathering test apparatus is 22° 54' 13S and 43° 12' W. The research building is near Guanabara’s Bay of Atlantic Sea at a distance of 570 m, with an altitude of 20 m from the sea level.

Standard specimens measuring 127 × 12.7 × 10 mm were fabricated for the Charpy impact test in accordance with ASTM D6110. With the number of seven samples, they were tested by impact with a PANTEC hammer pendulum.

The values obtained for the Charpy impact energy were interpreted by means of the Weibull statistics using the computer program Weibull Analysis. The Weibull statistical analysis is based on a cumulative distribution function.

$$F(x) = 1 - \exp[-(x/\theta)^\beta] \tag{1}$$

where θ and β are mathematically known as the shape and scale parameters. Equation 1 can be conveniently modified into a linear expression by double application of logarithm:

$$\ln \ln (1 \div (1 - F(x))) = \beta \ln x - (\beta \ln \theta) \tag{2}$$

Using the seven experimental specimens' data, the computer program constructed the linear graph of Eq. 2 and calculated the Weibull parameters. After impact tests, fragments of the ruptured specimens were collected and analyzed by scanning electron microscopy (SEM), in a model Quanta FEG FEI equipment.

Results and Discussion

Meteorological parameters are the major factors in our study. The climate of the Guanabara Bay as a whole is humid tropical, with a rainy season in summer, from December to April, and a dry season, between June and August. The climatic diversity can be evidenced by the very irregular distribution of precipitation in the region. Relative air humidity averages 78%. The average annual precipitation, measured at the *Aterro do Flamengo* Meteorological Station, is 1173 mm, and evaporation is 1198 mm. In addition, the annual average temperatures are 23.7 °C [16].

The climate of Guanabara Bay is influenced by several atmospheric factors, whether dynamic (air mass, for example) or geographic (static), such as topography, geographic position, maritime nature, continentality, among others. The duration of the test used in the composites was 2160 h.

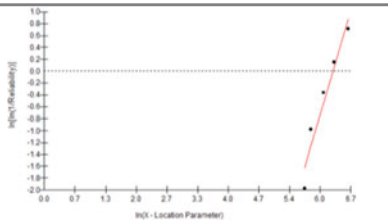
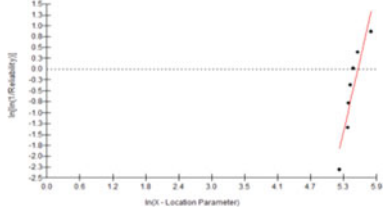
The degradation mechanisms of the composite may undergo during natural ageing are thermo-oxidative, photo-oxidative, and hydrolytic degradation [17]. However, significant degradation was observed through this study, demonstrating the dominating degradation mechanism of fique composite to be photo-oxidative. Literature reported that color fading after aging is caused by oxidation of lignin [17].

Microcracks that develop on a UV-irradiated surface provide pathways for rapid ingress of moisture and chemical agents. Water, especially in the form of condensation, can also remove soluble products of photo-oxidation reactions from a UV-irradiated surface and thereby expose fresh surfaces susceptible to further degradation by UV radiation [14, 17]. Atmospheric pollutants may cause degradation, but in combination with solar radiation and other weather factors they can be responsible for severe damage [14].

As Luz et al. [10], although the heaviest hammer available (22 J) was used in the impact test, samples of composites reinforced with 40 vol% in both conditions, aged and not aged, did not break completely. The fact that Fique composite Charpy samples did not break completely is an indicative of the high toughness of this composite, provided by Fique reinforcement. In fact, if there were a total rupture of this composite, the energy absorbed would be even higher.

Literature report that most of the increase in tenacity is due to the low natural fiber/polymer matrix interfacial shear stress. This phenomenon results in a higher absorbed energy as a consequence of a longitudinal propagation of the cracks throughout the interface, which generates larger rupture areas, as compared to a transversal fracture [6]. The decrease in E_{max} values reached 47% after the weathering of 2160 h in comparison on the composite no aged. One can see in Table 1 the Weibull parameters. In this statistical method the shape parameter, β , is one of

Table 1 Weibull parameters of the Charpy impact test

Materials	β	θ	R^2	Mean	Standard deviation	
Composite no aged	2.61	551.2	0.94	489.6	201.8	
Composite natural aged	5.55	262.1	0.84	242.1	50.4	

the most widely examined parameters because it helps indicate the types of failures occurring base on slope or the β value. If the value of $\beta > 1$, the failure rate will generally increase over time, this could be an indication of premature failure issues, lack of proper maintenance, or dictate the useful life of the material.

Due to the high complexity of the failure process in the Charpy test, scanning electron microscopy was used to analyze all the fractured samples in the close vicinity of the notch. Figure 3 shows a comparison of the fracture zones, close to the initial notch line in the no aged and aged composite. The rough appearance of the fiber surface (Fig. 3a) indicates a good bonding between fiber and matrix. The fiber failure surface was found to be very irregular and rough. The matrix clearly failed without fragmentation.

As aforementioned, the color of the specimens has changed obviously after aging, and the boundary between the fiber and matrix is more and more obvious (Fig. 3b). The failure mode of the aged specimen is mainly fiber fracture and the bond between the fique fabric and epoxy matrix. The bonding strength between the matrix and the fabric is decreased by the weathering aging of the composite, which indicates the degradation of fabric/matrix interface. This is a likely reason for the presence of a gap between the fiber and the matrix, increasing the pullout process. Failure results in a cross section, with irregularities, in a plane perpendicular to the fiber axis. The surface of the pulled fibers was smooth (Fig. 3b), and there were less matrix impurities around, which was also evidence of poor fabric/matrix adhesion.

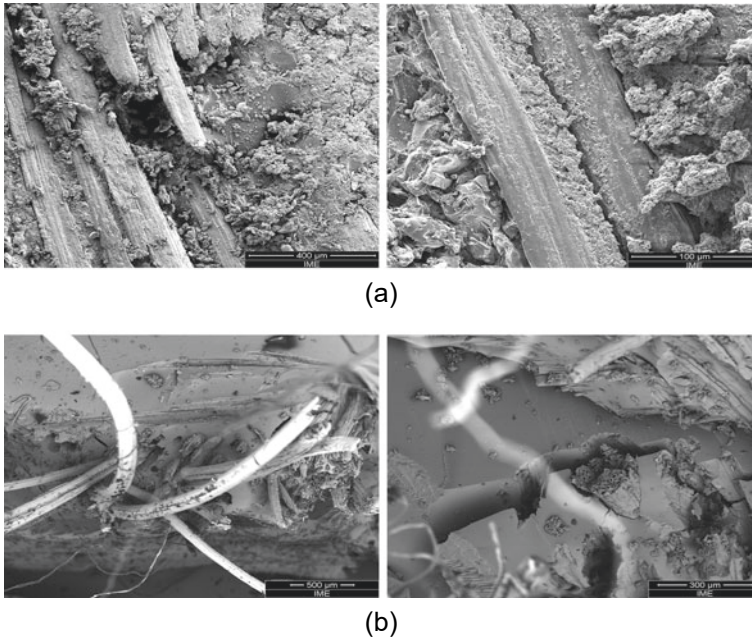


Fig. 3 SEM micrograph of the fracture for a 40 vol% fique fabric composite **a** no aged and **b** natural aging

Summary and Conclusions

- A significant degradation was observed through this study, demonstrating the dominating degradation mechanism of fique' composite to be photo-oxidative;
- The decrease in E_{max} values reached 47% after the weathering of 2160 h in comparison on the composite no aged;
- The shape parameter increased after the aging, this could be an indication of premature failure issues, lack of proper maintenance of the fique–epoxy composite;
- Failure mode of the aged specimen was mainly fique fiber fracture and the bond between the fique fabric and epoxy matrix.

Acknowledgements The authors thank the Brazilian agencies CAPES, FAPERJ, and CNPq for the financial support.

References

1. Monteiro SN, Drelich JW, Lopera HAC, Nascimento LFC, Luz FS, da Silva LC, ... Pereira AC (2019) Natural fibers reinforced polymer composites applied in ballistic multilayered armor for personal protection—an overview. In Ikhmayies S, Li J, Vieira C, Margem (Deceased) J, de Oliveira Braga F (eds) Green materials engineering. The minerals, metals & materials series. Springer, Cham, pp 33–47
2. Hassan KMF, Horvath PG, e Alpár T (2020) Potential natural fiber polymeric nanobiocomposites: a review. *Polymers* 12(5):1072
3. Mohammed L, Ansari MNM, Pua G, Jawaid M, Islam MS (2015) A review on natural fiber reinforced polymer composite and its applications. *Int J Polym Sci* 2015:1–15. <https://doi.org/10.1155/2015/243947>
4. Faruk O, Bledzki AK, Fink HP, Sain M (2014) Progress report on natural fiber reinforced composites. *Macromol Mater Eng* 299:9–26
5. Candido VS, da Silva ACR, Simonassi NT, da Luz FS, Monteiro SN (2017) Toughness of polyester matrix composites reinforced with sugarcane bagasse fibers evaluated by Charpy impact tests. *J Market Res* 6(4):334–338. <https://doi.org/10.1016/j.jmrt.2017.06.001>
6. Pereira AC, Monteiro SN, Assis FS de, Margem FM, Luz FS da, Braga F. de O (2017) Charpy impact tenacity of epoxy matrix composites reinforced with aligned jute fibers. *J Mater Res Technol* 6(4):312–316. <https://doi.org/10.1016/j.jmrt.2017.08.004>
7. Nascimento LFC, Monteiro SN, Louro LHL, Luz FS da, Santos JL dos, Braga F de O, Marçal RLSB (2018) Charpy impact test of epoxy composites reinforced with untreated and mercerized mallow fibers. *J Mater Res Technol*. <https://doi.org/10.1016/j.jmrt.2018.03.008>
8. Costa UO, Nascimento LFC, Garcia JM, Bezerra WBA, Monteiro SN (2019) Evaluation of Izod impact and bend properties of epoxy composites reinforced with mallow fibers. *J Market Res*. <https://doi.org/10.1016/j.jmrt.2019.10.066>
9. Ribeiro MP, Neuba L de M, da Silveira PHPM, da Luz FS, Figueiredo AB-H da S, Monteiro SN, Moreira MO (2021) Mechanical, thermal and ballistic performance of epoxy composites reinforced with Cannabis sativa hemp fabric. *J Mater Res Technol* 12:221–233. <https://doi.org/10.1016/j.jmrt.2021.02.064>
10. Luz FS da, Ramos FJHTV, Nascimento LFC, Figueiredo AB-H da S, Monteiro SN (2018) Critical length and interfacial strength of PALF and coir fiber incorporated in epoxy resin matrix. *J Mater Res Technol*. <https://doi.org/10.1016/j.jmrt.2018.04.025>
11. Monteiro SN, Lopes FPD, Nascimento DCO, da Silva Ferreira A, Satyanarayana KG (2013) Processing and properties of continuous and aligned curaua fibers incorporated polyester composites. *J Market Res* 2(1):2–9. <https://doi.org/10.1016/j.jmrt.2013.03.006>
12. Rua J, Buchely MF, Monteiro SN, Echeverri GI, Colorado HA (2021) Impact behavior of laminated composites built with fique fibers and epoxy resin: a mechanical analysis using impact and flexural behavior. *J Market Res* 14:428–438. <https://doi.org/10.1016/j.jmrt.2021.06.068>
13. Oliveira MS, Filho F da CG, Luz FS da, Pereira AC, Demosthenes LC da C, Nascimento LFC, ... Monteiro SN (2019) Statistical analysis of notch toughness of epoxy matrix composites reinforced with fique fabric. *J Mater Res Technol* 8(6):6051–6057. <https://doi.org/10.1016/j.jmrt.2019.09.079>
14. Sımmazçelik T (2006) Natural weathering effects on the mechanical and surface properties of polyphenylene sulphide (PPS) composites. *Mater Des* 27(4):270–277. <https://doi.org/10.1016/j.matdes.2004.10.022>
15. Oliveira MS, da Luz FS, Monteiro SN (2021) Research progress of aging effects on fiber-reinforced polymer composites: a brief review. In Book: characterization of minerals, metals, and materials 2021. https://doi.org/doi.org/10.1007/978-3-030-65493-1_51
16. Silva, Newton Thiago de Castro. Climate Diagnosis Guanabara Ecological Station Management Plan. <https://www.icmbio.gov.br>

17. Silva CB da, Martins AB, Catto AL, Santana RMC (2017) Effect of natural ageing on the properties of recycled polypropylene/ethylene vinyl acetate/wood flour composites. *Matéria (Rio de Janeiro)* 22(2). <https://doi.org/10.1590/s1517-707620170002.0168>

Evaluation of Recyclable Thermoplastics for the Manufacturing of Wind Turbines Blades H-Darrieus



Andres F. Olivera, Edwin Chica, and Henry A. Colorado

Abstract Wind energy is one of the most important clean energy sources. However, the manufacturing processes of turbine blades require rethinking when considering circular economy concepts. Rebuilt blades could be made with solid waste from the same turbines after their life cycle or from residual parts from other processes. The most direct adverse environmental effect is in the recycling of the wind turbines blades, since thermoset materials are the most typical material for the blades, which are not easily recycled at the end of their life cycle, worsened by the fibers that typically it contains in the blades. This research seeks to evaluate the mechanical strength of two types of thermoplastic materials, PLA and PETG, manufactured in a 3D printer. The PTEG material exhibited the most desirable mechanical strengths and will be the one used to manufacture the blades of an H-Darrieus wind turbine on a laboratory scale.

Keywords Wind turbine blade · 3D printing · Life cycle assessment · Tensile test · Flexion test

Introduction

The circular economy, responsible consumption, and affordable and non-polluting energy are part of the sustainable development objectives adopted by the United Nations (UN) [1]. This concept describes the entire process of designing, manufacturing, transporting, using, dismantling, recycling, and reusing a product before it is sent to the consumer market. If the planning process is carried out correctly, it

A. F. Olivera (✉) · H. A. Colorado

CCComposites Lab, Engineering school, Universidad de Antioquia (UdeA), Calle 70 No. 52-21, Medellín, Colombia
e-mail: andres.olivera@udea.edu.co

A. F. Olivera · E. Chica

Grupo Energia Alternativa, GEA, Engineering school, Universidad de Antioquia (UdeA), Calle 70 No. 52-21, Medellín, Colombia

© The Minerals, Metals & Materials Society 2022

M. Zhang et al. (eds.), *Characterization of Minerals, Metals, and Materials 2022*,

The Minerals, Metals & Materials Series,

https://doi.org/10.1007/978-3-030-92373-0_33

could be guaranteed that there will be responsible consumption based on the principle of the circular economy and thus beneficial for the near communities and for the sustainability of the planet [2].

The wind energy industry has undergone considerable growth in recent years and represents one of the sectors with the highest consumption of composite materials [3]. According to the Renewable energy Policy Network for the 21st Century-REN21, in 2019, the installed capacity of wind power expanded by 19%, with around 60 GW of new capacity added to the world's electricity grids. As of 2019, the reported energy generation capacity from wind power was 651 GW.

Given this increase in installed capacity, it is important to consider the life cycle of the equipment used for the transformation of the kinetic energy of the wind into electricity, especially the wind turbine [4]. The average useful life of a wind turbine can be between 20 and 25 years. Currently, there are very few ways to recycle the blades of a wind turbine in an economical and sustainable way, which is why landfills are the option most used today for final disposal [5, 6]. Different researchers around the world consider that in the next 25 years around 225,000 tons of waste from wind turbine blades will be produced [7–10].

Today, there are different alternatives for the upgraded design and manufacture of blades in wind turbines, leaving aside the common non-recyclable materials such as thermosetting resins and being replaced by thermoplastics that contain additions of glass and carbon fibers and have the capacity to be recycled and reused [11, 12]. The reduction, recycling, and reuse of these components has become a challenge, which is why a life cycle assessment must be carried to verify that the materials and processes to be used will meet the sustainable development goals set by the UN [13, 14]. The current project shows results regarding the construction of these wind turbine blades, recyclability of some of the used materials, and materials characterization. Although in Colombia the market is just starting, the potential of this technology is quite high and must agree with other initiatives that involve circular economy [15, 16], reuse and recycling of composites [17], and innovation [18] and sustainability via additive manufacturing [19].

Materials and Methods

Two mechanical tests were carried out, tension and flexion tests, for the two materials selected: Polylactic acid (PLA) and Polyethylene terephthalate glycol (PETG). The temperature of the material during the 3D printing processes were varied for manufacturing: 190, 210, and 230 °C for PLA and 230, 240, and 250 °C for PETG. The 3D printing process fabrication selected is fused deposition modeling (FDM), one of the most extensively used technologies in 3D fabrication due to the versatility of the process and low cost. For each material, at least three replicates were produced; 2 materials, with 3 temperatures and 3 replicates, 18 total test specimens were made. The testing methods are based on Standard Test Method for Tensile Properties of Plastics (ASTM D638– 14). The type I specimen shown in Fig. 1 was used [20].

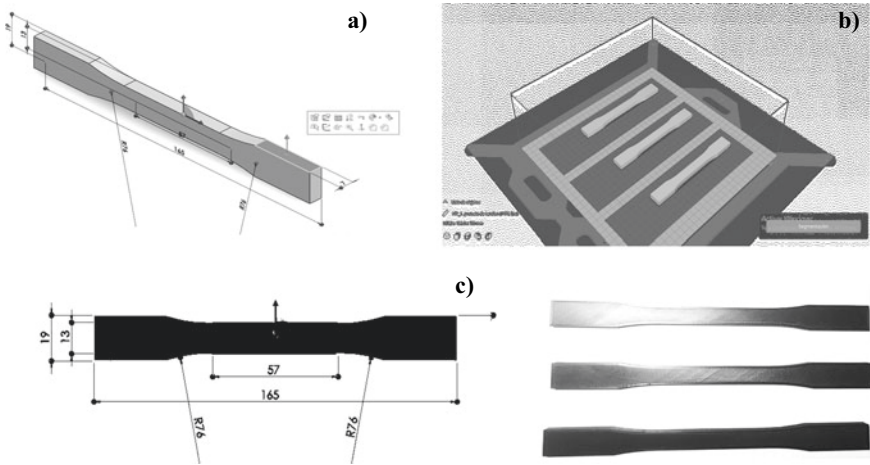


Fig. 1 a Isometric view of the layout of tensile specimen according to ASTM D638—14 specifications, b manufacturing process in a 3D printing software. c tensile specimen made according to the specifications of the standard

The type I specimen was designed in CAD software, as seen in Fig. 1a, later, this design was exported in an STL format, which is read by a 3D printer as shown in Fig. 1b. This process will lead into the manufacturing of the part, according to the initial design specifications. The fabricated specimens which will be tested in the machine for tension tests are shown in Fig. 1c, each one corresponding to the each of the manufactured batches.

For flexural tests, the Standard Test Methods for Flexural Properties of Unreinforced and Reinforced Plastics and Electrical Insulating Materials (D790-17) was used. Specimens must be solid and uniformly rectangular, as seen in Fig. 2a and

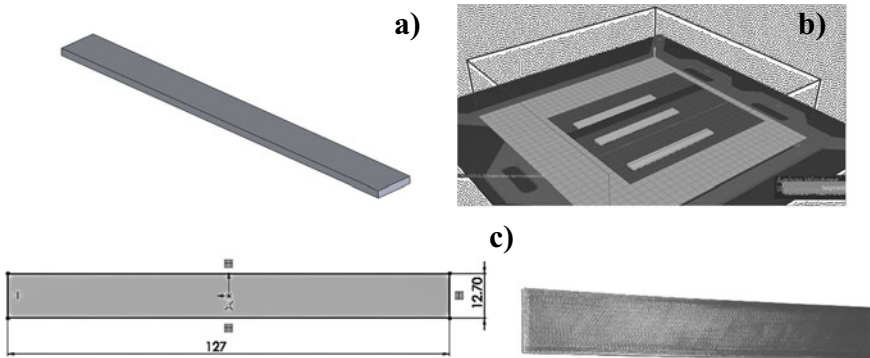


Fig. 2 a Isometric view of the layout of flexion specimen according to ASTM D790-17 specifications, b manufacturing process in a 3D printing software. c Flexion specimen made according to the specifications of the standard

b. The specimen rests on two supports and is loaded by means of a loading nose midway between the supports [21]. In Fig. 2 are shown 1 of the 36 test specimens made.

Results and Analysis

Figure 3 summarizes the tensile strength with respect to the manufacturing temperature of the specimen. PLA does not strengthen with increased printing temperature (in fact the performance worsens at 230 °C). On the other hand, PETG exhibits a strengthening effect with increased printing temperature. PETG samples showed a very low resistance at 230 °C, but in the other, values were quite competitive with respect to PLA.

Figure 4 shows typical stress–strain curves for some selected materials and temperatures. PETG materials with carbon fiber are much more ductile because of the action of the fibers, which is quite important in terms of the deformation solicitations. In a study carried out by the University of Windsor-Canada, they considered the design of wind turbines in 3D printing, using different plastic materials such as ABS, exhibiting an average tensile strength of 28.5 MPa and PLA which has exhibited resistance to 55.6 MPa tensile [22].

Similarly, in a study led by researchers from McGill University revealed the mechanical behavior of 3D printed materials for the manufacture of blades for wind turbines, with additions of fiberglass recycled from dismantled wind turbines, there it was established that pure PLA and the composite material, obtained a tensile strength of 51 and 50 MPa and deformation of 22–20%, respectively [23]. When comparing these results with other researchers with the results obtained in this investigation, where the maximum tensile strength of PLA and PETG was 51 and 49 MPa and

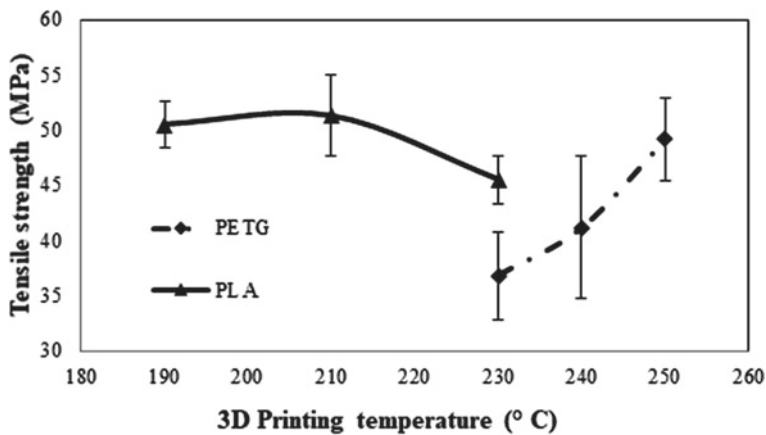


Fig. 3 Tensile strength behavior at different 3D printing temperatures

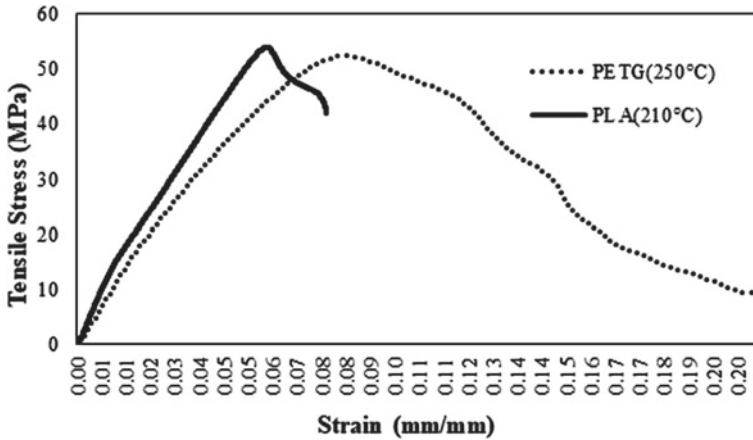


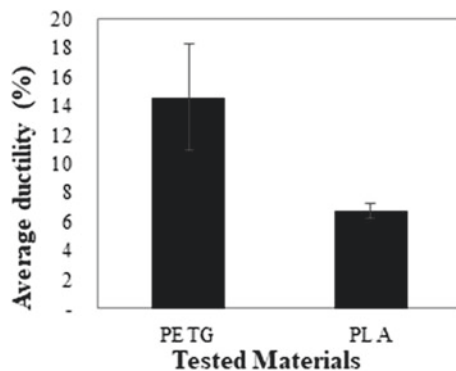
Fig. 4 Stress versus strain curve

the ductility was 7–15%, respectively, this is how the materials tested are within the normal range of wind turbine blade design.

Figure 5 shows the summary of results for all samples of each composition, clearly with PETG outperforming the PLA. Also, the materials resilience (a property that accounts for the materials capacity to recover from deformation, very important under high deformation such as in high deformation [24] or extreme weather conditions [25] was obtained, and once again, PETG showed to be better than PLA, see Fig. 6.

Figure 7 shows that PETG present lower flexural strength than PLA. PLA specimens show their best flexural strength at 210 °C, although at 230 °C the values do not significantly differ from PETG values. For the PETG samples, the strength values increased from samples tested from 230 to 250 °C, having its higher values at the maximum tested temperature 250 °C, with 93 MPa, same value for the worst results of PLA.

Fig. 5 Ductility results between different materials



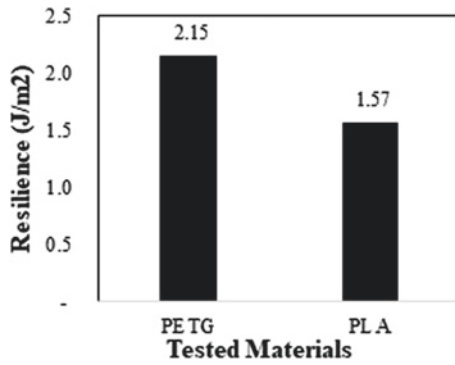


Fig. 6 Resilience results between different materials

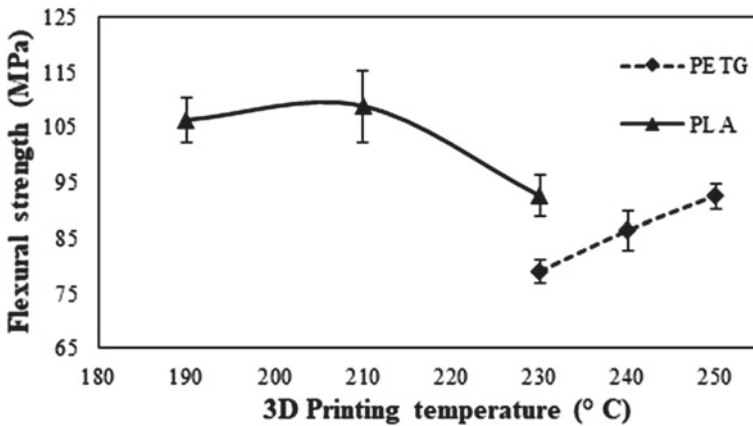


Fig. 7 Flexion strength behavior at different 3D printing temperatures

Figure 8 shows typical strain–stress values for the flexural tests, for samples with the best results in terms of the mechanical strength of Fig. 7. PLA supports greater flexural load, however, PETG is faraway much better in ductility result when compared to PLA.

Conclusions

After evaluating PLA and PETG as printing materials using FDM 3D printing technology in order to manufacture wind turbine blades and comparing these results with studies from other investigations which also analyzed materials to manufacture wind turbine blades, it was clear that PLA samples showed better results in terms of both tensile and flexural strength. However, the ductility was better for the PETG samples

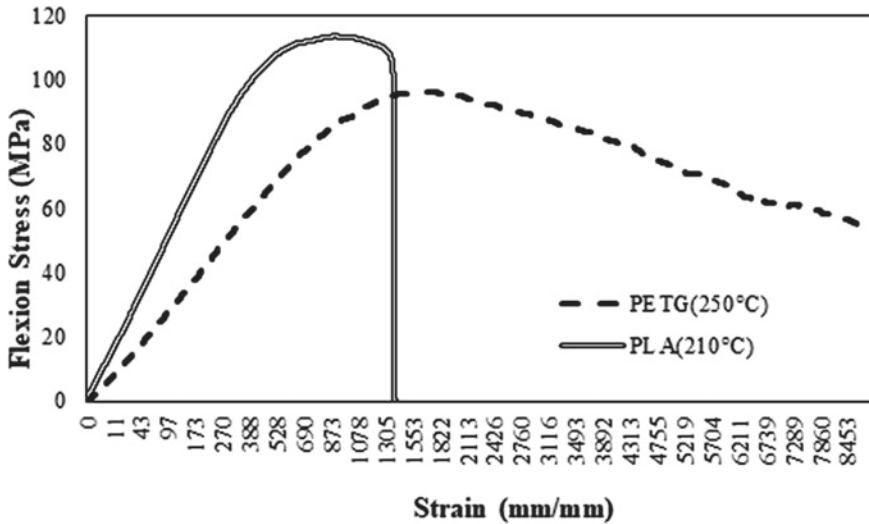


Fig. 8 Stress versus strain curve, Characterization of materials in stress and deformation (flexion)

(in both tests). Given that the values are not too different for the strength properties, and considering other aspects such as fatigue and deformation, the use of PETG is a real possibility since it offers better energy absorption which guarantees greater durability, for the conditions to which it will be exposed, this is very important in an H-Darrieus wind turbine application. For these reasons, although PLA is also a potential option, PETG appears to be a more suitable and versatile material for use in the blades of an H-Darrieus wind turbine.

References

1. Organización de las naciones unidas, objetivos de desarrollo sostenible (2015) Agosto 04, 2020, de naciones unidas Sitio web. <https://www.un.org/sustainabledevelopment/es/objetivos-de-desarrollo-sostenible>
2. Ratner S, Gomomov K (2020) Eco-design of energy production systems: the problem of renewable energy capacity recycling. Agosto 04, 2020, de MDPI
3. Albers H, Greiner S, Seifert H, Kühne U (2009) Recycling of wind turbine rotor blades—fact or fiction. DEWI Mag 34:32–41
4. REN21. Renewables 2020 Global Status Report (2020) 08/07/2020, de Renewable Energy Policy Network for the 21st Century Site web. <https://www.ren21.net/gsr-2020/>
5. Ming-Sung W, Cheng Jin B, Li X, Steven N (2019) A recyclable epoxy for composite wind turbine blades. Adv Manuf Poly Compos Sci 5(3):114–127. <https://doi.org/10.1080/20550340.2019.1639967>
6. Flizikowski J, Bielinski K (2013) Technology and energy sources monitoring: control, efficiency and optimization. IGI Global. ISBN 9781466626645
7. Fraile D, Mbistrova A (2018) Wind in power 2017. Annual combined onshore and offshore wind energy statistics. BrusselsWindEurope, Belgium

8. GWEC, Global Wind Report, Global Wind Energy Council, Brussels Haapala KR, Prempreeda P (2014) Comparative life cycle assessment of 2.0 MW wind turbines. *Int J Sustain Manuf* 3(2):170–185
9. Tazi N, Chatelet E, Bouzidi Y (2017) Using a hybrid cost-FMEA analysis for wind turbine reliability analysis. *Energies* 10(3):276
10. Global Wind Report, Global Wind Energy Council (2015)
11. Rashedi A, Sridhar I, Tseng K (2012) Multi-objective material selection for WTB and tower: Ashby's approach. *Mater Des* 37(5):521–532
12. Adolphs G, Skinner C (2011) Manufacturing, properties and applications, A volume in WHPS in composites science and engineering. Chapter 21–Non-crimp fabric composites in wind turbines, 48–493. Edited by Lomov SV. ISBN: 9781845697624. Available online 29 Jan 2014
13. Hollaway L (2014) A volume in WHPS in civil and structural engineering. Chapter 20—advanced fiber-reinforced polymer (FRP) CMs for sustainable energy technologies 2013:737–79. Edited by Bai J. ISBN: 978-0-85709-418-6
14. Tomporowski A, Piasecka I, Flizikowski J, Kasner R, Kruszelnicka W, Mrozinski A, Bielinski K (2018) Comparison analysis of blade life cycles of land-based and offshore wind power plants. *Pol Marit Res* 25:225–233
15. Colorado HA, Echeverri-Lopera GI (2020) The solid waste in Colombia analyzed via gross domestic product: towards a sustainable economy. *Revista Facultad de Ingeniería Universidad de Antioquia* 96:51–63
16. Rúa-Restrepo JJ, Echeverri GI, Colorado HA (2019) Toward a solid waste economy in Colombia: an analysis with respect to other leading economies and Latin America. In *REWAS 2019* (pp. 337–354). Springer, Cham
17. Agudelo G, Cifuentes S, Colorado HA (2019) Ground tire rubber and bitumen with wax and its application in a real highway. *J Clean Prod* 228:1048–1061
18. Colorado HA, Mendoza DE, Valencia FL (2021) A combined strategy of additive manufacturing to support multidisciplinary education in arts, biology, and engineering. *J Sci Educ Technol* 30(1):58–73
19. Colorado HA, Velásquez EIG, Monteiro SN (2020) Sustainability of additive manufacturing: the circular economy of materials and environmental perspectives. *J Market Res* 9(4):8221–8234
20. ASTM D638–14 (2015) Standard test method for tensile properties of plastics
21. ASTM D790–17 (2017) Flexural properties of unreinforced and reinforced plastics and electrical insulating materials
22. Bassett K et al (2015) 3D printed wind turbines part 1: design considerations and rapid manufacture potential. *Sustainable Energy Technol Assess*. <https://doi.org/10.1016/j.seta.2015.01.002>
23. Fayazbakhsh K et al (2019) Recycling of fiberglass wind turbine blades into reinforced filaments for use in Additive Manufacturing, *Composites Part B* 175 <https://doi.org/10.1016/j.compositesb.2019.107101>
24. Lehnhoff S, Gómez González A, Seume JR (2020) Full-scale deformation measurements of a wind turbine rotor in comparison with aeroelastic simulations. *Wind Energy Sci* 5(4):1411–1423
25. Diamond KE (2012) Extreme weather impacts on offshore wind turbines: lessons learned. *Nat Res Env't* 27:37

Evaluation of the Rheology of Mortars with Incorporation of Ornamental Stone Waste



E. B. Zanelato, A. R. G. Azevedo, M. T. Marvila, J. Alexandre, and S. N. Monteiro

Abstract The ornamental stone industry is a strategic market of great importance for many countries, however, the lack of an adequate destination for the waste generated causes a great environmental impact. The objective of this work is to evaluate the rheology of mortars with the incorporation of granite and marble residues for coating application. Particle grain size characterization tests were carried out of the materials used in the manufacture of the mortar and incorporated waste. The mortars were made with incorporations of 10, 20, 30, and 40% with each one of the residues replacing the sand. Water retention and mechanical resistance tests were carried out, in addition to the squeeze-flow test to evaluate the rheology. The results indicated that the marble residue improves both the mechanical strength and the rheology of mortars for application in coating. Granite residue increases mechanical strength similarly to marble and less in rheology.

Keywords Mortar · Residue · Rheology

Introduction

The adhesion of mortars to the substrate is the main property of mortars. The initial contact of the coating mortars with the surface of the substrates is directly influenced by the rheology of the mortar, since the casting is still carried out in a fresh state [1].

Both the initial contact and the spreading over the substrate are directly influenced by the rheology of the mortar. Rheology directly influences the surface tension

E. B. Zanelato (✉)

IFF—Federal Institute Fluminense, Rua Cel. Valter Kramer, 357—Parque Vera Cruz, Campos dos Goytacazes, Rio de Janeiro 28080-565, Brazil

A. R. G. Azevedo · M. T. Marvila · J. Alexandre

UENF—State University of the Northern Rio de Janeiro, LECIV—Civil Engineering Laboratory, Av. Alberto Lamago, 2000, Campos dos Goytacazes, Rio de Janeiro 28013-602, Brazil

S. N. Monteiro

IME—Military Institute of Engineering, Department of Materials Science, Square General Tibúrcio, 80, Rio de Janeiro 22290-270, Brazil

© The Minerals, Metals & Materials Society 2022

M. Zhang et al. (eds.), *Characterization of Minerals, Metals, and Materials 2022*,

The Minerals, Metals & Materials Series,

https://doi.org/10.1007/978-3-030-92373-0_34

present on the substrate surface at the moment they come into contact. Surface tension is a result of adhesion forces that must be strong and stable for adhesion between materials. The influence of rheology on surface tension is explained by the theory of interfacial bonds between a solid (substrate) and a liquid (mortar paste) [2].

The initial adhesion of the mortar with the substrate must occur in such a way that the liquid covers the solid surface as much as possible, reducing the gaps that generate adhesion failures at the interface. For the spreading of the liquid over the solid to occur with minimal defects, the liquid must have low viscosity, in addition, it is necessary that the process results in a decrease in free energy in the system [3]. This property of scattering liquids on solids is influenced by the reduction of the contact angle, the smaller the contact angle, the lower the surface tension and the greater the scattering. There are several factors that influence the reduction of the contact angle, including the use of air-incorporating and water-retaining additives or the increase in plasticity obtained by the addition of lime [4]. Furthermore, changes in the composition of the mortar, such as the increase in cement content, can favor adhesion, as it causes a reduction in surface tension [5].

The use of materials that change the surface tension of mortars directly influences the rheology and consequently its performance. The replacement of sand by waste promotes changes in surface tension and reduces environmental impacts [6].

In addition to replacing sand, a raw material that would be removed from nature for industrial use, the residue can be used in the manufacture of mortar, a destination with less environmental impact than its disposal in landfills [6].

The Brazilian ornamental stone industry alone exports 2.36 million tons of material, generating 800,000 tons of waste annually, whose most appropriate destination is sanitary landfills [7].

The use of residue in mortars has already been evaluated by several authors [8–10], where the mechanical performance has been improved. Studies related to mortar in its fresh state and mainly related to rheology are fundamental for deepening the knowledge related to the incorporation of the residue in mortar, since the main property of the mortar is its adherence to the substrate.

The objective of this work is to evaluate mortar produced with two different ornamental rock residues, granite and marble, in coating mortars. Granulometry and chemical analysis tests were carried out to characterize the materials used in the manufacture of mortar. Sand replacements were made by incorporating 10, 20, 30, and 40% with each residue, in addition to the reference without adding the residue. The performance of the mortars was evaluated by water retention and mechanical strength tests. Rheology was evaluated by the squeeze-Flow assay.

Materials and Methods

The materials used to make the mortar were characterized by grain size and grain density tests.

Table 1 Tests performed on mortar and respective standards

Test	Standard
Compressive strength	NBR 13,279 [12]
Flexural tensile strength	NBR 13,279 [12]
Water retention	NBR 13,277 [13]
Squeeze-flow	NBR 15,839 [14]

Two traces of mortar were used: 1:1:6 and 1:2:9 (Cement: Hydrated Lime: Sand). These traces were chosen because of their recurring use and proper plasticity for coating application. The 1:2:9 trace exhibits greater water retention and is widely used in locations that are most vulnerable to water loss by evaporation or absorption of the substrate where it was applied. The 1:1:6 trace exhibits greater mechanical strength as well as greater adhesion potential, however, depends on suitable application conditions where the coating does not suffer a large volume of water loss.

Granite and marble residues were incorporated in substitution of sand at 10, 20, 30, and 40% levels beyond the reference without incorporation.

The mortars were made as recommended by NBR 13,276 [11]. The tests performed and the respective standards are shown in Table 1.

Results

Figure 1 shows the particle size distribution obtained by the materials used in the preparation of mortar.

As can be seen in Fig. 1, marble has a similar grain size to cement, while granite has an intermediate grain size between cement and sand. Hydrated lime is the finest material used in making mortar.

The results obtained in the water retention test are shown in Fig. 2.

The results obtained in the test indicate that the water retention is directly influenced by the mortar mix, the type of residue, and the level of incorporation of the residue.

As already mentioned in the materials and methods, the 1:2:9 mix has a higher proportion of hydrated lime, the thinnest material in the mortar, which increases its water retention capacity.

The incorporation of marble was more effective than that of granite in increasing water retention. Because it is thinner and, therefore, has a greater surface area, marble was able to increase its water retention capacity, even less than that of hydrated lime.

The increase in water retention was verified as the level of incorporation of both waste used increased.

The results obtained in the mechanical strength test are shown in Figs. 3 and 4.

As can be seen in Figs. 3 and 4, the mix used significantly influences the mechanical strength, however, granite has a performance very similar to that of marble. The

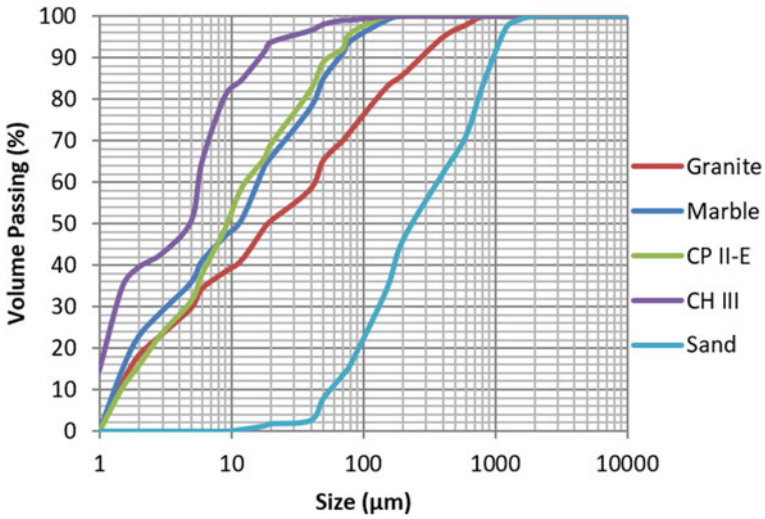


Fig. 1 Particle grain size

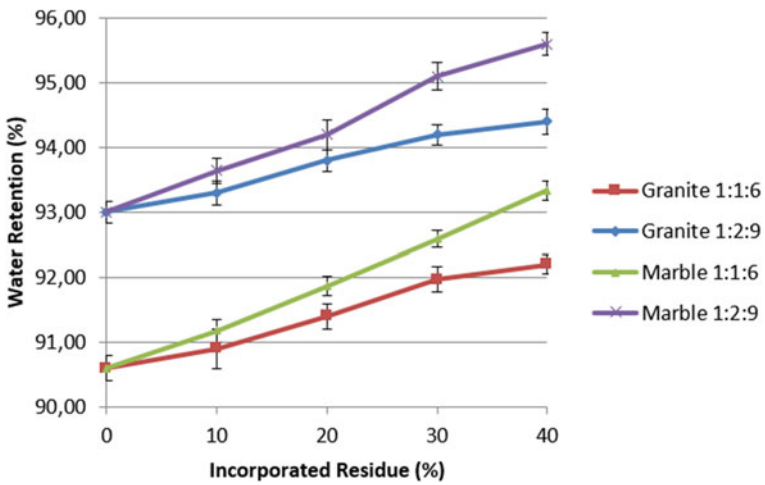


Fig. 2 Water retention

increase in the level of incorporation of the residue shows a slight tendency towards an increase in mechanical strength.

The better performance obtained by the 1:1:6 mix can be explained by the higher proportion of cement. The higher proportion of hydrated lime of the 1:2:9 mix increases water retention, as seen in Fig. 2, however, it generates loss of mechanical strength with a decrease in the proportion of cement.

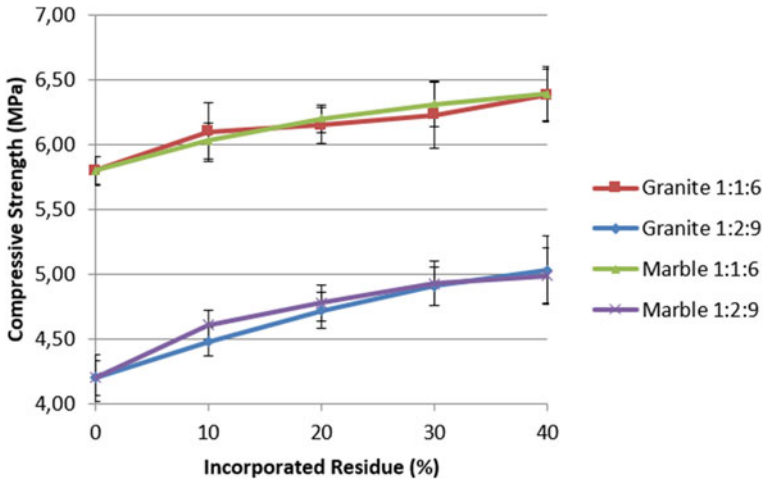


Fig. 3 Compressive strength

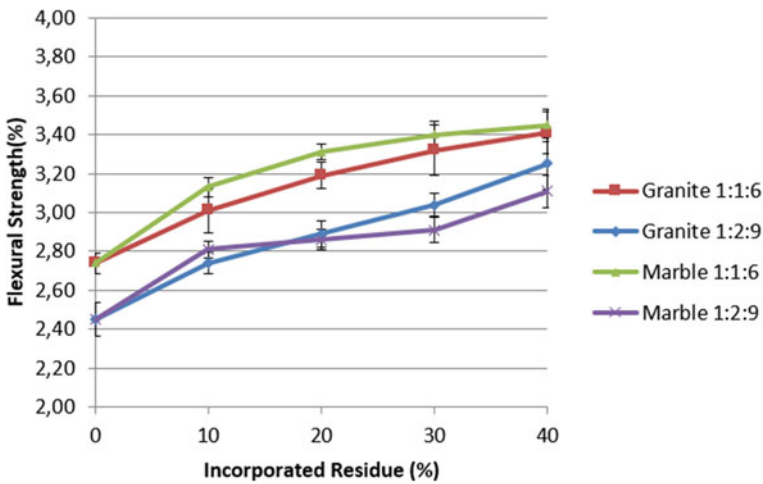


Fig. 4 Flexural strength

Marble and granite waste have very similar results across the levels of waste incorporation, especially when the standard deviation of the test is observed.

It is also verified in both tests that the mechanical resistance increases slightly as the residue incorporation increases.

The results of the squeeze-flow assay for each of the residues are shown in Figs. 5 and 6.

As can be seen in Figs. 5 and 6, the level of residue incorporation and especially the mix, directly influence the rheology of the mortars.

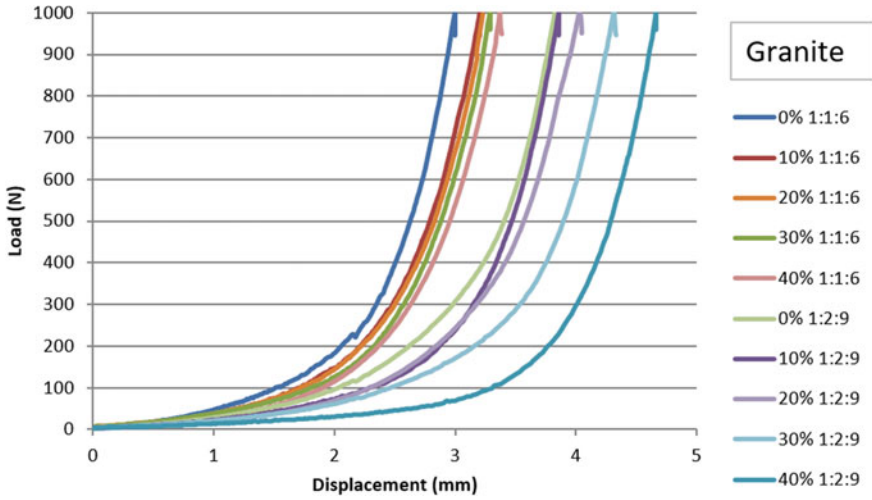


Fig. 5 Squeeze-flow: granite

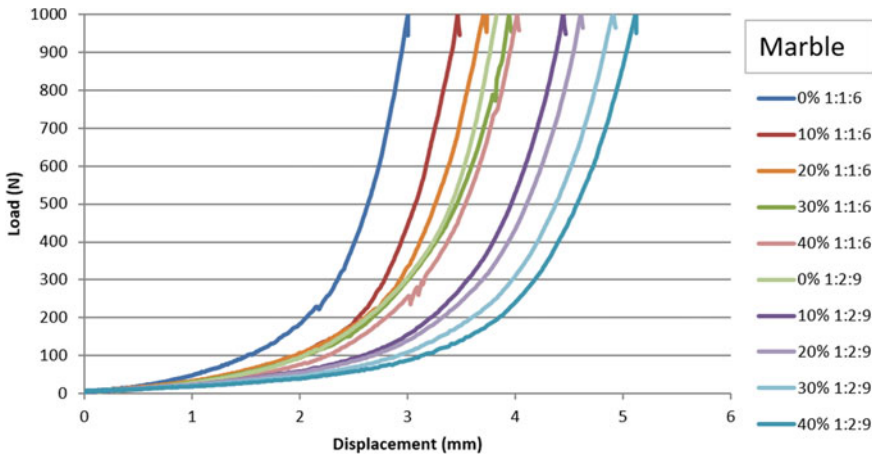


Fig. 6 Squeeze-flow: marble

The 1:2:9 mix presents greater spreading during the test for the same load compared to the 1:1:6 mix at any level of incorporation. This performance is justified by the presence of fines in the hydrated lime, which reduce internal friction during mortar spreading.

There is also an increase in scattering as the level of waste incorporation increases, both in Fig. 5 for granite and in Fig. 6 for marble in both analyzed traces.

The increase in spreading as the level of incorporation increases is also justified by the greater presence of fines, since sand is replaced, a material of greater granulometry among those used in the manufacture of mortar.

To compare the residuals, the results were grouped according to the trace in Figs. 7 and 8.

By grouping the data by trace, it is verified that marble has a significantly greater spread than granite. The incorporation of 10% of marble is already enough to overcome the spreading obtained by the incorporation of 40% of granite in the 1:1:6 mix.

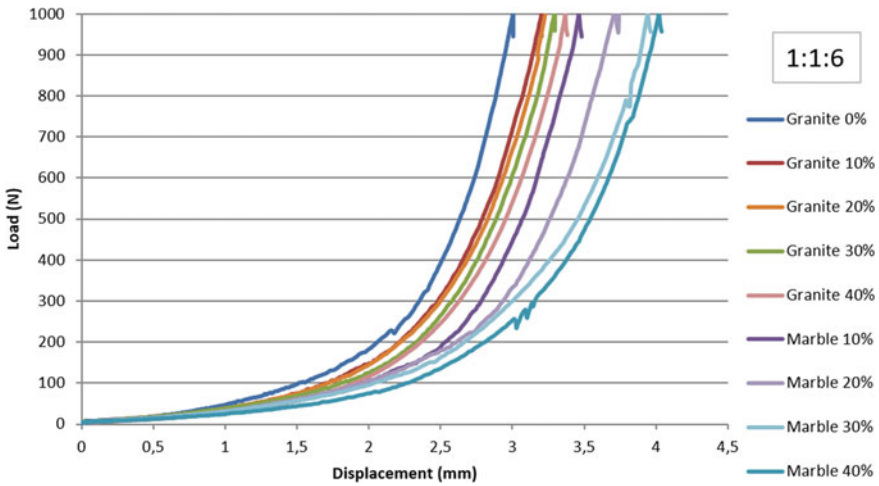


Fig. 7 Squeeze-flow: 1:1:6

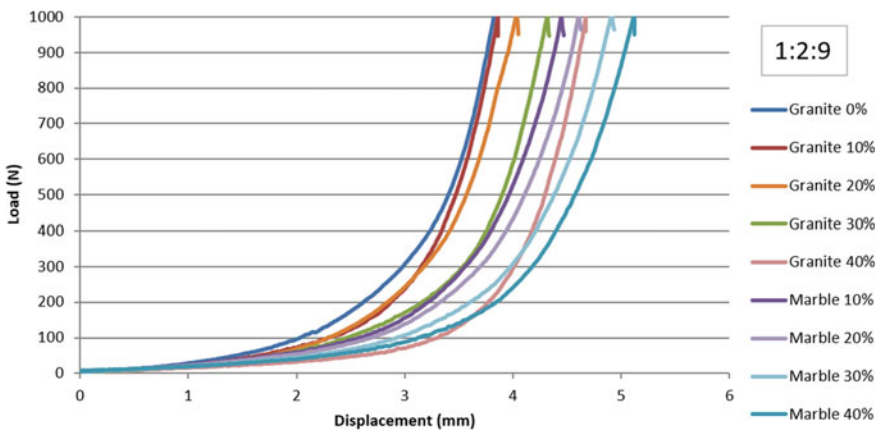


Fig. 8 Squeeze-flow: 1:2:9

For the 1:2:9 mix, the scattering obtained by incorporating 10% of marble is overcome by the incorporation of 40% of granite, the latter being surpassed by the scattering of 30% of marble.

Conclusion

In this work, it was possible to analyze how the incorporation of both marble and granite influence the properties of mortars, both in the highest strength (1:1:6) and in the most workable (1:2:9). The following conclusions can be made with the analysis of the results:

- The 1:1:6 trace has greater strength than the 1:2:9. The difference in resistance between the traces is not overcome until the incorporation of 40% of any waste used. As well as the rheology of the 1:2:9 mix is also not surpassed by the incorporation of up to 40% of the residues used.
- The type of residue significantly influences the fresh state, as seen in both the squeeze-flow and the water retention tests. However, the type of residue has little influence on the hardened state, evaluated by mechanical strength.
- The replacement of the area by both granite and marble residues brings better performance in the fresh state, keeping or even slightly increasing the hardened state.
- Marble residue showed similar performance to granite residue in the hardened state. In the fresh state, the marble residue performed considerably better than that of granite, which makes its use more recommended.

Acknowledgements The authors thank the Brazilian agencies CNPq, CAPES, and FAPERJ for the support provided to this investigation.

References

1. Stolz CM, Masuero AB (2015) Analysis of main parameters affecting substrate/mortar contact area through tridimensional laser scanner. *J Colloid Interface Sci* 455:16–23
2. Zanelato EB, Alexandre J, Azevedo ARG et al (2019) *Mater Struct* 52:53. <https://doi.org/10.1617/s11527-019-1353-x>
3. França MS, Cazacliu B, Cardoso FA, Pileggi RG (2019) Influence of mixing process on mortars rheological behavior through rotational rheometry. *Constr Build Mater* 223:81–90
4. Cardoso FA, John VM, Pileggi RG, Banfill PFG (2014) Characterisation of renderings mortars by squeeze-flow and rotational rheometry. *Cem Concr Res* 57:79–87
5. Cardoso FA, Fujii AL, Pileggi RG, Chaouche M (2015) Parallel-plate rotational rheometry of cement paste: influence of the squeeze velocity during gap positioning. *Cem Concr Res* 75:66–74

6. Azevedo ARG, Alexandre J, Pessanha LSP, Manhães RST, Brito J, Marvila MT (2019) Characterizing the paper industry sludge for environmentally-safe disposal. *Waste Manage* 95:43–52
7. ASSOCIAÇÃO BRASILEIRA DE EMPRESAS DE LIMPEZA PÚBLICA E RESÍDUOS ESPECIAIS (ABRELPE). Overview of solid waste in Brazil (2016) (in Portuguese)
8. Singh M, Choudhary K, Srivastava KS, Sangan Bhunia D (2017) A study on environmental and economic impacts of using waste marble powder in concrete. *J Build Eng* 13:87–95
9. Singh Y, Vyas AK, Kabeer KISA (2017) Compressive strength evaluation of mortars containing ISF slag and marble powder. *Mater Today Proc* 4(9):9635–9639
10. Munir MJ, Kazmi SMS, Wu Y, Hanif A, Khan MUA (2018) Thermally efficient fired clay bricks incorporating waste marble sludge: an industrial-scale study. *J Clean Prod* 174:1122–1135
11. ASSOCIAÇÃO BRASILEIRA DE NORMAS TÉCNICAS (2016) ABNT NBR 13276. Mortars applied on walls and ceilings—determination of the consistence index
12. ASSOCIAÇÃO BRASILEIRA DE NORMAS TÉCNICAS (2005) ABNT NBR 13279. Mortars applied on walls and ceilings—determination of the flexural and the compressive strength in the hardened stage
13. ASSOCIAÇÃO BRASILEIRA DE NORMAS TÉCNICAS (2005) ABNT NBR 13277. Mortars applied on walls and ceilings—determination of the water retentivity
14. ASSOCIAÇÃO BRASILEIRA DE NORMAS TÉCNICAS (2010) ABNT NBR 15839. Rendering mortar for walls and ceilings—rheological evaluation by squeeze-flow

Fundamental Study on Wettability of Pure Metal Using a Low Melting Temperature Alloy: A Theoretical Approach



Jun-ichi Saito, Yohei Kobayashi, and Hideo Shibutani

Abstract Studies on wettability control with liquid sodium have been conducted via many experiments and theoretical calculations. However, experiments using liquid sodium are challenging because of the high chemical reactivity of liquid sodium. Hence, we plan to perform experiments using a low melting temperature alloy, which is easy to use in air. In this study, the electronic structure of the interface between the substrate metal and the liquid metal was calculated using the molecular orbital method to understand the wettability of pure metal with the low melting temperature alloy. Results showed that the kind of liquid metal affected the atomic interaction at the interface. We obtained some atomic bonds representing a feature of the interface in order to understand the wettability by experiments.

Keywords Wettability · Liquid metal · Low melting temperature alloy · Atomic bonding · Electronic structure

Introduction

We conducted a fundamental study on wettability by liquid sodium [1, 2]. Our previous research showed a good correlation between the contact angle, which is an indication of wettability, and the atomic bonding generated by the electronic structure of the interface. Liquid sodium, which is used in wettability experiments, has high chemical activity and reacts violently with oxygen and moisture. Consequently, handling liquid sodium in experiments is generally challenging. Furthermore, a glove box filled with high-purity argon gas is necessary for experiments involving liquid

J. Saito (✉)

Japan Atomic Energy Agency, 1 Shiraki Tsuruga, Fukui 919-1279, Japan

e-mail: saito.junichi78@jaea.go.jp

Y. Kobayashi

National Institute of Technology, Maizuru College, 234 Shiroya Maizuru, Kyoto 625-8511, Japan

H. Shibutani

Kurume Institute of Technology, 2228-66 Kamitsu-cho Kurume, Fukuoka 830-0052, Japan

© The Minerals, Metals & Materials Society 2022

M. Zhang et al. (eds.), *Characterization of Minerals, Metals, and Materials 2022*,

The Minerals, Metals & Materials Series,

https://doi.org/10.1007/978-3-030-92373-0_35

sodium. Thus, instead of liquid sodium, we considered using a low melting temperature alloy, which is easy to handle in air during experiments, to understand the wettability between substrate and liquid metals.

In this study, the electronic structure of the interface between the liquid metal (the low melting temperature alloy) and the substrate metal was calculated to understand the wettability of pure metal with a low melting temperature alloy. The purpose of this study is to obtain new parameters (the atomic bond orders, which represent a feature of the interface between the pure metal and the low melting temperature alloy) to understand theoretically the wettability of pure metal with the low melting temperature alloy.

Theoretical Calculation

Calculation Method

Discrete variational (DV)- $X\alpha$ calculation, which is a molecular orbital calculation, was used for the theoretical calculation of the interface between the substrate metal and the liquid metal. There are many detailed papers about DV- $X\alpha$ calculation [3–6]. One of the advantages of this approach is that it easily performs not only solid-state calculations but also calculation of the interface between solids and liquids.

Low Melting Temperature Alloy and Substrate Metals

In this study, a low melting temperature alloy (U-alloy 60) manufactured by Osaka Asahi Co., Ltd., which will be used in future experiments, was regarded as the liquid metal. Its melting temperature is 333 K. This alloy consists of three metal elements: indium, bismuth, and tin. Its composition is as follows: 51 mass% In–32.5 mass% Bi–15.5 mass% Sn (60 mol% In–21 mol% Bi–19 mol% Sn). A component of structure metals was selected as the substrate metal. The crystal structures and the lattice constants of the substrate metal used in the calculation are shown in Table 1. The substrate metal has three types of crystal structures: body-centered cubic, face-centered cubic, and close-packed hexagonal (hereinafter called bcc, fcc, and hcp, respectively). The atomic radii of the three types of liquid metal atoms used in the calculation are shown in Table 2.

Table 1 Lattice constant of substrate metals used in calculation

Metal	Al	Ti	Fe		Ni
Crystal structure	fcc	hcp	bcc	fcc	fcc
Lattice constant (nm)	0.40496	a = 0.295 c = 0.468	0.28	0.36468	0.352
Substrate metal	Cu	Zr	Nb	Mo	
Crystal structure	fcc	hcp	bcc	bcc	
Lattice constant (nm)	0.36147	a = 0.323 c = 0.515	0.33	0.315	

Table 2 Atomic radius of liquid metals used in calculation

Liquid metal	In	Bi	Sn
Atomic radius (nm)	0.167	0.156	0.140

Cluster Models

A schematic drawing of the contact state of the liquid metal with the substrate metal is shown in Fig. 1. Figure 1a shows the interface between the substrate and liquid metals at the visual level. The liquid metal contacts the substrate metal. In detail, at the atomic level, the substrate metal atoms interact typically with the liquid metal atoms, as shown in Fig. 1b. When one atom contacts another atom, charge transfer and atomic bonding occur certainly between atoms. Therefore, the electronic structure of the interface between the substrate metal and the liquid metal is vital for a theoretical understanding of the wettability.

Cluster models were constructed on the basis of the interface between the substrate metal and the liquid metal, as shown in Fig. 2. Figure 2a illustrates the cluster model for the case of the fcc or hcp crystal structure. Figure 2b depicts the cluster model for the case of the bcc crystal structure. In these figures, the gray circles indicate the substrate metal atoms, whereas the white circles indicate the liquid metal atoms.

The interface between the substrate and liquid metals was selected as the close-packed plane of each crystal structure. In particular, the interfaces of fcc, hcp, and bcc

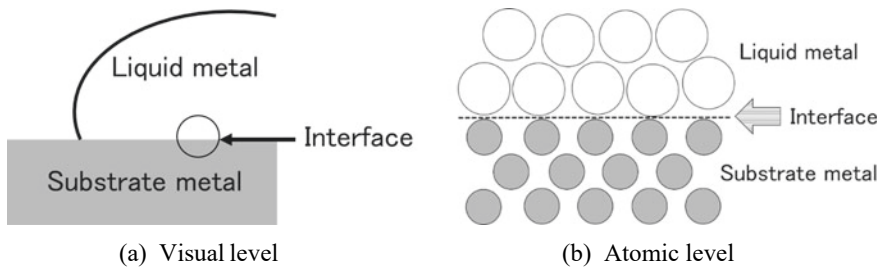


Fig. 1 Schematic drawing of the interface between substrate metal and liquid metal

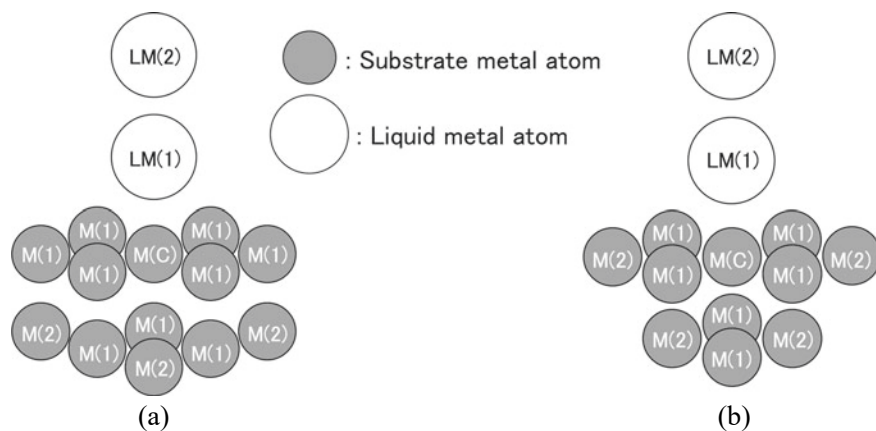


Fig. 2 Cluster models used for electronic structure calculation. **a** fcc or hcp substrate metal, **b** bcc substrate metal. In each cluster, M(C) is the centered atom of the substrate metal. M(1) and M(2) are the first- and second-nearest-neighbor substrate metal atoms, respectively, from M(C). LM(1) and LM(2) are the first- and second-nearest-neighbor liquid metal atoms, respectively, from M(C)

were (111), (0001), and (110), respectively. The liquid metal atoms were placed above the centered atom of the substrate metal. This cluster model consists of five kinds of atomic sites: the centered atom (M(C)) in the cluster model, the first-nearest-neighbor substrate metal atom (M(1)) from M(C), the second-nearest-neighbor substrate metal atom (M(2)) from M(C), the first-nearest-neighbor liquid metal atom (LM(1)) from M(C), and the second-nearest liquid metal atom (LM(2)) from M(C). The numbers of the first- and second-nearest-neighbor substrate metal atoms differ by the crystal structure of the substrate metal.

Electron States of Interface Between Substrate Metal and Liquid Metal

Electron Density of States

The calculated electron density of states of the interface between each substrate metal and each liquid metal is shown in Fig. 3. For example, for the electron density of states of Fig. 3a–c, the substrate metal is titanium, and the liquid metals are indium, bismuth, and tin. The horizontal axis denotes the electron density of states, and the vertical axis denotes the energy. E_f means the Fermi level. Due to space limitations, the shown density of states is for a 3d transition metal as the substrate metal.

These figures clarify that the main component is the d-orbital of the substrate metal. A peak of the d-orbital component exists near the Fermi level. The d-orbital component of the 3d transition metal shifts gradually to the low-energy side with

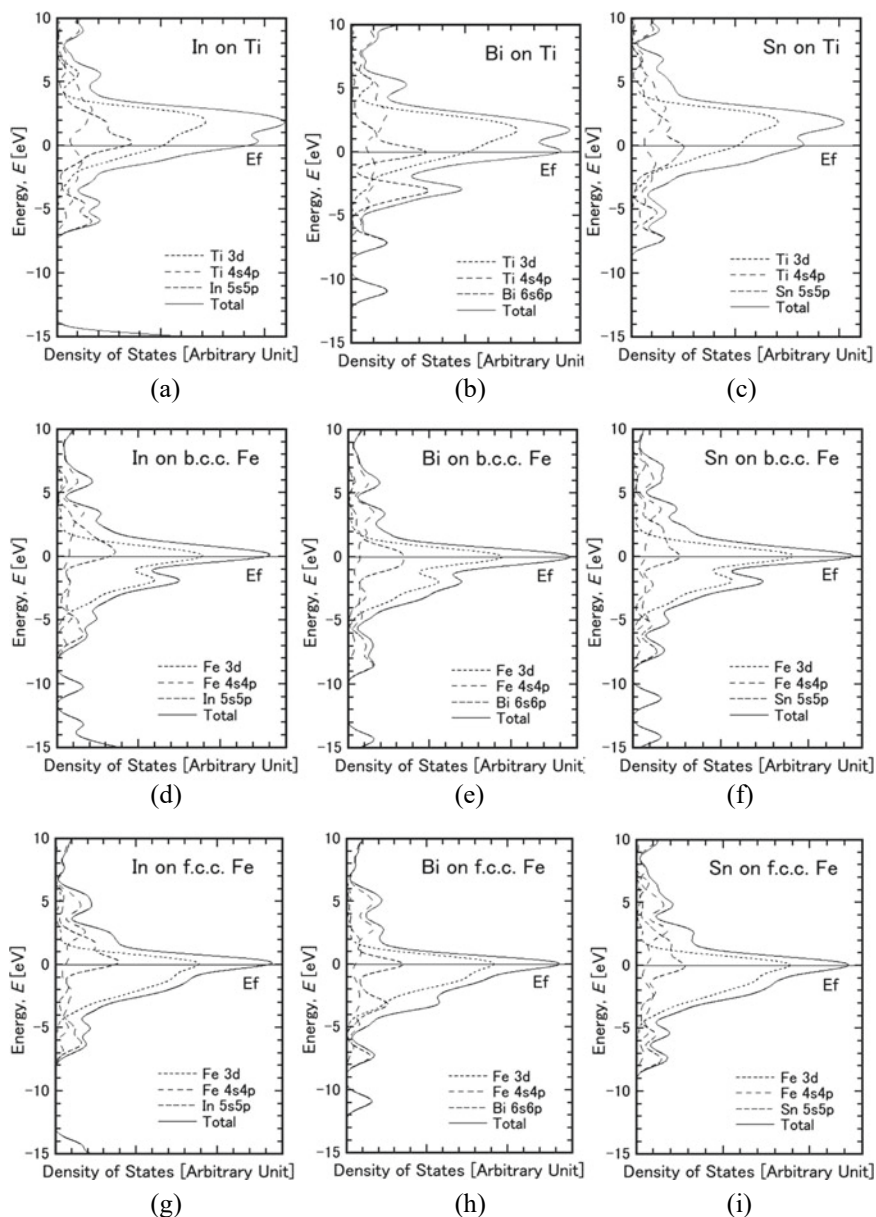


Fig. 3 Electron density of states at interface between substrate metal and liquid metal

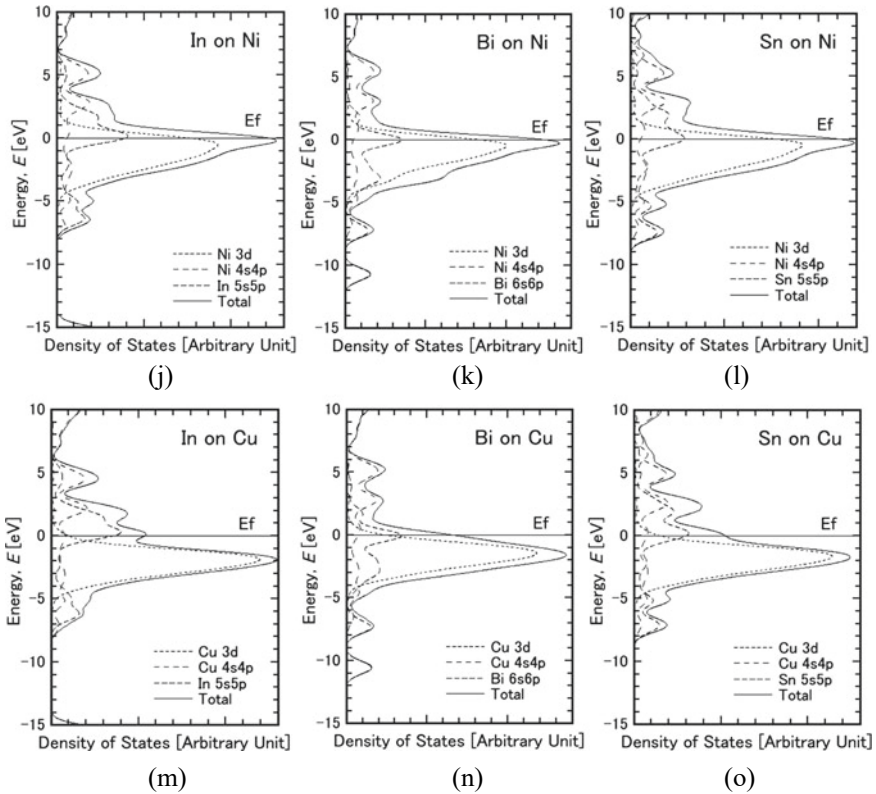


Fig. 3 (continued)

increasing atomic number. These electronic states of the substrate metal calculated in this study resemble those generated using band calculation [7–14]. The electronic state of the interface can also be represented by a small cluster model.

The main components of the indium, bismuth, and tin liquid metals are the s- and p-orbitals. Therefore, the components of the s- and p-orbitals of the liquid metal exist near the Fermi level. The shape of the electron density of states of the liquid metal remains constant irrespective of the kind of the substrate metal. The electron state of the liquid metal is assumed not to change considerably with a change in the substrate metal.

According to these results regarding the electron density of states, because the d-orbital component of the substrate metal and the s- and p-orbital components of the liquid metal exist near the Fermi level, their interactions are expected to affect the atomic interaction at the interface.

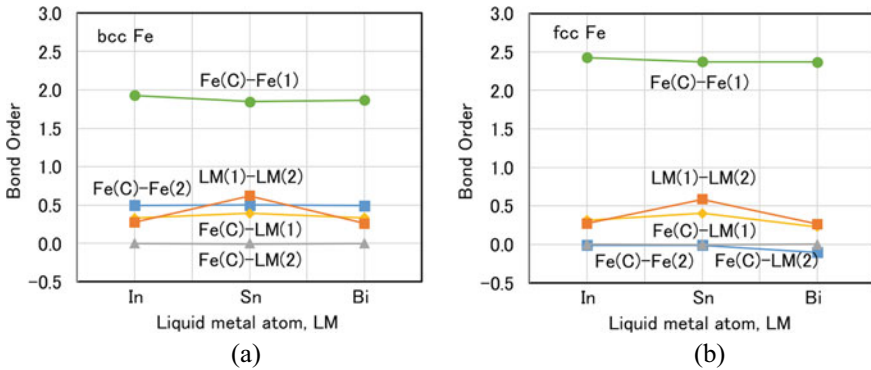


Fig. 4 Bond order of **a** substrate metal bcc Fe and **b** substrate metal fcc Fe

Bond Order

The bond order is a parameter showing the overlapping of the electron clouds between atoms. Therefore, this is a measure of the strength of the covalent bond between atoms.

The bond order calculated at the interface between the Fe substrate metal and the In, Sn, and Bi liquid metal are shown in Fig. 4a and b. Figure 4a shows the case where the substrate metal is bcc Fe, and Fig. 4b depicts the case where the substrate metal is fcc Fe. The horizontal axis denotes the kind of liquid metal. The vertical axis denotes the magnitude of the bond order. In these figures, Fe(C)-Fe(1) is the bond order between the centered Fe atom and the first-nearest-neighbor Fe atoms. Fe(C)-LM(1) is the bond order between the centered Fe atom and the first-nearest-neighbor liquid metal atom. Between Fig. 4a and b, there is a clear difference in Fe(C)-Fe(1) and Fe(C)-Fe(2). The Fe(C)-Fe(1) for fcc Fe is larger than that for bcc Fe. On the contrary, the Fe(C)-Fe(2) for fcc Fe is smaller than that for bcc Fe. The cause is the difference in the numbers of the nearest-neighbor atoms. In the case of fcc Fe (bcc Fe), there are nine (six) first-nearest-neighbor atoms and three (four) second-nearest-neighbor atoms. This result implies a need to normalize the number of bonding pairs considering the atomic interactions at the interface. On the contrary, the Fe(C)-LM(1) bond is not affected by the differences in crystal structures. It became clear from these figures the crystal structure affected the bond order.

The bond order between the substrate metal atom and the liquid metal atom at the interface (hereinafter called M-LM bond) and that between the substrate metal atoms (hereinafter called M-M bond) are shown in Fig. 5a and b, respectively. Each M-M bond is normalized with diatomic molecules using Eq. (1) or (2). The horizontal axis denotes the kind of substrate metal. In these figures, Fe(b) and Fe(f) mean bcc Fe and fcc Fe, respectively, which have different crystal structures. The vertical axis denotes the magnitude of the bond order.

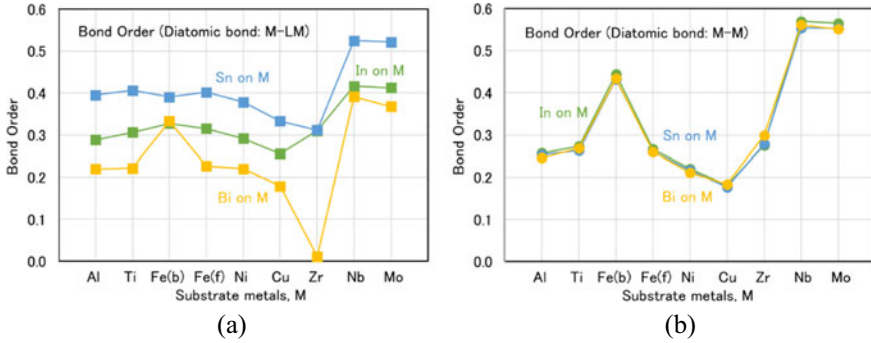


Fig. 5 **a** Bond order between substrate metal and liquid metal and **b** bond order between substrate metals

When the crystal structure of the substrate metal is fcc or hcp,

$$Bo(M - M) = \frac{1}{9} \times (M(C) - M(1)\text{bond}) + \frac{1}{3} \times (M(C) - M(2)\text{bond}). \quad (1)$$

When the crystal structure of the substrate metal is bcc,

$$Bo(M - M) = \frac{1}{6} \times (M(C) - M(1)\text{bond}) + \frac{1}{4} \times (M(C) - M(2)\text{bond}). \quad (2)$$

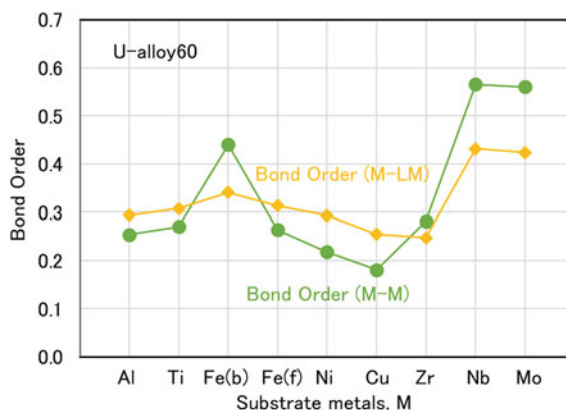
These results indicate that the M-LM bond changes largely by the kinds of the substrate and liquid metals. In particular, Fig. 5a shows that the kind of liquid metal affects the M-LM bond largely. This means the wettability can be modified even if the composition of the low melting temperature alloy is slightly different. On the contrary, there is almost no change in the M-M bond with the kind of the liquid metal, as shown in Fig. 5b. The kind of the liquid metal is not expected to affect the M-M bond. These results imply that the M-LM bond more significantly affects the wettability than does the M-M bond. The average value of the bond order for U-alloy 60 is defined using its component, as shown in Eqs. (3) and (4). The component used is mol% in place of mass%. The bond orders of the M-M and M-LM bonds for U-alloy 60 are shown in Fig. 6.

$$Bo(M - M)_{U\text{-alloy}60} = 0.06 \times Bo(M - M)_{In} + 0.21 \times Bo(M - M)_{Bi} + 0.19 \times Bo(M - M)_{Sn} \quad (3)$$

$$Bo(M - LM)_{U\text{-alloy}60} = 0.60 \times Bo(M - LM)_{In} + 0.21 \times Bo(M - LM)_{Bi} + 0.19 \times Bo(M - LM)_{Sn} \quad (4)$$

The magnitude of change of the M-LM bond is smaller than that of the M-M bond. The M-M bond of the 3d transition substrate metal is smaller than the M-LM

Fig. 6 Bond order of M–M bond and M–LM bond for U-alloy 60



bond except for Fe(b). On the contrary, the M–M bond of the 4d transition substrate metal is larger than the M–LM bond. Thus, the atomic bond of the interface is more complex. These findings indicate that these new two parameters, M–LM and M–M bonds, can be used to evaluate wettability theoretically.

Conclusion

The electronic structures of the interface were calculated using the DV- $X\alpha$ cluster method, which is a molecular orbital calculation, to understand the wettability of pure metal with a low melting temperature. Results showed that the kind of liquid metal affects the bond order between the substrate metal atom and the liquid metal atom at the interface. However, it does not affect the bond order between the substrate metal atoms. New parameters (bond orders) for understanding wettability were obtained from these calculation results.

References

1. Saito J, Shibutani H, Kobayashi Y (2020) Fundamental study on wettability of pure metal by liquid sodium. In: Li J et al (eds) Characterization of minerals, metals, and materials 2020. The minerals, metals & materials series. Springer, Cham, pp 563–571
2. Saito J, Kobayashi Y, Shibutani H (2021) Wettability of pure metals with liquid sodium and liquid tin. *Mater Trans* 62(10):1524–1532. <https://doi.org/10.2320/matertrans.MT-M2021107>
3. Adachi H, Tsukuda M, Satoko C (1978) Discrete variational $X\alpha$ cluster calculations. I. *Appl Metal Clust, J Phys Soc Jpn* 45:875–883. <https://doi.org/doi.org/10.1143/JPSJ.45.875>
4. Satoko C, Tsukada M, Adachi H (1978) Discrete variational $X\alpha$ cluster calculations. II. *Appl Surf Elect Struct MgO J Phys Soc Jpn* 45:1333–1340. <https://doi.org/doi.org/10.1143/JPSJ.45.1333>

5. Adachi H, Shiokawa S, Tsukada M, Satoko C, Sugano S (1979) Discrete variational $X\alpha$ cluster calculations. II. *Appl Phys Lett* 47:1528–1537. <https://doi.org/10.1143/JPSJ.47.1528>
6. Adachi H, Taniguchi K (1980) Discrete variational $X\alpha$ cluster calculations. IV. *Appl Phys Lett* 49:1994–1995. <https://doi.org/10.1143/JPSJ.49.1944>
7. Jafari M, Jamnezhad H, Nazarzadeh L (2012) Electronic properties of titanium using density functional theory. *Iranian J Sci Tech A* 36:511–515. <https://doi.org/10.22099/IJSTS.2012.2114>
8. Cornwell JF, Hum DM, Wong KG (1968) Density of states in iron. *Phys Lett A* 26:365–366. [https://doi.org/10.1016/0375-9601\(68\)90376-9](https://doi.org/10.1016/0375-9601(68)90376-9)
9. Fletcher GC (1952) Density of states curve for the 3d electrons in Nickel. *Phys Soc A* 65:192–202. <https://doi.org/10.1088/0370-1298/65/3/306>
10. Liu Z, Shang J (2011) First principles calculations of electronic properties and mechanical properties of bcc molybdenum and niobium. *Rare Met* 30:354–358. <https://doi.org/10.1007/s12598-011-0302-9>
11. Panda BP (2012) Electronic structure and equilibrium properties of hcp titanium and zirconium. *J Phys* 79:327–335. <https://doi.org/10.1007/s12043-012-0301-x>
12. Yasui M, Hayashi E, Shimizu M (1970) Self-consistent band calculations for vanadium and chromium. *J Phys Soc Jpn* 29:1446–1455. <https://doi.org/10.1143/JPSJ.29.1446>
13. Kolar M (1977) Surface density of states in a simple model of nickel. *Phys Status Solidi B* 80:521–531. <https://doi.org/10.1002/pssb.2220800213>
14. Williams GP, Norris C (1974) The density of states of liquid copper. *J Phys F* 4:L175L178. <https://doi.org/10.1088/0305-4608/4/8/001>

Influence of pH Regulating Additives on the Performance of Granite Waste-Based Paints



Márcia Maria Salgado Lopes, Leonardo Gonçalves Pedroti, Hellen Regina de Carvalho Veloso Moura, José Maria Franco de Carvalho, José Carlos Lopes Ribeiro, and Gustavo Henrique Nalon

Abstract The production of paints containing waste from granite processing has been studied as an alternative pathway to sustainable development. However, the low stabilization of polyvinyl acetate resin (PVA) due to the basic pH of the waste is a limitation of these paints. Therefore, the aim of this study is to evaluate the influence of pH regulating additives on the performance of PVA latex paints based on granite waste. The waste was characterized physically, chemically, and morphologically. Two pH-regulating additives (citric acid and sulfuric acid) were tested, considering different proportions of waste and resin used to produce the paints. The pH was adjusted to the range of 4.5–5.5. Experimental tests were carried out to determine the hiding power of the dry paint and the resistance to wet abrasion without abrasive paste. Paints produced with sulfuric acid showed better performance, as the additive positively influenced the abrasion resistance and did not significantly affect the hiding power of the paints. These results show that the granite waste has potential to be used in the manufacture of paints.

Keywords Granite waste · Paint · Performance · pH

M. M. S. Lopes (✉) · L. G. Pedroti · H. R. de Carvalho Veloso Moura · J. M. F. de Carvalho · J. C. L. Ribeiro · G. H. Nalon
Civil Engineering Department, Federal University of Viçosa, Av. Peter Rolfs, 36,570–000, Viçosa, Brazil

H. R. de Carvalho Veloso Moura
e-mail: hellen.moura@ufv.br

J. M. F. de Carvalho
e-mail: josemaria.carvalho@ufv.br

J. C. L. Ribeiro
e-mail: jcarlos.ribeiro@ufv.br

Introduction

The granite ornamental stone processing industry is responsible for the generation of large amounts of waste around the world, and the volume of this material is expected to increase continuously [1, 2]. In this context, professionals from different areas of knowledge have investigated possible solutions to minimize the environmental impacts caused by the disposal of this waste in landfills.

A new alternative is the use of granite waste as an inert pigment of paints for civil construction. Thus, it would be possible to reduce the amount of waste deposited in the environment and design a more sustainable and cheaper product to replace those traditionally used.

However, experimental tests performed by Lopes et al. [3] showed a negative interaction between the granite waste and the polyvinyl acetate resin (PVA). This negative interaction is probably associated with the basic pH of granite waste. Under alkaline conditions, PVA presents a low hydrolytic stability, impairing its binding properties [4].

In the paint industry, the use of pH regulating additives is a common practice to improve product performance. Cheng et al. [5], Croll and Taylor [6], and Godinez and Darnault [7] studied the influence of pH on the characteristics and properties of calcium carbonate pigments, titanium dioxide, and nano-titanium dioxide, respectively. In addition, Dillon et al. [8] studied the influence of pH on the performance of acrylic paints.

In this context, the objective of this work was to study the influence of pH on the hiding power and abrasion resistance of PVA latex paints based on granite waste. This study compared the performance of paints produced with granite waste without any special treatment with the performance of paints produced with granite waste and pH regulating additives.

Materials and Methods

Materials

In this work, granite waste was used as pigment, water as solvent, and PVA as binder of paints for civil construction. Moreover, two different pH-regulating additives were investigated: citrate buffer and sulfuric acid.

The granite waste was submitted to an initial treatment of deagglomeration and mechanical dispersion of particles in aqueous medium, using a Cowles disc coupled to a mechanical stirrer, at a speed of 1500 rpm, for 30 min. Then, sieving was performed in a wet medium, using an ASTM 80 mesh sieve (opening of 0.177 mm), as suggested by Cardoso et al. [9].

The water had a specific mass of 1.00 g/cm^3 and pH between 6.0 and 7.0. The resin presented a density of 1.05 g/cm^3 , a pH in the range of 4.0–5.0, and a solids content of 50%.

The pH regulating additives used in this study were a citrate buffer solution obtained from citric acid (CA) and pH adjustment with sodium hydroxide, and an aqueous solution of sulfuric acid.

Characterization of Granite Waste

The granite waste was characterized after being submitted to disaggregation, mechanical dispersion, and sieving. A physical characterization was carried out based on tests for determination of particle size distribution [10]; particle density [11]; and specific surface area by the BET method (Brunauer, Emmett, and Teller), using a Quantachrome NOVA equipment and nitrogen adsorption. Chemical characterization was developed based on the determination of pH of the materials [11]; and X-ray Fluorescence (XRF), using a Shimadzu EDX-700 equipment. For morphological characterization, scanning electron microscopy (SEM) was performed, using a Leo 1430VP equipment.

Preparation of Paints

The experimental model used in this study was the experimental planning of mixtures. The independent variables of the planning were the granite waste content with variations from 60 to 80%, and the resin content, ranging from 20 to 40% (considering the total resin system, i.e., both volatile and non-volatile fractions). These ranges of variation were defined based on pigment and resin contents of the commercial PVA latex paints studied by Silva and Uemoto [12]. Furthermore, these ranges are in line with the PVC (pigment volume concentration) values expected for an economical matte paint, with variations of approximately 55–80%.

The amount of water added to each mixture was defined to keep the viscosity within a constant range that ensures good practical application of the paint. Results of a series of preliminary tests indicated that the kinematic viscosity considered ideal for practical application of the paints corresponds to a flow time of $12 \pm 1 \text{ s}$, measured by a Ford cup viscometer with orifice number 4 [13].

Finally, the amount of citrate buffer solution or aqueous sulfuric acid solution (H_2SO_4) added to each mixture was determined based on the content needed to maintain the pH in the range of 4.5–5.5. This pH range was selected according to recommendations of Yamak [14], who verified that the optimum pH for polyvinyl acetate emulsions is included in this range.

The amounts of citric acid and sodium hydroxide used to prepare the citrate buffer were obtained from Eqs. 1 and 2. These equations defined relationships between the

mass of granite waste, the volume of water, and the masses of citric acid and sodium hydroxide necessary for keeping the pH of the solution within the defined range. The equations were defined based on the calculation of the force of the plug described by Oliveira [15], considering the acid–base effects associated with the resin. This calculation was performed based on results obtained from the potentiometric titrations of the water, granite waste, and sodium hydroxide (NaOH) system, using hydrochloric acid (HCl) at different concentrations. Aqueous solution of sulfuric acid (H_2SO_4) at 1.8 mol/L was added to the paint until the pH of the mixture was within the recommended range.

$$\text{Citric acid mass (g)} = 0.116 \times \text{Granite wastemass (g)} \times \text{Water volume (mL)} \quad (1)$$

$$\text{NaOH mass (g)} = 0.34 \times \text{citric acid mass (g)} \quad (2)$$

To produce the paints, granite waste pigments dispersed in water were mixed with the PVA, according to the previously defined proportions. The Cowles disc coupled to a mechanical agitator was used to ensure suitable mixture for 10 min at a speed of 500 rpm. In series containing citrate buffer solution, this additive was added to the mixture before the addition of the PVA, in amounts defined by Eqs. 1 and 2. In series containing aqueous solution of sulfuric acid, this additive was added to the mixture after the addition of the PVA.

Then, the viscosity of the paint was measured with a Ford cup viscometer with orifice number 4. When necessary, viscosity correction was carried out, based on the addition of one or more components to the mixture, followed by stirring and a new measurement of viscosity. This process was repeated until obtaining a flow time of 12 ± 1 s. It is noteworthy that such corrections always respected the proportions of granite waste and resin, as well as Eqs. 1 and 2.

The final formulations of each paint sample are shown in Table 1, as well as their mean flow time and PVC. PVC was obtained by the ratio between the volume of pigments (active and inert) and the total volume of solids in the dry film [16]. The experiment was reproduced three times. The first experiment consisted of reference paints containing granite waste (GWP). The second one was composed of paints containing granite waste and citrate buffer (GWP+CB). The third one was composed of paints containing granite waste and sulfuric acid (GWP+SA).

Characterization of the paint samples was carried out, based on the determination of their solids content [17] and the measurement of their pH with a pHmeter Digimed model DM-23. In addition, images of the paint films were performed using the Leo 1430VP scanning electron microscope.

Table 1 Mass composition, viscosity, and PVC of the paints

Exp	Paint sample	% Granite waste	% Resin	Granite waste (g)	Resin (g)	Water (g)	CA (g)	NaOH (g)	H ₂ SO ₄ (g)	Visc (s)	PVC (%)
GWP	1	80	20	500.0	125.0	385.0				12.8	76.6
	2	75	25	500.0	166.7	435.0				12.8	71.1
	3	70	30	500.0	214.3	485.0				12.9	65.7
	4	65	35	500.0	269.2	557.5				12.3	60.4
	5	60	40	500.0	333.3	640.0				12.5	55.2
GWP+CB	1	80	20	500.0	125.0	385.0	22.4	7.6		12.2	76.6
	2	75	25	500.0	166.7	435.0	24.8	8.4		11.9	71.1
	3	70	30	500.0	214.3	485.0	27.1	9.2		12.1	65.7
	4	65	35	500.0	269.2	557.5	30.1	10.2		12.1	60.4
	5	60	40	500.0	333.3	640.0	33.2	11.3		12.2	55.2
GWP+SA	1	80	20	500.0	125.0	385.0			2.6	12.5	76.6
	2	75	25	500.0	166.7	435.0			2.6	12.9	71.1
	3	70	30	500.0	214.3	485.0			2.6	12.9	65.7
	4	65	35	500.0	269.2	557.5			2.6	12.9	60.4
	5	60	40	500.0	333.3	640.0			2.6	12.9	55.2

Caption: Exp—experiment; CA—citric acid; NaOH—sodium hydroxide; H₂SO₄—sulfuric acid; Visc.—viscosity (paint flow time); PVC—pigment volume concentration; GWP—paints produced with granite waste; GWP+CB—paints produced with granite waste and citrate buffer; GWP+SA—paints produced with granite waste and sulfuric acid solution

Performance of Paints

Tests were carried out to determine the hiding power of dry paint and resistance to wet abrasion without abrasive paste, based on the requirements of Brazilian standards.

The hiding power of dry paint was determined based on the methodology of ABNT NBR 14942 [18]. This parameter is calculated as the maximum applied area (m^2) per unit of paint volume (L) so that the coverage has a contrast ratio of 98.5%. The contrast ratio is the ratio between the reflectance values measured on the black part and the white part of the test chart.

The resistance to wet abrasion without abrasive paste was determined according to ABNT NBR 15078 [19]. This parameter is calculated as the number of cycles that a paint film is able to withstand up to the wear of at least 80% of the area covered by the brush.

The desirability statistical function was used to determine the proportions of the components that optimize the performance properties. The target values were $4 \text{ m}^2/\text{L}$ for the hiding power of dry paint and 100 cycles for the resistance to wet abrasion without abrasive paste, as required by ABNT NBR 15079-1 [20], for the category of economical paints. Thus, an individual desirability value was calculated for each response variable, ranging from 0 (unacceptable value) to 1 (most desirable value). After that, the total desirability value was calculated as the simple geometric mean of the individual desirability values. The ideal proportion of components is the one whose total desirability value is closer to one [21].

Results and Discussion

Characterization of Granite Waste

Table 2 shows the results of the physical characterization and pH of the waste. Particle size influences paint properties in wet and dry state. The finer the particle size of the pigments, the better the product's performance, especially with regard to optical properties [22].

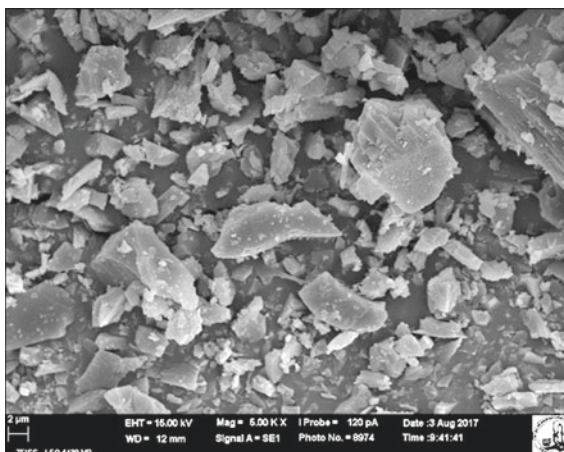
XRF results are shown in Table 3. It is observed that the granite waste is mainly composed of SiO_2 . Silica is one of the materials commonly used in the paint industry as an inert pigment, in order to improve the performance and durability of the product.

Table 2 Physical characterization of pigments

Pigment	Particle density (g/cm^3)	Specific surface (m^2/g)	Granulometry (%)			Average diameter (μm)	pH
			Similar to clay	Similar to silte	Similar to thin sand		
Granite waste	2.56	4.42	13.1	73.1	13.8	10	8.00

Table 3 XRF results of pigments

Pigment	SiO ₂	Al ₂ O ₃	K ₂ O	Na ₂ O	Fe ₂ O ₃	Others
Granite waste	73.35	16.09	6.47	1.83	0.54	1.74

Fig. 1 SEM of granite waste particles (Mag = 5000 X)

Regarding the morphological characterization, granite waste (Fig. 1) is a material with varied diameter distribution, since its particles present irregular morphology and angular corners. The shape and size of the particles affect their packaging and, consequently, the properties of the paint film [22].

Characterization and Performance of Paints

Table 4 shows the characterization results, i.e., solids content (SC) and pH of the paints produced in all experimental programs. It also shows their performance results, i.e., hiding power (HP) and abrasion resistance (AR). Desirability values (DSJ) for each sample are also presented.

Regarding the solids content (SC), it is observed that samples with the same percentage of resin and waste of the GWP, GWP+CB, and GWP+SA experiments have very similar SC values. It is attributed to the fact that the presence of the citrate buffer solution and the aqueous sulfuric acid solution did not change the amount of water needed to maintain the kinematic viscosity within the defined working range. Furthermore, it is observed that the higher the PVC, the higher the SC, as the amount of pigments is the factor that causes the highest impact to the solids content. According to Silva and Uemoto [12], the solids content of PVA latex paints available in the market ranges from 35.6 to 52%. One can notice that the SC of GWP,

Table 4 Characteristics and properties of paints

Paint	Sample	PVC	SC (%)	pH	HP (m ₂ /l)	AR (cycles)	DSJ
GWP	1	76.6	53.57	7.25	6.54	38.50	0.61
	2	71.1	50.46	7.19	5.05	53.30	0.74
	3	65.7	49.14	7.15	3.92	74.30	0.85
	4	60.4	45.82	7.03	2.75	83.70	0.79
	5	55.2	43.34	6.94	1.76	107.70	0.64
GWP+CB	1	76.6	54.70	4.87	5.61	33.33	0.59
	2	71.1	52.09	4.85	5.08	40.00	0.62
	3	65.7	49.76	4.93	2.87	44.00	0.62
	4	60.4	47.24	4.95	2.24	48.67	0.54
	5	55.2	45.21	4.85	1.78	49.83	0.43
GWP+SA	1	76.6	53.92	5.14	5.27	69.50	0.84
	2	71.1	51.84	5.16	4.42	93.83	0.97
	3	65.7	49.09	5.12	2.99	120.17	0.89
	4	60.4	46.43	5.05	1.79	146.17	0.74
	5	55.2	44.45	5.00	1.54	166.83	0.54

GWP+CB, and GWP+SA paints ranges from 43 to 55%, which is very similar to that of commercial paints.

Data concerning the pH of the paints indicated that GWP had a pH in the range of 6.9–7.3. Moreover, the higher the percentage of resin, the lower the pH, as the resin has a more acidic pH (pH between 4 and 5) in relation to the waste (pH = 8). In GWP+CB and GWP+SA, the pH was adjusted to the optimal pH range for the PVA, i.e., pH values close to 5.00, according to Yamak [14].

Regarding the hiding power (HP), GWP+CB and GWP+SA showed a reduction in the hiding power, when compared to GWP. It possibly happened because the addition of sulfuric acid or citric acid favored the dissolution of the smaller particles of granite waste. This phenomenon is related to Bronsted's acid–base processes and chemical kinematics, and can be experimentally proven by comparing Fig. 2a–c. In these SEM images, it is possible to observe a decrease in the number of smaller particles in paints with the addition of acids.

ABNT NBR 15079-1 [20] prescribes those economic paints must have a minimum hiding power of 4 m²/L. GWP, GWP+CB, and GWP+SA met the standard specifications only in formulations with PVC greater than 65%.

Regarding the abrasion resistance (AR), the best abrasiveness results were obtained in the case of GWP+SA, whereas the worst results were observed in GWP+CB. All these results are probably related to the adsorption of citrate, acetate (generated due to the hydrolysis of the polyvinyl acetate polymer and its natural degradation), and sulfate ions on the surface of granite waste pigments (linked to silicon and aluminum content groups). Such adsorption phenomena, mainly the one of citrate ions, was also reported by Lackovic et al. [23], and Mudunkotuwa and

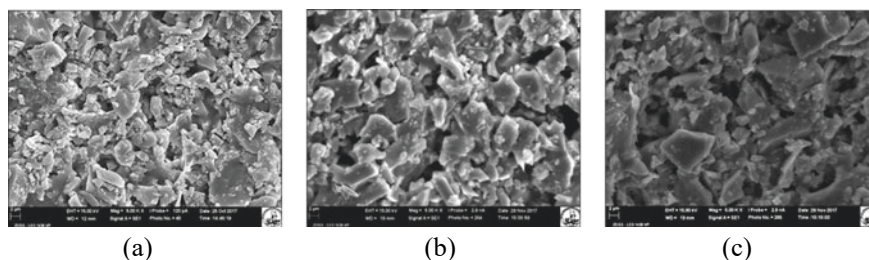


Fig. 2 SEM of paint films based on granite waste (Mag = 5000 X): **a** GWP sample 1; **b** GWP+CB sample 1; **c** GWP+SA sample 1

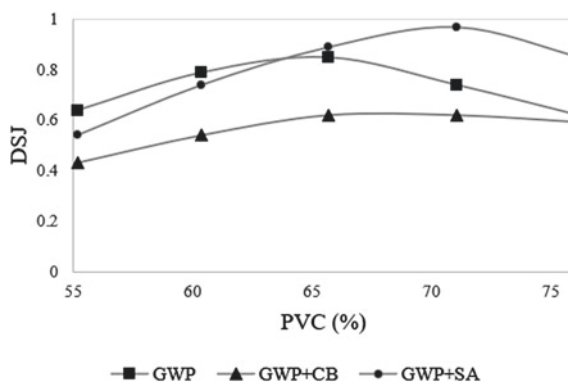
Grassian [24], considering particles of titanium dioxide, iron oxide, and aluminum oxide.

In the case of GWP+CB, the unsatisfactory abrasiveness results may be related to the presence of significant amounts of citrate ions (with 1-, 2-, and 3-charges) in a medium with pH between 4.5 and 5.5 [15]. These species, especially fully deprotonated citrate (with a 3-charge), may have been adsorbed on the granite waste particles, which must be positively charged in this pH range. The adsorption of citrate ions seems to have altered the adhesion between the waste particles and the resin, causing a decrease in the ability of PVA to bind pigments. In GWP samples, the positive surface charge is lower, due to the higher pH values (in the range of 7.0). Moreover, the effects of the adsorbed acetate ions should be less intense than those of citrate ions, as they lead to lower entropy increases. In the case of GWP+SA samples, the amount of acetate ions in pH close to 5.0 is about 50% smaller than in pH values above 5.0, which is the case with GWP. Thus, there is less adsorption of these anions on the pigment particles, which explains the high values of AR in GWP+SA samples.

ABNT NBR 15079-1 [20] prescribes that economic paints must have a minimum abrasion resistance of 100 cycles. The best AR results were observed in GWP+SA, since samples of this series met the standard specification in almost the entire range investigated in this research, i.e., in formulations with PVC below 70%. On the other hand, GWP reached AR values greater than 100 cycles only when the PVC was lower than 55%. Finally, GWP+CB presented the worst AR results, since GWP+CB samples did not meet the normative specification.

The desirability statistical parameters (Fig. 3) indicated that although the hiding power and abrasion resistance had an antagonistic effect, some formulations presented desirability values very close to 1.00. This means that the paints produced from these formulations simultaneously meet the hiding power and abrasion resistance requirements defined by ABNT NBR 15079-1 [20]. According to Fig. 3, the best formulation was GWP+SA with PVC close to 70%. This composition has a hiding power of 4.00 m²/l and abrasion resistance of 99.77 cycles so that its desirability was close to 1.00. In the GWP and GWP+CB cases, none of the formulations

Fig. 3 Desirability (DSJ) of the paints produced in this research



satisfied the minimum standard requirements. The best GWP formulation was verified in PVC close to 65%. In this formulation, the hiding power was 4.00 m²/l and abrasion resistance was 71.56 cycles, resulting in a desirability of 0.85. Finally, the best GWP+CB formulation presented PVC close to 68%, which provided a hiding power of 4.00 m²/l and an abrasion resistance of 41.23 cycles (desirability equal to 0.64). Therefore, the best paint formulations of all cases studied in this research do not present problems regarding opacity.

Conclusions

This study was carried out to explore the effect of pH on the performance of PVA latex paints containing granite waste. The results of the experimental tests provided the following conclusions:

- One of the alternatives for regulating the pH in the 4.5–5.5 range was the use of a citrate buffer solution. The use of this buffer in PVA latex paints containing granite waste impaired the abrasion resistance of the product, since the citrate ions were adsorbed on the surface of the pigments, possibly impairing their adhesion with the resin.
- Another alternative to regulate the pH in the mentioned range was the use of an aqueous solution of sulfuric acid at 1.8 mol/L. The use of this solution in PVA latex paints containing granite waste impaired the hiding power, but significantly increased the abrasion resistance. It was attributed to the greater stability of the PVA, as the pH of the solution was close to 5.0.
- According to the statistical desirability function, paints with aqueous solution of sulfuric acid that have PVC close to 70% meet Brazilian specifications of the economic paints category.

- The results of this work showed that the addition of certain pH regulating additives, such as sulfuric acid, improved the performance of PVA latex paints containing granite waste pigments.

Acknowledgements The authors want to thank the CNPq for the support provided to this investigation.

References

1. Souza AJ, Pinheiro BCA, Holanda JNF (2010) Processing of floor tiles bearing ornamental rock-cutting waste. *J Mater Process Technol* 210:1898–1904
2. Hojamberdiev M, Eminov A, Xu Y (2011) Utilization of muscovite granite waste in the manufacture of ceramic tiles. *Ceram Int* 37:871–876
3. Lopes MMS, Alvarenga RCSS, Pedroti LG, Ribeiro JCL, Carvalho AF, Cardoso FP, Mendes BC (2019) Influence of the incorporation of granite waste on the hiding power and abrasion resistance of soil pigment-based paints. *Constr Build Mater* 205:463–474
4. Suma KK, Jacob S, Joseph R (2009) Paint formulation using water based binder and property studies. *Macromol Symp* 277:144–151
5. Cheng B, Lei M, Yu J, Zhao X (2004) Preparation of monodispersed cubic calcium carbonate particles via precipitation reaction. *Mater Lett* 58:1565–1570
6. Croll SG, Taylor CA (2007) Hydrated alumina surface treatment on a titanium dioxide pigment: Changes at acidic and basic pH. *J Colloid Interface Sci* 314:531–539
7. Godinez IG, Darnault CJG (2011) Aggregation and transport of nano-TiO₂ in saturated porous media: effects of pH, surfactants and flow velocity. *Water Res* 45:839–851
8. Dillon CE, Lagalante AF, Wolbers RC (2014) Acrylic emulsion paint films: the effect of solution pH, conductivity, and ionic strength on film swelling and surfactant removal. *J Stud Conserv* 59:52–62
9. Cardoso FP, Alvarenga RCSS, Carvalho AF, Fontes MPF (2016) Production process and evaluation of performance requirements of soil pigments based paint for buildings. *Ambiente Construído* 16(4):109–125
10. ABNT NBR 7181 (2016) Soil-grain size analysis. Rio de Janeiro, Brazil (in Portuguese)
11. EMBRAPA (1997) Soil analysis methods manual. Brazil (in Portuguese), Rio de Janeiro
12. Silva JM, Uemoto KL (2005) Characterization of latex paints for civil construction: market diagnosis in the state of São Paulo. Technical Bulletin, Polytechnic School of the University of São Paulo, São Paulo, Brazil (in Portuguese)
13. ABNT NBR 5849 (2015) Paints-Viscosity determination by the ford cup. Rio de Janeiro, Brazil (in Portuguese)
14. Yamak HB (2013) Emulsion polymerization: effects of polymerization variables on the properties of vinyl acetate based emulsion polymers. In: *Polymer science*, chapter 2
15. Oliveira AF (2018) Chemical systems assessment-chemical equilibria in solution. Editora UFV, Viçosa, Brazil (in Portuguese)
16. Fazenda JMR (2009) *Paints and varnishes: science and technology*, 4th edn. Edgard Blücher, São Paulo, 1146p
17. ASTM D3723-05 (2017) Standard test method for pigment content of water-emulsion paints by low-temperature ashing. ASTM International, West Conshohocken, PA
18. ABNT NBR 14942 (2016) Paints for civil construction-method for evaluating the performance of paints for non-industrial buildings-Determination of covering power of dry paint. Rio de Janeiro, Brazil (in Portuguese)

19. ABNT NBR 15078 (2006) Paints for civil construction-Method for evaluating the performance of paints for non-industrial buildings-Determination of resistance to wet abrasion without abrasive paste. Rio de Janeiro, Brazil (in Portuguese)
20. ABNT NBR 15079-1 (2019) Paints for buildings-Minimum requirements for performance part 1: matte latex paint in light colors. Rio de Janeiro, Brazil (in Portuguese)
21. Barros Neto B, Scarminio IS, Bruns RE (2003) How to experiment: research and development in science and industry, 2nd edn, Campinas-SP, Brazil (in Portuguese)
22. Karakas F, Celik MS (2012) Effect of quantity and size distribution of calcite filler on the quality of water borne paints. *Prog Org Coat* 74:555–563
23. Lackovic K, Johnson BB, Angove MJ, Wells JD (2003) Modeling the adsorption of citric acid onto Muloorina illite and related clay minerals. *J Colloid Interface Sci* 267:49–59
24. Mudunkotuwa IA, Grassian VH (2010) Citric acid adsorption on TiO₂ nanoparticles in aqueous suspensions at acidic and circumneutral pH: surface coverage, surface speciation, and its impact on Na

Influence of the Sand Content on the Physical and Mechanical Properties of Metakaolin-Based Geopolymer Mortars



Igor Klaus R. Andrade, Beatryz C. Mendes, Leonardo G. Pedroti, Carlos M. F. Vieira, and J. M. Franco de Carvalho

Abstract Metakaolin is a naturally occurring calcined clay rich in aluminosilicates, and for this reason it is one of the most used precursors in the geopolymers' production. This work evaluates the influence of the sand content on the physical and mechanical properties of metakaolin-based geopolymer mortars, using sodium hydroxide solution with a concentration of 10 mol/L, thermal curing at 50 °C, and solution/precursor ratio of 0.90 ± 0.08 . The cylindrical and prismatic specimens were tested in flexural strength (1.6–4.7 MPa), compressive strength (2.3–7.4 MPa), bulk density (1.66–2.01 g/cm³), voids content (22.0–40.1%), and water absorption (12.3–30.7%). The addition of sand in the studied contents collaborated to a more compact and less porous composite formation, presenting better physical and mechanical performances. The 1:2 ratio (metakaolin:sand), when compared to the composite without sand, more than doubled the compressive strength of the mortars and reduced the porosity from 28.6 to 18.0%.

Keywords Geopolymer · Geopolymeric mortar · Metakaolin · Sand content

Introduction

Over the years, Portland cement has reached high consumption levels, with an average global production of 4.1 billion tons in 2019 [1]. Knowing the limitations of such material regarding its sustainability and durability, it is necessary to seek the development of new binders, such as the use of geopolymers based on industrial by-products [2, 3].

I. K. R. Andrade (✉) · B. C. Mendes · L. G. Pedroti · J. M. F. de Carvalho
DEC–Civil Engineering Department, UFV–Federal University of Viçosa, Av. Peter Rolfs, s/n,
Campus Universitário, Viçosa 36570-000, Brazil
e-mail: igor.klaus@ufv.br

C. M. F. Vieira
LAMAV–Advanced Materials Laboratory, UENF–State University of the Northern Rio de Janeiro,
Av. Alberto Lamego, 2000, Campos dos Goytacazes 28013-602, Brazil

Extensively studied in recent decades, the dosage of geopolymeric pastes and mortars using industrial by-products is an area still under consolidation. It is necessary to understand the best raw material processing conditions, dosing parameters, mixing, and curing to obtain the geopolymer matrix with the desired performance.

The production of geopolymers (materials with low calcium content) has explored several materials, with metakaolin being one of the most common in studies carried out [4–11]. Metakaolin is a naturally occurring calcined clay, also used as a primary source of aluminosilicate, and can be mixed with most industrial slag or used alone as a binding material [12].

Studies on the production of geopolymer mortars based on metakaolin found that the sand addition in some proportions reduces shrinkage and the formation of micro-cracks, reduces porosity, and increases the hardness and strength of the composites. Rashad, Hassan, and Zeedan [13] evaluated that the increment of quartz powder to geopolymers produced with metakaolin improved the paste workability and, despite increasing weight loss after heating, that increment promoted compressive strength gains before and after exposure to high temperatures, that is, increased residual resistance in post-fire situations.

Producing geopolymers with metakaolin, sodium silicate, and quartz sand of various particle sizes, Wan et al. [14] noticed that the quartz particles associated and involved by the geopolymer gel increased the mechanical strength of the geopolymers, working as an inert filling material, reaching approximately 5 MPa in compression, with the use of sand particles between 75 and 32 μm .

Autef et al. [15] produced geopolymers with metakaolin, adding different proportions of silica fume and unrefined crystallized quartz, and verified that the formed network depends on the nature of the silica source used. However, the polycondensation that leads to the formation of the geopolymer was dominant for mixtures with lower quartz contents, occurring a competition between the species in solution and the quartz, which is physically opposed to the polycondensation reaction.

In this sense, the ideal sand content for the production of geopolymers is the one that leads to the best filling of the matrix without compromising the geopolymerization reactions. In other words, a sand content that does not excessively limit the availability of reactive aluminosilicates or physically opposes the solubilized aluminosilicate species leaching.

Thus, this study aims to produce geopolymer mortars with low calcium content (geopolymers), based on metakaolin, using four different sand contents to observe the effect of increasing this content on the mechanical and physical properties of formed composites.

Materials and Methods

The geopolymeric mortars were produced with commercial metakaolin as a precursor, sand from the Piranga River (Minas Gerais, Brazil) with a particle size of

less than 2 mm (ASTM 10 mesh sieve), and a 10 mol/L sodium hydroxide solution (PASigma Aldrich, 99% purity).

The mineralogical composition was determined by X-ray diffractometry (Rigaku equipment, 2θ ranging from 3° to 70° , Co-K α radiation ($\lambda = 1.789 \text{ \AA}$), scan speed $0.119366^\circ/\text{s}$, and size of the step 0.0167113°). In addition, characterization tests determined the specific mass (2.61 g/cm^3) and specific area ($1478.26 \text{ m}^2/\text{kg}$) of metakaolin.

The composites were produced in different mixes by mass, as shown in Table 1, to evaluate the sand content effect in metakaolin-based geopolymer mortars. With preliminary studies, the range at 0.90 ± 0.10 for the solution/metakaolin ratio was determined to obtain consistencies that would allow the adequate molding of the specimens.

The production steps were:

- Preparation of the NaOH solution in distilled water 24 h before the geopolymers production;
- Manual mixing of precursors and solution (1 min);
- Mechanical mixing of the paste at low speed (2 min);
- Removal of paste adhered to the surface of the vat (1 min);
- Mechanical mixing with the slow and gradual addition of sand at low speed (2 min);
- Removal of paste adhered to the surface of the vat (1 min);
- Mechanical mixing at high speed (2 min);
- Measurement of material consistency;
- Mechanical mixing at high speed (1 min);
- Filling of molds in a single layer and densification on a vibrating table for 30 s;
- Coating of molds with plastic film to prevent water evaporation;
- The specimen sealed in the plastic film was subjected to curing at room temperature for 24 h, demolding and thermal curing at 50°C for 24 h, and curing in a humid chamber at room temperature until the test day.

For each mixture, four prismatic specimens with dimensions of ($20 \times 20 \times 80$) mm and six cylindrical samples with dimensions ($\text{Ø}35 \times 35$) mm were molded (Fig. 1a, b). Prismatic specimens were made of acrylic molds and the cylindrical samples in PVC molds, using vegetable oil as a release agent.

Table 1 Dosage of mixtures

ID	M:S	S:M
T120	1:2	0.97
T115	1:1.5	0.98
T110	1:1	0.88
T100	1:0	0.83

Abbreviations:

M:S – Metakaolin: Sand, by mass;

S:M – Solution: Metakaolin, by mass;

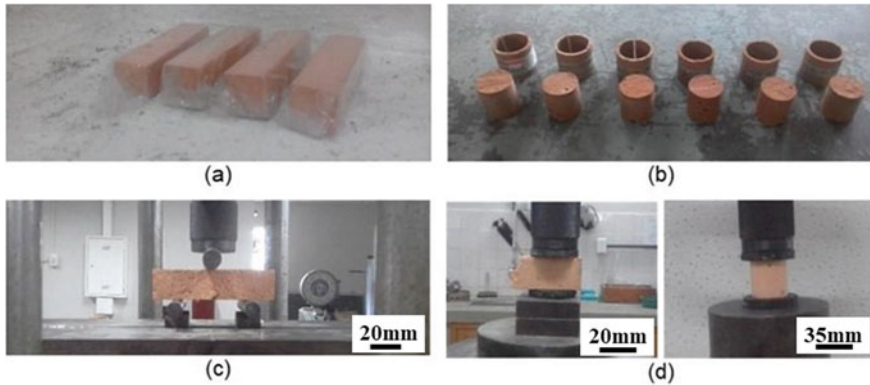


Fig. 1 Produced specimens and mechanical tests. **a** Prismatic specimens; **b** Cylindrical specimens; **c** Flexural strength test; **d** Compressive strength test

The mortars produced had their bulk density measured and were tested at 07 and 28 days for compressive strength and flexural strength (Fig. 1c, d) based on ABNT NBR 13,279 [16]. At 28 days, they were also tested for water absorption by immersion based on ABNT NBR 9778 [17].

Analyzes of variance were used to evaluate the precision of the values measured by the coefficients of variation and the statistical differences by the p-values of the ANOVA tables and using the Duncan’s test to compare the means.

Results and Discussion

Figure 2 shows the mineralogical composition of metakaolin with only quartz peaks. It appears that there is no residual kaolinite after the industrial heat treatment is applied and that the material obtained favors the geopolymerization process since the unstable phase allows the material to dissolve in an alkaline medium.

Fig. 2 Metakaolin XRD patterns (Q, quartz)

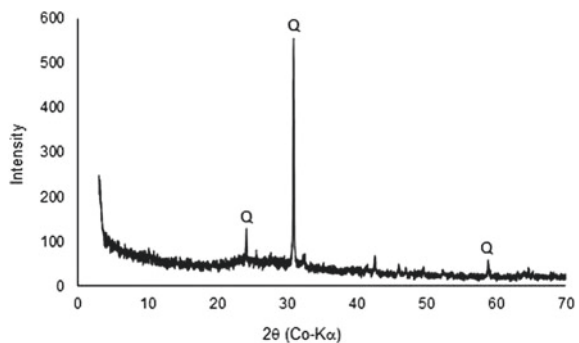


Table 2 Chemical composition of metakaolin (wt.%)

Oxide	SiO ₂	Al ₂ O ₃	CaO	MgO	Fe ₂ O ₃	TiO ₂	SO ₃	K ₂ O	Na ₂ O	Others
%	48.24	33.23	0.10	1.56	3.22	1.21	0.02	0.61	1.17	10.64

Table 2 shows the chemical composition of metakaolin. It is predominantly composed of silica (SiO₂) and alumina (Al₂O₃), the most common oxides that form metakaolinite and are necessary for the effectiveness of alkaline activation. Studies carried out indicate that the presence of iron oxide (Fe₂O₃) can inhibit geopolymerization reactions by replacing Al³⁺ ions with Fe³⁺ ions [18] and, therefore, must be controlled. However, the Fe₂O₃ content found is compatible with that expected for metakaolin [19]. Furthermore, the low presence of calcium oxide (CaO) allows characterizing the material produced as a geopolymer [20].

The physical and mechanical tests results were graphically compiled and presented in Fig. 3. The analysis of variance was performed, and the coefficients of variation were less than 10% for all tests, demonstrating a high precision of the values measured in the experiment. ANOVA table p-values were less than 5% in all trials. Tables 3 and 4 are present Duncan's test for multiple comparisons, and the letters "a, b, c, d" represent the results in descending order, and whose mixtures followed by equal letters do not differ statistically from each other.

The differences between the traces are significant for bulk density at 07 days, absorption and void content at 28 days. At 28 days, the bulk density of the mix T115 and T110 do not differ statistically. However, when analyzed together with the water absorption and void content results, there is an advantage in higher sand contents since the composites show a more compact and less porous configuration.

Kuenzel et al. [21] used silicate and sodium hydroxide to activate metakaolin mixtures with 0,10, 30, and 60% of silica sand and noticed an increase in density with an increase in the sand content (2.31 to 2 0.57 g/cm³). This increase in bulk density of approximately 11% with the increment of 60% of sand is in line with the results obtained in the matrices produced in this study, in which an increment of 100% sand (T110) increased the density by approximately 17% at 28 days.

As for the strengths, it was observed that the T120 and T115 mixes do not differ statistically, as well as the T110 and T100 admixtures. This evaluation allows the use of a more economical trace if the desired water absorption parameters are observed. An example is using a mortar with the greatest possible strength whose the desired water absorption is between 10 and 15%. Analyzing the absorption range, one could opt for the T120 or T115 mortar, and as the resistance results are statistically equal for these mixes, the choice falls on the economic criterion, and the mixture that will generate the lowest cost can be adopted.

Furthermore, we can observe that the results obtained are similar to the performance of conventional mixed mortars of cement, lime, and sand. Gołaszewska et al. [22] produced several 1:0.5:9 mix mortars (cement: lime: sand) and obtained bulk density, flexural strength, and compressive strength of approximately 2.01 g/cm³, 2.2 MPa, and 9.6 MPa, respectively.

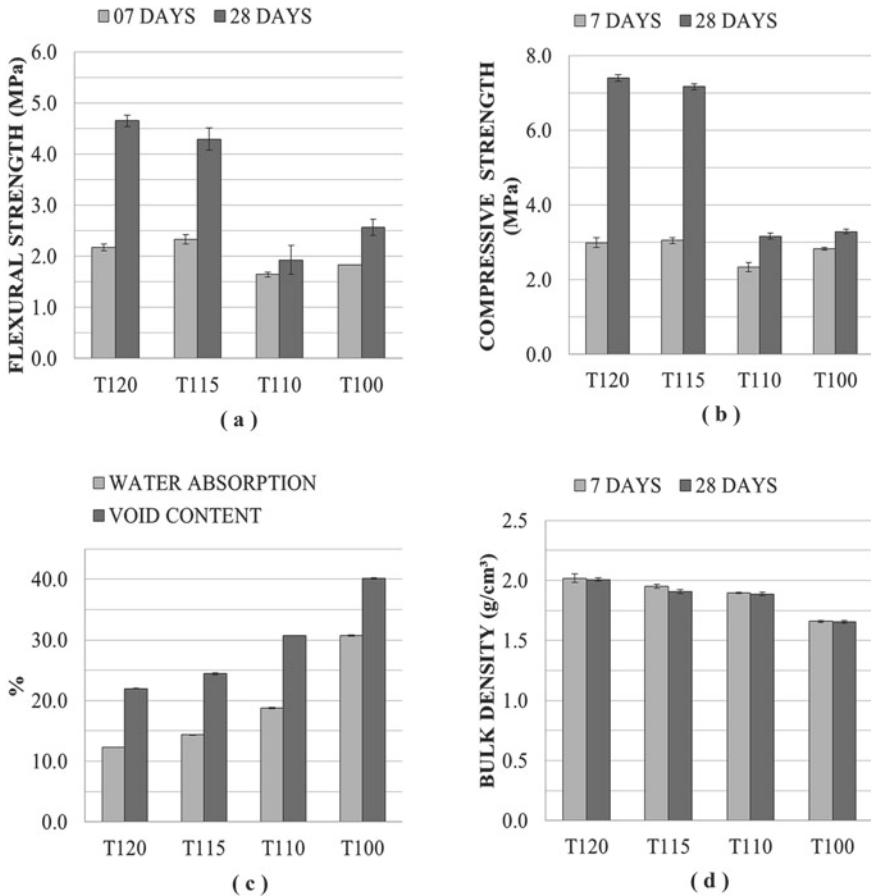


Fig. 3 Physical and mechanical tests results. **a** Flexural strength; **b** Compressive strength; **c** Water absorption and void content; **d** Bulk density

Table 3 Duncan’s test results for samples at 07 days

Bulk density	Flexural strength	Compressive strength
T120 a	T115 a	T115 a
T115 b	T120 a	T120 a
T110 c	T100 b	T100 a
T100 d	T110 b	T110 b

The addition of 200% sand (T120) more than doubled the compressive strength of the mortar and reduced the porosity from 28.6 to 18.0%. Buchwald et al. [23] found similar behaviors with using a sodium hydroxide solution (approximately 8 mol/L) and metakaolin showed that the additions of 20% of quartz reduced the porosity (from about 52 to 44%) and provided greater compressive strength (from 8 MPa

Table 4 Duncan's test results for samples at 28 days

Bulk density	Flexural strength	Compressive strength	Water absorption	Void Content
T120 a	T120 a	T120 a	T100 a	T100 a
T115 b	T115 a	T115 a	T110 b	T110 b
T110 b	T100 b	T100 b	T115 c	T115 c
T100 c	T110 b	T110 b	T120 d	T120 d

to about 11 MPa). Kuenzel et al. [21] found a variation in compressive strength between 4 and 40 MPa as the sand content increased and the amount of water in the mixture decreased. According to the authors, this is due to the strengthening that the sand particle generates to the geopolymer matrix (making it more effective for additions greater than 25% in volume) and the consequent reduction in the porosity of composites.

The solution/precursor ratio used presents a variation of less than 10% between the mixes, in this sense, it is assumed that the molar ratios of $\text{SiO}_2/\text{Al}_2\text{O}_3$, $\text{Na}_2\text{O}/\text{Al}_2\text{O}_3$, $\text{Na}_2\text{O}/\text{SiO}_2$ did not vary enough to generate significant changes in the composite, as they would promote similar alkaline conditions for geopolymer development. As the curing conditions were also standardized, the differences found in the tests are mainly due to the added sand content.

For the successful reactions of low calcium content systems (geopolymers), more aggressive conditions such as high alkalinity and thermal curing are needed [24, 25]. The thermal curing at 50 °C for 24 h (after a day of curing at room temperature) was positive for allowing an adequate demolding procedure and providing favorable conditions for polycondensation of aluminosilicates.

Thermal curing associated with the composition of raw materials did not generate visible disturbances due to excessive acceleration of reactions (such as non-hardening of the mixture, excessive expansion, or shrinkage). The specimens showed no apparent degradation such as cracks and efflorescence, maintained their integrity until the days tested, and showed resistance progression from 07 to 28 days, indicating the continuity of geopolymerization reactions.

Conclusions

This study observed the sand content effect on the mechanical and physical properties of composites from the alkali activation of metakaolin through the production of geopolymeric mortars using four different sand contents. Based on the results and discussions carried out, the following conclusions are presented:

- The solution/precursor ratio of 0.90 ± 0.08 provided good workability conditions, allowing for adequate molding.

- The differences between all mixtures regarding water absorption and void content are significant and indicated that the sand increment in the studied contents reduced the mortar's porosity.
- Comparing the T120 mortar and T100 paste, the sand increment increased the bulk density and tensile strengths in bending and compressive strength. In other words, the addition of sand in the studied contents tends to contribute to the formation of a more compact and less porous composite, and consequently, with better mechanical performance.
- Metakaolin-based geopolymer mortars showed results very similar to the usual ones for mixed cement, lime, and sand mortars. Thus, this material shows excellent potential for use when analyzed under the mechanical strength and physical behavior parameters.

Acknowledgements This study was financed in part by the Coordenação de Aperfeiçoamento de Pessoal de Nível Superior—Brasil (CAPES)—Finance Code 001. The authors also thank the Federal University of Viçosa, especially the Construction Materials Laboratory, for the exceptional support of this research.

References

1. U.S. Geological Survey, Mineral Commodity Summaries (2021) Cement 2021
2. ECRA (2017) Development of state of the art-techniques in cement manufacturing: trying to look ahead, RevisioBn 2017, Eur Cem Res Acad
3. Turner LK, Collins FG (2013) Carbon dioxide equivalent (CO₂-e) emissions: a comparison between geopolymer and OPC cement concrete. *Constr Build Mater* 43:125–130. <https://doi.org/10.1016/j.conbuildmat.2013.01.023>
4. Rashad AM (2013) Alkali-activated metakaolin: a short guide for civil engineer-an overview. *Constr Build Mater* 41:751–765. <https://doi.org/10.1016/j.conbuildmat.2012.12.030>
5. Granizo ML, Blanco-Varela MT, Palomo A (2000) Influence of the starting kaolin on alkali-activated materials based on metakaolin. Study of the reaction parameters by isothermal conduction calorimetry. *J Mater Sci* 35:6309–6315. <https://doi.org/10.1023/A:1026790924882>
6. Wang H, Li H, Yan F (2005) Synthesis and mechanical properties of metakaolinite-based geopolymer. *Colloids Surf A Physicochem Eng Asp* 268:1–6. <https://doi.org/10.1016/j.col surfa.2005.01.016>
7. Cwirzen A, Provis JL, Penttala V, Habermehl-Cwirzen K (2014) The effect of limestone on sodium hydroxide-activated metakaolin-based geopolymers. *Constr Build Mater* 66:53–62. <https://doi.org/10.1016/j.conbuildmat.2014.05.022>
8. Bernal SA, Rodríguez ED, Mejía De Gutiérrez R, Provis JL, Delvasto S (2012) Activation of metakaolin/slag blends using alkaline solutions based on chemically modified silica fume and rice husk ash. *Waste Biomass Valorization* 3:99–108. <https://doi.org/10.1007/s12649-011-9093-3>
9. Pouhet R, Cyr M (2016) Formulation and performance of flash metakaolin geopolymer concretes. *Constr Build Mater* 120:150–160. <https://doi.org/10.1016/j.conbuildmat.2016.05.061>
10. Tchakouté HK, Rüscher CH, Kong S, Kamseu E, Leonelli C (2016) Geopolymer binders from metakaolin using sodium waterglass from waste glass and rice husk ash as alternative activators:

- a comparative study. *Constr Build Mater* 114:276–289. <https://doi.org/10.1016/j.conbuildmat.2016.03.184>
11. Li X, Rao F, Song S, Ma Q (2019) Deterioration in the microstructure of metakaolin-based geopolymers in marine environment. *J Mater Res Technol* 8:2747–2752. <https://doi.org/10.1016/j.jmrt.2019.03.010>
 12. Samarakoon MH, Ranjith PG, Rathnaweera TD, Perera MSA (2019) Recent advances in alkaline cement binders: a review. *J Clean Prod* 227:70–87. <https://doi.org/10.1016/j.jclepro.2019.04.103>
 13. Rashad AM, Hassan AA, Zeedan SR (2016) An investigation on alkali-activated Egyptian metakaolin pastes blended with quartz powder subjected to elevated temperatures. *Appl Clay Sci* 132–133:366–376. <https://doi.org/10.1016/j.clay.2016.07.002>
 14. Wan Q, Rao F, Song S, Cholico-González DF, Ortiz NL (2017) Combination formation in the reinforcement of metakaolin geopolymers with quartz sand. *Cem Concr Compos* 80:115–122. <https://doi.org/10.1016/j.cemconcomp.2017.03.005>
 15. Autef A, Joussein E, Gasgnier G, Rossignol S (2013) Role of the silica source on the geopolymerization rate: a thermal analysis study. *J Non Cryst Solids* 366:13–21. <https://doi.org/10.1016/j.jnoncrysol.2013.01.034>
 16. Associação Brasileira de Normas Técnicas, NBR 13279 (2005) Argamassa para assentamento e revestimento de paredes e tetos: Determinação da resistência à tração na flexão e à compressão, pp 1–9
 17. Associação Brasileira de Normas Técnicas, NBR 9778 (2009) Argamassa e concreto endurecidos: Determinação da absorção de água, índice de vazios e massa específica, pp 1–4
 18. Kaze RC, Beleuk à Mougam LM, Cannio M, Rosa R, Kamseu E, Melo UC, Leonelli C (2018) Microstructure and engineering properties of Fe₂O₃(FeO)-Al₂O₃-SiO₂ based geopolymer composites. *J Clean Prod* 199:849–859. <https://doi.org/10.1016/j.jclepro.2018.07.171>
 19. Farhan KZ, Johari MAM, Demirbog R (2020) Assessment of important parameters involved in the synthesis of geopolymer composites a review. *Constr Build Mater* 264:120276. <https://doi.org/10.1016/j.conbuildmat.2020.120276>
 20. Provis JL (2014) Introduction and scope. In: Provis JL, van Deventer JSJ (Eds) Alkali activated materials. RILEM state-of-the-art reports, vol 13. Springer, Dordrecht. https://doi.org/10.1007/978-94-007-7672-2_1
 21. Kuenzel C, Li L, Vandeperre L, Boccaccini AR, Cheeseman CR (2014) Influence of sand on the mechanical properties of metakaolin geopolymers. *Constr Build Mater* 66:442–446. <https://doi.org/10.1016/j.conbuildmat.2014.05.058>
 22. Gołaszewska M, Gołaszewski J, Cygan G, Bochen J (2020) Assessment of the impact of inaccuracy and variability of material and selected technological factors on physical and mechanical properties of fresh masonry mortars and plasters. *Mater* 13(6):1382:1–29. <https://doi.org/10.3390/ma13061382>
 23. Buchwald A, Vicent M, Kriegel R, Kaps C, Monzó M, Barba A (2009) Geopolymeric binders with different fine fillers—phase transformations at high temperatures. *Appl Clay Sci* 46:190–195. <https://doi.org/10.1016/j.clay.2009.08.002>
 24. Palomo A, Krivenko P, Garcia-Lodeiro I, Kavalerova E, Maltseva O, Fernández-Jiménez A (2014) A review on alkaline activation: new analytical perspectives. *Mater Constr* 64:1–24. <https://doi.org/10.3989/mc.2014.00314>
 25. Provis JL, Fernández-Jiménez A, Kamseu E, Leonelli C, Palomo A (2014) Binder chemistry low-calcium alkali-activated materials. In: Provis JL, van Deventer JSJ (Eds) Alkali activated materials. RILEM state-of-the-art reports, vol 13. Springer, Dordrecht. https://doi.org/10.1007/978-94-007-7672-2_4

Mechanical and Microstructural Evaluation of Eco-Friendly Geopolymer Produced from Chamotte and Waste Glass



Beatryz Mendes, Leonardo Pedroti, José Maria Carvalho, Carlos Maurício Vieira, Igor Klaus Andrade, and Pedro Henrique Drumond

Abstract Geopolymers have been widely studied due to their potential to replace Portland cement. These materials are considered less aggressive to the environment because of the lower emission of carbon dioxide. In order to make the product more sustainable and solve the problem of incorrect disposal of solid wastes, the purpose of this work was the evaluation of alkali-activated pastes produced from chamotte and waste glass. Four types of sodium hydroxide (NaOH) solutions with molar concentration of 8 mol/L were prepared, with the addition of 0, 5, 10, and 15 g of waste glass per 100 ml of NaOH solution. Flexural and compressive strength tests were performed, as well as the microstructural analysis. The results showed that the waste glass improved the mechanical strength of the geopolymer. It can be applied as an alternative activator, acting as an extra source of soluble silica.

Keywords Geopolymer · Industrial wastes · Sustainability · Chamotte · Waste glass

Introduction

Alkali-activated binders have been widely studied around the world, especially in the last few decades [1–3]. These materials were developed as an alternative for replacement of Portland cement, applied in concretes, mortars, and pastes. The alkali-activated binders are considered less aggressive from the environmental point of view, due to the lower emission of CO₂ than the Portland cement industry [4, 5]. Furthermore, they demonstrate suitable mechanical characteristics and durability,

B. Mendes (✉) · L. Pedroti · J. Maria Carvalho · I. Klaus Andrade · P. Henrique Drumond
DEC–Civil Engineering Department, UFV-Federal University of Viçosa, Av. Peter Rolfs, s/n,
Campus Universitário, Viçosa 36570-000, Brazil
e-mail: beatryz.mendes@ufv.br

C. Maurício Vieira
LAMAV–Advanced Materials Laboratory, UENF-State University of the Northern Rio de Janeiro,
Av. Alberto Lamego, Campos dos Goytacazes 2000, 28013-602, Brazil

such as high resistance to heat. That fact has motivated several researchers to develop technological studies about this new class of material [6, 7].

According to Samarakoon et al. [8], there is a subgroup within the alkali-activated binder class, the geopolymer group. They consist of tridimensional aluminosilicates synthesized by an alkaline solution with high concentration (hydroxides or silicates). The precursors are materials rich in Si and Al, with low or zero content of calcium. Calcined clays (i.e. metakaolin), fly ashes, and mining tailings with high percentages of SiO_2 and Al_2O_3 can be used as raw materials [9]. The geopolymerization products are tridimensional silicoaluminates structures (N-A-S-H gel type, being N the alkaline cation). From the chemical point of view, geopolymers are also designated as poly(sialates), being sialate the abbreviation of silicon-oxo-aluminates. The crystalline poly(sialates) have structures similar to the zeolites, which are minerals formed by the alteration of pozzolanic rocks [10, 11].

Industrial by-products have been applied as precursors or activators in the production of geopolymers, in order to make the material more sustainable and to solve the problem of incorrect disposal of solid wastes. Some examples are the mining tailings, rice husk ashes, chamotte, waste glass, biomass ashes, construction, and demolition wastes, among others [12–18]. One requirement is that the waste may have reactive phases of SiO_2 e Al_2O_3 oxides, allowing the development of geopolymerization reactions [19].

Chamotte consists of broken ceramic pieces that are discarded after the firing process. Therefore, this waste presents similar behavior and characteristics to metakaolin, a conventional precursor. As it is generated after burning normally at around 800 °C [20], chamotte does not need any thermal treatment for its amorphization, already presenting itself in this condition. The only requirement for the application of the material in geopolymer is the reduction of particle size to values close to that of metakaolin. In turn, the waste glass is rich in SiO_2 and Na_2O and it already has fine particles that make the dissolution easier [21]. Thus, this waste shows promising physical and chemical characteristics for its use in the activating solution, replacing the sodium silicate that is normally applied.

Given the above, the objective of this research is to evaluate the mechanical behavior and microstructural of geopolymeric pastes, produced from industrial wastes (chamotte and waste glass) in both phases (precursor and alkaline solution). The effect of the addition of waste glass in NaOH-based alkaline solutions with molar concentration equal to 8.0 mol/L and the feasibility of using the waste to replace commercial sodium silicate were studied.

Materials and Methods

The materials used in this research were chamotte, waste glass (WG), sodium hydroxide, and distilled water. Chamotte was supplied by a company located at Ouro Branco, Brazil. The waste glass was obtained from glass cutting process and

Table 1 Characteristics of the alkaline solutions

Mixture	WG content (g/100 mL)	Molar concentration (mol/L)	SiO ₂ /Na ₂ O molar ratio
8 M-0	0	8.0	–
8 M-5	5	8.0	0.124
8 M-10	10	8.0	0.248
8 M-15	15	8.0	0.370

collected at NewTemper company, Brazil. The alkaline solutions were produced with the addition of NaOH pellets (CRQ P.A., 99% purity).

The raw materials (chamotte and waste glass) were characterized by particle size distribution, chemical, and mineralogical composition. The particle size was determined by means of Bettersize 2000 laser particle size analyzer, in a range of 0.02–2,000 μm . The chemical analysis was obtained by X-ray fluorescence technique, using a Shimadzu Micro-EDX-1300 spectrometer. The mineral phases of chamotte and waste glass were assessed by X-ray diffraction (XRD), through the D8 Discover (Bruker) diffractometer. The XRD was conducted with CuK α radiation (1.5418 \AA), 2θ varying from 3° to 70° , 0.05° 2θ step-scan, and 1.0 s/step.

Four types of alkaline solutions were prepared using NaOH 8 M solution and waste glass (Table 1). The production of the alternative sodium silicate solutions followed the methodology described by Torres-Carrasco and Puertas [22]. The waste glass was added to the NaOH solution and the mixture was magnetically stirred at 80°C for 3 h. Then, the mixture was filtered using a vacuum filtration apparatus. The liquid part was used as the final alkaline solution. The solutions were stored for at least 24 h before the production of geopolymeric pastes.

The geopolymeric pastes were produced by mixing the chamotte and the alkaline solution in a proportion of 1.0:0.4 (binder:solution). The materials were mixed using a mechanical process with the following steps: (1) 1 minute of manual mixing; (2) 1 minute at low velocity; (3) 1-minute interval; and (4) 2 minutes at high velocity. Prismatic specimens were molded with dimensions of $2\text{ cm} \times 2\text{ cm} \times 8\text{ cm}$. They were taken to the vibration table for 1 minute and covered with a plastic film. The specimens were kept at room temperature for 24 h. Subsequently, they were allocated in plastic bags and immersed in a thermal chamber at $60 \pm 1^\circ\text{C}$ for 24 h. After this period, they were kept at room temperature until the performance of mechanical tests.

Flexural and compressive strength tests were performed at the ages of 7 and 28 days, using an universal testing machine. Three samples of each mixture (by age) were tested for flexural strength, resulting in six results of compressive strength for each mixture. After performing the mechanical tests, the geopolymers were subjected to microstructural analysis, which were conducted in 28-day samples. The geopolymerization reactions were stopped using the methodology described by Reig et al.

[23]. XRD techniques and Fourier Transform Infrared (FTIR) spectroscopy (Spectrum 100 CAF 2/DTGS model) were applied. The infrared spectrum range was 400–4000 cm^{-1} with a resolution of 4 cm^{-1} and 64 scans by spectrum.

Results and Discussion

Characterization of Raw Materials

The particle size distribution of chamotte and waste glass is shown in Fig. 1. Chamotte is composed mostly by fine sand and silt, with about 10% of particles less than 2 μm . Waste glass presents finer particles than chamotte and it has higher percentage of clay (about 25%). The finer the material, the greater its reactivity and potential for geopolymerization.

Table 2 shows the chemical composition of chamotte and waste glass. One can notice that chamotte is basically composed of SiO_2 (49.74%) and Al_2O_3 (30.55), with minor content of Fe_2O_3 (5.29%). Waste glass has high percentage of SiO_2 (60.21%)

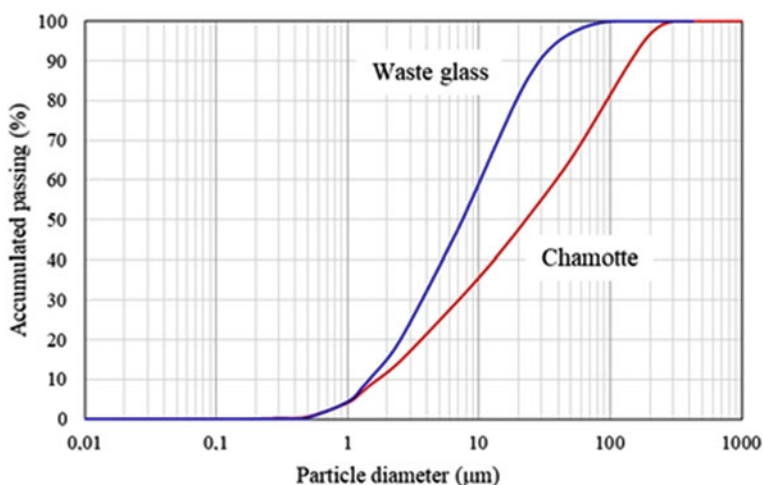


Fig. 1 Particle size distribution of chamotte and waste glass

Table 2 Chemical composition of chamotte and waste glass

Raw material	Chemical composition (%)									L.O.I. (%)
	SiO_2	Al_2O_3	Fe_2O_3	CaO	K_2O	MgO	Ti_2O	Na_2O	Other	
Chamotte	49.74	30.55	5.29	0.54	1.27	1.61	1.08	1.54	6.07	2.31
Waste glass	60.21	2.93	0.29	7.40	0.23	1.65	0.01	2.61	4.94	19.73

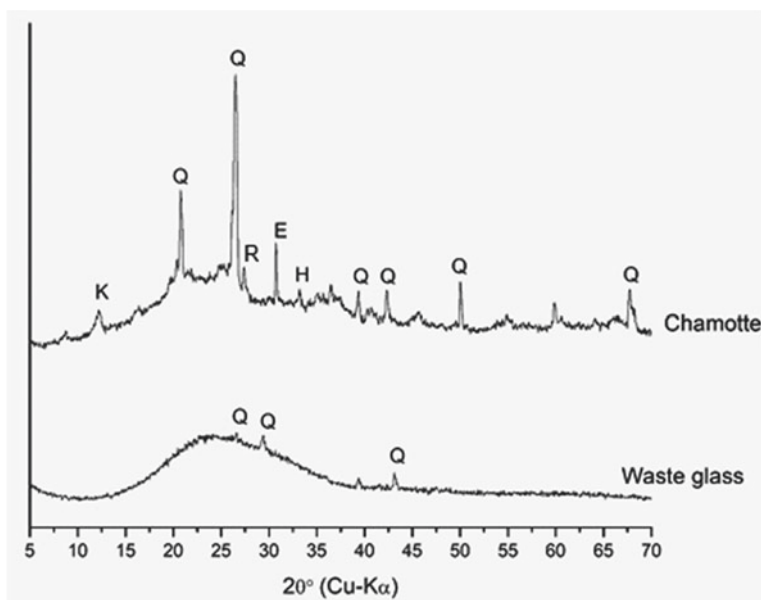


Fig. 2 XRD patterns of chamotte and waste glass (K—kaolinite; Q—quartz; E—epidote; R—rutile; H—hematite)

and small amounts of CaO (7.40%) and Na₂O (2.61%). The high content of silica is a key factor to choose an alternative activator [15].

Figure 2 shows the XRD patterns of chamotte and waste glass. Chamotte presents the following crystalline phases: kaolinite, quartz, epidote, rutile, and hematite. A diffused halo between 15° and 30° indicates the presence of amorphous phase. It is important, since the amorphous content is the reactive phase of the precursor. The waste glass is basically amorphous, with small peaks of quartz. It indicates that the waste glass has a great potential of dissolution and reaction.

Characterization of Geopolymeric Pastes

Figures 3 and 4 show the flexural and compressive strength of the four mixtures, respectively. One can notice that the increase of mechanical strength from 7 to 28 days was not significant. It probably occurred due to the higher availability of reactive silica at the beginning of the geopolymerization process and the influence of initial thermal curing (60 °C for 24 h) at early ages [17]. The rate of geopolymerization decreases over time, resulting in no significant changes in the geopolymer matrix and, consequently, its strength.

The addition of 5 g WG promoted few changes in both flexural and compressive strengths. Analyzing the averages at 28 days by the Tukey test ($\alpha = 0.05$), the flexural

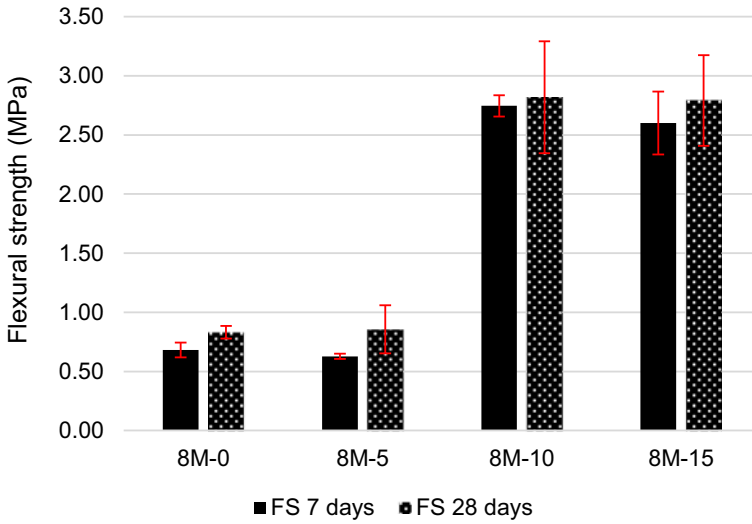


Fig. 3 Flexural strength of pastes at 7 and 28 days

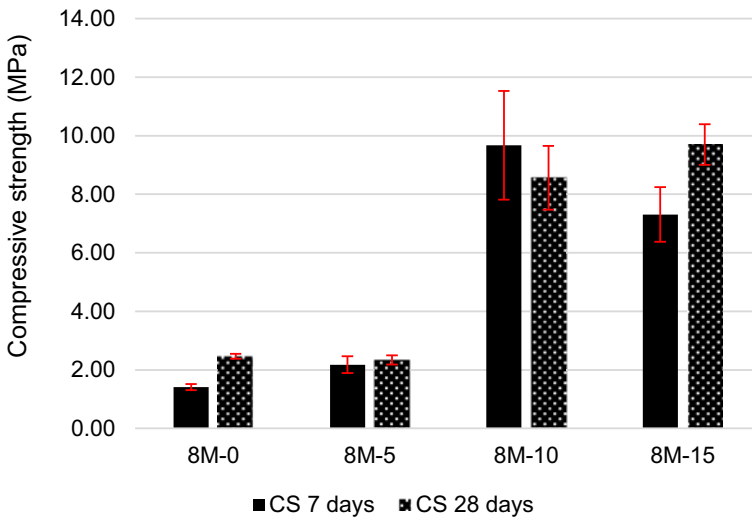


Fig. 4 Compressive strength of pastes at 7 and 28 days

strength results of 8 M-0 (0.83 MPa) and 8 M-5 (0.83 MPa) can be considered statistically equal. The same trend was observed in compressive strength results (2.47 MPa and 2.24 MPa, respectively).

There was an improvement of mechanical behavior for WG additions above 5 g. The mechanical results of 8 M-10 and 8 M-15 mixtures can be considered statistically

equal, although the absolute values of compressive strength of 8 M-15 mixture were higher than those of the 8 M-10. There was an increase of flexural strength of 240% comparing the results of 8 M-0 and 8 M-10 at 28 days. For the compressive strength that increase was 246%. Consequently, the higher the addition of WG, the higher the mechanical strength. This confirms the presence of reactive silica in WG and the importance of providing additional soluble silica to the alkaline system. Zhang et al. [24] mention that using activators with dissolved silicates is preferable over using only hydroxide, due to the fact that the products tend to develop higher strength and denser microstructure. In addition, the incorporation of waste glass in the solution changes its SiO₂/Na₂O molar ratio, which affects the mechanical strength of the geopolymer.

Figure 5 shows the diffractograms of the pastes. The XRD patterns of 8 M-0 and 8 M-5 do not show significant presence of crystalline geopolymeric products, only peaks of remaining compounds of the precursor and sodium carbonate hydrate. The addition of WG (above 5 g) promoted the formation of two kinds of zeolite—zeolite Y or faujasite and zeolite Na-X. Both structures are composed of silicon-oxygen and aluminum-oxygen tetrahedrons. The difference is the number of member rings that interconnect them and the combination of these units. The formation of faujasite crystal can be explained by the presence of Ca atoms in the composition of WG (CaO = 7.4%). The peaks of zeolites were observed only in geopolymers 8 M-10

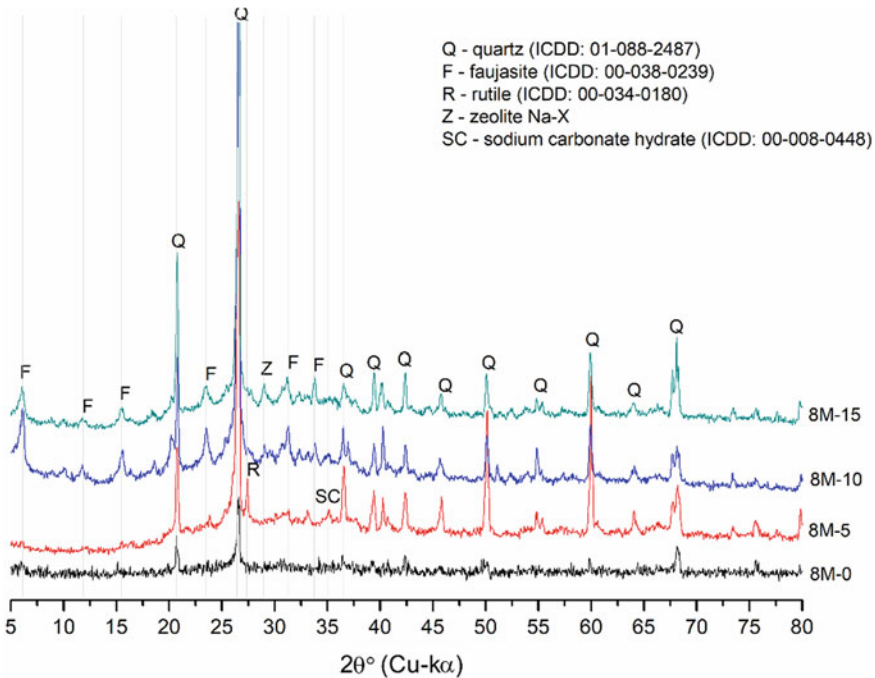


Fig. 5 XRD patterns of 8 M-0, 8 M-5, 8 M-10, and 8 M-15 pastes

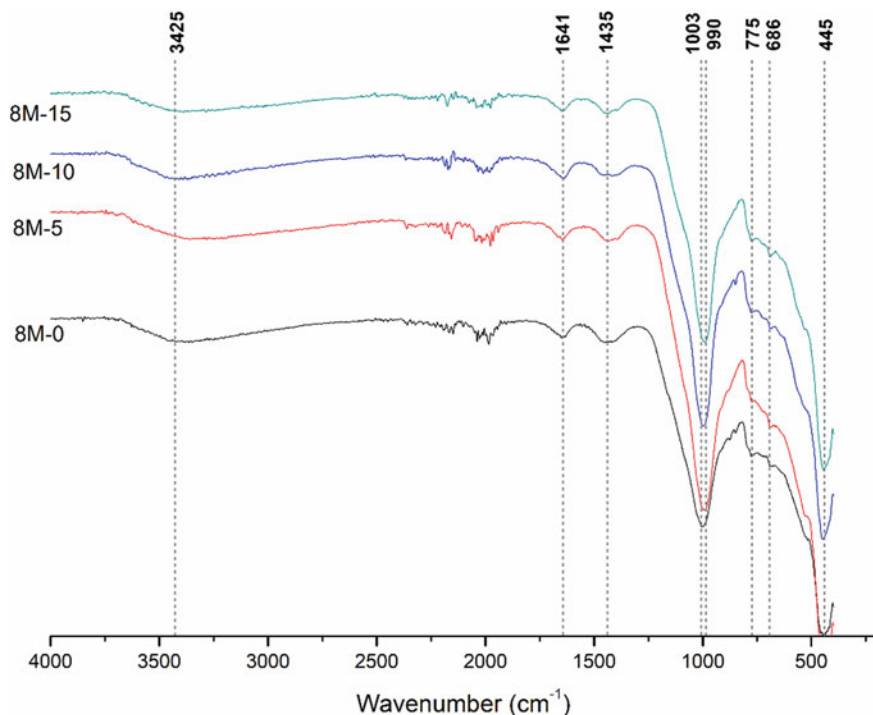


Fig. 6 FTIR spectrum of the pastes

and 8 M-15, indicating that these matrices have higher quality. The XRD patterns of 8 M-10 and 8 M-15 do not have significant differences, which is in agreement with the mechanical strength results.

The FTIR spectra of the pastes are shown in Fig. 6. The major band, related to the asymmetrical stretching of Si–O–T, being T Si or Al tetrahedral, occurred at 1003 cm^{-1} to 8 M-0 and 990 cm^{-1} to 8 M-15. The shift proves that the addition of waste glass increases the formation of geopolymeric products. At this band, higher wavenumbers are related to the lower inclusion of Al into the geopolymer structure [17]. It indicates the presence of greater amount of unreacted particles in the mixtures with less content of WG. The bands around 775 cm^{-1} are related to Si–O–Si symmetric stretching vibrations and O–Al–O bending vibrations. The band at 686 cm^{-1} is associated with the presence of zeolitic structures [25], which were also found in the diffractograms of geopolymers. The bands at 1435 cm^{-1} are associated to the inclusion of CO_3^{2-} . One can notice that the incorporation of waste glass tends to decrease the intensity of these bands, indicating that it can limit the carbonation of the pastes. The bands positioned at 1641 cm^{-1} and 3425 cm^{-1} are related to the vibration mode of O–H and H–OH, respectively.

Conclusions

This study aimed to evaluate the mechanical behavior and microstructure of geopolymeric pastes produced from chamotte and waste glass-based alkaline solutions. According to the experimental program and the statistical tools applied, one can conclude the following:

- Both chamotte and waste glass presented suitable characteristics for their application in the production of geopolymeric materials, such as the presence of amorphous phase and, in the case of chamotte, appropriate contents of SiO_2 and Al_2O_3 .
- The addition of waste glass (above 5 g/100 mL) in the NaOH-based alkaline solution promoted the improvement of mechanical strength of the pastes, due to the higher availability of soluble silica in the system. The addition of 10 g or 15 g did not promote significant differences on the results of flexural and compressive strength.
- The microstructural analyses showed that the waste glass led to the formation of zeolitic species in the pastes and reduced the carbonation reactions between Na and CO_2 . Also, a larger content of precursor was included in the geopolymerization reactions, since no peaks of remaining compounds were found in the XRD patterns of 8 M-10 and 8 M-15 pastes.
- Considering the mechanical results, chamotte and waste glass have potential to be applied in geopolymer products that do not request higher values of compressive strength, such as coating mortars. Thus, this work proves the possibility of producing geopolymers with industrial wastes in both parts (liquid and solid), which contributes to achieve higher level of sustainable.

Acknowledgements This study was financed in part by the Coordenação de Aperfeiçoamento Pessoal de Nível Superior—Brasil (CAPES)—Finance Code 001. The authors also thank the FAPEMIG agency for the financial support provided and the Sustainable and Innovative Construction Research Group (SICon) for the technical assistance.

References

1. Liu Y, Shi C, Zhang Z, Li N (2019) An overview on the reuse of waste glasses in alkali-activated materials. *Resour Conserv Recycl* 144:297–309. <https://doi.org/10.1016/j.resconrec.2019.02.007>
2. Provis JL (2014) Geopolymers and other alkali activated materials: Why, how, and what? *Mater Struct Constr* 47:11–25. <https://doi.org/10.1617/s11527-013-0211-5>
3. Shi C, Jiménez AF, Palomo A (2011) New cements for the 21st century: the pursuit of an alternative to Portland cement. *Cem Concr Res* 41:750–763. <https://doi.org/10.1016/j.cemconres.2011.03.016>
4. Kua T-A, Imteaz MA, Arulrajah A, Horpibulsuk S (2019) Environmental and economic viability of Alkali Activated Material (AAM) comprising slag, fly ash and spent coffee ground. *Int J Sustain Eng* 12:223–232. <https://doi.org/10.1080/19397038.2018.1492043>

5. Zhuang XY, Chen L, Komarneni S, Zhou CH, Tong DS, Yang HM et al (2016) Fly ash-based geopolymer: clean production, properties and applications. *J Clean Prod* 125:253–267. <https://doi.org/10.1016/j.jclepro.2016.03.019>
6. Gavali HR, Bras A, Faria P, Ralegaonkar RV (2019) Development of sustainable alkali-activated bricks using industrial wastes. *Constr Build Mater* 215:180–191. <https://doi.org/10.1016/j.conbuildmat.2019.04.152>
7. Heah CY, Kamarudin H, Mustafa Al Bakri AM, Bnhussain M, Luqman M, Khairul Nizar I et al (2012) Study on solids-to-liquid and alkaline activator ratios on kaolin-based geopolymers. *Constr Build Mater* 35:912–22. <https://doi.org/10.1016/j.conbuildmat.2012.04.102>
8. Samarakoon MH, Ranjith PG, Rathnaweera TD, Perera MSA (2019) Recent advances in alkaline cement binders: a review. *J Clean Prod* 227:70–87. <https://doi.org/10.1016/j.jclepro.2019.04.103>
9. Palomo A, Grutzeck MW, Blanco MT (1999) Alkali-activated fly ashes: a cement for the future. *Cem Concr Res* 29:1323–1329. [https://doi.org/10.1016/S0008-8846\(98\)00243-9](https://doi.org/10.1016/S0008-8846(98)00243-9)
10. Davidovits J (1987) Geopolymeric reactions in archaeological cements and in modern blended cements. *Concr Int* 9:23–29
11. Davidovits J (1991) Geopolymers-Inorganic polymeric new materials. *J Therm Anal* 37:1633–1656. <https://doi.org/10.1007/BF01912193>
12. Alonso MM, Gascó C, Morales MM, Suárez-Navarro JA, Zamorano M, Puertas F (2019) Olive biomass ash as an alternative activator in geopolymer formation: A study of strength, durability, radiology and leaching behaviour. *Cem Concr Compos* 104:103384. <https://doi.org/10.1016/j.cemconcomp.2019.103384>
13. Arulrajah A, Kua TA, Horpibulsuk S, Phetchuay C, Suksiripattanapong C, Du YJ (2016) Strength and microstructure evaluation of recycled glass-fly ash geopolymer as low-carbon masonry units. *Constr Build Mater* 114:400–406. <https://doi.org/10.1016/j.conbuildmat.2016.03.123>
14. Cristelo N, Fernández-Jiménez A, Vieira C, Miranda T, Palomo Á (2018) Stabilisation of construction and demolition waste with a high fines content using alkali activated fly ash. *Constr Build Mater* 170:26–39. <https://doi.org/10.1016/j.conbuildmat.2018.03.057>
15. Mejía JM, Mejía de Gutiérrez R, Puertas F (2013) Ceniza de cascarilla de arroz como fuente de sílice en sistemas cementicios de ceniza volante y escoria activados alcalinamente. *Mater Constr* 63:361–75. <https://doi.org/10.3989/mc.2013.04712>
16. Sassoni E, Pahlavan P, Franzoni E, Bignozzi MC (2016) Valorization of brick waste by alkali-activation: a study on the possible use for masonry repointing. *Ceram Int* 42:14685–14694. <https://doi.org/10.1016/j.ceramint.2016.06.093>
17. Villquirán-Caicedo MA (2019) Studying different silica sources for preparation of alternative waterglass used in preparation of binary geopolymer binders from metakaolin/boiler slag. *Constr Build Mater* 227:1–13. <https://doi.org/10.1016/j.conbuildmat.2019.08.002>
18. Ye J, Zhang W, Shi D (2017) Properties of an aged geopolymer synthesized from calcined ore-dressing tailing of bauxite and slag. *Cem Concr Res* 100:23–31. <https://doi.org/10.1016/j.cemconres.2017.05.017>
19. Rožek P, Król M, Mozgawa W (2019) Geopolymer-zeolite composites: a review. *J Clean Prod* 230:557–579. <https://doi.org/10.1016/j.jclepro.2019.05.152>
20. Azevedo ARG, Vieira CMF, Ferreira WM, Faria KCP, Pedroti LG, Mendes BC (2020) Potential use of ceramic waste as precursor in the geopolymerization reaction for the production of ceramic roof tiles. *J Build Eng* 29. <https://doi.org/10.1016/j.jobbe.2019.101156>
21. Pourabbas Bilondi M, Toufigh MM, Toufigh V (2018) Using calcium carbide residue as an alkaline activator for glass powder–clay geopolymer. *Constr Build Mater* 183:417–428. <https://doi.org/10.1016/j.conbuildmat.2018.06.190>
22. Torres-Carrasco M, Puertas F (2015) Waste glass in the geopolymer preparation: mechanical and microstructural characterisation. *J Clean Prod* 90:397–408. <https://doi.org/10.1016/j.jclepro.2014.11.074>
23. Reig L, Tashima MM, Borrachero MV, Monzó J, Cheeseman CR, Payá J (2013) Properties and microstructure of alkali-activated red clay brick waste. *Constr Build Mater* 43:98–106. <https://doi.org/10.1016/j.conbuildmat.2013.01.031>

24. Zhang Z, Wang H, Provis JL (2012) Quantitative study of the reactivity of fly ash in geopolymerization by FTIR. *J Sustain Cem Mater* 1:154–166. <https://doi.org/10.1080/21650373.2012.752620>
25. Mikuła A, Król M, Koleżyński A (2016) Experimental and theoretical spectroscopic studies of Ag- Cd- and Pb-sodalite. *J Mol Struct* 1126:110–116. <https://doi.org/10.1016/j.molstruc.2016.03.004>

Recycling Glass Packaging into Ceramic Bricks



G. C. G. Delaqua and C. M. F. Vieira

Abstract Wastes regularly discarded by the society, such as post-consumption packaging glass, are increasingly contributing to the environmental pollution. A possible solution could be its incorporation into a clay body to fabricate common fired ceramics for civil construction. The objective of this work is to evaluate the effect of the incorporation of this waste, at different particle sizes, in technological properties of clayey body. This glass powder was tested for X-ray fluorescence and optical dilatometry. Specimens were uniaxially pressed at 25 MPa and fired up to 1000 °C. The technological properties were evaluated in terms of water absorption, linear shrinkage, and flexural rupture strength. The results indicated that the waste incorporation improved both the ceramic water absorption and the mechanical strength. Finally, this work indicated that clay brick production is a viable and technically advantageous alternative for recycling this type of waste, also bringing benefits to the quality of ceramics.

Keywords Waste · Glass · Red ceramic

Introduction

The increase in the amount of waste generated through concerns related to final disposal [1, 2]. Demanding to the requirements of environmental agencies, alternatives have been sought for the correct disposal of solid waste generated [3], which is because they are not recycled naturally, and their incorrect disposal can cause serious environmental problems.

As glass is a 100% recyclable material, it can be reused infinite times without changing its initial composition, or also applied to other materials. According to the Business Commitment to Recycling—CEMPRE (2021) [4], Brazil produces an average of 1.3 million tons of glass packaging per year, using approximately 50% of recycled raw material in the form of shards. The reuse of packaging in the production

G. C. G. Delaqua (✉) · C. M. F. Vieira

Advanced Materials Laboratory-LAMAV, State University of the North Fluminense-UENF, Av. Alberto Lamego Campos dos Goytacazes, 2000, Rio de Janeiro 28013-602, Brazil

© The Minerals, Metals & Materials Society 2022

M. Zhang et al. (eds.), *Characterization of Minerals, Metals, and Materials 2022*,

The Minerals, Metals & Materials Series,

https://doi.org/10.1007/978-3-030-92373-0_39

process can directly contribute to the preservation of the environment, as in addition to consuming less raw material and energy, it avoids the emission of CO₂.

As it is an inert material, the glass discarded in the environment does not pollute, but it generates a great environmental liability, due to the poor management of this waste, increasing the significant amounts that are deposited in landfills. Thus, it is necessary to find viable technological alternatives that allow the recycling of these glasses in an economic and sustainable way [4, 5], as waste that is no longer used can return to the production cycle as a raw material [6].

Due to the characteristics of clay, the ceramic industry is one of the most outstanding in the recycling of different types of waste, which, due to its high monthly production volume, also allows the consumption of large amounts of waste [7]. In addition, this incorporation will act in such a way as to introduce non-plastic or inert elements to the material to the mass used, where, while one acts in reducing the energy expenditure of the burning stage, by supplying energy (exothermic reactions) [8], the another will contribute to reducing the sintering temperature of ceramic materials.

In the recycling process, the glass, to be used as a raw material for the glass industries, is preferably separated by color, to avoid changes in the visual pattern of the final product, [9], which would not be a problem for the ceramic industry, since most of the products are reddish in color.

By presenting in its chemical composition essential oxides for the ceramic industry, glass has considered levels of fluxing oxides that will help to reduce the initial temperature of liquid phase formation in the sintering process, reducing the firing temperature, thereby reducing expenses with fuel for heating the furnace [8]. To Dondi et al. (2009) [10], the glass residue used in the manufacture of ceramic products contributes to improving the final quality of the product, and Teixeira et al. (2008) [11] state that with the addition of glass the levels of flux oxides increase, which are responsible for the formation of the liquid phase and for the densification of the masses during the burning process, contributing to the improvement of properties.

In addition to the possibility of providing an environmentally correct destination for this type of waste, Bonet (2002) [12] points out that one of the issues of fundamental importance for society is the need to reuse waste as a way of preserving natural resources, saving energy, offering less degradation of the environment, and providing improvements in the living conditions of communities. Thus, this work aims to find a useful and environmentally viable application to multiple-use packaging, evaluating the influence of the incorporation of glass powder in different particle sizes on the physical–mechanical properties of a clayey mass used in the production of red ceramics.

Materials And Methods

Materials

The raw materials used in this work were a clayey mass containing 25% red clay and 75% yellow clay, and multiple-use packaging glass. The red clay comes from Itaboraí-RJ and the yellow one from Campos dos Goytacazes-RJ, both were donated by the company Arte Cerâmica Sardinha located in the municipality of Campos dos Goytacazes. The multiple-use packages were collected at a recycler—RECICAMPOS, in the municipality of Campos dos Goytacazes-RJ.

Methods

Initially, the clay was dried in an oven at 110 °C and processed by sieving in 40 mesh. The packaging glasses were broken with the aid of a crusher, and later placed in a ball mill to obtain the desired granulometry. The grinding time varied according to the particle size used.

Formulations were prepared containing 20% by weight of residue in clayey mass in the 40 and 100 mesh particle sizes. A 0% mass without addition of residue was used as a reference. Once prepared, the compositions were dry homogenized in a mill for 20 min. Then, they were moistened with 8% by weight of water and placed in plastic bags for 24 h to make the humidity uniform. Test specimens with 25 × 115 mm were made by uniaxial pressing at 25 MPa, which were oven dried at 110 °C for 24 h. The specimens were fired in a Muffle laboratory furnace, at a temperature of 800, 900, and 1000 °C, with a heating rate of 2 °C/min and an isotherm of 180 min at the plateau temperature. Cooling was done by natural convection, turning off the oven. After firing, the physical and mechanical properties were determined: water absorption, linear shrinkage, and flexural rupture strength.

The linear shrinkage of the burnt parts (LS) was determined according to the C326-09 [13] standard through Eq. 1:

$$Rlq = \left(\frac{L_s - L_q}{L_s} \right) * 100 \quad (1)$$

where L_s represents the length of the specimen after forming and drying and L_q represents the length of the specimen after firing.

The water absorption test (WA) was performed according to the NBR 15,270–17 standard [14]. In this test, the mass of each burnt specimen was measured, and then they were placed in a container with water, where they were kept boiling for 2 h. Afterwards, they were cooled to room temperature, where the surface water of each piece was removed and the mass of the specimens was recorded. Values were calculated using Eq. 2:

$$AA = \left(\frac{M_u - M_s}{M_s} \right) * 100 \quad (2)$$

The flexural rupture strength test (σ) was performed in accordance with ASTM C674-77 [15]. The load applied by the upper cutlass has a speed of 1 mm/min and the distance between the supporting cutlasses is 90 mm. The voltage was calculated using Eq. 3:

$$\sigma = \frac{3 * F * L}{2 * b * d^2} \quad (3)$$

where σ is the flexural failure stress (MPa); P is the load applied to the specimen at the moment of rupture (N); L is the distance between the support cleavers (mm); b is the width of the specimen (mm); and d is the thickness of the specimen (mm).

Results And Discussion

Table 1 shows the chemical compositions of red clay from Itaboraí and yellow clay from Campos dos Goytacazes and glass. It is observed that the predominant oxides in both clays are silica (SiO_2) and alumina Al_2O_3 , which mostly combine to form aluminum silicate, such as muscovite mica and kaolinite [16]. It is observed that the Fe_2O_3 content is high, which gives a reddish color to the pieces after firing. It is also possible to observe a considerable amount of losses due to fire. The high loss to fire indicates a large amount of clay minerals, as it is mainly associated with the dehydroxylation of kaolinite [1, 17].

In Table 1, the chemical composition of the glass is also presented, where it is possible to observe that the predominant oxide is SiO_2 , which is responsible for forming the vitreous phase, with significant presence of Na_2O and CaO . There is also a moderate amount of Fe_2O_3 . The presence of K_2O , which is a flux agent, contributes to the formation of liquid phases, responsible for closing porosity and improving technological properties.

Table 1 Chemical composition of clays and glass

	Al_2O_3	CaO	Fe_2O_3	K_2O	MgO	MnO	Na_2O	P_2O_5	SiO_2	TiO_2	LoL*
Red clay	24.29	0.12	6.36	1.69	0.97	<0.05	<0.05	0.08	56.85	1.02	8.54
Yellow clay	21.4	0.4	7.37	2.42	1.17	0,12	0.59	0.17	57.6	1.07	7.69
Glass	2.4	8.45	1.25	0.3	2.45	–	14	0.05	72	0.2	2.8

LoI = Loss on Ignition

Technological Properties

Figure 1 shows the linear shrinkage of the fired specimens. Note in the graph a high retraction of the pieces with packaging glass in relation to the standard mass. It is possible to observe that when the particle size of the residue decreased and the temperature increased, these values were higher. This property is of interest for the study of ceramic materials manufactured through sintering. Linear firing shrinkage has a direct correlation with sintering efficiency, since, during this step, the ceramic bodies tend to shrink, causing the particles to consolidate.

The recommendation for firing red ceramic is that the maximum shrinkage does not exceed 2% [18]. Analyzing the same figure, only the formulations with glass incorporation, and fired at a temperature of 1000 °C, would not meet the recommendation. This behavior was expected, given the ability of alkaline earth oxides to form a viscous flow with increased temperature, consequently, greater retraction.

Figure 2 shows the results of water absorption of ceramics containing 20% waste (40 and 100#), fired at the investigated temperatures (800, 900, and 1000 °C). It is possible to observe, comparing with the reference mass, that with the decrease in the particle size of the embedded glass residue and the increase in temperature, there was a decrease in water absorption. The alkaline and earth alkaline oxides present in the residue are important for ceramics, because due to the formation of a liquid phase during sintering, they cause the filling of the existing pores, thus causing a reduction in water absorption.

Figure 3 shows the flexural rupture strength graph of compositions containing 0 and 20% by weight of waste, in the granulometry of 40 and 100 mesh, fired at temperatures of 800, 900, and 1000 °C. Analyzing this graph, it is possible to observe an increasing trend of mechanical resistance attributed to the incorporation of the glass residue into the mass. This is due to the formation of the liquid phase of

Fig. 1 Linear shrinkage of mass as a function of temperature

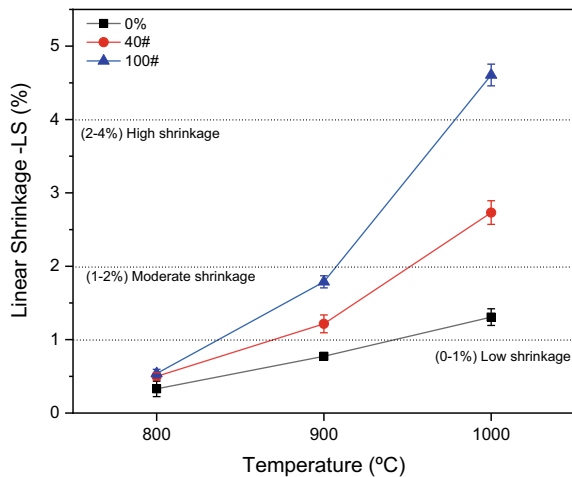


Fig. 2 Water absorption of formulations as a function of firing temperature

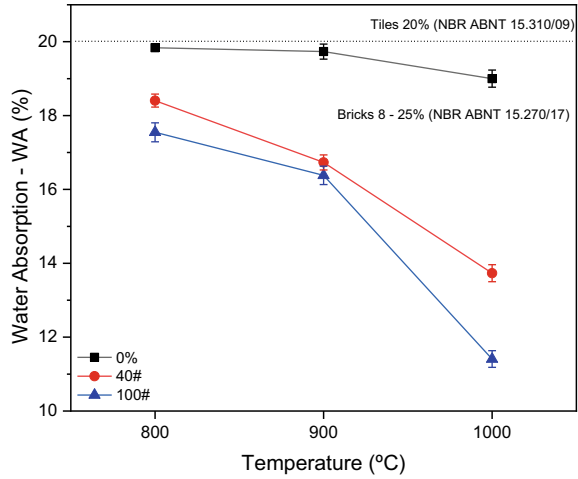
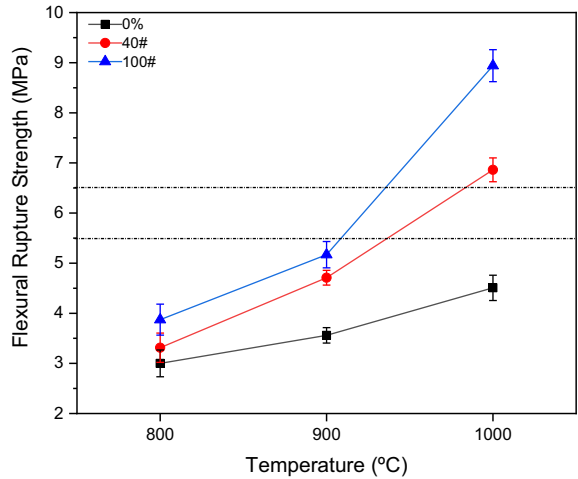


Fig. 3 Flexural rupture strength of the investigated mass and temperatures



the residue, providing improvements in mechanical properties through the closing of the pores. The finer particle size of the residue causes a good dispersion of the material, improving densification [19, 20], which, with the increase in temperature, contributed to a more efficient liquid phase formation. The pieces containing 20% of residue in a granulometry of 100#, fired at a temperature of 1000 °C, reached a resistance of 8.9 MPa.

In accordance with what is recommended by Santo (1989) [21], all the masses investigated in this work are suitable for the production of bricks (2 MPa), but only the masses with incorporation of waste burned at 1000 °C would meet the recommended for the production of blocks (5.5 MPa) and tiles (6.5 MPa).

The beneficial influence of the residue on the property of ceramics is notorious, where better quality pieces, fired at lower temperatures, would be possible.

Conclusions

With the results obtained, it was possible to conclude that glass has great potential to be reused in red ceramics, as it has a large amount of SiO_2 , followed by Na_2O and CaO , which contribute to reducing the sintering temperature of ceramics.

It was observed, at the investigated temperatures (800, 900 and 1000 °C), that the incorporation of the residue provided a decrease in the water absorption values and an increase in the breaking strength of the pieces, when compared to the reference mass (0%) which was burnt at the same temperatures.

Thus, it is concluded that glass has great potential to be reused in red ceramic, as in addition to contributing to the improvement of the properties of the pieces, it is an alternative for saving raw material, thus contributing to environmental preservation, already that the glass released into nature is not recycled naturally.

Acknowledgements The authors thank the Brazilian agencies, CNPq, proc. No. 301634/2018.1 and FAPERJ, proc. No. E-26/202.773/2017, for supporting this investigation, and Recicampos for providing the residue.

References

1. Monteiro SN, Alexandre J, Margem JI, Sanchez R, Vieira CMF (2008) Incorporation of sludge waste from water treatment plant into red ceramic. *Constr Build Mater* 22:1281–1287
2. Tallini Jr VMT, Mymrine V, Ribeiro RAC, Ponte HA (2007) Recycling of industrial waste into ceramic materials. In: 51st Proceedings of the electronic brazilian congress of ceramics. Salvador BA
3. Morais ASC, Caldas TCC, Monteiro SN, Vieira CMF (2013) Characterization of fluorescent lamp glass waste powder. *Mater Sci Forum* 727–728:1579–1584
4. CEMPRE-Business commitment to recycling. Recycling notebooks-the contribution of industry. <http://www.cempre.org.br>. Accessed 15 de julho 2021
5. Zaccaron A, Frizzo RG, Zanoni ET, Montedo ORK et al (2019) Effect of adding glass residue in masonry ceramic mass. *Subject (Rio de Janeiro)* 24(4):e12496. <https://doi.org/10.1590/s1517-707620190004.0821>
6. Lomasso ALM (2015) Benefits and challenges in the implementation of recycling: a case study at the Centro de Referencia em Residues in Minas Gerais (Cmrr). *Pensar Gestão e Administracao Magazine* 3(2):1–20
7. Wender AA, Baldo BB (1998) The potential of using a clayey waste in the manufacture of ceramic coating-part II. *Indus Ceram São Paulo* 3(1–2):34–36
8. Vieira CMF, M SN (2009) Incorporation of solid wastes in red ceramics-an updated review. *Revista Matéria* 14(3):881–905
9. Kanvasfer Glass CEMPRE–business commitment to recycling. http://www.cempre.org.br/ft_vidros.php

10. Dondi M, Guarini G, Raimondo M, Zanelli C (2009) Recycling PC and TV waste glass in clay bricks and roof tiles. *Waste Manage* 29:1945–1951
11. Teixeira SR, Costa FB, Souza AE, Santos GTA (2008) Reuse of glass cullet as aggregate for red ceramic clays. *Ciências Exatas* 2(1):12–16
12. Bonet II (2002) Recovery of foundry sand waste (RAF) incorporation in C.B.U.Q. dissertation submitted to the Federal University of Santa Catarina to obtain a Master's Degree in Engineering
13. ASTM-American Society For Testing And Materials (2018) C326-18-standard test method for drying and firing shrinkages of ceramic whiteware clays
14. ABNT-Associação Brasileira de Normas Técnicas (2017) NBR 15270. Componentes cerâmicos-Blocos e tijolos para alvenaria–parte I: requisitos
15. ASTM-American Society For Testing And Materials C674-77 (1977) Flexural properties of ceramic whiteware materials
16. Gonzalez JA, Carreras AC, Ruiz MC (2007) Phase transformations in clay and kaolins produced by thermal treatment in chlorine and air atmospheres. *Latin Am Appl Res* 37:133–139
17. Vieira CMF, Soares TM, Sánchez R, Monteiro SN (2004) Incorporation of granite waste in red ceramics. *Mater Sci Eng A* 373(1–2):115–121
18. Más E (2002) Quality and technology in red ceramics. Editora Pólo Produções Ltda, São Paulo
19. Godinho KO, Holanda JNF, Silva AGP (2005) Obtaining and evaluating technological properties of ceramic bodies based on clay and recycled glass. *Cerâmica (São Paulo)* 51(320):419–427
20. Marinoni N, Diella V, Confalonieri G, Pavese A, Francesco F (2017) Soda-lime-silica-glass/quartz particle size and firing time: their combined effect on sanitary-ware ceramic reactions and macroscopic properties. *Ceram Int* 43(14):10895–10904. <https://doi.org/10.1016/j.ceramint.2017.05.126>
21. Santos PS (1989) Clay science and technology, 2nd edn. Edgard Blücher, São Paulo, SP, 408, 91p

Study of the Collectorless Flotation Behavior of Galena in the Presence of Ferric Ion



Martín Reyes Pérez, Jimena Detzamin Trejo Martínez, Elia Palacios Beas, Iván A. Reyes Domínguez, Mizraim U. Flores Guerrero, Aislinn Michelle Teja Ruiz, Miguel Pérez Labra, Julio Cesar Juárez Tapia, and Francisco Raúl Barrientos Hernández

Abstract The presence of ferric ion in the pulp from the grinding is due to the galvanic reactions that take place between the sulfides and the grinding steel media, decisively influencing the flotation stage. In this research work, the behavior of different iron concentrations in galena collectorless flotation in acid and alkaline medium is studied. The results found indicate the depression of the mineral (27% w/w of flotation) in the presence of 25 mg/L of ferric ion at pH 10 and a pulp potential (Eh) of + 81 mV, with similar values of Eh and pH, but in the absence of the metal ion, a cumulative flotation of 59% w/w is obtained. While at slightly acidic pH 6.0, Eh of + 280 mV, and in the presence of 75 mg/L of iron, a cumulative flotation efficiency of 65% w/w is obtained.

Keywords Galena · Ferric ion · Pulp potential · Collectorless flotation · pH

Introduction

Galena (PbS) is a mineral of great industrial importance, it is the main source of lead in the world, and it is also considered as a semiconductor material [1]. It is one of the most common and important minerals. It often occurs with other similar minerals

M. R. Pérez (✉) · J. D. T. Martínez · A. M. T. Ruiz · M. P. Labra · J. C. J. Tapia · F. R. B. Hernández

Academic Area of Earth Sciences and Materials, Autonomous University of the State of Hidalgo, Road Pachuca-Tulancingo Kilometer 4.5 Mineral de la Reforma, Hidalgo 42180, México
e-mail: mreyes@uaeh.edu.mx

E. P. Beas
National Polytechnic Institute unit ESIQIE. C.P. 07738 ESIQIE, México

I. A. R. Domínguez
Institute of Metallurgy, Autonomous University of San Luis Potosí, San Luis Potosí 78210, SLP, México

M. U. F. Guerrero
Industrial Electromechanics Area, Technological University of Tulancingo, 43642 Hidalgo, México

such as pyrite or sphalerite [2]. The availability of galena, its well-defined crystal structure, and the absence of metal ions (impurities aside) that can easily change its oxidation state give galena the indisputable distinction of being the most studied mineral in the flotation. Despite this, the form of the adsorption of flotation reagents on the surface of the galena is still debated [3, 4].

In collectorless flotation, only in the presence of frother agent, the mineral particles tend to join the bubbles in the foam, due to the contact angle formed between the surface of the sulfide and the bubble. This phenomenon can be explained by the chemical charges of the mineral surface which are related to the interfacial electrochemical potentials of the system [5, 6].

So collectorless flotation takes advantage of the use of frother agent, favoring wettability and the contact angle between the bubble and the mineral surface, this process is also known as foam flotation [7, 8]. Regarding the natural buoyancy of mineral sulfides, this is due to the formation of elemental sulfur on the surface. The mineral sulfides that naturally possess this property are molybdenite, orpiment and realgar, molybdenum sulfide, and arsenic sulfides, respectively [9].

Galena flotation at laboratory and industrial scale can be carried out in the absence of a collector [10, 11]. Its surface is naturally hydrophobic, even if it is slightly oxidized can carry out the collectorless flotation, its surface state is rich in sulfur and deficient in metal. Importantly, and the nature of the surface state depends on whether the elements of the metal sulfide are oxidized or reduced. Heavily oxidized galena does not show collectorless flotation [10].

Regarding the presence of metal ions in flotation pulp, these affect positively or negatively the flotation process of minerals and the presence of metal ions in the pulp is for any of the following reasons: by intentional addition of an inorganic or organic chemical reagent that activates the mineral surface, or induced by grinding, during which a large amount of ions are released, as a result of the oxidation of iron from the grinding media, as well as the surface oxidation of the metallic elements of sulfide minerals such as iron from pyrite, chalcopyrite, pyrrhotite, and arsenopyrite, among others [12, 13].

Therefore, the nature and concentration of the iron III species adsorbed to the surface of the galena mineral strongly depend on the pH and the concentration of the metal ion in the pulp. The interaction mechanisms are controlled by the surface chemistry of galena, as well as by the speciation of iron III [14]. Therefore, the surface groups of galena (PbS) are controlled by the degree of oxidation, the pH, and have a determining role in flotation.

Therefore, in this research, the behavior of collectorless flotation of galena (PbS) is analyzed, depending on the pH, the oxide reduction potential, and the presence of different concentrations of Fe^{3+} ions in acidic and alkaline environments to establish its depressant or activating effect.

Experimental Methodology

To carry out the study of the behavior of collectorless flotation of galena (PbS) in the presence of different concentrations of ferric ion at acidic and alkaline pH values, a galena mineral was used, which is made up of a single phase from at Zimapán Hidalgo mining region, México. The mineral particles ground to a micrometric size in an agate mortar were characterized by X-ray diffraction (XRD), scanning electron microscopy in conjunction with energy dispersion microanalysis (SEM–EDS), Fourier transform infrared spectroscopy. (FTIR), and particle size analysis (PSA) by laser diffraction.

The flotation tests were carried out in a 1 L capacity laboratory Denver cell made of stainless steel, a diffuser, and impeller operated at 1200 rpm, the entry of air into the cell to form the bubbles was controlled with a valve opening and due to the stirring effect. The pH and the oxide reduction potential (ORP) were measured with a KCl internal solution electrode coupled to a Thermo Scientific Orion 3 Star potentiometer which was calibrated before each float test.

For all tests, deionized water and 99% $\text{Fe}_2(\text{SO}_4)_3$ ferric sulfate salt were used; to adjust the pH, sulfuric acid and 1 M sodium hydroxide were used; and methyl isobutyl carbinol (MIBC) was used as frother agent $\text{C}_6\text{H}_{14}\text{O}$ provided by Alkemin S.A, by S.R.L.

The collectorless flotation tests of galena in the presence of ferric ion were carried out under the following experimental procedure. The conditioning was performed inside the flotation cell using a volume of 1 L, then 60 mg/L of frother agent were added, later 4 g of mineral were added, as well as the ferric sulfate salt in quantities to give concentrations of 5, 25, and 75 mg/L of Fe^{3+} ion, the tests were conducted at pH 6 and 10, keeping the pulp in continuous stirring. At each change in the chemistry, the pulp was given a stabilization time of 3 min and then both the pH and the oxidation reduction potential (ORP) mV were measured.

The measured ORP was expressed in reference to the standard hydrogen electrode (SHE), by adding + 236 mV to the measured value, as cited in the bibliography [11]. Once the conditioning time was over, the flotation test was started by opening the air suction valve to generate the bubbles, obtaining concentrates in times of 0.5, 1, 2, 4, 6, 8, and 10 min. The wet concentrate was received in pre-weighed inert containers, one for each flotation time, and allowed to dry at room temperature. The float weight percentage obtained at each time was calculated with Eq. 1

$$\%w/w F = \frac{W_f - W_0}{4} * 100 \quad (1)$$

where % w/w F is the percentage by weight obtained in the flotation at each time, W_f is the weight of the container containing the floated dry mineral, W_0 is the weight of the empty container, four (4) is the quantity grams of ore used, and 100 to express the value as a percentage. The containers were weighed on a precision analytical balance.

Results

Figure 1 shows the X-ray diffraction spectrum, indexed using Match 1.1 software, the PDF JCPDS-ICDD (Joint Committee on Power Diffraction Standards-International Center for Diffraction Data) diffraction pattern that matches the mineral sample is 96-900–8695 indicating the presence of galena. Figure 2 shows the morphology of the galena mineral particles analyzed by scanning electron microscopy (SEM) with a magnification of 2000X, due to its low hardness of 2.5 to 3 Mohs it has a sub-conchoid type fracture, a wide variety is observed of sizes and tends to fracture into small rectangular prisms. Figure 3 shows the energy dispersion microanalysis, showing the characteristic elements of galena. The surface of the galena particle has a high lead content 87.49% w/w and a lower sulfur concentration 12.51% w/w.

Figure 4 presents the infrared spectrum of the galena particles pulverized in an agate mortar. Multiple absorption bands are observed. The identification of these bands was supported by obtaining FTIR spectra of chemically pure PbO_2 and PbO reagents. The absorption bands at 420, 461, 597, and 617 cm^{-1} correspond to the modes of vibration of the Pb–O bonds of Lead II oxide, PbO_2 . Regarding the Pb–O bonds of lead oxide PbO , these have vibration signals at 694 and 796 cm^{-1} . The presence of these modes of vibration caused by the covalent bonds of Pb–O indicates that as soon as the mineral is pulverized new surfaces are exposed, the lead atoms in

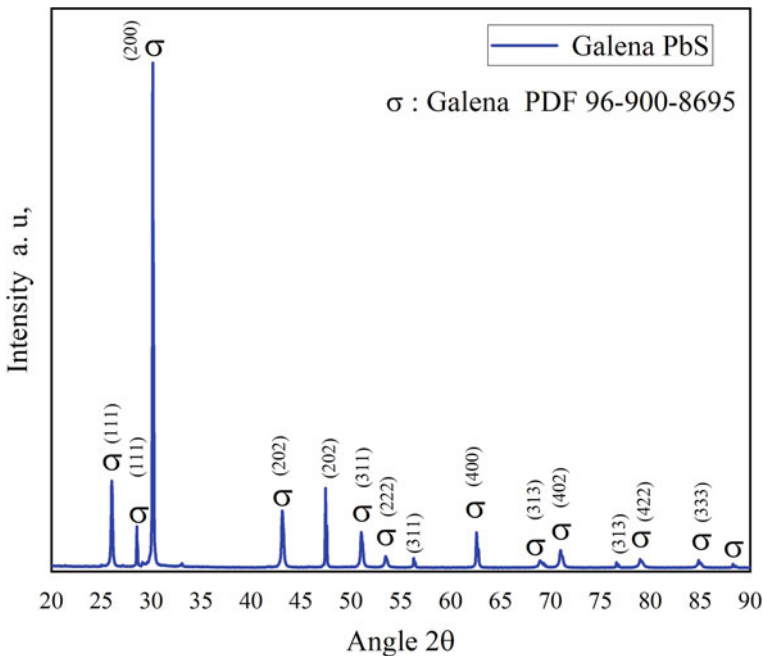


Fig. 1 XRD spectrum of galena PbS particles

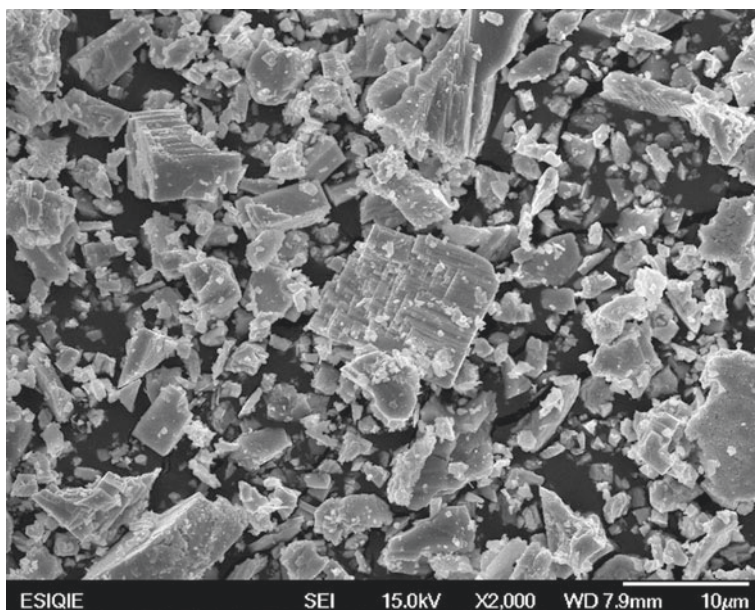


Fig. 2 SEM micrograph of galena PbS 2000X particles

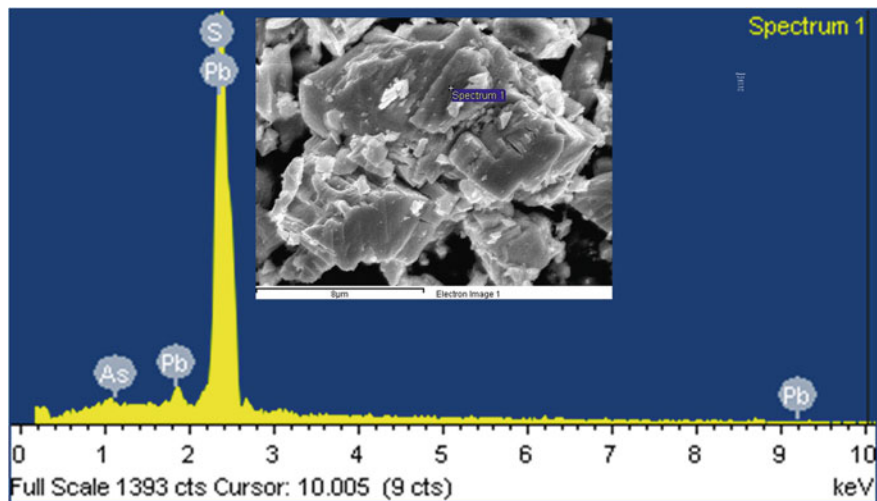
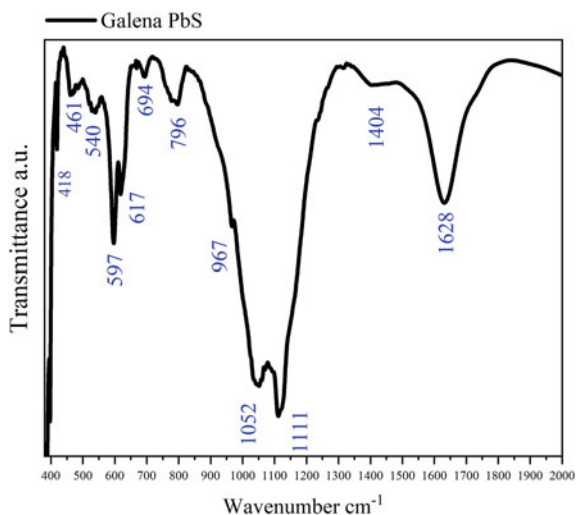


Fig. 3 EDS spectrum and semiquantitative microanalysis of galena

Fig. 4 Infrared spectrum of galena ore pulverized in agate mortar



the last surface layer are exposed to the atmosphere consisting of 21% oxygen O₂, which gives rise to covalent Pb-O bonds of lead oxides.

The presence of bands in 967, 1052, and 1111 cm⁻¹ is the result of the scission of the main band of the sulfate ion located at 1200 cm⁻¹, and these three absorption bands indicate that the surface sulfate is combined with lead in the form of a lead sulfate compound in a monodentate manner, where the main absorption band ν_1 of sulfate creates an active infrared, developing the triple degeneration ν_3 , which results in the division into two or three bands (depending on the structure formed). Regarding the analysis of the particle size (ATP) by laser diffraction of the galena used for the flotation tests, it indicates a mean population of 7.09 microns (μm).

Figure 5 shows the % w/w of cumulative flotation of galena in the presence of iron Fe³⁺ at concentrations 5 and 25 mg/L, at alkaline pH (10), and acidic pH (6.0). It is observed that in the absence of collector and Fe³⁺ metal ions at pH 10, the maximum cumulative flotation of galena was 59% w/w. The presence of only 5 mg/L of Fe³⁺ depresses flotation, having a cumulative flotation percentage of 54% w/w. Increasing the Fe³⁺ concentration to 25 mg/L further depresses the collectorless flotation, with the recovery being only 27% w/w, this test was performed at pH 10. In a similar experiment of collectorless flotation in the presence of 25 mg/L of Fe³⁺ but at pH 6.0, it is observed from Fig. 5 that the cumulative flotation tends to increase with time reaching 47% w/w separation of these results it is established that the negative effect of the presence ferric ion in the flotation can be minimized by lowering the pH to 6.0.

It is also observed that the presence of 75 mg/L of Fe³⁺ at pH 6.0 in the flotation pulp, not only the depression of galena due to the iron species is ruled out, but also the % w/w of cumulative recovery increases, with 65% w/w recovery. The results found in this work agree with those reported in similar investigations [14], where the

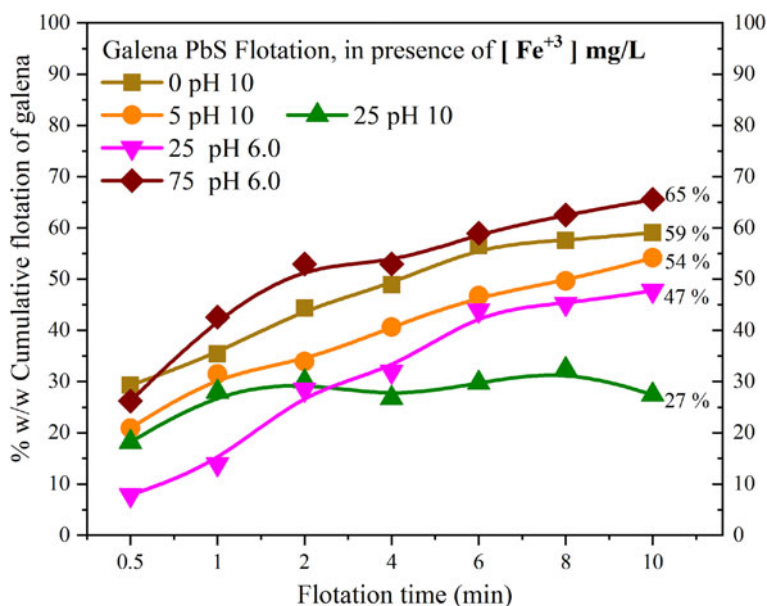


Fig. 5 % Accumulated galena flotation as a function of time (minutes) effect of Fe³⁺ concentration

separation of mineral sulfides (galena) by foam flotation or without collector can be hampered by the presence of hydrophilic surface layers of iron species.

The changes that occur in both the pH and the pulp potential Eh during conditioning help in the compression of the flotation results obtained. Figure 6 shows the behavior of the pulp potential Eh . This influences the adsorption affinity of metal ions and metal ion hydrolysis products on the surface of the galena mineral. Under alkaline pH conditions of 10 and in the presence of 5 mg/L and 25 mg/L of Fe³⁺, the pulp potential at the beginning of the flotation is around +81 mV, the chemical environment is weakly oxidizing, and the % w/w cumulative flotation at 10 minutes drops dramatically, this being 27% w/w.

Therefore, the presence of Fe³⁺ in concentrations of 5 and 25 mg/L at pH 10 not only decreases the oxidizing character of the pulp potential Eh , but also decreases the % w/w of cumulative flotation shown in Fig. 5, with similar potentials +81 mV, but in the absence of ferric ion, a considerably higher galena flotation of about 59% w/w is obtained.

On the other hand, the presence of the ferric ion (25, 75 mg/L) in the flotation pulp and under slightly acidic pH conditions (6.0) generates a strongly oxidizing pulp potential Eh of +300 mV. This means that the depressive effect of the ferric ion in the flotation pulp can be overcome if the pH of the process is slightly acidic. This is due to the dissolution of the phases formed on the surface of the galena.

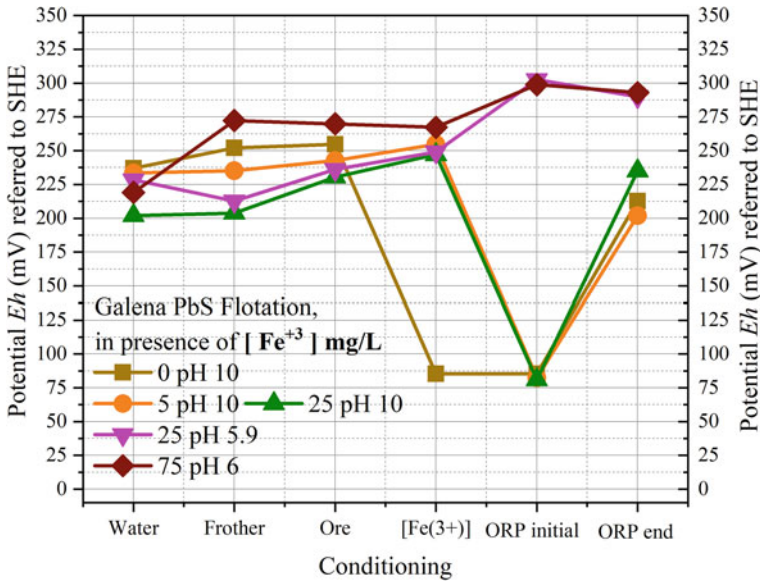


Fig. 6 Behavior of pulp potential, during initial and final flotation conditioning

Conclusions

Collectorless flotation of galena, only using foaming agent, can be carried out and is strongly altered by the presence of Fe^{3+} , only 5 mg/L of iron III alters the surface of the mineral, decreasing the flotation efficiency and 25 mg/L of the ferric ion seriously depress the flotation of galena having a 27% w/w at the 10 min of cumulative flotation, this under conditions of pH 10 and pulp potential Eh of +81 mV. With a slightly acidic flotation pulp at pH 6.0 and with Fe^{3+} contents of 25 mg/L and 75 mg/L, an adverse effect is found when the pulp has an alkaline pH, thus, under these pH conditions, the presence of ferric ion has a cumulative flotation of 47% w/w and 65% w/w, respectively. The adverse effect of the iron ion on the flotation pulp can be minimized if the flotation is carried out at a slightly acidic pH.

Acknowledgements To the Autonomous University of the State of Hidalgo, to the PRODEP Teacher Professional Development Program, and to the National Polytechnic Institute ESIQIE.

References

1. Klein C, Hurlblut JrC (1997) *Manual de Mineralogía (basado en la obra de J. DANA) 4^o Edición*, Editorial Reverté S.A. Barcelona, Bogotá, México
2. Wills BA, Finch JA (2016) Introduction. In: Wills BA, Finch JA (eds) *Wills' Miner. Process. Technol.*, Eighth Edi. Elsevier, Boston, pp 1–27
3. Ralston J (1994) The chemistry of galena flotation: principles & practice. *Miner Eng* 7 (5 y 6):715–735
4. Nowak P, Laajalehto K (2000) Oxidation of galena surface—an XPS study of the formation of sulfoxy species. *Appl Surf Sci* 157:101–111
5. Taggart AF (1930) Chemical reactions in flotation. *IMME* 312:3–33
6. Leya J, Schulman JH (1962) Molecular interaction between frothers and collectors. *Trans IMME* 72:417–423
7. Rao SR (2013) *Surface chemistry of froth flotation: volume 1: fundamentals*. Springer Science & Business Media.
8. Ralston J, Fornasiero D, Grano S (2007) *Pulp and solution chemistry. froth flotation: a century of innovation, USA*
9. Fuerstenau MC, Sabacky BJ (1981) On the natural floatability of sulfides. *Int J Miner Process* 8:79–84
10. Guy PJ, Trahar WJ (1984) The influence of grinding and flotation environments on the laboratory flotation of galena. *Int J Miner Process* 12:15–38
11. Hayes RA, Ralston J (1988) The collectorless flotation and separation of sulphide minerals by Eh control. *Int J Miner Process* 23:55–84
12. Huang G, Grano S (2005) Galvanic interaction of grinding media with pyrite and its effect on flotation. *Miner Eng* 18(12):1152–1163
13. Yongjun P, Stephen G, Daniel F, John R (2003) Control of grinding conditions in the flotation of galena and its separation from pyrite. *Int J Miner Process* 70:67–82
14. Clive AP, William MS, John R (1995) The interaction of iron (III) species with galena surfaces. *Colloids Surf A* 105:325–339

Study of the Determination of Hardbody Impact Resistance of Screened and Non-screened Ornamental Rocks of Different Thicknesses



M. F. Braga, E. D. F. Castilho, A. R. G. Azevedo, A. S. A. Cruz,
M. T. Marvila, and S. N. Monteiro

Abstract Ornamental stones have been increasingly used in civil construction and, therefore, knowing the technological characteristics of these materials is of paramount importance to determine which types of stone are most suitable for each application. This work studies ornamental stones applied as floors, where they are exposed to the possibility of cracking and breaking as a result of falling objects. For this, five different types of rock with different thicknesses were submitted to the screening process, which consists of applying a fiberglass screen on the unfinished face of the rock. Rocks with and without screens were then subjected to the hard body impact strength test. The results confirmed the screen's efficiency in increasing the impact strength of rocks and also showed that the thinner rocks with the screen reached higher strengths than the thicker rocks without the screen.

Keywords Hard body impact resistance · Screening · Ornamental stones

M. F. Braga · E. D. F. Castilho

IFES–Federal Institute of Education, Science and Technology of Espírito Santo; Rodovia Engenheiro Fabiano Vivacqua, 1568, Cachoeiro do Itapemirim, Espírito Santo 29322-000, Brazil
e-mail: matheus@uol.com

E. D. F. Castilho

e-mail: evanizis@ifes.edu.br

E. D. F. Castilho · M. T. Marvila

LAMAV–Advanced Materials Laboratory, UENF-State University of the Northern Rio de Janeiro, Av. Alberto Lamego, 2000, Campos dos Goytacazes, Rio de Janeiro 28013-602, Brazil

A. R. G. Azevedo (✉) · A. S. A. Cruz

LECIV–Civil Engineering Laboratory, UENF-State University of the Northern Rio de Janeiro, Av. Alberto Lamego, 2000, Campos dos Goytacazes, Rio de Janeiro 28013-602, Brazil

S. N. Monteiro

Department of Materials Science, IME-Military Institute of Engineering, Square General Tibúrcio, 80, Rio de Janeiro 22290-270, Brazil

© The Minerals, Metals & Materials Society 2022

M. Zhang et al. (eds.), *Characterization of Minerals, Metals, and Materials 2022*,

The Minerals, Metals & Materials Series,

https://doi.org/10.1007/978-3-030-92373-0_41

Introduction

Humanity's use of rocks dates back to the dawn of civilization. Since then, they have been used in the most diverse applications, as long as they are found in minimum conditions of use. In Brazil, ornamental stones have been used since the colonial period, imported from European countries such as Italy and Portugal [1].

Dimensional rocks are a mineral asset with diverse applications due to their great diversity and versatility. From them, blocks and plates are produced; cut in different ways; and that can undergo different processing processes, such as squaring and polishing. Dimensional stones can be used as decoration, in sculptures, on tables (as part of the structure or as a top), as countertops, as tombstones (and in funerary art in general), and in civil construction.

Exclusively in the civil construction sector, ornamental stones are used as coverings for walls, facades, and floors, both indoors and outdoors. Among the countless types of ornamental rocks, granites are the most used, as they have very varied textures, structures, and colors [2].

Due to its aesthetic importance, what conditions the trade and use of rocks is the beauty of the stone material, which, in turn, is related to the current fashion at each time. However, according to Frascá [2], the aesthetic aspect must be considered concurrently with the knowledge of the physical and mechanical properties of the rock, so that, once submitted to use requests, the chosen rock has a satisfactory performance.

It is clear, therefore, that the correct choice of material for different applications is extremely important, to ensure not only the beauty, but also the functionality of the project. The incorrect use of the material can result in a series of problems, bringing setbacks and the need for financial expenses.

The wide variety of applications to which ornamental stones can be used means that these materials are exposed to various situations of physical and chemical interaction with the environment of which they will be part. One of these situations is the fall of objects of different natures and heights, when rocks are used as floors. Various objects can impact a floor such as keys, cups, tools, and others. In this context, it is important to study the behavior of rocks in this situation and, therefore, it is necessary to adopt a technical criterion to determine which rocks can be used in these applications.

In the search to mitigate the appearance of breaks or cracks during the finishing and transport of rocks, in the 90s, the reinforcement technique called screening began to be used in Brazil. The technique consists of applying an epoxy system and a glass screen on the back of the plate, that is, on the opposite surface to which it will receive the polishing [3]. The screening must be applied to materials with low resistance to bending or when they present many fractures [4].

Based on the above, the present work seeks to compare the impact strength of hard body for five types of rocks (Arabesque, White Dallas, White Siena, Beige Ipanema, and Ubatuba Green) at different thicknesses (1.5 and 2.0 cm) with and without the use of screen, in order to determine the best thickness and the best finish for use of the rocks, based on the resistance obtained.

Materials and Methods

In this work, specimens of Arabesque, White Dallas, White Siena, Beige Ipanema, and Ubatuba Green rocks were subjected to the hard body impact strength test. The chosen rocks were provided by the companies VMA Granitos e Mármore, from Mimoso do Sul, and Du Muro's Granitos e Mármore, from Muqui.

The petrographic characterization of the rocks revealed that the Arabesco rock is classified as a medium to coarse classified tonalite. Portions of the rock have plagioclase porphyroclasts. Occasionally, some regions of the samples showed mineral orientation (biotite). The Bege Ipanema rock, in turn, is classified as a tonalite of massive structure, with fine to medium grain. The Branco Siena stony type is a leucocratic rock with a massive composition and structure and fine grain. The Verde Ubatuba rock is called Charnockito due to the large amount of orthopyroxene in the granite. It is a medium to coarse grained mesocratic rock with a massive structure. The White Dallas rock is a solid tonalitic rock, fine to medium grained. The mineralogical composition of the rocks can be seen in Table 1.

In order to carry out the hard body impact tests, 20 specimens of each type of rock were used, 10 with a thickness of 1.5 cm and 10 with a thickness of 2.0 cm, with 5 sealed samples and 5 unsealed samples for each thickness. The specimens were cut from use-finish plates and have dimensions of 200 × 200 mm.

The specimens were identified with letters and sequential numbers on one of the side faces of the sample, and also with Roman numerals on the other side, as can be seen in Fig. 1. The sides of the specimens were measured by placing the ruler on its sides, and the thickness of the samples was measured with the aid of a caliper [5].

To ensure that the center of the specimen would be accurately marked, the two diagonals of the specimens were demarcated with the help of a ruler.

The same procedures were performed for the screened samples, with the addition of the screening step. To carry out the mesh, the samples were first washed, in order to prevent particles, present in the rock from interfering with the process of adhesion of the mesh to the material. Afterwards, the samples were kept in an oven at 70 °C, for 24 h, for drying. This step is important because the removal of moisture ensures the effectiveness of the mesh adhesion process, by allowing the resin to be well absorbed by the rock [6].

Table 1 Mineralogical composition of rocks

	Quartz	Plagioclase (%)	Biotite	Grenade	Mafic minerals	Orthopyroxene
Arabesque	40	30	20%	10%	–	–
Beige Ipanema	30	45	20%	–	–	–
White Siena	30	50	–	15%	<5%	–
Ubatuba Green	25	40	15%	–	–	20%
White Dallas	20	70	5%	–	–	–

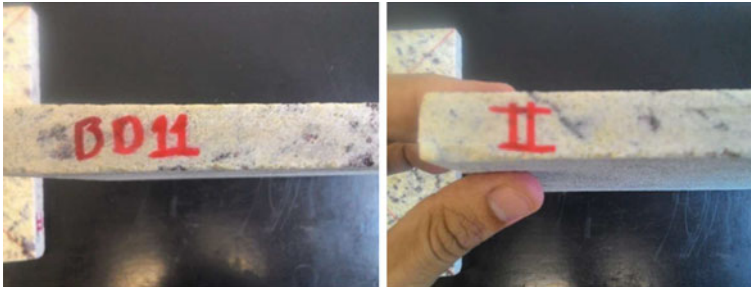


Fig. 1 Identification of the specimens

After the drying period in an oven, to apply the mesh to the rock, an epoxy resin and hardener were used, whose curing time is 24 h, according to information from the manufacturer. The proportion used for the mixture was 100% resin mass to 50% hardener mass, thus, for each specimen, 12.6 g of mixture were used, being 8.4 g of resin and 4.2 g of hardener. The screens are interwoven with 5×5 mm mesh polyester fabric with 1 mm diameter yarn.

The screens were placed on the unfinished face of the rock (backward), and the mixture (resin+hardener) was spread over the screen. After applying the mesh, the samples were dried at room temperature for a period of 24 h (Fig. 2).

The Hard Body Impact Resistance test was carried out in the Dimensional Stones laboratory of CETEM (Mineral Technology Center) in Cachoeiro do Itapemirim, Espírito Santo (Brazil) and followed the ABNT NBR 15,845–8 standard [5]. Five specimens were used for each sample, which were laid and leveled, one by one, on a sand mattress. Subsequently, the steel ball, weighing 1 kg, was raised to a height of 20 cm, and then abandoned it in free fall. From this point onwards, the procedure was repeated at intervals greater than 5 cm in height, until the height at which the specimen ruptured was observed. This height was noted and then an average of the results obtained from the five specimens used was made. The ball launch is vertical and standardized at the standard height and the materials are defined as standards

Fig. 2 Screened samples



for their density. The sand used must be of medium granulometry, for better impact absorption. The ball is expected to touch the rock sample in its central part, showing its impact.

Results and Discussion

Tables 2, 3, 4, 5 and 6 present the results of material tests with and without the use of screens, in different thicknesses.

The materials, Arabesco, Bege Ipanema, White Siena, and Verde Ubatuba without the use of a screen and with a thickness of 1.5 cm, do not meet the requirement of the ABNT 15,844:2010 standard, which sets the value as a reference for the hard body impact test of 0.30 m of breaking height of the specimens. The only material that meets the standard when 1.5 cm thick and without mesh is the White Dallas rock and, even so, it is very close to the established limit [7].

Table 2 Arabesque rock results for the hard body impact test

	Arabesque			
	2.0 cm		1.5 cm	
	With screening	Without screening	With screening	Without screening
Average break height (m)	0.61	0.31	0.48	0.26
Standard deviation	0.022	0.022	0.057	0.022
Average burst energy (J)	5.98	3.04	4.70	2.55
Average deviation	0.03			

Table 3 Arabesque rock results for the hard body impact test

	Beige Ipanema			
	2.0 cm		1.5 cm	
	With screening	Without screening	With screening	Without screening
Average break height (m)	0.65	0.34	0.52	0.26
Standard deviation	0.05	0.022	0.044	0.777
Average burst energy (J)	6.37	3.33	5.10	2.55
Average deviation	0.22			

Table 4 White Dallas rock results for the hard body impact test

	White Dallas			
	2.0 cm		1.5 cm	
	With screening	Without screening	With screening	Without screening
Average break height (m)	0.66	0.41	0.54	0.32
Standard deviation	0.065	0.022	0.022	0.027
Average Burst Energy (J)	6.47	4.02	4.02	3.13
Average deviation	0.03			

Table 5 White Siena rock results for the hard body impact test

	White Siena			
	2.0 cm		1.5 cm	
	With screening	Without screening	With screening	Without screening
Average break height (m)	0.72	0.32	0.64	0.29
Standard deviation	0.027	0.027	0.041	0.022
Average burst energy (J)	7.06	3.13	6.27	2.84
Average deviation	0.02			

Table 6 Ubatuba Green rock results for the hard body impact test

	Ubatuba Green			
	2.0 cm		1.5 cm	
	With screening	Without screening	With screening	Without screening
Average break height (m)	0.67	0.32	0.46	0.26
Standard deviation	0.044	0.027	0.022	0.022
Average burst energy (J)	6.57	3.13	4.51	2.55
Average deviation	0.02			

On the other hand, the use of the screen in samples with 1.5 cm caused a considerable increase in strength and, thus, the rocks that, without the use of the screen, did not achieve satisfactory performance before the standard reached the established minimum requirement.

The improvement in the performance of the rocks in the test was also observed with the increase in the thickness of the samples, that is, for samples with a thickness of 2.0 cm. It is noteworthy, however, that the resistance observed in samples with a thickness of 1.5 cm with the meshing process is higher than that observed in samples with a thickness of 2.0 cm without the use of a mesh [8].

At first, it was expected that materials that have more quartz (which hardness on the Mohs scale is 7 out of 10) would obtain greater resistance compared to others, due to the hardness of this mineral. However, the results showed that the Branco Dallas rock obtained greater strength for tests without the use of mesh, leading to the belief that other factors not only mineralogy influence the resistance to hard body impact.

It is notorious the increase in resistance due to the use of the screen. For a better analysis, the percentage increases in strength were calculated for each material when the mesh was used in both thicknesses, and the results of this analysis can be seen in Figs. 3, 4, 5, 6 and 7 [9].

The analysis of the graphics confirms the hypothesis that, for the same thickness, the use of the screen increases resistance. It is also interesting to note that the percentage quantification of the increase was considerable, in some cases very close to, or even greater than 100%.

The White Siena material stands out, which obtained the highest percentage increase in strength when compared to the values with and without the use of mesh, where the increase relative to the thickness of 2.0 cm without mesh and 1.5 cm with mesh was 50% [10].

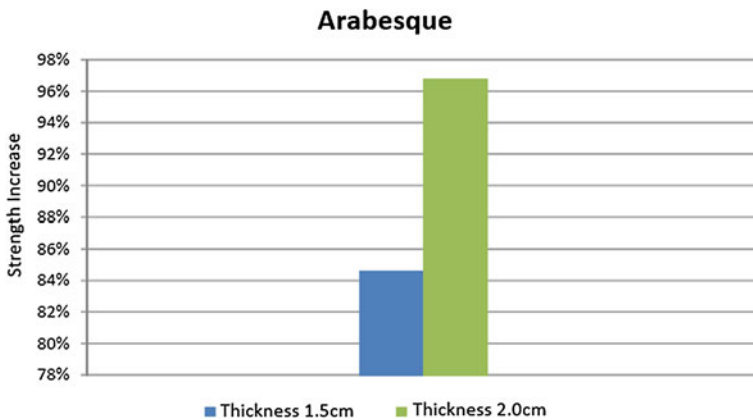


Fig. 3 Percentage increase in Arabesque rock strength

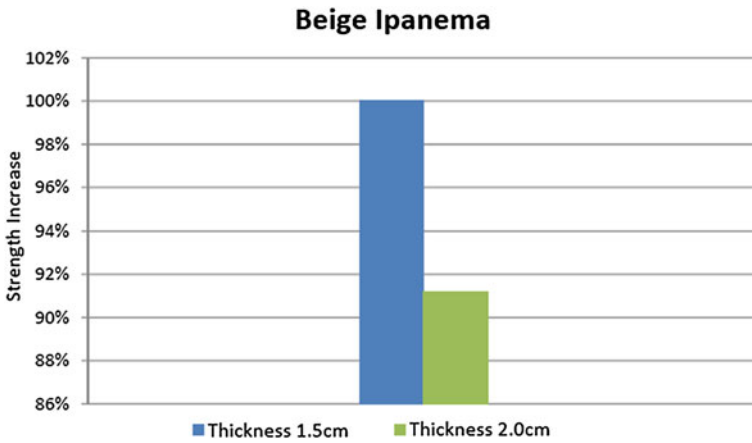


Fig. 4 Percentage increase in Beige Ipanema rock strength

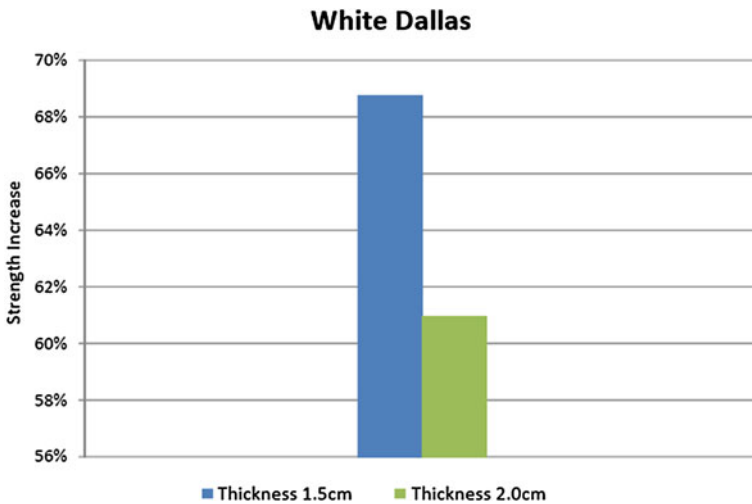


Fig. 5 Percentage increase in White Dallas rock strength

Conclusion

Through this work it was possible to conclude that the use of screens in ornamental stones for floors generates a greater use of the material, since the screen allows the production of more tiles, with less thickness, from the same block, ensuring a considerable increase in terms resistance to falling objects, delivering a technologically better product to the final consumer, as it is more resistant.

It can also be concluded that the materials, Arabesco, Bege Ipanema, Branco Siena, and Verde Ubatuba, with a thickness of 1.5 cm without screen coating would

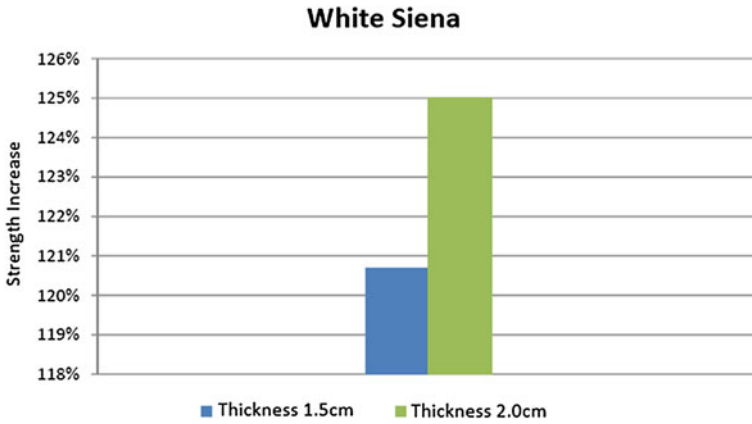


Fig. 6 Percentage increase in White Siena rock strength

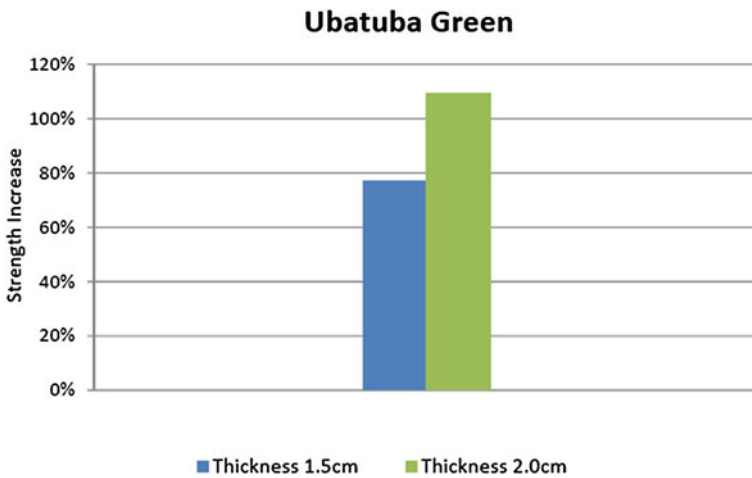


Fig. 7 Percentage increase in Ubatuba Green rock strength

not be indicated for floor coverings. Only after the application of the mesh could these materials be used in this application, due to the increased strength provided by the meshing process, which allowed these materials to reach the minimum strength provided for in the standard.

It is also important to point out that, according to the results obtained in the tests, the screening process made the samples with a smaller thickness (1.5 cm) to reach resistance greater than those of the rocks with a greater thickness (2.0 cm) without the use of a mesh. This is a relevant result, since it indicates that screening enables the production of thinner sheets without compromising the mechanical performance of the rock.

Acknowledgements The authors thank the Brazilian agencies: CNPq, CAPES, and FAPERJ for the support provided to this investigation.

References

1. Frascá MHBO (2003) Experimental studies of accelerated change in granitic rocks for cladding, Doctoral Thesis, Universidade de São Paulo, São Paulo
2. Frascá MHBO (2001) Qualification of ornamental stones and for coating of buildings: Technological characterization and alterability tests. SBRO/II SRON
3. Pazeto AA (2017) Experimental characterization of reinforcement solutions for ornamental stone slabs. Doctoral Thesis. Universidade de São Paulo, São Paulo
4. Silveira LLL et al (2014) Processing of ornamental stones. Rio de Janeiro, Cetem. http://mineralis.cetem.gov.br/bitstream/handle/cetem/1736/CCL00050014_CAPITULO_07_opt.pdf?sequence=1. Accessed 21 June 2016
5. ABNT-BRAZILIAN Association of Technical Standards (2015) NBR 15845: cladding rocks-part 8: determination of hard body impact resistance. Rio de Janeiro
6. Marvila MT, Azevedo ARG, Cecchin D, Costa JM, Xavier GC, de Fátima do Carmo D, Monteiro SN (2020) Durability of coating mortars containing açai fibers. *Case Stud Constr Mater* 13. <https://doi.org/10.1016/j.cscm.2020.e00406>
7. Neuba LM, Pereira Junio RF, Ribeiro MP, Souza AT, Lima ES, Filho FCG, Azevedo ARG, Monteiro SN (2020) Promising mechanical, thermal, and ballistic properties of novel epoxy composites reinforced with cyperus malaccensis sedge fiber. *Polymers* 12(8). <https://doi.org/10.3390/polym12081776>
8. de Azevedo ARG, Marvila MT, Tayeh BA, Cecchin D, Pereira AC, Monteiro SN (2021) Technological performance of açai natural fibre reinforced cement-based mortars. *J Build Eng* 33. <https://doi.org/10.1016/j.jobbe.2020.101675>
9. de Azevedo ARG, Marvila MT, Antunes MLP, Rangel EC, Fediuk R (2021) Technological perspective for use the natural pineapple fiber in mortar to repair structures. *Waste Biomass Valorization*. <https://doi.org/10.1007/s12649-021-01374-5>
10. Azevedo A, De Matos P, Marvila M, Sakata R, Silvestro L, Gleize P, De Brito J (2021) Rheology, hydration, and microstructure of portland cement pastes produced with ground açai fibers. *Appl Sci (Switzerland)* 11(7):15–26

Surface Modification of Jamesonite During Flotation; Effect of the Presence of Ferric Ion



Martín Reyes Pérez, Jazmin Terrazas Medina, Elia Palacios Beas, Iván. A. Reyes Domínguez, Mizraim U. Flores Guerrero, Aislinn Michelle Teja Ruiz, Miguel Pérez Labra, Julio Cesar Juárez Tapia, and Francisco Raúl Barrientos Hernández

Abstract In the present study, the analysis of the surface modification of jamesonite during flotation with and without a collector, in the presence of Fe^{3+} ions, was approached. It was found that the use of 25 mg/L of ferric ion acts as an activator during the collectorless flotation of jamesonite, obtaining a 79% w/w separation. Higher concentrations (75 mg/L of Fe^{3+}) do not increase efficiency, even though in the presence of 60 mg/L of xanthate, the cumulative flotation is 64% w/w. This is due to the surface modification, detecting the increase in the intensity of the absorption bands of lead oxide (PbO) in 419 cm^{-1} , of lead dioxide (PbO_2) in 617 cm^{-1} , of goethite ($\alpha\text{-FeOOH}$) in 881 cm^{-1} , of antimony oxides, and the formation of bidentate sulfates in coordination with the metal with four absorption bands identified by infrared.

Keywords Jamesonite · Surface · Infrared · Flotation

Introduction

Jamesonite is one of the most important mineral sulfides for obtaining metallic antimony, since it contains 30 to 40% antimony [1]. It is generally composed of 35.4% antimony (Sb), 21.7% sulfur (S), 2.7% iron (Fe), and 40.2% lead (Pb). The formula

M. R. Pérez (✉) · J. T. Medina · A. M. T. Ruiz · M. P. Labra · J. C. J. Tapia · F. R. B. Hernández
Academic Area of Earth Sciences and Materials, Autonomous University of the State of Hidalgo,
Road Pachuca-Tulancingo Kilometer 4.5 Mineral de la Reforma, Hidalgo 42180, México
e-mail: mreyes@uaeh.edu.mx

E. P. Beas
National Polytechnic Institute unit ESQIE, C.P. 07738 ESQIE, México

Iván. A. R. Domínguez
Institute of Metallurgy, Autonomous University of San Luis Potosí, San Luis Potosí 78210, SLP,
México

M. U. F. Guerrero
Industrial Electromechanics Area, Technological University of Tulancingo, 43642 Hidalgo,
México

for jamesonite is $\text{Pb}_4\text{FeSb}_6\text{S}_{14}$ and it is considered to form a solid solution of antimony sulfide and lead sulfide, and therefore the formula could also be written as $4\text{PbS}\cdot\text{FeS}\cdot 3\text{Sb}_2\text{S}_3$ [2, 3]. Each species is part of the crystalline structure and cannot be separated by physical means such as grinding or flotation [4].

The lead concentrates obtained by conventional flotation technologies contain mixtures of jamesonite and galena, which are sent directly to the smelting plants, or it is processed through hydrometallurgy for the separation of both phases, which leads to high consumption of energy [5, 6]. The flotation separation of polymetallic mineral sulfides from gangue is a subject that has been extensively studied. However, obtaining separate concentrates of jamesonite and galena is a poorly discussed topic [7]. The buoyancy of jamesonite is like that of galena [8]. Due to this, it is necessary to study the behavior of the flotation, activation, and depression of this mineral, prior to its selective separation.

During the last decades, there have been many studies on the buoyancy and the factors influencing the flotation of jamesonite [8–10], for example, has been investigating the use of five extracts of tannin from different trees, finding that larch tannin is the best reagent to improve the flotation of jamesonite [8]. In addition to considering chemical reagents that activate the surface of the mineral, it must be taken into account that during grinding, there is the galvanic contact between the grinding media and the minerals of the pulp, during this stage a carry out a number of reactions oxide-reduction and are the origin of the presence of metal ions in the pulp, one of the most abundant being iron and its surface adsorption or the formation of precipitates can negatively influence the separation of the valuable minerals.

The presence of hydrolyzed Fe^{3+} iron in the feed pulps of the flotation circuits is a common problem in the mineral-processing industry. The different solid iron species that can be found in flotation pulps are goethite ($\alpha\text{-FeOOH}$), lepidocrocite ($\gamma\text{-FeOOH}$), and akaganeite ($\beta\text{-FeOOH}$), among others and depending on the chemistry of the pulp, these species are hydrophilic and they become adsorbed to the surfaces of sulfides, causing a decrease in the hydrophobicity of the mineral, and directly influencing the flotation efficiency [11, 12].

To propose the optimal chemical conditions and an approach for the selective separation of jamesonite from galena, it is required to study separately the flotation of jamesonite without and with a collector and in the presence of different concentrations of inorganic depressants [13, 14]. From the above, the importance of flotation and separation of the mineralogical phases of jamesonite and galena is denoted, to mitigate environmental and economic problems. For this reason, this research work addresses the study of the activating or depressor effect on the presence of iron Fe^{3+} ions, in the flotation of jamesonite, results that can be applied in establishing the conditions of selective separation of these minerals.

Experimental Methodology

To perform the analysis of the surface modification of jamesonite during flotation, a jamesonite mineral was used with an appearance consisting of a single mineralogical phase, from the Carrizal mine located in Zimapán, Hidalgo Mexico. The mineral obtained in its entirety was pulverized in an agate mortar to a micrometric size. To characterize the mineral, X-ray diffraction, scanning electron microscopy in conjunction with SEM–EDS energy dispersion microanalysis were used, as well as elemental mapping and Fourier transform infrared spectroscopy FTIR.

For all the experimental tests, deionized water was used. To evaluate the effect of the ion concentration (Fe^{3+}) in the flotation without and with collector was employed a ferric sulfate salt ($\text{Fe}_2(\text{SO}_4)_3 \cdot n\text{H}_2\text{O}$), 60 mg/L methyl isobutyl carbinol (MIBC) as frother agent and 60 mg/L potassium amyl xanthate ($(\text{CH}_3)_2\text{CHCH}_2\text{OCSSK}$). Reagents provided by Alkemin S.A. de S.R.L. The tests were carried out in a 1 L laboratory Denver flotation cell, equipped with a diffuser and an impeller, both made of polypropylene material, the pulp inside the cell was kept under constant stirring of 1200 rpm.

During the conditioning of the pulp at the beginning and at the end of the flotation, the pH of the pulp and the oxide-reduction potential (ORP) mV were measured, using a KCl internal solution electrode coupled to a Thermo Scientific Orion 3 Star potentiometer calibrated to the start of floating.

A volume of 1 L of deionized water was used in each jamesonite flotation test. The conditioning of the pulp was carried out inside the cell and initially the pH and the ORP of the water were measured. Subsequently, 8 g of mineral were added, after 3 minutes of conditioning the frother agent, methyl isobutyl carbinol (MIBC) in a concentration of 60 mg/L, was added. Subsequently, the stoichiometric proportion of the salt was added, to have concentrations of 25, 50, and 75 mg/L of the metal ion (Fe^{3+}) with and without xanthate. Once the metal salt was dissociated, the physico-chemical properties that characterize the flotation process were measured. Figure 1 shows the flow chart of the experimental procedure.

After the conditioning time, the flotation test was started obtaining concentrates in times of 0.5, 1, 2, 4, 6, 8, and 10 min, the foam flotation was received in containers of inert material, previously weighed wet concentrate was allowed to dry at room temperature, and the flotation weight percent was calculated using Equation 1

$$\%w/wF = \frac{W_c - W_v}{8} * 100 \quad (1)$$

where W_c is the weight of the recipient containing the dried jamesonite mineral particles collected at each float time, W_v is the weight of the empty container, eight (8) is the number of grams of mineral used in each test, and 100 to express the value as % w/w F is the flotation weight percentage. A precision balance was used for weighing the containers.

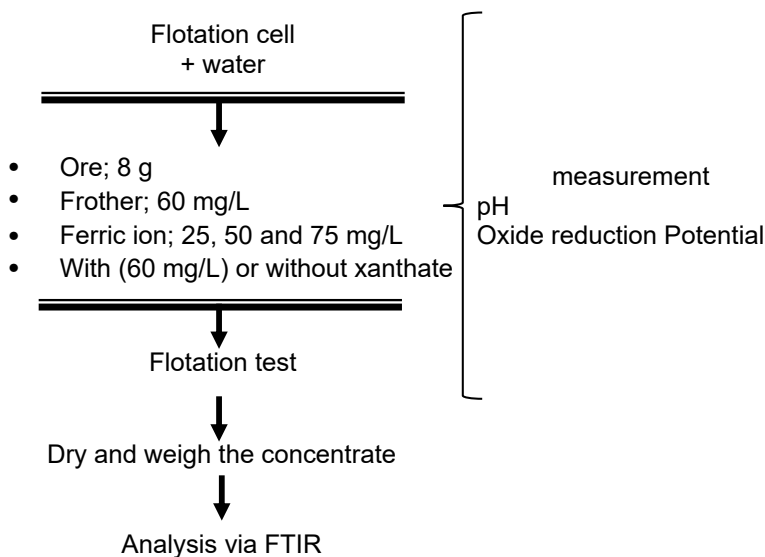


Fig. 1 Flow sheet of the experimental procedure

The particles obtained in 0.5 min of flotation were characterized by infrared spectroscopy to determine the surface speciation and in this way identify the phases that depress or activate surface of the jamesonite mineral in the presence of different concentrations of iron.

Results

Characterization of the Jamesonite Mineral

Figure 2 shows the X-ray diffraction spectrum of the jamesonite mineral, which confirms that it consists of a single crystalline phase identified with the PDF 96-901-2801 diffraction pattern as jamesonite, with a monoclinic crystal structure.

Figure 3 shows an SEM micrograph, elemental mappings, and semi-quantitative chemical analysis by energy dispersion microanalysis of the mineral jamesonite. Particles with a morphology made up of elongated crystals with smooth edges that fracture in the form of striae or needles are observed where one of their ends is at a right angle, the elemental mappings show the distribution of the elements that constitute the mineral of jamesonite, and in this analysis it was possible to detect the presence of zinc.

About Fourier transform infrared spectroscopy (FTIR), this technique was used to determine the species that have covalent bonds and are not detectable by XRD or

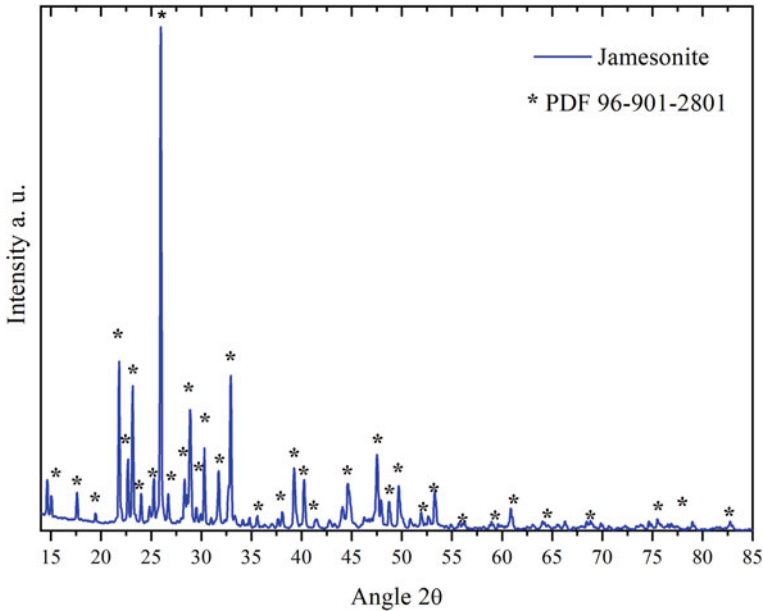


Fig. 2 X-ray diffraction spectrum (XRD) of jamesonite mineral

SEM–EDS. Figure 4 shows the FTIR analysis of the jamesonite particles. The band at 1648 cm^{-1} indicates the adsorption of OH^- ions. The spectral region between 1000 and 1200 cm^{-1} corresponds to the formation of sulfate ion, where the main band is the ion sulfate, which can split into three or four adsorption bands, so that the sulfate ion formed is incorporated into the metal of the sulfosalt mineral in the form of mono- or bidentate compounds.

The absorption band at 670 and 876 cm^{-1} is assigned to the stretching vibration mode of the Fe–O bond of goethite ($\alpha\text{-FeOOH}$), and the signals at 545 and 1407 cm^{-1} are attributed to the Sb–O bonds of Sb_2O_3 , while those found at 419 , 435 , 829 , and 1242 cm^{-1} indicate the presence of Pb–O bonds.

Flotation and surface modification of jamesonite

The presence of Fe^{3+} in the pulps fed to the flotation circuits is a common problem in the mineral-processing industry. Due to the galvanic reactions that take place during the grinding between the forged steel media and the mineral sulfides that contain iron, such as pyrite (FeS_2), chalcopyrite (CuFeS_2), pyrrhotite (FeS), and jamesonite, among others, they induce oxidation iron of the steel of the grinding medium to Fe^{2+} [15]. That, due to the chemical and thermodynamic conditions of the pulp, this ferrous ion continues to oxidize, passing to Fe^{3+} which hydrolyzes forming different solid iron species, such as goethite ($\alpha\text{-FeOOH}$), lepidocrocite ($\gamma\text{-FeOOH}$), and akaganeite ($\beta\text{-FeOOH}$), among others depending on the pulp chemistry [11, 12]. Due to this, in this experimental work, the effect of the concentration of ferric ion (Fe^{3+}) is studied

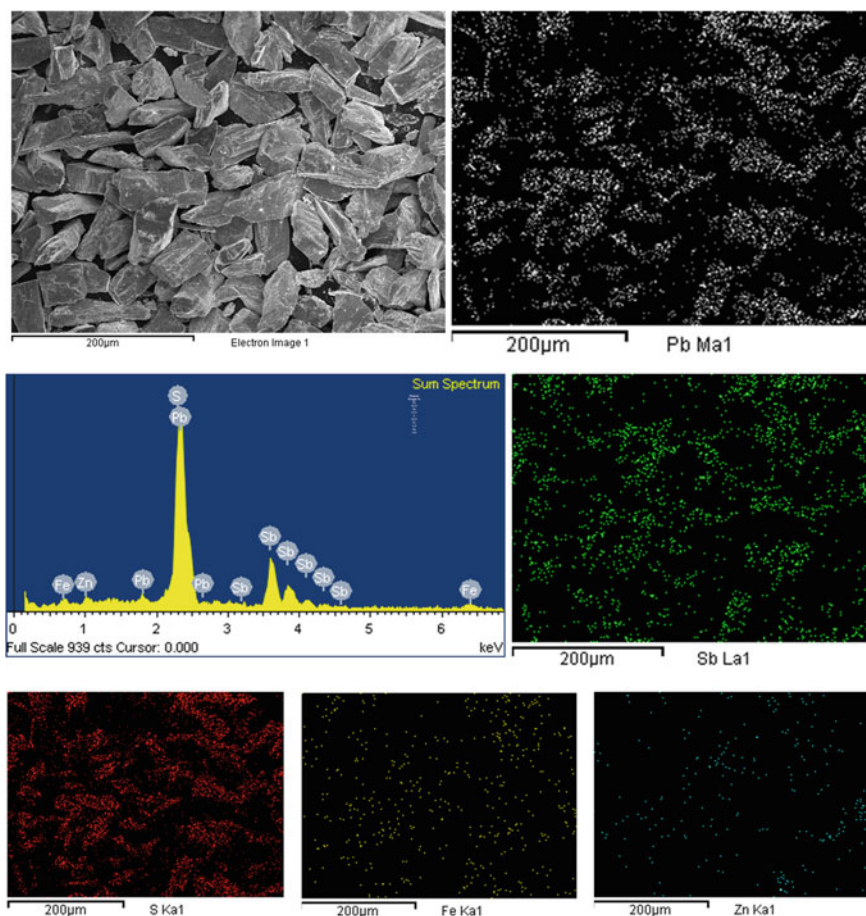


Fig. 3 SEM, EDS, and elemental mapping image of jamesonite ore

in the presence and absence of flotation collector, potassium amyl xanthate, with a slightly acidic pH.

Figure 5 shows results of the flotation of jamesonite with different concentrations of ferric ion, as well as in the presence of xanthate as a collector. It should be mentioned that, except where indicated, the flotation of jamesonite was carried out only using 60 mg/L of frother agent. It is observed that, in the absence of ferric ion Fe^{3+} , the collectorless flotation of jamesonite reaches 72% w/w of cumulative separation. Whereas, when there is a ferric ion concentration of 25 mg/L as ferric sulfate, it favors the flotation of jamesonite reaching a cumulative percentage of 79%. However, increasing the concentration of the ferric ion decreases the recovery of jamesonite, and these tests were performed at slightly acidic pH.

Under these conditions, the reactions that occur superficially between the iron Fe^{3+} which precipitated as iron oxyhydroxide, on the jamesonite, depressing flotation.

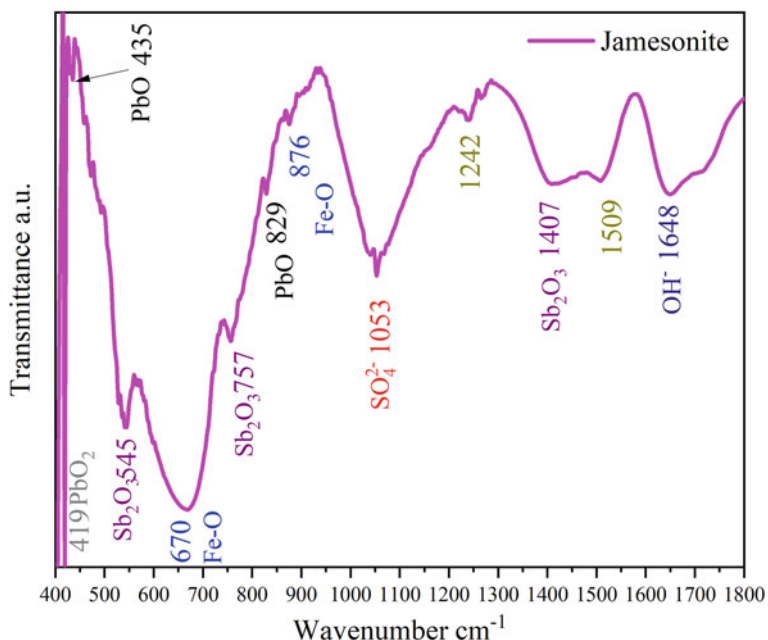


Fig. 4 Infrared spectrum of the Jamesonite mineral

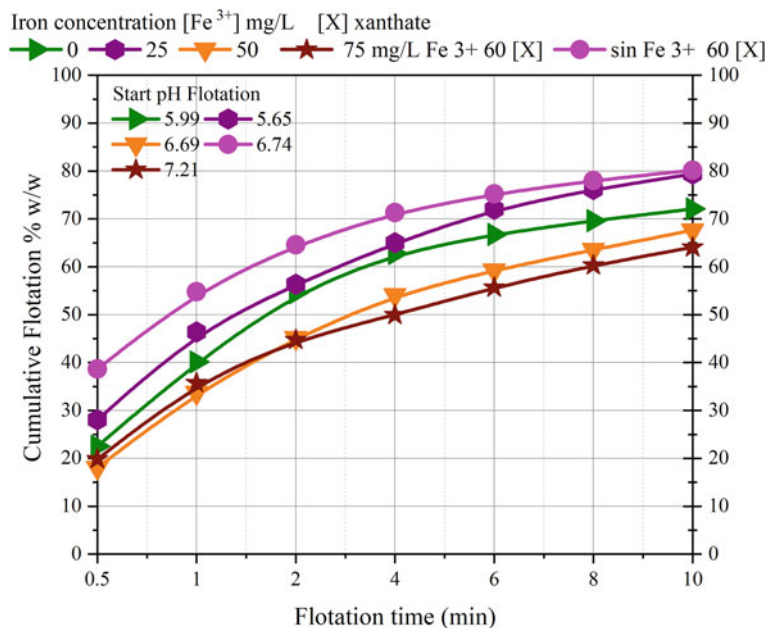


Fig. 5 % w/w cumulative flotation of Jamesonite versus time (min). Effect of the ferric ion Fe³⁺

Similarly, with the addition of 60 mg/L of xanthate to the pulp and containing ferric ion at a concentration of 75 mg/L, the flotation of jamesonite is depressed, and there is 64% w/w of flotation. In the literature, it is mentioned that iron oxidation species from sulfides and grinding media inhibit xanthate adsorption, which negatively impacts flotation [15].

As it happens in this work, for the Fe^{3+} concentration of 75 mg/L, the collector adsorption is inhibited, and the separation efficiency decreases. The inhibition of xanthate adsorption to the surface of the jamesonite mineral was verified, as shown in Fig. 4 previously presented, for the flotation test without the addition of ferric ion and using only 60 mg/L of xanthate and frother agent, a flotation efficiency of 80% w/w of cumulative flotation was achieved. This test was carried out at an initial pH of 6.74.

To identify the effect of the ferric ion Fe^{3+} on the surface of jamesonite during the flotation tests, the particles were characterized by Fourier transform infrared spectroscopy. Figure 6 shows the IR spectra of the collectorless flotation of jamesonite particles in the absence of Fe^{3+} (72% w/w F) and in the presence of 25 mg/L Fe^{3+} (79% w/w F), 50 mg/L of Fe^{3+} (67% w/w F), with 75 mg/L of Fe^{3+} , and 60 mg/L of xanthate (64% w/w F) and only containing 60 mg/L (80% w/w F) of xanthate. In the spectral zone corresponding to sulfur, there is the division of the main band of the sulfate ion into two bands and a weak absorption shoulder at 1051, 1088, and 1114 cm^{-1} .

The band at 881 cm^{-1} is attributed to the mode of vibration of the Fe–O bonds of goethite ($\alpha\text{-FeOOH}$), also expressed as $\text{Fe}_2\text{O}_3 \cdot \text{H}_2\text{O}$. At 1631 cm^{-1} , the absorption band is assigned to the bending mode of the OH- bond, which displaces the S_2^{2-} ion from the surface of the jamesonite mineral, the IR spectra presented show intense bands of the OH⁻ ion. At 1247 and 542 cm^{-1} , absorption bands are found corresponding to the Sb–O bonds of Sb_2O_3 , the band 1247 cm^{-1} is only presented for the analysis that contains 25 mg/L of Fe^{3+} , in about 1384 cm^{-1} and 1400 cm^{-1} . There is an intense band that represents the S=O bonds, this band generally occurs when the flotation system contains xanthate. Absorption bands at 459 cm^{-1} , 617 cm^{-1} indicate the presence of lead oxides (PbO_2) with the Pb–O bonds.

When the flotation pulp contains 75 mg/L and 60 mg/L of xanthate, the superficial depression of the jamesonite occurs at pH 7.21, as can be seen in Fig. 5 and this is mainly due to mechanisms of iron oxide formation, such as goethite ($\alpha\text{-FeOOH}$) represented by the binding band at 881 cm^{-1} , to the formation of antimony oxides (Sb_2O_3) band at 1051 cm^{-1} and the presence of sulfates with a single absorption band in 1088 cm^{-1} . Whereas when jamesonite floats in the presence of xanthate at pH 6.74 in the absence of ferric ion, it indicates mechanisms of formation of bidentate metal sulfate complexes where the metal binds with two oxygens, represented by the formation of four absorption bands in 1033, 1053, 1114, and 1163 cm^{-1} . Xanthate promotes the hydrophobicity of the particle to a greater degree, minimizing or canceling the formation of metal oxides, and the adsorption of xanthate is identified by the band at 1384 cm^{-1} . Figure 6 presents the IR spectrum of the flotation test with 50 mg/L of Fe^{3+} which in these conditions depresses the collectorless flotation of jamesonite, due to the mechanisms of formation of lead oxides PbO , PbO_2 , with

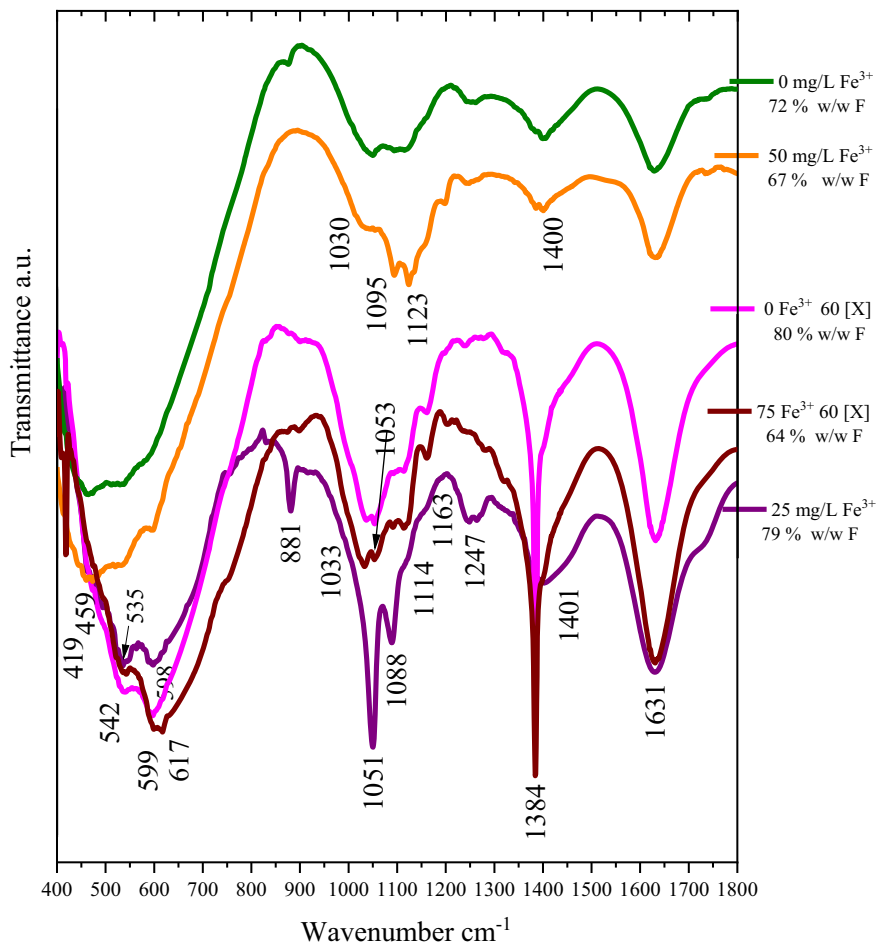


Fig. 6 Infrared spectra of the floating jamesonite in the absence and presence of Fe^{3+} and xanthate

absorption bands in 419 cm^{-1} , 459 cm^{-1} , and 542 cm^{-1} , respectively as well as by effect of the mechanisms of formation of bidentate sulfate compounds with four absorption bands. While the Fe^{3+} concentrations of 75 mg/L in the flotation pulp at pH 7.21 depresses the separation of jamesonite, even being in the presence of 60 mg/L of xanthate the cumulative flotation is 64% w/w. This is due to the increase in the intensity of the absorption bands of lead oxide (PbO) by 419 cm^{-1} , of lead dioxide (PbO_2) by 617 cm^{-1} , of goethite ($\alpha\text{-FeOOH}$) by 881 cm^{-1} , of antimony oxides in 1033 cm^{-1} , and the formation of bidentate sulfates in coordination with the metal with four absorption bands.

Discussion

The flotation of jamesonite can be carried out in the absence of collector, achieving a 72% w/w separation, the particles analyzed by FTIR show a surface containing Pb–O bonds, Lead (II) and (IV) oxide, Fe–O from goethite, Sb–O from Sb₂O₃, sulfate ion with weak absorption bands indicating the beginning of the division of the main band, and the presence of the hydroxide ion OH⁻. The addition of 25 mg/L of Fe³⁺ to the flotation pulp leads to an improvement in the % w/w of flotation reaching 79% due to the dissolution of the Pb–O bonds and the increase in the intensity of the Sb–O bonds detected in 535, 598, 1051, 1247, and 1401 cm⁻¹, as well as the presence of Fe–O and S–O bonds of the sulfate ion and the increase in the intensity of the OH⁻ band. The rise of the concentration of Fe³⁺ (50 mg/L) decreases the separation efficiency, having a maximum of 67%, and this is due as observed in Fig 6 to the dissolution of the bonds formed by Sb–O and Fe–O. The division of the main band of the sulfate ion into four absorption bands was also found, and this indicates the formation of bidentate compounds linked to the metal. The increase in the concentration of the ferric ion (75 mg/L) and despite the presence of xanthate (60 mg/L), a lower flotation efficiency (64% w/w) is obtained, due to the dissolution of the band Fe–O, the decrease of the Sb–O binding bands. The presence of the xanthate ion is detected in 1384 cm⁻¹.

Conclusions

The analysis of the surface modification of jamesonite during flotation with and without a collector, in the presence of Fe³⁺ ions, was addressed. It was found that the use of 25 mg/L of ferric ion acts as an activator during flotation without a jamesonite collector, obtaining a 79% w/w separation. Higher concentrations (75 mg/L of Fe³⁺) do not increase efficiency, even though in the presence of 60 mg/L of xanthate, the cumulative flotation is 64% w/w. This is due to the surface modification, detecting the increase in the intensity of the absorption bands of lead oxide (PbO) in 419 cm⁻¹, of lead dioxide (PbO₂) in 617 cm⁻¹, of goethite (α -FeOOH) in 881 cm⁻¹, of antimony oxides, and the formation of bidentate sulfates in coordination with the metal with four absorption bands identified by spectroscopy infrared.

Acknowledgements To the Autonomous University of the State of Hidalgo, to the PRODEP Teacher Professional Development Program, and to the National Polytechnic Institute ESIQIE.

References

1. Runqing L, Yanzhe G, Li W, Wei S, Hongbiao T, Yuehua H (2015) Effect of calcium hypochlorite on the flotation separation of galena and jamesonite in high-alkali systems. *Minerals Eng* 84:8–14 <https://doi.org/10.1016/j.mineng.2015.09.009>
2. Xu YL, Hua Y (2005) Research on a new process for separating lead and antimony from jamesonite China's. *Nonferrous Met Ind* 10(5):44–45
3. Zhao WD, Heng X, Yong D, Bin Y, Jin YZ, Yong ND, Jia JW (2015) Separation and enrichment of PbS and Sb₂S₃ from jamesonite by vacuum distillation. *Vacuum* 121:48–55. <https://doi.org/10.1016/j.vacuum.2015.07.009>
4. Sun W, Liu RQ, Hu YH (2005) Research on depression mechanism of jamesonite and pyrrhotite by organic depressant DMPS. *Mining Metal Eng* 25(6):31–34
5. Ran JC, Liu JT, Zhang CJ, Wang DY, Li XB (2013) Experimental investigation and modeling of flotation column for treatment of oily wastewater. *Int J Min Sci Technol* 23:665–668
6. Laxmi T, Srikant SS, Rao DS, Rao RB (2013) Beneficiation studies on recovery and in-depth characterization of ilmenite from red sediments of badlands topography of Ganjam District, Odisha, India. *Int J Min Sci Technol* 23:725–731
7. Runqing L, Yanzhe G, Li W, Wei S, Hongbiao T, Yuehua H (2015) Effect of calcium hypochlorite on the flotation separation of galena and jamesonite in high-alkali systems. *Miner Eng* 84(8):14
8. Chen JH, Li YQ, Long QR, Wei ZW, Chen Y (2011) Improving the selective flotation of jamesonite using tannin extract. *Int J Miner Process* 100(1–2):54–56
9. Zhang Q, Hu YH, Xu J, Chen TJ (2006) FTIR spectroscopic study of electrochemical flotation of jamesonite– diethyldithiocarbamate system. *J Trans Nonferrous Metals Soc China* 16(3): 493–496
10. Zhao RR, Jiang HY, Zhen-O Z, Qin YH, Xu S (1990) Behaviors of Sb, Sn, and As in leaching and electrowinning from jamesonite concentrate. *Acta Metall Sin* 3(10):265–270
11. Hug SJ (1997) In situ fourier transform infrared measurements of sulfate adsorption on Hematite in aqueous solutions. *J Colloid Interface Sci* 188(2):415–422
12. Reyes PM (2013) Modificación superficial de mineral de pirita y precipitados de Hierro: comportamiento en medios acuosos y de molienda. Ph.D. Thesis Morelia, Michoacán, México
13. Chen JH, LI YQ, Long QR (2010) Molecular structures and activity of organic depressants for marmatite, jamesonite and pyrite flotation. *Trans Nonferrous Met Soc China* 20(10):1993–1999
14. Liu RQ, Sun W, Hu YH, Xiong DL (2006) Depression mechanism of small molecular mercapto organic depressants on flotation behavior of complex sulfides. *China J Nonferrous Met* 16(4):746–751
15. Hu Y, Sun W, Wang D (2009) *Electrochemistry of flotation of sulphide minerals*. Tsinghua University Press, Dordrecht Beijing, New York

Synthesis and Electrical and Magnetic Characterization of Electroceramics Type $\text{Ba}_{1-x}\text{Eu}_x\text{Ti}_{1-x/4}\text{O}_3$ ($x = 0.001$ and $x = 0.005\%$ by Weight Eu^{3+})



J. P. Hernández-Lara, M. Pérez-Labra, A. Hernández-Ramírez,
J. A. Romero-Serrano, F. R. Barrientos-Hernández, J. C. Juárez-Tapia,
M. Reyes-Pérez, and V. E. Reyes-Cruz

Abstract In this work, the synthesis of solid solutions type $\text{Ba}_{1-x}\text{Eu}_x\text{Ti}_{1-x/4}\text{O}_3$ ($x = 0.001$ and $x = 0.005\%$ by weight Eu^{3+}) and its subsequent determination of electrical and magnetic properties were carried out. The samples were synthesized by the conventional solid-state reaction method. The grinding of the BaCO_3 , TiO_2 , and Eu_2O_3 precursor powders was carried out in an agate mortar with acetone as a control medium. The powders were mixed and calcined at $900\text{ }^\circ\text{C}$ and then green pellets were manufactured which were sintered at $1350\text{ }^\circ\text{C}$ for 5 h. The experimental results obtained by X-ray diffraction showed the presence of tetragonal BaTiO_3 phase in the BaTiO_3 sample doped with Eu^{3+} $x = 0.001$ and $x = 0.005\%$ by weight. Electrical measurements (Capacitance and permittivity) and magnetic measurements were made. Scanning electron microscopy results showed mostly sintered sub-rounded particles.

Keywords BaTiO_3 · Capacitance · Permittivity · Hysteresis

Introduction

With the production of Barium Titanate (BaTiO_3), the current era of dielectric ceramic materials began. Its high dielectric constant was first reported in the United States in 1942. This material has now become the basic dielectric material for building capacitors [1]. BaTiO_3 is generally made by reaction of BaCO_3 with TiO_2 at a temperature of approximately $1100\text{ }^\circ\text{C}$. Whatever the technique, the current trend is to produce powders with strict control of purity, Ba/Ti ratio, and particle size,

J. P. Hernández-Lara (✉) · M. Pérez-Labra · F. R. Barrientos-Hernández · J. C. Juárez-Tapia · M. Reyes-Pérez · V. E. Reyes-Cruz

Academic Area of Earth Sciences and Materials, Autonomous University of the State of Hidalgo, Pachuca-Tulancingo Km 4.5 Mineral de la Reforma, 42184 Hidalgo, México

A. Hernández-Ramírez · J. A. Romero-Serrano
Higher School of Chemical Engineering and Extractive Industries (ESIQIE)-IPN, Zacatenco 07738, México D.F., México

which affects the generation of reproducible microstructures and constant dielectric properties in the sintered product [1].

BaTiO₃ is a crystalline ceramic material that at room temperature has a tetragonal structure and has a ferroelectric behavior, but when this material exceeds the Curie temperature (T_c), which in this case is close to 125 °C, it undergoes a transformation to the phase cubic called Perovskite. This symmetric unit cell material is paraelectric [2], having a Perovskite structure, it presents barium atoms in the corners of a cube; oxygen atoms fill the face-centered sites and a titanium atom occupies the body-centered site.

One of the most important properties of ceramic materials is their dielectric behavior, this property prevents the flow of electric current, which goes beyond simply providing electrical insulation, since when an electric field is applied, both positive and negative charges tend to separate. and the material is polarized (electrical polarization) due to electrostatic interaction, appearing electric dipoles [3].

BaTiO₃ does not usually have magnetic properties; however, you can find ceramics with magnetic properties of great importance such as ferrites and garnets called ferromagnetic ceramics. In these ceramics, the different ions have different magnetic moments, which leads to a net magnetization when applying a magnetic field [4].

Impurities play an important role in balancing the defect chemistry of perovskite-type titanates. Because there is no evidence of interstitial impurities, only substitutional impurities are considered. Isovalent substitutional impurities have no effect on defect concentration, because they do not change local charge. On the other hand, anisovalent substitutional impurities, those whose charge differs from the ions being replaced, require the formation of opposite charge compensation defects to maintain total charge neutrality [5–8].

In this investigation, the results of X-ray diffraction, electrical properties (capacitance and relative permittivity), and magnetic (hysteresis) are reported, as well as scanning electron microscopy of the solid samples type Ba_{1-x}Eu_xTi_{1-x/4}O₃ ($x = 0.001$ and $x = 0.005\%$ by weight Eu³⁺) synthesized by the solid-state reaction technique.

Experimental Methodology

Solid solutions like Ba_{1-x}Eu_xTi_{1-x/4}O₃ ($x = 0.001$ and $x = 0.005\%$ by weight Eu³⁺) were synthesized using the solid-state reaction method. The precursor powders BaCO₃ (Sigma-Aldrich CAS 513-77-9, 99.9%), TiO₂ (Sigma-Aldrich, CAS No. 13463-67-7 99.9%), and Eu₂O₃ (Sigma-Aldrich, 99.9%) were dried at 300 °C in a LINDBERG Muffle for 4 h. Subsequently, they were ground in an agate mortar with acetone as a control medium for 25 min. The mixture of powders is placed in an alumina crucible and calcined at 800 °C for 12 h. Subsequently, the sintering of the mixtures was carried out at 1300 °C in a titanium crucible using a heating ramp of 4 °C/min. Once the sintered material had been obtained, the manufacture of green pellets with a diameter of 10 mm and a thickness of 5 mm was carried out

in a stainless-steel die and a hydraulic press. Next, the pellets were sintered on an alumina plate at 1350 °C for 5 h in a FURNACE THERMOLYNE model 46,200 oven, using a heating ramp of 4 °C/min. The electroceramics obtained were characterized by X-ray diffraction, electrical measurements (capacitance, relative permittivity), magnetic (hysteresis), and scanning electron microscopy.

Results and Discussion

X-Ray Diffraction

The X-ray diffraction patterns corresponding to the sintered samples with $x = 0.001$ and $x = 0.005\%$ by weight Eu^{3+} at 1350 °C are shown in Fig. 1. It can be seen that there is no presence of the species corresponding to precursor powders. However, the consolidation of Tetragonal BaTiO_3 (JCPDS 05-0626) is seen in positions $2\theta \approx 21.94^\circ, 31.49^\circ, 38.81^\circ, 45.20^\circ, 50.93^\circ, 56.17^\circ, 65.83^\circ, 70.42^\circ, 75.16^\circ, 79.43^\circ,$ and 83.68° . The highest intensity peak can be observed at $2\theta \approx 31.49^\circ$.

It should be mentioned that secondary phases were not detected in these samples due to the low concentrations of the Eu^{3+} dopant used, thus ensuring the doping of the compound without exceeding its solubility limit. Jankowska-Sumara et al. [9] mention that for concentrations lower than 3% of dopant, rare earth ions are

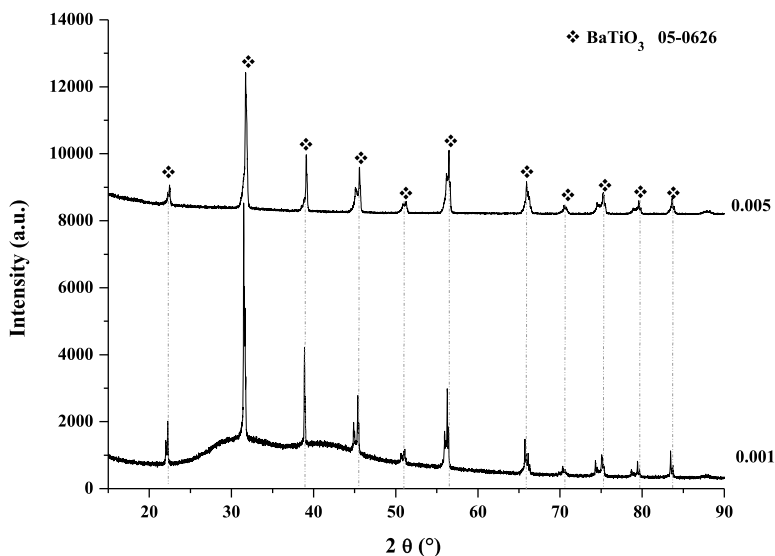


Fig. 1 Diffractograms of the sintered samples at 1350 °C with $x = 0.001$ and $x = 0.005\%$ by weight Eu^{3+}

incorporated into the A site of perovskite and act as donor impurities, which gives rise to ferroelectric properties.

Electrical Properties

Capacitance

The obtained capacitance values were measured at 120 Hz frequency. This value was chosen taking as reference the results obtained by West et al. [10] for BaTiO₃ base ceramics doped with La³⁺.

Figures 2 and 3 show the capacitance curves obtained for the compositions $x = 0.001$ and $x = 0.005\%$ by weight Eu³⁺. The maximum value of capacitance obtained was 2799 pF in the sample with $x = 0.001\%$ in weight Eu³⁺ registering the Curie temperature value of 103 °C, it should be mentioned that in the frequency used a change in slope is observed at 165 °C, approximately, and as the frequency increases the capacitance decreases.

For the sample with $x = 0.005\%$ by weight (Fig. 3), the obtained capacitance registered a maximum value of 1187 pF at 120 Hz, and at a Curie temperature of 102 °C in this sample there is also a change in slope approximately at 140 °C from which the capacitance takes on increasing values again. It is important to mention that

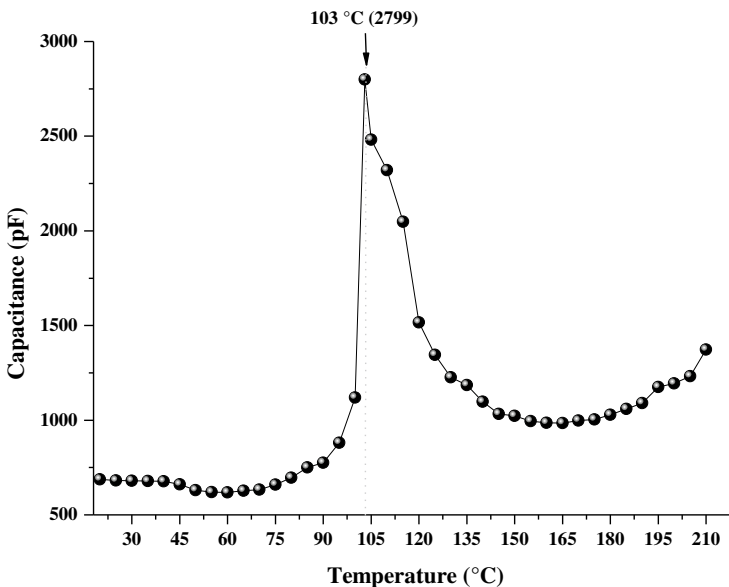


Fig. 2 Capacitance versus temperature for the sample with $x = 0.001\%$ by weight Eu³⁺

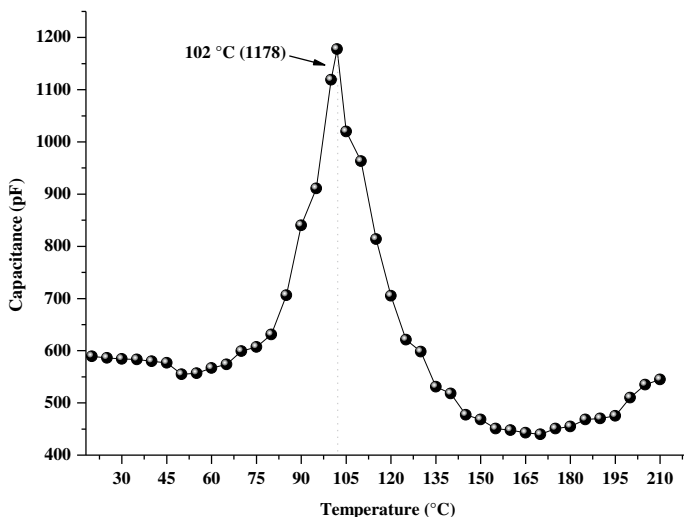


Fig. 3 Capacitance versus temperature for the sample with $x = 0.005\%$ by weight Eu^{3+}

it is desirable to lower the Curie temperature of BaTiO_3 (120°C) to room temperature. The Curie temperature is the temperature above which a ferroelectric body loses its electrical properties, behaving like a purely paraelectric material, so this change is expected to occur at temperatures that tend to be room temperature.

Relative Permittivity

Figure 4 shows the results of relative permittivity (ϵ) or dielectric constant obtained at 120 Hz frequency for samples with $x = 0.001$ in Eu^{3+} weight. The maximum value of relative permittivity for $x = 0.001\%$ by weight Eu^{3+} was 6149.30 and having a Curie temperature 103°C . For $x = 0.005\%$ by weight Eu^{3+} , the maximum relative permittivity was = 2866.89 at 120 Hz, with a Curie temperature of 102°C (Fig. 5). In this sample, a change in slope is observed approximately at 165°C from which the relative permittivity takes increasing values.

Magnetic Properties

Figure 6 shows the magnetic hysteresis curve of BaTiO_3 doped with Eu^{3+} for the composition $x = 0.001\%$ by weight Eu^{3+} , from which it is obtained that, at room temperature, this material presents a ferromagnetic order in which magnetic saturation is reached. Specific $M_s = 5.80$ emu/g applying a magnetic field close to $3.92 \times$

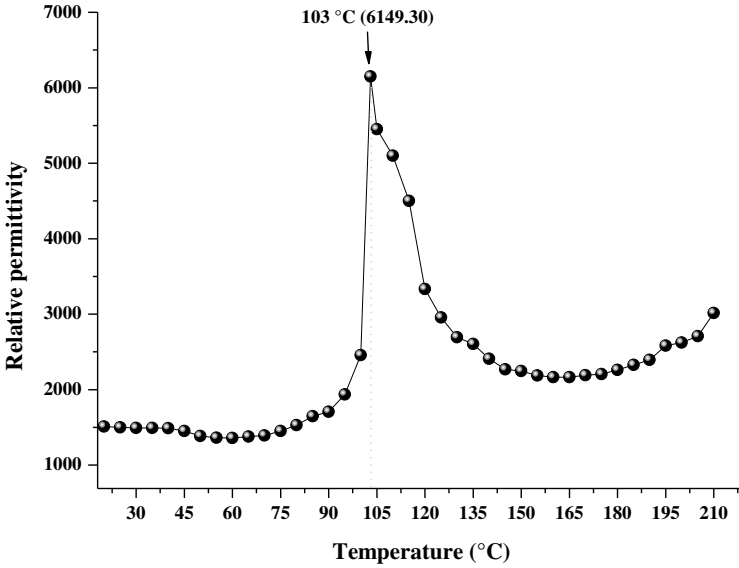


Fig. 4 Relative permittivity versus Curie temperature for $x = 0.001\%$ by weight Eu^{3+}

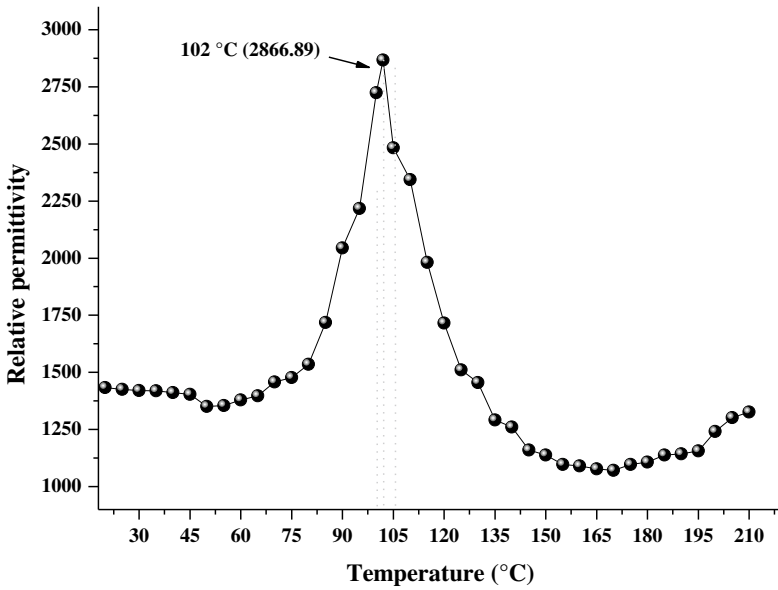


Fig. 5 Relative permittivity versus Curie temperature for $x = 0.005\%$ by weight Eu^{3+}

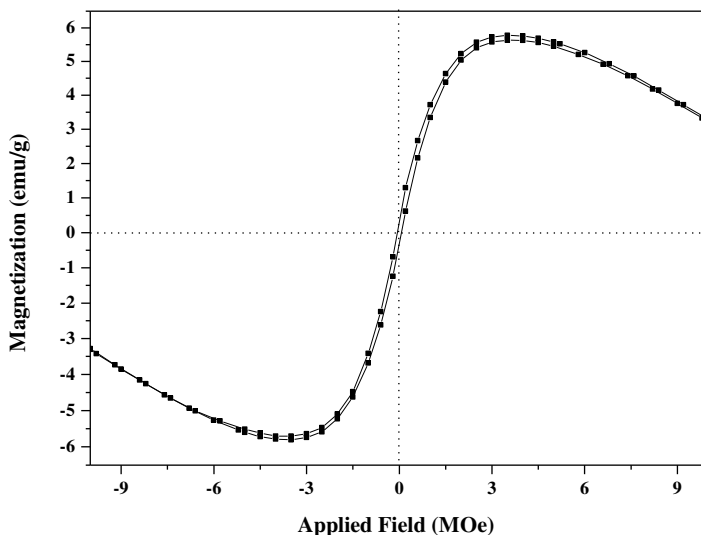


Fig. 6 Magnetic hysteresis curves for the sample with $x = 0.001\%$ by weight Eu^{3+}

106 Oe and a remanent magnetization $M_r = 0.22$ emu/g, and this value is obtained by extrapolating the saturation behavior of the magnetic hysteresis curve on the magnetization axis. These values indicate that BaTiO_3 with $x = 0.001\%$ by weight Eu^{3+} shows a ferromagnetic behavior and low coercivity, 0.060×10^6 Oe.

Figure 7 shows the magnetic hysteresis curve of BaTiO_3 doped with Eu^{3+} for the composition $x = 0.005\%$ by weight Eu^{3+} , and it presents a specific saturation magnetization $M_s = 9.92$ emu/g applying a magnetic field close to 2×10^6 Oe and a magnetization remnant $M_r = 1.16$ emu/g. These values indicate that the compositions show a tendency to paramagnetic behavior due to the decrease in the magnetization values and with the increase in the dopant (Eu^{3+}) it is more evidently compared to the sample with $x = 0.001\%$ by weight of Eu^{3+} (Fig. 6).

Scanning Electron Microscopy

The scanning electron microscopy analyses reported in this section were performed on sintered samples at 1350°C for 5 h for compositions of $x = 0.001$ and 0.005% weight Eu^{3+} (Fig. 8a, b), respectively.

In Fig. 8a, b, the morphology of the sample can be observed with $x = 0.001\%$ weight Eu^{3+} using an acceleration voltage 5.0 kV and a magnification of X 10,000. The micrograph shows individual particles and aggregates with various sizes with most grains tend to sphericity. It can also be noted that the microstructure is partially homogeneous. These individual particles are very similar to those reported by Hernandez-Lara et al. [11] and Barrientos Hernandez et al. [12] who carried out

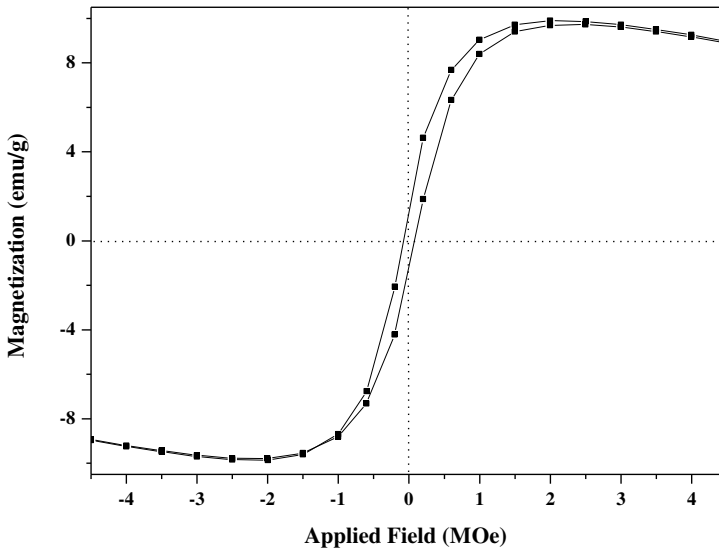


Fig. 7 Magnetic hysteresis curves for the sample with $x = 0.005\%$ weight Eu^{3+}

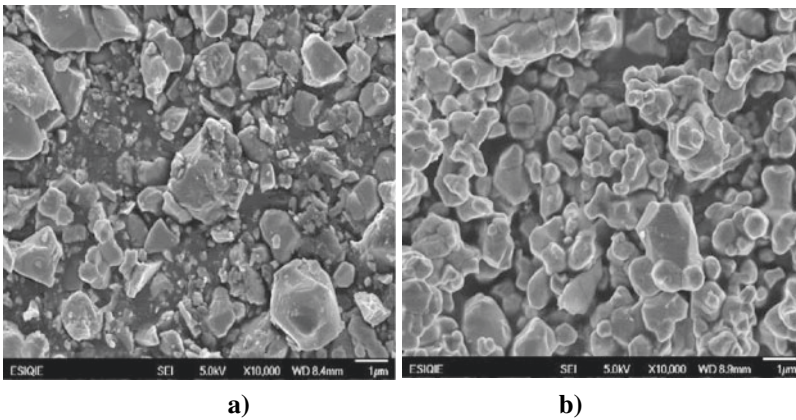


Fig. 8 Micrograph of the samples: **a** $x = 0.001\%$ weight Eu^{3+} and **b** $x = 0.005\%$ weight Eu^{3+} sintered at $1350\text{ }^{\circ}\text{C}$

studies on BaTiO_3 doped with Gd and Nb and attributed the increase in grain size to the increase in the amount of dopant used in the synthesis, the grains are spherical in shape with random orientation and agglomerates are formed, as well as porosity in different areas.

Conclusions

The conclusions derived from this research work are as follows.

The XRD patterns of the synthesized and sintered pickups at 1350 °C confirmed the formation of tetragonal BaTiO₃ (JCPDS 05-0626) consolidated at positions $2\theta \approx 21.94^\circ, 31.49^\circ, 38.81^\circ, 45.20^\circ, 50.93^\circ, 56.17^\circ, 65.83^\circ, 70.42^\circ, 75.16^\circ, 79.43^\circ,$ and 83.68° which highlights the highest intensity peak at $2\theta \approx 31.49^\circ$. The capacitance obtained in the BaTiO₃ samples doped with Eu³⁺ ($x = 0.001$ and $x = 0.005\%$ weight Eu³⁺) showed a tendency to decrease with increasing dopant content and decreasing Curie temperature without becoming totally paraelectric. It is important to lower the Curie temperature (120 °C for pure BaTiO₃) to room temperature; in this way, the temperature at which the compound will undergo the transition of crystalline structure will be lower than in the pure compound, generating spontaneous polarization at lower temperatures. than 120 °C. The relative permittivity in the BaTiO₃ samples doped with Eu³⁺ for $x = 0.001\%$ weight Eu³⁺ was 6149.30 at 120 Hz and a Curie temperature of 103 °C and for the sample with $x = 0.005\%$ weight Eu³⁺ was 2866.89 at 120 Hz, and Curie temperature of 102 °C. These values show a tendency to decrease as the dopant content increases without becoming totally paraelectric, similar to the tendency shown by the capacitance results. The magnetic hysteresis curves for the BaTiO₃ samples doped with Eu³⁺ $x = 0.001, 0.005\%$ by weight Eu³⁺ show a ferromagnetic behavior at room temperature and reached a magnetization of saturation $M_s = 5.80$ and $M_s = 9.92$ emu/g, respectively. The micrographs showed individual particles and aggregates of various sizes, a random orientation, and were mostly grains that tend to sphericity.

Acknowledgements This work has been partially carried out thanks to the support of the Autonomous University of the State of Hidalgo and Conacyt.

References

1. Kingery WD (1960) Introduction to ceramics. Wiley, New York
2. Smyth DM (2000) The defect chemistry of metal oxides. Oxford University Press. ISBN 0195110145, 9780195110142
3. Haertling GH (1999) Ferroelectric ceramics: history and technology. J Am Ceram Soc 82:797–818
4. Carter CB (2007) Norton Springer, n° 716
5. Kahn M (1971) Influence of grain growth on dielectric properties of Nb-doped barium titanate. J Am Ceram Soc 54:455–457
6. Chan HM (1988) Compensating defects in highly donor-doped BaTiO₃. J Am Ceram Soc 69(6):507–510
7. Nowotny J (1994) Defect structure: electrical properties and transport in barium titanate. VII chemical diffusion in Nb-doped BaTiO₃. Ceram Int 20:265–275
8. Shiransaki SI, Saito S (1985) Structure-property-relationships in perovskite electronic ceramics. de Fine Ceramics. Elsevier, New York, pp 150–161

9. Jankowska-Sumara I, Sitko D, Podgorna M, Pilch M (2017) The electromechanical behavior of europium doped BaTiO₃. *J Alloys Compd* 724:703–710
10. West AR, Adams TB, Morrison FD, Sinclair DC (2004) Novel high capacitance materials: BaTiO₃:La and CaCu₃Ti₄O₁₂. *J Eur Ceram Soc* 24:1439–1448
11. Hernández-Lara JP, Pérez-Labra M, Barrientos-Hernández FR, Romero-Serrano JA, Ávila-Dávila EO, Thangarasu P, Resendiz-Corona I (2016) Synthesis, structural and electrical properties of BaTiO₃ doped with Gd³⁺. *Mex J Mater Sci Eng* 3(1):7–12
12. Barrientos Hernández FR, Lira Hernández IA, Gómez Yáñez C, Arenas Flores A, Cabrera Sierra R, Pérez Labra M (2014) Structural evolution of Ba₈Ti₃Nb₄O₂₄ from BaTiO₃ using a series of Ba(Ti_{1-5x}Nb_{4x})O₃ solid solutions. *J Alloys Compd* 583:587–592

The Collectorless Flotation of Pyrargyrite, Surface Analysis via FTIR



Martín Reyes Pérez, Zaida Peralta García, Elia Palacios Beas, Iván. A. Reyes Domínguez, Mizraim U. Flores Guerrero, Aislinn Michelle Teja Ruiz, Miguel Pérez Labra, Julio Cesar Juárez Tapia, and Francisco Raúl Barrientos Hernández

Abstract In this work, the study of the collectorless flotation of pyrargyrite is presented to provide information for the selective separation of this mineral. The mineral used consists of a single phase with contents of 59.64% w/w Ag, 22.90% w/w Sb, and 17.46% w/w S. The flotation can be carried out using only 60 mg/L frother agent. The pH plays an important role and higher flotation efficiency is obtained at pH 6 and 10 with 66% w/w and 67% w/w of separation, respectively. Values pH 2, 2.54, and 4.97 depress the flotation of the mineral. The surface depression is attributed to the strong intensity of the absorption bands of the Sb–O bonds, the sulfate ion, and the hydroxyl ion OH⁻ species that give it a hydrophilic character, bonds determined by FTIR.

Keywords Pyrargyrite · Collectorless · Infrared · Depression · Activation

Introduction

Pyrargyrite Ag₃SbS₃ is a sulfosalt-type mineral, with a chemical composition of 59.7% Ag, 22.5% Sb, and 17.8% S, it crystallizes in the trigonal system and is found in polymetallic epithermal deposits of base metal sulfides [1, 2]. The term sulfosalt refers to a complex salt that contains oxygen, in pyrargyrite this is replaced by sulfur.

M. R. Pérez (✉) · Z. P. García · A. M. T. Ruiz · M. P. Labra · J. C. J. Tapia · F. R. B. Hernández
Academic Area of Earth Sciences and Materials, Autonomous University of the State of Hidalgo,
Road Pachuca-Tulancingo Kilometer 4.5 Mineral de la Reforma, Hidalgo 42180, México
e-mail: mreyes@uaeh.edu.mx

E. P. Beas
National Polytechnic Institute, ESIQIE, 07738 México D.F., Mexico

Iván. A. R. Domínguez
Institute of Metallurgy, Autonomous University of San Luis Potosí, San Luis Potosí 78210,
México

M. U. F. Guerrero
Industrial Electromechanics Area, Technological University of Tulancingo, 43642 Hidalgo,
México

Sulfosalt minerals have the general formula $A_xX_yS_z$ where “S” is for sulfur; “X” is assigned to Sb^{3+} , As^{3+} , Bi^{3+} , or Te^{4+} ; and “A” represents the metal in the structure, for example, Ag^+ , Sn^{2+} , Cu^{+1} , Pb^{+1} , Fe^{2+} , Mn^{2+} , and Hg^{2+} [3, 4].

The color of the pyrrargyrite crystals is brown, dark reddish to black with abundant internal reflections. It has a metallic luster and red streaks [5]. The crystal structure of this mineral contains covalent antimony–sulfur Sb–S bonds corresponding to the pyramidal chains of SbS_3 [6]. In Mexico, pyrrargyrite is found in sulfide-type mineral deposits in the states of Guanajuato, Zacatecas, and Guerrero [2]. During the concentration process, the pyrrargyrite is separated by flotation together with the sulfides, mainly with the galena. However, during pyrometallurgical processing, the silver from pyrrargyrite passes into slag and must be reprocessed to recover it, so it is convenient to study the selective separation of pyrrargyrite via collectorless flotation.

Regarding the collectorless flotation, it has been noted from the twentieth century as a process of separation of sulfide-type minerals, and it is favored when there is a surface deficient in metal and rich in sulfur [7], this modification superficial is caused by galvanic reactions that occur between sulfides and iron media during grinding, causing oxidation of the metallic components of sulfides [8]. Therefore, a requirement to carry out the collectorless flotation of sulfides is the presence of elemental sulfur, or layers of polysulfides on the mineral surface [9].

The hydrophobicity of sulfides is an important parameter in the collectorless flotation, and this is affected by both the pH and the pulp potential Eh (V), and therefore they are parameters that should be studied during the collectorless flotation. The application of collectorless flotation reduces the use of collector reagents, improves the degree of concentrate, and influences the number of flotation equipment necessary to achieve maximum separation, and another application is the depression of gangue minerals. However, for some mineral sulfides, due to their limited flotation, it is necessary to add a metal ion to improve flotation efficiency [10].

For this reason, in this research work, the collectorless flotation of pyrrargyrite is studied as a function of pH (acid and alkaline) and pulp potential Eh in order to provide information for the selective separation of this mineral sulfosalt type, as well as determining the surface speciation by means of Fourier transform infrared spectroscopy, to identify the species that depresses or activates the mineral surface during this process.

Experimental Methodology

To carry out the flotation tests, a pyrrargyrite mineral with a macroscopic appearance consisting of a single phase was used, from the mineral deposits of Guanajuato, Mexico, pulverized in an agate mortar. This silver sulfosalt mineral was characterized by X-ray diffraction (XRD), scanning electron microscopy in conjunction with energy dispersion microanalysis (SEM–EDS), Fourier transform infrared spectroscopy (FTIR), and size analysis of particle (SAP) by laser diffraction.

To adjust the pH of the pulp, a solution of sulfuric acid and 1 M NaOH was used. The flotation tests were carried out in a 1 L stainless steel cell, Denver brand, consisting of a diffuser and an impeller operated at 1200 rpm, the air to form the bubbles was controlled by a suction valve. To measure the pH and the oxidation reduction potential, an electrode with an internal solution of saturated KCl was used, connected to a calibrated Thermo Scientific Orion 3 Star potentiometer before starting each float test.

The experimental procedure for all the collectorless flotation tests of pyrrargyrite consisted of carrying out the conditioning inside the cell, one liter of deionized water was placed, then the 60 ppm frother agent, methyl isobutyl carbinol (MIBC) provided by Alkemin S.A. of S.R.L, plus 4 g of mineral, and finally adjust the pH either acid (2, 2.54, 4.97, 6) or alkaline (9 and 10), this stage was carried out under constant stirring and in each addition of reagents a time was given 3-min conditioning. During each chemical change of the pulp, the pH values and the oxide reduction potential (ORP) mV were measured and recorded. The measured ORP values were expressed in reference to the standard hydrogen electrode SHE, by adding +236 mV to the measured value, as cited in the bibliography [7].

Once the conditioning stage was concluded, the flotation test began and the concentrates were collected in times of 0.5, 1, 2, 4, 6, 8, and 10 min, in containers of inert material, which were previously weighed, the collected wet concentrates dried at room temperature and the percentage by weight (% w/w) at each flotation time was calculated with Eq. 1.

$$\% \text{ w/w } F = \frac{W_c - W_i}{4} * 100 \quad (1)$$

where % w/w F is the percentage of flotation by weight obtained at each time, W_c is the weight of the container containing the dry mineral particles floated in the previously established float time, W_i is the weight of the empty container, four is the number of grams of mineral used in each test, and 100 to express the value as a percentage. A precision analytical balance was used to weigh the containers.

The particles of the concentrate obtained in times of 0.5 and 10 min of flotation of most of the tests were characterized by Fourier transform infrared spectroscopy to determine the surface speciation and, in this way, infer the depression or activation of the pyrrargyrite mineral as a function of pH.

Results

Figure 1 shows the morphology of the pyrrargyrite particles that were mounted in epoxy resin, polished with abrasive, and characterized in SEM in conjunction with EDS, which also presents the elemental mapping of the pyrrargyrite mineral

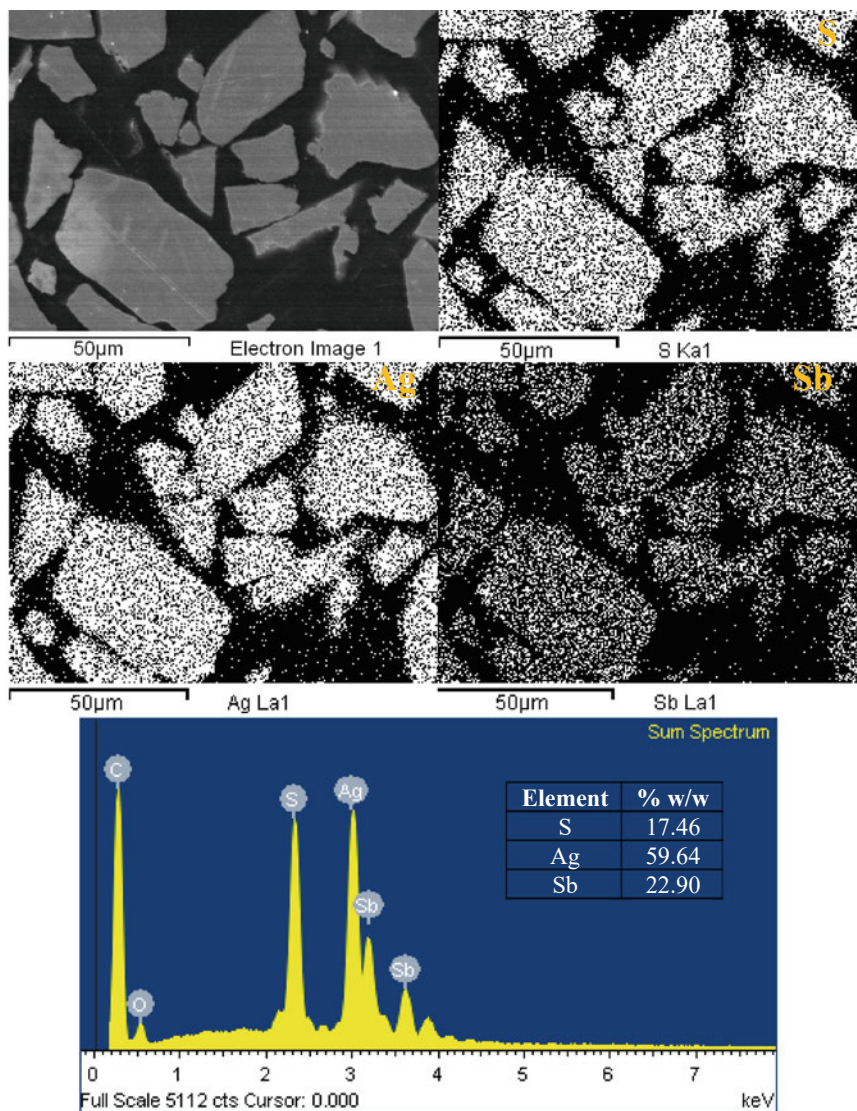


Fig. 1 SEM micrograph, elemental mapping, and energy dispersion microanalysis of pyrrargyrite

used for the flotation tests without collector, thus as the semi-quantitative chemical composition. Elongated sharp-edged particles are observed with a constituted semi-quantitative chemical composition of 17.46% w/w sulfur (S), 59.64% w/w silver (Ag), and 22.90% w/w antimony (Sb), oxygen is not quantified; however, it is detected in the EDS spectrum of Fig. 1.

Figure 2 shows the X-ray diffraction spectrum (XRD) of pyrrargyrite particles, identified with the Match software with the reference standard 96-101-1163 corresponding to pyrrargyrite with a trigonal crystal structure with hexagonal axes.

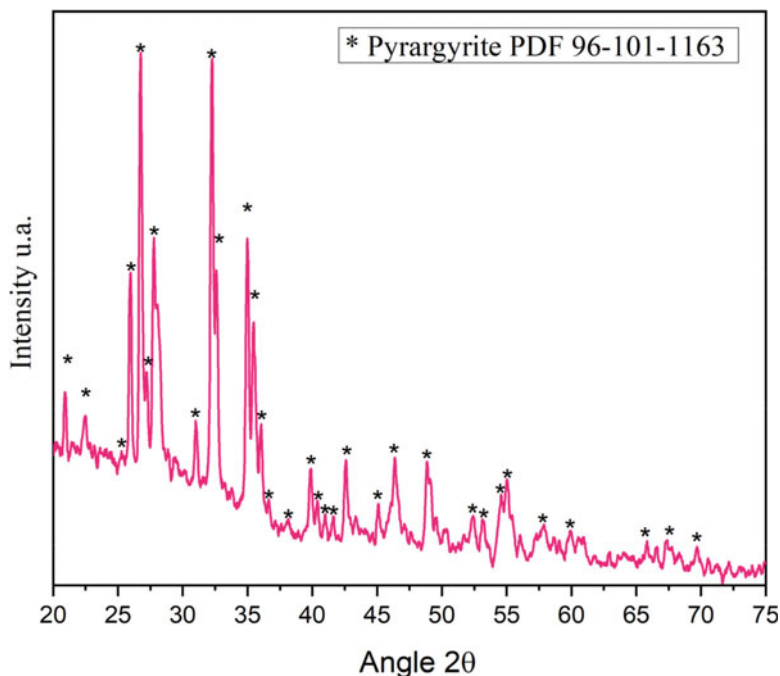


Fig. 2 X-ray diffraction spectrum (XRD) of pyrargyrite

Regarding the analysis of the particle size (APS) by laser diffraction of the pyrargyrite obtained in the final pulverized and which was used for the flotation tests, it indicates a mean population of 47.9 microns (μm).

Regarding the characterization by infrared spectroscopy of the pyrargyrite used for the flotation tests, it is presented in Fig. 3. Multiple absorption bands are observed derived from the surface alteration of the mineral during pulverized. The sulfur of pyrargyrite undergoes surface modification due to the division of the main sulfate band located 1200 cm^{-1} , into three absorption bands at 1001 , 1052 , and 1117 cm^{-1} indicating the formation of compounds of sulfur bonded to the metal in a monodentate way with three absorption bands.

While the bands at 537 , 610 , 658 , 797 , and 1405 cm^{-1} shown in Fig. 3 indicate the presence of surface bonds of Sb-O of the Sb_2O_3 compound. In 1630 cm^{-1} , the band assigned to the OH bond is found; this is due to the molecular absorption of water to the surface of the mineral. The band at 419 cm^{-1} may be attributed to the Sb_2S_3 bonds.

Figure 4 shows the behavior of the cumulative flotation % w/w of pyrargyrite as a function of pH, after 10 min of flotation. It should be remembered that flotation was carried out in the absence of a collector using only a frother concentration $[e]$ of 60 PPM, two zones are distinguished, when flotation is carried out at acidic pH (2, 2.54

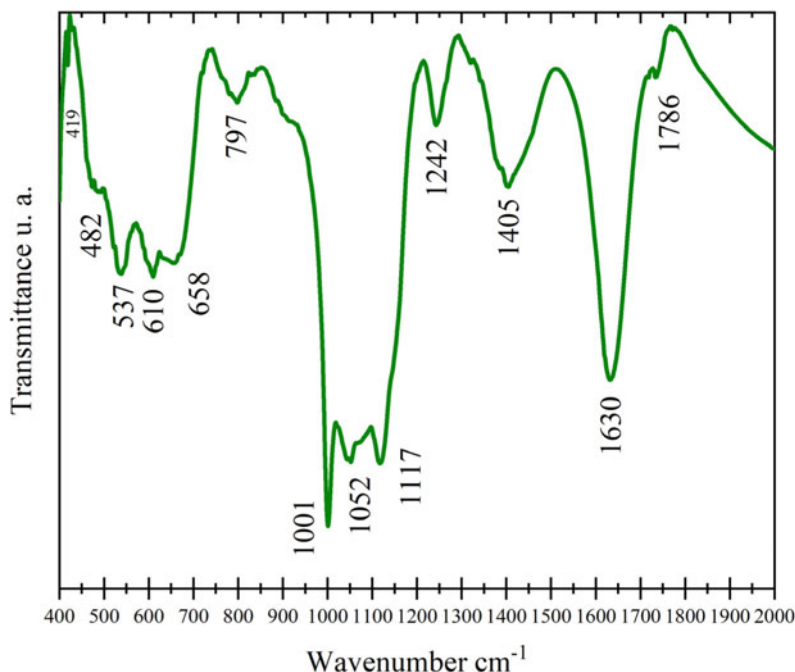


Fig. 3 Infrared spectrum of pyrrargyrite mineral

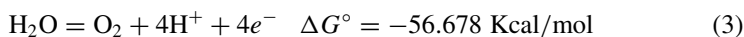
and 4.97) with efficiencies of recovery less than 58% w/w and when carried out at slightly acidic pH 6 and alkaline pH 10 with cumulative recoveries of 67% w/w.

This indicates that, under these chemical conditions at a pH greater than 6, the surface of the pyrrargyrite has greater hydrophobicity, verified with the greater separation achieved. Therefore, the pH of the pulp acts as a depressant medium for the surface of pyrrargyrite, decreasing the recovery at strongly acidic pH values, which leads to a reduction in the hydrophobicity of the mineral.

During the flotation tests, the pH value was measured. When the initial pH is very acidic (2 and 2.54), it practically remains unchanged at the end of the test. Meanwhile, when the collectorless flotation pH is 4.97 and 6.09 at the end of the tests, the pH of the pulp tends to increase, and this due to the generation of OH^- ions as indicated by reaction 2.



whereas when the initial pH is very alkaline (9 and 10) it tends to decrease at the conclusion of the flotation, and this is because of the decomposition of the water molecules into gaseous oxygen and hydrogen ion as it occurs in the reaction (3).



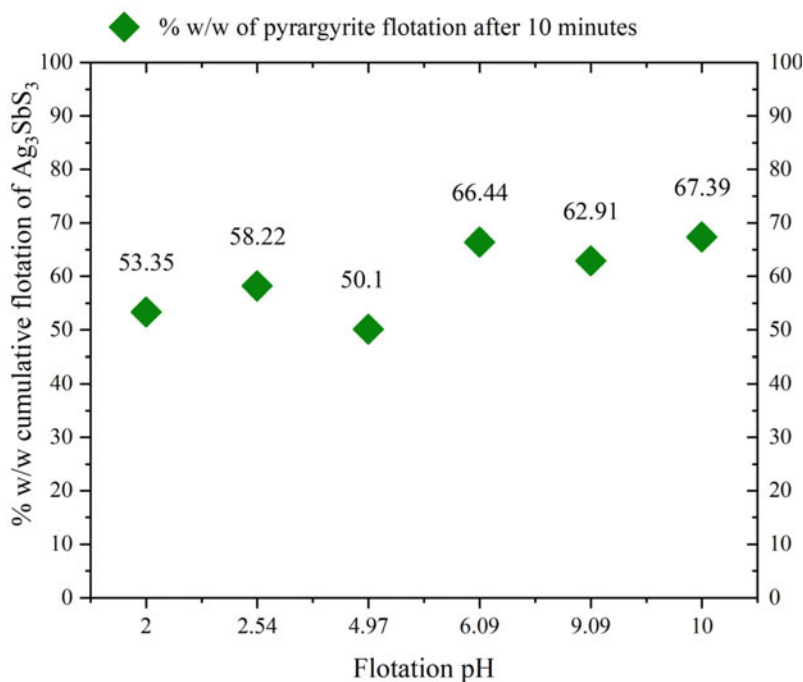


Fig. 4 % w/w cumulative flotation of pyrargyrite as a function of pH

Along with pH, the oxide reduction potential (ORP) mV is also monitored during conditioning and flotation. Pulp potential is an important parameter in flotation processes and together with pH they control the increase or decrease in flotation efficiency. For this research work of collectorless flotation of pyrargyrite, highly oxidizing potentials greater than +450 mV depress the mineral surface and decrease the percentage of flotation, while the optimal Eh where the maximum recovery of pyrargyrite occurs is at +100 mV.

To carry out the analysis of the surface of the pyrargyrite obtained in the flotation, the particles concentrated in 0.5 min of flotation were generally analyzed, and for this, an amount of 0.003 g was used mixed with 0.3 g of potassium bromide KBr-grade FTIR which were compressed into a tablet, which was placed in the equipment and the analysis was carried out. Figure 5 shows the spectra of the initial pyrargyrite without treatment and that obtained in 0.5 min of flotation at initial pH 9 and 10. It should be mentioned that the maximum separation efficiencies for these tests were 62% w/w and 67% w/w, respectively.

Similarity is observed in the absorption bands found for these tests; this is related to the little difference in the percentage of recovery obtained. The Sb–O bonds produced by the oxygenation of the pulp and the chemical conditions present multiple absorption bands located at 529, 595, 692, 777, and 1316 cm^{-1} , and some of these bands are not located in the spectrum of pyrargyrite floated at pH 9.

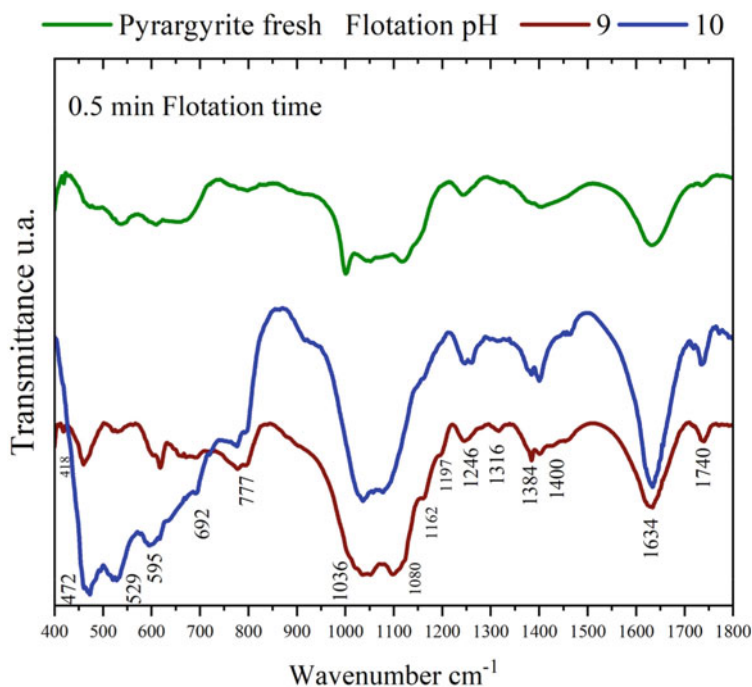


Fig. 5 IR Spectra of pyrrargyrite fresh and concentrated at 0.5 min pH 9 and 10

The bands located between 1000 and 1200 cm^{-1} correspond to the S–O bonds of the sulfate ion, and from Fig. 5 it is contemplated that the particles floating at pH 10 exhibit low intensity absorption bands, around 1036 and 1080 cm^{-1} , while for the pyrrargyrite floating at pH 9 and 0.5 min, the beginning of the division of the main band is presented, which indicates the formation of sulfate-type compounds coordinated with the metal, and the presence of three bands shows the metal coordinated with oxygen in a mono-toothed manner [11, 12] which as a first approximation can influence the decrease in flotation efficiency.

At 1634 cm^{-1} , the presence of water molecules bound to the mineral surface by the band corresponding to the hydroxyl ions OH^- was detected. It has been previously described in the literature that during flotation the hydration of the surfaces of sulfides, minerals are carried out due to the reaction of dissolved oxygen as indicated in Eq. 2 which leads to the formation of a variety of oxidized species leading to have a hydrophilic surface and affecting the success of flotation [13].

Conclusions

Collectorless flotation of pyrargyrite can be carried out over a wide range of pH and pulp potentials Eh . The optimum pH for flotation is greater than 6.0 and a 66.4% w/w of flotation is obtained with Eh of +287 mV. At pH 10 values there is a flotation efficiency of 67.4% w/w with Eh values of +100 mV. While at acidic flotation pH 2, 2.54 and 4.97 the cumulative recovery weight percentages are 53% w/w, 58% w/w, and 50% w/w, respectively, with pulp potentials of +345 mV, +476 mV, and +506 mV. The surface alteration, that is, the change from a mostly hydrophobic to a hydrophilic surface of the pyrargyrite analyzed by FTIR, indicated that the intensity of the binding bands of Sb–O, sulfate ion, and OH^- ions increases on the mineral surface. This formation of oxides and hydroxides and sulfates is greater on a hydrophilic surface, which negatively influences flotation efficiency.

Acknowledgements To the Autonomous University of the State of Hidalgo, to the PRODEP Teacher Professional Development Program, and to the National Polytechnic Institute ESIQIE.

References

1. Harlov DE, Sack RO (1995) Ag–Cu exchange equilibria between pyrargyrite, high-skinnerite, and polybasite solutions. *Geochim Cosmochim Acta* 59:867–874
2. García ME, Querol SF, Lowther GK (1991) Geology of the Fresnillo mining district, Zacatecas. In: Salas GP (ed) *Economic geology, Mexico, GSA DNAG*, vol 438, pp 383–394
3. Kostov I (1978) Sulphosalt minerals: crystal chemistry and morphology. *Krist Tech* 13(4):449–458
4. Sherif K, Stanislav J (2016) Raman spectroscopy of the Pb–Sb sulfosalts minerals: Boulangerite, jamesonite, robinsonite and zinkenite. *Vib Spectro* 85:157–166
5. František L, Jiří S, Michal D (2010) The role of silver in the crystal structure of pyrargyrite: single crystal X-ray diffraction study. *J Geosci* 55:161–167
6. Kutoglu A (1968) Die Struktur des Pyrostilpnits (Feuer blende) Ag_3SbS_3 . *Neu Jb Mineral Mh* 145–1160
7. Hayes RA, Ralston J (1988) The collectorless flotation and separation of sulphide minerals by Eh control. *Int J Miner Process* 23(1):55–84
8. Peng Y, Grano S (2010) Effect of grinding media on the activation of pyrite flotation. *Miner Eng* 23(8):600–605
9. Lekki J, Dryable J (1990) Flotometric analysis of the collectorless flotation of sulphide materials. *Colloids Surf* 44:179–190
10. Sajjad A, Seyed KM, Mahdi G (2015) Chemical and colloidal aspects of collectorless flotation behavior of sulfide and non-sulfide minerals, vol 225, pp 203–217
11. Nakamoto K (2008) *Infrared and Raman Spectra of inorganic and coordination compounds, theory and applications in inorganic chemistry*, 6th edn. Wiley, Hoboken, New Jersey
12. Reyes M (2013) Modificación superficial de mineral de pirita y precipitados de Hierro: comportamiento en medios acuosos y de molienda. Thesis doctoral, Morelia Michoacán México
13. Hidayet C, Cahit H, Taki G (2002) Collectorless flotation of lead and zinc sulphide from Dereköy ore deposit. *Physicochemical Probl Mineral Process* 36:197–208

The Elastic Constants Measurement in a Medical Ti–6Al–4V ELI Alloy by Using Ultrasonic Means



Hector Carreon and Maria Carreon-Garcidueñas

Abstract In this paper, we report the calculation of the elastic constants such as Poisson's ratio, elastic modulus, and shear modulus deduced from the ultrasonic propagating equations with two types of ultrasonic vibrations named longitudinal and transverse waves. The ultrasonic propagating velocity is measured at the microstructural evolution in a Ti–6Al–4V medical alloy with two varying microstructures, bimodal and acicular, respectively. The two different initial microstructures were treated thermally by aging at 515, 545, and 575 °C at different times from 1 min to 576 h to induce a precipitation process. Ultrasonic measurements of shear and longitudinal wave velocities, scanning electron microscopy (SEM) image processing, and microhardness were performed, establishing a direct correlation with the measurements of the ultrasonic velocity and the elastic properties developed during the thermal treatment of the artificial aging.

Keywords Elastic constants · Titanium alloys · Ultrasonic velocity

Introduction

Nowadays, many researchers are using ultrasonic nondestructive testing to evaluate the mechanical characteristics on metallic materials, mainly, due to its accuracy, besides being fast and very reliable. As we know, the ultrasonic detection methods are very popular in the medical inspection of the human body for a long time. Several researchers have focused on Young's modulus of the bone material or carotid artery measurement by using the ultrasonic technique [1, 2]. The use of the Ti–6Al–4V alloy in the biomaterial industry [3] has been accompanied by the need for further development of characterization techniques to determine the microstructure-property

H. Carreon (✉)

Instituto de Investigaciones Metalúrgicas, Edif. "U" C.U., 58000-888 Morelia, México
e-mail: hcarreon@umich.mx

M. Carreon-Garcidueñas

Facultad de Odontología, Estudios de Posgrado e Investigación (UMSNH-CUEPI), Morelia 58330, México

© The Minerals, Metals & Materials Society 2022

M. Zhang et al. (eds.), *Characterization of Minerals, Metals, and Materials 2022*,

The Minerals, Metals & Materials Series,

https://doi.org/10.1007/978-3-030-92373-0_45

relations in this metallic alloy. It is also of main importance to study the phase transformations that occur during processing in order to design microstructures that possess excellent properties specific to these applications. When the Ti–6Al–4V alloy is over-aged at 500–600 °C, nanometer-sized phases such as α_2 (Ti₃Al) can be homogeneously precipitated in the titanium alloy matrix, leading to enhance the mechanical properties of the metallic material [4]. On the other hand, the study of ultrasonic wave propagation in metals gives information on the microstructure, mechanical and physical properties of the material. The quantitative assessment of microstructural changes and properties can be carried out through the measurement of ultrasonic parameters such as attenuation and velocity [5]. The ultrasonic wave velocity depends on the elastic constants and density of the body while ultrasonic wave attenuation depends on microstructure and crystalline defects [6–8]. In the present research study, we applied the contact pulse-echo ultrasonic technique using a buffer media to measure the ultrasonic velocity of the Ti–6Al–4V alloy artificially aged. Combined with the theory of the ultrasonic propagating equations in a solid media, the effect of the two microstructures (bimodal and acicular) on the ultrasonic velocity at different aging conditions was discussed.

Experimental Procedure

The material used in this study was a Ti–6Al–4V ELI alloy plate (thickness: 6.76 mm) and its exact chemical composition is 6.10Al–3.93V–0.17Fe–0.18O–0.009C–0.005N–0.002H–Ti (wt%). This alloy plate was subjected to different heat treatments to get acicular and bimodal microstructures. The acicular microstructure was obtained by holding the material at 1020 °C for 20 min (above the β transformation temperature) followed by furnace cooling. The bimodal microstructure was obtained by holding at 950 °C ($\alpha + \beta$ region), for 1 h followed by water cooling/quenching. These two microstructures were over-aged at 515, 545, and 575 °C for different aging times ranging from 1 min to 576 h to promote the formation of very fine α_2 (Ti₃Al) precipitates. For SEM inspection, heat-treated specimens were mounted in Bakelite, ground and polished down to 1 μ m diamond cloth. Microstructural features were unveiled using Kroll's reagent (H₂O 100 ml, HF 100 ml, HNO₃ 100 ml). The size and volume fraction of each phase were measured using an image analyzer. To evaluate microhardness variations amongst the samples, Vickers hardness measurements were performed by applying a load of 500 g for 30 s on selected samples. Ultrasonic compressional and transverse velocities were determined by measuring the time taken for the ultrasonic waves to travel through the titanium samples. Figure 1 illustrates a schematic diagram of the ultrasonic measurements. A longitudinal-broadband transducer (Aerotech) with a central frequency of 10 MHz and diameter element size of 6 mm was used to generate compressional ultrasonic waves. A shear-broadband transducer (Aerotech) with a central frequency of 5 MHz and diameter element size of 12 mm was used to generate transverse ultrasonic waves. In order to avoid the non-uniform amplitude in the near field of transducer, a buffer

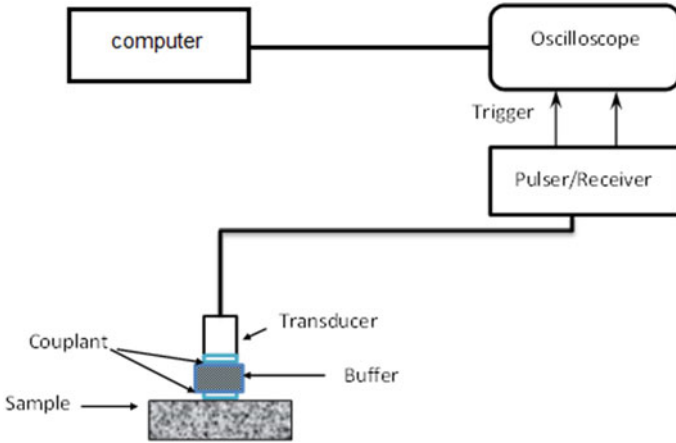


Fig. 1 Experimental set up for the velocity ultrasonic measurements

rod (fused silica) was employed to provide time delay between the excitation pulse and echoes returning from the measured simple [9]. The ultrasonic transducer was mounted on the specimen and excited by a Panametrics 5072PR broadband pulser-receiver. The ultrasonic signal was digitized and averaged by a LeCroy Wavesurfer 432 oscilloscope and then sent to the computer for further processing.

As we know, the wave propagating equation can be expressed as follows:

$$\frac{\partial^2 u}{\partial t^2} = C_c^2 \frac{\partial^2 u}{\partial x^2} \tag{1}$$

Thus, the propagating velocity of the ultrasonic longitudinal wave denoted as C_C is expressed as

$$C_c^2 = \frac{\lambda + 2G}{\rho} = \frac{E(1 - \mu)}{(1 + \mu)(1 - 2\mu)\rho} \tag{2}$$

When the propagating elastic wave is an ultrasonic transverse wave. The wave propagating equation can be simplified similarly as

$$\frac{\partial^2 v}{\partial t^2} = C_s^2 \frac{\partial^2 v}{\partial x^2} \tag{3}$$

So, the propagating velocity of the ultrasonic transverse wave denoted as C_S is expressed as

$$C_s^2 = \frac{G}{\rho} = \frac{E}{2(1 + \mu)\rho} \tag{4}$$

Combining Eqs. (2) and (4), the elastic constants of the detected material can be deduced by

$$\mu = \frac{1 - 2(C_C/C_S)^2}{2 - 2(C_C/C_S)^2} \quad (5)$$

$$E = \frac{C_C^2 \rho (1 + \mu)(1 - 2\mu)}{(1 - \mu)} \quad (6)$$

$$G = C_S^2 \rho \quad (7)$$

where E is Young's modulus (GPa), G is the shear modulus (GPa), μ is Poisson ratio, C_C is the compressional velocity (m/s), C_S is the transverse velocity (m/s), and ρ is the density of the sample (g/cm^3). From these equations, it is found that the elastic constants can be calculated after getting the elastic wave propagating velocities and the material density in two varying medical Ti–6Al–4V ELI alloy microstructures.

Experimental Procedure

Figure 2 shows the SEM micrographs of the acicular and bimodal microstructures. In the acicular microstructure, α phase grains (black/dark) have been developed along prior β grain boundaries (white/bright) and colonies of lath-type β and α lamellar structure are observed inside prior β grains (Fig. 2a). The colony size, thickness of α/β platelets, volume fraction of α phase, and volume fraction of β phase were measured to be 973 μm , 5 μm , 56% and 44%, respectively. The bimodal microstructure consists of equiaxed α grains (black/dark) and tempered martensite with a small amount of residual β (white/bright). The α grain size was measured to be 10 μm , and volume fractions of tempered martensite, α , and β were measured to be 52, 40,

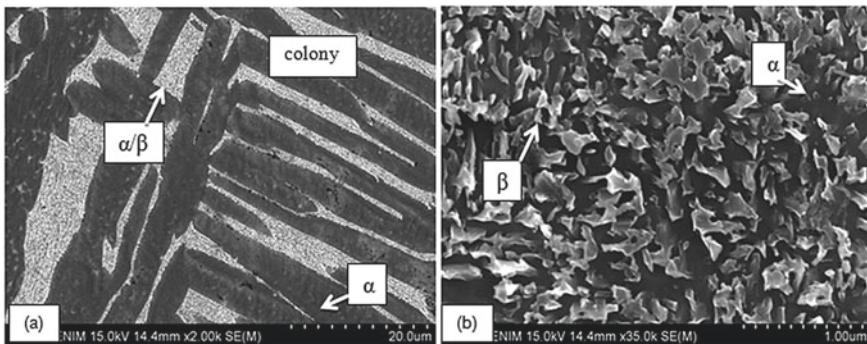


Fig. 2 SEM micrographs of the a acicular and b bimodal microstructures

and 8%, respectively, as shown in Fig. 2b. An understanding of the two Ti-6Al-4V ELI microstructures is essential to interpret the results of the ultrasonic velocities and elastic constant data. There are some differences in the high-magnification SEM micrographs of the aged acicular and bimodal microstructures as shown in Figs. 3 and 4. Fine α_2 phases of 50–200 nm in size are homogeneously distributed in the α (black/dark) phases in the acicular microstructure, see Fig. 3. In addition, in the acicular microstructure, the platelet size increases in size significantly with the ageing and, thus, a higher number density of nucleation sites available for the α_2 precipitates to be formed (Fig. 3a, b). On the other hand, Fig. 4 also shows that the amount of precipitates increases with respect to the aging time for the bimodal microstructure. Figure 4a correspond to an aging time of 144 h in which the presence of α_2 precipitates was observed in the grain boundaries of α (black/dark) phase. The size and morphology of the intermetallic precipitates α_2 remain constant. For the aging time at 576 h, these α_2 precipitates are found in a greater number, being located mainly

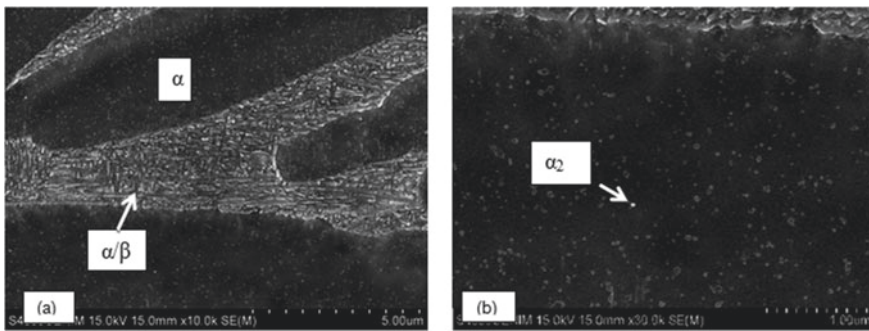


Fig. 3 SEM micrographs of the over-aged acicular microstructure at 30000X for 575 °C by different aging times **a** 144 h and **b** 576 h, showing very fine α_2 phases homogeneously distributed in the α phase

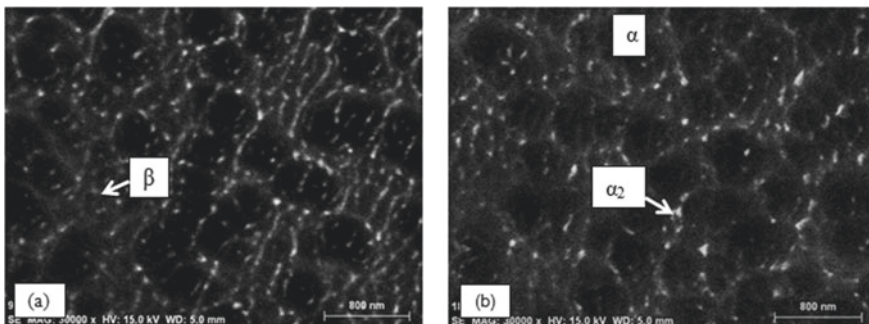


Fig. 4 SEM micrographs of the over-aged bimodal microstructure at 30000X for 575 °C by different aging times **a** 144 h and **b** 576 h, showing very fine α_2 phases homogeneously distributed in the α phase

in large groups (clusters) within the α matrix, as shown in Fig. 4b. The precipitation of these α_2 (Ti_3Al) nanoparticles induces hardening of the Ti–6Al–4V matrix.

Figure 5 shows the variation of Vickers microhardness in the two initial medical Ti–6Al–4V ELI microstructures: acicular and bimodal as a function of different aging times at 515, 545, and 575 °C. The microhardness of the bimodal microstructure is higher than that of the acicular microstructure. This is probably the result of having the presence of a huge volume fraction of the tempered martensite in the bimodal microstructure. The microhardness results of the medical Ti–6Al–4V ELI alloy show an important tendency to increase in the early aging times at both microstructures. This phenomena is attributed to the precipitation of α_2 (Ti_3Al) particles inside the α phase. This is the result of having a greater volume fraction of the α -phase after aging in both microstructure and, thus, a higher number density of nucleation sites available for the α_2 precipitates to be formed. The precipitation of these nanoparticles occurs mainly in the boundary and within the α phase, resulting in an increment of microhardness values. After 300 h, the hardness data tends to remain constant with increasing the aging time due to the thickening of the α/β platelets (acicular) and α grains (bimodal) at expense of the precipitates of smaller sizes.

Figure 6 shows the variations on the young and shear modulus in the acicular and bimodal microstructures with different aging parameters at the medical Ti–Al–4V ELI alloy. Young's and shear modulus were calculated from Eqs. (6) and (7), respectively, by using the diffraction correction of the ultrasonic compressional and transverse velocities, $\rho = 4.43 \text{ g/cm}^3$ and $\mu = 0.31$. Young's modulus of the bimodal microstructure is higher than that of the acicular microstructure as shown in Fig. 5a. Young's modulus of the bimodal microstructure is higher than that of the acicular microstructure as shown in Fig. 5b. In general, the ultrasonic velocities were found to be lower in coarse grain medium [5]. In the acicular microstructure, the α grains have different orientations from each other (Fig. 2). Strong preference orientation of

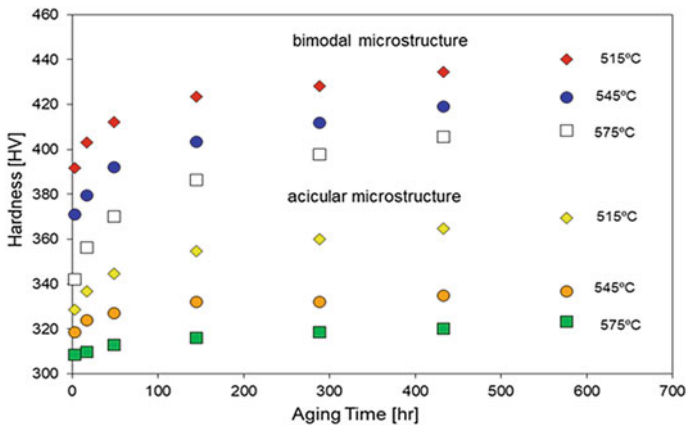


Fig. 5 Hardness measurements in the acicular and bimodal microstructures with different aging parameters in a medical Ti–Al–4V ELI alloy

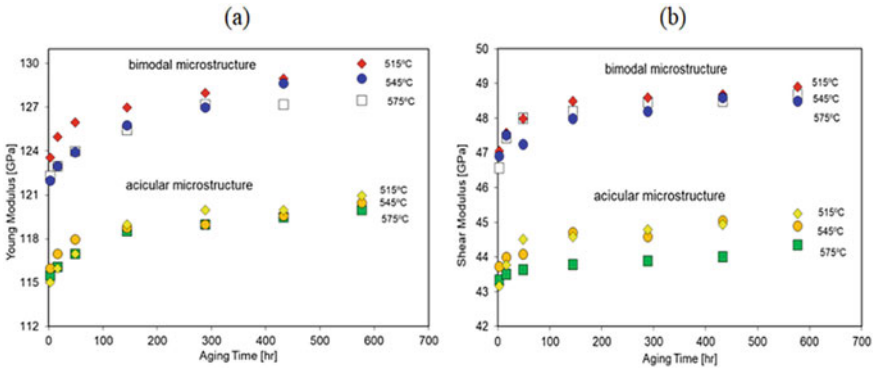


Fig. 6 Influence of the artificial aging in a medical Ti–Al–4V ELI alloy on the **a** Young modulus and **b** shear modulus with different microstructures

these α grains increases the morphological anisotropy (acicular) while equiaxed α grains (bimodal) decrease it. Due to the inverse relation between ultrasonic velocity and density, increasing in the ultrasonic velocity must be related to increase Young's and shear modulus.

From these results, it is evident that the ultrasonic velocity is very sensitive to the stages of the precipitation process in both Ti–6Al–4V ELI microstructures at different aging conditions. This is attributed to the fact that the ultrasonic velocities depend on Poisson's ratio of the material, which are very sensitive to any phase transformation and degree of morphological anisotropy [10]. The first stage of the precipitation (i.e., incubation) influences Poisson's ratio of the material and in turn the compressional and transverse ultrasonic velocities. The depletion of the precipitate-forming elements from the matrix induced by aging leads to a decrease in Poisson's ratio of at the bimodal medical Ti–6Al–4V ELI alloy microstructures as it is shown in Fig. 7.

Conclusions

The precipitation behavior in two varying medical Ti–6Al–4V ELI alloy microstructures (acicular and bimodal) has been studied using microscopy and ultrasonic techniques. The study clearly revealed that the changes of the ultrasonic compressional and transverse velocities arises mainly from the contrasting in the elastic properties of α and β phases which are affected by the degree of lattice distortion and misorientation. The ultrasonic compressional and transverse velocities are more sensitive to the initiation of the precipitation, whereas the influence of precipitation on hardness can be felt only after the precipitates attain a minimum size to influence the movement of dislocations. These observations are consistent with the electron microscopy studies. Finally, the proposed ultrasonic nondestructive method can be used for

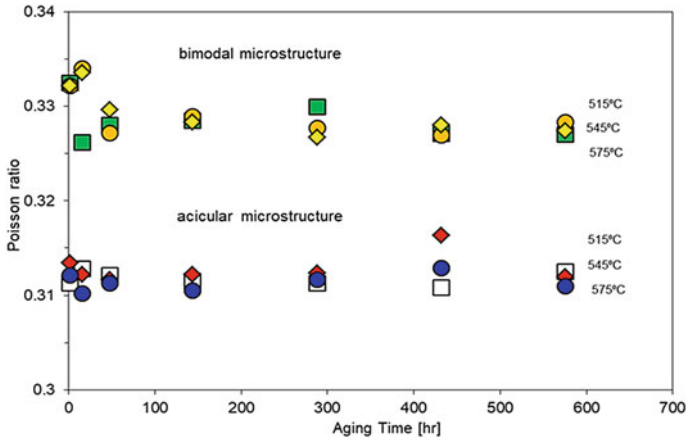


Fig. 7 Influence of the artificial aging in a medical Ti–Al–4V ELI alloy on the Poisson ratio with different microstructures

the metal material's elastic constants measurement. Based on the velocity extraction of the ultrasonic longitudinal wave and transverse wave, the elastic constants can be calculated in two varying medical Ti–6Al–4V ELI alloy microstructures conveniently.

Acknowledgements This work was partially funded from PRODEP-SEP (UMSNH-CA-140) and CIC-UMSNH.

References

1. Rho JY, Ashman RB, Turner H (1993) Young's modulus of trabecular and cortical bone material: ultrasonic and micro-tensile measurements. *J Biomech* 26:111–119
2. Riley WA, Barnes RW, Evans GW, Burke GL (1992) Ultrasonic measurement of the elastic modulus of the common carotid artery: the atherosclerosis risk in communities (ARIC) study. *Stroke* 23:952–956
3. Toyras J, Lyyra-Laitinen T, Niinimäki M (2001) Estimation of the Young's modulus of articular cartilage using an arthroscopic indentation instrument and ultrasonic measurement of tissue thickness. *J Biomech* 34:251–256
4. Carreon H, Carreon M, Dueñas A (2017) Assessment of precipitates of aged Ti-6Al-4V alloy by ultrasonic attenuation. *Philos Mag* 97:58–68
5. Rosen M, Ives L (1985) An investigation of the precipitation-hardening process in aluminium alloy 2219 by means of sound wave velocity and ultrasonic attenuation. *Mater Sci Eng* 74:1–10
6. Ping H (1998) Determination of ultrasonic parameters based on attenuation and dispersion measurements ultrasonic imaging, vol 20, pp 275–280
7. Bouda BA, Benchaala A, Alem K (2000) Ultrasonic characterization of materials hardness. *Ultrasonic* 38:224–227
8. Palanichamy P, Vasudevan M, Jayakumar T, Venugopal S, Raj B (2002) Ultrasonic velocity measurements for characterizing the annealing behaviour of cold worked austenitic stainless steel. *NDT&E Int* 33:253–259

9. Papadakis EP (1966) Ultrasonic diffraction loss and phase change in anisotropic materials. *J Acoust Soc Am* 40:863–876
10. Anish K, Jayakumar T, Baldev R (2006) Influence of precipitation of intermetallics on Young's modulus in nickel and zirconium base alloys. *Phil Mag Lett* 86:579–587

Use of Glass Waste as a Geopolymerization Reaction Activator for Ceramic Materials



A. R. G. Azevedo, M. T. Marvila, L. B. Oliveira, D. Cecchin, P. R. Matos,
G. C. Xavier, C. M. Vieira, and S. N. Monteiro

Abstract Geopolymeric materials have been widely studied due to technological and environmental advantages, which in the case of applications in ceramic materials is due to the non-need for sintering the parts. The objective of this work was to evaluate the potential of using the glass polishing residue as a constituent element of the activating solution, together with NaOH, in geopolymerization reactions, aiming at the production of ceramic artifacts. Specimens were submitted with thermal curing at 60 °C and ambient temperature of 23 °C with ratio to SiO₂/Al₂O₃ of 3 and 4. The prepared specimen was evaluated of technological properties such as apparent specific mass, linear shrinkage, water absorption, and mechanical resistance to flexion in the specimens. The results showed a potential for application of the glass polishing residue as a component of the alkaline solution, improving the properties evaluated when in thermal curing and with a SiO₂/Al₂O₃ ratio of 4.0.

Keywords Glass waste · Geopolymer · Ceramic materials

A. R. G. Azevedo (✉) · G. C. Xavier

LECIV—Civil Engineering Laboratory, UENF—State University of the Northern Rio de Janeiro, Av. Alberto Lamego, 2000, Campos dos Goytacazes, Rio de Janeiro 28013-602, Brazil

G. C. Xavier

e-mail: gxavier@uenf.br

M. T. Marvila · L. B. Oliveira · C. M. Vieira

LAMAV—Advanced Materials Laboratory, UENF—State University of the Northern Rio de Janeiro, Av. Alberto Lamego, 2000, Campos dos Goytacazes, Rio de Janeiro 28013-602, Brazil
e-mail: vieira@uenf.br

D. Cecchin

TER—Department of Agricultural Engineering and Environment, UFF—Federal Fluminense University, Rua Passo da Pátria, 341, Niterói, Rio de Janeiro 24210240, Brazil

P. R. Matos

Coordenadoria Acadêmica, UFSM—Federal University of Santa Maria, Rodovia Taufik Germano, 3013, Cachoeira do Sul, Rio Grande do Sul 96503-205, Brazil

S. N. Monteiro

Department of Materials Science, IME—Military Institute of Engineering, Square General Tibúrcio, 80, Rio de Janeiro 22290-270, Brazil

© The Minerals, Metals & Materials Society 2022

M. Zhang et al. (eds.), *Characterization of Minerals, Metals, and Materials 2022*,

The Minerals, Metals & Materials Series,

https://doi.org/10.1007/978-3-030-92373-0_46

Introduction

Knowing the wide use of binding materials, in other words, those that have binding properties and that on contact with water or solution form a paste capable of hardening by simple drying [1, 2], materials such as geopolymers are generated. These are basically a material with high initial mechanical resistance and resistant to attack by acids, sulfates, fire, and ice/thaw cycles [3].

Geopolymers, unlike traditional binders, are alkaline activated materials. Alkaline activation is the synthesis reaction of geopolymers, generalizing, as a hydration reaction of aluminum silicates present in the mixture. This reaction consists of the release of Si and Al, when it comes to kaolinitic precursors, where the highly alkaline medium is necessary, aiming at the formation and stabilization of the new molecular structure of the material [4].

In addition to showing great potential for alternative material to Portland cement, geopolymers are also able to behave like ceramic materials without the need to expose the artifacts to high temperatures, which is a determining factor in the final quality of the ceramic. Thus, instabilities during the burning process of the material directly imply the conformity and regularization of the obtained product. Sometimes maintaining these temperatures can become economically unviable measures [5].

This work seeks to develop a material with properties similar to conventional ceramics, from the application of known techniques of geopolymerization, as well as the improvement of its performance with the incorporation of glass polishing waste, as a constituent material of the activating solution responsible for the alkaline activation reactions.

Glass is a material that is easy to manufacture and abundant, since its composition is predominantly in sand, which in turn is rich in silica, around 72% [6]. Silicate-based activators promote the acceleration of geopolymerization reactions, and this is due to the fact that silica initiates the reaction with the solution's free alumina. The silicate acts in favor of the polymerization process, culminating in a product with a greater amount of Si and, consequently, with greater mechanical resistance [4]. Thus, the glass polishing waste has great potential to achieve the objectives proposed by this work.

Materials and Methods

The paste developed during the research was made from the mixture of the commercial metakaolin of the HP ultra-brand, acting as a precursor material, together with the alkaline solution, acting as an activating material, composed of sodium hydroxide (NaOH), polishing glass waste, and water, with quantity supplied as proposed by means of standard NBR 13276 [7] issued by the Brazilian Association of Technical Standards (ABNT).

The glass waste incorporated into the alkaline solution comes from the lapidation process of flat glass. Obtained from the sludge produced during the process, after drying it becomes solid and petrifies. Thus, for its proper application it was necessary to grind the material in a ball mill. That done, the material was placed in an oven at a temperature close to 105 °C, until it reached a constant mass [5]. Then, finally, it was sieved through the number 40 and 200 sieves, with openings of 0.42 mm and 0.074 mm, respectively.

Samples with SiO₂/Al₂O₃ molar ratios fixed at 3.0 and 4.0 were manually made, whereupon they were sent to a thermal and conventional curing process, at 60 and 23 °C, respectively. Thus, they were tested according to water absorption tests, apparent specific mass, linear retraction, and mechanical resistance to flexion [8].

The water absorption test was carried out after 7 days after molding. The specimens are weighed, still dry, and with the aid of a digital scale to then be immersed in water, where they remain for another 24 h. That done, the specimens are weighed again, now saturated. In this way, it was possible to calculate the water absorption rate as shown in Eq. 1.

$$WA = \left(\frac{M_{\text{saturated}} - M_{\text{dry}}}{M_{\text{dry}}} \right) \times 100 \quad (1)$$

where

WA water absorption;
 $M_{\text{saturated}}$ saturated mass; and
 M_{dry} dry mass.

The process previously exposed also allows us to calculate the apparent specific mass of the material if the mass of the specimen immersed in water is collected, that is, through Eq. 2.

$$SM = \left(\frac{M_{\text{dry}}}{M_{\text{saturated}} - M_{\text{immersed}}} \right) \quad (2)$$

where

SM apparent specific mass;
 M_{dry} dry mass;
 $M_{\text{saturated}}$ saturated mass; and
 M_{immersed} immersed mass.

In order to determine the linear retraction rate of the material, with the aid of a digital caliper, the largest measure of the dimensions of the specimen is collected after demolding and the curing period has elapsed, in this case, 7 days. Thus, the relationship between the initial length and the final length allows us to calculate the rate, using Eq. 3.

$$R_l = \left(\frac{L_i - L_f}{L_i} \right) \times 100 \quad (3)$$

where

R_l linear retraction;
 L_i initial length; and
 L_f final length.

Finally, to obtain the flexural resistance of the masses, they were placed on supports, with conventional distances where they were subjected to the flexing effort, with controlled loading speed, by means of a hydraulic press under the region without the supports. In this way, with the data collected from the test, it is possible to calculate, in MPa, the flexural strength of the paste, using Eq. 4 [8].

$$R_f = \left(\frac{1,50 \times L \times F}{b \times h^2} \right) \quad (4)$$

where

R_f mechanical strength to flexion (MPa);
 L distance between the supports;
 F supported tension by the specimens;
 b base measurement of the specimens; and
 h height of the specimens.

Result

Figure 1 shows the results of the water absorption test performed on the samples. As expected, there is a general tendency to reduce absorption rates as the $\text{SiO}_2/\text{Al}_2\text{O}_3$ molar ratio increases. Therefore, the molar ratio samples 4.0 present more coherent results. Making a parallel between the samples, those that were subjected to thermal curing, presented higher absorption rates, thus, in this aspect, conventional curing at room temperature became more effective and pertinent [9]. Therefore, the best result was of composition 4.0 submitted to curing at room temperature, reaching around 1.37% of water absorption rate [10].

The results obtained by the apparent specific mass test of the pastes are shown in Fig. 2. It can be seen that, as in the previous test, the molar ratio has a ratio inversely proportional to the apparent specific mass, given in g/cm^3 . Therefore, the most coherent would be to adopt the composition 3.0, which has a higher specific mass, which implies a less porous and mechanically more resistant material [11, 12]. The samples submitted to thermal curing showed higher values of specific mass when compared to the samples that were cured at room temperature, reaching around $1.75 \text{ g}/\text{cm}^3$, while the others were around $1.49 \text{ g}/\text{cm}^3$ [13].

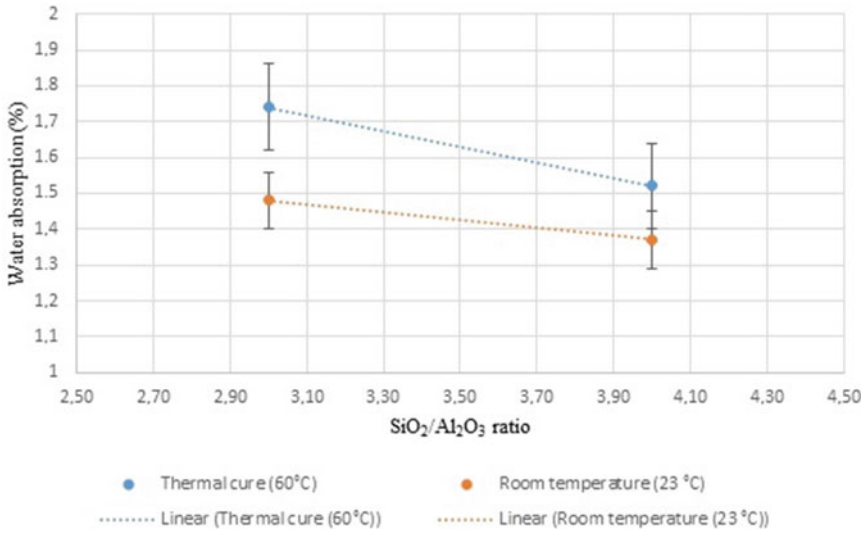


Fig. 1 Result of the water absorption test

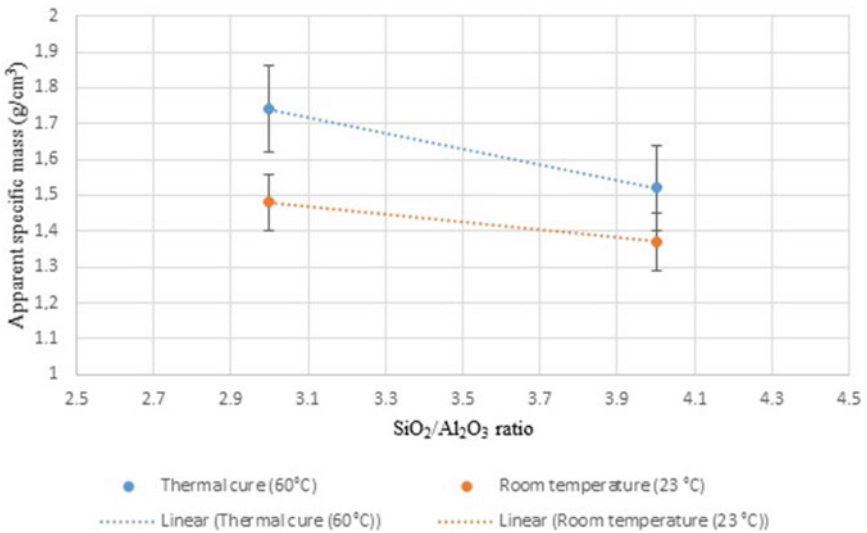


Fig. 2 Result of the apparent specific mass test

The results of the linear retraction tests can be seen in Fig. 3. This shows us a trend of decreasing linear retraction as the SiO₂/Al₂O₃ molar ratio increases. It is also possible to notice that the thermal cure increased the rates of linear shrinkage, which differs from the behavior desired by this work [14, 15].

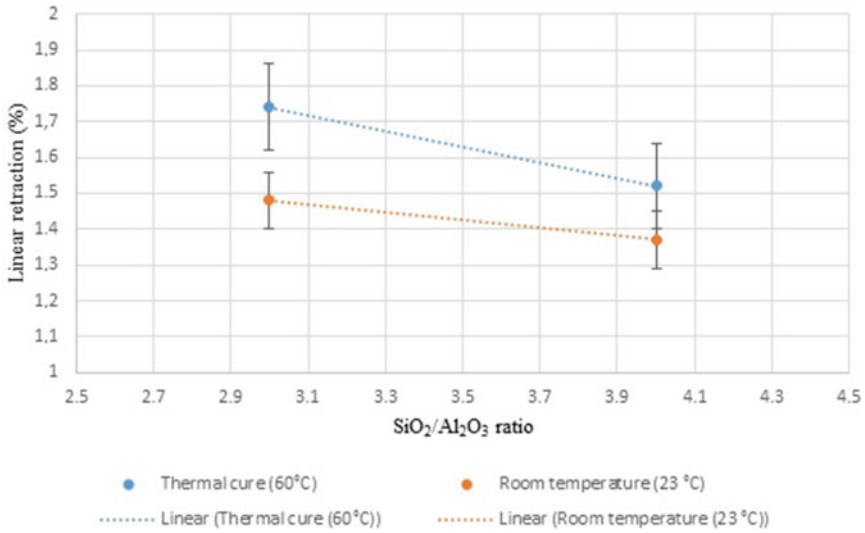


Fig. 3 Result of linear retraction test

Figure 4 refers to the results of the flexural strength test to which the samples were submitted. The curves plotted in the graph show us that the samples of composition 3,0 achieved higher resistances, as well as those that were subjected to thermal curing, these being the most coherent results according to the desired, reaching around 1.75 MPa [16–18].

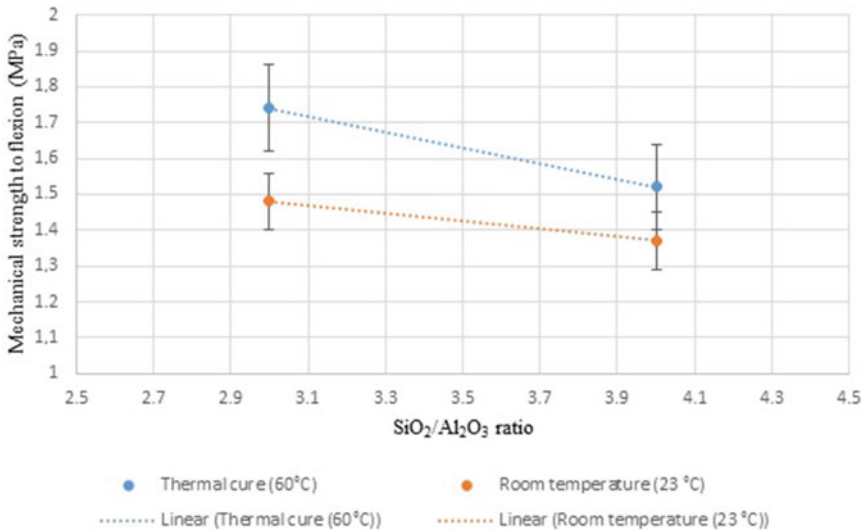


Fig. 4 Results of the mechanical strength to flexion tests

Conclusion

In this work, we sought to develop a material with properties and characteristics similar to ceramics, based on the knowledge subsequently obtained on geopolymerization techniques. Samples of molar ratio $\text{SiO}_2/\text{Al}_2\text{O}_3$ agreed on 3.0 and 4.0 were developed, which were applied with thermal curing, at 60°C and conventional curing at room temperature, 23°C , to then be tested according to the proposed tests, where it can be concluded that:

- The samples submitted to thermal curing presented more satisfactory results in the tests of apparent specific mass and, consequently, in the mechanical resistance to flexion, since a high specific mass index provides us with a less porous material. In addition, it was observed that among the compositions, the one with the best performance was the one with the lowest molar ratio, in this case, 3.0. This would be the most coherent option for the development of ceramic blocks, for example.
- The samples that passed through the curing period at room temperature, on the other hand, behaved more consistently in the water absorption and linear shrinkage tests. It was also noted that the samples of composition 4.0 obtained the best performances when compared to samples of smaller molar ratios and would be more viable choices for the development of ceramic tiles.

Acknowledgements The authors thank the Brazilian agencies: CNPq, CAPES, and FAPERJ for the support provided to this investigation.

References

1. Aires EKS (2019) Sustainability in civil construction: the case of a popular standard residence. Monography—UNINOVAFAPI University Center, Teresina (in Portuguese)
2. Hagemann SE (2011) Handout of basic building materials. Universidade Aberta do Brasil and Federal Institute Sul-rio-grandense. Available at: http://tics.ifsul.edu.br/matriz/conteudo/disciplinas/_pdf/apostila_mcb.pdf (in Portuguese)
3. de Azevedo AGS, Strecker K, Lombardi CT (2018) Production of geopolymers based on metakaolin and red ceramic. *Cerâmica (São Paulo)* 64(371):388–396. <https://doi.org/10.1590/0366-69132018643712420> (in Portuguese)
4. Severo C, Costa D, Bezerra I, Menezes R, Neves G (2014) Characteristics, peculiarities and scientific principles of alkaline activated materials. *Electr J Mater Processes South Am* 8(8):03 (in Portuguese)
5. Azevedo ARG, de Alexandre JIS, Zanelato E, Marvila MT, Cerqueira N (2017) Influence of the burning temperature on red ceramic articles, pp 258–263. <https://doi.org/10.5151/1516-392X-30162> (in Portuguese)
6. Civil Construction Materials and Materials Science and Engineering Principles—IBRACON (2010) Editor: Geraldo Cechella Isaia. Chapter 29: Portland Cement Concrete. Paulo Helene, Tibério Andrade (in Portuguese)
7. NBR. 13276 (2016) Mortar for laying and cladding walls and ceilings—determination of the consistency index. Brazilian Association of Technical Standards (in Portuguese)

8. Azevedo ARG, Vieira CMF, Ferreira WM, Faria KCP, Pedroti LG, Mendes BC (2020) Potential use of ceramic waste as precursor in the geopolymerization reaction for the production of ceramic roof tiles. *J Build Eng* 29(1):101–156
9. de Azevedo ARG, Alexandre J, Zanelato EB, Marvila MT (2017) Influence of incorporation of glass waste on the rheological properties of adhesive mortar. *Constr Build Mater* 148:359–368
10. de Azevedo ARG, Alexandre J, Marvila MT, Xavier GC, Monteiro SN, Pedroti LG (2020) Technological and environmental comparative of the processing of primary sludge waste from paper industry for mortar. *J Cleaner Prod* 32
11. Marvila MT, Azevedo ARG, Cecchin D, Costa J, Xavier GC, Carmo DF, Monteiro SN (2020) Durability of coating mortars containing açai fibers. *Case Stud Constr Mater* 13:10–21
12. De Azevedo ARG, Marvila MT, Rocha HA, Cruz LR, Vieira CM (2020) Use of glass polishing waste in the development of ecological ceramic roof tiles by the geopolymerization process. *Int J Appl Ceram Technol*
13. Oliveira PS, Antunes MLP, da Cruz NC, Rangel EC, de Azevedo ARG, Durrant SF (2020) Use of waste collected from wind turbine blade production as an eco-friendly ingredient in mortars for civil construction. *J Cleaner Prod* 274
14. Marvila MT, Azevedo ARG, Delaqua GCG, Mendes BC, Pedroti LG, Vieira CMF (2021) Performance of geopolymer tiles in high temperature and saturation conditions. *Constr Build Mater* 286:256–280
15. Marvila MT, de Azevedo ARG, de Matos PR, Monteiro SN, Vieira CMF (2021) Rheological and the fresh state properties of alkali-activated mortars by blast furnace slag. *Materials* 14(8):52–68
16. Azevedo A, De Matos P, Marvila M, Sakata R, Silvestro L, Gleize P, De Brito J (2021) Rheology, hydration, and microstructure of portland cement pastes produced with ground açai fibers. *Appl Sci (Switzerland)* 11(7):15–26
17. Mendes BC, Pedroti LG, Vieira CMF, Marvila M, Azevedo ARG, Franco de Carvalho JM, Ribeiro JCL (2021) Application of eco-friendly alternative activators in alkali-activated materials: a review. *J Build Eng* 35:136–145
18. de Azevedo ARG, Marvila MT, Barbosa de Oliveira L, Macario Ferreira W, Colorado H, Rainho Teixeira S, Mauricio Fontes Vieira C (2021) Circular economy and durability in geopolymers ceramics pieces obtained from glass polishing waste. *Int J Appl Ceram Technol* 25:56–62

Author Index

A

Adejo, A. O., 47
Alexandre, J., 247, 295, 349
Anashkina, Natalia E., 219
Andrade, Igor Klaus R., 381
Aniko, S. O., 101
Anyagou, D. I., 101
Aparicio-Durán, Abdon R., 155
Asphaug, Erik, 17
Ayomanor, B. O., 101
Azevedo, A. R. G., 39, 229, 239, 247, 267,
277, 287, 295, 315, 323, 349, 421,
473

B

Barrientos-Hernández, F. R., 443
Beas, Elia Palacios, 411, 431, 453
Braga, M. F., 421
Brainer, J. G. F., 267
Bunin, Igor Zh., 219

C

Campos, L. M., 287
Cao, Jiang, 81
Carreon-Garcidueñas, Maria, 463
Carreon, Hector, 463
Carvalho Veloso Moura de, Hellen Regina,
369
Castilho, E. D. F., 229, 277, 287, 315, 421
Cecchin, D., 473
Cerqueira, N. A., 323
Chattopadhyay, Aditi, 17
Chen, Dalin, 113
Chen, Guoju, 81

Chen, Jingbo, 163
Chica, Edwin, 341
Cobos-Murcia, José A., 207
Colorado, Henry A., 247, 341
Cotto-Figueroa, Desireé, 17
Cruz, A. S. A., 421
Cruz, L. R., 277

D

Dawuk, D. N., 101
de Carvalho, José Maria Franco, 369, 381
Delaqua, G. C. G., 403
Ding, Kai, 305
Domínguez, Iván. Reyes A., 411, 431, 453

E

Escobedo-Diaz, Juan Pablo, 57

F

Findley, K. O., 3
Flores-Guerrero, Mizraim U., 155
Freitas, M. G. S., 229
Frint, Philipp, 25
Fumpa, Nachikonde, 135

G

Gama, F. D., 39
Gao, Yulai, 305
Garcia Filho, Fabio da Costa, 333
García, Zaida Peralta, 453
Garkida, A. D., 47
Garvie, Laurence A. J., 17

Godínez-Garrido, Gildardo, 155
 Gonah, C. M., 47
 González-García, Karime A., 155
 González-Islas, Juan C., 155
 Gruber, Maximilian, 25
 Guerrero, Mizraim Flores U., 411, 431, 453
 Guo, Yan, 163
 Gu, Shouyu, 91

H

Han, Guihong, 71
 Hara, Rainford, 135
 Hara, Yotamu R. S., 135
 Henrique Drumond, Pedro, 391
 Hernández, Francisco Raúl Barrientos, 411, 431, 453
 Hernández-Lara, J. P., 443
 Hernández-Ramírez, A., 443
 Hilário, A. C., 315
 Hong-Su, 143
 Hou, Cuihong, 91
 Huang, Yanfang, 71
 Hu, Qingqing, 123

I

Illgen, Christian, 25
 Iyen, C., 101
 Iyen, I. S., 101

J

Jesika, 81
 Juárez-Tapia, Julio Cesar, 207, 443
 Júnior, Linhares J. A. T., 229

K

Kaluba, Golden, 135
 Khabarova, Irina A., 219
 Khafagy, Khaled H., 17
 Klaus Andrade, Igor, 391
 Kobayashi, Yohei, 359
 Krishnaraj, V., 57
 Kuang, Yucen, 195

L

Labra, Miguel Pérez, 411, 431, 453
 Lawrence, S. K., 3
 Lechner, Philipp, 25
 Le, Dinghao, 113
 Li, Luyi, 91

Lima, T. E. S., 247, 315
 Li, Shun, 305
 Liu, Bingbing, 71
 Liu, Yongjie, 123
 Li, Yuanyuan, 81
 Lopes, Márcia Maria Salgado, 369
 Luo, Guanwen, 81
 Lu, Sujun, 81
 Luz da, Fernanda Santos, 333

M

Ma, Donglai, 123, 257
 Maria Carvalho, José, 391
 Martínez, Jimena Detzamin Trejo, 411
 Marvila, M. T., 39, 229, 239, 247, 267, 277, 287, 295, 315, 323, 349, 421, 473
 Matos, P. R., 473
 Maurício Vieira, Carlos, 391
 Mbah, V., 101
 Medina, Jazmin Terrazas, 431
 Mendes, Beatryz C., 381, 391
 Monteiro, Sergio Neves, 39, 229, 239, 247, 267, 277, 287, 295, 315, 323, 333, 349, 421, 473

N

Nalon, Gustavo Henrique, 369
 Nascimento, Lucio Fabio Cassiano, 333
 Ndiriza, S. D., 101

O

O'Brien, M. K., 3
 Old, Alexander, 135
 Oliveira, L. B., 323, 473
 Oliveira, Michelle Souza, 333
 Olivera, Andres F., 341
 Omonokhua, M., 101
 Opoku, E. V., 47

P

Pérez-Labra, Miguel, 207, 443
 Pedroti, Leonardo Gonçalves, 369, 381, 391
 Pereira, Artur Camposo, 333
 Prasanth, A. S., 57

R

Rabbi, Fazle M., 17
 Ramesh, R., 57
 Ren, Wei, 163, 195
 Reyes-Cruz, Víctor Esteban, 207, 443

Reyes-Perez, Martin, 207, 411, 431, 443, 453
Ribeiro, José Carlos Lopes, 369
Rocha, D. L., 247
Rocha, S., 277
Romero-Serrano, J. A., 443
Ruiz, Aislinn Michelle Teja, 411, 431, 453
Ryazantseva, Maria V., 219

S

Saito, Jun-ichi, 359
Shankar, Krishna, 57
She, Xuefeng, 177
Shibutani, Hideo, 359
Silva, T. R., 287
Simonassi, Noan Tonini, 333
Soto, Jesús Iván Martínez, 207
Spoerer, Thomas, 25
Sun, Xintao, 113
Su, Shengpeng, 71

T

Tapia, Julio Cesar Juárez, 411, 431, 453
Teja-Ruiz, Aislinn M., 207

U

Uahengo, Foibe D. L., 135
Urbano-Reyes, Gustavo, 207

V

Vieira, Carlos M. F., 39, 239, 323, 381, 403, 473
Volk, Wolfram, 25

W

Wagner, Martin F.-X., 25
Wang, Haobin, 91
Wang, Jianshen, 57
Wang, Jie, 91
Wang, Jing-Song, 143, 177
Wang, Tingting, 91
Wang, Yubi, 71
Wang, Yue, 123
Wang, Zibiao, 113
Warren, Georgia, 57

X

Xavier, G. C., 267, 473
Xue, Qing-Guo, 143, 177

Y

Yan, Ganggang, 113
You, Xiaomin, 177
You, Zhixiong, 123, 257

Z

Zanelato, E. B., 39, 239, 247, 287, 295, 349
Zhang, Lechi, 195
Zhang, Li, 305
Zhang, Shengfu, 163, 195
Zhang, Xijun, 113
Zhao, Bingge, 305
Zhao, Jianbo, 257
Zhao, Lian-Da, 143
Zhou, Hanghang, 257

Subject Index

A

AA5083, 57–67
Açaí, 248, 249, 252
Acetic acid, 113–115, 120, 121
Activated alkali cements, 239, 245
Activation, 34, 42, 45, 79, 240–245, 326, 327, 385, 387, 432, 455, 474
Adsorption sequence, 82, 84
Aging materials, 333
Aluminum AA7075, 25, 30, 32
Ammonia, 47, 49, 123, 124, 127–129
Anneal, 101
Areas degraded, 267
Arnu-Audibert's dilatometer, 196, 198, 200–202
Artificial rock, 229, 230, 232–237
Atomic absorption spectrophotometry, 155–157
Atomic bonding, 359, 361

B

BaTiO₃, 72, 443–447, 449–451

C

Caking index, 195–198, 200, 202
CaO-containing carbon pellets, 177–189
Capacitance, 443–447, 451
Carbothermal, 71, 102, 123
Cementite, 3–13
Ceramic, 39, 40, 42, 57–62, 64, 67, 74, 231, 267–269, 272, 273, 278, 295–297, 300–303, 316, 328, 392, 403, 404, 407, 409, 443–446, 473, 474, 479

Ceramic materials, 39, 40, 231, 268, 295, 404, 443, 444, 473, 474
Chamotte, 391–395, 399
Characterization, 3, 4, 13, 17, 18, 22, 28, 74, 75, 93, 94, 109, 155, 156, 181, 229–231, 239–241, 245, 267–270, 288, 292, 295, 316, 342, 347, 349, 371, 372, 374, 375, 383, 394, 395, 423, 434, 457, 463
Coal macromolecular, 178, 182, 188
Cobalt, 47, 50, 54, 81–86, 88, 113–121, 135–137, 139, 141
Co-continuous ceramic composites (C4), 57–62, 64, 67
Coke performance, 163
Collectorless, 411–413, 416, 418, 436, 438, 453–455, 458, 459, 461
Collectorless flotation, 411–413, 416, 418, 436, 438, 453–455, 458, 459, 461
Compressive strength, 143, 144, 147, 150–153, 163, 165, 167, 170–172, 174, 177, 178, 180–182, 185, 187–189, 239, 240, 245, 248, 323, 325–329, 351, 353, 381, 382, 384–388, 391, 393, 395–397, 399
Construction cladding, 292
Cooling rate, 18, 66, 67, 305, 306, 308–312
Cyanex272, 113–115, 117, 120, 121

D

Density Functional Theory (DFT), 123–125, 128, 129
Depression, 411, 416, 432, 438, 453–455
Dielectric barrier discharge, 219–223, 225
Diffusion performance, 143

Digital image correlation, 17–20, 22, 28, 29
 Dimension stone, 230, 231, 278, 297
 Direct reduction, 257, 258, 260

E

Effective conversion, 91, 92, 94–100
 Elastic constants, 463, 464, 466, 467, 470
 Electrode potential, 219, 222–224
 Electron Backscatter Diffraction (EBSD),
 3, 4, 6–9, 11, 13, 67
 Electronic structure, 359–362, 367
 Epoxy resin, 288, 289, 334, 335, 424, 455
 Equal Channel Angular Pressing (ECAP),
 25–34
 Extraction separation, 119

F

Failure mechanism, 17–20
 Ferric ion, 411, 413, 416–418, 431,
 435–438, 440
 Fiber, 247–253, 288, 333, 334, 336–338,
 341, 342, 344
 Fique fabric, 333–335, 337, 338
 Flexion test, 342, 478
 Flotation, 220, 222–225, 411–413,
 416–418, 431–440, 453–461
 Flue Gas Desulfurization waste (FGD),
 39–42, 44, 45, 323–329
 Furnace, 28, 72, 73, 94, 102–104, 124, 144,
 146, 163, 164, 166, 167, 169, 170,
 178, 179, 181, 239, 240, 242, 243,
 245, 257, 295–297, 300–303, 324,
 328, 329, 404, 405, 445, 464
 Fused calcium magnesium phosphate
 fertilizer, 91, 92

G

Galena, 220, 222, 223, 411–418, 432, 454
 Gas-pressure infiltration, 57–67
 Geopolymeric mortar, 328, 382, 387
 Geopolymers, 39–45, 242, 323–329,
 381–383, 385, 387, 388, 391–393,
 395, 397–399, 474
 Gibeon, 17–22
 Glass, 40, 47–49, 51–55, 74, 91, 92, 96,
 100, 244, 288, 289, 307, 316, 342,
 391–395, 397–399, 403–407, 409,
 422, 473–475
 Glass waste, 40, 474, 475
 Goethite adsorption, 82, 86
 Granite waste, 353, 369–379

Grinding, 75, 83, 105, 107, 207–211,
 213–216, 241, 242, 324, 405, 411,
 412, 432, 435, 438, 443, 454

H

Hard body impact, 315–318, 321, 421, 423,
 425, 427
 Hard body impact resistance, 315, 424
 Heat treatment, 26, 27, 30–32, 34, 59, 84,
 163–167, 169–174, 384, 464
 Heavy metals, 47–49, 54, 55, 81, 82
 High-power nanosecond pulses, 219–221,
 223
 High-titanium slag, 71–73, 75, 76, 79
 Hot tensile test, 28
 Humic acid, 71, 72, 74, 76–79
 Hysteresis, 114, 444, 445, 447, 449–451

I

Image segmentation, 155, 156
 Industrial wastes, 247, 392, 399
 Influence of temperature and pH, 86, 87
 Infrared, 103, 106, 178, 196, 240, 394, 413,
 414, 416, 431, 433, 434, 437–440,
 454, 455, 457, 458
 Interaction couple, 143–150, 153
 Iron meteorite, 17, 18, 22

J

Jamesonite, 431–440

L

Leaching, 79, 82, 102, 103, 106, 107, 109,
 135, 136, 139, 140, 207–216, 382
 Life cycle assessment, 342
 Liquid metal, 359–367
 Liquid-metal infiltration, 57
 Low melting temperature alloy, 359, 360,
 366

M

Macerals of coal, 196, 199, 200, 202–204
 Mechanical performance, 290, 292, 325,
 350, 381, 388, 429
 Mechanical properties, 18, 20, 22, 25–27,
 31–34, 40, 58, 60, 63, 248, 288, 328,
 333, 334, 381, 404, 405, 408, 422,
 464

- Melting temperature, 91, 92, 94, 97, 99,
100, 257, 258, 260, 261, 263, 264,
359, 360, 366, 367
- Melting time, 98
- Metakaolin, 39, 40, 241, 323–329,
381–388, 392, 474
- Metal growth, 258, 262
- Metallothermic, 101, 103, 107
- Metallurgical transformation, 71
- Metal–slag separation, 258, 259, 262–264
- MgO additives, 144, 146, 149
- Microhardness, 18, 219–222, 224, 225
- Microstructure, 6, 13, 18, 26, 28, 31–34,
57, 67, 74, 102, 105, 124, 144, 147,
165, 259, 262, 263, 307, 397, 399,
444, 449, 463, 464, 466–470
- Mining activity, 267–269
- Mortar, 40, 73, 247–253, 296, 323–329,
349–351, 353–356, 381–388, 391,
399, 413, 414, 416, 433, 443, 444,
454
- N**
- Nanocalorimetry, 305–307, 310, 312
- Nickel-cobalt, 114
- Nickel laterite ore, 257, 260
- O**
- Ornamental rock, 230, 231, 287, 295–297,
299–302, 315, 316, 321, 350, 422
- Ornamental stones, 230, 231, 277, 278,
284, 288, 295, 302, 316, 349, 350,
370, 421, 422, 428
- P**
- Paint, 29, 47, 48, 230, 369–379
- Performance, 40, 79, 81, 123, 144, 163,
196, 214, 237, 229, 288, 290, 292,
295, 296, 300–303, 325, 344,
350–352, 354, 356, 369, 370, 374,
375, 378, 379, 381, 382, 385, 388,
393, 422, 427, 429, 474, 479
- Permittivity, 447, 448, 451
- PH, 81–88, 104, 113, 114, 116–119, 121,
135–141, 208, 222–224, 272, 279,
369–372, 374–379, 411–413,
416–418, 433, 436, 438, 439,
453–455, 457–461
- Phase identification, 3, 4, 7, 11–13, 74
- Photocatalytic degradation, 72, 74, 75, 78
- Plastic layer, 196, 198, 200–202
- Pulp potential, 411, 417, 418, 454, 459, 461
- Purple fluorite, 155–158
- Pyrrargyrite, 453–461
- Q**
- Quartz (%), 74, 93, 99, 102, 137, 138, 164,
219–221, 224, 225, 272, 290, 382,
384, 386, 395, 423, 427
- R**
- Raman spectroscopy, 104, 177, 178, 181,
182
- Raw, 51, 53, 72, 73, 81, 91, 92, 94, 102,
103, 105, 106, 123, 124, 129, 144,
145, 163, 167, 171, 172, 177, 198,
200–202, 272, 287, 289, 291, 292,
296, 315–321, 324, 350, 382, 387,
392–394, 403–405, 409
- Recoveries, 28, 31, 113, 135, 137,
139–141, 208, 223, 268, 272–274,
416, 436, 458, 459, 461
- Recycled post consumer glass, 48–55
- Red ceramic, 295, 296, 404, 407, 409
- Reductant, 135, 139, 140
- Residue, 104, 135, 137, 208, 241, 242,
295–297, 299–303, 324, 328, 329,
349–353, 356, 404, 405, 407–409,
473
- Resin, 82, 277, 278, 281–284, 287–289,
292, 315–317, 319–321, 334, 335,
342, 369–372, 375–378, 423, 424,
455
- Resinate, 315
- Resistance heating, 28, 29, 32
- Rheology, 349, 350, 353, 356
- Rice husk ash, 101–109, 392
- Roasting pretreatment, 214
- Roughness, 48, 224, 305, 306, 309–312
- S**
- Sand content, 381–383, 385, 387
- Scanning electron microscopy, 67, 102,
135, 161, 219, 221, 240, 307, 336,
337, 371, 413, 414, 433, 443–445,
449, 454, 463
- Screened, 137, 317, 318, 320, 423, 424
- Screening, 174, 317, 321, 421–423, 425,
426, 429
- Semi-quantitative analysis, 155
- SiC foam, 57–60, 63–67
- Si thin film, 305–312

Sodium Meta-Bi-Sulphate (SMBS), 135, 136, 138–141
Staining, 229–237, 277–284
Substrate, 47, 48, 305–312, 349–351, 360–367
Sulfide minerals, 221, 223–225
Surface, 7, 12, 17–22, 29, 30, 47, 54, 72, 102, 105–107, 114, 123–126, 128–130, 155, 156, 164, 173, 219–225, 230–234, 240, 241, 242, 245, 247–249, 251, 270, 278–281, 283, 284, 288, 289, 309–312, 315, 326, 336, 337, 349–351, 371, 376–378, 383, 405, 412, 414, 416–418, 422, 431–435, 438, 440, 453–455, 457–461
Surface morphology, 105, 219, 220, 222, 223, 311
Sustainability, 268, 323, 324, 329, 342, 381

T

Technological characterization, 229–231, 288, 292, 316
Tensile test, 25, 28, 32–34
Textured coat, 47–51, 55
3D printing, 342–344, 346
Titanate, 71–75, 79, 443, 444
Titanium alloys, 464

U

Ultrasonic velocity, 463, 464, 467–469
Undercooling, 305–312

V

V₂O₅, 123–130
Vanadium nitride, 123, 124

W

Waste, 39, 40, 42, 48, 72, 81, 82, 101, 102, 207, 208, 210–212, 215, 216, 242, 247, 295, 296, 299, 300, 302, 303, 323–329, 341, 342, 349–351, 353, 354, 356, 369–379, 391–395, 397–399, 403, 404, 407, 474, 475
Waste glass, 391–395, 397–399
Wettability, 258, 359–361, 366, 367, 412
Wind turbine blade, 342, 345, 346

X

X-ray diffraction, 72–76, 83, 93, 99, 101, 103, 104, 107, 109, 114, 128, 150–152, 163, 165, 168, 172–174, 177, 178, 181–183, 186–188, 239, 240, 243, 270, 384, 393–395, 397–399, 413, 414, 433–435, 443–445, 451, 454, 456, 457